Physics of the Solid State, Vol. 46, No. 5, 2004, pp. 789–824. Translated from Fizika Tverdogo Tela, Vol. 46, No. 5, 2004, pp. 769–803.

REVIEWS

Magnetoplastic Effects in Solids

Yu. I. Golovin

Tambov State University, Tambov, 392622 Russia

e-mail: golovin@tsu.tmb.ru

Received May 28, 2003; in final form, August 4, 2003

Abstract—This paper is an overview of the studies into the effect of weak magnetic fields on the structure and mechanical properties of nonmagnetic solids of various nature (ionic, covalent, molecular, and metallic crystals, polymers, etc.). The various effects and aftereffects initiated by static, pulsed, and microwave magnetic fields that have been discovered over the past 15 years are classified and critically analyzed. The thermodynamic and kinetic aspects of the magnetic-field sensitivity of real solids with structural defects containing paramagnetic centers (electrons, holes, radicals, excitons, etc.) are discussed. Possible mechanisms for the effect of a weak magnetic field on the defect structure of crystals are considered. Special attention is given to the most developed chemical-physical theory of spin-dependent reactions between mobile particles and unpaired electrons. Interpretation of magnetoplastic effects is proposed in terms of the spin, electron, molecular, and dislocation dynamics of the complex multistage processes initiated by a magnetic field in a system of metastable structural defects.

CONTENTS

1. INTRODUCTION

The effect of a magnetic field (MF) on the properties of magnetic (or, more precisely, magnetically ordered) materials has been known for thousands of years and has been consistently explained in terms of the current quantum theory of magnetism [1]. The possibility that the macroscopic properties of "nonmagnetic" solids (para- and diamagnets, characterized by a disordered magnetic structure) are significantly affected by weak MFs[1] is by no means evident and is frequently questioned despite numerous publications in which various "magnetic" effects observed in these materials are described.

It should be remembered that weak MFs are part of the environment; they affect processes occurring on Earth without interruption and should be subject to technical and health regulations based on clear physical notions and established facts [2]. MFs both occur in nature and can be created by man; for instance, they can be produced intentionally to suppress hostile electronic equipment or can arise during powerful explosions (e.g., of nuclear devices). Finally, MFs are efficient tools for studying the fine structure of materials (in EPR, NMR, ENDOR, and other magnetic-resonance spectroscopy methods), where it is important to be confident that the probe field will not significantly affect the processes in the object under study. A similar problem arises in the development of highly sensitive exper-

[1] In what follows, MFs are called weak if $\mu_B B \ll kT$ (and, for metals, $\omega = Be/m \ll \omega_c$), where μ_B is the Bohr magneton, B is the induction of the MF, k is the Boltzmann constant, ω is the cyclotron frequency, e and m are the charge and mass of an electron, and ω_c is the collision frequency of an electron with scattering centers.

1063-7834/04/4605-0789$26.00 © 2004 MAIK "Nauka/Interperiodica"

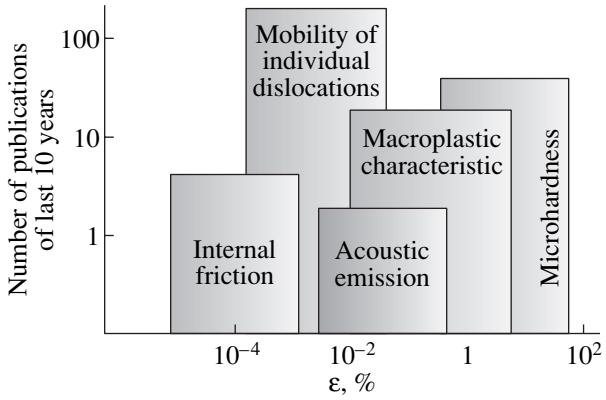

Fig. 1. Amount of publications (over the past ten years) on the MPE observed in various strain ranges.

imental setups (e.g., a gravity-wave antenna) and in interpreting the results obtained with these setups. In such cases, it is necessary to take into account that weak MFs and variations in them can affect the operation of precision measuring instruments and the results they give, including through the physical-mechanical parameters of the brackets, electromechanical cavities, pendulums, etc. Therefore, it is important to be aware of the mechanisms of the possible effects of weak MFs on the structure and properties not only of magnetically ordered solids but also of nonmagnetic materials.

It is widely believed that weak MFs cannot significantly change the structure and properties of nonmagnetic solids (for such materials, laboratory fields $B \le 10$ T can be considered weak at room temperature T_R). Indeed, the effect produced by a field $B \sim 1$ T in systems at thermodynamic equilibrium is of the order of $(\mu_B B/kT_R) \sim 10^{-3}$, which is far less than the typical measurement errors encountered in studying mechanical properties. For this reason, the few earlier attempts to detect the influence of MFs on the structure [3–8] and physical-mechanical characteristics [9–12] of diamagnetic crystals did not attract considerable attention. Moreover, most researchers considered the results obtained in those studies to be suspect, as they were inclined to believe that the results were artifacts. However, in the 1960s–1980s, luminescence [13–15], photoelectric [16–19], and radiospectroscopy studies [20–25] of various diamagnetic crystals revealed a number of magnetic effects and the validity of those findings was more than once confirmed in independent investigations.

The data on the magnetoplastic effects reported in [26–31] were apparently the first that were beyond question and had clear physical interpretation. The effect of static and low-frequency ac magnetic fields on the dislocation mobility and macroplasticity in ferromagnets revealed in those studies was explained in terms of interaction of dislocations with domain walls, which move when magnetization is produced or reversed. After the theoretical paper by Kravchenko [32], the effect of magnetic fields $B \sim 5$–10 T on the plasticity of pure diamagnetic metals at liquid-helium temperatures was intensively studied experimentally [33–42] and theoretically [43, 44]. Many of those studies are reviewed in [45–47]. Note that, in those experimental studies (as well as in the relevant studies of ferromagnets [26–31]), the MFs were not weak and the results were explained in terms of MF-induced variations in the viscosity of an electron gas and in electron–dislocation friction. However, this interpretation is not full and disagrees with experimental data in certain cases.

Several studies were devoted to the inverse effect, namely, the influence of plastic deformation and dislocation structure on the magnetic properties of semiconductors [48], transition metals [49–52], and ionic crystals [53]. To the best of our knowledge, the results of [53], a study that was widely debated (see, e.g., [54, 55]), have not been reproduced by anybody. As for studies [33, 34], their results were also subject to criticism, because, as shown in [56], they depended strongly on the effect MFs exhibit on the movable parts of the test machine employed (despite the fact that those parts were made of nonferromagnetic austenitic steel). After this effect was taken into account and removed, the magnetoplastic effect persisted but became an order of magnitude smaller.

In 1987, Al'shits and coworkers [57] reported the observation of a phenomenon which was paradoxical at first glance and attracted considerable interest: dislocations produced by a weak impact into NaCl single crystals were observed to move under the action of a static magnetic field $B < 1$ T in the absence of an external load. The experiments were performed at room temperature (like the majority of experiments described in this review); therefore, the MFs could be considered weak and the observed effect was regarded with caution even by the authors themselves.

However, later, the authors of [57] and then several other independent research groups confirmed the existence of such effects not only in NaCl but also in other materials, such as LiF, KCl, KBr, CsI, InSb, Al, Zn, Si, $NaNO_2$, ZnS, C_{60}, polymers, etc. (see Section 2). Furthermore, many related phenomena have been discovered that testify to MFs having a significant effect on various physical-mechanical and other structure-sensitive characteristics of nonmagnetic materials (see Section 3). These phenomena were observed in static, ac, pulse, and mw magnetic fields with almost the entire range of techniques used for studying microstructure and mechanical properties (Fig. 1) and various load modes in different temperature ranges.

In terms of time characteristics, the magnetoplastic effects (MPE) can be divided into three basic groups, namely, effects that occur only during the action of MFs and effects that exist for a long time after an MF is switched off and can, in turn, be completely reversible

or relax slowly with time (Fig. 2). In certain cases, the time dependences of the response to the application of MFs were more complex and characterized by a latent period after the MF was switched off or were nonmonotonic and even changed sign.

These and other thermodynamic and kinetic features of observed MPE suggest that the most important and necessary factor that causes high sensitivity of a defect structure to external and internal MFs is nonequilibrium, which exists from the outset in a crystal or is maintained externally (using loading, illumination, irradiation, etc.). Note that the occurrence of large responses to weak perturbations in a system that is far from equilibrium does not contradict the basic principles of thermodynamics.

The existence of such effects is presently a firmly established fact. However, their nature is not completely understood. It is not even clear whether a single mechanism or several different mechanisms control the effect of MFs on the mechanical properties of materials that differ in terms of bonding, defect structure, etc. This situation is similar in certain respects to that in magnetobiology, where the effect of weak MFs on various living organisms and processes occurring in them has been firmly established using very precise modern techniques [58–61], but the mechanisms of this effect are poorly understood. A great number of papers have been published in this field; some of them did not conform to the standards of natural science (it is enough to mention the term "magnetized water"), and some were obviously only speculative. As a result, the skepticism about the possible effects of weak MFs on nonmagnetic substances is often extended to other, nonbiological objects.

Since the study of the magnetoplastic effects in weak MFs has a short history, no monographs have been published on this subject; there are only a few brief review articles [62–65], in which the authors primarily give an overview of their own studies and concentrate on separate aspects of the problem. This review also does not pretend to be complete (if for no other reason than its limited size) but aims at calling the attention of researchers to the most prominent and, without doubt, reliable results obtained recently by several independent groups. These results open up a new area in the physics of plasticity whose basic principles should be treated on the electron-spin or even nuclear-spin level.

2. EFFECT OF WEAK MAGNETIC FIELDS ON THE PHYSICAL-MECHANICAL CHARACTERISTICS OF REAL DIAMAGNETIC CRYSTALS

The physical-mechanical properties of solids are determined by the elastic characteristics and inelastic processes that proceed at the atomic, dislocation, mesoscopic, and macroscopic structural levels. The mechanical properties of an ideal nonmagnetic crystal can be changed by applying very high magnetic fields (≥100 T). In rare cases, e.g., in certain metals (Bi, Be, Al, Nb, etc.), oxides, and alloys in which the bands overlap slightly or are separated by a narrow gap ($\Delta U \sim 10^{-2}$ eV), the magnetic energy $U_m \sim \mu_B B$ becomes larger than ΔU at $B \sim$ 10 T; i.e., the "quantum limit" is reached. In these cases, a so-called magnetic breakdown occurs at liquid-helium temperatures, which can affect the equilibrium properties (including the mechanical ones) of a nonmagnetic crystal [66].

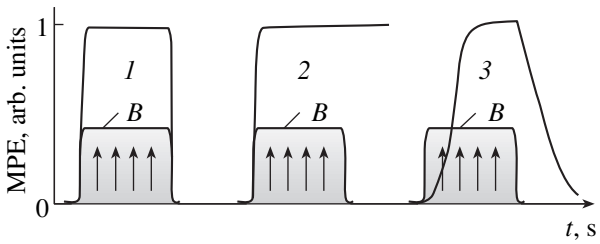

Fig. 2. Three main types of behavior of nonmagnetic materials in a magnetic field: (*1*) *in situ* effects, (*2*) irreversible aftereffects, and (*3*) aftereffects with slow relaxation.

We will not discuss these interesting aspects of the effect of MFs on weakly magnetic materials taking place in the perfect crystal lattice approximation. This review is dedicated primarily to the effect of much weaker MFs on the structure-sensitive inelastic characteristics, which are mainly determined by structural defects and their mobility and interaction. Obviously, a weak MF can affect the properties of nonmagnetic crystals only through structural defects. Therefore, we consider results that allow one to elucidate the effect of MFs on the dynamics of defects determining the inelastic properties, namely, dislocations and small atomic complexes that hinder the motion of dislocations in easy-slip planes. Different techniques are used depending on the amount of deformation and the level of structural hierarchy at which the deformation is analyzed. The available experimental data are classified in accordance with these differences.

2.1. Depinning of Dislocations in a Magnetic Field

Systematic studies into the effect of weak MFs on the mechanical properties of nonmagnetic crystals began with the work of Al'shits *et al.* [57], where the following phenomenon, paradoxical at first glance, was observed. The motion of edge dislocations in NaCl single crystals was initiated by a uniform static magnetic field B (varied from 0.1 to 1.6 T) in the absence of external stresses. It was found that the dislocation path length L (which can be determined using the highly reliable standard double-selective-etching method) increased with the square of the magnetic field B and in proportion to the duration t_B of the exposure to the MF and reached several hundred micrometers. The direc-

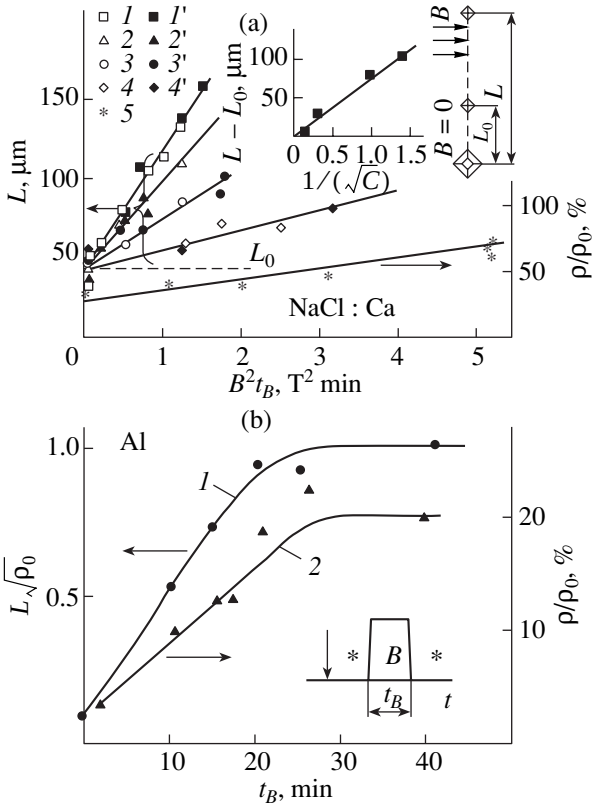

Fig. 3. Regularities of MF-stimulated depinning of dislocations in various materials. (a) Dependence of the path length L of edge dislocations on magnetic field and exposure time t_B for NaCl crystals with a Ca concentration of (*1*, *1*') 0.5, (*2*, *2*') 1, (*3*, *3*') 10, and (*4*, *4*') 100 ppm obtained (*1*–*4*) from the $L(B)$ dependence and (*1*'–*4*') from the $L(t_B)$ dependence; (*5*) the proportion of starting dislocations; insets show the concentration dependence of L for $B = 0.5$ T and the diagram representing the experiment; L_0 is the path length in etchant. (b) (*1*) Dislocation path lengths in Al normalized to the average distance between dislocations $\lambda = 1\sqrt{\rho_0}$, where ρ_0 is their average density, and (*2*) proportion of starting dislocations as functions of the duration t_B of exposure to a magnetic field $B = 1.2$ T. Inset shows the consecutive order of procedures: arrow means production of dislocations, asterisk stands for etching, and B means exposure to an MF; $T = 293$ K.

tion of motion of dislocations did not change as the field was reversed, from which it was concluded in [57] that the effect was not due to the ponderomotive forces caused by the magnetic field and to the vortex electric field that arises when an MF is switched on or when a sample is placed in it. Later, analogous results were obtained by this research group for other wide-band-gap crystals (LiF, CsI, InSb) [67–75] and metals Zn [76] and Al [77]. These results are partly represented in Fig. 3. The path length L depended on temperature only weakly (or not at all in certain cases); this behavior of mobile dislocations under MPE conditions differs drastically from that under a stress field alone.

Estimations show that the force exerted on dislocations by an MF (for any possible mechanism) is several orders of magnitude less than the internal stresses, let alone the starting dislocation stresses. In [78], a great number of dislocation paths ($N > 10^3$) were measured in different widely separated ($\geqslant 1$ mm) regions of a crystal and it was found that the quantity of shifted dislocations and their mean path lengths were the same in the four equivalent crystallographic directions (for the fcc structure) and were independent of the MF direction (provided the dislocation lines were perpendicular to this direction). It follows that dislocations move in the random field of internal stresses and an MF only lowers the height of barriers to dislocation motion.

Note that these data do not indicate conclusively whether the barriers are lowered when dislocations interact with them or before this interaction as a result of changes in the dislocation cores and pinning centers. The fact that the average density of forest dislocations in these crystals was ~10^3–10^4 cm^{-2} (and, therefore, the average spacing between them was several hundred micrometers) suggests that MFs affect the interaction of moving dislocations with impurity centers and, probably, change their internal structure. Special experiments were carried out in which the composition and state of impurities were varied using different thermal treatments, and it was shown that a high sensitivity to MFs did not always take place. For example, an increase in Ca concentration in NaCl crystals from 0.5 to 100 ppm effected an increase in the MF threshold value from 0.03 to 0.25 T and a decrease in L from 100 to several micrometers in a field $B = 0.5$ T (see inset to Fig. 3). The introduction of Pb and Cu with a concentration of several tens of parts per million caused pile-ups of dislocations and a loss of MF-sensitivity, whereas doping with Ni (<0.06 ppm) enhanced the MPE significantly [71, 79]. The observation of a great number of dislocations that were close together and traveled large distances in the same direction and of the path length L increasing directly with the duration of MF exposure up to several hundred or even a few thousand micrometers in high-purity crystals at $B = 1.6$ T suggests that dislocations were driven, for the most part, by large-scale macroscopic internal stresses rather than by fields of individual dislocations (which were much closer together), as assumed in [80] when discussing the possible mechanisms for the MPE.

Further modifications of these experiments provided many new data. For example, in [79, 81, 82], samples were rotated with various angular velocity ν about the [001] axis during exposure to a static MF and it was found that the MF sensitivity decreased sharply at $\nu > \nu_c^i$, where ν_c^i is one or several critical frequencies (see Subsections 3.1, 3.3) and varied as B^2 but were independent of temperature and impurity concentration (Fig. 4). From these data, the upper estimate of the shortest duration of exposure to an MF of a certain orientation sufficient for efficient depinning of disloca-

tions was found to be $\tau_{dp} \sim 10^{-2}$ s. Note that depinning is not an elementary event but rather occurs in several steps (for more details, see Section 4, Fig. 20); therefore, there is no *a priori* reason to assign the time τ_{dp} to one of these steps, e.g., the spin-evolution stage, and assume it to be dominant neglecting the waiting time for excitation of the dislocation–pinning center complex and the time required for the bond-breaking products to leave the reaction cell. We can only state that the results under discussion agree qualitatively with the experimentally observed dependence of the MPE on the mutual orientation of the magnetic field **B**, the dislocation line **l**, and the Burgers vector **b** (see, e.g., [79]).

Double selective etching has a very poor time resolution (not better than a few tens of seconds) and gives no way to determine the actual time of dislocation motion or even elucidate whether this time is longer or shorter than the duration of MF exposure. Additional information on the dislocation motion kinetics [67] and the MF aftereffect was obtained in [83, 84] using continuous etching. A crystal was subjected simultaneously to a short MF pulse (B = 7 T, pulse duration t_B = 10 ms) and to etching in the absence of external stresses. On the crystal surface there appeared chains of etching pits progressively decreasing in size, which suggests that dislocations moved discontinuously. Using such patterns and the preliminarily measured growth rate of etching pits, one can determine the quantity of jumps, the dislocation velocity in a jump, the jump waiting time, the correlation coefficients between various events, etc. Figure 5 shows the dependence of the average velocity of edge dislocations $\langle V \rangle$ on the distance traveled in NaCl crystals not subjected to a pulse magnetic field and in those subjected to this treatment. After the MF exposure, the velocity $\langle V \rangle$ increased several times. Note that MFs favored dislocation depinning and (what is more important) subsequent dislocation motion for several tens of seconds after the MFs were switched off; i.e., *an aftereffect took place*. Small values of the correlation coefficient (<0.1) between the average time spent at a pinning center and the dislocation velocity after depinning indicate that these two parameters are not related to each other. This result is easily understood; indeed, MFs could not affect the interaction of dislocations with the majority of pinning centers in these experiments, because almost the entire path lengths of dislocations were traveled in the absence of an MF and the MPE arose due to the magnetic field having acted on pinning centers before dislocations approached them.

These experiments made it possible to directly determine the minimum duration of an MF pulse t_{min} sufficient for depinning of dislocations. It can be seen from Fig. 6 that, for NaCl crystals with a total divalent-impurity content of ~10 ppm at T = 293 K, t_{min} is of the order of 10^{-6} s [85, 86] and is independent of B (in contrast to the experiments with rotating MFs [79–82]). Of course, this time is not a constant even for a single

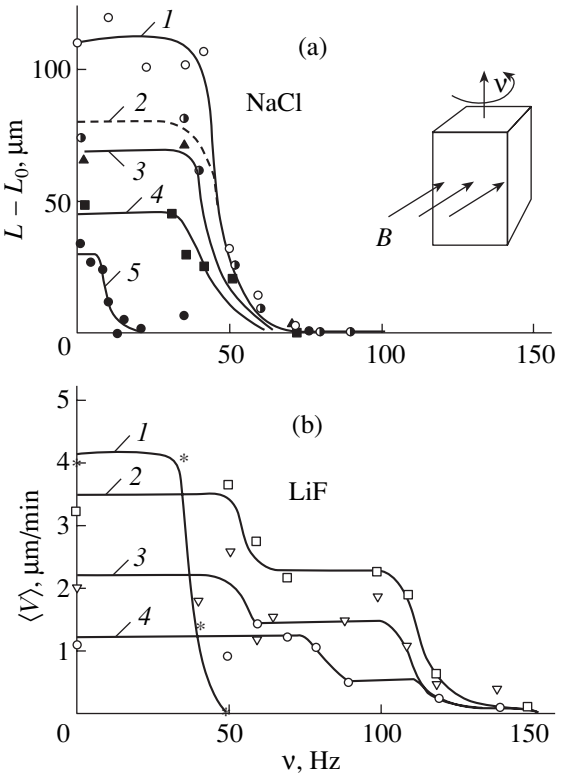

Fig. 4. Regularities of depinning of dislocations under a rotating MF (a) in NaCl for (*1*) B = 0.5 T, T = 293 K; (*2*) B = 0.5 T, T = 77 K; in NaCl : Ca for (*3*) C = 1 ppm, B = 0.5 T, T = 293 K; (*4*) C = 10 ppm, B = 0.5 T, T = 293 K; (*5*) B = 0.3 T, T = 293 K; and (b) in LiF preliminarily subjected to x-ray irradiation over t_R for B = 0.5 T, T = 293 K, and t_R equal to (*1*) 0, (*2*) 10, (*3*) 20, and (*4*) 30 s. Inset shows the diagram representing the experiment.

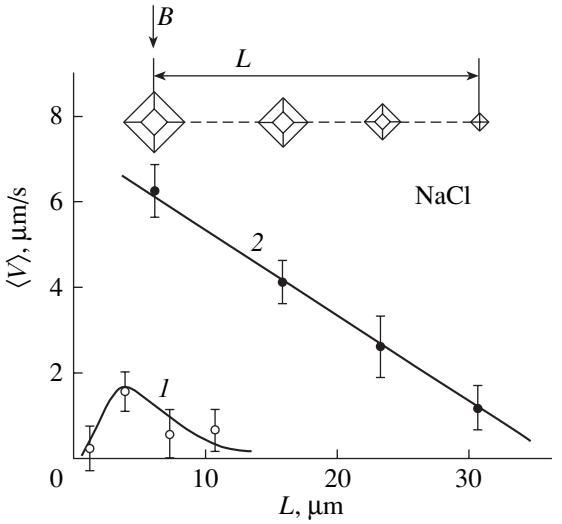

Fig. 5. Average velocity of edge dislocations in NaCl single crystals as a function of distance traveled after depinning in (*1*) etchant and (*2*) a magnetic field B = 7 T, t_B = 10 ms, obtained using the continuous-etching method at T = 293 K. Inset illustrates measurements.

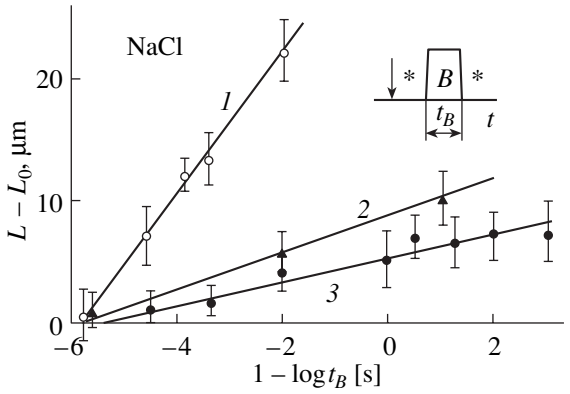

Fig. 6. Dependence of the path lengths of edge dislocations in NaCl single crystals on the duration of an MF that stimulates depinning: (*1*) $B = 7$, (*2*) 2, and (*3*) 1 T. Inset shows the consecutive order of procedures. Notation is the same as that in Fig. 3b.

material, but it gives an idea of the scale of characteristic times in the dynamics of depinning. Note that, from these data (as well as from the critical frequencies ν_c measured in the experiments with rotating MFs; see Fig. 4), it does not follow that this time characterizes a certain electronic process proceeding in the dislocation–pinning center system, because only the final result (depinning of a dislocation segment) is considered. These events cannot occur without involvement of the slow molecular and dislocation dynamics, i.e., correlated motion of a large number of atoms entering into the dislocation core. The large difference between the time τ_{dp} obtained in [79, 81, 82] and the time τ_{min} found in [84, 85] can be due to differences in the doping level, internal stresses, the state of impurity complexes, the MF geometry (the action of a pulsed MF of fixed orientation is not equivalent to that of a rotating field **B** with fixed magnitude), etc.

The above-described simple experiments on the effect of MFs alone on a crystal made it possible to detect MF-stimulated dislocation depinning and investigate its general features. However, the physical interpretation of these experiments is hampered by a number of specific features inherent to the techniques employed. First, there is no information on the internal stresses (their sign, strength, range), which are responsible for depinning and the motion of dislocations in these experiments. Second, dislocations begin to move at different instants of time rather than at the instant an MF is switched on (Fig. 3). Therefore, dislocations that start earlier have a chance to move under an MF for a longer period (though this will not necessary happen for all of them, because part of them will be arrested before the MF is switched off and the other part will continue moving after the MF is switched off). Thus, the path lengths alone do not characterize the effect in question, because the time spent at a pinning center is not taken into account. In other words, the ensembles of objects and events involved in this effect are not in a steady state, because, first, the number of dislocations in an ensemble increases after an MF is switched on and, second, the driving stresses vary constantly in time and space.

This fundamental feature must be taken into account when performing a statistical treatment of such data. It should be noted that this problem is associated with the dislocation dynamics in the case of very low stresses (close to the depinning stresses) rather than with the MPE itself. At least two cases should be distinguished here: an ensemble of dislocations that progressively increase in number and an ensemble in which the number of moving dislocations is maintained constant dynamically.

When interpreting the experiments described above, as Fig. 5 suggests, one should consider not only the effect of MFs on the interaction of dislocations with pinning centers but also the possible effect of MFs on the electronic and atomic structures of dislocation cores and pinning centers (the latter can consist of several impurity atoms and cation vacancies and vary in composition [87, 88]). Furthermore, one should take into account that they can be affected not only by the MF alone but also (what is even more possible) by the combined action of the MF, high stresses, and electric fields in their "contact" interaction. Indirect evidence of this effect is the fact that, after an MF is switched on, dislocations do not immediately began to move, but rather the displaced dislocations gradually increase in number over several minutes (Fig. 3). In the case of normal relaxation of internal stresses, the opposite occurs; namely, the moving dislocations gradually decrease in number.

Much more diverse data on the dislocation dynamics can be obtained by applying a magnetic field in combination with external stresses. The corresponding experiments and their results are described in the following subsection.

2.2. Mobility of Individual Dislocations

We define the mobility of dislocations (by analogy with the mobility of elementary carriers in transport phenomena) as the dislocation velocity averaged over a steady-state ensemble in a unit field or as the average path length, when a square stress pulse of a fixed amplitude and duration is applied. Magnetic fields can be switched on at different stages of the experiment (see below), which makes it possible to vary the experimental conditions, more specifically, the stresses acting on dislocations, the type and state of defects subjected to a field, etc.

In [89–92], in order to separate the mechanisms of the effect of MFs on the defect structure of a crystal, several series of experiments were performed in which an MF was switched on at different stages and could influence different objects and processes. In other

words, only the consecutive order of different procedures was changed, while the main experimental characteristics, such as the duration of MF pulses and applied stresses, the temperature, and the way in which new dislocations were produced (scratching of the surface of a crystal), remained unchanged.

As seen from Fig. 7, the application of an MF before producing dislocations caused the path length L of dislocations to increase in the subsequent loading test (curve *2*) as compared to the path length L^* in the reference samples not subjected to an MF. In these experiments, the magnetic field could have an effect only on point defects and their complexes, which then became pinning centers for moving dislocations. An even greater increase in L was observed when MFs were applied *after new dislocations had been produced* (curve *3*). In this case, an MF could have an effect not only on pinning centers but also on the dislocations; therefore, the observed additional increase in L (in comparison to curve *2*) could be due to a change in the state of dislocations themselves or to an enhancement of the former process in the presence of dislocations. In these experiments (in contrast to those described in [67–72]), the application of a magnetic field alone did not cause depinning and the motion of dislocations, because the content of "nonmagnetic" impurities was higher than that in [67–72]. Thus, by switching on an MF and applying stresses separately, one can detect a prolonged aftereffect of MFs and, furthermore, can separate magnetically sensitive and insensitive pinning centers and investigate them. Aftereffects of MFs have been observed not only in ionic but also in molecular and covalent crystals [93–95].

Finally, in the case where an MF and stresses were applied simultaneously and $\mathbf{B} \perp \mathbf{l}$, a 6-s exposure to an MF caused the same increase in L as in the experiments described above after an exposure of crystals to MFs for over ~10^3 s (point *4* in Fig. 7). This enhancement of the effect of the MF can be explained by either (a) a third mechanism of the effect of the MF beginning to operate, namely, the influence of the MF on the interaction of dislocations with pinning centers (this mechanism was absent in the experiments corresponding to curves *2* and *3* in Fig. 7, because the MF had been switched off before the application of stresses), or (b) the processes proceeding in pinning centers and dislocation cores under the influence of the MF becoming faster by a factor of ~10^2 to 10^3 in the presence of externally applied stresses. Which of these two possible effects actually occurs can be established by performing special experiments. In the case of $\mathbf{B} \parallel \mathbf{l}$, the MPE was not observed, as in [67–72].

In [83, 84, 92, 96], the "mechanical" mobility of dislocations in ionic crystals in the presence of an MF was investigated using a high-resolution (~1 μs) *in situ* method of measuring the dislocation electric polarization; this method makes it possible to discriminate between the stages of depinning of dislocations and

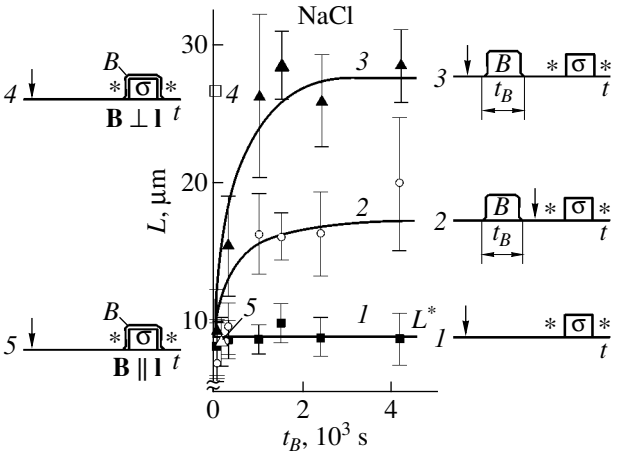

Fig. 7. Dependence of the path lengths of edge dislocations in NaCl single crystals caused by the same mechanical loading (σ = 0.1 MPa, duration 6 s, pulse rise time 10 ms) on the set and consecutive order of procedures and the duration of exposure to a static magnetic field B = 1 T at T = 293 K: (*1*) reference tests in the absence of an MF (average path length L^*); (*2*) dislocations are produced after exposure to an MF; (*3*) dislocations are produced before exposure to an MF; and (*4*, *5*) simultaneous loading and exposure to an MF (t_B = 6 s) with different orientation of vector **B** with respect to dislocation line **l**: (*4*) $\mathbf{B} \perp \mathbf{l}$ and (*5*) $\mathbf{B} \parallel \mathbf{l}$. Insets show the consecutive order of procedures for different types of test: σ means mechanical loading; the remainder of the interpretation is the same as in Fig. 3b.

their subsequent motion. In KCl : Ca crystals, MFs increased the quantity of dislocations and decreased the time spent by dislocations at pinning centers while affecting the average velocity of dislocations only weakly.

By applying two successive MF pulses or an MF pulse and a pulse of stress σ, one can perform a time-resolved spectroscopic study of relaxation processes in the system of point defects and elucidate their kinetic features (Fig. 8). We will refer to the former study as the B test and to the latter as the σ test. The idea of such experiments is to first treat only MF-sensitive point defects with an MF pulse and then, after a certain time, produce dislocations and cause them to move using the two different methods in order to investigate magnetically sensitive and insensitive pinning centers separately. It can be seen from Fig. 8a that prior magnetic treatment of pinning centers caused L to increase in a σ test and to decrease much more significantly in a B test. As time goes on, the aftereffect of an MF applied to point defects vanishes and the path lengths become equal to the value L^* in the reference samples (not subjected to prior magnetic treatment) in the former case and to a somewhat smaller value than L^* in the latter case. At first glance, it would seem that the point defects affected by the first MF pulse recover during the pause. If this were the case, the defects would again become sensitive to an MF a sufficiently long time after the first MF pulse. However, subsequent magnetic

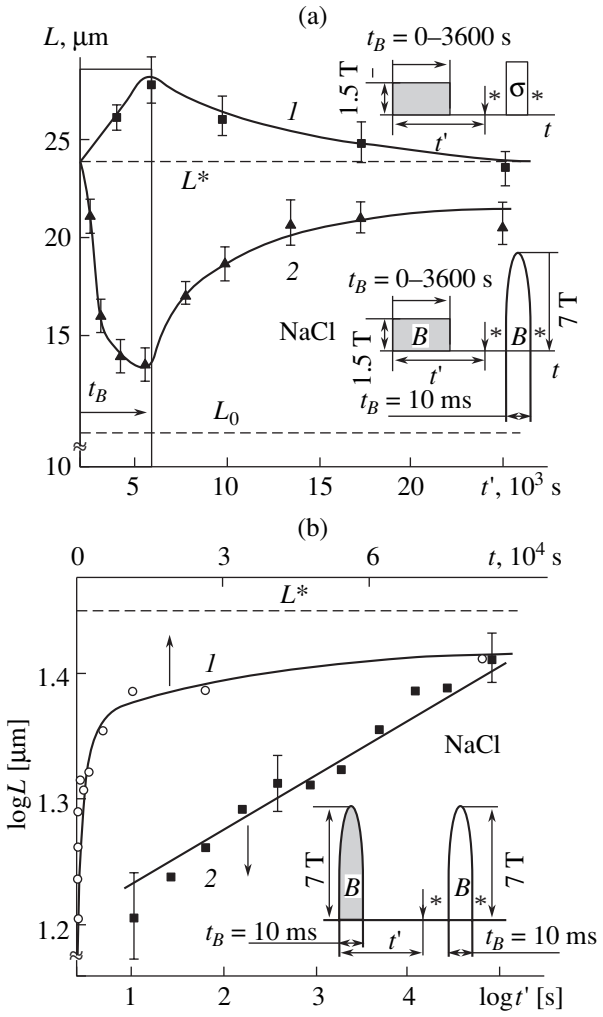

Fig. 8. Dependence of the path lengths L of edge dislocations in NaCl single crystals (a) on the duration t_B of prior exposure to a static magnetic field B = 1.5 T and on the time t' after which dislocations are produced; dislocation motion is caused by (*1*) stresses σ and (*2*) an MF pulse B = 7 T, t'_B = 10 ms; and (b) on the duration of pause t' between two successive MF pulses B = 7 T, t_B = 10 ms plotted on (*1*) semilogarithmic and (*2*) logarithmic scales. T = 293 K, L_0 is the path length in etchant, and L^* is the path length in reference samples not subjected to MF before dislocations are produced. Insets show the consecutive order of procedures. Notation in insets is the same as that in Fig. 7.

treatment did not affect the path lengths of dislocations regardless of the duration of the pause after the first treatment. Therefore, although the mobility of dislocations in a σ test returns to its initial value a certain time after an MF pulse is applied to the crystal, the point defects, once transformed by the field, become no longer sensitive to MF; i.e., their state is changed irreversibly by the first MF pulse (of sufficient amplitude and duration). Thus, the nonmonotonic time dependence of the dislocation path lengths in both tests (Fig. 8a) is due to the two-step relaxation process caused by the first MF pulse. The long relaxation times (tens of thousand of seconds) indicate that the process proceeds on the atomic–molecular level.

Note that the irreversibility of the MPE observed in the experiments described above is due to the weakness of the applied stresses σ, which exceed the depinning stresses only slightly. Such stresses do not produce new dislocations and do not increase the internal stresses during the motion of the dislocations present. As we will see further on (Subsection 2.4), the MPE can occur repeatedly as a crystal is deformed by applying $\sigma > \sigma_y$ (where σ_y is the yield stress).

The mechanism of the MF-stimulated transformation of depinning centers can be suggested by the kinetic dependences. Indeed, it is well known that monomolecular (intracenter) reactions are characterized by exponential kinetics (as in the case of radioactive decay), which is described by straight lines in the semilogarithmic coordinates, whereas bimolecular reactions (such as recombination) follow a power law, which is described by a straight line in the logarithmic coordinates [97]. It can be seen from Fig. 8b that the kinetics of the second stage of the MF-initiated relaxation process is described by a straight line in the log–log coordinates, which is indicative of random walks and collisions of two reagents derived from the decomposition of point complexes under the action of the first MF pulse [86, 98, 99]. Obviously, due to the dissociation of impurity–vacancy polyatomic complexes, as-produced dislocations are pinned predominantly by magnetically insensitive pinning centers. For this reason, the dislocation path lengths decrease after the action of the second MF pulse, because there are no pinning centers that can be affected by this pulse. On the other hand, the total concentration of magnetically sensitive and insensitive pinning centers decreases after the magnetic treatment, which is favorable to the motion of dislocations in the σ test.

In [83, 91, 96, 99, 100], it was shown that an MF differently affects the dislocation mobility in the stage where the load is decreased and in the stage where the load does not change. Here, we again face the problem of the influence of the nonsteady state of ensembles of moving dislocations. It is clear that, in the region of the plateau of a loading pulse, the ensemble is closer to a steady state than in the region where stresses progressively increase and are comparable to the depinning stresses.

In silicon, which has remained the base material for microelectronics for the past few decades, the MPE is of special interest. In this material, dislocations can act as getters for impurities and affect the electronic, optical, and transport properties, which is of considerable practical importance. In [101], an aftereffect of a prior exposure of *n*-type silicon samples (resistivity 0.01–0.1 Ω m) to a static magnetic field B = 0.7 T at room temperature over 15 min on the mobility of dislocations (which were not specified in [101]) under mechanical

stresses $\sigma = 20$ MPa at $T = 850$–950 K was found. After the magnetic treatment, the dislocation path lengths increased approximately twofold. A model of the MPE in Si was proposed in [102] in which three types of obstacles for dislocations (Peierls barriers, impurity atoms, forest dislocations) were taken into account.

In [95], using the selective etching method, a twofold decrease in the depinning (start) stresses τ_{st} was observed for individual 60° dislocations in Cz–Si grown using the Czochralski method (i.e., containing a large amount of oxygen) after a prior exposure of the sample to a magnetic field $B = 2$ T over 3 h. The magnetic treatment of a crystal with dislocations produced beforehand was performed at room temperature, and the dislocation mobility was measured at 600°C under shear stresses τ varied from zero to 70 MPa. The MF exposure had a smaller effect on the velocity of broken-away dislocations than on τ_{st}. In floating-zone silicon (where the oxygen content is less than in Cz–Si by two orders of magnitude), the effect of MFs on the dislocation mobility was not detected. Based on these observations, it was assumed in [95] that the MF affected the state of oxygen molecules adsorbed by dislocation cores, thereby changing the position of the molecules and the binding energy between them and dislocations.

2.3. Internal Friction

Measurement of the parameters of internal friction (IF) is a very subtle and sensitive method that has been used over many decades to investigate the dynamics of defects (in particular, dislocations and point defects) in a stress field. The effect of MFs on the parameters of IF in ferromagnets has been studied in considerable detail [103, 104].

Internal friction in nonmagnetic materials in the presence of an MF has been much more poorly investigated. Several attempts at detecting magnetic effects in diamagnets were made in the 1970s–1980s. Sometimes, the results were positive but, as a rule, highly contradictory [10, 105] and very difficult to interpret. For this reason, those results have not attracted the attention of researchers (except in studies performed for polymers [106]). For example, in [10], the logarithmic decrement of bending vibration of a plate of silicon (KÉF 7.5/0.1, *n*-type conductivity $\sim 10^{-2}\ \Omega^{-1}\ \mathrm{cm}^{-1}$) was observed to decrease under the action of a static MF, with the decrease being fourfold in a field $B = 0.09$ T. However, no data on strains and applied stresses were presented (hence, it is unclear whether the results are related to amplitude-independent or amplitude-dependent IF) and no explanation of the observed phenomenon was offered in [10]. The effect of MFs on dislocation IF in copper was studied in [105]. It was found that, at $T = 4.2$ K, the decrement (in the amplitude-independent region) increased by a factor of 2.5 in a sample subjected to a field $B = 0.3$ T and by a factor of 1.7 in the same sample and field after plastic deformation. A further increase in the field up to 1.2 T did not cause the softening to increase. Attempts to explain these results in terms of the electron drag of dislocations in an MF [47] (the single mechanism for the effect of an MF on the plasticity of diamagnetic metals having been proposed by that time) were not successful, and the authors (as far as we know) did not continue this study at a later date.

Starting in the mid 1990s, the effect of MFs on the amplitude-dependent dislocation IF in a number of ionic crystals (LiF, NaCl, KBr, KCl) at room temperature has been the subject of much study [107–110]. It has been established that magnetic fields $B \approx 0.1$–0.75 T have an effect (surprising in certain cases) on many IF parameters. In KBr samples subjected to a field $B = 0.2$ T, Young's modulus decreased while the decrement increased, which is indicative of an increase in the dislocation mobility in the presence of an MF. It was shown that the increase in damping was associated with charged edge dislocations escaping from Debye–Hückel clouds and with an increase in the probability of oscillating dislocations breaking away from local pinning centers [108]. Prior exposure to an MF, on the contrary, had an inverse effect, namely, hardening of the samples [110]. Magnetic fields suppressed dislocation sources localized at the boundaries of blocks [107], with the consequence that dislocation structures characteristic of high-temperature loading of alkali halide crystals formed at room temperature. The papers mentioned above also did not discuss the mechanisms for the effect of MFs on the primary acts of interaction between dislocations and pinning centers.

In the 1980s–1990s, a great number of papers were published describing the phenomenology of the effect of weak MFs on internal friction and structural relaxation in other nonmagnetic materials at room temperature (glass ceramics, oxide glasses, nonferrous alloys, polycrystalline aluminum of technical purity grade, etc.) [111–116]. However, those papers do not contain any data on the dislocation structure and, hence, do not discuss the role played by this structure in the observed MF-induced effects.

2.4. Macroplasticity and Hardness

It is well known that there is no direct relation between the mobility of individual dislocations and the macroscopic plastic characteristics. Therefore, it was of interest to elucidate the effect of MFs on the plastic flow for large deformations ε. This effect was investigated for the first time in [117–119]. NaCl single crystals were subjected to uniaxial compression up to $\varepsilon \approx 5\%$ for 10–15 min. A static magnetic field $B = 0.7$ T was applied over a short time (5–10 s) at different stages of compression (Fig. 9). The strain hardening coefficient $G = \partial\sigma/\partial\varepsilon$ measured during these short periods (G_B) was found to decrease twofold at most. The application of an MF pulse ($B = 7$ T, $t_B = 10$ ms) caused G to

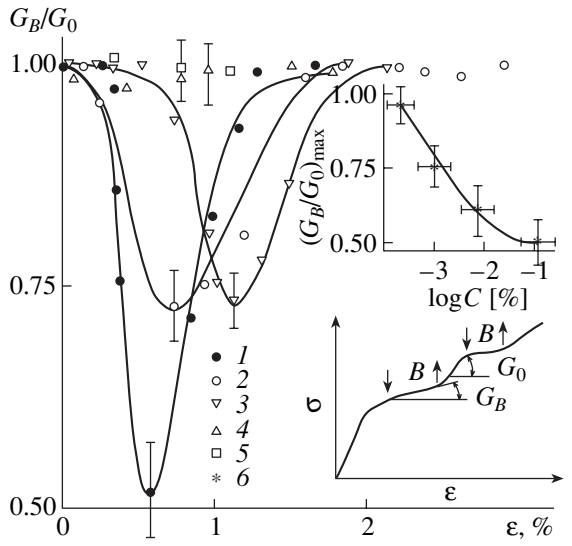

Fig. 9. Strain hardening coefficient as a function of strain ε and impurity composition for ionic crystals subjected to macroscopic deformation in a static magnetic field $B = 0.7$ T at $T = 293$ K: (*1*) NaCl : Ca (0.1%), (*2*) KCl : Ca (0.03%), (*3*) LiF : Mg (0.03%), (*4*) KCl : Pb (0.03%), and (*5*) KCl : Mn (0.03%); NaCl : Ca (concentration dependence).

decrease in a jump of 50–100 ms after the MF pulse. Then, a period followed over which G increased and an MF had no noticeable effect on it. A few seconds later, G became equal to its value G_0 before the application of the MF pulse. The softening effect became a maximum immediately after the yield point had been reached, and then, at $\varepsilon \approx 2$–3%, the softening decreased slowly in both cases of static and pulsed MFs. The fact that the MPE depends on ε and reaches a maximum at the easy-slip stage indicates that the MF favors dislocations overcoming point obstacles of impurity origin and has a slight effect on the penetrability of a dislocation forest.

The most MF-sensitive crystals (among the crystals studied) were found to be those doped with Ca, whose ionic radius (0.197 nm) is close to the ionic radius of Na^+ (0.186 nm) in the NaCl lattice. Crystals doped with Eu, In, and Mg to concentrations definitely exceeding the background values also exhibited sensitivity to MFs. The MPE was not observed in crystals doped with Mn and Pb (as was the case in the individual-dislocation mobility experiments). The dependence of the MPE on the Ca content C in NaCl is shown in Fig. 9. The fact that the MPE depends on the impurity type and concentration is indicative of the close involvement of impurity atoms in MF-sensitive processes and macroscopic deformation.

However, from a comparison of the concentration dependences shown in the insets to Figs. 3 and 9 for the same NaCl : Ca crystals in which the MF-induced dislocation depinning was studied, it can be seen that, with increasing C, the MPE decreases in unloaded crystals and increases (tending to saturation) in macroscopically deformed crystals. This feature can be explained by the dual role played by a different-valence impurity in crystals subjected to an MF. On the one hand, an increase in C leads to an increased amount of pinning centers; hence, the depinning stress and the yield stress become higher. On the other hand, the quantity of MF-sensitive objects and their fraction of the total amount of pinning centers increase with concentration C. Obviously, the former factor is more important in the case where the MPE is associated with low internal stresses, and the latter factor is more significant under conditions of macroscopic deformation, where the external stresses are sufficiently strong for the majority of local pinning centers to be overcome.

In [120–123], the yield stress σ_y in ionic crystals was found to decrease by a factor of up to 2.5 in an MF of ~1 T and possible reasons for this effect were discussed. In [124], the effect of a static magnetic field $B = 0.2$ T on the creep rate of ferroelectric $NaNO_2$ crystals and LiF single crystals was studied. It was established that in both materials the creep rate $\dot{\varepsilon}_B$ increased after the application of an MF and recovered its original value $\dot{\varepsilon}_0$ after the MF was switched off. The ratio $\dot{\varepsilon}_B/\dot{\varepsilon}_0$ depended heavily on the strain rate before the application of an MF and reached 7 for $\dot{\varepsilon}_0 \approx 0.2 \times 10^{-5}$ s^{-1} in $NaNO_2$, whereas in LiF this ratio did not exceed 1.6. The reason for this high MF sensitivity of $NaNO_2$ remains unclear. In [125], the effect and aftereffect of static MFs of 0.2 to 2 T on the creep rate were studied *in situ* in molecular crystals of fullerite C_{60}. The sign of the effect was found to depend on temperature (the phase state of the sample). The MF caused the strain rate to increase at $T = 293$ K (fcc lattice) and decrease at $T = 110$ K (simple cubic lattice), with the strain rate becoming zero several seconds after the MF was switched off. Earlier, sign reversal of the MPE was observed in C_{60} at the phase transition point in [126], where the aftereffect of an MF on the microhardness of the fullerite was studied at temperatures of MF exposure from 200 to 300 K.

The magnetic effects observed in polymers stand out against the long series of MPEs discovered in the past years. These materials were subjected to magnetic fields during polymerization or consolidation or in a high-elasticity state above the vitrification temperature, and then their properties were studied at lower temperatures. The magnetic field caused changes in the structure and the dielectric and mechanical properties. In most cases, the authors associated these effects with MF-initiated orientation processes in the polymer structure. For details, see the review by Rodin [127].

In [128–130], the effect of static fields $B = 0.2$–0.4 T on the kinetics of creep was observed in polymers (PMMA, PVC, etc.,) in the glassy state (at $T \approx 300$ K). The *in situ* effect of an MF on the creep rate and on the magnitude and rate of strain microjumps was found to

increase considerably if, before deformation in the presence of a magnetic field, samples were subjected to the same or a stronger field over a long period of time (up to 700 h). The authors related the observed effects to the diamagnetic susceptibility of individual monomer chains and its anisotropy; however, no detailed mechanism was proposed for the effect of the MF on these characteristics (including the problems mentioned above, which are inherent in "force" models of this kind).

Magnetic treatments of ionic, mixed ionic–covalent, and molecular (C_{60}) crystals and other materials cause aftereffects, more specifically, long-term changes in microhardness H [12, 93, 94, 126, 131–136]. As an example, Fig. 10 shows the dependences of H on the elapsed time t from the application of an MF pulse for NaCl, C_{60}, and PMMA. Clearly, only the effect of the MF on the initial structure was studied in this case, because loadings and measurements of H were performed a certain time after the MF exposure of the sample.

The aftereffect of short MF pulses (B = 30 T, t_B = 25–1300 μs) on the mechanical properties of polymers in the glassy state was studied in [131–133]. It was found that the softening effects observed after the action of an MF pulse are reversible (the time required for H to relax to the initial value was several tens of hours at T = 300 K) and cannot be explained in terms of reorientation of links of macromolecules (because of the short duration of MF pulses). However, the values of the dipole and magnetic moments of side groups of a chain were observed to correlate with the MPE characteristics.

In [137–139], the *in situ* effect of a magnetic field B = 0.2 T on the microhardness of Bi single crystals was studied ignoring the highly probable errors that could be introduced by the influence of the MF on the test machine (see, e.g., [35]). A magnetic field was applied during indentation. An increase in H and a decrease in the size of twin layers around a dent were observed to occur.

2.5. Fracture

Plastic flow and fracture are related and often correlated processes. The nucleation and slow growth of cracks to the critical size, as a rule, are controlled by the mobility and interaction of dislocations. Therefore, the effect of the MF on the dynamics of dislocations must reflect on the behavior of cracks. Furthermore, the MF can have an effect on quasi-brittle fracture, fatigue, wear, etc., through other mechanisms not involving dislocations [140].

We restrict our consideration to the results related to the fracture of ionic crystals in a static MF. In [141], the crack growth in a LiF single crystal was observed to change direction when the crack tips entered a region where there was an MF (B = 0.1–1 T). In this case, a

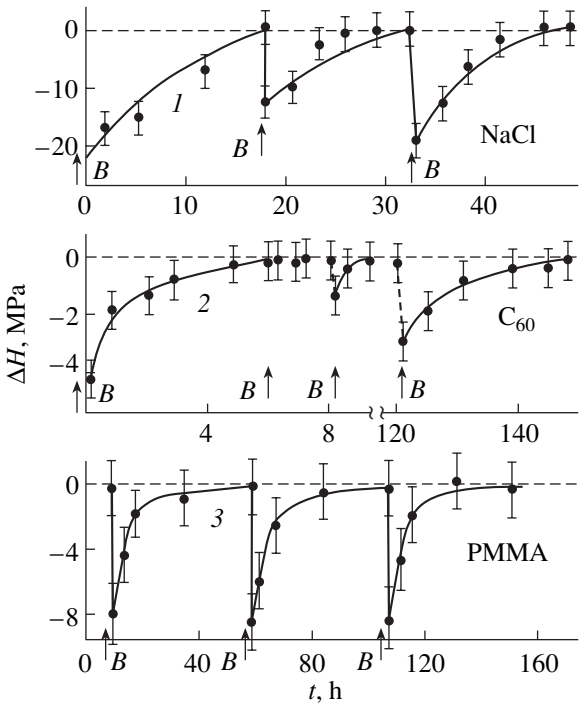

Fig. 10. Dependences of the change in microhardness H on elapsed time t from the exposure to an MF pulse (B = 24 T, $t_B = 10^{-4}$ s) for (*1*) NaCl and (*2*) C_{60} single crystals and (*3*) PMMA. Values of H before application of an MF are shown by dashed lines, and the moments at which the MF is switched on are indicated by arrows. T = 293 K.

crack passed from a (100)-type cleavage plane (typical of alkali halide crystals) to a (110)-type plane (with a higher surface energy), which is an easy-slip plane for edge dislocations. This effect was interpreted in [141] in terms of the model proposed by Molotskiĭ [142]. In this model, the avalanche relaxation of surface electric charges on the opposite faces of a crack is blocked in the presence of an MF because of the magnetron effect. However, according to [142], in order for an electron avalanche cutoff to occur in the cavity of a growing crack, magnetic fields in excess of 30 T are required, which are two orders of magnitude higher than those used in [141]. At the time paper [141] was published, it was not known that the dislocation mobility in LiF can be considerably enhanced in the presence of much lower MFs. It is most likely that the softening in the slip plane of the most mobile dislocations was the reason why cracks passed into this plane. In [143, 144], the same authors reported on the observation of an increase in the fracture load by a factor of up to 1.4 and an increase in the number of acoustic emission pulses before fracture by a factor of 2.5 in LiF samples subjected to MFs (B = 0.4 T). As follows from the σ–ε curves presented in those papers, the MF-induced strengthening was due to the increased plasticity resource at large values of ε rather than to an increase

in $G = \partial\sigma/\partial\varepsilon$. Based on the currently available data on magnetoplastic effects, it is reasonable to suggest that the observed MF-induced increase in the load-carrying ability was due to the increased dislocation mobility, which made stress relaxation easier in the stress concentration region. Thus, there are strong grounds to believe that much more complex and less well-understood processes of flow and fracture at large deformations are also sensitive to MFs and should be covered by the science dealing with the mechanical properties of solids in electromagnetic fields.

Let us sum up the results of early studies of the MPE in diamagnetic materials. Although the available data are inconsistent and contradictory in certain cases because of the lack of information on the experimental conditions, prior history of the samples, the impurity content, and the state of impurities, differences in the interpretation of the experimental data, etc., the following facts have been well established.

(1) The effect of weak MFs on the inelastic and plastic properties of solids of different nature takes place on various structural levels and for any deformation (from 10^{-5} to 1).

(2) Both *in situ* effects and aftereffects (long-term or permanent memory of the MF exposure) occur in nonmagnetic materials. These effects, as a rule, are characterized by threshold values of the magnetic field and its duration and reach saturation at fields of several teslas. There are at least two reasons for saturation, one of which is associated with magnetically sensitive processes proceeding in the defect structure and the other, with finite path lengths of dislocations limited by insurmountable pinning centers. Note that the existence of threshold and saturating values of the magnetic field for the MPE is indirect evidence that the MF has a selective effect on certain defects and degrees of freedom in crystals whereas the others are not affected. In other words, the MF changes the relations between various factors controlling the physical-mechanical properties of crystals.

(3) In magnetic fields of 0.1 to 1–2 T, the magnitude of the effect is usually proportional to B^2 and is independent of the direction of the vector **B** if this vector lies in the plane perpendicular to the dislocation line **l**; in the case of **B** || **l**, the MPE does not occur.

(4) In order for the MPE to occur, a sample must have a nonequilibrium structure, which either can be its inherent property or must be continuously sustained. In the former case, the MPE can occur only once and then, after structural relaxation caused by an MF pulse of sufficient amplitude and duration, will not be reproduced in subsequent magnetic treatments.

(5) The MPE depends strongly on the type and state of impurities. The effect is usually the largest in crystals with a different-valence impurity, which does not produce large dilatational strains in the lattice.

(6) There are a few mechanisms through which the MF affects the structure and properties of the crystal. Therefore, the magnetic field can induce multistage (concurrent–consecutive) relaxation processes in the defect structure; certain of them are unique and cannot be initiated using thermal treatments, mechanical effects, etc. The most important processes initiated by MFs are dislocation depinning, disintegration of impurity complexes, and subsequent recombination of the fragments with possible involvement of other defects of the structure.

3. COMBINED AND RELATED PHENOMENA STIMULATED BY A MAGNETIC FIELD IN SOLIDS

Plastic flow is one of the relaxation phenomena observed in solids and has much in common with analogous phenomena that are controlled by the dynamics of defects of the atomic structure or electronic excitations. Certain of those phenomena are also highly sensitive to weak MFs, which was discovered even earlier than the MPE. Although the responses observed in those phenomena are not mechanical, the elementary events can be analogous in nature. Certain advantages of such experiments are that the measured quantity can be associated with processes that are more closely related to the elementary events of the MF influence than in mechanical tests and that this quantity can be less inertial. Furthermore, electronic excitations can be affected using other means (light, electric field, ionizing radiation), which provides additional information on the dynamics of these excitations in the presence of an MF. For this reason, we briefly consider several groups of "magnetic" effects that are observed in magnetically disordered solids subjected to weak MFs and are close to the MPE.

3.1. Electromagnetoplastic Effects

Leaving aside purely electroplastic effects (EPEs), which have been studied in dielectrics, semiconductors, metals, alloys, etc., over approximately half a century [145–151], we restrict our discussion to the combined action of a magnetic and an electric field (EF) on an object. There have been studies in which these fields were applied successively or simultaneously. However, the following important factors should be taken into consideration. Strictly speaking, a "static" magnetic field cannot be considered absolutely time-independent, because it must be switched on and off, or a sample must be placed in the field or removed from it, etc. Therefore, the possible effect of the vortex EFs that arise in these cases (to say nothing of pulsed and high-frequency ac magnetic fields) must be taken into account. On the other hand, the application of an electric field produces an electric current in the conductor and, hence, the magnetic field associated with the current. In ionic and semiconducting crystals of the A^3B^5 and A^2B^6 types, nucleation and motion of dislocations produce a dynamic pattern of internal electric fields,

whose effect on other defects (in particular, local and extended barriers for dislocations) can be added to the effect of external stresses and magnetic fields. Therefore, individual elements of the structure and of a sample as a whole are always subjected to a combination of electric and magnetic fields. On general grounds and on the basis of a large body of data, it is clear that in reality the combined effect can be much more complicated then in a model that allows for the effect of each field separately.

We will focus our attention on a few prominent examples of nontrivial effects produced by the joint action of magnetic and electric fields, though there are a great number of such examples. In [152–156], the effect of a weak electric field $E = 0.25$–5 kV/m, applied in combination with a magnetic field $B = 0.05$–0.5 T, on the mobility of as-produced dislocations was observed in LiF and NaCl crystals with Ca, Ni, Cu, and Pb impurities. EFs of up to 1.5 kV/m did not cause dislocations to move in the absence of an MF. After the application of a magnetic field $B \geq 0.15$ T, even an electric field $E = 250$ V/m caused an increase in the mobility of edge dislocations. When the direction of the EF was reversed, the majority of dislocations also reversed their direction of motion, which correlates well with the observed linear dependence of the path lengths of dislocations on the value of E. The dislocation mobility reached a maximum when the vector **E** lied in the slip plane of dislocations and was perpendicular to the dislocation lines. If a weak temperature dependence of the dislocation mobility was observed at $E = 0$ (see Subsection 2.1 for details), then this dependence disappeared in the presence of an EF in the temperature range from 77 to 300 K. It is important that, in the case of rotating MFs ($B = 0.5$ T), the application of an EF ($E = 1.2$ kV/m) increased the mobility of edge dislocations only (without a change in the threshold frequency ν_c of the MF rotation) but had no effect on the mobility parameters of screw dislocations. Based on the results of those studies, it was concluded that the EF affected the velocity of dislocations moving between MF-sensitive pinning centers but (because the EF was weak) did not have a significant effect on the probability of MF-induced dislocation depinning. By decreasing the FE further and monitoring the direction of motion of dislocations broken away from pinning centers, one could have estimated the magnitude and distribution of internal stresses in the crystals under study. Note that, in addition to the mechanisms of the magnetoelectroplastic effect in ionic crystals discussed in the papers mentioned above, it is appropriate to take into account the possible injection plastic effect [157–159], because in the experiments in question the EF was produced using galvanic coupling between electrodes and a sample.

In [160], the combined effect of a static MF ($B = 0.1$–0.4 T) and a static EF ($E = 0$–5 kV/m) on the macroscopic deformation of NaCl crystals subjected to compression at a constant strain rate $\dot{\varepsilon}$ lying in the range 5×10^{-5} to 2×10^{-3} s^{-1} was studied. It was found that, in the entire ranges of B and $\dot{\varepsilon}$ covered, the application of an EF caused an additional loss of strength (the yield stress σ_y decreased by a factor of up to 2), which saturated with electric field at $E \approx 1$ kV/m. Simultaneously, the strain strengthening rate and dislocation density were observed to increase. Note that analogous phenomena occurring in the absence of an MF are well known and have been intensively studied; however, these phenomena are observed only in fields $E \geq 10^3$ kV/m. Therefore, the application of a magnetic field $B = 0.4$ T can increase the sensitivity of the macroscopic properties of NaCl to an EF by more than three orders of magnitude.

An increase in the EF-stimulated mobility of dislocations was observed in a silicon single crystal after the application of a magnetic field $B = 0.05$–1 T [161–164]. The magnetic effect was detected using the acoustic-emission method [161] and, later, using selective etching. It was established that, for a current density of 3×10^5 A/m^2, a magnetic field of 1 T increases the dislocation path lengths in n-Si by a factor of up to 40. These results are of practical importance, because semiconductor devices and chips are influenced simultaneously by a current and an MF under conventional service conditions.

Paper [163] was devoted to studying the effect of prior exposure of Czochralski-grown silicon single crystals (doped with phosphorus and boron) to an MF ($B = 0.17$ T) at room temperature over 7 days on the mobility of dislocations observed subsequently at $T = 923$ K in the absence of an MF. It was found that, due to the preliminary magnetic treatment, dislocations were pinned and the velocity $\langle V \rangle$ of dislocations moving under external stresses ($\sigma = 63.5$ MPa) decreased. Passing the electric current of a density of 10^6 A/mm^2 simultaneously with mechanical loading caused the velocity $\langle V \rangle$ to increase by 15 times, whereas in samples subjected to prior magnetic treatment the velocity increased by only 5 times. In other words, the prior exposure to a weak MF decreased the EF-stimulated mobility of (presumably 60°) dislocations by three times in a doped silicon crystal. The activation energy for dislocation motion was $\cong 0.75$ eV against 2.03 eV in the reference samples not subjected to an MF and through which no current was passed during mechanical loading. Unfortunately, an MF was applied after dislocations were produced in a sample; therefore, different mechanisms for the MPE (modification of point defects and their complexes, of the structure of the cores of dislocations and their environment, or of the interaction of dislocations with potential pinning centers) could not be separated.

In [165], edge-dislocation depinning caused by a series of MF pulses ($B = 7$ T, $t_B \cong 10$ ms) was studied in NaCl : Ca crystals. A crystal was subjected to the first MF pulse before dislocations were produced, and it was found that, for a long time after this treatment, the next

MF pulse had no effect on dislocations. At room temperature, an MF regained its ability to cause depinning of as-produced dislocations after ~10^3 s (as in the experiments represented in Fig. 9). The application of an ac electric field (f = 400 Hz, $E = 3 \times 10^5$ V/m) after the first MF pulse decreased the time it took for the magnetic sensitivity of depinning to be restored by a factor of ~10^2. The result also depended on the order in which the treatments were performed; if dislocations were produced before the application of an EF, the effect of the EF on the dislocation mobility was two times larger than in the case where dislocations were produced after the exposure of the sample to the EF [92]. This dependence indicates that there are several mechanisms for the effect of the EF (as well as for the effect of the MF; Fig. 7) on the structure of a crystal. In the absence of dislocations, the EF could affect the system of point defects only and did not changed the MPE significantly. The effect became even more noticeable when the EF affected pinning centers, dislocations, and the interaction between them.

The electroplastic effects observed in metals [149–151] can be explained more adequately on the basis of the elegant hypothesis (made by Molotskii and Fleurov [166, 167]) that depinning of dislocations can be caused by the magnetic field produced by the electric current flowing through a sample. It is believed that all quantitative and qualitative regularities of electroplasticity can be explained in this way. For example, the quadratic dependence of the EPE on current I can be due to the quadratic dependence of the MPE on B (which is proportional to I) and the threshold values of the amplitude and duration of the current can exist for the same reasons as those dictating the magnetic depinning of dislocations.

3.2. Photomagnetoplastic Effects

Studies into the combined effect of light and an MF on plasticity are important, because the elementary events of this effect involve electrons and electronic excitations in structural defects, which makes it possible to gain a better understanding of the electronic structure of MF-sensitive centers and to control the MPE using optical methods. The well-known series of papers on photoplasticity by Osip'yan and coworkers (see [148] for a review) made it clear for the first time that the physical-mechanical properties of real solids can be understood on the fundamental level only in terms of the electronic properties of dislocations and obstacles surmounted by them.

Contrary to heat treatment or the application of stresses and EFs, monochromatic light can cause selective (photostimulated) transformations of certain structural defects, excite or suppress certain transitions in the electron subsystem, etc. A number of papers have been dedicated to the detection and study of the mutual influence of the photoplastic and magnetoplastic effects [168–175]. Those studies were of both theoretical and experimental interest, because in the case where mixed, photomagnetoplastic effects occur the illumination of a sample has to be controlled when studying the MPE.

Figure 11a shows the dependence of the photostimulated change in path lengths of edge dislocations in NaCl crystals on photon energy for two cases, where dislocation motion is caused by applying stresses or an MF (B = 7 T, duration t_B = 10 ms). It is significant that the influence of light on as-produced dislocations and on their interaction with pinning centers was eliminated in these experiments, because dislocations were produced after illumination of a sample. Therefore, light could affect only the structure of potential pinning centers (point defects and their complexes); the path lengths of as-produced edge dislocations were much shorter than the average distance between forest dislocations. It can be seen from Fig. 11a that the maxima of the spectral photosensitivity in both cases coincide in position; however, in the σ test, the mobility slightly increases, whereas in the B test the mobility decreases significantly (as in the experiments represented in Fig. 8). The most important difference between these two tests is that stresses can cause dislocations to break away from any pinning center, whereas a magnetic field can only cause dislocations to break away from MF-sensitive pinning centers.

A comparison between the data presented in Figs. 11a and 8 shows that light with photon energies E = 2–5 eV selectively affects the structure of MF-sensitive pinning centers (with a maximum in spectral sensitivity at E_{max} = 3.5 eV); namely, light causes photochemical reactions in pinning centers, thus decreasing their ability to retard dislocation motion. In the σ test, due to this influence, the height of local barriers will decrease, on average, and the dislocation mobility will increase. When dislocations are produced in such a crystal, they are pinned, for the most part, by magnetically insensitive centers; therefore, when an MF is applied to cause dislocation depinning in the B test, there will be no pinning centers that can be affected by this field. Simultaneously, we arrive at a negative answer to the question of whether the vortex EF can affect dislocation depinning caused by a pulsed strong MF (of 7 T in these experiments). Analogous results were obtained on KCl and LiF crystals, with the only difference that here E_{max} varied regularly with the lattice parameter a (as a^{-2}) and was 2.8 and 6.6 eV, respectively.

The photoinduced changes in the state of point defects were reversible and relaxed with a characteristic time of ~10^3 s at T = 300 K (Fig. 11b). The kinetics of this relaxation was bimolecular in character (see inset to Fig. 11b), which indicates that the reaction between the products of photochemical decomposition was of the recombination type. Illumination with IR light (E_{max} < 1.5 eV) during this relaxation increased its rate by a factor of several tens. In [176], the dislocation

mobility was observed to be anisotropic in the equivalent (110)-type planes; more specifically, after illumination of a crystal with light polarized in the direction coinciding with one of the {110} axes, the fraction of dislocations moving in the plane of polarization under the action of an MF was greater than in the perpendicular plane by a factor of 1.5. No difference was observed in the path length of dislocations.

In another series of experiments, γ-irradiated KCl crystals were illuminated with *F* light (λ = 555 nm), with the result that electrons were selectively excited from *F* centers into the conduction band [175, 176]. Check experiments (without illumination) showed that the application of an MF (B = 2 T, t_B = 20 s) to such samples caused a long-term (a few tens of hours) but reversible 8% decrease in microhardness. *F*-light illumination of samples preliminarily subjected to an MF partly restored the hardness (increasing it by 4% in 5 s). The subsequent application of an MF again decreased the hardness to the previous value. Such MF-induced softening and *F*-light-induced strengthening alternating with each other can be repeated many times over a period of a few minutes. Analogous experiments on crystals containing not only MF-sensitive pinning centers that are characterized by deep levels lying in the band gap but also by less deep *F* centers make it possible to change the population of the former levels by illuminating the crystal with light with the appropriate photon energy *E* and control the magnitude and character of the MPE. The fact that light with certain wave lengths has a considerable effect on the sensitivity of the mechanical properties of wide-band-gap crystals to MFs is indicative of the electronic nature of the MPE observed in such crystals and suggests that the impurity complexes whose structure is changed by light and MFs are the same.

3.3. Radiation-Magnetoplastic Effects

The effects produced on a solid by fluxes of optical, x-ray, and γ-ray photons and of light particles (e.g., β^-) are similar to a considerable extent; initially, electronic excitations are produced, whose decay results in ionization, photochemical reactions, and displacements of atoms from lattice sites. This similarity makes radiations a convenient tool for studying the MPE and various combined effects, which can be nonlinear and nonadditive and difficult to predict. Furthermore, the simultaneous action of a weak MF and background radiation is a characteristic feature of our environment, which makes the study of combined effects vitally important. Unfortunately, the physical aspects of the problem have not been adequately investigated, whereas whole institutes have conducted research on its biomedical aspects (see [177] for a review).

The effect of prior low-dose (<1 Gy) x-ray irradiation on the MPE in LiF and NaCl crystals with various impurities was detected in [178] and described in detail

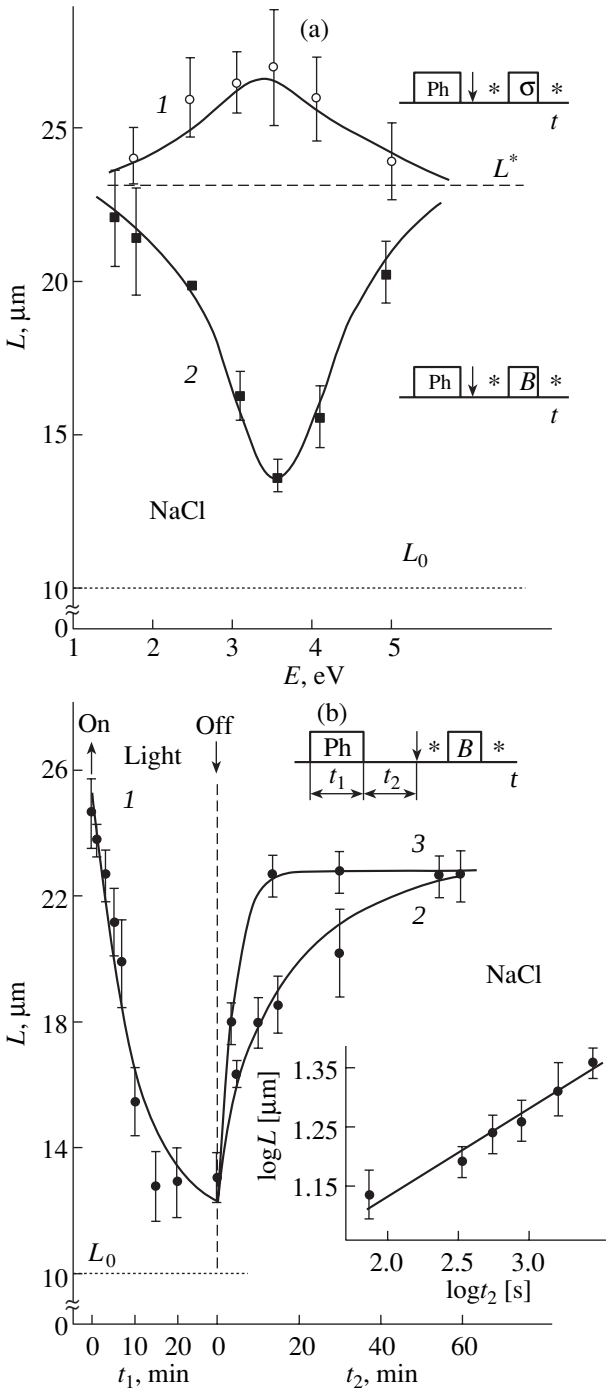

Fig. 11. (a) Dependence of the path lengths of edge dislocations in NaCl single crystals, caused by (*1*) mechanical loading and (*2*) magnetic field, on the photon energy *E* of prior illumination of samples. Dashed lines show the path length L^* in crystals not subjected to illumination and the background path length L_0 in etchant. Insets show the consecutive order of procedures; Ph stands for photoexposure, and the remainder of the notation is the same as that in Fig. 7. (b) Dependence of the path lengths of edge dislocations in NaCl caused by an MF on (*1*) the duration of photoexposure with photon energy E = 3.6 eV and the "rest" duration (*2*) in the dark or (*3*) under IR illumination with E < 1.5 eV. B = 7 T, t_B = 10 ms, and T = 293 K.

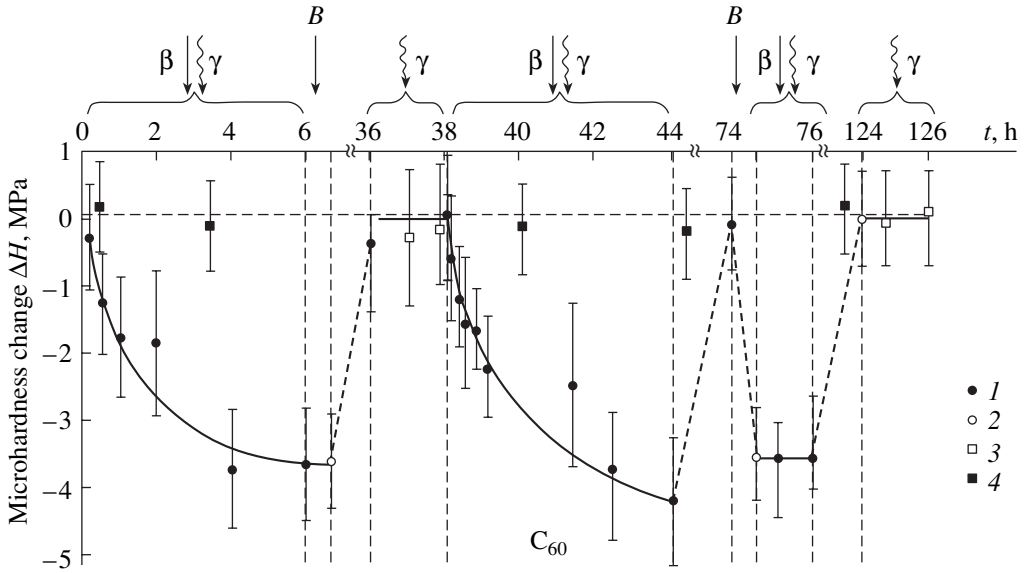

Fig. 12. Changes in the microhardness H of fullerite C_{60} single crystals caused by successive exposure to radiation and MF pulses (B = 25 T, $t_B = 10^{-4}$ s): (*1*) β + γ radiation, (*2*) magnetic treatment, (*3*) γ radiation, and (*4*) after polishing of the surface.

in [155, 179]. In all cases, an increase in the dose caused a decrease in the path length of dislocations moving in a static MF (B = 0.3–0.6 T). However, much more interesting results were obtained in the case of rotating MFs. In addition to the one critical frequency in the dependence of the path lengths of dislocations on the angular frequency of rotation of the applied MF, another, higher frequency appeared (Fig. 4b), which was insensitive to radiation dose (in contrast to the former frequency, associated with impurities). Therefore, irradiation brought about the formation of another type of MF-sensitive pinning centers characterized by a shorter depinning time. This feature appears to be explicable if the depinning time is controlled by the molecular dynamics, because radiation-induced pinning centers (especially in the case of low radiation doses) are smaller in size than polyatomic impurity complexes. Although the crystals thus obtained were not tested by applying stresses in the experiments under discussion, it can be said with confidence that no changes in the mechanical properties would have been detected in conventional tests. Measurements of the MF-stimulated mobility of dislocations made it possible to detect the presence of the new type of defects, even though their concentration certainly could not be detected by using EPR or optical spectroscopy.

In [180], the influence of even lower doses of β^- radiation (<1 cGy) on the MPE was observed in C_{60} single crystals (Fig. 12). The influence was reversible; more specifically, the MPE disappeared immediately after irradiation, but the sensitivity to MF was restored after relaxation ($\tau_r \sim 50$ h at T = 293 K). Conversely, the magnetic treatment of a crystal made it "radiation-resistant" over the same time τ_r; i.e., the mechanical properties of the crystal became insensitive to radiation. This feature is likely to indicate that the MF and β^- particles act on the same objects in the crystal. The effects described above are still not clearly understood and call for further investigation. However, it is clear that, in ionic and molecular crystals (as well as in semiconductors; see Subsection 3.6), a combination of even very low radiation doses and the MF can have a fairly noticeable effect.

3.4. Magnetoplastic Effects in Strong Magnetic Fields

So far, we have discussed the effects induced by weak MFs for which the quantity $\Delta U_m = 2\mu_B gMB$ is small compared to $U_T \sim kT$ (where g is the spectroscopic splitting factor, M is the magnetic quantum number). On general grounds, it is clear that, as the magnetic field B increases, the mechanisms for its effect on the structure of a material will progressively increase in number. For high-spin states (with large M), ΔU_m becomes comparable to kT in fields of a few tens of teslas at room and lower temperatures. Therefore, such fields can also affect the processes proceeding in systems close to thermodynamic equilibrium. Indeed, break-away and motion of dislocations in NaCl caused by a pulsed magnetic field $B \approx 15$ T was observed in [9] (as was already mentioned in the Introduction); depinning of dislocations in NaCl was studied in [135, 171, 181], and various softening aftereffects were also investigated in other crystals (ionic–covalent ZnS [94], molecular C_{60} [93]) and polymers (PMMA, PVC [131–133]) in pulsed MFs of up to 30 T. The main phenomenological distinctions of the effect of such MFs from

the effect of weak fields were reversibility (except in ZnS) and high threshold values of B (~20 T) in certain cases (Fig. 13). In experiments where the change in microhardness ΔH was measured after the exposure of samples (NaCl, C_{60}, polymers) to a pulsed MF, the characteristic relaxation times of the states induced by the field were equal to several hours or even days, which unambiguously indicates that the processes proceeded on the atomic–molecular level.

In a special series of experiments, it was established that, although the magnitude of the MPE depends on the duration and rate of rise of MF pulses (which was also observed in weak fields in most cases), the vortex electric field does not make a dominant contribution to softening. For example, in ionic crystals, the minimum duration of an MF pulse causing depinning was ~10^{-6} s and was independent of the rate of rise and amplitude of MF pulses (Fig. 6). In polymers, on the contrary, the MPE was observed only when the rate of pulse rise was higher than a certain critical value.

The fact that the effects in question can be reproduced many times without a decrease in amplitude on the same sample (in the case of a sufficient time elapsing between successive MF pulses) indicates that, in a strong field, metastability of the initial structure is not a necessary condition for the magnetic sensitivity to arise. It is likely that the energy of an MF suffices to activate certain multistage reactions in the defect structure. By performing an appropriate heat treatment, the contributions from different defects to the MPE were separated. For example, as seen from Fig. 13, the field dependence of dislocation path lengths exhibits a maximum at B = 20 T in as-quenched NaCl crystals, whereas in an aged crystal this field is the threshold for depinning. Therefore, the weak and strong MFs act on different objects in the crystals.

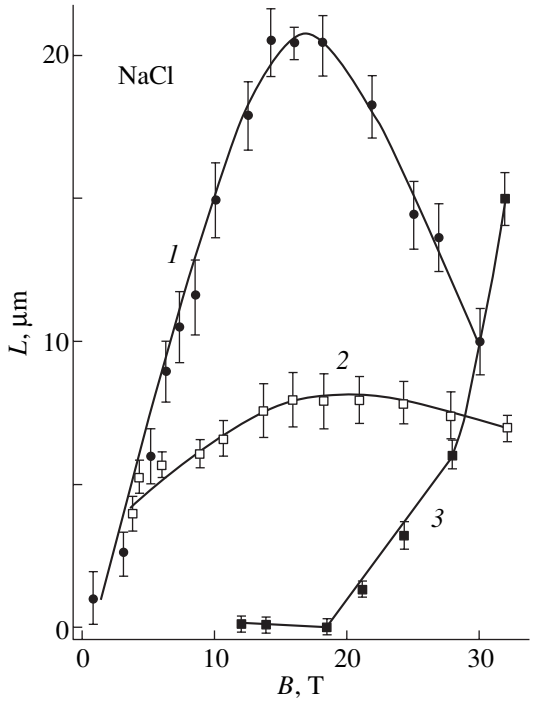

Fig. 13. Dependence of the path lengths L of edge dislocations in NaCl single crystals on the amplitude of an MF pulse stimulating depinning with duration $t_B = 10^{-4}$ s: (*1*) as-quenched (from T = 750 K) crystals, T = 293 K; (*2*) same at T = 120 K; and (*3*) aged crystals, T = 293 K.

3.5. Effect of a Magnetic Field on Phase Transformations

On general grounds, it is clear that, near a phase transition point, a real system can be in an unstable state (e.g., superheated or supercooled relative to the line of phase equilibrium). In this state, weak external forces can produce a noticeable effect in the system. Indeed, the effects of MFs on the nucleation, morphology, growth kinetics, and properties of a new phase in various materials (ferromagnets, nonmagnetic metals and alloys, dielectric and semiconducting crystals, amorphous systems, polymers, etc.) have been discovered and intensively studied [5, 6, 182–191]. Certain inventions in this area have been known for hundreds of years; among them is the storm-glass, which is a sealed glass ampoule filled with a supersaturated solution of salts that form a dynamic dendrite structure, whose morphology and volume are believed to vary according to variations in the geomagnetic field.

In this review, we consider the effect of a weak MF on the physical properties of new phases, which are nucleated and grow either in the presence of an MF or after magnetic treatment of the initial material. In [186, 187], it was shown that the treatment of oxide glass $MgO–Al_2O_3–SiO_2$ by applying a series of a few thousand MF pulses ($B \approx 0.1$–1 T) at $T \approx 300$ K decreases the temperatures of glass formation and crystallization and the level of internal stresses, changes the activation energies for various relaxation processes, etc. In [188], the effect of an analogous series of MF pulses was studied on the phase composition, structure, and mechanical properties of a Cu–Sn-based cast alloy during cooling of its melt. A decrease in the quantity of the eutectoid phase and grain size and an increase in microhardness were observed. Melts of flexible-chain polymers subjected to an analogous series of MF pulses exhibited a decreased concentration of nucleation centers and subsequent growth of larger dendrites than in reference samples [188–191]. The spectra of thermostimulated polarization and depolarization (in the solid state) also changed noticeably in shape.

3.6. Microstructure and Nonmechanical Structure-Sensitive Properties

MF-induced mechanical responses are the result of a complex, multistage process, which starts with elec-

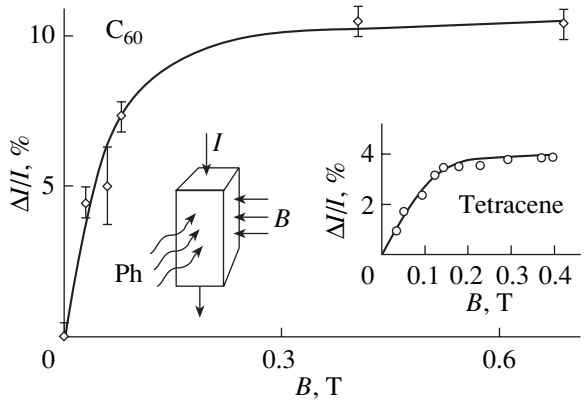

Fig. 14. Increase in photocurrent ΔI caused by application of a static MF as a function of this field B for C_{60} single crystals. Insets show an analogous $\Delta I(B)$ dependence for tetracene [202] and the diagram representing the test.

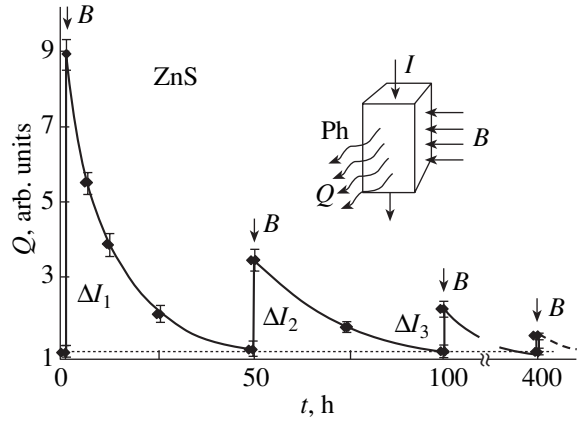

Fig. 15. Dependence of the electroluminescence intensity of an ZnS single crystal on elapsed time from the first application of an electric field (E = 1 kV/mm, f = 800 Hz) under conditions where several successive MF pulses are applied (B = 7 T, τ_B = 10 ms). Arrows indicate the moments at which MF is switched on. T = 293 K. Inset shows the diagram representing the test.

tronic excitations in structural defects. In order to decrease the number of intermediate steps in the branching chain between the primary act of the MF influence and the measured response, it is advisable to measure responses that are close to the processes proceeding in the electronic subsystem. Such responses are the photoconductivity and optical, luminescence, radiospectroscopy, and other characteristics, which are associated with purely electronic processes. Changes in the atomic structure of defects are intermediate between these characteristics and macroscopic mechanical properties. We will consider only the most prominent examples of numerous publications on this subject.

As described in Section 2, the microhardness of C_{60} fullerite molecular crystals is sensitive to weak MFs and ultralow doses of β radiation (Fig. 12). In [192–194], it was found that a magnetic field $B < 1$ T produced a nontrivial effect on the photoconductivity of C_{60}. The increase in photocurrent ΔI caused by the application of an MF was independent of the mutual orientation of the magnetic field and the direction of the current density and reached saturation at $B \approx 0.2$ T (Fig. 14). The MF had no effect on the magnitude of a dark current. Therefore, the observed phenomenon is not a classical galvanomagnetic effect (such as the Hall effect, magnetoresistance, etc.). This effect is close to the influence of the MF on the photoconductivity of molecular crystals of aromatic hydrocarbons (this influence was explained in terms of the spin-dependent recombination of electron–hole pairs [195, 196]). Such an interpretation of the effect observed in C_{60} is supported by the fact that the increase in photocurrent ΔI becomes larger under the conditions of paramagnetic resonance in a static MF and a perpendicular microwave MF [193]. Analogous effects of weak MFs on microwave and photoconductivity and fluorescence in single crystals of silicon [197–199], polyacetylene [24, 200], polyvinil carbazole [201], tetracene [202], rubrene [203], anthracene [204], and even clorophyll molecules [205] have also been interpreted consistently as spin-dependent processes controlled by an MF.

It is important that the application of a magnetic field ($B \approx 10^{-2}$–10^{-1} T) changed the quantities measured in the studies mentioned above by at most a few percent at liquid-helium temperatures and even less significantly at room temperature, whereas the plastic characteristics can change by tens and even hundreds of percentage points in the same fields. This testifies once again that mobile dislocations are highly sensitive to the state of the electronic subsystem of defects and can be used as an atomic-scale probe to study individual small atomic complexes in slip planes.

A record-large magnetic effect (up to 100%) was observed in ZnS in [206], where the intensity of electroluminescence (EL) and its change caused by MF pulses of amplitude B = 7 T and duration 10 ms were measured (Fig. 15). It was assumed that such a drastic MF-induced EL amplification is due to depinning of dislocations, which sweep electrons out of traps and transfer them to pores (dislocation sinks), where the electrons are accelerated by the strong electric field produced by these same dislocations. The vortex electric field was much weaker than the electric field applied to a sample and had no significant effect, as follows from simple estimates and the very slow decay of the increased EL intensity (lasting tens of hours) after the application of a millisecond pulse of an MF.

The effect of a weak MF on the ferroelectric and dielectric properties of ferroelectrics (coercive field, Curie temperature, permittivity, dielectric losses, etc.) was detected and studied in [207, 208] and on the tem-

perature coefficient of resistance of $YBa_2Cu_3O_{7-x}$ near the superconducting transition temperature in [209]. Of particular interest are the effects of MFs and their long-term aftereffects (lasting a few months) on semiconducting materials and structures (Si [210–213], Sb–As [214], InAs [215, 216], $Cd_{0.5}Zn_{0.5}S$ [217], and others [218, 219]), where multistage rearrangements of impurity complexes and structural transformations were observed. In the majority of cases, the effects were interpreted in terms of spin-dependent primary interactions, which give rise to atomic diffusion processes in a metastable system.

In concluding this section, the series of studies [220–223] should be mentioned in which the aftereffects of weak MFs (~0.1 T) alone or in combination with low-dose irradiation were observed on the operating parameters of silicon-based MIS structures, which are extensively applied in field-effect semiconductor devices and integrated circuits. It was shown that magnetic treatment can be used to cull potentially unreliable items, stabilize the characteristics of nondefective ones, etc.

4. NATURE OF THE MAGNETIC-FIELD SENSITIVITY OF NONMAGNETIC MATERIALS

4.1. Main Problems in Interpreting Magnetoplastic Effects

The abundance and diversity of experimental data obtained independently by numerous research groups using radically different techniques provide conclusive evidence of the existence of the (paradoxical, at first glance) anomalously strong effect of very weak MFs on the physical-mechanical and other structure-sensitive properties of solids. This raises the fundamentally important question of the nature of these phenomena. Can they be explained in terms of a single universal mechanism (or in the framework of a single approach) or do the reasons depend on the materials and test conditions? Early, unsuccessful attempts to interpret the MPE drew on the Lorentz force exerted on moving charged dislocations by the MF, the vortex EF arising when a magnetic field is switched on or off, the forces caused by the magnetization of ferromagnetic precipitates in a diamagnetic matrix, the forces associated with gradients of the magnetic susceptibility caused by lattice strains near dislocation cores, etc.

In the models mentioned above, insurmountable obstacles arise even at the first step and are associated with the fact that the relevant forces and energies $\Delta U_m \sim \mu_B g B$ derived by any structural element in a magnetically ordered medium from magnetic fields $B \sim 1$ T are small; therefore, under these conditions, the MF cannot change the state of a system at thermodynamic equilibrium. In particular, direct action of the MF cannot change the probability of dislocations breaking away from pinning centers, because the activation energy for this process is $U_a \gg kT_R \gg \mu_B g B$ (Fig. 16).

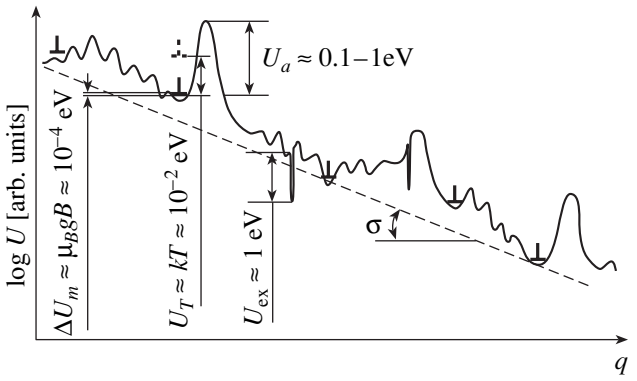

Fig. 16. Potential profile for dislocations in a crystal under conditions where there are internal and external stresses, exchange forces, and an MF (schematic). U_a, U_{ex}, U_T, and U_m are the activation energy for surmounting an obstacle, exchange interaction energy between a dislocation and an obstacle, thermal energy, and Zeeman energy of an electron in the MF; q is a configuration coordinate.

Another group of difficulties encountered in explaining the MPE is associated with the fact that the plastic flow is a complex multistage process and that the usually recorded macroscopic responses are distantly related to the primary acts, whose dynamics can be affected by the MF. Between changes in the state of electrons (which only the MF can influence) and, say, the yield stress (or even the mobility of individual dislocations), there are several poorly understood hierarchical levels of the dynamics of the defect structure of a solid. An (incomplete) enumeration of these levels can be given as follows: a change in the spin and spatial quantum numbers of electrons in interacting defects, atomic rearrangement of the quasi-molecule formed by a pinning center and a short section of a dislocation core in contact, dislocation break-away from a pinning center and motion to another strong pinning center, multiplication and interaction of moving dislocations, and the macroscopic response of the detector used. Most of these processes can be treated in terms of the popular string model of dislocations, which, in fact, ignores the atomic structure of the dislocation core. The dynamics of the first several processes, which are of very short duration (roughly, ~10^{-12}–10^{-6} s), are poorly studied in the physics of plasticity; however, only the dynamics can be affected by the MF. Thus, analysis of the possible nature of the MPE has revealed many gaps in our knowledge on the mechanisms of dislocation motion and break-away from pinning centers in general, not only in the presence of a magnetic field.

The problems that arose in explaining the MPE and could not be solved in the framework of the elementary approaches indicated above stimulated a search for other methods that invoke chemical kinetics, chemical physics of spin-dependent processes, the theory of catalysis of chemical reactions, and other interdisciplinary sciences that had been successfully used to interpret profound magnetic effects in nonmagnetic media.

4.2. Spin-Dependent Processes in Solids

In pioneering papers [16–25], well before the discovery of the MPE in diamagnetic crystals, Frankevich and coworkers described the effects of a weak magnetic field (B = 0.1–1 T) on the dark- and photoconductivity of organic semiconductors, their fluorescence, and other photoelectric properties at close to room temperature. Those effects were fundamentally different from the well-known galvanomagnetic effects in that they reached saturation in fields $B < 1$ T (Fig. 14), were independent of the mutual orientation of the field **B** and the current density **j**, etc. The effect of a static MF on the radical reactions proceeding in solutions was first observed in 1972 [224]. In the reaction of pentafluoride benzyl chloride with *n*-butyllithium, the ratio between the products changed by tens of percent after the application of a magnetic field B of approximately 2 T. In [225], this effect was interpreted as the result of singlet–triplet transitions in a radical pair. Later on, studies performed by Buchachenko, Molin, Sagdeev, Salikhov, Frankevich, and other researchers extended the range of MF-dependent phenomena and the range of materials in which these phenomena were observed (see reviews [195, 196]).

Radical progress toward an understanding of the nature of such phenomena was achieved in experiments [226–228], the notion of which was suggested as long ago as 1967 in [229]. In those experiments, sudden changes in the intensity of fluorescence, dark currents, and photocurrents were observed to occur in organic semiconductors of the polyacene series in crossed static and microwave MFs satisfying the conditions of electron paramagnetic resonance (EPR) for particles with spin $S = 1/2$ and a spectroscopic splitting factor g close to 2. These changes strongly suggest that the MF has an effect on the spin degrees of freedom (rather than orbital magnetic moments, moving charges, etc.). The experiments were similar, in principle, to the classical radiospectroscopy technique, except that a change in the intensity of the photoelectric and luminescence processes rather than a sharp change in the absorption of microwave energy in a resonator containing a sample was observed in the system under study as resonance was approached. One of the most interesting features of this method of detecting and studying EPR is the very high sensitivity to the presence of paramagnetic centers in a system. In exceptional cases, the sensitivity was so high that several paramagnetic centers could be detected. Later on, a wide range of analogous techniques was given the name reaction yield–detected magnetic resonance (RYDMR), i.e., resonance detected using the magnitude of a response (yield) to the application of an MF. The results obtained using this method were described in detail in [230]. Analogous approaches are used in the well-known optically detected magnetic resonance (ODMR) method [231, 232] and in studies of EPR spectra of dislocation dangling bonds in Si, which are detected by measuring the change in photocurrent at resonance [196, 198]. A number of effects have been explained in terms of the Kaplan–Solomon–Mott theory of spin-dependent electronic processes [233]. An even wider range of magnetic phenomena (the effect of a weak MF on the kinetics and yield of certain radical reactions, the selective influence of crossed static and microwave MFs satisfying the EPR conditions on these characteristics, polarization of electronic and nuclear spins caused by a chemical reaction, radio-wave radiation accompanying the relaxation process in chemically polarized spin subsystems, spin catalysis, etc.) is covered by the theory of spin-dependent phenomena in chemical physics [234–236]. This theory, as applied to the kinetics of radical reactions, is based on the following facts following from the angular momentum conservation law for a closed system and the Pauli exclusion principle, which permits at most one electron to be in any single electronic state in the system:

(1) Only those thermodynamically possible reactions occur that satisfy the spin conservation law.

(2) Since the electrons that reside in a reaction cell for a period of time interact with the environment (including the external MF and the intrinsic nuclear MF), certain thermodynamically possible spin-forbidden reaction channels can become partially or fully allowed, which, in turn, can change the reaction rates and the ratios between the yields of reaction products.

(3) A weak MF can have a significant effect only on nonequilibrium (spin, molecular) systems that go, in the course of their evolution, through short-lived excited states whose multiplicity can be changed. A macroscopic effect is produced only when the molecular dynamics keep pace with the spin dynamics and ensure fast removal of new products (forming under the MF) from the reaction cell before their recombination occurs and the excitation relaxes to the initial state.

(4) A reaction should have several thermodynamically possible channels, and the changeover between them should be effected by an MF.

Thus, the MF can produce an effect by making spin-forbidden reactions allowed rather than by changing their energetics (Fig. 17). Therefore, the apparent contradiction between the smallness of the magnetic energy and the noticeable effect produced is resolved.

However, for this effect to occur, several conditions must be satisfied simultaneously. First, the mechanisms indicated above must not contradict thermodynamics. Clearly, these mechanisms can operate in a system where the final state is thermodynamically favored over the initial state rather than in a system at thermodynamic equilibrium. Furthermore, conditions should be provided under which a weak MF can maintain a noticeable nonequilibrium polarization in the spin subsystem; otherwise, there will be no noticeable macroscopic effects.

The simplest radical pair with spins $s = \pm 1/2$ residing in a reaction cell can be in two possible states, namely, a singlet (S) with $\sum_{1,2} s_i = 0$ or a triplet (T) with $\sum_{1,2} s_i = 1$ depending on the mutual orientation of the spins (Fig. 18a). The difference in exchange energy between these states is ~1 eV when the distance between the members of a pair is of the order of the interatomic distance r_0 in condensed media. Clearly, a magnetic field $B \sim 1$ T cannot change the state of a radical pair under these conditions. At larger distances ($r \gg r_0$), we have $U_T - U_S = 0$ and the MF also has no effect. The MF can reverse the spins only in the intermediate range $r_0 \le r \le 2r_0$, where $\Delta U_m \sim 2\mu_B g M B \approx U_T - U_S$. A radical pair can transfer to this state either through its excitation from the ground state caused by thermal fluctuations, mechanical deformations of bonds, ionizing radiation, etc., or by its members approaching each other from the position where they were widely spaced. The lifetime τ^* of this intermediate state has to be longer than the spin conversion time τ_{S-T} due to any possible mechanism under an MF in order for this conversion to have a chance to occur. On the other hand, in a solid, in order for the MF-induced change in the occupation of states to have no time to relax, the time τ^* has to be shorter than the spin–lattice relaxation time τ_{S-L}. Therefore, there is a range of values of the lifetime of a short-lived MF-sensitive state

$$\tau_{S-T} < \tau^* < \tau_{S-L}, \qquad (1)$$

within which the MF can have a noticeable effect on a spin-dependent reaction. Obviously, an increase in the MF strength extends this range to shorter times by increasing the spin conversion rate in a radical pair, whereas a decrease in temperature extends this range to longer times. The decay time τ_r of a radical pair in the T state should be shorter than the time of the inverse (T–S) transition, $\tau_r < \tau_{T-S}$ otherwise, the radical pair reverts to the initial position and the effect of the MF vanishes. Clearly, the probability that the members of a radical pair in the T state will move farther apart increases with temperature.

Thus, significant changes in the reaction rate and channeling can occur only as a result of a delicate balance between the spin, chemical, and molecular (as well as dislocation, in plasticity) dynamics. It should be noted that the scheme described above follows from "first principles" and is independent of the assumptions (made further) regarding the mechanisms of intercombination transitions in radical pairs, the characteristic times of elementary events, the nature of paramagnetic centers involved in the reaction, etc.

As for the specific mechanisms of spin conversion in an MF, Brocklehurst [237] and Kaptein and Oosterhoff [238] came up with the fundamental notions of the importance of S–T transitions in the recombination of radical pairs and the possible mechanisms of the influ-

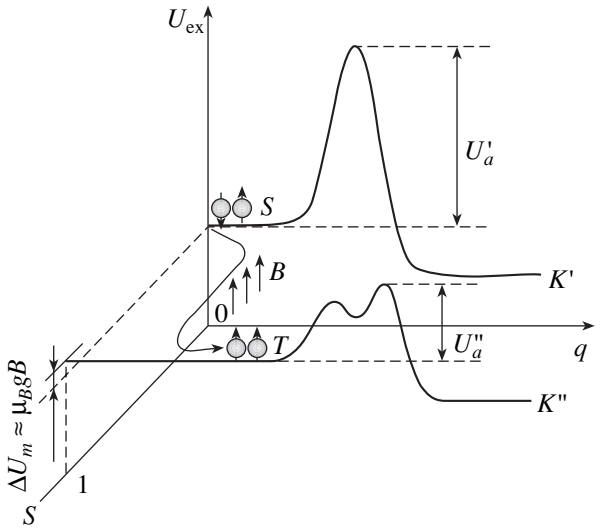

Fig. 17. Change in the rate constant of a spin-selective chemical reaction K caused by an external MF: U'_a is the activation energy for decay of a molecule in the S state, and U''_a is the same for the T state.

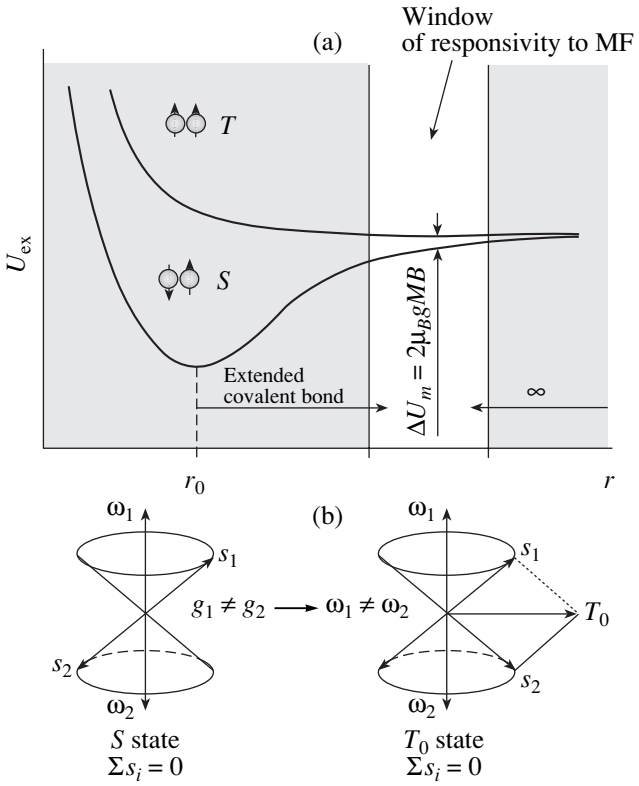

Fig. 18. Mechanisms for spin conversion in an external MF. (a) Change in multiplicity of the state of a short-lived radical pair and (b) Δg mechanism for spin conversion in a radical pair; ω_1 and ω_2 are the frequencies of Larmor precession for paramagnetic centers with g factors g_1 and g_2, respectively.

ence of an external MF and the internal nuclear MF on this process. These ideas (and their modifications) have been used to the present time, and the corresponding mechanisms can be reduced to three, called the Δg, *HFI*, and ΔJ mechanisms, or to combinations of them [239, 240]. In the first mechanism, the spin state of a radical pair changes in an MF because of the difference in the g factors of the two interacting radicals. In the second, the hyperfine interaction is assumed to be of importance and the effect of the magnetic moments of the atomic nuclei of radicals on the spin state of electrons is taken into account. Finally, in the third mechanism, the spin catalysis of transformations involving the spin of a third particle that approaches a radical pair is of importance.

For a number of reasons, the Δg mechanism is assumed to be the most probable in the spin conversion under a magnetic field $B \sim 1$ T; due to a small difference (usually, of the order of 10^{-3}–10^{-4}) in the g factors of two radicals, the precession frequencies of their spins in an MF are slightly different and the radical pair transfers from the S to the T state and vice versa with a frequency $f \approx \mu_B \Delta g B/h \approx 10^8$–$10^9$ s^{-1}, where (h is Planck's constant (Fig. 18b).

The spin conversion in the system will be irreversible and continuous and saturation will not be reached in the spin system if the reaction products are rapidly removed from the reaction cell; therefore, the molecular dynamics should follow the spin and chemical dynamics.

The MF will not produce a noticeable effect following the scheme described above if one of the conditions indicated above is not satisfied.

4.3. Plastic Flow as a Chemical Reaction Proceeding in a Crystal

In the early 1990s, Al'shits and Molotskiĭ proposed using these ideas in the physics of plasticity [67, 241], in particular, with the aim to explain the nature of the MPE. At that time, there were no strong grounds for this. However, it was known that dislocation cores contain paramagnetic centers (not only in covalent crystals, where it is clear that these centers are associated with dangling bonds, but also in ionic, metallic, and ionic–covalent crystals, where electrons are captured by jogs, kinks, and other specific features of cores); the concentration of these centers usually increases with increasing strains [242–248]. There were also analogous data on paramagnetic centers in impurity–vacancy complexes in ionic and ionic–covalent crystals, glasses, etc. Therefore, in these macroscopic diamagnetic materials, paramagnetic centers (localized electrons, holes, triplet excitons, ion radicals) are always present and can be involved in exchange interaction.

As follows from the experimental data presented in Sections 2 and 3, the type and state of impurities are of decisive importance for the MPE in ionic and covalent crystals. This sensitivity to impurities manifests itself differently, depending on the experimental conditions. In many cases, its manifestations can differ radically, as in σ and B tests (Figs. 8, 11) or in the dependences of the path lengths of individual dislocations and the strain-hardening coefficient on the Ca concentration in the case of macroscopic plastic flow (Figs. 3a, 9). We explain these illusory contradictions in the corresponding subsections.

The height of a local barrier produced by an impurity to dislocation motion is determined by many factors, such as the ionic radius, charge, spin, and number of impurity atoms in the complex. In general, the interaction energy U between a dislocation and a pinning center can be written as the sum of three terms:

$$U = U_d + U_e + U_{\text{ex}}, \tag{2}$$

where U_d is the elastic interaction energy with the dilatation field of the pinning center and U_e and U_{ex} are the electrostatic and exchange energies, respectively.

Experimental data on the influence of impurities on the MPE are scarce and cover a very narrow range of impurities. These data are insufficient to determine and predict the strength of pinning centers associated with certain impurity atoms. However, based on the experimental data, the following conclusions can be drawn.

In all studies into the MPE, dislocations moved under conditions where local obstacles are overcome through thermal activation. In this regime, after a dislocation (or, more specifically, its segment) is locked by an obstacle, it takes time for an appropriate thermal fluctuation to arise and allow the dislocation to cross or skirt the obstacle. The strength spectrum of obstacles in a real crystal is always very wide, even for one type of impurity and for dislocation path lengths shorter than the average distance between forest dislocations (which is typical for the majority of experimental studies described above).

In order to compensate the excess ionic charge, a different-valence impurity in an ionic crystal (Ca, Cu, Pb, Mn, Eu) is usually combined with a cation vacancy to form an impurity–vacancy dipole (IVD). These dipoles can exist in the isolated state; however, a high proportion of them form complexes of two, three, and more dipoles (dimers, trimers, and so on), which gives a gain in energy (per pair) of approximately 0.1 eV. There are always complexes that differ in the number Z of IVDs in them, with their distribution in Z depending on the sample history (the growth technique, heat treatment, temperature, aging time, etc.). From elementary considerations and a great body of experimental data (see, e.g., [249]), it follows that pinning centers containing from a few IVDs to tens of IVDs are of utmost importance in the plasticity of a crystal. The strength of pinning centers increases with Z, but their proportion decreases (since the mass of the impurity in the sample is conserved). Complete equilibrium between these

states of impurity is practically never reached, and relaxation processes in this system can last for years. Therefore, the history of a crystal, which influences the mechanical mobility of dislocations, is also quite important for the MPE. Indeed, the type of impurity and its state, which can be changed by heat treatment, illumination, and irradiation, were observed to play an important part in the MPE (see Sections 2, 3). For example, a Ca impurity with an ionic radius of 0.197 nm made NaCl crystals sensitive to an MF in all experiments (the ionic radius of Na is 0.186 nm), whereas the Cu and Mn impurities (ionic radii of 0.127 and 0.136 nm, respectively) suppressed the MPE. It is clear that, even if the exchange energies are equal, the last two impurities produce much larger dilatational strains in the lattice than the Ca impurity; therefore, the spin state of these impurities can affect the value of U in Eq. (2) only slightly.

Intensive plastic deformation or relaxation of the structure due to internal stresses brings about the formation, motion, interaction, annihilation, and other transformations of the defect structure of a crystal, which can be treated as chemical reactions between various reagents (Fig. 19). The conditions of the reactions between structural defects in a crystal and between reagents in the liquid and gaseous phases (which are usually dealt with in spin chemistry) differ radically for the following reasons:

(1) Contrary to a chemical reaction in a test tube, a real crystal contains a host of different reagents capable of reacting, especially under conditions of plastic deformation (point defects, their complexes and aggregates, different types of dislocations, defects captured by dislocation cores, etc.). Many of them cannot be considered chemically unchanged, because they represent complex quasi-molecules capable of undergoing changes in structure and even composition.

(2) All structural defects are in environments that can affect their properties by changing their electronic structure and restricting their possible orientations, positions, and mobility.

(3) The time that two radicals entering into interacting defects spend in a reaction cell is determined by the external and internal stresses rather than by the random thermal motion, as in a liquid.

(4) The spin–lattice relaxation in a crystal destroys spin correlations in pairs faster.

Nevertheless, the existing notions and theories of spin-dependent and magnetic effects in radical reactions can be taken as a starting point for analyzing the nature of the MPE in solids.

In the absence of detailed information on the dynamics of the short-run stages of the interaction between a dislocation and a pinning center, we can make only rough estimates of their characteristic times. Let us represent the motion of a dislocation through a random network of obstacles in a slip plane as a cycle

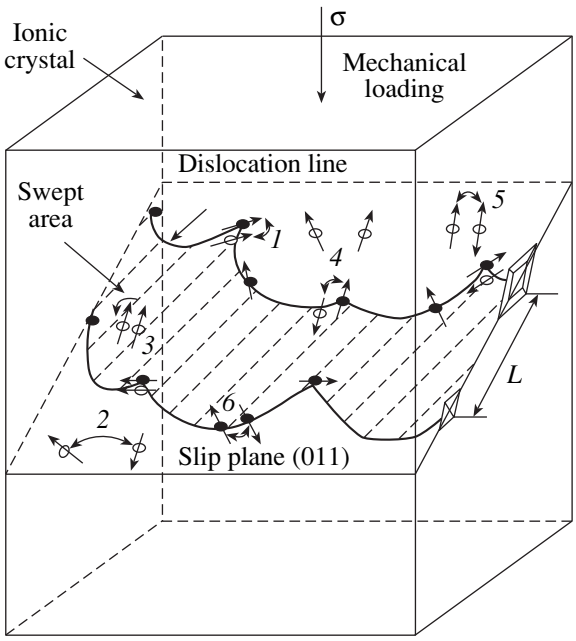

Fig. 19. Plastic deformation as solid-state chemical reactions between structural defects: (*1*, *2*, *3*) monomolecular reactions of dislocation break-away from an obstacle, decay of a complex of point defects, and its reorientation, respectively; and (*4*, *5*, *6*) bimolecular reactions of dislocation pinning, formation of a complex of point defects, and recombination of paramagnetic centers in a dislocation core, respectively.

repeated many times (Fig. 20). We consider separate stages in this cycle and estimate their characteristic times t^*.

The macroscopic velocity $\langle V \rangle$ of a dislocation is determined by the average distance between obstacles in the slip plane $\lambda = a\sqrt{Z/C}$, the average (waiting) time spent near an obstacle t_w, and the time of viscous motion of the dislocation between obstacles $t_m = \lambda B/\tau b$ (where a is the lattice parameter, B is the coefficient of viscosity for a moving dislocation, τ is the shear stress in the slip plane), namely, $\langle V \rangle = \lambda/(t_w + t_m)$. By neglecting t_m (which is a good approximation for the majority of the data described in Sections 2, 3), we obtain $t_w \approx a\sqrt{Z/C}/\langle V \rangle$. Numerical estimates show that, in experiments on dislocation depinning under an MF, $t_w \approx 10^{-2}$–1 s; in experiments where the mobility of individual dislocations is measured, $t_w \approx 10^{-3}$–10^{-1} s; and in experiments on macroscopic deformation, $t_w \approx 10^{-5}$–10^{-3} s (depending on the type and concentration of the impurities, stresses, temperature, etc.). These times are much shorter than the characteristic times of the spin dynamics.

When forced against an obstacle by stresses, a dislocation makes many attempts to overcome it, with the attempt frequency being determined by the phonon fre-

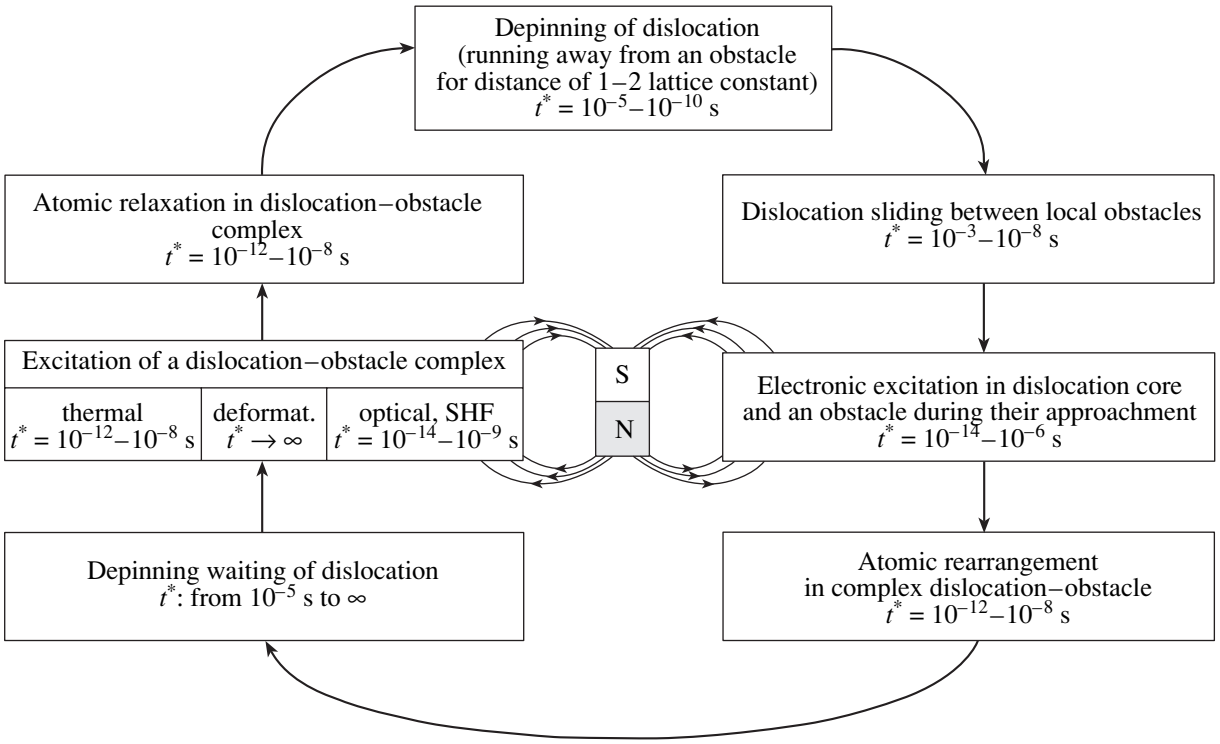

Fig. 20. Main stages of one cycle of dislocation motion through a random network of local obstacles and their characteristic times. A magnetic field can affect only short-lived excited states of electrons in interacting defects.

quencies (f_{ph} = 10^6–10^{13} Hz) and the natural frequencies of vibration of the dislocation structure [250]:

$$f_n = (n/2\pi\lambda)\sqrt{12\gamma/m}$$
$$\approx (0.4n/\lambda)\sqrt{G_S/\rho} \approx n(10^8\text{–}10^9)\ \text{Hz},$$

where γ is the linear stress, m is the effective linear mass of the dislocation line, G_S is the shear modulus, ρ is the density, and n is the harmonic number.

Thus, a dislocation makes millions of attempts before it succeeds in overcoming a barrier. During these short-lived excitations, spin conversion can occur under the action of an MF. Molotskiĭ [251] assumed that a dislocation surmounts an obstacle through the motion of a kink along the dislocation line; the characteristic interaction time in this case was found to be ~10^{-7}–10^{-9} s. It is unlikely that this mechanism for dislocations overcoming local barriers is dominant in ionic crystals; however, with this mechanism, one can estimate the duration of this stage.

In actuality, there are also several intermediate stages. As a dislocation approaches an obstacle, there appears electronic and molecular excitation of the structure of the interacting segment of the dislocation and atoms of the obstacle and only then does the waiting period for an appropriate dislocation begin (if the obstacle was not surmounted immediately). The characteristic times of this stage are determined by the time required for the terms of the interacting atoms to approach each other, $t^* \approx B/\tau = 10^{-10}$–$10^{-9}$ s, and by the eigenfrequencies of the dislocation string and the phonon spectrum.

Analogously, after the spin conversion in a radical pair occurs, time is required for the decelerated dislocation segment to be displaced by several lattice parameters away from the pinning point. During this time, the segment can be pinned again by other parts of the impurity complex. In other words, an obstacle can be surmounted step by step. In this case, the characteristic time required for the segment to move to a noticeable distance from the obstacle can be much longer than $t^* \approx B/\tau$ and amount to a noticeable proportion of the time t_w.

When analyzing the MPE, it is often assumed *a priori* that the molecular and dislocation dynamics are of minor importance and that the spin-conversion stage determines the magnitude of the macroscopic response. For example, in [252], the dislocation-depinning time is identified with the duration of the spin evolution in the dislocation–obstacle system and this latter time is estimated as the product of $1/\nu_c \approx 10^{-1}$–10^{-2} s (see Subsection 2.1 and Fig. 4) by an arbitrarily chosen coefficient ~10^{-2}. The assumption that the MPE decreases sharply as the vector **B** is rotated through an angle of 10^{-2} rad or less is not substantiated and contradicts the data obtained in the case of quasi-static MFs; more specifically, in the majority of experimental studies on the MPE (if not always), the magnetic field was oriented

relative to the crystallographic axes with an accuracy far worse than to within 10^{-2} rad, but this did not prevent different independent research groups from observing the MPE. Furthermore, the time ~10^{-4} s, obtained in [252] using the estimation described above, is still much longer than the characteristic times of the spin dynamics and the spin–lattice relaxation times in ionic crystals at room temperature (which can be estimated to be 10^{-8}–10^{-6} s).

We stress once again that the estimates presented above are qualitative and should be considered a reference point in further analysis of the contributions from separate short-run stages to the MPE.

4.4. Theory of Spin-Dependent Dislocation Depinning

For the sake of simplicity, we assume that all weak obstacles and dislocation cores are paramagnetic. In this case, when sweeping out an area dS, the Nth dislocation interacts with $dn \cong adS_N C/Z$ weak obstacles. The plastic strain rate $\dot{\varepsilon}$ can be expressed in terms of the rate constant $K = dn/Cdt$ of the monomolecular reaction of the breaking of the bond between the paramagnetic center in the dislocation core $\dot{R}_D$ and the paramagnetic center in an obstacle $\dot{R}_{\mathrm{Obs}}$ ($Q \longrightarrow \dot{R}_D + \dot{R}_{\mathrm{Obs}}$) as follows:

$$d\varepsilon/dt = \sum_N A\frac{dS_N}{dt} = \sum_N A\frac{dn}{aCdt} = \alpha K. \qquad (3)$$

Here, $\alpha = A/a$ is a geometric constant.

Thus, measurements of the dislocation mobility or the macroscopic flow rate are equivalent to determining the rate constant K of disintegration of quasi-molecules Q formed by dislocations and obstacles. In a more rigorous treatment, one should take into account nonparamagnetic obstacles, the pure elastic interaction between them and dislocations, and the diffusion of paramagnetic centers both in the bulk of the crystal and along the dislocation core. The currently available methods for measuring the mobility of individual dislocations make it possible to determine MF-induced changes in the rate constant K in elementary events of the reaction $Q \longrightarrow \dot{R}_D + \dot{R}_S$.

The spin-dependent stage of dislocations overcoming paramagnetic obstacles was analyzed in the series of papers [241, 251, 253–260]. In the model at hand, it is assumed that the transfer of a radical pair $\dot{R}_D + \dot{R}_S$ to the S state implies capture and deceleration of the slip dislocation; the transfer of the pair to the T state means that there is no pinning and that the dislocation moves unhindered through the obstacle. In this approximation, the path lengths of dislocations in the presence of an MF are determined by the population ρ_S of the S states in pairs.

In spin chemistry, it is commonly assumed that a radical pair can form in the following three ways: through the decay of a molecule, the transformation of one radical pair into another (disproportionation reaction), and an encounter of two radicals in a solution. All these events can also take place during plastic flow of a crystal. We will restrict our consideration to the following two initial cases. In one case, a dislocation is pinned by an obstacle via a covalent bond and the population ρ is close to unity. In the other case, a dislocation encounters an obstacle and forms a pair with it in a random fashion. Therefore, the probability of each of the four possible states (S, T_0, T_+, T_-) is the same and equal to 1/4. The effect of an MF reduces to a change in the population ρ_S due to the S–T conversion through the Δg mechanism. In this model, the population $\rho_S(B)$ depends on the magnetic field B, the time τ^* it takes for the pair to pass through the resonance region (where $U_S - U_T \approx \mu_B gB$), and the longitudinal (T_1) and transverse (T_2) relaxation times of the correlated spin state. Even the order of magnitude of all these quantities (except for B) is unknown; therefore, only a qualitative analysis can be performed. In the presence of an MF, according to the theory in question, we have

$$\rho_S(B) = \rho_S(0) \times \frac{(1 + T_1/\tau^*)(1 + T_2/\tau^*) + B^2/2B_m^2}{(1 + T_1/\tau^*)(1 + T_2/\tau^*) + (1 + \tau^*/2T_1)(B^2/B_m^2)}, \qquad (4)$$

where $B_m = h/\Delta g\mu_B\sqrt{T_1T_2}$ is a characteristic MF under which intercombination transitions become of importance (a rough estimation of this field gives several teslas).

The population $\rho_S(B)$ determines the concentration of obstacles that form covalent bonds in the presence of the MF:

$$C(B) = C_0\rho_S(B), \qquad (5)$$

where C_0 is the concentration of obstacles for $B = 0$.

In the majority of models proposed, the average velocity and path lengths L of dislocations depend on the concentration of efficient pinning centers as $C^{-1/2}$; therefore, the magnetic field causes a decrease in $\rho_S(B)$ and $C(B)$ and, hence, an increase in L, in accordance with the relation

$$L(B) = L^*\sqrt{\rho_S(0)/\rho_S(B)}, \qquad (6)$$

where L^* is the path length of dislocations for $B = 0$ under the same stresses. Substituting Eq. (4) into Eq. (6), we obtain the following field dependence for $B \ll B_m$:

$$L(B) = L^*[1 + (B^2/4B_m^2)(T_1/\tau^*)(1 + T_2/\tau^*)]. \qquad (7)$$

According to theory, saturation of the MPE takes place in fields $B \gg B_m$.

Experimentally, both a quadratic field dependence and saturation of the MPE in strong fields were observed (see Section 2). However, these facts cannot be taken as evidence of the validity of the theory described above, because there are other models that also predict a quadratic field dependence and saturation [234, 235].

Indirect evidence favoring the approach and assumptions described above is provided by the weak temperature dependence of the MPE and the fact that the effect of an MF on the depinning of dislocations is stronger than that on their subsequent motion, because these properties are indicative of the decisive role played by the spin dynamics, at least in experiments on ionic crystals. Indeed, the insulation of a correlated pair from the crystal lattice (for a time of the order of the spin relaxation time) can decrease the sensitivity of the process of spin conversion under an MF to temperature, and the four times greater population of the S state of pinned dislocations compared with that of moving dislocations can make the effect of the MF on dislocation depinning stronger than that on the subsequent motion of the dislocations. Later on, these arguments were used to explain a number of anomalies observed in the temperature dependences of the strength and magnetostriction of iron–nickel alloys [257, 258].

The mechanism for the MPE described above implies that the limiting stage of the process in which dislocations approach an obstacle, attempt to overcome it, and finally break away from it (Fig. 20) is intercombination S–T transitions in the short-lived intermediate state of a radical pair. In actuality, this assumption is valid only in the case where the chemical, molecular, and dislocation dynamics ensure the removal of the dislocation segment with a paramagnetic center from the reaction cell before the excited T state relaxes to the S state. In [253–260], this inverse transition is ignored, although its probability is not zero in the presence of an MF, especially in the case of the Δg mechanism for spin conversion assumed to operate in those papers.

Perhaps the occurrence of these transitions was the reason why, in certain cases, exposure of a sample to an MF over a long period of time ($\sim 10^3$ s) was required (Figs. 3, 6–8) to accumulate a sufficient number of rare positive events of spin-dependent transformations despite the fact that, in the theory under discussion, the MF duration is of no consequence (provided that this duration is longer than the intercombination transition time $\Delta t \sim h/\Delta g m_B B$; for typical values of $\Delta g = 10^{-3}$–10^{-4} and $B = 0.1$–1 T, we have $\Delta t \approx 10^{-6}$–10^{-8} s).

On the other hand, by ignoring the molecular dynamics, one can apply this theory to other related processes, such as the MF-induced decay of metastable complexes of point defects containing paramagnetic particles. From the experimental data (see Section 2), it follows that, in such complexes, the MF initiates first-order reactions causing a long-term aftereffect, more specifically, slow variations in the structure-sensitive properties observed after the MF is switched off. Analogous considerations were applied in [261] to explain the structural relaxation in oxide glasses.

Finally, in [255], the contribution from the hyperfine interaction to the MPE was considered in much the same way as the nuclear-spin selectivity of certain radical reactions is analyzed in spin chemical physics [234–236, 262]. The nuclear-spin relaxation time is typically many orders of magnitude longer than the electronic spin relaxation time, which makes it possible to consider the behavior of a radical pair in an effective magnetic field B_{eff}. This field is the sum of the external field B and the nuclear field $B_N = A/2\Delta g$, $B_{\text{eff}} = B \pm B_N$, where A is the hyperfine interaction constant. The plus and minus signs correspond to two projections of the nuclear spin, +1/2 and –1/2, onto the direction of an external MF in the simple (and commonly encountered) case where only one of the nuclei of a radical pair possesses an uncompensated spin. With allowance for the hyperfine interaction, we have $\rho_S(B) = (1/2)[\rho_S(B + B_N) + \rho_S(B - B_N)]$. For typical values $\Delta g = 10^{-3}$–10^{-4} and $A = 10^{-4}$–10^{-2} T, the field B_N can lie in the range 0.05–5 T. Therefore, one might expect the isotope effect (i.e., the dependence on the isotopic composition) to take place in the MPE in fields $B < B_N$, which lie within the MF ranges covered in many studies. In magnetic fields $B > B_N$, the nuclear-spin effects are insignificant. Thus, the study of the mechanical properties and, in particular, the MPE can be related to the nuclear and isotopic level of the structure of materials.

4.5. Magnetic-Resonance Softening of Ionic Impurity Crystals

The mechanisms for the MPE discussed in Subsection 4.4 agree with various indirect evidence and considerations [69, 72, 98, 263, 264]. However, qualitative agreement between the experimental and theoretical field dependences of the MPE, characteristic times, critical fields, etc., is not conclusive evidence of the spin-dependent nature of elementary events of the MPE, because there is no theory capable of predicting even the order of magnitude of the quantities under discussion; therefore, different schemes can give results and field dependences that coincide to within this accuracy. Unambiguous proof of the effect of the MF on the spin degrees of freedom could be provided by the fact that measured values of the g factor of the objects subjected to the MF are close to two or an even integer. The purely orbital magnetic moments also experience an external MF, but the g factor for them is equal to unity. The two-times difference in the value of g factors can be easily determined even without the use of a high-precision method. For this purpose, it was proposed in [253] to study the mechanical characteristics in crossed static and microwave MFs under EPR conditions using RYDMR spectroscopy adapted to the physics of plasticity. Experimentally, such EPR techniques were used

to study NaCl : Eu and NaCl : Ca crystals in the following three standard tests: (1) measurement of the path lengths L of individual edge dislocations using selective etching, (2) macroscopic compression of a sample and recording stress–strain curves, and (3) measurement of the Vickers microhardness H [265–270].

As in the traditional EPR study, a sample was placed in a microwave resonator near an antinode of the standing wave (ν_m = 9.5 GHz). A static magnetic field $\mathbf{B}_0$ was applied perpendicular to the microwave magnetic field $\mathbf{B}_1$ and was changed in small steps in the range 0–0.8 T. In the second test, the *in situ* effect was measured, while in the first and third tests, the aftereffect of the crossed static and microwave fields was studied.

The exposure of NaCl : Eu crystals with as-produced dislocations to a magnetic field $\mathbf{B}_0 \perp \mathbf{B}_1$ over 15 min caused a resonance increase in L at $B_0^{(1)} = 0.32 \pm 0.03$ T, $B_0^{(2)} = 0.18 \pm 0.02$ T, and $B_0^{(3)} = 0.12 \pm 0.02$ T (Fig. 21a). These values of the static MF correspond to resonance transitions between Zeeman levels at frequency ν_m = 9.5 GHz for $g_1 = 2.1 \pm 0.2$, $g_2 = 3.8 \pm 0.3$, and $g_3 = 5.7 \pm 0.7$. In the case where only the static MF was applied or the crossed static and microwave MFs satisfied the condition $\mathbf{B}_0 \parallel \mathbf{B}_1$, an ordinary monotonic field dependence of $L(B)$ was observed. These features indicate that the resonance peaks are magnetic in nature.

Experiments at the frequency of a microwave MF ν_m = 152 MGz revealed a resonance increase in L for $B_0 = 5.1 \pm 0.5$ mT [266], which corresponds to $g = 2 \pm 0.2$. This value of the MF is likely the lowest at which the MPE was observed. Note that, in principle, resonance softening can occur even in lower MFs (e.g., a geomagnetic field ~0.05 mT, which corresponds to the resonance frequency $\nu_m \sim 1$ MHz for $g = 2$). Al'shits *et al.* [271] reported that they detected such resonance in their early unpublished study on the MPE but could not explain the phenomenon at that time.

The combined effect of a microwave and a static magnetic field $\mathbf{B}_0 \perp \mathbf{B}_1$ on macroscopic plastic flow in NaCl : Ca was also observed to be resonant in character (Fig. 21b). In this case, a change in the strain-hardening coefficient was measured after the application of a microwave MF (a static MF was applied over the entire period of deformation, and, hence, its individual contribution to the observed effect could be excluded). Analogous results were obtained for the microhardness of the same crystals measured after a 15-min exposure of a sample under the same conditions.

Modulating the microwave field with square pulses varied in duration from 10^{-8} to 1 s made it possible to determine the minimum duration of an MF pulse τ_{min} for which the MPE still occurs (Fig. 21c). At T = 293 K, τ_{min} was ~10^{-6} s, which agrees with the result obtained by initiating dislocation motion with MF pulses of a variable duration (Fig. 6). These results strongly suggest that the MF acts on particles with spin 1/2 and 3/2 and initiates spin-dependent reactions between dislocations and obstacles and inside point complexes, which

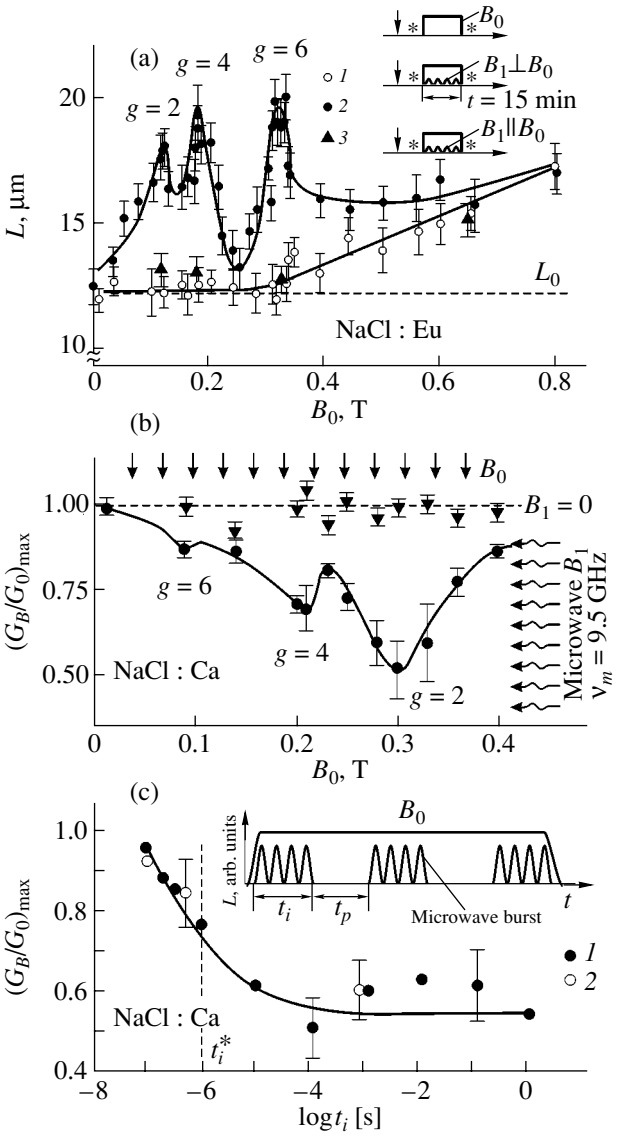

Fig. 21. MF-stimulated softening under EPR conditions. (a) Resonant increase in dislocation mobility in a NaCl single crystal doped with Eu (100 ppm) after prior treatment of the sample by crossed static and microwave MFs; (b) resonant macroscopic softening (a decrease in strain-hardening coefficient) in a Ca-doped NaCl single crystal subjected to active deformation and to simultaneously applied crossed static and microwave MFs (G_B is strain-hardening coefficient under simultaneously applied microwave and static MFs, G_0 is the same in the absence of the microwave MF); and (c) softening of NaCl : Ca under EPR conditions (B_0 = 0.32 T) in the case where the microwave MF is modulated with square pulses as a function of the duration of pulses t_i and the duration of a pause between them t_p: (*1*) $t_p = 10^{-3}$ and (*2*) 10^{-7} s. Insets show the consecutive order of procedures in different series of tests. Notation is the same as that in Fig. 7.

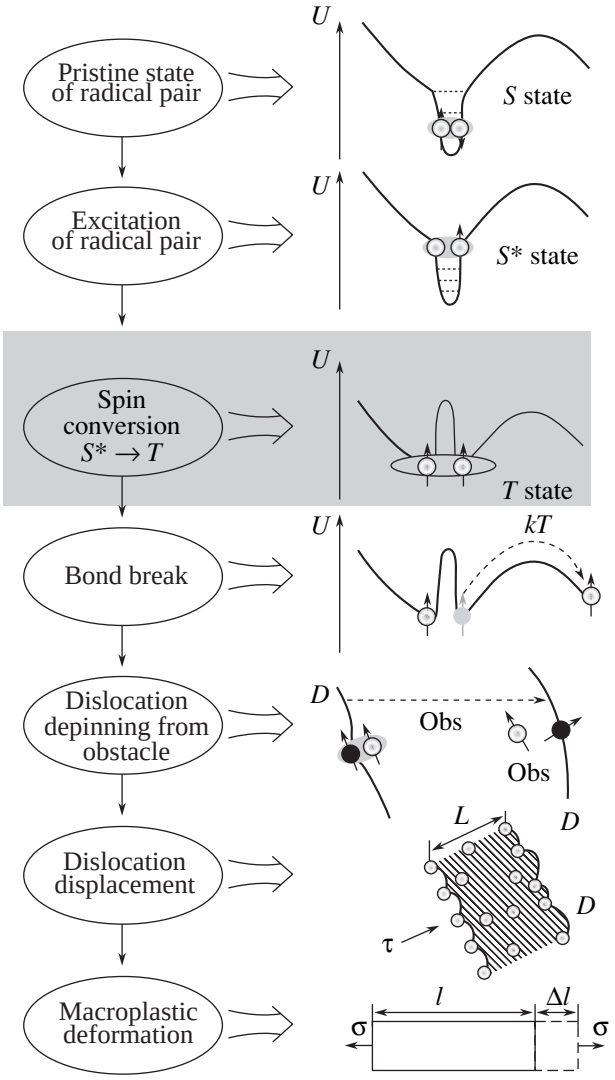

Fig. 22. Schematic diagram of different stages of MPE associated with acceleration of dislocation depinning due to an MF. *D* stands for dislocation, *L* is its path length, Obs stands for obstacle, τ and σ are applied stresses, and *l* and Δ*l* are the length of a sample and its change due to deformation, respectively; (*1*, *2*) elastic and exchange parts of interaction between defects in a crystal, respectively.

then become local obstacles for slip dislocations. In [272, 273], a detailed description is given of the conditions, objects, and the kinetics of transformations occurring in impurity–vacancy complexes in ionic crystals that are initiated by the MF and affect the luminescence, radiospectroscopic, plastic, and other characteristics of ionic crystals. In a wide range of point complexes, polyatomic aggregates consisting of 3 to 5 impurity–vacancy dipoles were found to be the most favorable to the MPE.

From the above discussion, it follows that the mechanical properties of macroscopic diamagnetic crystals with structural defects containing paramagnetic centers can be significantly affected by a weak MF in accordance with the scheme shown in Fig. 22. Certain stages, especially short-run steps, are poorly understood and should be thoroughly studied using high-resolution techniques; the kinetics and even the existence of these steps can be presently inferred only from indirect evidence. Such studies are of importance not only because the electronic-spin dynamics determines the physics of magnetoplastic effects but also since it has an effect on the macroscopic properties of real crystals in the absence of MFs; this effect is masked by other contributions determining the mechanical characteristics of real crystals.

Formally, the effect produced by the MF on the plastic properties of solids by changing the rate constants of reactions proceeding in a crystal is a subject of mechanochemistry or magnetochemistry. However, the MPE has specific features. Indeed, mechanochemistry deals with mechanically stimulated reactions involving the entire volume (or surface) of a solid [274, 275], whereas the MPE is determined by events occurring in nanoscale volumes, which amount to a negligible portion of the solid. The spin-dependent interaction of short-lived paramagnetic particles has also little in common with the traditional subject matter of magnetochemistry, namely, the interrelation between the macroscopic chemical and magnetic properties (most commonly, magnetic susceptibility) of a material [276]. Nominally, all materials in which the MPE has been detected are diamagnetic (except Al, which is weakly paramagnetic, according to handbooks). The presence of paramagnetic impurities (of a typical concentration) does not change this property. While being potentially important, the quantity of a paramagnetic impurity is not the decisive factor for the sensitivity of the mechanical properties to an MF. Since the excited states (which are the only states that can be affected by a weak MF) are short-lived, their instantaneous concentration is extremely small and cannot be detected using standard EPR spectroscopy. This concentration is only indirectly related to the original concentration of the paramagnetic impurity and, hence, to the static magnetic susceptibility, with which magnetochemistry usually deals.

In terms of the chemical-physical classification of magnetic effects, the resonance softening of crystals caused by an MF can be considered as a further extension of RYDMR spectroscopy. This effect provides a unique possibility to investigate short-run stages of the interaction between structural defects in crystals with the goal of not only elucidating the nature of the MPE but also of gaining better insight into the dynamics of nanoscale objects in the absence of an MF.

Controlling the mechanical properties of solids via the spin conversion in nanoclusters of structural defects is physically much closer to spintronics, a new area in physics and high technology, where the desired change in a characteristic of nanoscale objects is obtained by

influencing the spin state of electrons rather than their coordinate wave function.

4.6. Other Possible Mechanisms

Considering the advances made in the theory of spin-selective reactions and the fact that such reactions play a decisive role in the MPE observed in ionic impurity crystals, it is tempting to explain all magnetic effects observed in weakly magnetic solids in terms of this mechanism.

Indeed, the theory of spin-dependent reactions between short-lived paramagnetic particles possesses a number of attractive features. This theory removes the thermodynamic restriction associated with the smallness of the magnetic energy (the MF only catalyzes plastic flow rather than energetically activates it) and solves the problem of thermal noise, because the reacting spins can be considered to be isolated from the lattice and at $T \sim 0$ K over the short period of fast spin conversion caused by the MF. Since the primary MF-sensitive events associated with the MPE occur in nanoclusters of structural defects, the solvent matrix is of minor importance and only indirectly affects the molecular dynamics, spin–lattice relaxation times, etc. These features of local spin-dependent reactions depend only slightly on the nature of a material. However, it seems unlikely that the wide range of phenomena described in Sections 2 and 3 occurring in such differing materials as ionic and semiconducting crystals, metals and alloys, polymers and oxide glasses, fullerenes and ferroelectrics are of the same nature. Other interpretations have also been proposed. For example, the MPE observed in polymers is likely due to the orientation of side groups and segments of chains possessing magnetic moments [277]. However, the mechanisms for energy accumulation in a weak MF and thermalization effects are not discussed in such interpretations.

In [278], using a standard EPR technique, an attempt was made to detect dangling covalent bonds in polycaproamide subjected to prolonged loading. The result was negative, and the conclusion was drawn that the MPE cannot be explained in terms of spin-dependent reactions of covalent-bond breaking in any material. However, Zakrevskiĭ *et al.* [278] failed to detect the MPE in polycaproamide; therefore, their experimental results cannot considered strong evidence against the influence of an MF on the spin degrees of freedom in materials where the MPE is observed. Furthermore, the lifetime of the free radicals formed is, as a rule, short; therefore, even if they are generated at a high rate (which is unlikely in the case of creep tests), their effective instantaneous concentration can be below the threshold of sensitivity of an EPR spectrometer.

In a number of papers concerned with the effect of weak MFs, it is advocated that the magnetic effect can be coherent in space and time (which, in principle, can be the reason for the accumulation of energy in a large number of particles over a long time) and that thermal noise is always incoherent [61]. In other words, it is insufficient to compare these two kinds of energy in value alone. However, well-founded mechanisms were not proposed for the subsequent transfer of the accumulated energy to a smaller number of particles reacting at a given moment of time.

Conjectures that the MPE is associated with a ferromagnetic impurity forming polyatomic clusters are not substantiated by experimental data or even qualitative estimates in the overwhelming majority of cases. For concentrations of Fe, Ni, and other impurities typical of ionic and semiconducting crystals and polymers, even if impurity atoms aggregate in relatively large precipitates, where their magnetic ordering is possible, the concentration is insufficient to have an effect on plasticity.

As already discussed, in the majority of cases, vortex electric fields and currents also cannot be the chief cause of the MPE, although they can contribute to this effect. In a deformed sample, which is an open nonequilibrium system, self-assembling effects and an enhancement of weak external influences can occur; however, these possible effects have not been analyzed yet.

Thus, despite notable advances in the theory of spin-dependent reactions between nonequilibrium structural defects, the mechanisms for the MPE are not clearly understood. However, a physical basis has been provided for further detailed studies of these widespread (as is clear now) phenomena in weakly magnetic materials.

5. CONCLUSIONS

The results of intensive studies performed over the past decade have convinced even skeptics that weak magnetic fields can significantly affect the mechanical properties of many nonmagnetic materials. A basis has been provided for studying the conditions, regularities, and mechanisms not only of the MPE but also of a wider range of multistage processes that proceed in a system of structural defects. Those studies will make it possible to develop a fundamentally new, highly sensitive, high-resolution method of magnetic spectroscopy of short-run phenomena occurring in real solids. In order to adequately describe the MPE in certain materials, not only dislocation-microscopic analysis should be performed but also electronic processes should be considered on the electron-spin and even nuclear-spin level.

The results described above are of fundamental importance for the physics of condensed matter and the physics of plasticity in particular (where, using direct methods, it has been shown for the first time that the spin degrees of freedom of structural defects play an important part in the formation of the mechanical properties of nonmagnetic materials and the sensitivity of

other macroscopic properties to a magnetic field). Furthermore, these results can be used in interdisciplinary sciences. For example, magnetic treatment can be performed, in certain cases, instead of a more prolonged and power-consuming heat treatment, which is applied to stimulate relaxation and stabilize the defect structure in various materials. The study of the regularities and physical mechanisms of the effect of MFs on various properties of solids is part of the more extended study of the effect of low doses (of radiation, chemical action, electromagnetic fields, etc.) on open nonequilibrium systems in animate and inanimate nature, and the effect itself is an important factor of the environment. For example, geodynamics and tectonics are likely to have to take into account the possible softening of the Earth's crust caused by the combined action of the geomagnetic field and its high-frequency fluctuations. Magnetobiology and biochemistry can also employ the lines of reasoning and physical models developed and tested for simpler crystal systems. In any case, progress toward an understanding of magnetoplastic effects has given impetus to the study of other MF-sensitive (electric, optical, luminescence) properties of practically important diamagnetic materials (semiconductors, polymers, fullerites, high-spin organic compounds [279], etc.).

ACKNOWLEDGMENTS

The author is grateful to A.A. Buchachenko, Yu.A. Osip'yan, V.I. Al'shits, Yu.V. Baranov, V.L. Berdinskiĭ, P.Yu. Butyagin, A.I. Deryagin, V.A. Zakrevskiĭ, M.I. Molotskiĭ, V.V. Kveder, V.P. Kisel', N.L. Klyachko, N.A. Tyapunina, S.Z. Shmurak, and many other colleagues for useful discussions and criticism and to his coworkers and followers A.A. Dmitrievskiĭ, V.I. Ivolgin, D.V. Lopatin, R.B. Morgunov, I.A. Pushnin, A.I. Tyurin, and others for their contributions to the long-term studies into magnetoplastic effects performed at the Tambov State University. The author also thanks both reviewers for helpful comments and ideas conducive to improving this work.

This work was supported by the Russian Foundation for Basic Research (project nos. 02-02-17571, 01-02-16573), the Ministry of Education of the Russian Federation (project no. E 02-3.4-263), the federal program "Fundamental Studies, Universities of Russia" (project no. UR 01.01.013), and the federal program "Fullerenes and Atomic Clusters" (project no. 541-02).

REFERENCES

1. S. V. Vonsovskiĭ, *Magnetism* (Nauka, Moscow, 1971; Wiley, New York, 1974).
2. N. T. Ptitsyna, J. Villoresi, L. I. Dorman, N. Iucci, and M. N. Tyasto, Usp. Fiz. Nauk **168** (7), 769 (1998) [Phys. Usp. **41**, 687 (1998)].
3. G. I. Distler, V. M. Kanevskiĭ, V. V. Moskvin, S. N. Postnikov, L. A. Ryabinin, V. P. Sidorov, and G. D. Shnyrev, Dokl. Akad. Nauk SSSR **268** (3), 591 (1983) [Sov. Phys. Dokl. **28**, 43 (1983)].
4. V. M. Kanevskiĭ, G. I. Distler, A. E. Smirnov, Yu. M. Gerasimov, E. I. Kortukova, A. A. Urusovskaya, and E. S. Goryunov, Izv. Akad. Nauk SSSR, Ser. Fiz. **48** (12), 2408 (1984).
5. S. A. Dembovskiĭ, E. A. Chechetkina, and S. A. Kozyukhin, Pis'ma Zh. Éksp. Teor. Fiz. **41** (2), 74 (1985) [JETP Lett. **41**, 88 (1985)].
6. S. A. Dembovskiĭ, S. P. Vikhrov, V. N. Ampilogov, and E. A. Chechetkina, Pis'ma Zh. Tekh. Fiz. **11** (20), 1267 (1985) [Sov. Tech. Phys. Lett. **11**, 523 (1985)].
7. N. V. Kukushkin, S. N. Postnikov, Yu. I. Terman, and V. M. Kedyarkin, Zh. Tekh. Fiz. **55** (10), 2083 (1985) [Sov. Phys. Tech. Phys. **30**, 1227 (1985)].
8. V. N. Davydov, I. I. Fefelova, and E. A. Loskutova, Izv. Akad. Nauk SSSR, Neorg. Mater. **23** (9), 1438 (1987).
9. N. V. Zagoruĭko, Kristallografiya **10** (1), 63 (1965) [Sov. Phys. Crystallogr. **10**, 50 (1965)].
10. I. I. Soloshenko and A. F. Zolotarev, in *Internal Friction Mechanisms in Semiconductor and Metallic Materials* (Nauka, Moscow, 1972), p. 35.
11. S. T. Kishkin and A. A. Klypin, Dokl. Akad. Nauk SSSR **211** (2), 325 (1973) [Sov. Phys. Dokl. **18**, 502 (1973)].
12. A. E. Smirnov and A. A. Urusovskaya, Fiz. Tverd. Tela (Leningrad) **29** (3), 825 (1987) [Sov. Phys. Solid State **29**, 485 (1987)].
13. R. C. Johnson, R. E. Merrifield, P. Avakian, and R. B. Flippen, Phys. Rev. Lett. **19** (6), 285 (1967).
14. R. E. Merrifield, J. Chem. Phys. **48** (12), 4318 (1968).
15. H. Hayashi, Y. Sakaguchi, and H. Abe, Physica B (Amsterdam) **164**, 217 (1990).
16. E. L. Frankevich and E. I. Balabanov, Pis'ma Zh. Éksp. Teor. Fiz. **1** (6), 33 (1965) [JETP Lett. **1**, 169 (1965)].
17. E. L. Frankevich and E. I. Balabanov, Fiz. Tverd. Tela (Leningrad) **8** (3), 855 (1966) [Sov. Phys. Solid State **8**, 682 (1966)].
18. V. I. Lesin, V. P. Sakun, A. I. Pristupa, and E. L. Frankevich, Phys. Status Solidi B **84** (2), 513 (1977).
19. E. L. Frankevich, M. M. Tribel, and I. A. Sokolik, Phys. Status Solidi B **77** (1), 265 (1976).
20. E. L. Frankevich, A. I. Pristupa, and V. I. Lesin, Chem. Phys. Lett. **47** (2), 304 (1977).
21. E. L. Frankevich and A. I. Pristupa, Izv. Akad. Nauk SSSR, Ser. Khim. **50** (2), 220 (1986).
22. E. L. Frankevich, A. I. Pristupa, and V. I. Lesin, Pis'ma Zh. Éksp. Teor. Fiz. **26** (11), 725 (1977) [JETP Lett. **26**, 561 (1977)].
23. E. L. Frankevich, V. I. Lesin, and A. I. Pristupa, Zh. Éksp. Teor. Fiz. **75** (2), 415 (1978) [Sov. Phys. JETP **48**, 208 (1978)].
24. E. L. Frankevich, I. A. Sokolik, D. I. Kadyrev, and V. M. Kobryanskiĭ, Pis'ma Zh. Éksp. Teor. Fiz. **36** (11), 401 (1982) [JETP Lett. **36**, 486 (1982)].
25. E. L. Frankevich, A. I. Pristupa, and V. M. Kobryanskiĭ, Pis'ma Zh. Éksp. Teor. Fiz. **40** (1), 13 (1984) [JETP Lett. **40**, 733 (1984)].
26. L. A. Chebotkevich, A. A. Urusovskaya, and V. V. Veter, Kristallografiya **10** (5), 688 (1965) [Sov. Phys. Crystallogr. **10**, 578 (1965)].

27. L. A. Chebotkevich, A. A. Urusovskaya, V. V. Veter, and A. D. Ershov, Fiz. Tverd. Tela (Leningrad) **9**, 1093 (1967) [Sov. Phys. Solid State **9**, 854 (1967)].
28. S. Hayashi, S. Takahashi, and M. Yamamoto, J. Phys. Soc. Jpn. **25**, 910 (1968).
29. S. Hayashi, S. Takahashi, and M. Yamamoto, J. Phys. Soc. Jpn. **30** (2), 381 (1971).
30. S. Hayashi, S. Takahashi, and M. Yamamoto, J. Phys. Soc. Jpn. **32** (2), 349 (1972).
31. S. Hayashi, S. Takahashi, and M. Yamamoto, Phys. Lett. A **42A**, 171 (1972).
32. V. Ya. Kravchenko, Pis'ma Zh. Éksp. Teor. Fiz. **12** (11), 551 (1970) [JETP Lett. **12**, 391 (1970)].
33. J. M. Galligan, T. N. Lin, and C. S. Pang, Phys. Rev. Lett. **38** (8), 405 (1997).
34. J. M. Galligan and C. S. Pang, J. Appl. Phys. **50** (10), 6253 (1979).
35. V. V. Abraimov, Fiz. Nizk. Temp. **6** (10), 1334 (1980) [Sov. J. Low Temp. Phys. **6**, 651 (1980)].
36. V. S. Krylovskiĭ, V. P. Lebedev, and V. I. Khotkevich, Fiz. Nizk. Temp. **7** (12), 1550 (1981) [Sov. J. Low Temp. Phys. **7**, 750 (1981)].
37. V. P. Lebedev and V. S. Krylovskiĭ, Fiz. Tverd. Tela (Leningrad) **27** (5), 1285 (1985) [Sov. Phys. Solid State **27**, 777 (1985)].
38. J. M. Galligan, Scr. Metall. **18** (7), 653 (1984).
39. V. P. Lebedev and V. S. Krylovskiĭ, Fiz. Tverd. Tela (Leningrad) **32** (3), 544 (1990) [Sov. Phys. Solid State **32**, 315 (1990)].
40. J. M. Galligan, P. D. Goldman, L. Motowidlo, and J. Pellegrino, J. Appl. Phys. **59**, 3747 (1986).
41. C. S. Kim and J. M. Galligan, Scr. Metall. **26**, 1769 (1992).
42. C. S. Kim and J. M. Galligan, Acta Mater. **44**, 775 (1996).
43. V. D. Natsik and L. G. Potemina, Zh. Éksp. Teor. Fiz. **67** (1), 240 (1974) [Sov. Phys. JETP **40**, 121 (1975)].
44. A. M. Grishin, E. A. Kaner, and E. P. Fel'dman, Zh. Éksp. Teor. Fiz. **70** (4), 1445 (1976) [Sov. Phys. JETP **43**, 753 (1976)].
45. J. M. Galligan, in *Physical Acoustics*, Ed. by W. P. Mason (Academic, New York, 1982), Vol. 16, p. 173.
46. V. I. Startsev, in *Dislocations in Solids*, Ed. by F. R. N. Nabarro (North Holland, Amsterdam, 1983), Vol. 6, p. 143.
47. M. I. Kaganov, V. Ya. Kravchenko, and V. D. Natsik, Usp. Fiz. Nauk **111** (4), 655 (1973) [Sov. Phys. Usp. **16**, 878 (1974)].
48. V. A. Grazhulis and Yu. A. Osip'yan, Zh. Éksp. Teor. Fiz. **58** (4), 1259 (1970) [Sov. Phys. JETP **31**, 677 (1970)].
49. V. A. Pavlov, I. A. Pereturina, and N. L. Pecherkina, Phys. Status Solidi **57** (2), 449 (1980).
50. A. I. Deryagin, V. A. Pavlov, K. B. Vlasov, and S. P. Grubova, Fiz. Met. Metalloved. **32** (6), 1231 (1971).
51. K. B. Vlasov, A. I. Deryagin, and V. A. Pavlov, Fiz. Met. Metalloved. **44** (6), 1206 (1977).
52. A. I. Deryagin and R. Sh. Nasyrov, Fiz. Met. Metalloved. **49** (6), 1199 (1980).
53. E. J. Sharp and D. A. Avery, Phys. Rev. **158** (2), 511 (1967).
54. A. M. Kosevich and V. N. Shklovskiĭ, Zh. Éksp. Teor. Fiz. **55** (3), 1131 (1968) [Sov. Phys. JETP **28**, 590 (1969)].
55. V. L. Pokrovskiĭ, Pis'ma Zh. Éksp. Teor. Fiz. **11** (4), 233 (1970) [JETP Lett. **11**, 146 (1970)].
56. D. N. Bol'shutkin and V. A. Desnenko, Fiz. Nizk. Temp. **7** (5), 652 (1981) [Sov. J. Low Temp. Phys. **7**, 321 (1981)].
57. V. I. Al'shits, E. V. Darinskaya, T. M. Perekalina, and A. A. Urusovskaya, Fiz. Tverd. Tela (Leningrad) **29** (2), 467 (1987) [Sov. Phys. Solid State **29**, 265 (1987)].
58. A. N. Kuznetsov, *Biophysics of Low-Frequency Impacts* (Mosk. Fiz.–Tekh. Inst., Moscow, 1994).
59. S. Ueno and M. Iwasaka, J. Appl. Phys. **79** (8), 4705 (1996).
60. V. A. Kovarskiĭ, Usp. Fiz. Nauk **169** (8), 889 (1999) [Phys. Usp. **42**, 797 (1999)].
61. V. N. Binhi and A. V. Savin, Usp. Fiz. Nauk **173** (3), 265 (2003) [Phys. Usp. **46**, 259 (2003)].
62. Yu. I. Golovin and R. B. Morgunov, Chem. Rev. (Part 2) **23**, 22 (1998).
63. V. I. Al'shits, E. V. Darinskaya, O. L. Kazakova, M. V. Koldaeva, E. Yu. Mikhina, and E. A. Petrzhik, Materialovedenie, No. 12, 2 (1999).
64. Yu. I. Golovin and R. B. Morgunov, Materialovedenie, Nos. 3–6, 2 (2000).
65. Yu. I. Golovin and R. B. Morgunov, Priroda (Moscow), No. 8, 49 (2002).
66. *Conduction Electrons*, Ed. by M. I. Kaganov and V. S. Édel'man (Fizmatlit, Moscow, 1984).
67. V. I. Al'shits, E. V. Darinskaya, and E. A. Petrzhik, Fiz. Tverd. Tela (Leningrad) **33** (10), 3001 (1991) [Sov. Phys. Solid State **33**, 1694 (1991)].
68. V. I. Al'shits, E. V. Darinskaya, and E. A. Petrzhik, Fiz. Tverd. Tela (St. Petersburg) **35** (2), 320 (1993) [Phys. Solid State **35**, 162 (1993)].
69. V. I. Al'shits, E. V. Darinskaya, O. L. Kazakova, E. Yu. Mikhina, and E. A. Petrzhik, Pis'ma Zh. Éksp. Teor. Fiz. **63** (8), 628 (1996) [JETP Lett. **63**, 668 (1996)].
70. V. I. Al'shits, E. V. Darinskaya, and O. L. Kazakova, Fiz. Tverd. Tela (St. Petersburg) **40** (1), 81 (1998) [Phys. Solid State **40**, 70 (1998)].
71. E. V. Darinskaya and M. V. Koldaeva, Pis'ma Zh. Éksp. Teor. Fiz. **70** (3), 226 (1999) [JETP Lett. **70**, 228 (1999)].
72. V. I. Al'shits and E. V. Darinskaya, Pis'ma Zh. Éksp. Teor. Fiz. **70** (11), 749 (1999) [JETP Lett. **70**, 761 (1999)].
73. E. V. Darinskaya, E. A. Petrzhik, S. A. Erofeeva, and V. P. Kisel', Pis'ma Zh. Éksp. Teor. Fiz. **70** (4), 298 (1999) [JETP Lett. **70**, 309 (1999)].
74. E. V. Darinskaja, E. A. Petrzhik, and S. A. Erofeeva, J. Phys.: Condens. Matter **14**, 12883 (2002).
75. E. A. Petrzhik, E. V. Darinskaya, S. A. Erofeeva, and M. R. Rukhman, Fiz. Tverd. Tela (St. Petersburg) **45** (2), 254 (2003) [Phys. Solid State **45**, 266 (2003)].

76. V. I. Al'shits, E. V. Darinskaya, I. V. Gektina, and F. F. Lavrent'ev, Kristallografiya **35** (4), 1014 (1990) [Sov. Phys. Crystallogr. **35**, 597 (1990)].
77. V. I. Al'shits, E. V. Darinskaya, and E. A. Petrzhik, Fiz. Tverd. Tela (St. Petersburg) **34** (1), 155 (1992) [Sov. Phys. Solid State **34**, 81 (1992)].
78. Yu. I. Golovin, R. B. Morgunov, and S. E. Zhulikov, Kristallografiya **43** (3), 586 (1998) [Crystallogr. Rep. **43**, 538 (1998)].
79. V. I. Al'shits, E. V. Darinskaya, O. L. Kazakova, E. Yu. Mikhina, and E. A. Petrzhik, Izv. Ross. Akad. Nauk, Ser. Fiz. **57** (11), 2 (1993).
80. V. I. Al'shits, E. V. Darinskaya, and M. V. Koldaeva, Fiz. Tverd. Tela (St. Petersburg) **43** (9), 1635 (2001) [Phys. Solid State **43**, 1703 (2001)].
81. V. I. Al'shits, R. Voska, E. V. Darinskaya, and E. A. Petrzhik, Fiz. Tverd. Tela (St. Petersburg) **35** (1), 70 (1993) [Phys. Solid State **35**, 37 (1993)].
82. V. I. Al'shits, R. Voska, E. V. Darinskaya, and E. A. Petrzhik, Fiz. Tverd. Tela (St. Petersburg) **35** (1), 70 (1993) [Phys. Solid State **35**, 37 (1993)].
83. Yu. I. Golovin, R. B. Morgunov, and A. V. Tyutyunnik, Izv. Ross. Akad. Nauk, Ser. Fiz. **10**, 3 (1995).
84. Yu. I. Golovin, R. B. Morgunov, and V. E. Ivanov, Fiz. Tverd. Tela (St. Petersburg) **39** (4), 630 (1997) [Phys. Solid State **39**, 550 (1997)].
85. Yu. I. Golovin, R. B. Morgunov, and S. E. Zhulikov, Izv. Ross. Akad. Nauk, Ser. Fiz. **61**, 965 (1997).
86. Yu. I. Golovin, R. B. Morgunov, S. E. Zhulikov, V. A. Kiperman, and D. V. Lopatin, Fiz. Tverd. Tela (St. Petersburg) **39** (4), 634 (1997) [Phys. Solid State **39**, 554 (1997)].
87. R. W. Dreyfus and R. B. Laibowitz, Phys. Rev. **135** (5), 1413 (1964).
88. M. Hartmanova, Phys. Status Solidi **79** (2), 303 (1971).
89. Yu. I. Golovin and R. B. Morgunov, Pis'ma Zh. Éksp. Teor. Fiz. **58** (3), 189 (1993) [JETP Lett. **58**, 191 (1993)].
90. Yu. I. Golovin, O. L. Kazakova, and R. B. Morgunov, Fiz. Tverd. Tela (St. Petersburg) **35** (5), 1384 (1993) [Phys. Solid State **35**, 700 (1993)].
91. Yu. I. Golovin and R. B. Morgunov, Fiz. Tverd. Tela (St. Petersburg) **35** (9), 2581 (1993) [Phys. Solid State **35**, 1280 (1993)].
92. Yu. I. Golovin, R. B. Morgunov, and A. V. Tyutyunnik, Phys. Status Solidi B **189** (1), 75 (1995).
93. Yu. A. Osip'yan, Yu. I. Golovin, D. V. Lopatin, R. B. Morgunov, R. K. Nikolaev, and S. Z. Shmurak, Pis'ma Zh. Éksp. Teor. Fiz. **69** (2), 110 (1999) [JETP Lett. **69**, 123 (1999)].
94. Yu. I. Golovin, R. B. Morgunov, A. A. Baskakov, M. V. Badylevich, and S. Z. Shmurak, Pis'ma Zh. Éksp. Teor. Fiz. **69** (2), 114 (1999) [JETP Lett. **69**, 127 (1999)].
95. M. V. Badylevich, Yu. L. Iunin, V. V. Kveder, V. I. Orlov, and Yu. A. Osip'yan, Zh. Éksp. Teor. Fiz. **124** (7), 664 (2003) [JETP **97**, 601 (2003)].
96. Yu. I. Golovin and R. B. Morgunov, Fiz. Tverd. Tela (St. Petersburg) **37** (5), 1352 (1995) [Phys. Solid State **37**, 734 (1995)].
97. *Experimental Methods of Chemical Kinetics*, Ed. by N. M. Émanuel' and M. G. Kuz'min (Mosk. Gos. Univ., Moscow, 1985).
98. Yu. I. Golovin and R. B. Morgunov, Dokl. Akad. Nauk **354** (5), 632 (1997).
99. Yu. I. Golovin, R. B. Morgunov, V. E. Ivanov, S. E. Zhulikov, and D. V. Lopatin, Kristallografiya **44** (5), 885 (1999) [Crystallogr. Rep. **44**, 825 (1999)].
100. M. V. Koldaeva, E. A. Darinskaya, and V. I. Al'shits, Kondens. Sredy Mezhfaz. Granitsy **2** (3), 229 (2000).
101. A. A. Skvortsov, A. M. Orlov, and L. I. Gonchar, Zh. Éksp. Teor. Fiz. **120** (1), 134 (2001) [JETP **93**, 117 (2001)].
102. A. M. Orlov, A. A. Skvortsov, and A. A. Solov'ev, Fiz. Tverd. Tela (St. Petersburg) **45** (4), 613 (2003) [Phys. Solid State **45**, 643 (2003)].
103. I. B. Kekalo, Itogi Nauki Tekh., Ser.: Metalloved. Term. Obrab. **7**, 5 (1973).
104. M. S. Blanter, I. S. Golovin, S. A. Golovin, A. A. Il'in, and V. I. Sarrak, *Mechanical Spectroscopy of Metal Materials* (MIA, Moscow, 1994).
105. R. Jemielniak and J. Krolikowski, J. Phys. Colloq. **46** (C10), 163 (1985).
106. G. M. Bartenev and A. G. Barteneva, *Relaxation Properties of Polymers* (Khimiya, Moscow, 1992).
107. A. A. Svetashov, V. L. Krasnikov, and É. P. Belozerova, Kristallografiya **42** (3), 493 (1997) [Crystallogr. Rep. **42**, 446 (1997)].
108. É. P. Belozerova, A. A. Svetashov, and V. L. Krasnikov, Izv. Ross. Akad. Nauk, Ser. Fiz. **61** (1), 291 (1997).
109. N. A. Tyapunina, V. L. Krasnikov, and É. P. Belozerova, Fiz. Tverd. Tela (St. Petersburg) **41** (6), 1035 (1999) [Phys. Solid State **41**, 942 (1999)].
110. N. A. Tyapunina, V. L. Krasnikov, and É. P. Belozerova, Kristallografiya **45** (1), 156 (2000) [Crystallogr. Rep. **45**, 150 (2000)].
111. V. I. Alekseenko, T. K. Volkova, T. E. Konstantinova, I. K. Nosolev, and I. B. Popova, Fiz. Tverd. Tela (St. Petersburg) **36** (6), 1597 (1994) [Phys. Solid State **36**, 873 (1994)].
112. O. I. Datsko, V. I. Alekseenko, and A. D. Shakhova, Fiz. Tverd. Tela (St. Petersburg) **38** (6), 1799 (1996) [Phys. Solid State **38**, 992 (1996)].
113. V. I. Alekseenko, T. K. Volkova, I. B. Popova, I. K. Nosolev, and T. E. Konstantinova, Pis'ma Zh. Éksp. Teor. Fiz. **66** (1), 49 (1996) [JETP Lett. **66**, 52 (1996)].
114. V. I. Alekseenko, T. K. Volkova, I. B. Popova, I. K. Nosolev, and T. E. Konstantinova, Pis'ma Zh. Éksp. Teor. Fiz. **67** (10), 30 (1998).
115. O. I. Datsko and V. I. Alekseenko, Fiz. Tverd. Tela (St. Petersburg) **39** (7), 1234 (1997) [Phys. Solid State **39**, 1094 (1997)].
116. O. I. Datsko, V. I. Alekseenko, and A. L. Brusova, Fiz. Tverd. Tela (Leningrad) **41** (11), 1985 (1999) [Phys. Solid State **41**, 1821 (1999)].
117. Yu. I. Golovin and R. B. Morgunov, Pis'ma Zh. Éksp. Teor. Fiz. **61** (7), 583 (1995) [JETP Lett. **61**, 596 (1995)].

118. Yu. I. Golovin and R. B. Morgunov, Fiz. Tverd. Tela (St. Petersburg) **37** (7), 2118 (1995) [Phys. Solid State **37**, 1152 (1995)].
119. Yu. I. Golovin, R. B. Morgunov, S. E. Zhulikov, and A. M. Karyakin, Izv. Ross. Akad. Nauk, Ser. Fiz. **60** (9), 173 (1996).
120. A. A. Urusovskaya, V. I. Al'shits, A. E. Smirnov, and N. N. Bekkauér, Pis'ma Zh. Éksp. Teor. Fiz. **65** (6), 470 (1997) [JETP Lett. **65**, 497 (1997)].
121. A. A. Urusovskaya, A. E. Smirnov, and N. N. Bekkauér, Izv. Ross. Akad. Nauk, Ser. Fiz. **61** (5), 937 (1997).
122. V. I. Al'shits, N. N. Bekkauér, A. E. Smirnov, and A. A. Urusovskaya, Zh. Éksp. Teor. Fiz. **115** (3), 951 (1999) [JETP **88**, 523 (1999)].
123. V. I. Al'shits, A. A. Urusovskaya, A. E. Smirnov, and N. N. Bekkauér, Fiz. Tverd. Tela (St. Petersburg) **42** (2), 270 (2000) [Phys. Solid State **42**, 277 (2000)].
124. B. I. Smirnov, N. N. Peschanskaya, and V. I. Nikolaev, Fiz. Tverd. Tela (St. Petersburg) **43** (12), 2154 (2001) [Phys. Solid State **43**, 2250 (2001)].
125. B. I. Smirnov, V. V. Shpeĭzman, N. N. Peschanskaya, and R. K. Nikolaev, Fiz. Tverd. Tela (St. Petersburg) **44** (10), 1915 (2002) [Phys. Solid State **44**, 2009 (2002)].
126. Yu. A. Osip'yan, Yu. I. Golovin, R. B. Morgunov, R. K. Nikolaev, I. P. Pushnin, and S. Z. Shmurak, Fiz. Tverd. Tela (St. Petersburg) **43** (7), 1333 (2001) [Phys. Solid State **43**, 1389 (2001)].
127. Yu. P. Rodin, Mekh. Kompoz. Mater., No. 3, 490 (1991).
128. N. N. Peschanskaya, V. Yu. Surovova, and P. N. Yakushev, Fiz. Tverd. Tela (St. Petersburg) **34** (7), 2111 (1992) [Sov. Phys. Solid State **34**, 1127 (1992)].
129. N. N. Peschanskaya and P. N. Yakushev, Fiz. Tverd. Tela (St. Petersburg) **39** (9), 1690 (1997) [Phys. Solid State **39**, 1509 (1997)].
130. N. N. Peschanskaya, Fiz. Tverd. Tela (St. Petersburg) **43** (8), 1418 (2001) [Phys. Solid State **43**, 1478 (2001)].
131. Yu. I. Golovin, R. B. Morgunov, and S. Yu. Liksutin, Vysokomol. Soedin., Ser. A **42** (2), 277 (2000).
132. Yu. I. Golovin and R. B. Morgunov, Fiz. Tverd. Tela (St. Petersburg) **43** (5), 827 (2001) [Phys. Solid State **43**, 859 (2001)].
133. R. B. Morgunov, Yu. I. Golovin, D. V. Yakunin, and I. N. Trofimova, Vysokomol. Soedin., Ser. A **44** (1), 1 (2002).
134. V. A. Zhorin, L. L. Mukhina, and I. V. Razumovskaya, Vysokomol. Soedin., Ser. A **40** (7), 1213 (1998).
135. Yu. I. Golovin, R. B. Morgunov, D. V. Lopatin, and A. A. Baskakov, Phys. Status Solidi A **160**, R3 (1997).
136. Yu. I. Golovin, R. B. Morgunov, D. V. Lopatin, A. A. Baskakov, and Ya. E. Evgen'ev, Fiz. Tverd. Tela (St. Petersburg) **40** (11), 2065 (1998) [Phys. Solid State **40**, 1870 (1998)].
137. A. I. Pinchuk and S. D. Shavreĭ, Fiz. Tverd. Tela (St. Petersburg) **43** (1), 39 (2001) [Phys. Solid State **43**, 39 (2001)].
138. A. I. Pinchuk and S. D. Shavreĭ, Fiz. Tverd. Tela (St. Petersburg) **43** (8), 1416 (2001) [Phys. Solid State **43**, 1476 (2001)].
139. A. I. Pinchuk and S. D. Shavreĭ, Pis'ma Zh. Tekh. Fiz. **28** (12), 80 (2002) [Tech. Phys. Lett. **28**, 525 (2002)].
140. M. S. C. Bose, Phys. Status Solidi A **86** (2), 649 (1984).
141. N. I. Gershenzon, D. O. Zalpimiani, P. V. Mandzhgaladze, and O. A. Pokhotelov, Fiz. Tverd. Tela (Leningrad) **28** (3), 708 (1986) [Sov. Phys. Solid State **28**, 394 (1986)].
142. M. I. Molotskiĭ, Fiz. Tverd. Tela (Leningrad) **19** (9), 1834 (1977) [Sov. Phys. Solid State **19**, 1071 (1977)].
143. N. I. Gershenzon, D. O. Zalpimiani, P. V. Mandzhgaladze, and O. A. Pokhotelov, Fiz. Tverd. Tela (Leningrad) **30** (7), 2209 (1988) [Sov. Phys. Solid State **30**, 1273 (1988)].
144. P. F. Biadzhi, N. I. Gershenzon, D. O. Zalpimiani, P. V. Mandzhgaladze, O. A. Pokhotelov, V. Sgrin'ya, and Z. T. Chelidze, Fiz. Tverd. Tela (Leningrad) **32** (8), 2328 (1990) [Sov. Phys. Solid State **32**, 1352 (1990)].
145. A. A. Urusovskaya, Usp. Fiz. Nauk **96** (1), 39 (1968) [Sov. Phys. Usp. **11**, 631 (1968)].
146. N. A. Tyapunina and É. P. Belozerova, Usp. Fiz. Nauk **156** (4), 683 (1988) [Sov. Phys. Usp. **31**, 1060 (1988)].
147. L. B. Zuev, *Physics of Electroplasticity of Alkaline-Haloid Crystals* (Nauka, Novosibirsk, 1990).
148. *Electron Properties of Dislocations in Semiconductors*, Ed. by Yu. A. Osip'yan (Éditorial URSS, Moscow, 2000).
149. V. I. Spitsyn and O. A. Troitskiĭ, *Electroplastic Deformation of Metals* (Nauka, Moscow, 1985).
150. Yu. V. Baranov, O. A. Troitskiĭ, Yu. S. Avramov, and A. D. Shlyapin, *Physical Fundamentals of Pulsed Electrical and Electroplastic Treatments and New Materials* (MGIU-IMASh RAN, Moscow, 2001).
151. H. Conrad and A. F. Sprecher, in *Dislocations in Solids*, Ed. by F. R. N. Nabarro (North-Holland, Amsterdam, 1989), Vol. 8, p. 497.
152. V. I. Al'shits, E. V. Darinskaya, E. Yu. Mikhina, and E. A. Petrzhik, Fiz. Tverd. Tela (St. Petersburg) **35** (5), 1397 (1993) [Phys. Solid State **35**, 706 (1993)].
153. V. I. Alshits, E. V. Darinskaya, O. L. Kazakova, E. Yu. Mikhina, and E. A. Petrzhik, J. Alloys Compd. **211/212**, 548 (1994).
154. V. I. Al'shits, E. V. Darinskaya, O. L. Kazakova, E. Yu. Mikhina, and E. A. Petrzhik, Fiz. Tverd. Tela (St. Petersburg) **38** (8), 2426 (1996) [Phys. Solid State **38**, 1333 (1996)].
155. V. I. Alshits, E. V. Darinskaya, O. L. Kazakova, E. Yu. Mikhina, and E. A. Petrzhik, Mater. Sci. Eng., A **234–236**, 617 (1997).
156. V. I. Al'shits, E. V. Darinskaya, E. Yu. Mikhina, and E. A. Petrzhik, Fiz. Tverd. Tela (St. Petersburg) **38** (8), 2426 (1996) [Phys. Solid State **38**, 1333 (1996)].
157. Yu. A. Osip'yan and V. F. Petrenko, Zh. Éksp. Teor. Fiz. **63** (6), 1735 (1972) [Sov. Phys. JETP **36**, 916 (1973)].
158. Yu. A. Osip'yan and V. F. Petrenko, Zh. Éksp. Teor. Fiz. **69** (4), 1362 (1975) [Sov. Phys. JETP **42**, 695 (1975)].
159. Yu. A. Osip'yan and V. F. Petrenko, Zh. Éksp. Teor. Fiz. **75** (1), 296 (1978) [Sov. Phys. JETP **48**, 147 (1974)].
160. A. A. Urusovskaya, V. I. Al'shits, N. N. Bekkauér, and A. E. Smirnov, Fiz. Tverd. Tela (St. Petersburg) **42** (2), 267 (2000) [Phys. Solid State **42**, 274 (2000)].
161. A. A. Skvortsov, A. M. Orlov, V. A. Frolov, L. I. Gonchar, and O. V. Litvinenko, Fiz. Tverd. Tela (St. Peters-

burg) **42** (10), 1814 (2000) [Phys. Solid State **42**, 1861 (2000)].
162. A. M. Orlov, A. A. Skvortsov, and L. I. Gonchar, Fiz. Tverd. Tela (St. Petersburg) **43** (7), 1207 (2001) [Phys. Solid State **43**, 1252 (2001)].
163. V. A. Makara, L. P. Steblenko, N. Ya. Gorid'ko, V. M. Kravchenko, and A. N. Kolomiets, Fiz. Tverd. Tela (St. Petersburg) **43** (3), 462 (2001) [Phys. Solid State **43**, 480 (2001)].
164. A. A. Skvortsov, L. I. Gonchar, and A. M. Orlov, Fiz. Tverd. Tela (St. Petersburg) **45** (6), 1603 (2003) [Phys. Solid State **45**, 1683 (2003)].
165. Yu. I. Golovin, R. B. Morgunov, A. V. Tyutyunik, S. E. Zhulikov, and N. M. Afonina, Fiz. Tverd. Tela (St. Petersburg) **40** (12), 2184 (1998) [Phys. Solid State **40**, 1981 (1998)].
166. M. I. Molotskii and V. Fleurov, Phys. Rev. B **52** (22), 15829 (1995).
167. M. I. Molotskii, Mater. Sci. Eng. A **287**, 248 (2000).
168. Yu. I. Golovin, R. B. Morgunov, M. V. Badylevich, and S. Z. Shmurak, Fiz. Tverd. Tela (St. Petersburg) **39** (8), 1389 (1997) [Phys. Solid State **39**, 1232 (1997)].
169. Yu. I. Golovin, R. B. Morgunov, S. E. Zhulikov, and V. I. Ivolgin, Kristallografiya **43** (5), 912 (1998) [Crystallogr. Rep. **43**, 858 (1998)].
170. Yu. I. Golovin, R. B. Morgunov, and S. Z. Shmurak, Dokl. Akad. Nauk **355** (3), 299 (1998) [Dokl. Phys. **43**, 340 (1998)].
171. Yu. I. Golovin, R. B. Morgunov, D. V. Lopatin, and A. A. Baskakov, Kristallografiya **43** (6), 1115 (1998) [Crystallogr. Rep. **43**, 1056 (1998)].
172. Yu. I. Golovin and R. B. Morgunov, Izv. Vyssh. Uchebn. Zaved., Fiz. **41** (7), 31 (1998).
173. Yu. I. Golovin, R. B. Morgunov, A. A. Dmitrievskiĭ, and S. Z. Shmurak, Kristallografiya **45** (1), 154 (2000) [Crystallogr. Rep. **45**, 148 (2000)].
174. Yu. I. Golovin, R. B. Morgunov, S. E. Julikov, and A. A. Dmitrievskiĭ, Kristallografiya **45** (4), 738 (2000) [Crystallogr. Rep. **45**, 676 (2000)].
175. Yu. I. Golovin, R. B. Morgunov, A. A. Dmitrievskiĭ, and S. Z. Shmurak, Izv. Akad. Nauk, Ser. Fiz. **62** (7), 1296 (1998).
176. Yu. I. Golovin, R. B. Morgunov, and D. V. Lopatin, Izv. Vyssh. Uchebn. Zaved., Fiz. **42** (4), 66 (1999).
177. E. B. Burlakova, Ross. Khim. Zh. **43**, 5 (1999).
178. V. I. Al'shits, E. V. Darinskaya, and O. L. Kazakova, Pis'ma Zh. Éksp. Teor. Fiz. **62** (4), 352 (1995) [JETP Lett. **62**, 375 (1995)].
179. V. I. Al'shits, E. V. Darinskaya, and O. L. Kazakova, Zh. Éksp. Teor. Fiz. **111** (2), 615 (1997) [JETP **84**, 338 (1997)].
180. Yu. I. Golovin, A. A. Dmitrievskiĭ, R. K. Nikolaev, and I. A. Pushnin, Fiz. Tverd. Tela (St. Petersburg) **45** (1), 187 (2003) [Phys. Solid State **45**, 197 (2003)].
181. Yu. I. Golovin, R. B. Morgunov, S. E. Zhulikov, and D. Yu. Golovin, Fiz. Tverd. Tela (St. Petersburg) **38** (10), 3047 (1996) [Phys. Solid State **38**, 1666 (1996)].
182. L. N. Blinov, G. Yushka, K. Arlauskas, and M. S. Gutenev, Fiz. Khim. Stekla **9** (6), 748 (1983).
183. M. D. Samsonenko, T. V. Zhmykhov, V. Sh. Zonn, and V. K. Aksenov, Zh. Strukt. Khim. **20** (5), 1116 (1979).
184. T. V. Zhmykhov, V. I. Borul'ko, I. A. Klyuchnik, V. G. Pitsyuga, G. V. Zakharov, and E. V. Reshetnikova, Fiz. Khim. Stekla **15** (1), 52 (1989).
185. S. A. Kozyukhin, L. M. Ilizarov, V. G. Podkopaev, and S. A. Dembovskiĭ, Materialovedenie **1** (2), 18 (1997).
186. V. I. Alekseenko, G. K. Volkova, I. B. Popova, T. E. Konstantinova, and O. I. Datsko, Pis'ma Zh. Tekh. Fiz. **18** (21), 37 (1992) [Sov. Tech. Phys. Lett. **18**, 703 (1992)].
187. V. I. Alekseenko, G. K. Volkova, I. B. Popova, I. K. Nosolev, and T. E. Konstantinova, Zh. Tekh. Fiz. **67** (10), 30 (1997) [Tech. Phys. **42**, 1141 (1997)].
188. E. G. Pashinskaya and V. V. Pashinskiĭ, Fiz. Met. Metalloved. **85** (6), 120 (1998).
189. M. N. Levin and N. N. Matveev, Zh. Fiz. Khim. **75** (10), 1886 (2001).
190. M. N. Levin, V. V. Postnikov, and N. N. Matveev, Vysokomol. Soedin., Ser. A **45** (2), 217 (2003).
191. M. N. Levin, V. V. Postnikov, and N. N. Matveev, Zh. Fiz. Khim. **77** (4), 1 (2003).
192. Yu. A. Osip'yan, Yu. I. Golovin, D. V. Lopatin, R. B. Morgunov, R. K. Nikolaev, and S. Z. Shmurak, Fiz. Tverd. Tela (St. Petersburg) **41** (11), 2097 (1999) [Phys. Solid State **41**, 1926 (1999)].
193. Yu. A. Osipyan, Yu. I. Golovin, D. V. Lopatin, R. B. Morgunov, R. K. Nikolaev, and S. Z. Smurak, Phys. Status Solidi B **223** (3), R14 (2001).
194. Yu. I. Golovin, D. V. Lopatin, R. K. Nikolaev, A. V. Umrikhin, and S. Z. Shmurak, Dokl. Akad. Nauk **387** (6), 1 (2002) [Dokl. Phys. **47**, 849 (2002)].
195. I. A. Sokolik and E. L. Frankevich, Usp. Fiz. Nauk **111** (2), 261 (1973) [Sov. Phys. Usp. **16**, 687 (1973)].
196. Ya. B. Zel'dovich, A. L. Buchachenko, and E. L. Frankevich, Usp. Fiz. Nauk **155** (1), 3 (1988) [Sov. Phys. Usp. **31**, 385 (1988)].
197. V. V. Kveder, Yu. A. Osip'yan, and A. I. Shalynin, Zh. Éksp. Teor. Fiz. **83** (2), 699 (1982) [Sov. Phys. JETP **56**, 389 (1982)].
198. L. V. Vlasenko and V. A. Khramtsov, Pis'ma Zh. Éksp. Teor. Fiz. **42** (1), 32 (1985) [JETP Lett. **42**, 38 (1985)].
199. V. V. Kveder and Yu. A. Osip'yan, Izv. Akad. Nauk SSSR, Ser. Fiz. **51** (4), 626 (1987).
200. E. L. Frankevich, D. I. Kadyrov, I. A. Sokolik, and V. M. Kobryanskiĭ, Khim. Fiz. **2** (7), 1642 (1983).
201. K. Okamoto, N. Oda, A. Itaga, and S. Kusabayashy, Chem. Phys. Lett. **35** (8), 483 (1975).
202. M. Pope, N. E. Gescintov, and F. Fogel, Mol. Cryst. Liq. Cryst. **6**, 83 (1969).
203. B. M. Rumyantsev, V. I. Lesin, and E. L. Frankevich, Opt. Spektrosk. **38** (1), 89 (1975) [Opt. Spectrosc. **38**, 49 (1975)].
204. G. Klein, R. Voltz, and M. Schott, Chem. Phys. Lett. **19** (4), 391 (1973).
205. E. L. Frankevich, M. M. Tribel, A. A. Sokolik, L. I. Kolesnikova, and Yu. I. Stolovitskii, Phys. Status Solidi B **107** (2), 423 (1981).
206. Yu. I. Golovin, R. B. Morgunov, A. A. Baskakov, M. V. Badylevich, and S. Z. Shmurak, Pis'ma Zh. Éksp. Teor. Fiz. **69** (2), 114 (1999) [JETP Lett. **69**, 127 (1999)].

207. S. A. Gridnev, K. S. Drozhdin, and V. V. Shmykov, Fiz. Tverd. Tela (St. Petersburg) **42** (2), 318 (2000) [Phys. Solid State **42**, 326 (2000)].
208. M. N. Levin, V. V. Postnikov, M. Yu. Palagin, and A. M. Kostsev, Fiz. Tverd. Tela (St. Petersburg) **45** (3), 513 (2003) [Phys. Solid State **45**, 542 (2003)].
209. M. N. Levin, V. V. Postnikov, and M. A. Dronov, Pis'ma Zh. Tekh. Fiz. **29** (11), 7 (2003) [Tech. Phys. Lett. **29**, 444 (2003)].
210. M. N. Levin and V. M. Maslovsky, Solid State Commun. **90** (12), 813 (1994).
211. V. M. Maslovskiĭ, Yu. A. Klimov, N. S. Samsonov, and E. V. Simanovich, Fiz. Tekh. Poluprovodn. (St. Petersburg) **28** (5), 772 (1994) [Semiconductors **28**, 453 (1994)].
212. M. N. Levin and B. A. Zon, Zh. Éksp. Teor. Fiz. **111** (4), 1373 (1997) [JETP **84**, 760 (1997)].
213. M. N. Levin and B. A. Zon, Mater. Res. Soc. Symp. Proc. **583**, 278 (2000).
214. M. N. Levin, G. V. Semenova, T. P. Sushkova, V. V. Postnikov, and B. L. Agapov, Fiz. Tverd. Tela (St. Petersburg) **45** (4), 609 (2003) [Phys. Solid State **45**, 639 (2003)].
215. M. N. Levin, G. V. Semenova, T. P. Sushkova, É. A. Dolgopolova, and V. V. Postnikov, Pis'ma Zh. Tekh. Fiz. **28** (19), 50 (2002) [Tech. Phys. Lett. **28**, 818 (2002)].
216. M. N. Levin, G. V. Semenova, and T. P. Sushkova, Dokl. Akad. Nauk **388** (2), 1 (2003) [Dokl. Phys. **48**, 62 (2003)].
217. M. N. Levin, V. N. Semenov, and Yu. V. Meteleva, Pis'ma Zh. Tekh. Fiz. **27** (10), 37 (2001) [Tech. Phys. Lett. **27**, 411 (2001)].
218. V. P. Vlasov, V. M. Kanevskiĭ, and A. A. Purtskhvadze, Fiz. Tverd. Tela (Leningrad) **33** (7), 2194 (1991) [Sov. Phys. Solid State **33**, 1236 (1991)].
219. V. N. Davydov, E. A. Loskutova, and E. P. Naĭden, Fiz. Tekh. Poluprovodn. (Leningrad) **23** (9), 1596 (1989) [Sov. Phys. Semicond. **23**, 989 (1989)].
220. Yu. A. Klimov, V. M. Maslovskiĭ, and V. V. Tarasenko, Élektron. Tekh. **3** (5(139)), 25 (1990).
221. Yu. A. Klimov, V. M. Maslovskiĭ, and K. V. Kholodnov, Élektron. Tekh. **3** (5(144)), 22 (1991).
222. A. G. Kadmenskiĭ, S. G. Kadmenskiĭ, M. N. Levin, V. M. Maslovskiĭ, and A. V. Chernyshev, Pis'ma Zh. Tekh. Fiz. **19** (3), 41 (1993) [Tech. Phys. Lett. **19**, 86 (1993)].
223. M. N. Levin, Yu. O. Lichmanov, and V. M. Maslovskiĭ, Pis'ma Zh. Tekh. Fiz. **20** (4), 27 (1994) [Tech. Phys. Lett. **20**, 145 (1994)].
224. R. Z. Sagdeev, T. V. Leshina, and M. A. Kamkha, Izv. Akad. Nauk SSSR, Ser. Khim. **9**, 2128 (1972).
225. R. Z. Sagdeev, K. M. Salikhov, T. V. Leshina, M. A. Kamkha, S. M. Sheĭn, and Yu. N. Molin, Pis'ma Zh. Éksp. Teor. Fiz. **16** (7), 599 (1972) [JETP Lett. **16**, 422 (1972)].
226. E. L. Frankevich and A. I. Pristupa, Pis'ma Zh. Éksp. Teor. Fiz. **24** (4), 397 (1976) [JETP Lett. **24**, 362 (1976)].
227. E. L. Frankevich, A. I. Pristupa, M. M. Tribel', and I. A. Sokolik, Dokl. Akad. Nauk SSSR **236**, 1173 (1977).
228. E. L. Frankevich, M. M. Tribel, I. A. Sokolik, and A. I. Pristupa, Phys. Status Solidi B **87** (2), 337 (1978).
229. R. C. Johnson, R. E. Merrifield, P. Avakian, and R. B. Flippen, Phys. Rev. Lett. **19** (5), 285 (1967).
230. A. L. Buchachenko and E. L. Frankevich, *Chemical Generation and Reception of Radio- and Microwaves* (VCH, New York, 1994).
231. B. C. Cavenett, Adv. Phys. **30** (4), 475 (1981).
232. P. G. Baranov and N. G. Romanov, Izv. Akad. Nauk SSSR, Ser. Fiz. **50** (2), 224 (1986).
233. P. Kaplan, I. Solomon, and N. E. Mott, Europhys. Lett. **39**, L51 (1978).
234. K. M. Salikhov, Y. N. Molin, R. A. Sagdeev, and A. L. Buchachenko, *Spin Polarization and Magnetic Effects in Radical Reactions* (Nauka, Novosibirsk, 1978; Elsevier, Amsterdam, 1984).
235. A. L. Buchachenko, R. Z. Sagdeev, and K. M. Salikhov, *Magnetic and Spin Effects in Chemical Reactions* (Nauka, Novosibirsk, 1978).
236. A. L. Buchachenko, Chem. Rev. **95** (7), 2507 (1995).
237. B. Brocklehurst, Nature **221**, 921 (1969).
238. R. Kaptein and J. L. Oosterhoff, Chem. Phys. Lett. **4**, 195 (1969).
239. U. E. Steiner and T. Ulrich, Chem. Rev. **89**, 51 (1989).
240. A. L. Buchachenko and V. L. Berdindky, J. Phys. Chem. **100**, 18292 (1996).
241. M. I. Molotskiĭ, Fiz. Tverd. Tela (Leningrad) **33** (10), 3112 (1991) [Sov. Phys. Solid State **33**, 1760 (1991)].
242. V. V. Zyryanov, Izv. Sib. Otd. Akad. Nauk SSSR, Ser. Khim. Nauk **6** (19), 9 (1988).
243. V. R. Regel', A. I. Slutsker, and É. E. Tomashevskiĭ, *Kinetic Nature of the Strength of Solids* (Nauka, Moscow, 1974).
244. P. Yu. Butyagin, A. M. Dubinskaya, and V. A. Radtsig, Usp. Khim. **36** (5), 593 (1969).
245. M. V. Vlasova and N. G. Kakazeĭ, *Electron Paramagnetic Resonance in Failed Solids* (Naukova Dumka, Kiev, 1979).
246. K. V. Vlasov, A. I. Deryagin, and V. A. Pavlov, Phys. Met. Metalloved. **44**, 1204 (1977).
247. V. A. Radtsig, Kinet. Katal. **20** (2), 456 (1979).
248. V. A. Zakrevskiĭ, Fiz. Khim. Stekla **14** (2), 256 (1988).
249. A. S. Argon and G. E. Padaver, Philos. Mag. **25** (5), 1075 (1972).
250. A. S. Nowick and B. S. Berry, *Anelastic Relaxation in Crystalline Solids* (Academic, New York, 1972; Atomizdat, Moscow, 1975).
251. M. I. Molotskiĭ, Fiz. Tverd. Tela (St. Petersburg) **35** (1), 11 (1993) [Phys. Solid State **35**, 5 (1993)].
252. V. I. Al'shits, E. V. Darinskaya, M. V. Koldaeva, and E. A. Petrzhik, Kristallografiya **48** (5), 826 (2003) [Crystallogr. Rep. **48**, 768 (2003)].
253. M. Molotskii and V. Fleurov, Philos. Mag. Lett. **73** (1), 11 (1996).
254. M. Molotskii and V. Fleurov, J. Phys. Chem. B **104**, 3812 (2000).
255. M. I. Molotskii and V. Fleurov, Phys. Rev. B **56** (18), 56 (1997).

256. M. I. Molotskii and V. Fleurov, Phys. Rev. Lett. **78** (3), 1 (1997).

257. M. I. Molotskii and V. Fleurov, Phys. Rev. B **63**, 184421 (2001).

258. M. I. Molotskii and V. Fleurov, Phys. Rev. B **63**, 132102 (2001).

259. M. I. Molotskii, R. E. Kris, and V. N. Fleurov, Phys. Rev. B **51**, 12531 (1995).

260. V. Fleurov and M. Molotskii, in *Microwaves: Theory and Application in Materials Processing, V: Proceedings of the Second World Congress on Microwave and Radio Frequency Processing* (Orlando, USA, 2000), pp. 57–63.

261. V. M. Shatalov, Fiz. Tekh. Vys. Davleniĭ **6** (3), 81 (1996).

262. A. L. Buchachenko, Usp. Khim. **64** (9), 863 (1995).

263. Yu. I. Golovin and R. B. Morgunov, Izv. Ross. Akad. Nauk, Ser. Khim. **46** (4), 739 (1997).

264. Yu. I. Golovin and R. B. Morgunov, Zh. Éksp. Teor. Fiz. **115** (2), 605 (1999) [JETP **88**, 332 (1999)].

265. Yu. I. Golovin, R. B. Morgunov, V. E. Ivanov, S. E. Zhulikov, and A. A. Dmitrievskiĭ, Pis'ma Zh. Éksp. Teor. Fiz. **68** (5), 400 (1998) [JETP Lett. **68**, 426 (1998)].

266. Yu. I. Golovin, R. B. Morgunov, A. I. Tyurin, and V. I. Ivolgin, Dokl. Akad. Nauk **361** (3), 352 (1998).

267. Yu. I. Golovin, R. B. Morgunov, V. E. Ivanov, and A. A. Dmitrievskiĭ, Fiz. Tverd. Tela (St. Petersburg) **41** (10), 1778 (1999) [Phys. Solid State **41**, 1631 (1999)].

268. Yu. I. Golovin, R. B. Morgunov, V. E. Ivanov, and A. A. Dmitrievskiĭ, Zh. Éksp. Teor. Fiz. **117** (6), 1080 (2000) [JETP **90**, 939 (2000)].

269. Yu. I. Golovin, R. B. Morgunov, and A. A. Dmitrievskii, J. Mater. Sci. Eng. **28/2**, 261 (2002).

270. Yu. Golovin, R. Morgunov, and A. Baskakov, Mol. Phys. **100** (9), 1291 (2002).

271. V. I. Al'shits, E. V. Darinskaya, M. A. Legen'kov, and V. A. Morozov, Fiz. Tverd. Tela (St. Petersburg) **41** (11), 2004 (1999) [Phys. Solid State **41**, 1839 (1999)].

272. R. B. Morgunov, S. Z. Shmurak, B. K. Ponomarev, A. A. Baskakov, and V. I. Kulakov, Pis'ma Zh. Éksp. Teor. Fiz. **76** (5), 336 (2002) [JETP Lett. **76**, 307 (2002)].

273. R. B. Morgunov and A. A. Baskakov, Fiz. Tverd. Tela (St. Petersburg) **43**, 1632 (2001) [Phys. Solid State **43**, 1700 (2001)].

274. P. Yu. Butyagin, Chem. Rev. (Part 2) **23**, 91 (1998).

275. G. Heinike, *Tribochemistry* (Akademie, Berlin, 1984; Mir, Moscow, 1987).

276. A. V. Gubanov, A. I. Likhtenshteĭn, and A. V. Postnikov, *Magnetism and Chemical Relations in Crystals* (Khimiya, Moscow, 1985).

277. N. N. Peschanskaya and P. N. Yakushev, Fiz. Tverd. Tela (St. Petersburg) **45** (6), 1130 (2003) [Phys. Solid State **45**, 1185 (2003)].

278. V. A. Zakrevskiĭ, V. A. Pakhotin, and A. V. Shul'dinger, Fiz. Tverd. Tela (St. Petersburg) **44** (11), 1990 (2002) [Phys. Solid State **44**, 2083 (2002)].

279. T. G. Prokhorova, S. S. Khasanov, L. V. Zorina, L. I. Buranov, V. A. Tkacheva, A. A. Baskakov, R. B. Morgunov, M. Gener, E. Canadell, R. P. Shibaeva, and E. V. Yagubskii, Adv. Funct. Mater. **13** (5), 1 (2003).

Translated by Yu. Epifanov

Physics of the Solid State, Vol. 46, No. 5, 2004, pp. 825–832. Translated from Fizika Tverdogo Tela, Vol. 46, No. 5, 2004, pp. 804–810.

SEMICONDUCTORS AND DIELECTRICS

Metastable *X* Centers in Cadmium Telluride Single Crystals

P. N. Tkachuk*, V. I. Tkachuk*, P. N. Bukivsky, and M. V. Kurik****

** Chernovtsy National University, Chernovtsy, 58012 Ukraine*
e-mail: ptkachuk@chnu.cv.ua
*** Institute of Physics, National Academy of Sciences of Ukraine, pr. Nauki 46, Kiev, 03028 Ukraine*
e-mail: bukivsky@iop.kiev.ua
Received July 8, 2003

Abstract—A model is proposed for metastable *DX* centers formed through Jahn–Teller distortion of the crystal lattice of cadmium telluride, i.e., through the displacement of a D_{Cd} residual donor impurity atom (where *D* is a Group III element of the periodic table) to the region of a nearest neighbor interstice. The configuration-coordinate diagram for a V_{Cd}–D_i associated defect is constructed with due regard for the tetrahedral and hexagonal positions of interstitial atoms. The Stokes shift, *n*-type conductivity, location of the Fermi level, specific features of photoluminescence, and some other effects are explained in terms of the configuration-coordinate diagram. The results of experimental investigations of the energy spectrum of *DX* centers in cadmium telluride single crystals are in agreement with available theoretical data. © *2004 MAIK "Nauka/Interperiodica".*

1. INTRODUCTION

The presence of technologically uncontrollable impurities, intrinsic defects of the crystal lattice, and complexes of different types in II–VI semiconductor compounds, for example, in cadmium telluride, brings about the formation of impurity centers with deep-lying levels. In the crystal lattice of cadmium telluride, cation vacancies are the primary defects forming complexes and can exist in several charge states, such as V_{Cd}^{0}, V_{Cd}^{-}, and V_{Cd}^{--} [1, 2]. In particular, doubly charged cadmium vacancies and impurities of Group III and VII elements of the periodic table form associated defects, i.e., the so-called double acceptors and *A* centers, which are localized in the band gap of the compound and play an important role in recombination processes.

The data available in the literature on the energy spectra of deep-level centers in cadmium telluride are contradictory [1, 2]. This is especially true in regard to the nature of the acceptor level at an energy E_c – 0.06 eV, which belongs to a group of local states that have not been identified to date. It is known that this level can be attributed to both an intrinsic defect and a complex formed by an intrinsic defect and an impurity. Unfortunately, the data obtained by different researchers for the binding energy of this defect do not always correlate (see, for example, [3]).

In recent years, the majority of theoretical investigations into the shallow–deep transitions in II–VI and III–V semiconductor compounds have been performed in the framework of the microscopic model of an *X* center [4–7]. According to this model, the *X* center is formed through the Jahn–Teller distortion of the crystal lattice, i.e., through the displacement of a center-forming atom along the [111] direction to the region of the nearest neighbor interstice. As a result of the Jahn–Teller distortion, the bond with an atom of the adjacent sublattice is broken and the symmetry of the center lowers from tetrahedral (T_d) to trigonal (C_{3v}) symmetry. In the case of donor impurities, structural relaxation is accompanied by trapping of an extra electron into a neutral donor state d^0: $2d^0 \longrightarrow d^+ + DX^-$.

For III–V semiconductor compounds, *X* centers have been adequately investigated both theoretically and experimentally. However, *X* centers in II–VI compounds have been examined predominantly using theoretical approaches. Nonetheless, it has been established that the formation of deep-level centers of Group III elements in cadmium telluride and in a number of III–V compounds (GaAs, GaAlAs) occurs through similar mechanisms [6, 7]. Park and Chadi [6] revealed that the *DX* centers formed by aluminum, indium, and gallium impurities in cadmium telluride are localized at energy levels 0.55, 0.61, and 0.54 eV below the conduction band bottom and have binding energies of 0.42, 0.04, and 0.08 eV, respectively. However, the results of theoretical calculations require further experimental verification.

The purpose of the present work was to develop a model of *DX* centers in cadmium telluride single crystals and to identify the electronic states of these centers. We studied single-crystal samples with the impurity-defect composition most frequently used in the technology for fabricating nuclear radiation spectrometric semiconductor detectors based on semi-insulating cadmium telluride. However, the preparation of such a material required compensation of the contribution from the donor impurities introduced. This was

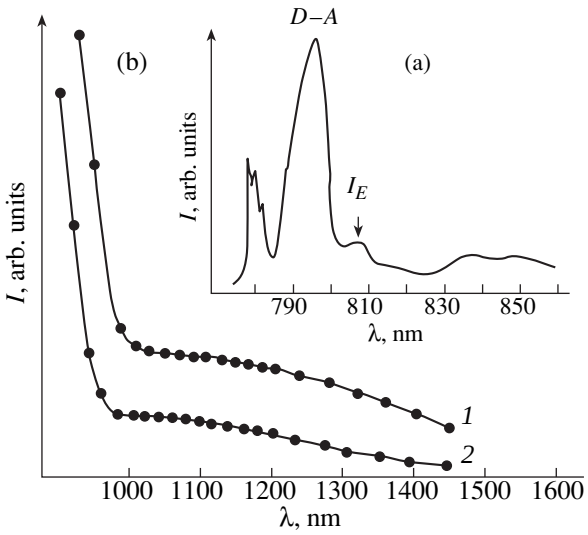

Fig. 1. (a) Photoluminescence spectrum of the *n*-CdTe⟨Cl⟩ single crystal ($N_{Cl} = 5.0 \times 10^{17}$ cm^{-3}) at $T = 4.5$ K. (b) Photocurrent spectra of *n*-CdTe⟨Cl⟩ crystals at $T = 300$ K. Chlorine concentration N_{Cl} = (*1*) 5.0×10^{17} and (*2*) 1.0×10^{19} cm^{-3}.

achieved using compounds with an excess of tellurium as compared to the stoichiometric composition.

2. SAMPLE PREPARATION AND EXPERIMENTAL TECHNIQUE

Cadmium telluride single crystals were grown using the Bridgman method from a melt. The technique of doping single crystals by Cl_{Te} impurities and the compensation mechanisms were described in our previous work [8].

Samples CdTe + Te were prepared in the following way. By virtue of the specific features of the *P–T–X* phase equilibrium diagram of cadmium telluride, the cadmium telluride crystals grown from a melt contain an insignificant excess of tellurium (~10^{17} cm^{-3}) as compared to the stoichiometric composition [1, 2]. For more efficient saturation of the cadmium telluride compound with tellurium, the single crystals were grown by the static and dynamics methods from the gas phase [9]. In this case, we used CdTe or CdTe(In) compounds that were preliminarily synthesized at the temperature of the initial melt.

Compared to the *p*-CdTe crystals grown from the melt, the *n*-CdTe + Te single crystals grown from the gas phase have a slightly more imperfect structure. In particular, the latter crystals contain tellurium inclusions (10^2–10^4 cm^{-2}) and the mean density of dislocations increases by one order of magnitude and amounts to approximately 10^5 cm^{-3}.

As was shown by Rudolph [10], the total concentration of technologically uncontrollable (residual) donor impurities (Ga, In, Al, Tl, Cl) in cadmium telluride single crystals grown by the Bridgman method can be as high as 10^{17} cm^{-3}. The maximum concentrations of the Group III elements under investigation are as follows: $N_{Ga} = 2.0 \times 10^{16}$ cm^{-3} and $N_{In} = 3.0 \times 10^{16}$ cm^{-3}.

We studied the initial (unsaturated) compound *p*-CdTe ($p \sim 10^{14}$ cm^{-3}, μ = 80–90 cm^2/(V s)) and the tellurium-saturated samples *n*-CdTe ($n \sim 10^{14}$ cm^{-3}, μ = 600–700 cm^2/(V s)), *n*-CdTe⟨In⟩ ($n \sim 10^7$ cm^{-3}, μ = 400–800 cm^2/(V s)), and *n*-CdTe⟨Cl⟩ ($n \sim 10^6$ cm^{-3}, μ = 300–500 cm^2/(V s)).

The low-temperature photoluminescence and exciton reflection spectra were recorded for natural cleavages of single crystals upon excitation of the studied samples under argon laser radiation at a power of ~10^{22} cm^{-2} s^{-1}. The photoelectric recording and synchronous detection were accomplished using standard techniques. The dispersion was provided by an SDL-1 spectrometer (linear dispersion, 6 Å/mm). The low-temperature investigations were performed with the use of an UTREKS temperature controller, which made it possible to maintain a constant temperature of the samples with an accuracy of 0.05 K.

In the case when the exciton photoluminescence spectra were measured in the range 1.606–1.580 eV (Fig. 1a), the activation energy E_b of isolated defects was determined from the binding energy E_b^{ex} of exciton–impurity complexes with the use of the Hines empirical relationship ($m_h^*/m_e^* = 4$) [1, 2]:

$$E_b^{ex} = \alpha E_b, \tag{1}$$

where α = 0.24, 0.2, and 0.1 for the ionized donor, neutral donor, and neutral acceptor, respectively.

The edge photoluminescence spectra of CdTe single-crystal samples with a dopant concentration of less than 10^{18} cm^{-3} in the range 1.57–1.50 eV (Fig. 1a) contain bands *D–A* and I_E. An increase in the dopant concentration leads to a considerable decrease in the intensity of the edge photoluminescence. According to Agrinskaya *et al.* [11], the mechanism of recombination responsible for the appearance of band I_E at an energy of 1.54 eV is consistent with the band–impurity scheme. Therefore, the thermal activation energy for the acceptor level (E_t = 0.06 eV) can be determined from the expression

$$E_t = E_g - h\nu(I_E), \tag{2}$$

where E_g = 1.606 eV at 4.5 K.

For low-resistance (uncompensated) samples, the same value of thermal activation energy E_t was obtained from the temperature dependences of the conductivity.

The optical activation energy E_0 was estimated from the long-wavelength edge of the photocurrent spectrum in the impurity region (Fig. 1b) or from the spectral

dependence of the IR quenching of photoconduction [11]. For all the samples studied, the optical activation energies fall in the range E_0 = 0.75–0.80 eV.

3. EXPERIMENTAL RESULTS AND DISCUSSION

The exciton photoluminescence spectrum of the *p*-CdTe single crystal at 4.5 K is shown in Fig. 2 (curve *1*). As can be seen, the spectrum contains the luminescence lines *A*, *D*, and *C* due to the annihilation of exciton–impurity complexes and also the broadened lines I_β (in the longer wavelength range) and *X* (at the frequency of free excitons). Agrinskaya *et al.* [12] assigned the *C* line at an energy of 1.5915 eV to the emission of several free excitons bound to one impurity atom. According to available data [2, 13], the *A* line at an energy of 1.5900 eV is associated with the annihilation of excitons bound to neutral acceptors (A^0, *X*), which are responsible for *p*-type conductivity. The competitive effect of *n*-type conductivity manifests itself in the fact that the exciton photoluminescence spectrum contains the *D* line at an energy of 1.5935 eV, which has a lower intensity and corresponds to the emission of excitons bound to neutral donors (D^0, *X*). The role of neutral states can be played by isolated residual impurities, intrinsic defects of the crystal lattice, and complexes formed by impurities and defects [2, 13].

The saturation of cadmium telluride single crystals with tellurium (Fig. 2, curve *2*) leads to an increase in the intensity and a narrowing of the lines I_β (at 1.5860 eV) and *X* (at 1.5965 eV) and the appearance of the dominant line I_α (at 1.5924 eV). In [2, 14], the I_α line is attributed to the emission of excitons bound to ionized donors (D^+, *X*). It should be noted that this shape of the exciton photoluminescence spectrum corresponds to *n*-type conductivity of the samples, even though an increase in the content of the anion component of the CdTe compound is accompanied by the generation of V_{Cd} acceptors [1, 2].

As regards the luminescence line I_β, the following interesting data are available in the literature. As was noted by Agrinskaya *et al.* [16], this line is typical of the exciton photoluminescence spectra of single crystals that are heavily doped with chlorine. However, according to our earlier data [8] and the results obtained in [16], the I_β line is also characteristic of the exciton photoluminescence spectra of CdTe + Te crystals. Worshech *et al.* [17] interpreted the I_β line as the phonon replica of the A^0–*X* line at a transverse acoustic phonon energy of 4.3 meV. Of the greatest interest, in our opinion, are the results obtained by Taguchi *et al.* [14], who explained the origin of the I_β line in terms of the recombination of a hole of the valence band and an electron trapped by a center with trigonal symmetry.

According to this mechanism of radiative recombination, the binding energy of electrons in traps (E_b = 0.02 eV) is determined from a relationship similar to expression (2) [14], that is,

$$E_b = E_g - h\nu(I_\beta). \quad (3)$$

Note that the trigonal symmetry is consistent with the microscopic model of an *X* center; i.e., the origin of the I_β line can be interpreted from this point of view.

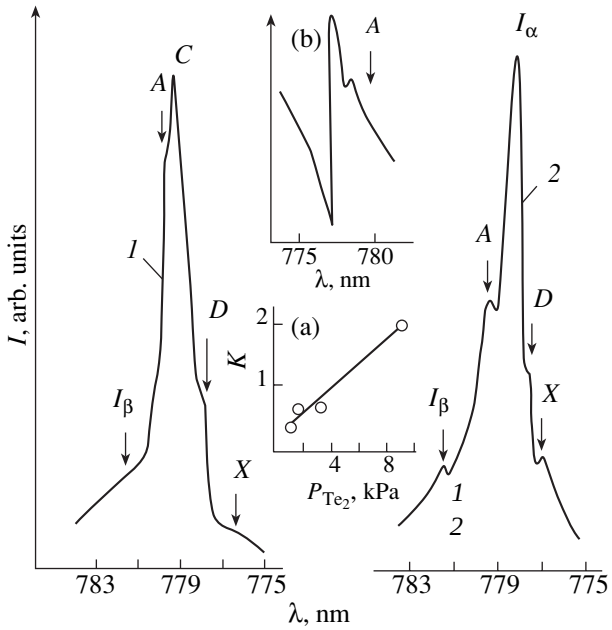

Fig. 2. Exciton photoluminescence spectra of (*1*) *p*-CdTe and (*2*) *n*-CdTe single crystals at *T* = 4.5 K. Tellurium vapor pressure in the cell P_{Te_2} = (*1*) 0.1 and (*2*) 3.0 kPa. Insets shows (a) the dependence of the intensity ratio *K* of line I_β to line *D* on the tellurium vapor pressure and (b) typical exciton reflection spectrum.

The problem of determining the conditions favorable for the formation of *X* centers is rather complicated and calls for special complex investigation. An analysis of the available data on the microstructure and x-ray diffraction of CdTe + Te single crystals allows us to draw the inference that tellurium precipitates are primarily responsible for the long-range elastic forces associated with the elastic stresses arising from the mismatch between the matrix and particles of the other phase. In our opinion, it is these stresses induced in the crystal lattice that bring about the displacement of residual impurities from sites to interstices. This assumption is confirmed by the increase in the intensity of the I_β line with an increase in the tellurium partial pressure upon saturation with tellurium (Fig. 2, inset (a)).

Figure 2 shows the exciton reflection spectrum for free (*n* = 1) and bound (line *A*) exciton states (see inset (b)). We assume that the *A* line observed at an energy of 1.5900 eV in the photoluminescence and exciton reflection spectra can be attributed to cadmium vacancies in the surface layer of the samples.

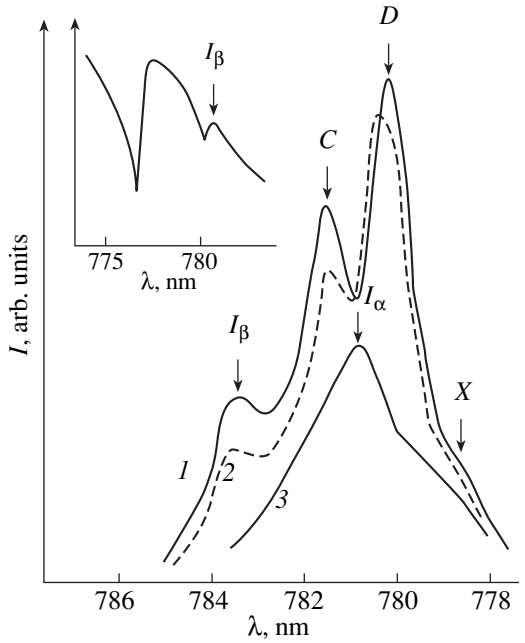

Fig. 3. Exciton photoluminescence spectra of the *n*-CdTe⟨Cl⟩ single crystal ($N_{Cl} = 5.0 \times 10^{17}$ cm^{-3}) at temperatures T = (*1*) 4.5, (*2*) 10, and (*3*) 20 K. The inset shows the exciton reflection spectrum.

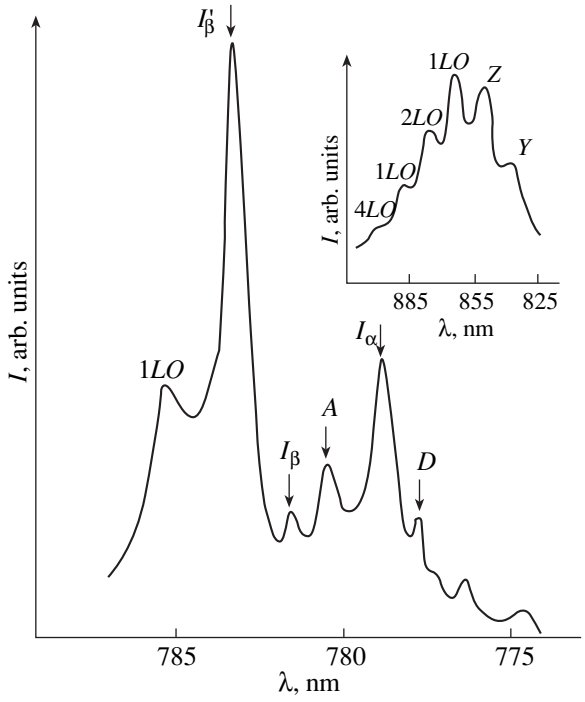

Fig. 4. Exciton photoluminescence spectrum of the CdTe⟨In⟩ semi-insulating single crystal grown from the gas phase (P_{Te_2} ~ 3.0 kPa) with the use of an indium-doped batch of synthetic cadmium telluride. The inset shows the typical emission spectrum of *A* centers in CdTe samples.

It is of interest to trace the evolution of the exciton photoluminescence spectra of CdTe⟨Cl⟩ compensated crystals ($N_{Cl} = 10^{17}$–10^{20} cm^{-3}) with variations in temperature (Fig. 3). At T = 4.5 K, the exciton photoluminescence spectra of CdTe⟨Cl⟩ crystals contain the *C*, *D*, and I_β lines, which are also observed in the spectra of *n*-CdTe low-resistance samples. An increase in the temperature is accompanied by quenching of exciton photoluminescence. As can be seen from Fig. 3, the exciton lines completely disappear in the temperature range 15–20 K. However, at $T \sim 20$ K, the spectra of CdTe⟨Cl⟩ crystals (irrespective of the chlorine concentration) contain the I_α line, which is absent at 4.5 K.

The exciton reflection spectrum shown in the inset to Fig. 3 does not exhibit the *A* line but contains the I_β line at an energy of 1.5860 eV, as is the case in the photoluminescence spectra of these samples. The *A* line disappears with a decrease in the concentration of isolated cadmium vacancies due to the formation of V_{Cd}–$2Cl_{Te}$ neutral complexes [8]. In turn, the appearance of the I_β line is associated with the formation of more electrically active complexes with V_{Cd} vacancies.

The exciton photoluminescence spectrum of the CdTe⟨In⟩ semi-insulating single crystal ($N_{In} \sim 5 \times 10^{16}$ cm^{-3}) is depicted in Fig. 4. It can be seen that the I'_β line observed at an energy of 1.5938 eV is dominant in the exciton photoluminescence spectrum. In [13, 17], this line is attributed to the annihilation of excitons bound to indium centers. The low-intensity line I_β is assigned to concomitant residual impurities.

As was shown by Agrinskaya *et al.* [16], the emission spectrum of *A* centers (see inset to Fig. 4) is associated with the transitions occurring inside an electrically active complex of a V_{Cd} vacancy with a donor impurity. The emission spectrum consists of several longitudinal optical phonon replicas of the zero-phonon line *Z* at an energy of 1.450 eV. The relative intensity of individual longitudinal optical phonon lines is adequately described by a Poisson distribution. The origin of the *Y* line at an energy of 1.477 eV remains unclear. Some authors assigned this band to tellurium precipitates [18].

The lattice distortion observed upon the formation of a *DX* center, as in the case of a Frenkel defect, is accompanied by the generation of an associated pair that consists of a vacancy (or part of a vacancy) and an interstitial donor. The aforementioned specific features of the photoluminescence and exciton reflection spectra of single crystals count in favor of the model of an associated defect being formed by a cation vacancy (V_{Cd}) and a residual donor impurity (D_{Cd}), which will be identified in Section 3.2.

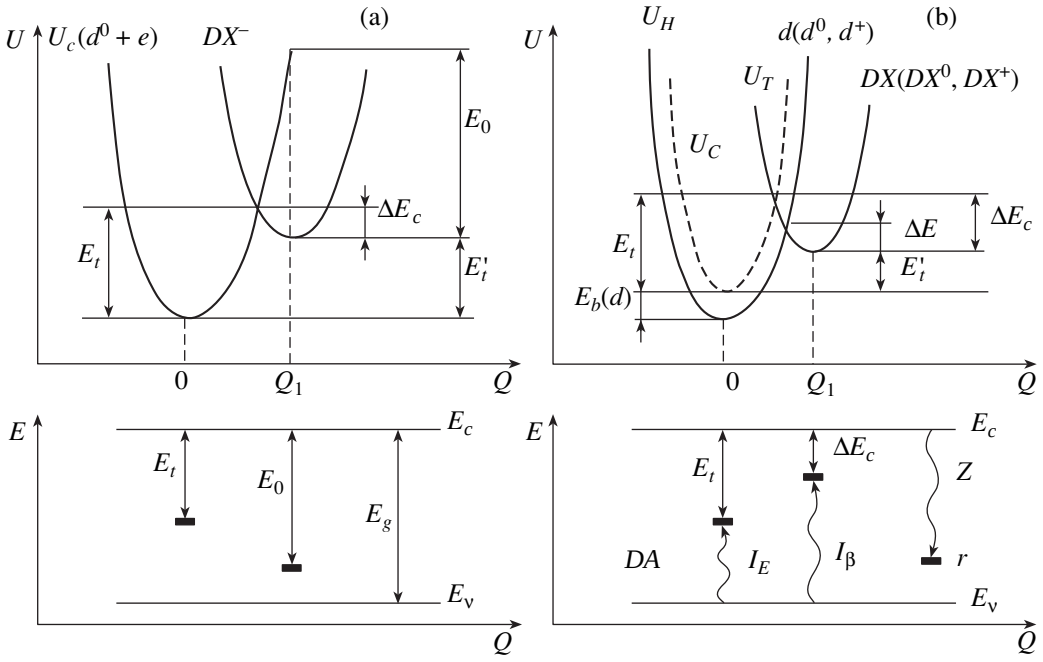

Fig. 5. Configuration-coordinate diagrams for metastable *X* centers: (a) a typical DX^- center [4–6] and (b) a V_{Cd}–D_i associated defect (D_i is an interstitial atom of the center-forming donor impurity). Designations: $U_{T(H)}$ is the energy of the "crystal–*X* center" system in the case of a tetrahedral (hexagonal) position of the interstitial center-forming atom, U_c is the energy of the "crystal–free electron" system, *E* is the energy of the free charge carrier, and *Q* is the configuration coordinate.

3.1. Configuration-Coordinate Diagram

Since the lines *D* (D^0, *X*) and I_α (D^+, *X*), which are characteristic of isolated hydrogen-like states of donors in cadmium telluride, are dominant in the exciton photoluminescence spectra of the studied crystals, we can draw the inference that the *X* centers are unstable upon high-intensity optical excitation of the system. In this respect, it is expedient to consider the model of a typical metastable DX^- center (Fig. 5a), which was proposed by Chadi and Park in [4–6]. First and foremost, we should make the following refinements. According to the configuration-coordinate diagram, the thermal activation energy E_t' is equal to the binding energy $E_b(DX^-)$ for a DX^- center. On the other hand, the experimentally measured activation energy E_t is determined by the height of the vibronic barrier between the ionized ($d^0 + e$) and unionized (DX^-) states of the deep-level center; that is,

$$E_t = E_b(DX^-) + \Delta E_c, \tag{4}$$

where ΔE_c is the height of the energy barrier to back thermally induced transfer of the carrier to the conduction band. For the most part, the value of ΔE_c is small compared to the binding energy $E_b(DX^-)$ and, hence, $E_t \sim E_t'$.

The optical activation energy E_0 determines the trap depth with respect to the conduction band. The appreciable difference between the activation energies E_t and E_0 can be explained on the basis of the Franck–Condon principle regarding the constancy of the configuration coordinate *Q* upon optical transition.

The above variant of the configuration-coordinate diagram corresponds to an undoped CdTe compound whose composition is close to stoichiometric. It will be shown below that the model of an *X* center, as applied to the studied crystals, should take into account both the impurity-defect structure of the samples and the difference between the positions of the center-forming atoms located in interstices.

A high degree of doping of a semiconductor compound can lead to a change in the charge state of DX^- centers. In particular, Chadi and Chang [7] described the transformation of Si : DX^- centers into the neutral state d^0 upon doping of the GaAs crystal with boron impurities. In this case, the impurities do not necessarily interact directly with *X* centers; however, under the action of dopant atoms, the DX^- centers become unstable.

In *n*-CdTe⟨Cl⟩ single crystals, the *DX* centers can undergo similar transformations in the field of Cl_{Te}^+ charged defects at high concentrations; that is,

$$DX^- + Cl_{Te}^+ \longrightarrow DX^0 + Cl_{Te}^0. \tag{5}$$

It should be noted that the occurrence of reaction (5) is a further factor accounting for the known effect of

"self-purification" of cadmium telluride crystals [19], i.e., the transformation of electrically active impurities into a neutral state due to the introduction of chlorine impurities.

In *n*-CdTe and *n*-CdTe⟨In⟩ single crystals with an excess of the anion component, the DX^- centers are most probably affected by neutral cadmium vacancies:

$$DX^- + V_{Cd}^0 \longrightarrow DX^+ + V_{Cd}^{2-}. \quad (6)$$

It follows from reactions (5) and (6) that the DX^- states in the above compounds are unstable with respect to the DX^0 and DX^+ states, which, in turn, in the absence of energy barriers [7], readily transform into the d^0 and d^+ states, respectively.

The configuration-coordinate diagram for a V_{Cd}–D_i associated defect (Fig. 5b) takes into account not only the transformations due to reactions (5) and (6) but also the possibility of an interstitial atom occupying two positions, namely, tetrahedral (*T*) and hexagonal (*H*) positions. This possibility is confirmed by the splitting of the photoluminescence line I_β under uniaxial compression along the [111] direction [14]. A similar model was used for V_{Zn}–Ga and V_{Se}–As associated defects in ZnSe single crystals [20] and Cl_{Te}–Cl_i pairs in CdTe single crystals [21].

The curves $U_H(Q)$ and $U_C(Q)$ lie close to each other, and their positions at $Q = 0$ differ by the binding energy of the charge carrier for a neutral (d^0) or ionized (d^+) donor. In this variant of the configuration-coordinate diagram, the optical activation energy E_0 (determined from the photoluminescence data) also corresponds to the trap depth with respect to the conduction band. Making allowance for the transition $DX^- \longrightarrow DX^+(DX^0)$, the thermal activation energy E_t can be represented in the form

$$E_t = E_b(DX) + \Delta E_c, \quad (7)$$

where $\Delta E_c = E_b(d) + \Delta E$. It is evident that ΔE_c in relationship (7) corresponds to the binding energy of the D_i element in the V_{Cd}–D_i associated pair. Therefore, compared to the binding energy $E_b(d^0) = 0.014$ eV [11, 22] for the isolated donor d^0, the binding energy for the D_i element increases by the barrier height ΔE and, according to expression (3), is equal to 0.02 eV. Consequently, we have the barrier height $\Delta E = 0.006$ eV and no spontaneous transformations of the type $DX^0 \longrightarrow d^0$ or $DX^+ \longrightarrow d^+$ occur at sufficiently low temperatures.

In the framework of the configuration-coordinate diagram of an associated defect, the specific features of exciton photoluminescence in CdTe single crystals can be explained as follows.

Let us assume that an *X* center is in the ground state DX^0 (*T* configuration) at liquid-helium temperature and is excited by high-power laser radiation. Upon optical excitation, the crystal lattice transforms into a nonequilibrium state and the center undergoes a jumpwise transformation into the *H* configuration, i.e., the d^0 state. In the photoluminescence spectra, these transformations manifest themselves in a substantial increase in the intensity of the *D* line. An increase in the temperature leads to defreezing of the neutral donor, and the I_α (D^+, *X*) line appears in the photoluminescence spectra and is dominant at 20 K. It is obvious that, when the DX^+ center is the initial state, the I_α line should also be dominant at $T = 4.5$ K.

According to Chadi and Chang [7], the probability that photoexcited charge carriers have the minimum energy necessary for the formation of *DX* centers can be written in the form

$$f(E_b) = [1 + \exp(E_b - E_F)/kT]^{-1}. \quad (8)$$

The stability of the *DX* center in the *T* configuration is associated with the stabilization of the Fermi level E_F at an energy level lying above $E_c = 0$ [7] by the binding energy of the center ($E_b = E_F$).

It should be noted that the stabilization of the Fermi level E_F in the conduction band manifests itself in a number of effects. In particular, the high-energy tail of the edge photoluminescence should be observed in the range of energies above $E_c = 0$ [20], which is considered to be a distinguishing feature of degenerated semiconductors. However, such effects are not observed in our photoluminescence spectra. Therefore, as was assumed above, the DX^0 (DX^+) states are unstable with respect to the d^0 (d^+) states at negative binding energies.

In this situation, we can use traditional statistics for compensated nondegenerated semiconductors [23]. For CdTe⟨Cl⟩ crystals, the Fermi energy at $T = 0$ coincides with the energy E_c. As the temperature increases, the Fermi energy decreases in accordance with the expression

$$E_F = E_c + kT \ln \frac{N_D - N_A}{N_c}, \quad (9)$$

where $N_D - N_A = n$ and N_c is the effective density of states in the conduction band of the CdTe compound.

At 20 K, the Fermi energy decreases by ~0.05 eV, which corresponds to complete ionization of states of the *X* center in the *H* configuration. This raises the question as to the stability of the associated defects, because the recombination barrier separating the interstice from the vacancy drastically decreases upon ionization of one of the elements forming an associated defect [24]. In the framework of the simplest model described in [24], the probability of recombination of a pair is determined by a relationship similar to expression (8) and is close to zero in the temperature range under consideration.

The model representations for the three types of deep-level centers responsible for the photoluminescence bands I_β, I_E, and *Z* are given in Table 1. The

scheme of the radiative transitions corresponding to these bands is shown at the bottom of Fig. 5b. For the studied crystals, the following two important remarks need to be made. (i) According to the model proposed in the present work, the local state of the *DA* double acceptor can be treated as a result of the transition between the configurations *T* and *H* of the optically excited *DX* center. (ii) As was shown for ZnSe crystals in [20], the presence of concomitant *A* centers can account for the fact that the studied samples do not exhibit a characteristic effect, namely, residual photoconductivity at sufficiently low temperatures [6].

3.2. Identification of the Electronic States of the DX Center

According to Chadi and Chang [7], we can write the relationship

$$E_b(DX^-) = 2E_b(DX)^0. \quad (10)$$

Relationships (1), (3), (7), and (10) were used to calculate the binding energies presented in Table 2. The binding energy $E_b(DX^-)$, which was determined using the parameters obtained above, coincides with the theoretical binding energy for a Ga : *DX* center [6]. Therefore, gallium residual impurities are the most probable center-forming donors that are responsible for the photoluminescence line I_β. This inference is supported by the results of analyzing the photoluminescence spectra of CdTe⟨In⟩ single crystals. Moreover, unlike other Group III elements, the Ga_{Cd} impurities form metastable *DX* centers (with a lower stability as compared to hydrogen-like states) [6], which is consistent with the model representations proposed in present work.

The binding energy of the DX^+ state for the CdTe and CdTe⟨In⟩ single crystals can be estimated in the same manner. In particular, the value of $E_b(DX^+)$ for the *n*-CdTe crystal is comparable to the binding energy $E_b(DX^0)$ for the *n*-CdTe⟨Cl⟩ crystal. However, we cannot make any generalizing inferences, because reliable theoretical data necessary for comparison are not available.

Now, we consider other experimental results in support of the proposed model of an *X* center. According to Takebe *et al.* [3], the double-acceptor level at an energy $E_c - 0.06$ eV is associated with a trap at an energy $E_c - 0.04$ eV, which was identified by deep-level transient spectroscopy. In our opinion, this level is identified with the level of the *DX* center in the *H* configuration. Since the cadmium telluride samples studied in [3] were annealed in cadmium vapors at high partial pressures p_{Cd}, proper allowance must be made for the effect of Cd_i interstitial atoms. The formation of the impurity energy band of Cd_i shallow levels ($E_c - 0.013$ eV [2]) in the vicinity of the Γ minimum of the CdTe crystal should lead to a sharp decrease in the binding energy of an isolated d^0 donor associated with a residual impurity.

Table 1. Radiative-recombination deep centers formed by cation vacancies and residual donor impurities in the CdTe compound

Center type	Designation	Photoluminescence band (at 4.5 K)	Model representation
V_{Cd}–D_i	*DX*	I_β	Frenkel-type defect in the *T* configuration
V_{Cd}^{2-}–d_i^+	*DA*	I_E	*D*X center in the *H* configuration
V_{Cd}^{2-}–d_{Cd}^+	*r*	*Z*	*A* center

Table 2. Characteristics of the energy spectrum of metastable *D*X centers in CdTe⟨Cl⟩ single crystals

State	Binding energy E_b, eV	Photoluminescence band $h\nu$, eV
d^+	0.015	I_α (1.5924)
d^0	0.015	*D* (1.5935)
	0.014 [11]*	
D_i	0.02	I_β (1.5860)
DX^0	0.04	
DX^-	0.08	
	0.08 [6]**	

* More exact value obtained from the Debye–Conwell equation.
** Theoretical value for a Ga : *D*X center.

In this case, according to relationship (7), we obtain $E_t \approx E_b(DX)$.

4. CONCLUSIONS

Thus, the main results obtained in this work can be summarized as follows.

(1) A model was proposed for *DX* centers in CdTe single crystals. According to this model, the displacement of a D_{Cd} residual donor impurity atom to the region of the nearest neighbor interstice brings about the formation of a V_{Cd}–D_i Frenkel-type defect (where *D* is a Group III element).

(2) The configuration-coordinate diagram for a V_{Cd}–D_i associated defect was constructed taking into account the tetrahedral and hexagonal positions occupied by the center-forming atom. The Stokes shift, *n*-type conductivity and the location of the Fermi level upon optical excitation of crystals, specific features of photoluminescence, and some other effects were explained on the basis of the configuration-coordinate diagram.

(3) The results of experimental investigations of the energy spectrum of *DX* centers in CdTe crystals are in agreement with available theoretical data.

REFERENCES

1. *Physics and Chemistry of II–VI Compounds*, Ed. by M. Aven and J. S. Prener (North-Holland, Amsterdam, 1967; Mir, Moscow, 1970).
2. K. R. Zanio, in *Semiconductors and Semimetals*, Vol. 13: *Cadmium Telluride*, Ed. by R. K. Willardson and A. C. Beer (Academic, New York, 1978).
3. T. Takebe, J. Saraie, and H. Matsunami, J. Appl. Phys. **53** (1), 457 (1982).
4. D. J. Chadi, Phys. Rev. Lett. **72** (4), 534 (1994).
5. D. J. Chadi, Appl. Phys. Lett. **59** (27), 3589 (1991).
6. C. H. Park and D. J. Chadi, Phys. Rev. B **52**, 11884 (1995).
7. D. J. Chadi and K. J. Chang, Phys. Rev. B **39**, 10063 (1989).
8. P. N. Tkachuk, V. I. Tkachuk, V. M. Tsmots', and V. S. Shtym, Neorg. Mater. **36**, 1443 (2000).
9. A. V. Savitskiĭ, P. N. Tkachuk, V. I. Chobotar, P. P. Beĭsyuk, P. N. Bukivskiĭ, and I. I. Blisko, Izv. Akad. Nauk SSSR, Neorg. Mater. **26**, 2661 (1990).
10. R. Rudolph, Prog. Cryst. Growth Charact. **29**, 275 (1994).
11. N. V. Agrinskaya, E. N. Arkad'eva, and O. A. Matveev, Fiz. Tekh. Poluprovodn. (Leningrad) **5** (5), 863 (1971) [Sov. Phys. Semicond. **5**, 762 (1971)].
12. N. V. Agrinskaya, N. N. Zinov'ev, O. A. Matveev, and I. D. Yaroshetskiĭ, Fiz. Tekh. Poluprovodn. (Leningrad) **14** (1), 55 (1980) [Sov. Phys. Semicond. **14**, 30 (1980)].
13. V. I. Gavrilenko, A. M. Grekhov, D. V. Korbutyak, and V. G. Litovchenko, *Optical Properties of Semiconductors: A Handbook* (Naukova Dumka, Kiev, 1987).
14. T. Taguchi, J. Shirafuji, and Y. Inuishi, Phys. Status Solidi B **68**, 727 (1975).
15. S. Seto, A. Tanaka, Y. Masa, and M. Kawashima, J. Cryst. Growth **117**, 271 (1992).
16. N. V. Agrinskaya, E. N. Arkad'eva, and O. A. Matveev, Fiz. Tekh. Poluprovodn. (Leningrad) **5** (5), 869 (1971) [Sov. Phys. Semicond. **5**, 767 (1971)].
17. L. Worshech, W. Ossau, F. Fisher, A. Waag, and G. Landwehr, J. Cryst. Growth **161**, 134 (1996).
18. V. N. Babentsov, Fiz. Tekh. Poluprovodn. (St. Petersburg) **30** (8), 1426 (1996) [Semiconductors **30**, 750 (1996)].
19. O. A. Matveev, E. N. Arkad'eva, and L. A. Goncharov, Dokl. Akad. Nauk SSSR **221** (2), 325 (1975) [Sov. Phys. Dokl. **20**, 220 (1975)].
20. P. N. Tkachuk, Fiz. Tverd. Tela (St. Petersburg) **44** (12), 2113 (2002) [Phys. Solid State **44**, 2211 (2002)].
21. R. Legros, Y. Marfaing, and R. Triboulet, J. Phys. Chem. Solids **39**, 179 (1978).
22. N. V. Agrinskaya, M. V. Alekseenko, E. N. Arkad'eva, O. A. Matveev, and S. V. Prokof'ev, Fiz. Tekh. Poluprovodn. (Leningrad) **9** (2), 320 (1975) [Sov. Phys. Semicond. **9**, 208 (1975)].
23. V. D. Popovich, G. M. Grigorovich, R. M. Peleshchak, and P. N. Tkachuk, Fiz. Tekh. Poluprovodn. (St. Petersburg) **36** (6), 674 (2002) [Semiconductors **36**, 636 (2002)].
24. J. Bourgoin and M. Lannoo, *Point Defects in Semiconductors: Experimental Aspects* (Springer, New York, 1983; Mir, Moscow, 1985).

Translated by O. Borovik-Romanova

Physics of the Solid State, Vol. 46, No. 5, 2004, pp. 833–835. Translated from Fizika Tverdogo Tela, Vol. 46, No. 5, 2004, pp. 811–812.

SEMICONDUCTORS AND DIELECTRICS

Band Structure and Permittivity of the $TlGaTe_2$ Compound

É. M. Godzhaev, G. S. Orudzhev, and D. M. Kafarova

Azerbaijani Technical University, pr. Dzhavida 25, Baku, Az1073 Azerbaijan

e-mail: Dilara-22@mail.ru

Received July 17, 2003

Abstract—The band structure of the $TlGaTe_2$ compound is calculated by the pseudopotential method. The spectral dependences of the real and imaginary parts of the complex permittivity are determined in the case when the polarizations are parallel and perpendicular to the optic axis of the crystal. © *2004 MAIK "Nauka/Interperiodica".*

1. INTRODUCTION

The triple compound $TlGaTe_2$ is a semiconductor of the TlSe type. This compound is the least known representative of the triple analogs of thallium selenide. The $TlGaTe_2$ compound, like the TlSe compound, has a body-centered tetragonal lattice with symmetry group D_{4h}^{18} (*I*4/*mcm*). Guseinov *et al.* [1, 2] determined the band gaps of the $TlGaTe_2$ semiconductor from electrical measurements. It was found that the band gaps differ drastically and amount to 2.3 eV [1] and 1.2 eV [2]. Moreover, the authors of [1] determined the temperature coefficient of the band gap (-3.14×10^{-4} eV/K).

All compounds of the aforementioned type have one feature in common; more specifically, they are compounds of univalent thallium (Tl^+) with the corresponding anionic radicals and consist of trivalent metals and chalcogens: $Tl^+(Me^{3+}X_2^{2-})$. In the $TlGaTe_2$ compound, the gallium atoms and their nearest environment (four tellurium atoms) form chains along the tetragonal axis **c**. The tetragonal axis is the optic axis of the crystal. The univalent thallium atoms have an octahedral environment consisting of eight tellurium atoms. The compounds under consideration are semiconductors, and their semiconducting properties are satisfactorily explained on the basis of the chemical bonding model proposed by Mooser and Pearson [3].

The band structure of the $TlGaTe_2$ compound was first calculated by Gashimzade and Orudzhev [4] using the empirical pseudopotential method. The form factors of the atomic pseudopotentials were calculated from an analytical expression proposed by Konstantinov *et al.* [5]. These calculations demonstrated that the valence band top is located at the high-symmetry point *T* (0, $2\pi/a$, 0) at the Brillouin zone boundary, whereas the conduction band bottom is aligned along the line *D* (π/a, π/a, *k*) at the Brillouin zone boundary. Those authors drew the conclusion that, for the $TlGaTe_2$ compound, the direct transition is forbidden by the selection rules.

Tables of the characters of simple irreducible and double-valued irreducible representations of groups in terms of the wave vectors relating to the space group D_{4h}^{18} (*I*4/*mcm*) were obtained by Gashimzade [6]. The compatibility conditions for irreducible representations of the simple and double-valued groups D_{4h}^{18} and the schematic drawing of the Brillouin zone (Fig. 1) for a body-centered tetragonal lattice with an axial ratio $c/a < 1$ are also presented in [6].

In this work, the band structure of the $TlGaTe_2$ compound was calculated by the pseudopotential method.

2. THEORETICAL BACKGROUND

The nonlocal ionic pseudopotentials in configurational space were constructed according to the scheme proposed by Bachelet *et al.* [7]. When calculating the band structure of the $TlGaTe_2$ compound, the screening

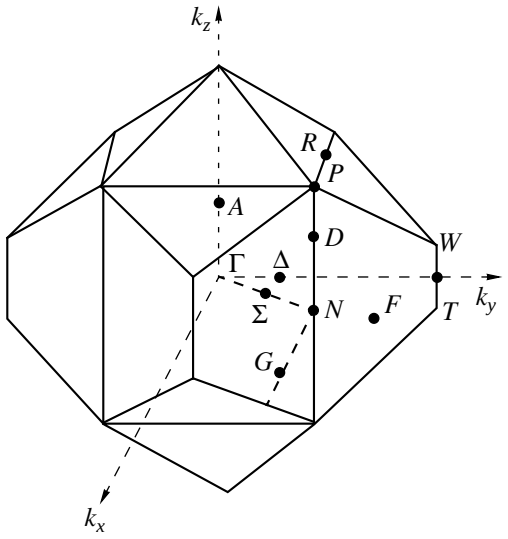

Fig. 1. Schematic drawing of the Brillouin zone for a body-centered tetragonal lattice of the $TlGaTe_2$ compound.

1063-7834/04/4605-0833$26.00 © 2004 MAIK "Nauka/Interperiodica"

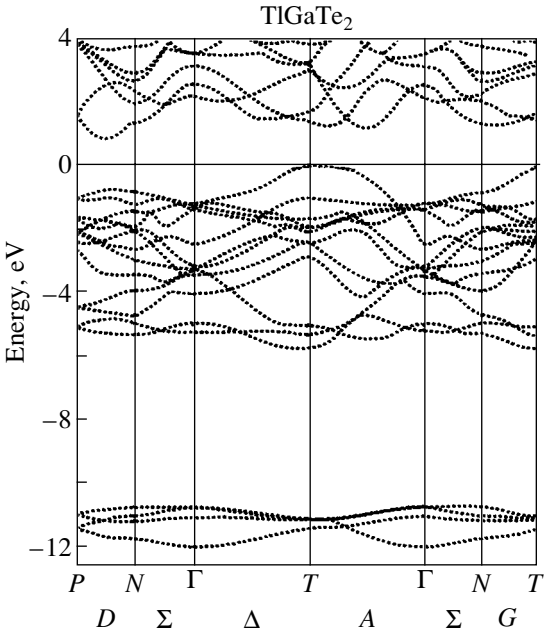

Fig. 2. Band structure of the $TlGaTe_2$ compound.

of the ion charge and the exchange–correlation effects were taken into account in the framework of the dielectric formalism using the Hubbard–Sham model with a sampling charge distribution around each ion. We used approximately 1800 plane waves in the expansion of the wave function. The maximum kinetic energy of the plane waves included was equal to 16 Ry.

For the $TlGaTe_2$ compound, the lattice parameters $a = 8.429(6)$ Å and $c = 6.865(4)$ Å and the parameter of the chalcogen $x = 0.170$ were taken from [8].

The band structure of the $TlGaTe_2$ compound is presented in Fig. 2. From analyzing these data, we can draw the following general conclusions.

(i) The valence band top is located at the high-symmetry point T on the surface of the Brillouin zone and corresponds to the irreducible representation T_3. The conduction band bottom is aligned along the line D at an equal distance from the points P (π/a, π/a, π/c) and N (π/a, π/a, 0), which corresponds to the irreducible representation D_1. The direct transition at the lowest energy occurs between the states T_3 and T_4 and is forbidden in the dipole approximation. According to our calculations, the band gap is equal to 0.86 eV.

(ii) The valence bands can be conventionally divided into three groups. The first group, which is characterized by the lowest energy (≈–11 eV) and consists of four bands, is formed by the Te 5*s* states. The second group, which is located in the energy range from –6 to –4 eV and composed of four bands, is predominantly formed by the Tl 6*s* and Ga 4*s* states. The third group, which is located in the energy range from –4 to 0 eV and consists of ten bands, is predominantly formed by the Te 5*p*, Tl 6*p*, and Ga 4*p* states. Our results concerning the origin of the energy bands are consistent with the data obtained by Okazaki *et al.* [9]. In [9], the authors investigated the photoemission spectra and performed the augmented plane wave calculation of the band structure of the $TlGaTe_2$ compound. However, these calculations demonstrated that, in the band structure, the valence band overlaps with the conduction band, which is in contradiction with the experimental data.

Our results and the data obtained in [9] do not confirm the theoretical inference made in [4] that, at the valence band top of the $TlGaTe_2$ semiconductor, there is an isolated group consisting of two bands. Apparently, this disagreement can be associated with the incorrect inclusion of the screening of the pseudopotential in the empirical method.

The optical properties of the $TlGaTe_2$ compound have not been adequately studied. In this respect, the purpose of the present work was to investigate the optical properties of the $TlGaTe_2$ compound theoretically. To accomplish this, we calculated the real and imaginary parts of the complex permittivity and the effective number of valence electrons in the case when the polarizations were parallel and perpendicular to the optic axis of the crystal.

In order to determine the frequency dependence of the imaginary part of the complex permittivity, we used the following relationship [10]:

$$\varepsilon_i(\omega) = \frac{4\pi^2 e^2}{m_e^2 \omega^2} \sum_{v,c} \int_{\text{zB}} \frac{2d^3k}{(2\pi)^3} \left|\mathbf{eM}_{cv}(\mathbf{k})^2\right| \times \delta(E_c(\mathbf{k}) - E_v(\mathbf{k}) \hbar\omega). \quad (1)$$

Here,

$$\mathbf{eM}_{cv}(\mathbf{k}) = \langle \psi_{c\mathbf{k}}(\mathbf{r}) | \mathbf{ep} | \psi_{v\mathbf{k}}(\mathbf{r}) \rangle = \mathbf{e} \int \psi^*_{c\mathbf{k}}(\mathbf{r}) (-i\hbar\nabla) \psi_{v\mathbf{k}}(\mathbf{r}) d^3r,$$

where the integral on the right-hand side represents the matrix element of the momentum operator $\mathbf{p} = -i\hbar\nabla$; v and c are the indices numbering the states of the valence and conduction bands, respectively; $\mathbf{k}$ is the wave vector; and $\mathbf{e}$ is the polarization unit vector. The integration is performed with respect to the unit cell volume of the crystal.

In expression (1), the integration with respect to the Brillouin zone was replaced by summation in the unit cell of the reciprocal lattice. For this purpose, the unit cell volume was divided into eight equal parts in which points of the wave vector $\mathbf{k}$ were chosen in a random way. A total of 1280 points were taken into account, and a smooth histogram was constructed from them. Then, this histogram was normalized according to the formula

$$\int_0^\infty \omega \varepsilon_i(\omega) d\omega = \frac{\pi}{2} \omega_p^2 = \frac{\pi}{2} \frac{4\pi n_e e^2}{m_e},$$

where ω_p is the plasma frequency of electrons, m_e is the electron mass, and n_e is the mean density of electrons in the crystal. The calculation showed that $\hbar\omega_p$ = 14.25 eV.

The histogram was constructed with a step of ≈0.2 eV. All transitions $v \longrightarrow c$ at an energy of up to 15 eV were taken into account. The frequency dependence of the imaginary part of the complex permittivity $\varepsilon_i(\omega)$ in the vicinity of 15 eV was extrapolated by the standard formula $\varepsilon_i(\omega)|_{\omega\to\infty} \sim \frac{1}{\omega^3}$.

The real part of the permittivity was calculated from the Kramers–Kronig integral dispersion relation

$$\varepsilon_r(\omega) = 1 + \frac{2}{\pi}P\int_0^\infty \frac{\omega'\varepsilon_2(\omega')d\omega'}{\omega'^2 - \omega^2}. \qquad (2)$$

Here, P stands for the principal value of the integral.

The effective number of valence electrons (per atom) involved in transitions at an energy $E \le \hbar\omega$ is determined by the expression

$$n_{\text{eff}} = \frac{m_e}{2\pi^2 e^2}\frac{1}{n_a}\int_0^\omega \varepsilon_i(\omega')\omega' d\omega', \qquad (3)$$

where n_a is the density of atoms in the crystal.

3. RESULTS

Figure 3 presents the results of our calculations of the optical functions in the energy range from 0 to 12 eV. The maxima of the principal peak in the spectrum $\varepsilon_r(\omega)$ for polarizations **e** ∥ **c** and **e** ⊥ **c** are located at energies of ≈2.72 and ≈2.50 eV, respectively. The maxima of the principal peak in the spectrum $\varepsilon_i(\omega)$ for polarizations **e** ∥ **c** and **e** ⊥ **c** are observed at energies of ≈1.85 and ≈1.19 eV, respectively. For the polarization **e** ⊥ **c**, the spectrum $\varepsilon_i(\omega)$ exhibits two additional peaks at energies of ≈1.63 and ≈3.37 eV. For the polarization **e** ∥ **c**, these additional peaks are located at energies of ≈2.28 and ≈3.81 eV but are considerably less pronounced. The effective number n_{eff} of valence electrons involved in transitions at an energy of less than 12 eV is equal to 3 for both polarizations. As should be expected, at higher energies, this number approaches 4.5.

The maximum permittivities ε_i for polarizations **e** ∥ **c** and **e** ⊥ **c** are approximately equal to 25.29 and 15.40, respectively. Such a difference is characteristic of chain crystals with strong anisotropy. The permittivities $\varepsilon_r(0)$ for polarizations **e** ∥ **c** and **e** ⊥ **c** are equal to 12.59 and 13.14, respectively.

Our theoretical results are in qualitative agreement with the experimental data on the optical properties of the TlSe compound studied earlier in [11].

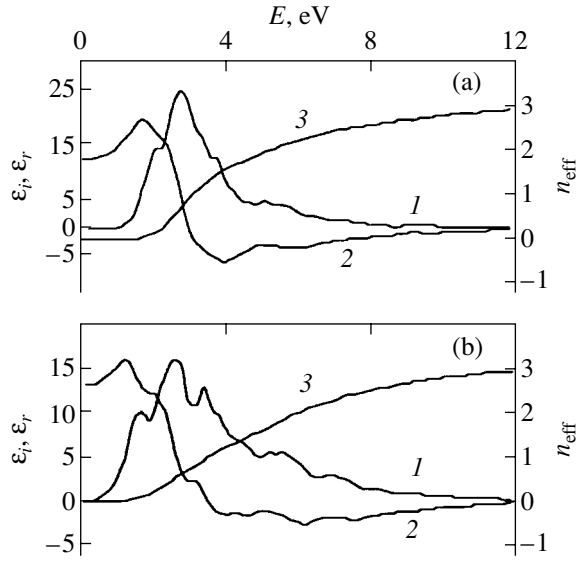

Fig. 3. Spectral dependences of (*1*) the imaginary ε_i and (*2*) real ε_r parts of the complex permittivity and (*3*) the effective number n_{eff} of valence electrons per atom in the $TlGaTe_2$ compound for polarizations (a) **e** ∥ **c** and (b) **e** ⊥ **c**.

ACKNOWLEDGMENTS

We would like to thank F.M. Gashimzade for his continuous interest in this work and for helpful remarks.

REFERENCES

1. G. D. Guseinov, G. B. Abdullaev, S. M. Bidzinova, F. M. Seidov, M. Z. Ismailov, and A. M. Pashaev, Phys. Lett. A **33A** (27), 421 (1970).
2. G. D. Guseinov, A. M. Ramazanzade, E. M. Kerimova, and H. Z. Ismailov, Phys. Status Solidi **22** (2), k117 (1967).
3. E. Mooser and W. B. Pearson, J. Electron. **1** (6), 629 (1956).
4. F. M. Gashimzade and G. S. Orudzhev, Dokl. Akad. Nauk AzSSR **36** (12), 18 (1980).
5. O. V. Konstantinov, Sh. K. Nasibullaev, and M. M. Panakhov, Fiz. Tekh. Poluprovodn. (Leningrad) **11** (5), 881 (1977) [Sov. Phys. Semicond. **11**, 519 (1977)].
6. F. M. Gashimzade, Fiz. Tverd. Tela (Leningrad) **2** (12), 3040 (1960) [Sov. Phys. Solid State **2**, 2700 (1960)].
7. G. B. Bachelet, D. R. Hamann, and M. Schluter, Phys. Rev. B **26** (8), 4199 (1982).
8. D. Muller, G. Eulenberger, and H. Hahn, Z. Anorg. Allg. Chem. **398**, 207 (1973).
9. K. Okazaki, K. Tanaka, J. Matsuno, A. Fujimori, L. F. Mattheiss, S. Iida, E. Kerimova, and N. Mamedov, Phys. Rev. B **64**, 045210 (2001).
10. Yu. I. Ukhanov, *Optical Properties of Semiconductors* (Nauka, Moscow, 1977).
11. L. L. Yanulenis, G. A. Babonas, M. A. Nizametdinova, G. S. Orudzhev, and A. Yu. Shileĭka, Litov. Fiz. Sb. **22** (3), 63 (1982).

Translated by I. Volkov

Physics of the Solid State, Vol. 46, No. 5, 2004, pp. 836–841. Translated from Fizika Tverdogo Tela, Vol. 46, No. 5, 2004, pp. 814–819.

SEMICONDUCTORS AND DIELECTRICS

Edge Photoluminescence Spectra and the Intensity of the Intracenter *f–f* Transitions in Er- and Sm-Doped GaN Crystals

V. V. Krivolapchuk, V. V. Lundin, M. M. Mezdrogina, A. V. Nasonov, S. V. Rodin, and N. M. Shmidt

Ioffe Physicotechnical Institute, Russian Academy of Sciences, Politekhnicheskaya ul. 26, St. Petersburg, 194021 Russia
e-mail: vlad.krivol@mail.ioffe.ru, margaret.m@mail.ioffe.ru

Received July 14, 2003; in final form, September 1, 2003

Abstract—Doping of GaN crystals prepared by various methods (HVPE and MOCVD) with various degrees of perfection of the mosaic structure, using rare-earth (RE) ions has been studied. An analysis of the shape of the photoluminescence spectra obtained before and after the doping showed that, as the defect concentration decreases, the intracenter *f–f* transitions characteristic of RE ions, at 1.54 and 0.54 μm in Er^{3+} and 0.72 μm in Sm^{2+}, become observable. The intracenter *f–f* transitions of RE ions are seen, as a rule, in epitaxial layers with well-aggregated and relaxed domains and are absent in the case of a mosaic structure containing domains in the near-surface part of the epitaxial layer that are not fully coalesced. RE doping of the crystals under study was observed to initiate defect gettering. © *2004 MAIK "Nauka/Interperiodica".*

1. INTRODUCTION

Doping the wide- and direct-band-gap gallium nitride GaN by rare-earth (RE) ions (GaN⟨RE⟩) makes this semiconductor a promising material for use in materials intended for visualization of information, including optical fiber devices if Er is used as a dopant [1]. It is known that photoluminescence (PL) at a wavelength of 1.54 μm (corresponding to minimum losses in the optical fiber) is observed at room temperature in the doped material GaN⟨Er⟩, which makes it possible to develop GaN⟨Er⟩-based *p–i–n* structures operating at $T = 300$ K. Another Er^{3+} transition, at a wavelength of 540–560 nm, i.e., in the green spectral region, was also found to have application potential.

Despite the considerable progress reached in the investigation of GaN⟨Er⟩, its application presently meets with difficulties associated with an insufficiently high quantum yield both at the wavelengths characteristic of the bound-exciton radiation, i.e., at the energies $E = 3.463$ eV (358 nm) and 2.29 eV (540 nm), and at the wavelength in the IR region, $E = 0.82$ eV (1.54 μm). It was also shown that only 1% Er of the total concentration of the impurity inserted into the semiconductor matrix is optically active [2]. This is why codoping (the introduction of additional impurities), in particular, of Mg, is used to form complexes with a large carrier capture cross section [3], which provides a high efficiency of electronic excitation transfer to the Er ions. Also, it is desirable to exclude other recombination channels for the electrons injected into the matrix. One of the most efficient channels of radiative recombination in GaN crystals is the donor–acceptor recombination, which is indicated by the presence of a broad band in the PL spectra at energy $E = 3.09$–3.26 eV. This emission band is usually associated with the donor–acceptor PL (D–A PL) and is due to the existence of shallow donor–acceptor pairs, whose depth, according to various estimates, is 25 meV for the donors and 220–240 meV for the acceptors [4]. The D–A PL was observed [5] to exist in Mg-doped GaN crystals, as well as in undoped ones [4]. The origin of the D–A PL in Mg-doped samples is assigned [4, 5] to a nonuniform distribution of the impurity and to its interaction with defects of the starting crystal. The appearance of D–A PL in the undoped material may indicate the presence of residual impurities and their interaction with crystal growth defects [6]. The growth of an epitaxial layer is accompanied by domain wall coalescence with simultaneous trapping of impurities, such as oxygen, silicon, and carbon, which form centers that act as shallow donors in nitrides. Hence, such a system may contain (depending on the actual growth conditions, the formation of a nuclei layer, and the extent of domain coalescence) a broad spectrum of impurity complexes with native defects. Note that the strained walls of an incompletely relaxed domain structure can spatially separate defects of the donor and acceptor types. All these structural features are conducive to the appearance of the D–A PL.

The question of what levels (donor or acceptor) are created by RE ions doping the GaN semiconducting matrix has not yet been considered, and there are no data whatsoever on the defects produced by RE ions in the band gap of this matrix [7, 8].

1063-7834/04/4605-0836$26.00 © 2004 MAIK "Nauka/Interperiodica"

Our purpose was to study how the characteristics of a system of extended defects (in particular, the degree of perfection of the mosaic structure) in the RE-doped original GaN layers influence the spectra of near-edge (NE) and D–A PL of the matrix and of the intracenter *f–f* RE transitions and establish mutual correlation between these spectra.

2. EXPERIMENT

The starting crystals were prepared by different techniques, namely, HVPE and MOCVD. Studies were conducted on two groups of samples differing in the degree of mosaic structure perfection; more specifically, in the first group, the domains in the near-surface region of the epitaxial layer were not completely aggregated, while in the second, the epitaxial layers were made up of well-aggregated and relaxed domains.

We studied two species of REs, Er and Sm. Samarium was chosen as a dopant because, in contrast to Er, which can reside, as a rule, in one charge state only, 3+, Sm can exist in two charge states, 2+ and 3+. Both dopants, Er and Sm, were introduced by diffusion, as in [9, 10]. The impurity diffused in the samples of the first and second groups by different mechanisms. In samples of the first group, diffusion involves grain boundaries (with strained and dangling Ga–N and N–H bonds at the grain boundaries), and in samples of the second group, crystal dislocations and defects.

A nitrogen laser (3371 Å) served to excite the PL. The PL spectra were measured with an SDL-2 spectrometer in the time-correlated photon-counting mode. To make the radiation spectra of different samples comparable, the controllable parameters, namely, the angle of light incidence, the excitation intensity, and temperature, were maintained constant. Measurements were made at 77 and 300 K.

3. RESULTS AND DISCUSSION

We studied the radiation at wavelengths of 1.54 and 0.54 μm for GaN⟨Er⟩ and at 0.72 μm for GaN⟨Sm⟩, as well as in the region 0.34–0.43 μm corresponding to the NE PL. The most essential characteristics are the position of the line due to excitons bound to shallow defects, its intensity, and the FWHM. Therefore, the main attention in analyzing the PL spectra was focused on the variation in these NE PL line characteristics of GaN crystals doped by RE metals.

In general, the radiation intensity I_r at an excitation level $G = f(I_{ex})$ depends on the total lifetime of nonequilibrium carriers τ. The total lifetime is determined, in turn, by the radiative, τ_r, and nonradiative, τ_{nr}, carrier recombination times: $\tau^{-1} = \tau_r^{-1} + \tau_{nr}^{-1}$. Therefore, the radiation intensity can be written as $I_r = G/(1 + \tau_r/\tau_{nr})$. Because for the given material (GaN) and our experimental conditions τ_r = const, the radiation intensity depends on τ_{nr}. The nonradiative recombination time τ_{nr} is determined by exciton trapping (with a cross section σ_i) to deep states (with concentration N_i), whose existence is due to various defects: $\tau_{nr}^{-1} = \Sigma_i v \sigma_i N_i^{NR}$ (here, v is the thermal velocity and i labels the defect type). From this it follows that, with all other experimental conditions being the same, samples with different PL intensities should differ primarily in the concentration of nonradiative recombination centers associated with deep levels. The lower the concentration of the nonradiative recombination centers (deep levels) N_i^{NR}, the higher the integrated PL intensity, and vice versa. Furthermore, the intensity of the radiation involving local centers is determined by the number of shallow centers taking part in the formation of the emission line, N_p, and by the transport of nonequilibrium charge carriers (due to excitation) to the trapping (shallow and deep) centers, as well as by their mutual positions in the lattice. For these reasons, the intensity and FWHM of the radiation lines (D^0, x; A^0, x) can be correlated to a certain extent.

Indeed, it is known that the emission line of defect-bound excitons is inhomogeneously broadened. Inhomogeneous broadening appears because the excitons bound to different centers differ slightly in the wavelength of the radiation they produce. This difference stems from the dispersion in the thermal activation energy of shallow levels ΔE_{DT} (and, hence, of the excitons bound to them) as a result of the local potential V_{loc} being different for various shallow defects. Doping of the starting crystal with REs may give rise to the appearance of an additional concentration of nonradiative states, restricted transport to the emission centers (D^0, A^0), and a nonuniform mutual distribution of shallow and deep centers. These factors bring about a restriction of the number of centers, N_p, involved in the emission line formation and may cause a significant correlated decrease in the intensity and FWHM of the emission lines (D^0, x; A^0, x). This behavior is characteristic of the emission lines of RE-doped (Er, Sm) crystals (see below).

Figures 1–4 present PL spectra of GaN crystals of the first group with various ratios of NE PL and D–A PL intensities measured before and after their doping with Er. Here, curves labeled *a* and *b* refer to undoped and Er-doped crystals, respectively.

Sample 1 is free-standing, and samples 2–4 are not separated from the substrate and differ from one another in the growth rate used, i.e., in the crystallite size and surface nonuniformity. The NE PL intensity (E_{max} = 3.46 eV) in the undoped crystals can be both substantially higher than the intensity of the D–A PL emission lines at E_{max} = 3.25 and 3.17 eV (Figs. 1, 2) and lower than it (Figs. 3, 4).

Doping the crystals with Er changes the shape of the PL spectra, depending on the PL spectrum of the start-

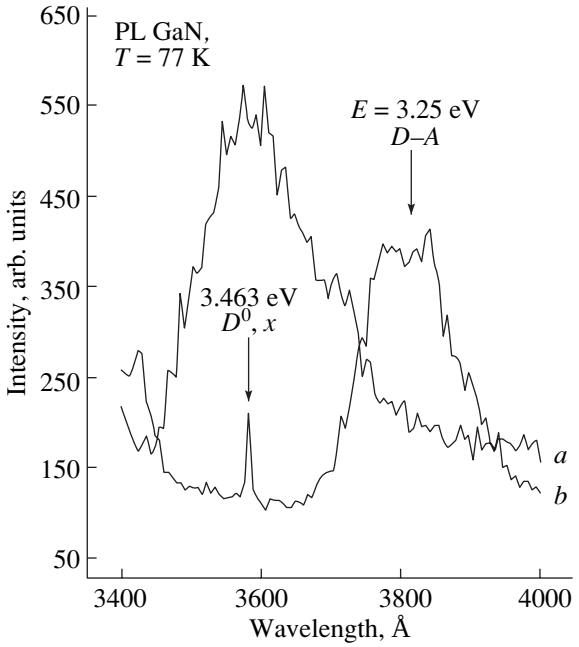

Fig. 1. Variation of near-edge photoluminescence of free-standing GaN crystal 1 (of the first group). (*a*) Starting crystal and (*b*) Er-doped sample.

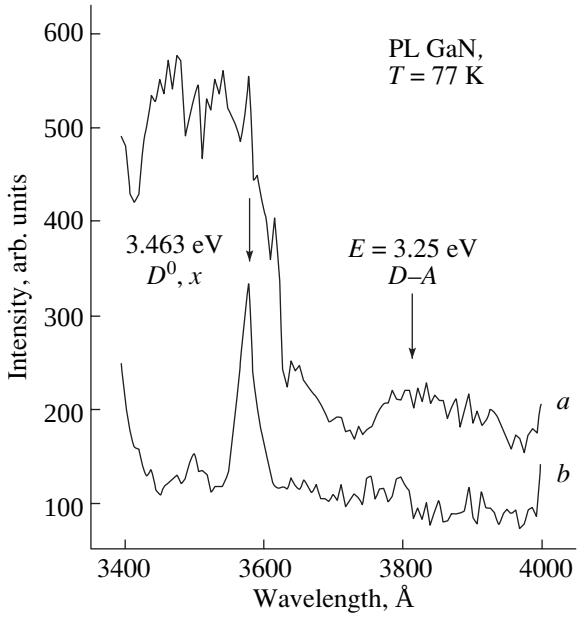

Fig. 2. Variation of near-edge photoluminescence of GaN crystal 2 (of the first group) not separated from the substrate. The notation is the same as that in Fig. 1.

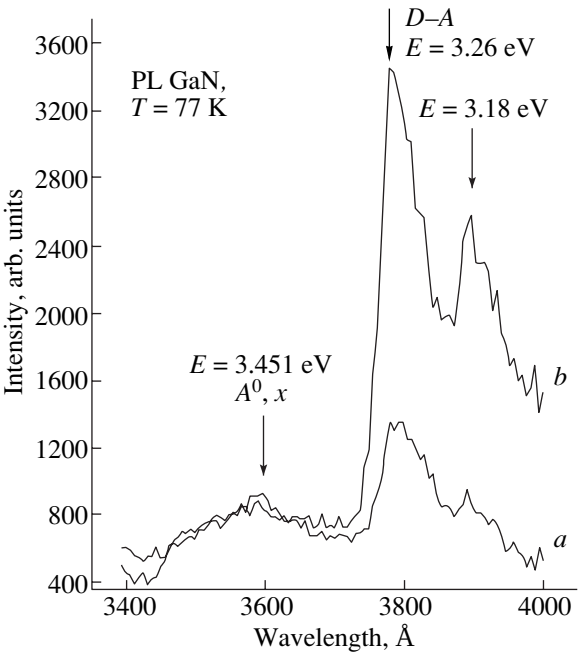

Fig. 3. Effect of Er doping on the donor–acceptor emission of GaN crystal 3 (the first group). The notation is the same as that in Fig. 1.

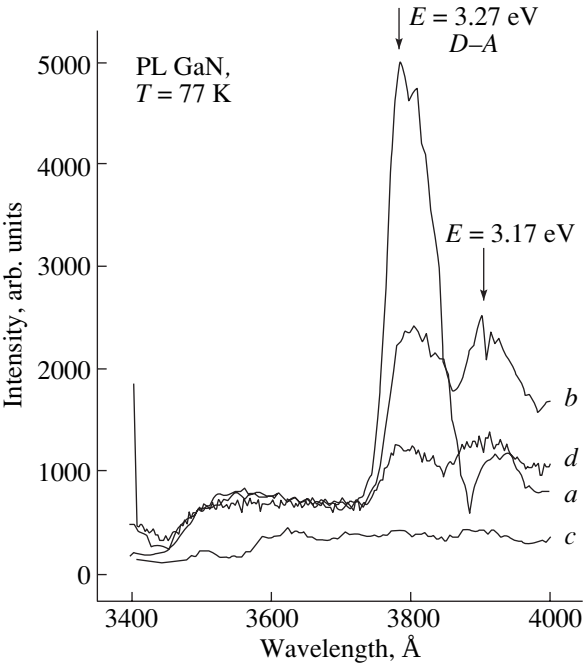

Fig. 4. Photoluminescence spectra of GaN crystal 4 (the first group). (*a*) Starting crystal, (*b*) Er-doped, (*c*) after polishing, and (*d*) following polishing and Er doping.

ing crystal. Crystal 1 (Fig. 1) exhibits, in place of NE PL, a peak with a substantially smaller FWHM (7.4 against 181 meV) and a considerably lower intensity than that of the starting crystal. (Note that this decrease in the FWHM may also be evidence of a decrease in carrier concentration [11].) In addition, a much stronger D–A PL band appears, which originates from shallow-donor–acceptor pairs [5]. The NE PL to D–A PL

intensity ratio in the starting crystal 2 (Fig. 2) differs only insignificantly from that in crystal 1. The spectrum observed after the doping consists only of one emission line peaking at 3.46 eV (NE PL, 358 nm). In both crystals, one observes a decrease both in the NE PL intensity and in the magnitude of the FWHM (down to 28 meV; the original value was 300 meV), with practically no D–A PL seen, which indicates the absence of shallow acceptor centers. This provides supportive evidence for the misfit strains (caused by the difference in the lattice parameters between the substrate and the crystal grown on it) not playing a significant role in the formation of PL spectra. Figure 3 displays spectra of crystal 3, whose ratio of the D–A PL to NE PL intensities is larger than that of the preceding two crystals. After the doping, the shape of the spectrum in the NE PL region does not change, whereas the D–A PL intensity increases strongly. This suggests a substantial increase in the shallow acceptor concentration. Therefore, the influence of the Er dopant is similar to that of Mg [12]. Figure 4 shows spectra of sample 4, where the intensity of the D–A PL band exceeds that of the NE PL by nearly an order of magnitude. Crystal 4 differs from sample 3 in that it has a smaller crystallite size, because it was obtained at a higher growth rate. After the doping, the D–A PL intensity decreased, but (similar to the case with sample 3) no increase in the NE PL intensity was observed. It may be assumed that here we have an increase in concentration either of the deep centers (because the shallow levels became deep) or of the shallow donors, a situation similar to the changes in GaAs [13]. Several explanations can be given for such transformations of the shallow to deep levels (i.e., a change in the localization length): (i) lattice reconstruction, (ii) a high concentration of surface and metastable states, and (iii) strain relaxation, which transfers part of the impurities (including the extrinsic ones) from lattice to interstitial sites, thus in the end changing the defect charge state.

These results suggest that the part played by each factor can be determined by varying the concentrations of both the impurity and the surface and metastable states. To do this, one needs to vary the parameters of the diffusion properly, as well as of the growth process of the starting crystals. Therefore, crystal 4 was subjected to additional mechanical treatment, including grinding followed by polishing.

Figures 1–4 (curves *c*, *d*) show spectra of crystal 4 polished to a depth of 20 μm. Polishing removed the emission lines characteristic of the NE PL and D–A PL, which indicates an increase in the concentration of nonradiative recombination centers. After the doping, the PL spectra of crystal 4 (GaN⟨Er⟩) exhibit D–A PL and NE PL, the intensity of the latter being equal to that observed before the polishing. The intensity of D–A PL exceeds that of NE PL. Such a change in spectral shape (curve *b* in Fig. 3 illustrates a similar behavior) may be evidence of an increase in the donor–acceptor pair concentration caused by a transformation of the contributions due to various defects of the matrix.

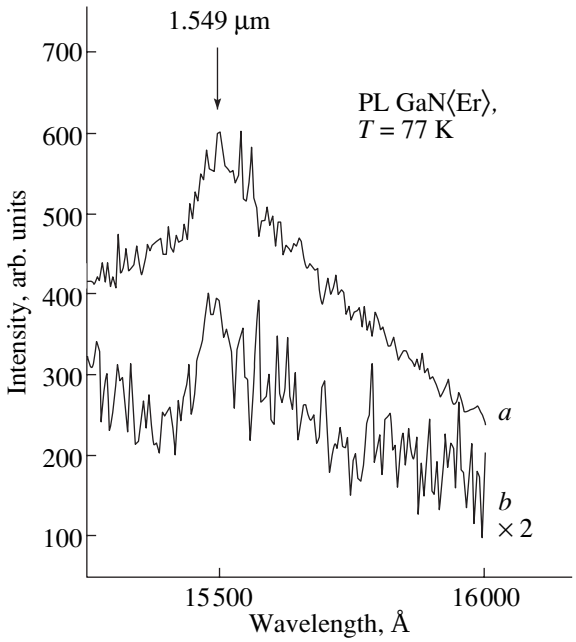

Fig. 5. IR emission spectra of GaN⟨Er⟩ crystals of (*a*) the second and (*b*) first groups.

It should be noted that the long-wavelength emission lines characteristic of the Er^{3+} *f–f* intracenter transition (0.54 μm) are present in the spectra of crystals 1 and 2 but are not observed in crystals 3 and 4. The IR emission line (1.54 μm) is observed in crystal 4 (although its intensity is weak) and is not detected in crystals 1–3. Observation of the D–A PL in a crystal indicates the existence of an additional recombination channel in the short wavelength region of the spectrum. This channel, which is more important for the recombination, most likely hampers the population of the rare-earth centers, which accounts for these crystals not emitting at a wavelength of 1.54 μm. Note that the intensity of the green emission line (0.54 μm) is high enough for it to be detected with the sensitivity of the instruments used in the present study.

In the long-wavelength region (1.54 μm), one observes PL in MOCVD-grown crystals of the second group which do not feature the D–A PL band (curve *a* in Fig. 5) and, hence, do not have additional nonradiative recombination channels.

Figure 5 (curve *b*) shows the PL spectrum of crystal 4. The intensity of the 1.54-μm line of crystals of the second group is seen to be considerably higher than that of crystal 4 (first group).

The short-wavelength NE PL spectra of the starting and doped GaN crystals of the second group are practically identical, which implies that doping did not bring about any significant changes in spectral shape. By analogy with [14], the presence of the D–A PL band

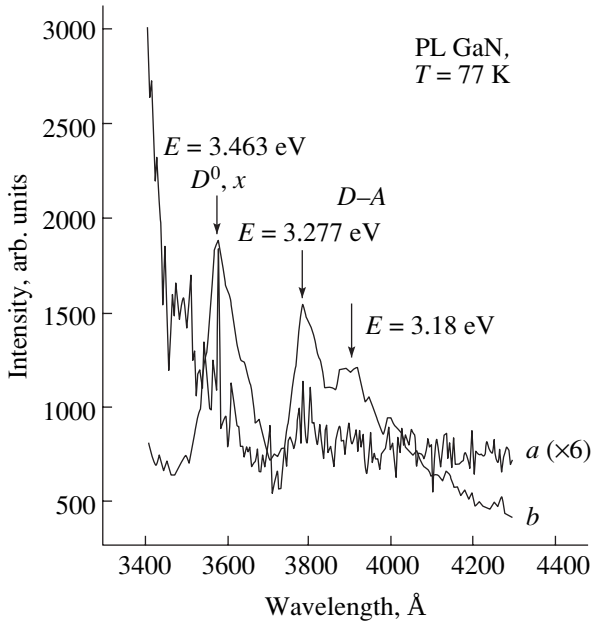

Fig. 6. Variation of the near-edge photoluminescence spectrum of a GaN crystal of the first group (*a*) before and (*b*) after Sm doping.

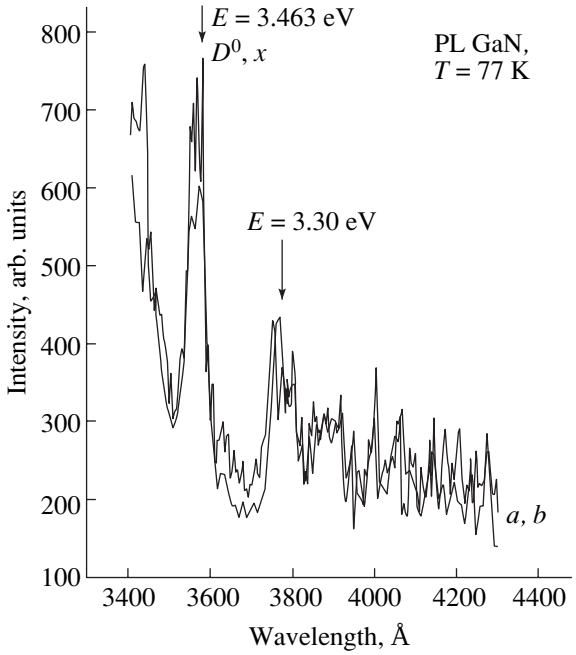

Fig. 7. Variation of the near-edge photoluminescence spectrum of a GaN crystal of the second group (*a*) before and (*b*) after Sm doping.

can be assigned to nonuniformities in the structural morphology of the crystals under study.

Earlier studies [9] revealed the transformation of shallow to deep states in GaN⟨Er⟩ crystals. This effect was observed with the dopant having two charge states, Eu^{2+} and Eu^{3+}, which is supported by Mössbauer charge-state measurements [15]. Measurements of optical transmission spectra established Er to enter substitutionally on the Ga sites in the GaN crystal lattice [16]. Thus, one may consider Er to be a substitutional impurity that can interact both with the matrix and the defects of the starting crystal. An EXAFS study [17] showed the Ga–N bond length (1.95 Å) to be smaller than the Er–N length (2.42 Å), so insertion of Er into the crystal lattice should induce tensile misfit strains. At the same time, optical reflectivity and PL studies have shown [4, 10] that undoped crystals are characterized, as a rule, by compressive strains. One can thus suggest that the introduction of Er^{3+} (as an isovalent impurity) should be conducive to stress relaxation and a decrease in defect concentration as a result of the decrease in the concentration of stressed or dangling Ga–N and N–H bonds and, hence, to various changes in both the NE PL and D–A PL spectra.

Doping of GaN crystals with samarium, which was chosen because its ions, like those of Eu, can reside in two charge states, 2+ and 3+, was carried out with the purpose of determining the probability of defect transformation in the matrix. These two RE metals differ substantially in chemical activity, a factor that can affect the mechanism of doping of GaN crystals, because in the case of Eu^{2+} the precipitates (Eu^{2+} + oxygen) are possibly capable of diffusion and insertion into the hexagonal crystal lattice, while in the case of Sm, the bonding type can convert from ionic–covalent (characteristic of Ga–N) to ionic (typical of RE–N) because of the RE metals and Ga having different electronegativities (1.1–1.3 against 1.8) [18]. Figure 6 pre-

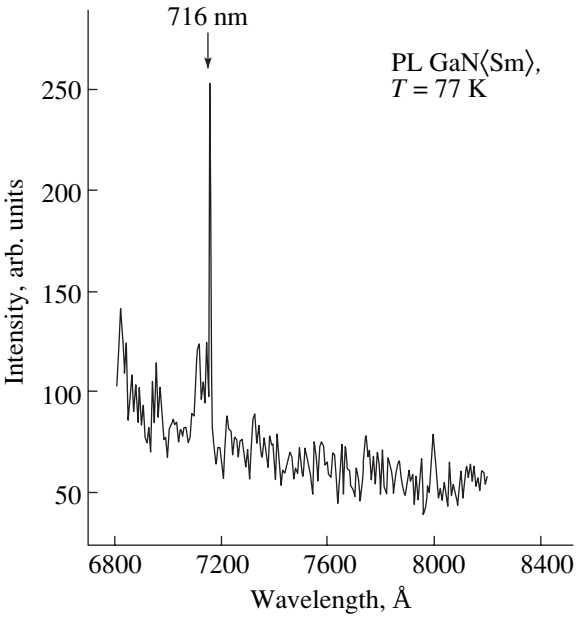

Fig. 8. Intracenter emission of the Sm ion in a GaN crystal of the second group.

sents NE PL spectra of a crystal of the first group (*a* corresponds to the starting crystal, *b* to the crystal doped with Sm). As in [9], the change in spectral shape is most likely due to the transformation of deep to shallow defects, because one readily sees the D–A PL band and, in addition, a gettering effect (the NE PL intensity increased after the doping even though the FWHM also increased). Figure 7 displays spectra of a GaN crystal of the second group (*a* corresponds to the starting crystal, *b* to the crystal doped with Sm). The spectra are seen to be practically identical; indeed, doping affected neither the NE PL intensity nor the FWHM of the band. Shown in Fig. 8 is the long-wavelength spectrum of the doped crystal, which clearly exhibits a peak at 716 nm (characteristic of the Sm^{2+} emission line) corresponding to the *f–f* intracenter transition.

4. CONCLUSIONS

The intensity of the 0.54- and 1.54-μ m emission lines in GaN crystals is higher, the lower the intensity of the D–A PL band. A study of the evolution of the D–A PL spectra of GaN⟨Er⟩ crystals has established that a decrease or increase in the concentration of the donor–acceptor pairs responsible for the D–A PL intensity depends on the degree of perfection of the mosaic structure of the starting sample; namely, insertion of a dopant (Er^{3+}) into a more perfect matrix can increase the D–A PL intensity, as in the case of Mg^{2+} doping. Introduction of Er^{3+} and Sm (which can reside in two charge states, 2+ and 3+, as in the case of Eu doping) produces similar changes in the PL spectra and reveals the gettering effect. The results obtained in this study suggest that reducing the defect concentration in the starting semiconductor matrix is a necessary condition for efficient RE doping of GaN crystals (irrespective of the actual growth method used).

REFERENCES

1. A. J. Steckl and B. Birkhahn, Appl. Phys. Lett. **73**, 1700 (1998).
2. A. J. Steckl, M. Garter, B. Birkhahn, and J. D. Scofield, Appl. Phys. Lett. **74**, 2161 (1999).
3. S. Kim, S. J. Rhee, D. A. Turnbull, X. Li, J. J. Coleman, S. G. Bishop, and P. B. Klein, Appl. Phys. Lett. **71**, 2662 (1997).
4. P. H. Lim, B. Schnieler, O. Schon, and H. Heino, J. Cryst. Growth **205**, 1 (1999).
5. V. Yu. Nekrasov, L. P. Belyakov, O. M. Sreseli, and N. N. Zinov'ev, Fiz. Tekh. Poluprovodn. (St. Petersburg) **33**, 1428 (1999) [Semiconductors **33**, 1284 (1999)].
6. N. A. Cherkashin, N. A. Bert, Yu. G. Musikhin, S. V. Novikov, T. S. Cheng, and C. T. Foxon, Fiz. Tekh. Poluprovodn. (St. Petersburg) **34**, 903 (2000) [Semiconductors **34**, 867 (2000)].
7. M. Cadoret, J. Cryst. Growth **205**, 123 (1999).
8. S. M. Myles, A. F. Wright, G. A. Peterson, C. H. Seager, W. R. Wampler, M. H. Crawford, and J. Han, J. Appl. Phys. **88**, 4676 (2000).
9. V. V. Krivolapchuk, M. M. Mezdrogina, A. V. Nasonov, and S. V. Rodin, Fiz. Tverd. Tela (St. Petersburg) **45** (9), 1556 (2003) [Phys. Solid State **45**, 1634 (2003)].
10. Yu. V. Zhilyaev, V. V. Krivolapchuk, M. M. Mezdrogina, S. D. Raevskiĭ, A. P. Skvortsov, and Sh. A. Yusupova, in *Proceedings of International Symposium on Photo- and Electroluminescence of Rare-Earth Elements in Semiconductors and Dielectrics* (St. Petersburg, 2001), p. 27.
11. E. Illipoulus, D. Doppalaudi, H. M. Hg, and T. D. Moustakas, Appl. Phys. Lett. **73**, 375 (1998).
12. Y. Golan, X. H. Wu, J. S. Speck, R. P. Vaudo, and V. M. Phase, Appl. Phys. Lett. **73**, 3090 (1998).
13. V. V. Krivolapchuk, M. M. Mezdrogina, and N. K. Poletaev, Fiz. Tverd. Tela (St. Petersburg) **45** (1), 29 (2003) [Phys. Solid State **45**, 28 (2003)].
14. S. Kim, S. J. Rhee, X. Li, J. J. Coleman, and S. C. Biscop, Appl. Phys. Lett. **76** (17), 2403 (2000).
15. Yu. V. Kozhanova, V. V. Krivolapchuk, M. M. Mezdrogina, S. V. Rodin, and Yu. V. Zhilyaev, in *Proceedings of the 2nd All-Russian Conference on Gallium, Indium, and Aluminum Nitride: Structures and Devices* (St. Petersburg, 2003), p. 6.
16. V. V. Krivolapchuk, M. M. Mezdrogina, S. D. Raevskiĭ, A. P. Skvortsov, and Sh. A. Yusupova, Pis'ma Zh. Tekh. Fiz. **28** (7), 19 (2002) [Tech. Phys. Lett. **28**, 270 (2002)].
17. P. H. Citrin, P. A. Northrup, and B. Birkhahn, Appl. Phys. Lett. **76**, 2865 (2000).
18. P. Perlin, T. Suski, M. Leszezynski, and H. Teisseyre, in *GaN and Related Materials,* Ed. by S. Pearton (Gordon and Breach, Amsterdam, 1997), p. 315.

Translated by G. Skrebtsov

Physics of the Solid State, Vol. 46, No. 5, 2004, pp. 842–847. Translated from Fizika Tverdogo Tela, Vol. 46, No. 5, 2004, pp. 820–825.

SEMICONDUCTORS AND DIELECTRICS

Intrinsic Ultraviolet Luminescence of LiB_3O_5 Single Crystals under Inner-Shell Excitation

I. N. Ogorodnikov*, V. A. Pustovarov*, and M. Kirm**

**Ural State Technical University, ul. Mira 19, Yekaterinburg, 620002 Russia*

e-mail: ogo@dpt.ustu.ru

***Institut für Experimentalphysik der Universität Hamburg, Luruper Chaussee 149, Hamburg, D-22761 Germany*

Received July 28, 2003

Abstract—Ultraviolet photoluminescence (PL) of LiB_3O_5 (LBO) crystals has been studied under selective excitation by photons in the vacuum ultraviolet and ultrasoft x-ray regions, including the *K*-absorption edges of the Li and B cations and O anion. Radiative recombination of electron–hole pairs was established to be the main channel of the intrinsic PL excitation at 4.2 eV. Features were observed in the PL excitation spectra near the lithium and boron *K*-absorption edges originating from excitation of the cation 1*s* core excitons. Experimental evidence of the multiplication of Li 1*s* excitons in LBO was obtained. It is shown that excitation of the O 1*s* core excitons does not affect the PL yield noticeably. The differences in the appearance of the Li, B, and O 1*s* excitons in the excitation spectra of the LBO ultraviolet PL are discussed. © *2004 MAIK "Nauka/Interperiodica".*

1. INTRODUCTION

Studies of the relaxation and multiplication of intrinsic electronic excitations in various optical materials performed with the use of synchrotron radiation under selective photoexcitation in the vacuum ultraviolet (VUV) spectral region have been recently attracting considerable interest. High-sensitivity luminescence methods have been employed to explore the generation of secondary anion excitons and electron–hole pairs following VUV photon absorption in alkali halide crystals [1]; wide-band-gap oxides [2–4], including crystals promising for use in nonlinear optics [5–7]; and other systems. Secondary electronic excitations can also be produced by hot photoelectrons and, in some cases, by hot photoholes created in core state excitation [8–10]. Secondary cation excitations and electron–hole pairs in wide band-gap oxides are produced, as a rule, at higher excitation energies in the ultrasoft x-ray energy region. This accounts for the substantial difficulties of a technical nature that arise in the corresponding experimental studies.

The possibility of performing experiments in time-resolved luminescence spectroscopy on the BW3 channel (HASYLAB, DESY) [11] stimulated investigation of the cation and anion core excitations in wide band-gap crystals, including oxides [2, 12], fluorides [12, 13], noble gas cryocrystals [14], and other compounds. However, no studies have been carried out thus far on nonlinear optical crystals in this excitation energy region even though they have high application potential. This is why we chose for our study nonlinear optical crystals of lithium triborate LiB_3O_5 (LBO), on which a wealth of experimental information on the dynamics of electronic excitations in the VUV spectral region has already been amassed [5, 7]. The *K*-absorption edges for the atoms making up the LBO lie at 54.99 (Li), 187.99 (B), and 537.00 eV (O). The corresponding peaks in the x-ray photoelectron spectra of LBO are observed at 55.5, 192.0, and 531.6 eV [15].

The present study dealt with the processes involved in the formation of the primary and secondary cation and anion excitations, as well as with their decay channels in lithium triborate crystals, which were probed using time-resolved luminescence spectroscopy under selective excitation by synchrotron radiation in the VUV and ultrasoft x-ray spectral regions.

2. EXPERIMENT

The time-resolved photoluminescence (PL) spectra in the range 2.5–8.3 eV, time-resolved PL excitation spectra (40–200 eV, 520–610 eV), and PL decay kinetics were measured under selective photoexcitation by synchrotron radiation from the BW3 beam line of HASYLAB at DESY. The excitation was performed by undulator radiation through a Zeiss SX700 monochromator, which produced a photon flux $I_{max} \leq 5 \times 10^{12}$ photons/s in the energy region extending from 40 to 2000 eV [11]. The spectral resolution of the Zeiss SX700 monochromator was typically 50 and 900 meV at the lithium and oxygen *K*-absorption edges, respectively. The excitation spectra were normalized against the incident photon flux by means of an AXUV-100 photodiode (International Radiation Detector, Inc.). Luminescence was measured with a vacuum monochromator (0.4 m, Seya–Namioka arrangement) and a microchannel photomultiplier (MCP 1645 U-09, Hamamatsu). Time-resolved spectra were recorded

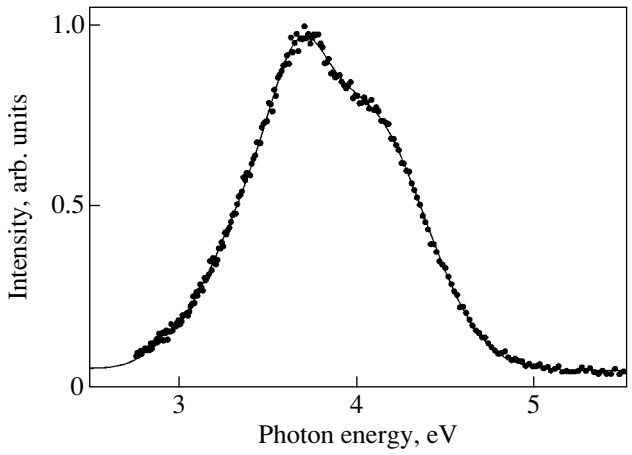

Fig. 1. Normalized PL spectra of an LBO crystal obtained at 290 K under selective excitation by 25-eV photons.

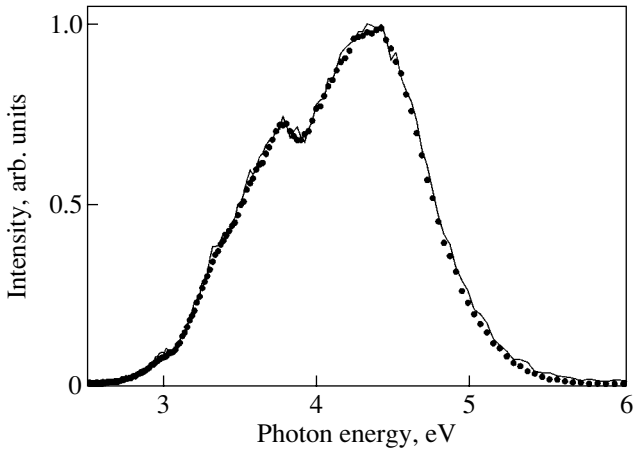

Fig. 2. Normalized PL spectra of an LBO crystal obtained at 290 K under selective excitation by photons of energy 140 (points) and 600 eV (solid line).

with a gate Δt wide, which could be delayed by a time δt with respect to the excitation pulse of the synchrotron radiation. We performed measurements with three independent gates with the following parameters: δt_1 = 0.2 ns and Δt_1 = 6.4 ns; δt_2 = 19.5 ns and Δt_2 = 20.5 ns; and δt_3 = 43 ns and Δt_3 = 107 ns. These measurements were carried out parallel by recording spectra without time resolution, i.e., time-integrated spectra. The PL spectra are presented here without correction for the spectral sensitivity of the analyzing channel. The effective time resolution of the measurement system was about 250 ps (FWHM).

The spectral and kinetics measurements at incident photon energies of 4–35 eV were carried out under selective photoexcitation by synchrotron radiation at the SUPERLUMI experimental station [16] of the HASYLAB, DESY laboratory. The equipment and measurement techniques employed were described in our earlier publications [5, 6].

We used nonactivated crystals of lithium triborate LiB_3O_5 of a high optical quality grown at the Single-Crystal Research and Technology Institute (Siberian Division, Russian Academy of Sciences, Krasnoyarsk). The technique used to grow the crystals is described in [5, 17]. Samples $8 \times 8 \times 1$ mm in size with polished laser-quality plane-parallel faces were used. The LBO sample faces were perpendicular to the [001] direction (2_1 crystallographic axis). The sample was mounted in the crystal holder of a flow-type helium cryostat, which was inserted into a chamber of oil-free vacuum of about 10^{-9} mbar.

Incident photons with energy E_{ex} in the interband transition region give rise to the appearance of various bands in the range 2.5–5.5 eV of the LBO PL spectrum (Figs. 1, 2). Our interest was focused on investigating the excitation mechanisms of the ultraviolet (UV) band in the LBO intrinsic PL at 4.2 eV (referred to subsequently as the UV band). This band is dominant in the room-temperature PL spectrum; therefore, all measurements were conducted at 290 K. The time-resolved and time-integrated PL spectra of LBO were measured under selective excitation by photons of various energies. An analysis of the spectra shows the relative yield of the PL UV band to increase with increasing photon energy in the VUV region of the spectrum (Figs. 1, 2). Note that this change in the observed PL spectral profile, rather than being caused by instrumental factors, is associated with the redistribution of intensity between the long-wavelength and the UV bands of the LBO PL. The long-wavelength PL band seen at 290 K was assigned by us earlier to the luminescence of the defects on the oxygen sublattice of LBO, which are localized primarily in the near-surface region [7]. As the excitation energy increases above 25 eV, the LBO absorption coefficient decreases and the depth of photon penetration into the sample increases, as does the excitation efficiency of the "bulk" UV band. Excitation in the soft x-ray region did not reveal any differences between the profiles of the time-resolved and time-integrated PL spectra or their dependence on the exciting photon energy (Fig. 2). For this reason, Fig. 2 presents only time-integrated LBO PL spectra measured at two different excitation energies.

The kinetics of luminescence decay, which was measured under selective excitation by photons of various energies in different PL bands, follows the same pattern and consists of a fast exponential subnanosecond-range component and slow components in the micro- and millisecond ranges, which are seen in our case in the form of a pedestal (Fig. 3). The relative contribution of the pedestal increases as one goes from the long- to short-wavelength part of the PL spectrum. The amplitude ratio of the pedestal to the fast component at the maximum of the PL UV band grows as the incident photon energy is increased to 35 eV. This ratio remains, however, unchanged (1 : 0.38) with a further increase in excitation energy (Fig. 3). Deconvolution made under

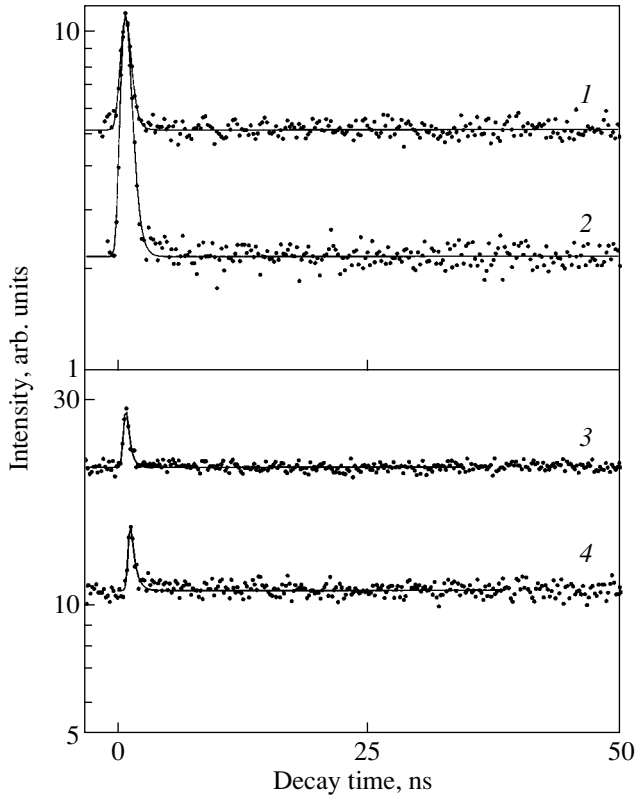

Fig. 3. PL decay kinetics in the band at (*2*) 3.4 eV and (*1*, *3*, *4*) 4.3 eV obtained on an LBO crystal at 290 K under selective excitation by photons of energy (*1*, *2*) 25, (*3*) 140, and (*4*) 600 eV.

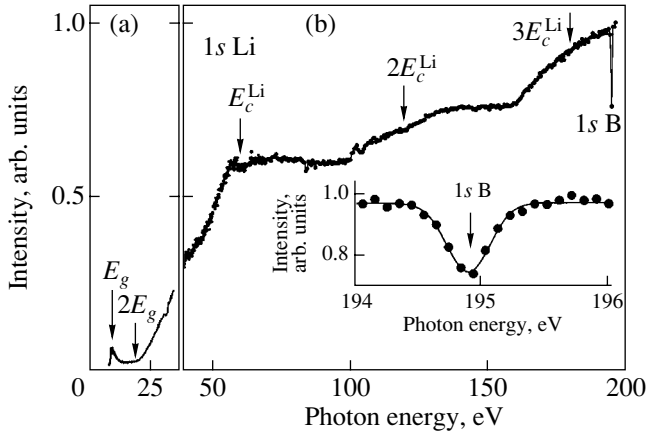

Fig. 4. PL excitation spectra of an LBO crystal obtained at a photon energy of 4.3 eV at 290 K in the energy ranges (a) 4–35 and (b) 40–200 eV. Inset: PL excitation spectrum in the region of the boron *K*-absorption edge.

the assumption of a Gaussian shape of the excitation pulse (FWHM = 400 ps) yielded 350–450 ps for the time constant of the fast component.

Figure 4 displays excitation spectra of the PL UV band of the LBO crystal obtained at 290 K in the excitation energy ranges 4–35 and 40–200 eV. The spectra reveal a common trend of a monotonic linear growth in the PL yield with increasing excitation energy above 18 eV, against which a number of features are observed. For instance, at $E_{ex} \approx 60$ eV, a shoulder appears in the PL excitation spectrum. As the excitation energy is increased even further, the PL excitation spectrum exhibits a periodic structure with a repetition period of about 60 eV. The arrows in Fig. 4 identify the energies corresponding to the three periods of this structure. In between these positions, one can see two nearly horizontal sections. Another feature is a narrow dip (FWHM = 0.41 eV) in the PL excitation spectrum near the boron *K*-absorption edge (Fig. 4).

Figure 5 displays the PL excitation spectrum of LBO measured in the region of the oxygen *K*-absorption edge. The spectrum is almost structureless, with the exception of a small (3%) dip at 532 eV and a hump with a height of about 6% at 540 eV.

3. DISCUSSION OF THE RESULTS

Our previous studies of the intrinsic luminescence of LBO [5, 7, 17, 18] show that the PL UV band of this crystal arises from radiative annihilation of the recombination-type self-trapped exciton with a hole nucleus in the form of a 2*p* hole, which occupies oxygen levels near the valence band top. At low temperatures, the PL intensity is comparatively low and is due primarily to recombination of the electron–hole pairs created by photons with energies only slightly in excess of the interband transition threshold ($E_g \approx 9$ eV). When heated above the temperature of delocalization of the major lattice defects, the electronic B^{2+} and the hole O^- centers (not producing activator luminescence bands), the UV band intensity increases by 1.5–2 orders of magnitude. This is due to the increasing probability of recombination involving these defects. At room temperature, the UV band dominates in the LBO PL spectrum. The long-wavelength boundary of the PL excitation spectrum coincides with the long-wavelength fundamental absorption edge near 8 eV (Fig. 4). The increase in the efficiency of recombination PL excitation in the exciton region below E_g, which is observed to occur at room temperature (Fig. 4), originates from thermal dissociation of the exciton.

As the exciting photon energy is increased still further, the PL yield remains at a comparatively low level without any noticeable changes up to energy $2E_g \approx$ 18 eV. Above 18 eV, the PL yield grows with increasing excitation energy and exhibits several features (Fig. 4). The monotonic pattern of the increase in the PL yield indicates that the dominant in the PL excitation mechanism role is played by the multiplication of electronic excitations, which is caused by inelastic scattering of hot photoelectrons (as is the case in alkali halide crystals [1, 8]) and hot photoholes. This scattering generates secondary low-energy electron–hole pairs, which contribute to PL excitation.

The rise in the PL yield continues up to excitation energies corresponding to the lithium *K*-absorption edge. The 1*s*-electron ionization energy in the lithium atom is 54.9 eV [19]. Interaction with the crystal field usually shifts the absorption peak in energy [20]. For instance, in LiF, the Li 1*s* photoionization energy is 62.0 eV [21]. We are not aware of any direct experimental measurements of this quantity for LBO. However, in [22], the reflectance spectra of the LBO crystal were measured in the range 55–71 eV at 290 K and were used to calculate the absorption spectra. The main peak near the Li *K*-absorption edge was reported [22] to lie at E_c^{Li} = 60 eV (FWHM = 0.3 eV). Several more weak overlapping peaks are seen to exist in the range 62–67 eV. We believe that it is these absorption peaks that are responsible for the shallow dip in the LBO PL excitation spectrum at 59–67 eV (Fig. 4). The comparatively small drop in the absorption coefficient in the vicinity of the peak, $(0.6–1) \times 10^6$ cm^{-1} [22], accounts for the accordingly small (about 3%) depth of the dip in the excitation spectra (Fig. 4).

When excited by x-ray photons with energies in the region of core transitions, many compounds exhibit a correlation between the dips in the PL excitation spectra and the peaks in the x-ray absorption spectra. The depth of the dips observed in the PL excitation spectra under excitation near the 1*s* transitions of the corresponding atoms can be as high as 5% for Ca in CaF_2 [9]; 5% for C in $NaC_7H_5O_3$ [23]; 16 and 35% for K in KCl and KBr, respectively [24]; and 46% for Cl in KCl [24]. It is usually believed that the modulation of PL excitation spectra originates primarily from surface energy losses. Selective reflection in this spectral region does not play a significant role because of the smallness of the reflectance. We note for comparison that the reflectance near the Li *K* edge in LBO is 0.3–0.6% [22]. Therefore, the reverse patterns of behavior of the PL excitation and absorption spectra observed in different crystals is caused by the same factors. This also accounts for the PL excitation spectra having the same profile.

At photon energies above the Li 1*s* exciton creation energy, E_c^{Li} = 60 eV, hot photoelectrons become scattered from the Li 1*s* core-level electrons. The photoelectron energy left after the scattering is, however, not high enough for the subsequent formation of a self-trapped exciton, whose radiative annihilation produces the observed PL. The core hole decays (i.e., the hole state becomes occupied by an electron) either nonradiatively in the Auger process or in the course of x-ray fluorescence. In alkali halide crystals, this brings about the termination of the rise in the intrinsic PL yield with increasing excitation energy and provides a constant PL yield up to energy $E_c + \Delta E$, where $\Delta E \approx E_g$ or $2E_g$ [8]. Following from [8], after the excitation energy has reached $E_c + \Delta E$, the energy of the scattered photoelectron is again high enough to form secondary electron excitations, which contribute in the final count to the observed PL. This again results in a rise in the PL yield with increasing excitation energy. For the LBO crystal, $E_c^{\mathrm{Li}} + 2E_g$ = 78 eV. At the same time, as follows from Fig. 4, the PL yield in LBO remains constant up to at least 100 eV; i.e., ΔE for the LBO is 40 eV. On the one hand, this value is comparable, from a formal viewpoint, to the energy position of the oxygen 2*s* quasi-core levels in the LBO crystal. According to our data [15], they lie 25 eV below the Fermi level, which corresponds to 34 eV below the conduction band bottom. In accordance with the selection rules, the O 2*s* states usually do not manifest themselves in optical spectra; however, one cannot exclude the possibility of scattering of the hot photoelectrons and photoholes from electrons of the oxygen 2*s* quasi-core levels.

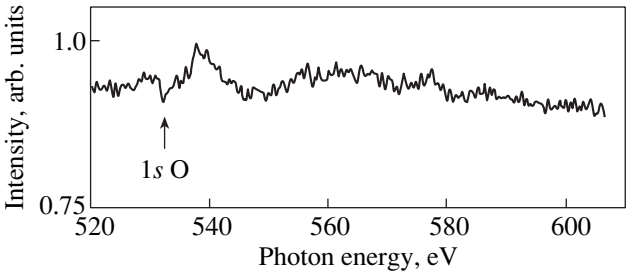

Fig. 5. PL excitation spectra of an LBO crystal obtained at a photon energy of 4.3 eV at 290 K in the energy range near the O *K*-absorption edge.

Another possible origin of the observed features in the excitation spectrum of the UV band may consist in the comparatively isolated position of the lithium ion in the LBO lattice and the absence in the Li atom of outer electron shells, which would screen the core hole. At exciting photon energies above E_c^{Li}, the core-hole Coulomb field prevents breakup of the (Li 1*s*) core-hole–conduction-electron pair. This results in nonradiative relaxation to the E_c^{Li} lowest excited level. This may be followed by radiative or nonradiative decay of the core excitation, as occurs at the E_c^{Li} excitation energy. The radiative decay of the cation Li 1*s* *K* exciton has been studied in a number of materials (LiF [25–27], LiCl and LiBr [28]). The intensity of the x-ray emission exciton peak is a fundamental characteristic of an atom in a compound [29]. In all cases, the part played by phonon relaxation was found to be significant. Considered along the lines of this assumption, the threshold at $E_c^{\mathrm{Li}} + \Delta E \approx 100$ eV (Fig. 4) should be treated as the excitation energy above which the electron component of a pair has a kinetic energy high enough to overcome the Coulomb field of the Li 1*s* core hole. It should be stressed that, here, the numerical value of ΔE is not associated with the height of the potential barrier of this process; it serves rather to specify the energy interval in

the excitation spectrum above which the PL yield efficiency again starts to rise monotonically (Fig. 4).

Above $2E_c^{\mathrm{Li}} = 120$ eV, the energy of a photoelectron scattered by the Li 1*s* core electrons is high enough to excite one more Li 1*s* electron. This accounts for the structure with a period of $E_c^{\mathrm{Li}} = 60$ eV observed in the excitation spectrum (Fig. 4). Despite the diffuse character of the appearance of the $2E_c^{\mathrm{Li}}$ threshold in the PL excitation spectrum, above 130 eV one again sees a constant level of the PL yield. This level extends exactly up to the energy $2E_c^{\mathrm{Li}} + \Delta E = 160$ eV. A further increase in the exciting photon energy again initiates a monotonic rise in the PL yield, which, following the above ideas, should reach a constant level at $3E_c^{\mathrm{Li}} + \Delta E = 220$ eV.

Analysis of the experimental data reveals a narrow, well-resolved dip in the PL excitation spectrum, which becomes clearly pronounced near the boron *K*-absorption edge (Fig. 4). In the region of the dip, the PL excitation spectrum can be approximated by a Gaussian,

$$I(E) = I_0 - A\exp(-(E - E_0)^2/2\sigma^2), \qquad (1)$$

where I_0 is the PL intensity outside the dip region. The fitting parameters are $E_0 = 194.9$ eV and $\sigma = 170$ meV, and the dip depth A is 24% of the I_0 level.

The *K*-absorption spectra of boron exhibit narrow lines in many compounds. These lines are of exciton nature and can be identified with boron *K* shell electron transitions to states at the conduction band bottom related genetically to the boron 2*p* atomic orbital [30–32]. We are not aware of any data on the x-ray absorption spectra of the LBO crystal in this region. However, in B_2O_3 films at 290 K, near the boron *K* edge, a sharp, well-resolved strong peak of Gaussian shape (σ = 190 meV) with a maximum at 194.7 eV was observed, which derives from absorption of the B 1*s* cation excitons [33]. The parameters of this peak compare well to our data for the dip in the PL excitation spectrum of the LBO crystal (Fig. 4). This suggests that the dip at 194.9 eV observed in the LBO PL excitation spectrum is due to modulation of the PL excitation spectra by the absorption peak of the cation B 1*s* excitons.

The Gaussian shape of the absorption line is due to the phonon-interaction-induced broadening, and the σ parameter is defined by the relation [33]

$$\sigma^2 = S(\hbar\omega)^2\coth(\hbar\omega/k_bT), \qquad (2)$$

where S is the average number of phonons emitted in the transition. For a well-localized core transition, ω is close to the longitudinal acoustic vibration frequency. Taking $\hbar\omega_{\mathrm{LA}} = 90$ meV and the value $\sigma = 170$ meV (Fig. 4), we arrive at the estimate $S = 4.5$.

The next expected feature in the PL excitation spectrum corresponds to the energy region in the vicinity of the oxygen *K*-absorption edge near 532 eV. The exciting photon energy is high enough to ionize the oxygen 1*s* shell, which creates a short-lived core excitation made up of the conduction electron and an O 1*s* core hole. Decay of such a core exciton gives rise to an efficient creation of conventional anion excitons and electron–hole pairs, with the hole in the oxygen valence band. The main channels contributing to population of the O 1*s* hole state are the x-ray emission and the Auger cascades, which eventually result in the formation of valence-band 2*p* holes serving as a nucleus for the subsequent creation of anion excitons. Note that at room temperature other channels of excitation of this PL in LBO are thermally quenched. The absence of other competing PL excitation channels that would be anywhere near efficient is, in our opinion, the main reason for the weak manifestation of the oxygen *K*-absorption edge in the LBO PL excitation spectra. This correlates with the results of theoretical study [34], where competing PL excitation channels are considered to be the decisive factor determining the character and intensity of manifestation of the *K*-absorption edge in PL excitation spectra. A similar situation in the region of the O 1*s* transitions was observed earlier in experiments on excitation of intrinsic PL in Al_2O_3 and MgO crystals [2].

4. CONCLUSIONS

We have reported on a first study of ultraviolet PL in LiB_3O_5 crystals produced under selective excitation by photons in the VUV and ultrasoft x-ray spectral regions. The experimental data obtained indicate that recombination is the major channel of the intrinsic PL excitation at 4.2 eV. The continuous monotonic growth in the PL yield as the photon energy is increased from $2E_g$ to the lithium *K*-absorption edge is caused by the scattering of hot photoelectrons and photoholes from valence-band electrons, which brings about the formation of secondary low-energy electron–hole pairs contributing to the excitation of the recombination PL. Features were observed in the PL excitation spectra near the lithium and boron *K*-absorption edges originating from excitation of the cation 1*s* core excitons. Experimental evidence was obtained of the multiplication of Li 1*s* excitons. The observed differences between the manifestations of the Li 1*s* and B 1*s* cation excitons in PL excitation spectra are assigned to specific features in the crystallographic and electronic structure of LBO; namely, lithium cations are located in voids of the boron–oxygen network, occupy an isolated position in the LBO lattice, and do not contribute to electronic states near the conduction band bottom. The Li 1*s* core excitations are virtually of intraatomic character; therefore, within a broad range of excitation energies above the Li *K*-absorption edge ($\Delta E \approx 40$ eV), electrons transfer from highly excited states to the lowest excited state of the Li 1*s* exciton in a nonradiative way. By contrast, the boron cation is part of the continuous boron–oxygen LBO network and boron orbitals contribute to the formation of the electronic structure of the valence

band and of the conduction band bottom, thus providing conditions conducive to migration of the electronic component of the pair that is made up of the electron in a conduction-band state coupled genetically with the boron 2*p* atomic orbital and the B 1*s* core hole. This dramatically restricts the energy region of the observed manifestation of the B 1*s* exciton in the PL excitation spectra. Excitation of the O 1*s* core transition provides still more favorable conditions for migration of the electronic component, because the oxygen 2*p* orbitals in LBO not only make a leading contribution to the formation of valence band states but are parts of the boron–oxygen orbitals from which the conduction band bottom is derived. In the absence of competing PL UV-band excitation channels at room temperature, this accounts for the very weak manifestations of O 1*s* core transitions in the PL excitation spectra.

ACKNOWLEDGMENTS

The authors are indebted to L.I. Isaenko for providing the crystals for the study and to Professor G. Zimmerer for interest in the work and support.

This study was supported by the Russian Foundation for Basic Research (project no. 02-02-16322), the Ministry of Education of the Russian Federation (project no. E02-3.4-362), and, in part, by Deutsche Bundesministerium für Bildung and Forschung (grant no. 05 KS8GUD 1).

REFERENCES

1. A. Lushchik, E. Feldbach, R. Kink, C. Lushchik, M. Kirm, and I. Martinson, Phys. Rev. B **53** (9), 5379 (1996).
2. M. Kirm, A. Lushchik, C. Lushchik, S. Vielhauer, and G. Zimmerer, J. Lumin. **102–103**, 307 (2003).
3. V. A. Pustovarov, V. L. Petrov, É. I. Zinin, M. Kirm, G. Zimmerer, and B. V. Shul'gin, Fiz. Tverd. Tela (St. Petersburg) **42** (2), 246 (2000) [Phys. Solid State **42**, 253 (2000)].
4. V. A. Pustovarov, V. Yu. Ivanov, M. Kirm, A. V. Kruzhalov, A. V. Korotaev, and G. Zimmerer, Fiz. Tverd. Tela (St. Petersburg) **43** (7), 1189 (2001) [Phys. Solid State **43**, 1233 (2001)].
5. I. N. Ogorodnikov, V. A. Pustovarov, A. V. Kruzhalov, L. I. Isaenko, M. Kirm, and G. Zimmerer, Fiz. Tverd. Tela (St. Petersburg) **42** (3), 454 (2000) [Phys. Solid State **42**, 464 (2000)].
6. I. N. Ogorodnikov, V. A. Pustovarov, A. V. Kruzhalov, L. I. Isaenko, M. Kirm, and G. Zimmerer, Fiz. Tverd. Tela (St. Petersburg) **42** (10), 1800 (2000) [Phys. Solid State **42**, 1846 (2000)].
7. I. N. Ogorodnikov, V. A. Pustovarov, M. Kirm, A. V. Kruzhalov, and L. I. Isaenko, Fiz. Tverd. Tela (St. Petersburg) **43** (8), 1396 (2001) [Phys. Solid State **43**, 1454 (2001)].
8. J. H. Beaumont, A. J. Bourdillon, and M. N. Kabler, J. Phys. C: Solid State Phys. **9** (15), 2961 (1976).
9. A. Bianconi, D. Jackson, and K. Monahan, Phys. Rev. B **17** (4), 2021 (1978).
10. H. Mizouchi, Phys. Rev. B **58** (23), 15557 (1998).
11. C. U. S. Larsson, A. Beutler, O. Björneholm, F. Federmann, U. Hahn, A. Rieck, S. Verbin, and T. Möller, Nucl. Instrum. Methods Phys. Res. A **337** (2–3), 603 (1994).
12. M. Kirm, A. Lushchik, C. Lushchik, V. Makhov, E. Negodin, S. Vielhauer, and G. Zimmerer, Nucl. Instrum. Methods Phys. Res. A **486** (1–2), 422 (2002).
13. M. Kirm, S. Vielhauer, G. Zimmerer, A. Lushchik, and C. Lushchik, Surf. Rev. Lett. **9** (2), 1363 (2002).
14. S. Vielhauer, M. Kirm, V. Kisand, E. Negodin, E. Sombrowski, B. Steeg, and G. Zimmerer, Surf. Rev. Lett. **9** (2), 1333 (2002).
15. A. Yu. Kuznetsov, M. V. Kuznetsov, I. N. Ogorodnikov, A. V. Kruzhalov, and V. A. Maslov, Fiz. Tverd. Tela (St. Petersburg) **36** (3), 845 (1994) [Phys. Solid State **36**, 465 (1994)].
16. G. Zimmerer, Nucl. Instrum. Methods Phys. Res. A **308** (1–2), 178 (1991).
17. I. N. Ogorodnikov, E. A. Radzhabov, L. I. Isaenko, and A. V. Kruzhalov, Fiz. Tverd. Tela (St. Petersburg) **41** (2), 223 (1999) [Phys. Solid State **41**, 197 (1999)].
18. I. N. Ogorodnikov, L. I. Isaenko, A. V. Kruzhalov, and A. V. Porotnikov, Radiat. Meas. **33** (5), 577 (2001).
19. T. A. Callcott, E. T. Arakawa, and D. L. Ederer, Phys. Rev. B **16** (12), 5185 (1977).
20. M. A. Blokhin, E. G. Orlova, and I. G. Shveĭtser, Zh. Strukt. Khim. **18** (4), 667 (1977).
21. F. Bassani, Appl. Opt. **19** (23), 4093 (1980).
22. T.-J. Chen, R. N. Zitter, R. Tao, W. R. Hunter, and J. C. Rife, Phys. Rev. B **52** (19), 13703 (1995).
23. D. B. M. Klaassen, Phys. Rev. B **38** (14), 9974 (1988).
24. M. Yanagihara, Y. Kondo, T. Hanyu, and S. Yamaguchi, Solid State Commun. **68** (3), 345 (1988).
25. E. T. Arakawa and M. W. Williams, Phys. Rev. Lett. **36** (6), 333 (1976).
26. A. A. Maiste, A. M.-E. Saar, and M. A. Elango, Pis'ma Zh. Éksp. Teor. Fiz. **18** (3), 167 (1973) [JETP Lett. **18**, 97 (1973)].
27. A. A. Maiste, A. M.-E. Saar, and M. A. Elango, Fiz. Tverd. Tela (Leningrad) **16** (6), 1720 (1974) [Sov. Phys. Solid State **16**, 1118 (1974)].
28. K. E. Miyano, D. L. Ederer, T. A. Callcott, Q.-Y. Dong, J. J. Jia, L. Zhou, and D. R. Mueller, Phys. Rev. B **49** (9), 5929 (1994).
29. R. D. Carson and S. E. Schnatterly, Phys. Rev. Lett. **59** (3), 319 (1987).
30. T. M. Zimkina and V. A. Fomichev, *Ultrasoft X-ray Spectroscopy* (Leningr. Gos. Univ., Leningrad, 1971).
31. B. M. Davies, F. Bassani, F. C. Brown, and C. G. Olson, Phys. Rev. B **24** (6), 3537 (1981).
32. V. A. Fomichev, Fiz. Tverd. Tela (Leningrad) **13** (3), 907 (1971) [Sov. Phys. Solid State **13**, 754 (1971)].
33. A. Mansour and S. E. Schnatterly, Phys. Rev. Lett. **59** (5), 567 (1987).
34. S. Emura, T. Moriga, J. Takuzawa, M. Nomura, K. R. Bauchspiess, T. Murata, K. Harada, and H. Maeda, Phys. Rev. B **47** (12), 6918 (1993).

Translated by G. Skrebtsov

Physics of the Solid State, Vol. 46, No. 5, 2004, pp. 848–852. Translated from Fizika Tverdogo Tela, Vol. 46, No. 5, 2004, pp. 826–829.

SEMICONDUCTORS AND DIELECTRICS

The Genesis of Energy Bands Formed by Sublattice States in Alkaline-Earth Metal Oxides and Sulfides

Yu. M. Basalaev, Yu. N. Zhuravlev, A. V. Kosobutskiĭ, and A. S. Poplavnoĭ

Kemerovo State University, ul. Krasnaya 6, Kemerovo, 650043 Russia

e-mail: zhur@kemsu.ru

Received July 30, 2003

Abstract—The self-consistent electron energy band spectra of crystals and charged sublattices of alkaline-earth metal oxides and sulfides are calculated in the framework of the density functional theory within the pseudopotential approximation in the basis set of localized orbitals. The charge states of sublattices (such as neutral sublattices, empty metal sublattices, and doubly charged anion sublattices) are analyzed with due regard for the electrical neutrality of the crystal. It is demonstrated that the valence bands of the studied crystals are very similar to the valence bands of the doubly charged anion sublattices. The distributions of the valence electron densities of the crystals are virtually identical to those of the anion sublattices. The lower conduction bands of the crystals and doubly charged anion sublattices also almost coincide with each other for MgO and MgS but differ substantially for CaO and CaS. This is associated with the difference between the contributions from the anions and cations to the conduction band of the crystals. It is found that these contributions depend on the relative energy positions of *p* and *d* unoccupied states. © *2004 MAIK "Nauka/Interperiodica".*

1. INTRODUCTION

In our recent works [1–3], we developed a sublattice method for studying the electronic structure of crystalline solids. It was established that the specific features in the electron density of crystals are governed by long-range interactions between identical atoms of the sublattices. The coupling between the sublattices is characterized by the difference density. This quantity is determined by subtracting the valence electron densities of all the sublattices constituting the crystal from the total valence electron density of the crystal. As was shown in [1, 3], the sublattices of ionic crystals undergo weak hybridization. For a cation sublattice of alkali or alkaline-earth metals, the valence electron density is determined primarily by the anion states and satisfies the following relationship:

$$|\rho_{cr}| \approx |\rho_A| \gg |\rho_{Me}| > |\Delta\rho|, \quad (1)$$

where ρ_{cr}, ρ_A, and ρ_{Me} are the valence electron densities of the crystal, the anion, and the metal, respectively, and $\Delta\rho$ is the difference density. Hence, it can be expected that the energy band states of the crystal should be very similar to those of the sublattices. Therefore, the hybridization between the sublattices can be adequately described in the framework of the perturbation theory. In this case, it is desirable for the perturbation to be minimum. Recall that the sublattices are separated in such a way that the resultant distribution of the valence electron density ensures the electrical neutrality of the sublattices. As a result, the occupancy of energy band states of the sublattices differs from that of the crystal. In this respect, the problem now is to determine the initial charge distribution over the sublattices that would coincide to the greatest extent with the charge distribution over the crystal. One way to solve this problem is as follows. In the calculation of the band structure for the compound under investigation, the occupation numbers of the anion sublattice are varied until the valence band spectrum of this sublattice coincides to the greatest possible extent with the valence band spectrum of the crystal and, consequently, the perturbing effect of the sublattice hybridization becomes minimum in at least the given spectral range. Further calculations of the energy states of the metal sublattice are performed with occupation numbers that ensure electrical neutrality of the crystal.

2. OBJECTS OF INVESTIGATION AND COMPUTATIONAL METHOD

In this work, the above technique was applied to model objects, such as crystals of alkaline-earth metal oxides and sulfides with an NaCl lattice. These compounds provide a good example of a homologous series of crystals with predictable physical and physicochemical properties. From the practical standpoint, the great interest expressed in oxides and sulfides of magnesium and calcium is associated with their extensive use as refractory materials (MgO); constituents of glass-formers and glass-ceramic–forming materials (CaO); and highly efficient photoluminescent, cathodoluminescent, and x-ray phosphors (MgS, CaS). It should be noted that, at present, the electronic structure of alkaline-earth metal sulfides and oxides (primarily, magnesium oxide) has been investigated in sufficient detail. Magnesium oxide is one of the most suitable model

Energy parameters of the valence band and band gaps

Crystal, sublattice	Energy ranges, eV					
	valence band					band gap
	$LVB_{\Gamma-L}$	$LVB_{\Gamma-X}$	$UVB_{\Gamma-L}$	$UVB_{\Gamma-X}$	total width of the valence band ΔE_{VB}	ΔE_g
MgO	1.1	1.5	4.6	4.3	17.8	4.6 Γ_{15}–Γ_1
			5 [9]		16 [9]	4.7 [9]
O^{-2}	1.1	1.4	4.0	3.4	17.7	2.9 Γ_{15}–Γ_1
MgS	1.5	2.0	5.0	4.4	13.0	2.2 Γ_{15}–X_1 3.2 Γ_{15}–Γ_1
					13 [9]	2.6 [9] 3.5 [9]
S^{-2}	1.5	2.0	4.4	3.9	13.0	1.7 Γ_{15}–X_1
						3.2 Γ_{15}–Γ_1
CaO	0.5	0.3	2.8	1.9	16.9	3.5 Γ_{15}–X_4
						5.6 Γ_{15}–Γ_1
O^{-2}	0.4	0.6	2.2	1.9	16.9	1.5 Γ_{15}–Γ_1
CaS	0.7	0.7	3.3	2.6	11.4	2.1 Γ_{15}–X_4
						4.3 Γ_{15}–Γ_1
S^{-2}	0.7	1.0	2.8	2.5	11.5	2.0 Γ_{15}–X_1
						2.4 Γ_{15}–Γ_1

Designations: VB is the valence band, and LVB and UVB are the widths of the lower and upper valence bands, respectively.

objects for use in the development of new methods for studying the electronic structure. There are dozens of theoretical works devoted to the calculation of the band structure of magnesium oxide. The most complete list of references and basic results obtained in MgO band calculations performed up to 1984 inclusive are presented by Tauran *et al.* [4]. Brief reviews of recent works dealing with the entire series of alkaline-earth metal compounds are given in [5, 6].

We calculated the electron energy band spectra and valence electron densities of crystals and their sublattices in the framework of the density functional theory within the pseudopotential approximation [7] according to the technique described in our earlier work [8]. In these calculations, the basis set additionally included the localized O 3*s*, O 3*p*, S 4*s*, and S 4*p* atomic orbitals.

3. RESULTS AND DISCUSSION

The band structure and valence electron densities of the anion sublattices of the crystals of alkaline-earth metal oxides and sulfides were calculated for different charge states. For neutral sublattices, the total widths of the valence bands of the crystals and their sublattices proved to be close to each other. However, the widths of the allowed valence bands of the sublattices were found to be approximately half as large as those of the crystals. Our calculations demonstrated that the distributions of the valence electron densities of the neutral anion sublattices are qualitatively similar to the distributions of the valence electron densities of the crystals, but the numerical values of the distribution parameters differ substantially. The energy parameters of the valence bands of the crystals and sublattices are close to each other in the case when the valence electrons of the metal completely transfer to the anion sublattice (see table). The table also presents the results of the band calculations performed by de Boer and de Groot [9]. It can be seen that our results are in reasonable agreement with the data obtained in [9].

The energy band spectra of metal anion crystals and the energy band spectra of O^{-2} and S^{-2} charged sublattices are depicted in Fig. 1. In this figure, the energy band spectra of the crystals and sublattices are superimposed on each other such that the tops of their upper valence bands coincide. The energy is reckoned from these tops. As can be seen from the table and Fig. 1, the valence bands of the crystals are very similar to the valence bands of the charged sublattices. The partial analysis of the valence states of the crystals showed that the lower valence band is predominantly formed by the *s* states of the anion; in this case, the maximum contribution of the metal amounts to 10% at the boundary points of the Brillouin zone. As regards the upper valence band, the maximum contribution of the metal at the boundary points of the Brillouin zone can be as large as 30%. It is this contribution that is responsible for the difference between the numerical parameters of the upper valence bands of the crystals and the sublattices (see table).

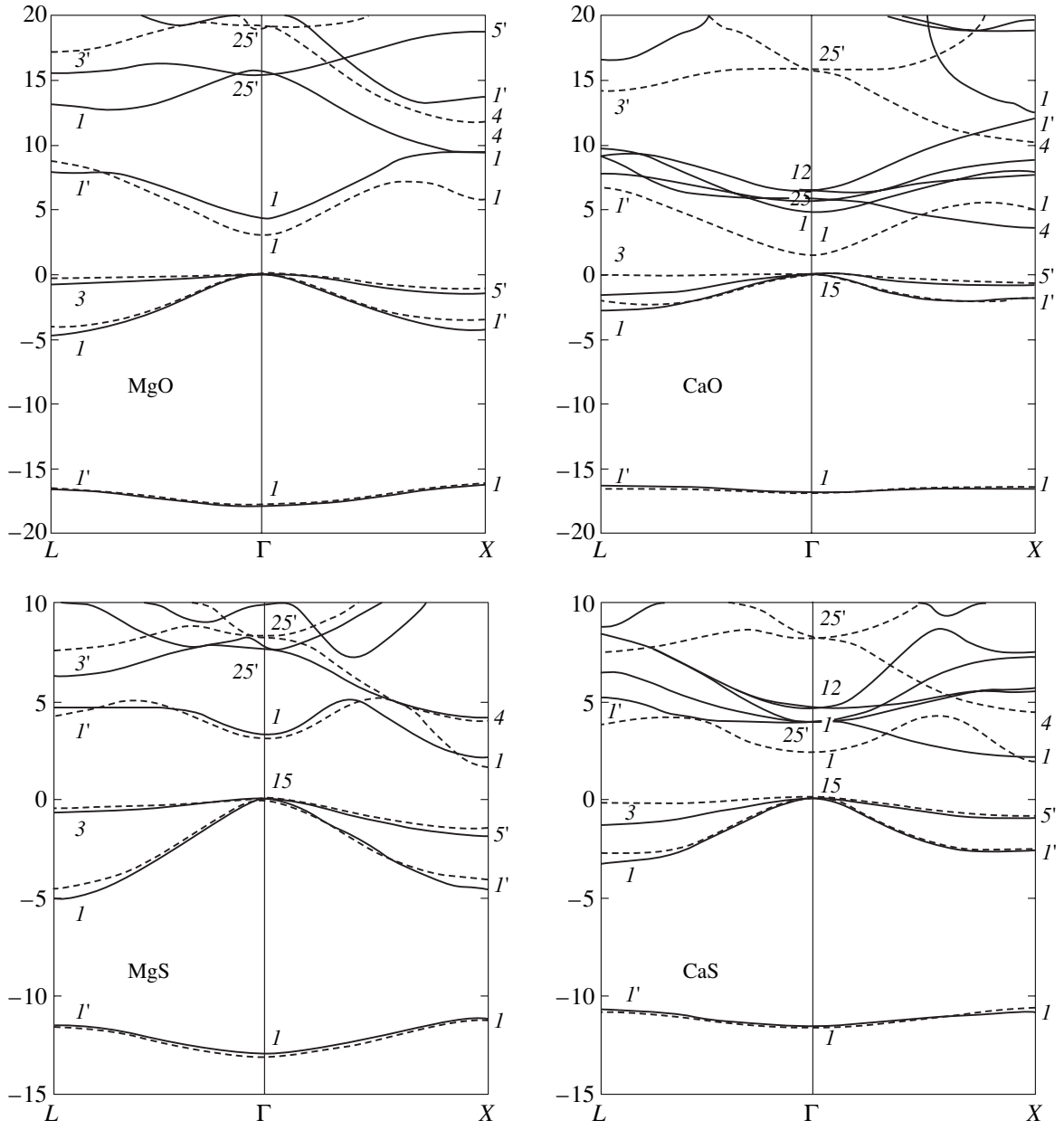

Fig. 1. Energy band spectra of metal anion crystals (solid lines) and the energy band spectra of O^{-2} and S^{-2} charged sublattices (dashed lines).

Figure 2 presents the distributions of the valence electron densities of MgO and MgS crystals and their charged sublattices in the (100) plane. The valence electron densities are expressed in terms of $e \cdot Å^{-3}$ (where e is the elementary charge). It can be seen from Fig. 2 that the complex distributions of the valence electron densities almost completely coincide with each other. A very similar situation is observed for calcium compounds. The question arises as to why the valence electron densities of the crystals and sublattices almost completely coincide, whereas the parameters of the valence bands (particularly those of the upper valence bands) and their partial contributions differ considerably. First and foremost, as was noted in our earlier work [1], the major portion of the electron density is transferred from the metal to the anion site. The second reason is more formal in character: for charged sublattices, the role of the wave functions of the metal is played by virtual wave functions of the anion. This provides reproducibility of the valence electron density and, as much as possible, of the structure of the valence energy bands. To put it differently, in the case of a

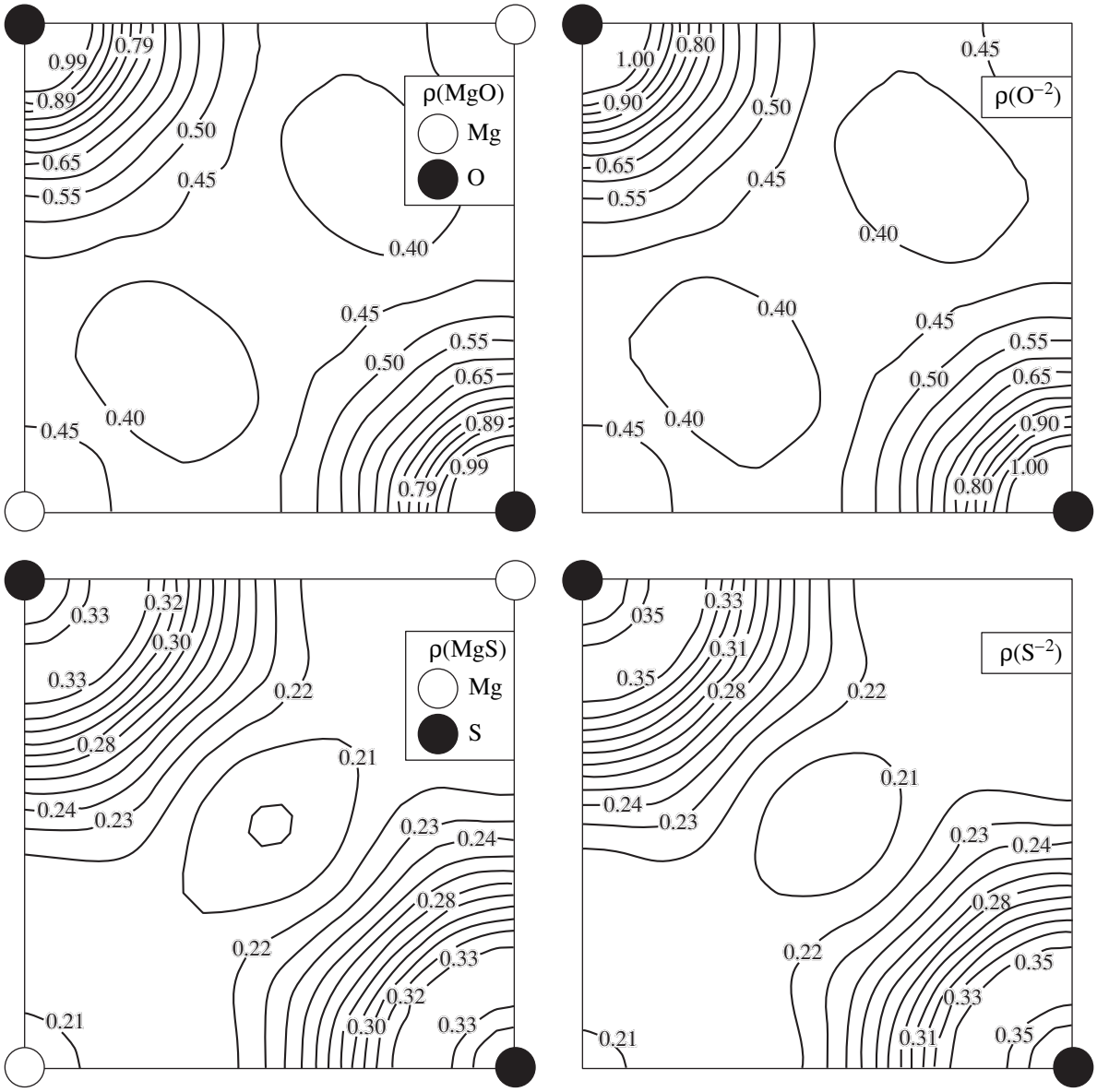

Fig. 2. Distributions of the valence electron densities of MgO and MgS crystals and the valence electron densities of O^{-2} and S^{-2} charged sublattices.

restricted basis set, the reproducibility of the valence electron density is better than that of the energy spectrum.

Let us now consider conduction bands in crystals and charged sublattices of alkaline-earth metal oxides and sulfides. First, we note the surprising fact that, for a charged anion sublattice in magnesium sulfide crystals, the two lower conduction bands of the crystal are reproduced fairly well, whereas the third band is reproduced somewhat worse. A different situation occurs with magnesium oxide crystals. The lower conduction band is reproduced well along the Γ–*L* direction and somewhat worse along the Γ–*X* direction. However, the next two conduction bands are reproduced only qualitatively. A considerably more complex situation arises with calcium compounds, in which the Γ_1, $\Gamma_{25'}$, and Γ_{12} energy levels are located at the Γ point in the vicinity of the conduction band bottom of the crystal, whereas the conduction bands of the O^{-2} and S^{-2} sublattices do not involve such a group of levels.

De Boer and de Groot [9] also carried out a comparative analysis of the energy states in the conduction band of the MgS crystal and the energy states in the conduction band of the S^{-2} charged sublattice. Note that the energy band spectra obtained in [9] for the MgS crystal and S^{-2} charged sublattice are similar to those shown in Fig. 1. Reasoning from these spectra, de Boer and de Groot made the inference that the energy states

in the conduction band exhibit a purely anionic nature and that the metal acts as a stabilizer of the crystal lattice. Unfortunately, in [9], the authors did not perform a consistent analysis of the band structure of the MgO crystal and only presented the energy band spectrum of this crystal. We can agree only in part with the inferences made in [9]. The partial analysis of the energy states in the conduction band of magnesium sulfide demonstrated that the contributions from the energy states of the anion at the *L* point and along the Γ–*L* line of the Brillouin zone actually exceed 90%. This provides an explanation of the similarity between the first conduction band of the MgS crystal and the first conduction band of the S^{-2} sublattice along the Γ–*L* line of the Brillouin zone. However, along the Γ–*X* line, the metal and the anion make approximately identical contributions to the energy states of the first conduction band. At the same time, the contribution of the metal to the energy states at the center of the Brillouin zone is predominant. For subsequent conduction bands, the contributions from the energy states of the metal and the anion vary from 10 to 90% along different directions of the Brillouin zone.

In the band structure of CaO and CaS compounds, the Γ_1, $\Gamma_{25'}$, and Γ_{12} energy levels are closely spaced in the vicinity of the conduction band bottom of the crystal. This can be explained by the hybridization of the virtual *p* and *d* states of the metal and the anion. It is worth noting that, at the center of the Brillouin zone, the main contribution is made by the *d* states. That is why this group of energy levels is not reproduced by the states of the O^{-2} and S^{-2} charged sublattices. Therefore, the partial contributions from the energy states of the cations and anions to the conduction band of alkaline-earth metal sulfides and oxides depend on the mutual arrangement of the virtual states of the metal and the anion. On this basis, we can make the inference that, in magnesium compounds, the lower conduction bands are substantially anionic in nature. However, the lower conduction bands in calcium compounds have a different nature.

4. CONCLUSIONS

Thus, it was established that, in alkaline-earth metal oxides and sulfides, the valence bands of doubly charged anion sublattices are very similar to the valence bands of the crystals. The distributions of the valence electron densities of the anion sublattices also almost coincide with those of the crystals. The conduction bands of the crystals and charged anion sublattices can either be similar to each other or differ substantially depending on the degree of hybridization of the crystal orbitals of the cations and anions.

ACKNOWLEDGMENTS

This work was supported by the scientific program "Russian Universities" of the Ministry of Education of the Russian Federation, project no. UR.01.01.047.

REFERENCES

1. Yu. N. Zhuravlev and A. S. Poplavnoĭ, Zh. Strukt. Khim. **42** (5), 860 (2001).
2. Yu. N. Zhuravlev and A. S. Poplavnoĭ, Fiz. Tverd. Tela (St. Petersburg) **43** (11), 1984 (2001) [Phys. Solid State **43**, 2067 (2001)].
3. Yu. N. Zhuravlev and A. S. Poplavnoĭ, Fiz. Tverd. Tela (St. Petersburg) **45** (1), 37 (2003) [Phys. Solid State **45**, 36 (2003)].
4. O. E. Taurian, M. Srpingborg, and N. E. Christensen, Solid State Commun. **55** (4), 351 (1985).
5. V. A. Sashin, H. E. Dorself, M. A. Bolorizaden, S. A. Camey, and M. Y. Ford, J. Chem. Phys. **113** (18), 8175 (2000).
6. Yu. N. Zhuravlev, Yu. M. Basalaev, and A. S. Poplavnoĭ, Izv. Vyssh. Uchebn. Zaved., Fiz. **8**, 104 (2000).
7. G. B. Bachelet, D. R. Hamann, and M. Schluter, Phys. Rev. B **26** (8), 4199 (1982).
8. Yu. G. Zhuravlev, Yu. M. Basalaev, and A. S. Poplavnoĭ, Izv. Vyssh. Uchebn. Zaved., Fiz. **3**, 96 (2000).
9. P. K. de Boer and R. A. de Groot, J. Phys.: Condens. Matter **10**, 10241 (1998).

Translated by O. Borovik-Romanova

Physics of the Solid State, Vol. 46, No. 5, 2004, pp. 853–857. Translated from Fizika Tverdogo Tela, Vol. 46, No. 5, 2004, pp. 830–833.

SEMICONDUCTORS AND DIELECTRICS

Hyperfine Interactions in $Pb^{3+}F_8^-F_a^-$ Clusters in Fluorite Crystals

V. I. Murav'ev

Scientific and Industrial Enterprise "Izmeritel'," Ul'yanovsk, 432008 Russia

Received August 11, 2003

Abstract—The parameters of hyperfine interactions in $Pb^{3+}F_8^-F_a^-$ tetragonal clusters of MeF_2 crystals (*Me* = Ca, Sr, Ba) are interpreted. The contributions of the spin polarization to the parameters of the proper hyperfine interaction and additional (ligand) hyperfine interactions are calculated in the approximation of weak binding between a charge-compensating ion F_a^- and a cubic fragment in the tetragonal cluster. It is demonstrated that correct inclusion of the contributions from the spin polarization to the ligand isotropic hyperfine interaction for the F_a^- ion leads to anomalously large parameters of this interaction for MeF_2 crystals. These results are in agreement with experimental data. © *2004 MAIK "Nauka/Interperiodica".*

Investigations into the electron paramagnetic resonance (EPR) of a Pb^{3+} : MeF_2 $6s^1$ (*Me* = Ca, Sr, Ba) ion in fluorites at temperature $T < 100$ K have revealed that the fluorite crystals contain $Pb^{3+}F_8^-F_a^-$ tetragonal clusters in which the charge-compensating ion F_a^- is located in an interstice of the second shell. Moreover, EPR studies have elucidated the specific features of the hyperfine interactions in these compounds. In particular, Mikheev and Stepanov [1] found that the measured *g* factor, hyperfine parameter *A*, and additional (ligand) hyperfine parameters for fluorine ions of a cubic fragment of the F_i^- tetragonal cluster (components of the A^{F_i} tensor) coincide with those for the $Pb^{3+}F_8^-$ cubic cluster [2], whereas the ligand hyperfine parameters for the F_a^- ion (components of the A^{F_a} tensor), on average, exceed the components of the A^{F_i} tensor by a factor of 1.5 for MeF_2 crystals. On the one hand, the experimental results can be explained by the fact that the distance from the Pb^{3+} ion to the F_a^- ion is shorter than the distance from the Pb^{3+} ion to a F_i^- ion [3]. On the other hand, the observed isotropy of the *g* factor and hyperfine parameter *A*, as well as the equivalency (within the limits of experimental error) of the F_i^- ions with respect to the center of the cubic fragment in the $Pb^{3+}F_8^-F_a^-$ tetragonal cluster, suggest that the nearest environment of the Pb^{3+} ion is cubic in shape and that the charge-compensating ion is bound to the cubic fragment through a weaker covalent bond ($Pb^{3+}F_8^-F_a^-$) than the covalent bond inside the fragment.

The experimental results presented in Table 1 indicate that the main contributions to the ligand hyperfine parameters are made by the isotropic parts of the A^{F_i} and A^{F_a} tensor components. Earlier [4, 5], we analyzed the effect of spin polarization on the hyperfine parameters *A* and ligand isotropic hyperfine parameters for

Table 1. Experimental EPR data for $Pb^{3+}F_8^-F_a^-$ clusters in MeF_2 crystals [1]*

Crystal	*A*, GHz	$A_\parallel^{F_i}$, Gs	$A_\perp^{F_i}$, Gs	A_i, Gs	B_i, Gs	$A_\parallel^{F_a}$, Gs	$A_\perp^{F_a}$, Gs	A_a, Gs	B_a, Gs
GaF_2	52.85	+200	+69	+112.7	+43.7	+340	(+188.8)	(+239.2)	(+50.4)
SrF_2	51.7	+190	+60	+103.3	+43.3	+290	(+138.8)	(+189.2)	(+50.4)
BaF_2	49.6	+171	+50	+90.3	+40.3	+220	+68.8	+119.2	+50.4

* Parenthetic numbers are the hypothetical parameters of ligand hyperfine interactions for the F_a^- ion, determined by analogy with anisotropic parameters $B_i \approx$ const for MeF_2 crystals.

1063-7834/04/4605-0853$26.00 © 2004 MAIK "Nauka/Interperiodica"

$Me^{n+}F_8^-$ cubic clusters (where Me^{n+} is an ns^1 ion) in fluorite crystals. In this work, we consider the effect of spin polarization on these parameters for $Pb^{3+}F_8^-F_a^-$ tetragonal clusters in MeF_2 crystals in the weak-binding approximation.

1. The energy spectrum of a tetragonal cluster can be represented in the form of interacting systems of energy levels of the cubic fragment and the F_a^- ion. The sequence of electron shells whose spin polarization makes nonzero contributions to the hyperfine parameters A and ligand isotropic hyperfine parameters is as follows (C_{4v}, $S = I/2$):

$$[a_1^b(2s_\sigma^i)]^2[a_1^b(2s_\sigma^a)]^2[a_1^b(2p_\sigma^i)]^2[a_1^b(2p_\sigma^a)]^2 \times [a_1^*(6s)]^1 = {}^2A_1. \quad (1)$$

Here, the character of the molecular orbital (MO) of electrons of the corresponding shell (the shell character) is given in parentheses and the superscript * refers to the antibonding (bonding) state. The molecular orbital of the tetragonal cluster is represented by a superposition of the molecular orbital of the cubic fragment and the atomic orbital (AO) of the F_a^- ion. In open form, the molecular orbitals can be written as follows (in the MO LCAO method, the $2p_\sigma$ and $2s_\sigma$ atomic orbitals of fluorine ions are mixed in a zero approximation):

$$\begin{aligned}
a_1^*(6s) &= \{x_0(6s) - x_1(2p_\sigma^i) - x_2(2s_\sigma^i)\}_{\text{cub}} - x_3(2p_\sigma^a) - x_4(2s_\sigma^a),\\
a_1^b(2p_\sigma^a) &= \{v_0(6s) - v_1(2p_\sigma^i) - v_2(2s_\sigma^i)\}_{\text{cub}} + v_3(2p_\sigma^a) - v_4(2s_\sigma^a),\\
a_1^b(2p_\sigma^i) &= \{y_0(6s) + y_1(2p_\sigma^i) - y_2(2s_\sigma^i)\}_{\text{cub}} + y_3(2p_\sigma^a) - y_4(2s_\sigma^a),\\
a_1^b(2s_\sigma^a) &= \{w_0(6s) + w_1(2p_\sigma^i) - w_2(2s_\sigma^i)\}_{\text{cub}} + w_3(2p_\sigma^a) + w_4(2s_\sigma^a),\\
a_1^b(2s_\sigma^i) &= \{z_0(6s) + z_1(2p_\sigma^i) + z_2(2s_\sigma^i)\}_{\text{cub}} + z_3(2p_\sigma^a) + z_4(2s_\sigma^a).
\end{aligned} \quad (2)$$

Here, the molecular orbitals of the cubic fragment are given in curly brackets; x, y, z, v, and w are the coefficients of expansion of the molecular orbitals in the LCAO basis set (coefficients of the molecular orbitals); sign combinations of the coefficients of the molecular orbitals correspond to expression (1); and $a_1^*(6s)$ is the molecular orbital in the ground state (unpaired electron).

2. Let us consider a cubic fragment of the tetragonal cluster. Expressions for the hyperfine interaction and ligand hyperfine interaction parameters in the case of an $Me^{n+}F_8^-$ cube ($Me^{n+} = Zn^+, Cd^+, Pb^{3+}$; O_h; $S = 1/2$) in terms of spin polarization of the $2p_\sigma^i$ shell were derived in my previous work [5]. Taking into account the spin polarization of the $2s_\sigma^i$ shell with the use of the molecular orbitals represented by expressions (2) and ignoring the effect of the F_a^- ion, we obtain the following relationships for the hyperfine and ligand hyperfine parameters in the one-center approximation:

$$A = A_0x_0^2(1 + \delta), \quad (3)$$

$$A_\parallel^{F_i} = A_i + 2B_i; \quad A_\perp^{F_i} = A_i - B_i, \quad (4)$$

where the isotropic (A_i) and anisotropic (B_i) parts of the A^{F_i} tensor components are defined by relationships (9) in [5] and the parameter of the ligand isotropic hyperfine interaction is given by the formula

$$A_{s_i} = A_{0_i}f_{s_i}(1 + \delta_i). \quad (5)$$

In expressions (3) and (5), $A_{0_{(i)}}$ is the parameter of the isotropic hyperfine interaction of a free ion; $f_{s_i} = (x_2/\sqrt{8})^2$ is the spin density at the $3s_\sigma^i$ atomic orbital in the ground state; and $\delta_{(i)}$ is the polarization correction, which, for the F_i^- ion, can be represented in the following form (similar to the expression for the Pb^{3+} ion):

$$\delta_i = \alpha_i x_0^2 + \beta_i x_1^2 + \gamma_i x_2^2, \quad (6)$$

where

$$\begin{aligned}
\alpha_i &= 2K(6s, 6s)\left(\frac{x_0}{x_2}\right)\left(\frac{y_0y_2}{\Delta_{p_i}} - \frac{z_0z_2}{\Delta_{s_i}}\right),\\
\beta_i &= -\frac{1}{4}K(2p_\sigma, 2p_\sigma)\left(\frac{x_1}{x_2}\right)\left(\frac{y_1y_2}{\Delta p_i} - \frac{z_1z_2}{\Delta_{s_i}}\right),\\
\gamma_i &= \frac{1}{4}K(2s_\sigma, 2s_\sigma)\left(\frac{y_2^2}{\Delta_{p_i}} + \frac{z_2^2}{\Delta_{s_i}}\right).
\end{aligned} \quad (7)$$

Here, $K(j, j)$ are the exchange integrals and $\Delta_{p(s)_i}$ are the intervals of transitions $b \longrightarrow *$. In expression (3), the first term corresponds to the isotropic hyperfine interaction of the 6s electron localized at the Pb^{3+} ion in the ground state with its own nucleus. In relationship (5), the first term describes the delocalization contribution. It follows from formula (6) that the polarization correction δ_i is associated with the spin polarization of the Pb^{3+}–F_i^- covalent bond by unpaired electrons localized

Table 2. Covalency parameters for cubic fragments of $Pb^{3+}F_8^-F_a^-$ clusters in MeF_2 crystals

Crystal	x_0^2	x_1^2	x_2^2	y_0^2	y_1^2	y_2^2	z_0^2	z_1^2	z_2^2
CaF_2	0.73	0.56	0.05	0.44	0.69	0.01	0.01	~0	0.96
SrF_2	0.72	0.55	0.04	0.33	0.51	0.01	0.03	~0	0.94
BaF_2	0.72	0.52	0.04	0.30	0.52	0.04	0.04	~0	0.93

Table 3. Polarization corrections, hyperfine parameters A, and ligand isotropic hyperfine parameters A_{s_i} for cubic fragments of $Pb^{3+}F_8^-F_a^-$ clusters in MeF^2 crystals

Crystal	δ_p	δ_s	$\delta = \delta_p + \delta_s$	A, GHz	δ_{p_i}	δ_{s_i}	$\delta_i = \delta_{p_i} + \delta_{s_i}$	A_{s_i}, Gs
CaF_2	−0.11	+0.01	−0.10	+53.6	−0.05	+0.01	−0.04	+108.7
SrF_2	−0.12	~0	−0.12	+52.2	−0.13	+0.03	−0.10	+93.4
BaF_2	−0.14	−0.01	−0.15	+49.7	−0.23	−0.03	−0.26	+70.0

at the 6*s*, $2p_\sigma^i$, and $2s_\sigma^i$ atomic orbitals, respectively. The coefficients α_i, β_i, and γ_i in formula (6) account for the exchange interaction of the unpaired electron with α electrons of the $[a_{1g}^b(2p_\sigma^i)]^2$ and $[a_{1g}^b(2s_\sigma^i)]^2$ shells, which is described by the first and second terms in expressions (7), respectively.

In order to calculate the contributions to the hyperfine and ligand hyperfine parameters, we determine the coefficients of the molecular orbitals from the experimental data (Table 1) according to expressions (3)–(5). For this purpose, expressions (3)–(5) are complemented by the orthonormality conditions of the molecular orbitals and the orbital contributions (second terms) in relationships (9) from [5] are disregarded. Then, the exchange and overlap integrals are calculated using the atomic orbitals taken from [6, 7]. The $\Delta_{p(s)_i}$ values are varied in the interval (0.1–1) au. The atomic parameters used in our calculations are taken from [8]. The squares of the coefficients of the molecular orbitals (covalency parameters) are given in Table 2. In the calculation, we use different sign combinations of the ligand hyperfine parameters. The sign combination presented in Table 1 is chosen in accordance with the structure of delocalized bonds from Table 2. The electron shells are characterized by different electron density distributions. For the $[a_{1g}^*(6s)]^1$ and $[a_{1g}^b(2p_\sigma^i)]^2$ shells, the electron density is appreciably redistributed between the Pb^{3+} and F_i^- ions and is localized predominantly at the $2p_\sigma^i$ atomic orbital of the ligand. For the $[a_{1g}^b(2s_\sigma^i)]^2$ shell, the electron density is shifted toward the ligand and is almost completely localized at the $2s_\sigma^i$ atomic orbitals of the fluorine ions. The calculation demonstrated that the orbital contributions to the isotropic A_i and anisotropic B_i parts of the A^{F_i} tensor components do not exceed three percent of the experimental components of the A^{F_i} tensor. As a result, we found that $A_i = A_{s_i}$. The main contribution to the anisotropic part B_i is associated with the dipole interaction between the unpaired electron localized at the $2p_\sigma^i$ atomic orbitals of fluorine ions and the ligand nucleus.

The polarization corrections presented in Table 3 are separated into the contributions from the $2p_\sigma^i$ and $2s_\sigma^i$ shells in accordance with the first and second terms in expressions (7). An analysis of the polarization corrections demonstrates that the spin polarization of the shell $[a_{1g}^b(2p_\sigma^i)]^2$ is predominant. The character and scale of the variations in the theoretical parameters A and A_{s_i} with due regard for the polarization corrections are in agreement with the experimental data (Table 1).[1] The contribution from the spin polarization to the parameter A is approximately equal to 10%, and the contribution to the parameter A_{s_i} reaches 30%. The inefficiency of spin polarization of the $[a_{1g}^b(2s_\sigma^i)]^2$ shell is associated both with the insignificant localization of the spin density at the $2s_\sigma^i$ atomic orbitals of the fluorine ions in the ground state and with the inequality $\Delta_{s_i} > \Delta_{p_i}$ (for a free fluorine atom, we have $\Delta E(2s, 2p) = 220 \times 10^3$ cm^{-1} [9]). The contribution of the first term to the polarization correction defined by expression (6) is small due to

[1] The inferences made in this work coincide with the qualitative results obtained in [4, 5].

Table 4. Covalency parameters in the ground state, polarization corrections, and ligand isotropic hyperfine parameters A_{s_a} for the F_a^- ion of $Pb^{3+}F_8^-F_a^-$ clusters in MeF_2 crystals

Crystal	x_0^2	x_1^2	x_2^2	x_3^2	x_4^2	δ_{p_a}	δ_{s_a}	$\delta_a = \delta_{p_a} + \delta_{s_a}$	A_{s_a}, Gs
CaF_2	0.70	0.56	0.05	0.08	0.01	−0.05	+0.09	+0.04	+255.1
SrF_2	0.65	0.55	0.04	0.08	0.01	−0.13	+0.15	+0.02	+192.5
BaF_2	0.66	0.52	0.04	0.08	0.01	−0.23	+0.23	0	+113.5

the inequality $K(6s, 6s) \approx 0.1$ au $< K(2p_\sigma, 2p_\sigma) \approx K(2s_\sigma, 2s_\sigma) \approx 1$ au. The main contribution to the polarization correction in expression (6) is made by the second term. In a fairly good approximation, we obtain $\delta_i = \beta_i x_1^2$. Here, β_i is the coefficient defined by expression (7), for which the contribution from Δ_{p_i} should be taken into account. Therefore, despite the small admixture of the $2s_\sigma^i$ atomic orbitals in molecular orbitals of electrons of the $2p_\sigma^i$ shell, the behavior of the parameter A_{s_i} depends on the spin polarization of this shell. This is a consequence of localization of the spin density at the $2p_\sigma^i$ atomic orbitals of the fluorine ions in the ground state.

3. Let us now consider a tetragonal cluster. The expressions describing the ligand hyperfine parameters for the F_a^- cluster coincide (substitution $i \longrightarrow a$) with formulas (4) and (5). The polarization correction δ_a with allowance made for the spin polarization of the $2p_\sigma^a$ and $2s_\sigma^a$ shells can be written in the form

$$\delta_a = (\alpha_a x_0^2 + \beta_a x_3^2 + \gamma_a x_4^2) + (\varepsilon_a x_1^2 + \omega_a x_2^2). \quad (8)$$

Here, the first parenthetic term is an analog of expression (6) with coefficients (7), the second parenthetic term is an additional contribution from spin polarization of the shells due to the spin density at the $2p_\sigma^i$ and $2s_\sigma^i$ atomic orbitals of the fluorine ions in the ground state, and the coefficients ε_a and ω_a are given by the formulas

$$\varepsilon_a = \frac{1}{4}K(2p_\sigma, 2p_\sigma)\left(\frac{x_1}{x_4}\right)\left(\frac{\nu_1\nu_4}{\Delta_{p_a}} + \frac{w_1 w_4}{\Delta_{s_a}}\right),$$
$$\omega_a = \frac{1}{4}K(2s_\sigma, 2s_\sigma)\left(\frac{x_2}{x_4}\right)\left(\frac{\nu_2\nu_4}{\Delta_{p_a}} - \frac{w_2 w_4}{\Delta_{s_a}}\right). \quad (9)$$

The molecular orbitals of electrons of the polarizing shells can be represented in the following form:

$$a_1^b(2p_\sigma^a) \approx \nu_0(6s) + \nu_3(2p_\sigma^a) - \nu_4(2s_\sigma^a),$$
$$a_1^b(2s_\sigma^a) \approx w_0(6s) + w_1(2p_\sigma^i) + w_4(2s_\sigma^a). \quad (10)$$

The covalency parameters for the tetragonal cluster in the ground state (Table 4) are calculated from the experimental parameters of the ligand hyperfine interaction under the normalization condition for the $a_1^*(6s)$ molecular orbitals. The unpaired electron in the tetragonal cluster is localized at the cubic fragment. For the Pb^{3+}–$F_{a,i}^-$ bonds, the greater part of the spin density of the ligands is localized at the $2p_\sigma^{a,i}$ atomic orbitals of the fluorine ions. By using relationships (10), the first term in expression (8) can be represented in the form $\delta_{p_a} = \beta_a x_3^2$. Here, the expression for the coefficient β_a follows from a formula similar to expression (7) at $w_3 = 0$ and accounts for the spin polarization of the $2p_\sigma^a$ shell. From relationships (9) and (10), we obtain $\omega_a = 0$. The second term in expression (8) is given by the formula $\delta_{s_a} = \varepsilon_a x_1^2$, where the expression for the coefficient ε_a follows from relationship (9) at $\nu_1 = 0$ and takes into account the spin polarization of the $2s_\sigma^a$ shell. Since $\beta_a < 0$ and $\varepsilon_a > 0$, the contributions for $\delta_a = \delta_{p_a} = \delta_{s_a}$ cancel each other out. When estimating the polarization corrections, we assume that $\delta_{p_a} \approx \delta_{p_i}$, which follows from the coincidence of the characters of the spin density delocalization at the Pb^{3+}–$F_{a,i}^-$ bonds. The contribution δ_{s_a} is estimated under the assumption that $w_0^2 \approx z_0^2$ and that the fraction of the $2p_\sigma^i$ atomic orbital in the $a_1^b(2s_\sigma^a)$ molecular orbital is approximately equal to 1%. The calculation demonstrated that the scales of the contributions δ_{p_a} and δ_{s_a} coincide. Hence, the compensation of the contributions to the polarization correction δ_a from the spin polarization of the $2p_\sigma^a$ and $2s_\sigma^a$ shells leads to the inequality $A_{s_a} > A_{s_i}$ (compare the data presented in Tables 3 and 4). Since the second term in relationship (9) taken from [5] is small (less than 3%), we have $A_a = A_{s_a}$. In this case, the anomalous isotropic parts of the A^{F_a} tensor compo-

nents can be explained by the effect of the additional contribution to the polarization correction (8) on the ligand isotropic hyperfine parameter, i.e., the contribution from the spin polarization of the shell with the $2s^a_\sigma$ character of the spin density localized at the $2p^i_\sigma$ atomic orbitals of the F^-_i ions in the ground state of the tetragonal cluster. It is quite possible that the anisotropic parts of the $A^{F_{a,i}}$ tensor components contain contributions from the spin polarization in addition to the dipole contributions. The effect of the contributions from the spin polarization explains the behavior of the anisotropic parts B_a and B_i of the $A^{F_{a,i}}$ tensor components.

In conclusion, it should be noted that, in $Pb^{3+}F^-_8F^-_a$ clusters, spin polarization exhibits a pronounced ligand nature. This is associated with the specific electronic structure of the clusters consisting of ns^1 ions, because both the ground and polarizing states are covalent σ states, which is favorable for exchange interaction in the ligands.

REFERENCES

1. Yu. A. Mikheev and V. G. Stepanov, Fiz. Tverd. Tela (Leningrad) **27** (1), 253 (1985) [Sov. Phys. Solid State **27**, 154 (1985)]; Fiz. Tverd. Tela (Leningrad) **27** (10), 3177 (1985) [Sov. Phys. Solid State **27**, 1915 (1985)].
2. V. F. Krutikov, N. I. Silkin, and V. G. Stepanov, *Paramagnetic Resonance* (Kazan. Gos. Univ., Kazan, 1978), No. 10, p. 113; No. 13, p. 79.
3. Yu. A. Mikheev, Candidate's Dissertation (Kazan State Univ., Kazan, 1987).
4. V. I. Murav'ev and V. G. Stepanov, Fiz. Tverd. Tela (Leningrad) **25** (11), 3495 (1983) [Sov. Phys. Solid State **25**, 2014 (1983)].
5. V. I. Murav'ev, Fiz. Tverd. Tela (Leningrad) **29** (2), 567 (1987) [Sov. Phys. Solid State **29**, 323 (1987)].
6. A. A. Misetich and R. E. Watson, Phys. Rev. **143** (2), 335 (1966).
7. E. Clementy, D. L. Raumondi, and W. P. Reinhard, J. Chem. Phys. **47** (4), 1300 (1967).
8. J. R. Morton and K. F. Preston, J. Magn. Res. **30** (2), 577 (1978).
9. I. B. Bersuker, *Structure and Properties of Coordination Compounds* (Khimiya, Leningrad, 1971), p. 89.

Translated by N. Korovin

Physics of the Solid State, Vol. 46, No. 5, 2004, pp. 858–860. Translated from Fizika Tverdogo Tela, Vol. 46, No. 5, 2004, pp. 834–836.

DEFECTS, DISLOCATIONS, AND PHYSICS OF STRENGTH

Starting Stress for the Onset of Dislocation Motion in Ruby Single Crystals

M. E. Bosin*, I. F. Zvyagintseva, V. N. Zvyagintsev**, F. F. Lavrent'ev*, and V. N. Nikiforenko***

** Institute of Measurement Equipment "Tsiklon," Kharkov, 61001 Ukraine*
e-mail: bosin@yandex.ru
*** Institute of Single Crystals, National Academy of Sciences of Ukraine, pr. Lenina 60, Kharkov, 61001 Ukraine*
Received August 26, 2003

Abstract—For the purpose of preparing ruby single crystals with a high degree of structural perfection, the evolution of their structural state is investigated using four-point loading at $T = 1490$°C and chemical etching pits. The starting stress τ_{st} for the onset of the dislocation motion is measured. The regularities of the arrangement of dislocations in single-crystal samples of ruby are established. The starting stress for the onset of the dislocation motion is found to be $\tau_{st} = 2$ MPa. The results obtained make it possible to determine the optimum parameters of thermomechanical treatment of the single crystals and, in the future, to solve the problem of their long-term serviceability. *© 2004 MAIK "Nauka/Interperiodica".*

1. INTRODUCTION

The shear stress necessary for the onset of dislocation motion is a fundamental characteristic of a crystal. By measuring the starting stress in defect-free crystals, it is possible to estimate the resistance of the crystal lattice to dislocation motion, i.e., the Peierls–Nabarro stress in the plane and in the direction of the dislocation motion. Moreover, with knowledge of the starting stress measured in real crystals, one can determine the internal long-range stress fields generated by dislocations and their pileups. In this work, we investigated the structural evolution and measured the starting stress of the onset of dislocation motion in ruby single crystals under high-temperature loading.

2. SAMPLE PREPARATION AND EXPERIMENTAL TECHNIQUE

In our experiments, we used ruby single crystals (Al_2O_3 + 3%CrO_3) grown by the Verneuil method [1]. Samples were cut using a diamond saw from the single crystals grown and had the form of rectangular parallelepipeds ($90 \times 15 \times 2$ mm in size) faceted by the (0001) and $(11\bar{2}0)$ planes with the longitudinal axis along the $[1\bar{1}00]$ direction. The samples were loaded by four-point bending around the $[11\bar{2}0]$ axis at a temperature $T = 1490$°C.

Figure 1 shows the shape, the crystallographic orientation, and the scheme of four-point loading of the sample. The loading points lie on the upper and lower (0001) planes of the sample. The structure of the samples was investigated by selective chemical etching of the planes of the prism and the basis according to the procedure described in [2].

3. RESULTS AND DISCUSSION

For the chosen geometry and method of loading of the studied samples, there are virtually no shear stresses in the easy basal slip system. The secondary prismatic slip system is characterized by the shear stress components responsible for structural changes in the sample. A structure with a high density of dislocations is observed in local regions subjected to the strongest stress, i.e., in the vicinity of the external, contracted, and extended (0001) planes, whereas a structure with a low density of dislocations is formed along the neutral $[1\bar{1}00]$ axis in the region containing low-angle tilt boundaries with a linear density of edge dislocations $N_c = 1.5 \times 10^3$ cm^{-1} and low-angle twist boundaries with a linear density of screw dislocations $N_b = 3 \times 10^3$ cm^{-1}.

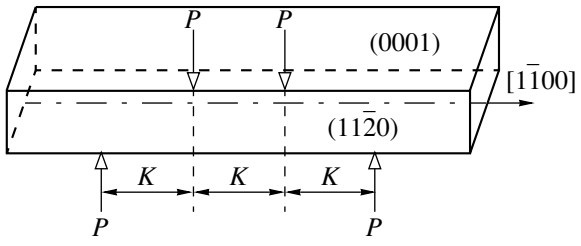

Fig. 1. Shape and crystallographic orientation of the sample for four-point loading. Arrows indicate points where the load P is applied.

1063-7834/04/4605-0858$26.00 © 2004 MAIK "Nauka/Interperiodica"

A dislocation network of twist boundaries is formed as a result of the reaction

$$\frac{1}{3}[2\bar{1}\bar{1}0] + \frac{1}{3}[\bar{1}2\bar{1}0] + \frac{1}{3}[\bar{1}\bar{1}20] = 0. \quad (1)$$

This reaction is accompanied by the formation of triple nodes that hinder the motion of the network of basal dislocations. It can be seen from Fig. 2 that, in general, the dislocation structure is symmetric with respect to the neutral axis and the density of screw dislocations increases toward the periphery of the sample. At the center, i.e., in the vicinity of the neutral axis of the sample, the edge and screw dislocations move through slip. This motion is attended by the formation of polygonal boundaries from both edge and screw dislocations. However, the edge dislocations can glide only in their own slip plane [in our case, the $(\bar{1}\bar{1}00)$ plane] and the polygonal boundaries formed from these dislocations are straight lines, whereas the polygonal boundaries formed from screw dislocations are bent. In the sample regions adjacent to the (0001) surface, the edge dislocations move through climb, whereas the screw dislocations move through cross slip. The probability of cross slip increases as the number of screw dislocations and temperature increase.

Using the results obtained, we can measure the starting stress for the onset of dislocation motion. It can be seen from Fig. 2 that, in accordance with the stress diagram, the prismatic dislocations in the $(1\bar{1}00)[11\bar{2}0]$ slip system move in a variable field of shear stresses from the strongest stresses at the upper and lower surfaces of the sample toward the neutral axis. The dislocations cease to move near the neutral axis at the points where the stress applied to the sample is equal to the resistance of the crystal lattice to dislocation motion, i.e., where it is equal to the internal stresses or the starting stress. To process the experimental data, we use the following expression for the shear stress σ_{sh} [3]:

$$\sigma_{sh} = \frac{6Pk}{ah^3}y, \quad \sigma_{sh} = 5 \text{ MPa}, \quad (2)$$

where $P = 5$ kg is the load applied to the sample; $k = 15$ mm is the distance between the loading points on the sample surface; $a = 15$ mm and $h = 2$ mm are the width and the height of the sample, respectively; and $y = 3 \times 10^{-1}$ mm is the distance from the neutral axis to the point where the dislocations stop.

Knowing the geometry of the sample and the method of its loading and using the parameters from relationships (2), we can determine the starting shear stress τ_{st} for the onset of dislocation motion. For this purpose, we use the relationship

$$\tau_{st} = \sigma_{sh}\sin\varphi\cos\psi, \quad \tau_{st} = 2 \text{ MPa}, \quad (3)$$

where φ is the angle between the $(1\bar{1}00)$ plane of the prism and the neutral axis of the sample and ψ is the angle between the $[11\bar{2}0]$ shear stress and the neutral axis of the sample.

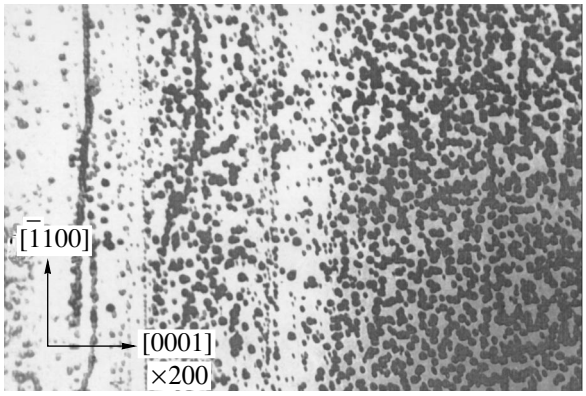

Fig. 2. Etch pattern on the $(11\bar{2}0)$ plane of the sample after loading.

As can be seen from Fig. 2, there are no dislocation pileups at the points where the dislocations stop. Consequently, local internal stresses are also absent. Therefore, the measured starting stress can be related to the Peierls–Nabarro resistance in the $(1\bar{1}00)[11\bar{2}0]$ prismatic slip system.

Nikitenko and Petukhov [4] noted that the technique of measuring the starting stress for the onset of dislocation motion is most effective for experimental determination of the resistance of the crystal lattice to dislocation motion in an ideal crystal. We compared the starting shear stress τ_{st} for the onset of dislocation motion and the critical shear stress determined by the macroscopic method from the hardening curve. It turned out that the critical shear stress is several times greater than the stress measured by the microscopic method. Such a large difference can be associated with strong internal stresses caused by macroscopic strains due to the presence of dislocation pileups inducing internal long-range stresses in the crystal.

It should be noted that ruby single crystals are widely used in laser technology. In our previous works [5, 6], we established that the long-term serviceability of lasers substantially depends on the degree of structural perfection of ruby single crystals. In a ruby single crystal, laser emission gives rise to thermoelastic stresses, which, in turn, initiate the nucleation of microcracks in the vicinity of stress concentrators, such as dislocation pileups, subgrain boundaries, etc. The development of microcracks in the course of the laser action leads to breakdown of the single crystal. In this respect, the starting stress has to be measured in order to determine the optimum conditions of thermomechanical treatment of a ruby single crystal with the aim of increasing the degree of its structural perfection. We confirmed the efficiency of this treatment for model zinc single crystals in our experiment. The total density

of dislocations was found to decrease by three to four orders of magnitude, and the subgrain boundaries were found to decompose and then be eliminated from the single crystal.

4. CONCLUSIONS

Thus, the above investigations into the evolution of the structural state in ruby single crystals made it possible for the first time to determine the starting shear stress for the onset of dislocation motion and to consider the criteria for choosing the optimum conditions of thermomechanical treatment of ruby single crystals for the purpose of improving the degree of their structural perfection. This is important for solving the problem of long-term serviceability of lasers.

ACKNOWLEDGMENTS

We would like to thank A.V. Ashukin for his assistance in preparing the samples used in our experiments.

REFERENCES

1. A. A. Blistanov, *Crystals of Quantum and Nonlinear Optics* (Mosk. Inst. Stali Splavov, Moscow, 2000).
2. M. V. Klassen-Neklyudova, *Ruby and Sapphire* (Nauka, Moscow, 1974).
3. S. P. Timoshenko, *Strength of Materials*, 3rd ed. (Van Nostrand, New York, 1956; NTL, Moscow, 1965).
4. V. I. Nikitenko and B. V. Petukhov, in *Abstracts of XXXII All-Russia Conference Dedicated to 100-Year Anniversary of Academician T. V. Kurdyumov, Chernogolovka* (Moscow, 2002).
5. M. E. Bosin, J. F. Zvyagintseva, V. N. Zvyagintsev, F. F. Lavrentyev, and V. N. Nikiforenko, Func. Mater. **9** (1), 154 (2002).
6. M. E. Bosin, I. F. Zvyagintseva, V. N. Zvyagintsev, F. F. Lavrent'ev, and V. N. Nikiforenko, Vopr. At. Nauki Radiat. Materialoved. **70** (4), 162 (1998).

Translated by N. Korovin

Physics of the Solid State, Vol. 46, No. 5, 2004, pp. 861–866. Translated from Fizika Tverdogo Tela, Vol. 46, No. 5, 2004, pp. 837–841.

MAGNETISM AND FERROELECTRICITY

Structure of a Bloch Domain Wall in a Cubic Crystal

O. A. Antonyuk, A. V. Tychko, and V. F. Kovalenko

Shevchenko National University, Vladimirskaya ul. 64, Kiev, 01033 Ukraine

e-mail: lab124@univ.kiev.ua

Received May 13, 2003; in final form, July 15, 2003

Abstract—Planar Bloch domain walls with different senses and paths of rotation of the magnetization vector are studied in a cubic crystal with a negative first constant of magnetic anisotropy. © *2004 MAIK "Nauka/Interperiodica".*

1. The substructure of domain walls in magnetically ordered media has been a subject of basic and applied research [1–8]. Bloch domain walls consisting of regions with different senses of rotation of the magnetization vector **M** have been observed in uniaxial and multiaxial crystals [1, 5–8]. In uniaxial magnets, 180° domain walls with anticlockwise and clockwise senses of rotation have been found to have the same energy [1, 8]. Earlier, Graham and Neurath [3, 4] analyzed the orientation dependences of the specific energy of planar Bloch domain walls with different senses and paths of rotation of the magnetization vector **M** in cubic crystals with a positive first constant K_1 of crystalline magnetic anisotropy. In this work, we investigated the properties of planar Bloch domain walls with different paths and senses of rotation of the magnetization vector **M** in cubic crystals with a negative first constant of magnetic anisotropy.

2. The spatial distribution of the magnetization **M** in the bulk of a Bloch domain wall for $|M|$ = const can be described by a unit vector $\boldsymbol{\alpha}$: $\mathbf{M} = M\boldsymbol{\alpha}$, where M is the saturation magnetization; $\boldsymbol{\alpha} = (\alpha_1, \alpha_2, \alpha_3)$; and α_1, α_2, and α_3 are the direction cosines in the *Oxyz* coordinate system whose axes are aligned parallel to the ⟨100⟩ directions. For Bloch domain walls that are characterized by the divergence div**M** = 0, the energy density of domain walls is determined only by the volume densities of the exchange energy $e_{EX} = A[\sum_{j=1}^{3}(\nabla\alpha_j)^2]$ and the magnetic anisotropy energy $e_{MA}(\boldsymbol{\alpha})$, where A is the exchange constant [1, 2, 8].

In the coordinate system under consideration (Fig. 1), the $O\tilde{z}$ axis is aligned parallel to the normal **n** and the $O\tilde{y}$ axis coincides with the direction of the vector $\Delta\mathbf{M} = \mathbf{M}_2 - \mathbf{M}_1$, where $\mathbf{M}_1 = M\mathbf{m}_1$, $\mathbf{M}_2 = M\mathbf{m}_2$, and $\mathbf{m}_1$ and $\mathbf{m}_2$ are the unit vectors specifying the extreme attainable directions of the magnetization **M** in the bulk of domains separated by a Bloch domain wall (at $\tilde{z} \longrightarrow -\infty$ and $\tilde{z} \longrightarrow +\infty$, respectively). From the condition **Mn** = const, it follows that $\Delta\mathbf{Mn} = 0$; i.e., all possible orientations of the normal **n** coincide with directions perpendicular to the vector $\Delta\mathbf{M}$.

The angle λ between the normal **n** and the plane of the unit vectors $\mathbf{m}_1$ and $\mathbf{m}_2$ characterizes the rotation of the normal **n** about the vector $\Delta\mathbf{M}$ and specifies the orientation of the plane of the Bloch domain wall. (For 180° domain walls, the angle λ will be defined in Section **4**.) The angle 2α between the vectors $\mathbf{m}_1$ and $\mathbf{m}_2$ determines the type of 2α-degree domain wall. This angle can be calculated from the expression $\alpha = \arccos\sqrt{[1 + (\mathbf{m}_1\mathbf{m}_2)]/2}$. The magnetic anisotropy energy is specified in the *Oxyz* coordinate system whose axes coincide with the ⟨100⟩ crystallographic directions. The *Oxyz* coordinate system and the coordinate system corresponding to the $(O\tilde{x}\tilde{y}\tilde{z})$ plane of the Bloch domain wall (Fig. 1) are related by the transformation $A(\lambda)$:

$$\tilde{\boldsymbol{\alpha}} = A(\lambda)\boldsymbol{\alpha}, \qquad (1)$$

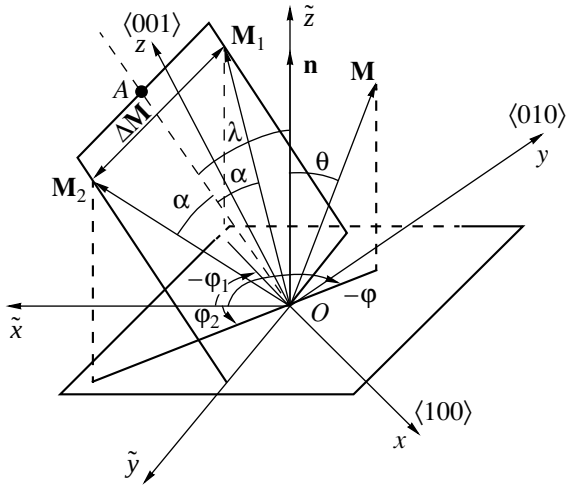

Fig. 1. Coordinate system.

1063-7834/04/4605-0861$26.00 © 2004 MAIK "Nauka/Interperiodica"

where $\tilde{\boldsymbol{\alpha}} = (\tilde{\alpha}_1, \tilde{\alpha}_2, \tilde{\alpha}_3)$ and $\tilde{\alpha}_1$, $\tilde{\alpha}_2$, and $\tilde{\alpha}_3$ are the direction cosines of the magnetization vector **M** in the $O\tilde{x}\tilde{y}\tilde{z}$ coordinate system. For arbitrary orientations of the vectors $\mathbf{m}_1$ and $\mathbf{m}_2$, we can write the following relationships:

$$A(\lambda) = \begin{bmatrix} \cos\lambda & 0 & \sin\lambda \\ 0 & 1 & 0 \\ -\sin\lambda & 0 & \cos\lambda \end{bmatrix} [\mathbf{e}_1^T \ \mathbf{e}_2^T \ \mathbf{e}_3^T]^{-1}, \quad (2)$$

$$\boldsymbol{\alpha} = [\mathbf{e}_1^T \ \mathbf{e}_2^T \ \mathbf{e}_3^T] \begin{bmatrix} \cos\lambda & 0 & -\sin\lambda \\ 0 & 1 & 0 \\ \sin\lambda & 0 & \cos\lambda \end{bmatrix} \tilde{\boldsymbol{\alpha}},$$

$$\mathbf{e}_1 = \frac{\mathbf{m}_2 \times \mathbf{m}_1}{|\mathbf{m}_2 \times \mathbf{m}_1|}, \quad \mathbf{e}_2 = \frac{\mathbf{m}_2 - \mathbf{m}_1}{|\mathbf{m}_2 - \mathbf{m}_1|}, \quad (3)$$

$$\mathbf{e}_3 = \frac{\mathbf{m}_2 + \mathbf{m}_1}{|\mathbf{m}_2 + \mathbf{m}_1|}, \quad \alpha < \pi/2 \quad (\mathbf{m}_1 \neq -\mathbf{m}_2),$$

$$\mathbf{e}_1 = \mathbf{e}_2 \times \mathbf{e}_3, \quad \mathbf{e}_2 = (\mathbf{m}_2 - \mathbf{m}_1)/|\mathbf{m}_2 - \mathbf{m}_1|,$$

$$\mathbf{e}_3 \perp \mathbf{e}_2 \quad (|\mathbf{e}_3| = 1), \quad \alpha = \pi/2 \quad (\mathbf{m}_1 = -\mathbf{m}_2).$$

In relationship (2), the first factor corresponds to the rotation of the coordinate system about the vector $\Delta\mathbf{M}$ and the second factor accounts for the transformation of the coordinate system from the initial position into the position at $\lambda = 0$.

Let us consider the case where the direction of the magnetization **M** is specified by the polar (θ) and azimuthal (φ) angles, which are reckoned from the $O\tilde{z}$ and $O\tilde{x}$ axes, respectively. Then, the spatial distribution of the magnetization **M** in the bulk of the Bloch domain wall is determined by the variable φ. Note that the angle θ is indefinable in the bulk of the Bloch domain wall due to the conservation of the normal component of the magnetization **M**. The orientations of the vectors $\mathbf{m}_1$ and $\mathbf{m}_2$ are specified by the angles φ_1 and φ_2, respectively. The angle θ depends on the orientation and type of the Bloch domain wall and is related to the parameters α and λ by the expression

$$\sin\theta = \sqrt{1 - \cos^2\alpha\cos^2\lambda}. \quad (4)$$

Next, we write the following relationships:

$$e_{11} = (\alpha_2^{(2)}\alpha_3^{(1)} - \alpha_3^{(2)}\alpha_2^{(1)})/|\mathbf{m}_2 \times \mathbf{m}_1|,$$

$$e_{12} = (\alpha_3^{(2)}\alpha_1^{(1)} - \alpha_1^{(2)}\alpha_3^{(1)})/|\mathbf{m}_2 \times \mathbf{m}_1|,$$

$$e_{13} = (\alpha_1^{(2)}\alpha_2^{(1)} - \alpha_2^{(2)}\alpha_1^{(1)})/|\mathbf{m}_2 \times \mathbf{m}_1|,$$

$$e_{2i} = (\alpha_i^{(2)} - \alpha_i^{(1)})/|\mathbf{m}_2 - \mathbf{m}_1|,$$

$$e_{3i} = (\alpha_i^{(2)} + \alpha_1^{(1)})/|\mathbf{m}_2 + \mathbf{m}_1|, \quad i = 1, 3,$$

where $\alpha_1^{(1)}$, $\alpha_2^{(1)}$, $\alpha_3^{(1)}$ and $\alpha_1^{(2)}$, $\alpha_2^{(2)}$, $\alpha_3^{(2)}$ are the direction cosines of the vectors $\mathbf{M}_1$ and $\mathbf{M}_2$ in the *Oxyz* coordinate system, respectively. If the above relationships are satisfied, we obtain

$$\alpha = \begin{bmatrix} (e_{11}\cos\lambda + e_{31}\sin\lambda)\sin\theta\cos\varphi \\ + e_{21}\sin\theta\sin\varphi + (e_{31}\cos\lambda - e_{11}\sin\lambda)\cos\theta \\ (e_{12}\cos\lambda + e_{32}\sin\lambda)\sin\theta\cos\varphi \\ + e_{22}\sin\theta\sin\varphi + (e_{32}\cos\lambda - e_{12}\sin\lambda)\cos\theta \\ (e_{13}\cos\lambda + e_{33}\sin\lambda)\sin\theta\cos\varphi \\ + e_{23}\sin\theta\sin\varphi + (e_{33}\cos\lambda - e_{13}\sin\lambda)\cos\theta \end{bmatrix}. \quad (5)$$

Since the angle φ is a cyclic variable, there are two possible senses of rotation of the magnetization vector **M** in the bulk of the Bloch domain wall. In these cases, the vector **M** rotates along two different parts of the lateral surface of a cone on which the lateral surface is divided by the generatrices parallel to the vectors $\mathbf{m}_1$ and $\mathbf{m}_2$. The base of this cone is parallel to the Bloch domain wall. If the angle φ_0 is half the angle between the projections of the vectors $\mathbf{m}_1$ and $\mathbf{m}_2$ onto the plane of the Bloch domain wall, the angle φ varies upon rotation of the magnetization vector **M** in the following ranges: $\varphi_1 = -\varphi_0 < \varphi < \varphi_2 = +\varphi_0$ and $\varphi_1 = \varphi_0 < \varphi < \varphi_2 = 2\pi - \varphi_0$ for the clockwise and anticlockwise senses of rotation magnetization vector **M**, respectively. The dependence of the angle φ_0 on the parameters λ and α can be represented in the form

$$\varphi_0 = \arccos(\cos\alpha\sin\lambda/\sqrt{1 - \cos^2\alpha\cos^2\lambda}), \quad (6)$$

where $\alpha < \varphi_0 < \pi - \alpha$.

In this work, we will consider long ($\varphi_2 - \varphi_1 > \pi$) and short ($\varphi_2 - \varphi_1 < \pi$) paths of rotation of the magnetization vector **M** in the bulk of the Bloch domain wall. The path of rotation of the vector **M** can be characterized by the parameter $L(\lambda) = (\varphi_2 - \varphi_1)\sin\theta$, which represents the length of the curve formed by directions of the magnetization vector **M** in the Bloch domain wall on the spherical surface of unit radius.

3. For a planar isolated Bloch domain wall, the spatial distribution $\bar{z}$ of the angle of rotation φ and the specific energy σ_ω can be represented in the form [1, 8]

$$\bar{z}(\varphi) = \int_0^\varphi \sqrt{A\sin^2\theta/(e_{MA}(\theta, \zeta) - e_{MA}(\theta, \varphi_1))}\,d\zeta, \quad (7)$$

$$\sigma = 2\int_{\varphi_1}^{\varphi_2} \sqrt{A\sin^2\theta(e_{MA}(\theta, \varphi) - e_{MA}(\theta, \varphi_1))}\,d\varphi. \quad (8)$$

For Bloch domain walls with clockwise and anticlockwise senses of rotation of the magnetization vector **M**, the specific energies σ_0 and σ_π can be written as

$$\sigma_0 = 2\int_{-\varphi_0(\lambda,\alpha)}^{\varphi_0(\lambda,\alpha)} \sqrt{A\sin^2\theta(e_{MA}(\theta,\varphi)-e_{MA}(\theta,\varphi_1))}\,d\varphi, \quad (9a)$$

$$\sigma_\pi = 2\int_{\varphi_0(\lambda,\alpha)}^{2\pi-\varphi_0(\lambda,\alpha)} \sqrt{A\sin^2\theta(e_{MA}(\theta,\varphi)-e_{MA}(\theta,\varphi_1))}\,d\varphi. \quad (9b)$$

The function $A\sin^2\theta[e_{MA}(\theta, \varphi) - e_{MA}(\theta, \varphi_1)]$ is transformed with a change in the orientation of the plane of the Bloch domain wall in accordance with relationships (3)–(5) and (8). The angles λ corresponding to equal energies of the Bloch domain walls with different senses of rotation are zeros of the function $\Delta\sigma(\lambda) = \sigma_0 - \sigma_\pi$ on a bounded interval $\lambda \in [-\pi/2; \pi/2]$. An analytical function that is not identically equal to zero has a finite number of zeros on a bounded interval. For $\lambda = +\pi/2$, the vector **M** rotates in the plane of the vectors $\mathbf{m}_1$ and $\mathbf{m}_2$ ($\theta = \pi/2$). Except for crystals with unidirectional magnetic anisotropy, the relationship $e_{MA}(\pi/2, \varphi) = e_{MA}(\pi/2, \pi - \varphi)$ is satisfied. Therefore, with due regard for expression (6), the analytical function $\Delta\sigma(\lambda)$ is identically equal to zero for $\alpha = \pi/2$ ($\theta = \pi/2$, $\varphi_0 \equiv \pi/2$) at arbitrary angles λ and takes on nonzero values that are opposite in sign but equal in magnitude for $\alpha \neq \pi/2$ at $\lambda = \pi/2$ ($\varphi_0 = \alpha$) and $\lambda = -\pi/2$ ($\varphi_0 = \pi - \alpha$). Consequently, there exists at least one position of the Bloch domain wall in which domain-wall regions with different senses of rotation have the same energy. For a 180° domain wall, the identity $\sigma_0 \equiv \sigma_\pi$ is satisfied for arbitrary orientations of the domain-wall plane. In the case of 2α-degree domain walls at $\alpha < \pi/2$, there is a finite number of orientations of the domain-wall plane for which the specific energies satisfy the equality $\sigma_0 = \sigma_\pi$ at $\lambda \in [-\pi/2; \pi/2]$.

4. For a cubic crystal, the energy density of magnetic anisotropy has the form [8, 9]

$$e_{MA} = K_1(\alpha_1^2\alpha_2^2 + \alpha_2^2\alpha_3^2 + \alpha_1^2\alpha_3^2) + \ldots, \quad (10)$$

where K_1 is the first magnetic anisotropy constant. In our calculations of the domain-wall structure in cubic crystals with a magnetic anisotropy constant $K_1 < 0$, when the vectors $\mathbf{m}_1$ and $\mathbf{m}_2$ are aligned along the $\langle 111\rangle$ directions, the vector $\Delta\mathbf{M}$ is taken to be coincident with the $\langle 001\rangle$, $\langle \bar{1}10\rangle$, and $\langle \bar{1}11\rangle$ crystallographic directions for the 71°, 109°, and 180° domain walls, respectively. For the 180° domain wall, the $O\tilde{z}$ and $O\tilde{x}$ axes at $\lambda = 0$ are chosen parallel to the $\langle 1\bar{1}2\rangle$ and $\langle 110\rangle$ directions, respectively.

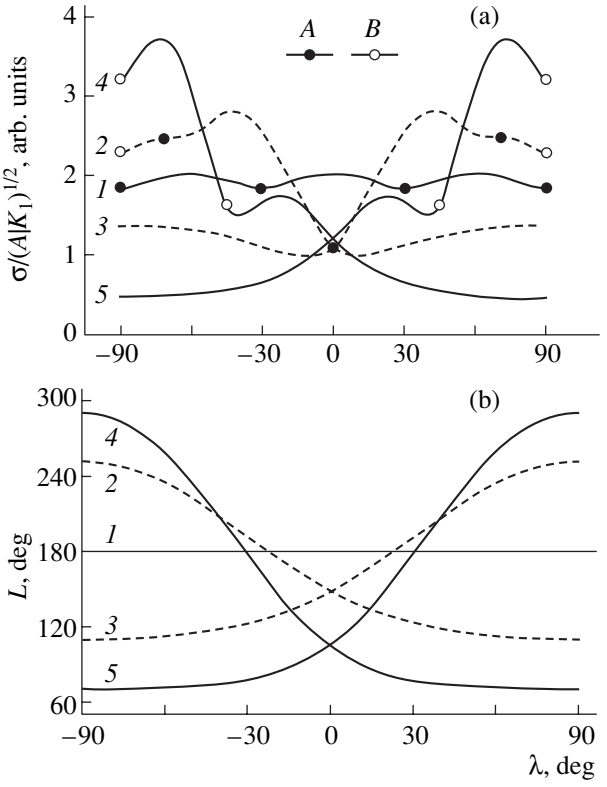

Fig. 2. Orientation dependences of (a) the specific energy and (b) the path length L for rotation of (*1*) 180°, (*2*, *3*) 109°, and (*4*, *5*) 71° domain walls in an infinite cubic crystal upon (*2*, *4*) clockwise and (*3*, *5*) anticlockwise senses of rotation of the magnetization vector **M**.

The orientation dependences of the specific energies σ_0 and σ_π for 180°, 109°, and 71° domain walls are plotted in Fig. 2a. The energy density of these domain walls exhibits minima for rotations of the magnetization vector **M**, whose trajectories either pass through the easy magnetization axis of the crystal or are close to this axis. Points *A* and *B* in Fig. 2a correspond to the orientations of the Bloch domain wall for which the trajectory of rotation of the magnetization vector **M** intersects one and two easy magnetization axes, respectively. The energy density of the 180° domain wall is minimum at $\lambda = \pm 30°$ and $\pm 90°$. This result is in agreement with the inferences made in [1, 3, 4]. The trajectory of rotation of the magnetization vector **M** in the 109° domain wall passes through the easy magnetization axis in the cases when the normal to the plane of the Bloch domain wall is aligned parallel to the fourfold, threefold, and twofold axes of the cubic crystal at $\lambda = 0°, \pm 70.53°, \pm 90°$, respectively. As a result, the orientation dependences of the specific energies σ_0 and σ_π exhibit local minima at $\lambda = 10°9', -90°$ and $-10°9', 90°$, respectively (Fig. 2a, curves *2*, *3*). For the 71° domain wall, the trajectory of rotation of the magnetization vector **M** intersects two easy magnetization axes at $\lambda = -45°$ and 90° for the specific energy σ_0 and at $\lambda = 45°$ and

Table 1. Equilibrium parameters of Bloch domain walls in an infinite crystal with a cubic magnetic anisotropy constant $K_1 < 0$

Type of Bloch domain wall	Path of rotation	Parameters of Bloch domain walls			
		λ, deg	$\varphi_2 - \varphi_1 = \Delta\varphi$, deg	L, deg	$\sigma/\sqrt{A\lvert K_1\rvert}$
180°	$\Delta\varphi \equiv 180°$	30	180	180	1.8291981
		90	180	180	1.8291981
109°	$\Delta\varphi < 180°$	10.15	165.8	149.2	0.9814107
	$\Delta\varphi > 180°$	90	250.5	250.5	1.3680489
71°	$\Delta\varphi < 180°$	90	70.5	70.5	0.4611492
	$\Delta\varphi > 180°$	39.73	264.2	206.1	1.4966010
		90	289.5	289.5	3.1971460

Table 2. Equilibrium parameters of Bloch domain walls in the (110) plate with a cubic magnetic anisotropy constant $K_1 < 0$

Type of Bloch domain wall	Path of rotation	Parameters of Bloch domain walls				
		λ, deg	ψ, deg	$\varphi_2 - \varphi_1 = \Delta\varphi$, deg	L, deg	$\sigma/\sqrt{A\lvert K_1\rvert}$
180°	$\Delta\varphi \equiv 180°$	7.21	82.79	180	180	1.98787
109°	$\Delta\varphi < 180°$	8.48	81.52	168.1	158	0.9834806
	$\Delta\varphi > 180°$	–	–	–	–	–
71°	$\Delta\varphi < 180°$	35.22	54.78	101.6	75.69	0.6029033
	$\Delta\varphi > 180°$	35.62	54.38	258.9	193.66	1.5436966

$-90°$ for the specific energy σ_π. In this case, the normal to the Bloch domain wall is aligned with the fourfold ($\lambda = \pm 45°$) and twofold ($\lambda = \pm 90°$) axes. The former orientation is responsible for the local minima in the orientation dependences of σ_0 at $\lambda = -39°44'$ and σ_π in the case of a long path of rotation (Fig. 2a, curves *4*, *5*).

For the 180° domain wall, the orientation dependences are identical (Figs. 2a, 2b, curves *1*): $\sigma_0 = \sigma_\pi$ at arbitrary angles λ and $L \equiv \pi$. In the case of 109° or 71° domain walls, the minima of the energy density at $\lambda \neq 90°$ are shifted toward angles λ corresponding to shorter paths of rotation of the magnetization vector **M** (Figs. 2a, 2b). For these domain walls, we obtain $\sigma_0 = \sigma_\pi$ at $\lambda = 0$ (Fig. 2a). A similar inference holds true for 90° domain walls in a cubic crystal with a magnetic anisotropy constant $K_1 > 0$ [4]. The orientation dependences for the 71° domain wall (Fig. 2a, curves *4*, *5*) are most pronounced because of the stronger dependence of the parameter L on the orientation of the Bloch domain wall (Fig. 2b, curves *4*, *5*). The orientation dependences for Bloch domain walls with opposite senses of rotation of the magnetization vector **M** (Fig. 2a) are symmetric with respect to the orientation of the domain wall at $\lambda = 0$ due to cubic symmetry of the crystal. Upon replacing $\mathbf{e}_1 \longrightarrow -\mathbf{e}_1$, $\lambda \longrightarrow -\lambda$, and $\varphi \longrightarrow \pi - \varphi$ in expression (6), we found that $\alpha_1 \longrightarrow -\alpha_2$, $\alpha_2 \longrightarrow -\alpha_1$, and $\alpha_3 \longrightarrow \alpha_3$ for the 109° domain wall and $\alpha_3 \longrightarrow -\alpha_3$ for the 71° domain wall. In this case, the value of e_{MA} [see relationship (10)] remains unchanged. As a consequence, Bloch domain walls with opposite senses of rotation whose planes are symmetric with respect to the orientation at $\lambda = 0$ have the same energy.

The behavior of the orientation dependences of the surface energy density of Bloch domain walls is governed by the sense and path of rotation of the magnetization vector **M** (Fig. 2b). In the case of 2α-degree domain walls ($\alpha < \pi/2$), the long (short) path for the clockwise (anticlockwise) senses of rotation of the magnetization vector **M** changes to the short (long) path when the sign of the angle λ changes from negative to positive. At arbitrary angles λ, the short path of rotation of the magnetization is characterized by lower specific energies of the 109° domain wall (Fig. 2a) in an infinite crystal with cubic magnetic anisotropy. This means that Bloch domain walls with a short path of rotation of the magnetization vector **M** are energetically favorable. The basic parameters that characterize the equilibrium position of Bloch domain walls with different paths of rotation of the magnetization vector **M** in an infinite crystal are presented in Table 1.

In a spatially bounded magnetically ordered medium, the energetically favorable orientations of the plane of a Bloch domain wall depend on its orientation with respect to the surface of the medium [5]. The

change in the surface area of the Bloch domain wall upon deviation of the domain-wall plane from the surface of the medium is included in the factor $(1/\sin\psi)$: $S = S_0/\sin\psi$, where ψ is the angle of rotation of the domain-wall plane about the line of intersection of the domain wall with the surface of the medium ($\psi = 0$ when the domain-wall plane coincides with the surface of the medium) [2, 5]. In this case, we obtain $\cos\psi = \sin\delta\sin\lambda$, where δ is the angle between the vector $\Delta\mathbf{M}$ and the normal to the plate. When the vectors $\mathbf{m}_1$ and $\mathbf{m}_2$ lie in the (110) plane, the orientation dependences of the specific energies σ_0 and σ_π for the (110) plate of a cubic crystal with magnetic anisotropy $K_1 < 0$ are symmetric with respect to the domain-wall orientation at $\lambda = 0$. The orientation dependences of the specific energies σ_0 and σ_π at $\pi/2 > \lambda > 0$ are depicted in Fig. 3.

Table 2 presents the parameters characterizing the equilibrium position of Bloch domain walls with different paths of rotation of the magnetization vector **M** in a cubic (110) crystal with a magnetic anisotropy constant $K_1 < 0$. The parameters of the Bloch domain wall with a minimum surface energy density are in good agreement with the results obtained in [1, 2, 5]. The inclusion of the change in the surface area of the Bloch domain wall leads to an increase in the energy density of the domain wall, a decrease in the equilibrium angle λ, and an increase in the angle $2\varphi_0$ for non-180° domain walls. In the (110) plates, 180° domain walls with different paths of rotation of the magnetization vector **M** do not differ from each other (Fig. 3a). In these plates, the 109° and 71° domain walls with short paths and the 71° domain walls with a long path of rotation of the magnetization vector **M** are equilibrium domain walls. The width of the 71° domain wall with a long path of rotation is substantially greater than that of the 71° domain wall with a short path of rotation. This can be explained by the longer path of rotation of the magnetization vector **M** and the slower change in the orientation of the magnetization vector **M** in the bulk of the Bloch domain walls (Fig. 4).

5. Thus, it was established that there exist orientations of the plane of a planar Bloch domain wall for which the energies of Bloch domain walls with clockwise and anticlockwise senses of rotation of the magnetization vector **M** are equal to each other. For 180° domain walls, this equality is satisfied at arbitrary (all) orientations of the domain-wall plane. For other types of Bloch domain walls, the above equality holds for a finite number of orientations of the normal to the domain-wall plane. This means that there exist ranges of orientations of the domain-wall plane in which the domain wall, with a specific sense of rotation of the vector **M**, has a minimum energy. Crystals with a negative first constant of cubic magnetic anisotropy are characterized by only one of these orientations, which, according to the results obtained in this work, corresponds to $\lambda = 0$.

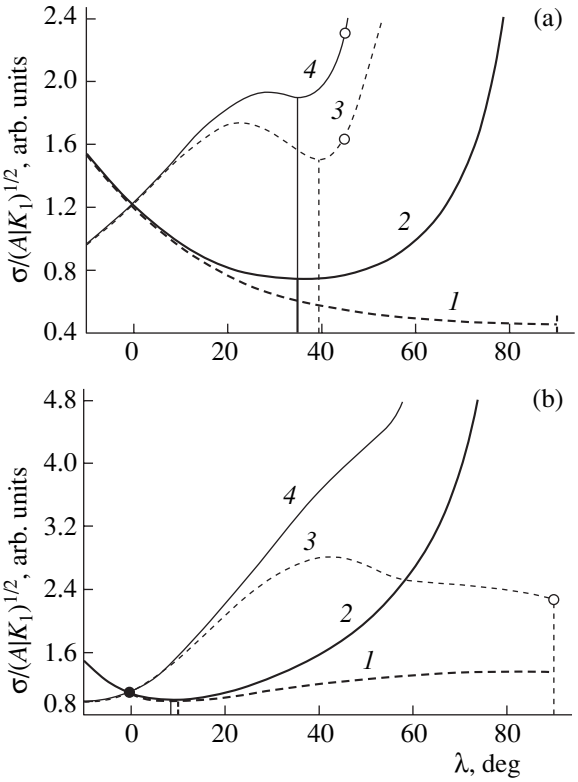

Fig. 3. Orientation dependences of the specific energy for (a) 71° and (b) 109° domain walls in an infinite cubic crystal upon (*1*, *3*) clockwise and (*2*, *4*) anticlockwise senses of rotation of the magnetization vector **M**.

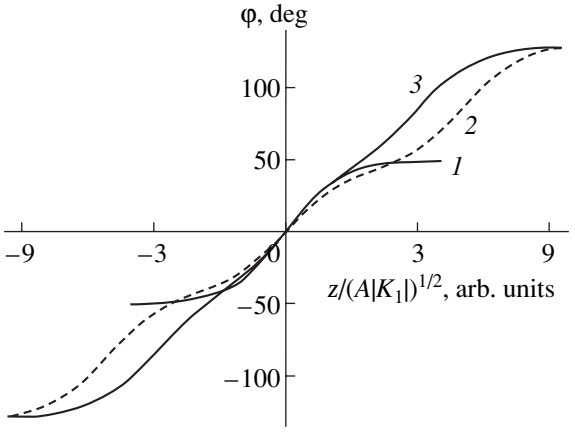

Fig. 4. Distributions of the magnetization **M** in an equilibrium 71° domain wall with (*1*) short and (*2*, *3*) long paths of rotation of the magnetization vector **M** in (*1*, *3*) the (110) plate and (*2*) an infinite cubic crystal with a magnetic anisotropy constant $K_1 < 0$.

In an infinite cubic crystal with a negative first constant of magnetic anisotropy, the Bloch domain walls with a short path of rotation of the magnetization vector **M** are energetically favorable irrespective of the type of

domain walls and the sense of rotation of the vector **M**. All the considered equilibrium orientations of the domain-wall plane either coincide with the orientations for which the path of rotation of the magnetization vector **M** passes through the easy magnetization axis or are shifted toward the orientations characterized by a shorter path of rotation of the magnetization. The orientation with a minimum surface energy density only for 71° domain walls corresponds to a minimum path of rotation of the magnetization.

In the (110) plate with a negative first constant of cubic magnetic anisotropy, the 71° domain walls with long and short paths of rotation of the magnetization vector **M** and 109° domain walls with a short path of rotation are equilibrium domain walls. Planar 109° Bloch walls with a long path of rotation of the magnetization vector are nonequilibrium in these plates. The width and surface energy density of 71° domain walls with a long path of rotation of the magnetization vector exceed those of 71° domain walls with a short path of rotation of the magnetization.

REFERENCES

1. A. Hubert, *Theorie der Domanenwande in Geordneten Medien* (Springer, Berlin, 1974; Mir, Moscow, 1977).
2. B. A. Lilley, Philos. Mag. **41**, 792 (1950).
3. C. D. Graham and P. W. Neurath, J. Appl. Phys. **28** (8), 888 (1957).
4. C. D. Graham, Jr., J. Appl. Phys. **29** (10), 1451 (1958).
5. V. L. Vlasko-Vlasov, L. M. Dedukh, and V. I. Nikitenko, Zh. Éksp. Teor. Fiz. **71** (6), 2291 (1976) [Sov. Phys. JETP **44**, 1208 (1976)].
6. B. E. Argyle and E. Terrenzio, J. Appl. Phys. **55** (6), 2569 (1984).
7. J. J. Basterfield, J. Appl. Phys. **39** (12), 5521 (1968).
8. A. Hubert and R. Shager, *Magnetic Domains: The Analysis of Magnetic Microstructures* (Springer, Berlin, 1998).
9. P. Hansen, in *Physics of Magnetic Garnets*, Ed. by A. Paoletti (North-Holland, Amsterdam, 1978), pp. 56–133.

Translated by O. Borovik-Romanova

Physics of the Solid State, Vol. 46, No. 5, 2004, pp. 867–871. Translated from Fizika Tverdogo Tela, Vol. 46, No. 5, 2004, pp. 842–845.

MAGNETISM AND FERROELECTRICITY

Spin-Wave Spectrum of an Ideal Multilayer Magnet upon Modulation of All Parameters of the Landau–Lifshitz Equation

V. V. Kruglyak, A. N. Kuchko, and V. I. Finokhin

Donetsk National University, Universitetskaya ul. 24, Donetsk, 83055 Ukraine

e-mail: kuchko@dongu.donetsk.ua

Received July 22, 2003

Abstract—The spectrum of exchange spin waves in a multilayer magnet is theoretically investigated without regard for dissipation upon periodic modulation of all magnetic material parameters (uniaxial anisotropy constant, exchange interaction constant, saturation magnetization, gyromagnetic ratio) entering into the Landau–Lifshitz equation. A graphical method is proposed for analyzing the dependence of the propagation of spin waves on the depth of modulation of the material parameters. Practical application of the results obtained and the effect of dissipation on the propagation of spin waves in the system are discussed. © *2004 MAIK "Nauka/Interperiodica".*

1. INTRODUCTION

In recent works devoted to the properties of multilayer systems, the trend has been toward a changeover from ideal structures to increasingly realistic models of magnetic materials. Great interest has been expressed by researchers in the phenomena associated with magnetic viscosity, finite thickness and irregular arrangement of interlayer boundaries, and the presence of defects in multilayer structures. In particular, Ignatchenko *et al.* [1, 2] performed a theoretical investigation into the evolution of the spectrum and damping of spin waves due to inhomogeneities in the period of the superlattice, Gulyaev and Nikitov [3] considered the localization of spin-wave modes in the vicinity of a single defect, and Gorobets *et al.* [4] and Ignatchenko *et al.* [5] studied spin waves in multilayer magnets with diffuse interfaces. In our earlier work [6], we investigated the influence of periodic inhomogeneities in the distribution of the magnetic viscosity parameter on the propagation and damping of spin waves. Zyuzin *et al.* [7] analyzed the effect of these inhomogeneities on the linewidth of spin-wave resonance.

However, the authors of the aforementioned works, as a rule, analyzed the modulation of only a few of the parameters characterizing a magnetic system (see, for example, [1–5, 8]). Since this approach is sufficiently simple and, in some cases, corresponds to real situations with magnetic systems, it has made it possible to reveal the main regularities in the propagation and damping of spin waves in multilayer materials. At the same time, from the experimental and practical standpoints, the properties and parameters of real magnetic materials need to be considered in a more general case. This is essential to the understanding of the contribution of the previously proposed models to the solution of the problem under consideration and for the possible application of the obtained results to a greater variety of materials used in practice.

In this work, the spin-wave spectrum of a multilayer magnet was theoretically investigated in the continuum approximation upon modulation of all magnetic material parameters entering into the Landau–Lifshitz equation without regard for dissipation.

2. THEORETICAL BACKGROUND

As in our previous work [6], we consider an infinite sample consisting of two types of alternating plane-parallel homogeneous layers that are uniformly magnetized to saturation. These layers have thicknesses d_1 and d_2 and are characterized by exchange interaction constants α_1 and α_2, uniaxial anisotropy constants β_1 and β_2, easy magnetization axes lying parallel to each other in the layer planes, saturation magnetizations M_1 and M_2, and gyromagnetic ratios g_1 and g_2 ($g_j > 0$, $j = 1, 2$). An external dc magnetic field **H** is aligned with the easy magnetization axis. The Cartesian coordinate system is chosen so that the *OX* axis is perpendicular to the layer planes and the *OZ* axis is parallel to the easy magnetization axis.

The dynamics of the magnetic moment can be described by the Landau–Lifshitz equation [9]

$$\frac{\partial \mathbf{M}}{\partial t} = -g\left[\mathbf{M}\times\left\{(H+\beta(\mathbf{Mn}))\mathbf{n}+\frac{\partial}{\partial \mathbf{r}}\left(\alpha\frac{\partial \mathbf{M}}{\partial \mathbf{r}}\right)\right\}\right], \quad (1)$$

1063-7834/04/4605-0867$26.00 © 2004 MAIK "Nauka/Interperiodica"

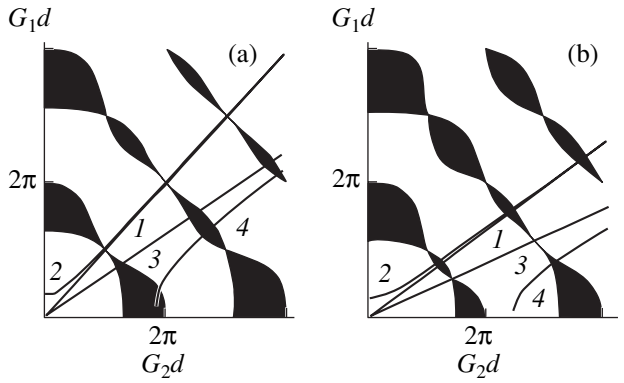

Fig. 1. Diagram for determining the boundaries of the forbidden and allowed energy bands in a multilayer material with equal layer thicknesses ($d_1 = d_2$) and identical saturation magnetization ($M_1 = M_2 = M_0$) for different modulations $\Delta\varepsilon$ of the material parameters [$\Delta\varepsilon = (\varepsilon_2 - \varepsilon_1)/\langle\varepsilon\rangle$ and $\langle\varepsilon\rangle = (\varepsilon_2 + \varepsilon_1)/2$, where ε is a modulated parameter]. The spectral lines in the diagram correspond to the following cases of modulation of the material parameters: (*1*) $\Delta\beta = 0$, $\Delta g = 0$, and $H = 0$; (*2*) $\Delta\beta = -0.8$, $\Delta g = 0$, and $H = 0$; (*3*) $\Delta\beta = -0.8$, $\Delta g = 0.8$, and $H = 0$; and (*4*) $\Delta\beta = -0.8$, $\Delta g = 0.8$, and $H = 10M_0$. $\Delta\alpha$ = (a) 0 and (b) 0.8.

where **M** stands for the magnetization distribution in the multilayer material and **n** is the unit vector aligned parallel to the *OZ* axis.

Let us now analyze the small deviations $\mathbf{m}_j$ of the magnetization from the ground state, i.e., the magnetization along the easy magnetization axis. For this purpose, the magnetization distribution can be represented in the form

$$\mathbf{M}_j(\mathbf{r}, t) = \mathbf{n}M_j + \mathbf{m}_j(\mathbf{r}, t), \quad |\mathbf{m}_j| \ll M_j. \tag{2}$$

For a monochromatic plane spin wave that has a frequency ω and a wave number G_j and propagates perpendicularly to the layer interfaces, we can write the following expressions:

$$\begin{aligned} \mathbf{m}_j(\mathbf{r}, t) &= \mathbf{m}_j \exp\{i\omega t\}, \\ \mathbf{m}_j &\sim B_j^+ \exp\{+iG_j x\} + B_j^- \exp\{-iG_j x\}, \end{aligned} \tag{3}$$

where $B_j^\pm$ stands for the spin-wave amplitudes in the *j*th layer. In an approximation linear with respect to the magnetization deviations $\mathbf{m}_j$, from the Landau–Lifshitz equation (1) with due regard for expressions (2) and (3), we obtain the following dispersion relation for spin waves in a homogeneous material of the *j*th layer:

$$G_j = \sqrt{\frac{1}{\alpha_j}\left(\frac{\omega}{g_j M_j} - \frac{H}{M_j} - \beta_j\right)}. \tag{4}$$

The spin-wave spectra of the multilayer material can be determined using the Bloch theorem [10]. The solution of the Landau–Lifshitz equation (1) for the *j*th layer can be represented in the form of expression (3). In the case under consideration, the exchange boundary conditions (A10) must be satisfied at the layer interfaces [7, 11–13]:

$$\left.\frac{\mathbf{m}_1}{M_1}\right|_{X_n} = \left.\frac{\mathbf{m}_2}{M_2}\right|_{X_n}, \quad \left.\frac{A_1}{M_1}\frac{\partial \mathbf{m}_1}{\partial x}\right|_{X_n} = \left.\frac{A_2}{M_2}\frac{\partial \mathbf{m}_2}{\partial x}\right|_{X_n}, \tag{5}$$

where X_n is the interface coordinate and $A = \alpha M^2/2$. The physical meaning of the first condition is as follows: when the exchange interaction between the layers is dominant, the magnetizations on both sides of the interface are parallel to each other. The second condition ensures the continuity of the normal (to the interface) vector component of the energy flux density [9].

Moreover, the solution must satisfy the condition of periodicity. This means that the magnetizations $\mathbf{m}_j$ at boundaries of the period ($x = 0$ and $x = d = d_1 + d_2$) can differ by only the phase factor; that is,

$$\mathbf{m}(0) = \exp(iKd)\mathbf{m}(d), \tag{6}$$

where *K* is the quasi-wave number.

Upon substituting expression (3) into relations (5) and (6), we obtain the following system of linear equations for the amplitudes $B_j^\pm$ of the incident and reflected waves:

$$\frac{B_1^+ \exp\{iG_1d_1\} + B_1^- \exp\{-iG_1d_1\}}{B_2^+ \exp\{iG_2d_1\} + B_2^- \exp\{-iG_2d_1\}} = \frac{M_1}{M_2},$$

$$\frac{B_1^+ \exp\{iG_1d_1\} - B_1^- \exp\{-iG_1d_1\}}{B_2^+ \exp\{iG_2d_1\} - B_2^- \exp\{-iG_2d_1\}} = \frac{M_1A_2G_2}{M_2A_1G_1},$$

$$\frac{1}{M_1}[B_1^+ + B_1^-]\exp\{iKd\} = \frac{1}{M_2}[B_2^+ \exp\{iG_2d\} + B_2^- \exp\{-iG_2d\}],$$

$$\frac{A_1G_1}{M_1}[B_1^+ - B_1^-]\exp\{iKd\} = \frac{A_2G_2}{M_2}[B_2^+ \exp\{iG_2d\} - B_2^- \exp\{-iG_2d\}].$$

The criterion for consistency of these equations is that the determinant consisting of the coefficients of the system must be equal to zero. By simplifying the corresponding equality, we found that the spin-wave spectrum of the multilayer material with due regard for the modulation of all the structural parameters can be adequately described by an expression similar to the relation derived earlier in [6], that is,

$$\begin{aligned} \cos(Kd) &= \cos(G_1d_1)\cos(G_2d_2) \\ &- \frac{1}{2}\left(\frac{A_2G_2}{A_1G_1} + \frac{A_1G_1}{A_2G_2}\right)\sin(G_1d_1)\sin(G_2d_2). \end{aligned} \tag{7}$$

Dispersion relation (7) will be analyzed with the use of the diagram depicted in Fig. 1, where the black and

white regions in the G_1–G_2 plane represent the forbidden bands (corresponding to imaginary values of the quasi-wave number) and allowed bands (corresponding to real values of the quasi-wave number), respectively. Figure 1 also depicts the "spectral lines" for different variants of the modulation of the parameters of the multilayer material. These lines are specified by the parametric dependence of the wave number on the spin-wave frequency in layers [see dispersion relation (4)] and are described by the equation

$$\alpha_1 g_1 M_1 G_1^2 - \alpha_2 g_2 M_2 G_2^2 = \beta_2 g_2 M_2 - \beta_1 g_1 M_1 + (g_2 - g_1)H. \quad (8)$$

The diagram presented in Fig. 1 permits one to determine the edges of the forbidden and allowed bands (the points of intersection of the spectral lines with boundaries of the black and white regions in the figure, respectively) for a specified modulation of the material parameters.

3. RESULTS AND DISCUSSION

The characteristic spin-wave spectra (frequency dependences of the quasi-wave number) calculated from dispersion relation (7) are shown in Fig. 2.

The specific feature of multilayer materials with a modulated gyromagnetic ratio is that the application of an external dc magnetic field does not lead to a simple scaling of the anisotropy constant and a shift of the reference point of the spin-wave frequency (as is the case with a multilayer material at a constant gyromagnetic ratio in the layers [4, 6]). Specifically, the frequency enters into dispersion relation (4) in combination with the saturation magnetization and the gyromagnetic ratio, whereas the magnetic field appears in this relation in combination with the saturation magnetization alone. Therefore, the field dependence cannot be obtained from the frequency dependence by scaling, as was done earlier in [6] for a homogeneous distribution of the gyromagnetic ratio. In the absence of modulation of the gyromagnetic ratio, the dependence of the wave number on the frequency and field is reduced to the single self-similar variable ω–gH [6]. In the case when the gyromagnetic ratio varies from layer to layer, this self-similarity is absent. As a consequence, in an external dc magnetic field, the spectral lines pass through regions of the diagram that are inaccessible at a reasonable depth of modulation of the parameters for a material with a constant gyromagnetic ratio.

The aforementioned specific feature can be used in practice. It can be seen from Fig. 1a (line *1*) that, in the absence of modulation of the exchange interaction ($\alpha_1 = \alpha_2$) and the saturation magnetization ($M_1 = M_2$), the region along the bisector, which emerges from the origin of the coordinates ($G_1 = G_2$) and corresponds to the homogeneous material, is occupied by the allowed bands. It is in the vicinity of this bisector that the spectral lines are arranged at a constant gyromagnetic ratio in a zero external magnetic field even at a considerable depth of modulation of the other material parameters (for example, line *2* in Fig. 1a). In this case, the spectral lines in the G_1–G_2 plane appear to be independent of the external magnetic field. Indeed, it can be seen from Eq. (8) for the spectral lines that, at $g_1 = g_2$, the external magnetic field is not explicitly included in the expression and the dependence on the field manifests itself only through the above self-similarity.

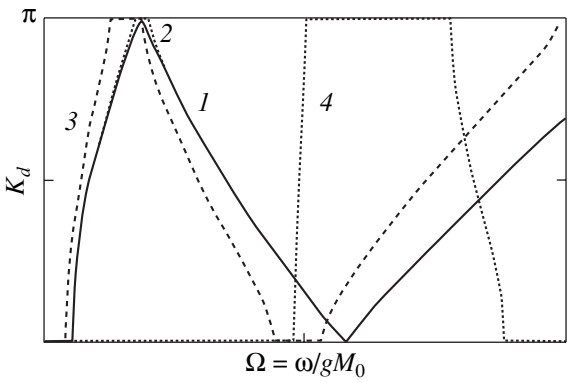

Fig. 2. Dependences of the quasi-wave number on the spin-wave frequency in reduced Brillouin zones. Material parameters are the same as in Fig. 1a.

The size of the forbidden bands substantially increases as the coordinate axes are approached, which corresponds to a system with significantly differing parameters of the material. It is in these regions that the spectral lines (Fig. 1a; lines *3*, *4*) are shifted by the magnetic field in the case of a modulated gyromagnetic ratio and, thus, are characterized by a strong dependence on the external magnetic field [see expression (8)].

For modulation of the exchange interaction and (or) the saturation magnetization (Fig. 1b), the specific feature under consideration is even more pronounced. Actually, there always exists a magnetic field $H = H_0$, where

$$H_0 = \frac{\beta_2 g_2 M_2 - \beta_1 g_1 M_1}{g_1 - g_2}, \quad (9)$$

for which the right-hand side of expression (8) is equal to zero. In this case, the spectral lines represent straight lines passing through the origin of the coordinates. Under the additional condition

$$\alpha_1 M_1^3/g_1 = \alpha_2 M_2^3/g_2, \quad (10)$$

the spectral lines are described by the equation $A_1 G_1 = A_2 G_2$ (Fig. 1b, line *3*). As can be seen from dispersion relation (7) and Fig. 1b, this situation corresponds to a continuous spectrum without forbidden bands.

Thus, conditions (9) and (10) determine the parameters of a "quasi-homogeneous" material, i.e., a multi-

layer magnet that has no band gaps and all of whose parameters, like wave numbers (4) of spin waves in layers, are distributed inhomogeneously. The deviation of the external dc magnetic field from H_0 disturbs the balance in the system and leads to the appearance of forbidden bands in the spectrum (Fig. 1b, line *4*). As a result, this system can be used as a functional element that is highly sensitive to magnetic field in a spin-wave device (switch, filter).

In this work, all calculations were performed in the absence of damping. The inclusion of damping should lead to the appearance of the imaginary part of the quasi-wave number for allowed bands and the real part of the quasi-wave number for forbidden bands [6]. As a consequence, the diagram depicted in Fig. 1 loses its meaning. Furthermore, in the case when the magnetic viscosity parameter is spatially modulated, the resultant damping of spin waves exhibits a nontrivial dependence on the depth of modulation of the other parameters [6]. However, in the regions of the forbidden bands obtained within the dissipationless model, the damping of spin waves remains sufficiently strong compared to the damping in the allowed bands of the spectrum [6]; therefore, the conclusions drawn in the present work are qualitatively valid.

APPENDIX

In order to derive boundary conditions (5), we consider a discrete one-dimensional model of a ferromagnet that is consistent with the Landau–Lifshitz equation (1). It is evident that we can restrict our consideration to the exchange approximation. In this case, the equations of motion have the form

$$\hbar\frac{\partial \mathbf{S}_n}{\partial t} = -\left[\mathbf{S}_n \times \frac{\partial W}{\partial \mathbf{S}_n}\right], \tag{A1}$$

where $W = -\frac{1}{2}\sum_{n,m} J_{nm}\mathbf{S}_n\mathbf{S}_m$, $\mathbf{S}_n$ is the spin of a site of the nth chain, and J_{nm} is the exchange integral of the nth and mth spins.

We will use the nearest neighbor approximation and, for definiteness, assume that the interface of materials passes through the sites 0 and 1; i.e., $J_{01} = J_{10} = \tilde{J}$ and $J_{nm} = J_0$ at $n, m \le 0$ and $J_{nm} = J_1$ at $n, m \ge 1$.

The boundary conditions are determined by the equations of system (A1) at $n = 0, 1$; that is,

$$\begin{aligned}\hbar\frac{\partial \mathbf{S}_0}{\partial t} &= [\mathbf{S}_0 \times (J_0\mathbf{S}_{-1} + \tilde{J}\mathbf{S}_1)],\\ \hbar\frac{\partial \mathbf{S}_1}{\partial t} &= [\mathbf{S}_1 \times (\tilde{J}\mathbf{S}_0 + J_1\mathbf{S}_2)].\end{aligned} \tag{A2}$$

Since the spin $\mathbf{S}_0$ obeys the identity $\mathbf{S}_0 \times \mathbf{S}_0 \equiv 0$, the first equation can be rewritten in the form

$$\hbar\frac{\partial \mathbf{S}_0}{\partial t} = [\mathbf{S}_0 \times (J_0(\mathbf{S}_{-1} - \mathbf{S}_0) + \tilde{J}\mathbf{S}_1)]. \tag{A3}$$

With the aim of changing over to the continuum approximation, as is customary, we introduce the function $\mathbf{S}(x)$: $\mathbf{S}(x_n) = \mathbf{S}_n$, where $x_n = an$ and a is the lattice constant. In our case, $\mathbf{S}(x)$ is a continuous function that is continuously differentiable in the ranges $x < x_0$ and $x > x_1$. As a consequence, we have

$$(\mathbf{S}_0 - \mathbf{S}_{-1}) = \frac{\partial \mathbf{S}(x_0)}{\partial x}a + O(a^2). \tag{A4}$$

By considering the linear oscillations and ignoring terms of the order of $\hbar\omega/J$, from expressions (A3) and (A4) to a first approximation nonvanishing in a, we find

$$\left[\mathbf{S}_0 \times \left(J_0 a\frac{\partial \mathbf{S}(x_0)}{\partial x} - \tilde{J}\mathbf{S}_1\right)\right] = 0. \tag{A5}$$

Similarly, from the second equation in system (A2), we obtain the expression

$$\left[\mathbf{S}_1 \times \left(J_1 a\frac{\partial \mathbf{S}(x_1)}{\partial x} + \tilde{J}\mathbf{S}_0\right)\right] = 0. \tag{A6}$$

Subtraction of expression (A6) from formula (A5) gives

$$J_0\mathbf{S}_0 \times \frac{\partial \mathbf{S}_0}{\partial x} = J_1\mathbf{S}_1 \times \frac{\partial \mathbf{S}_1}{\partial x}. \tag{A7}$$

In the long-wavelength limit $ka \ll 1$ (where k is the wave vector), from formulas (A5) and (A6), we obtain the following expression accurate to within terms of the order of $(J_{0.1}/\tilde{J})\mathbf{ka}$:

$$\mathbf{S}_0 \times \mathbf{S}_1 = 0. \tag{A8}$$

Hence, it follows from the condition $\mathbf{S}^2 = \text{const}$ that the vectors $\partial\mathbf{S}/\partial x$ and $\mathbf{S}$ are orthogonal to each other. Taking into account the collinearity of the vectors $\mathbf{S}_0$ and $\mathbf{S}_1$ [which follows from equality (A8)], relation (A7) can be rewritten in the form

$$J_0\mathbf{S}_0\frac{\partial \mathbf{S}_0}{\partial x} = J_1\mathbf{S}_1\frac{\partial \mathbf{S}_1}{\partial x}. \tag{A9}$$

In the case when $\mathbf{S}_{0,1} = \text{const}$ and $\mathbf{S}_0 \parallel \mathbf{S}_1 \parallel \mathbf{n}$ (where $\mathbf{n}$ is the unit vector aligned parallel to the magnetization direction in the ground state) at equilibrium, conditions (A8) and (A9) in terms of the amplitudes of small deviations $\mathbf{s}_0$ and $\mathbf{s}_1$ ($\mathbf{S}_m = S_m\mathbf{n} + \mathbf{s}_m$, $m = 0, 1$) from the equilibrium position take the form

$$\frac{\mathbf{s}_0}{S_0} = \frac{\mathbf{s}_1}{S_1}, \quad J_0S_0\frac{\partial \mathbf{s}_0}{\partial x} = J_1S_1\frac{\partial \mathbf{s}_1}{\partial x}. \tag{A10}$$

ACKNOWLEDGMENTS

We would like to thank Yu.I. Gorobets for helpful remarks.

REFERENCES

1. V. A. Ignatchenko, Yu. I. Man'kov, and A. V. Pozdnyakov, Zh. Éksp. Teor. Fiz. **116** (4), 1335 (1999) [JETP **89**, 717 (1999)].
2. V. A. Ignatchenko, Yu. I. Mankov, and A. A. Maradudin, J. Phys.: Condens. Matter **11**, 2773 (1999).
3. Yu. V. Gulyaev and S. A. Nikitov, Dokl. Akad. Nauk **380** (4), 469 (2001) [Dokl. Phys. **46**, 687 (2001)].
4. Yu. N. Gorobets, A. E. Zyubanov, A. N. Kuchko, and K. D. Shedzhuri, Fiz. Tverd. Tela (St. Petersburg) **34** (5), 1486 (1992) [Sov. Phys. Solid State **34**, 790 (1992)].
5. V. A. Ignatchenko, Yu. I. Mankov, and A. A. Maradudin, Phys. Rev. B **62** (3), 2181 (2000).
6. V. V. Kruglyak and A. N. Kuchko, Fiz. Met. Metallogr. **92** (3), 3 (2001).
7. A. M. Zyuzin, A. G. Bazhanov, S. N. Sabaev, and S. S. Kidyaev, Fiz. Tverd. Tela (St. Petersburg) **42** (7), 1279 (2000) [Phys. Solid State **42**, 1317 (2000)].
8. S. A. Nikitov, Ph. Tailhadesa, and C. S. Tsai, J. Magn. Magn. Mater. **236**, 320 (2001).
9. A. I. Akhiezer, V. G. Bar'yakhtar, and S. V. Peletminskiĭ, *Spin Waves* (Nauka, Moscow, 1967; North-Holland, Amsterdam, 1968).
10. F. G. Bass, A. A. Bulgakov, and A. P. Tetervov, *High-Frequency Properties of Semiconductors with Superlattices* (Nauka, Moscow, 1989).
11. A. M. Zyuzin, S. N. Sabaev, V. V. Radaĭkin, and A. V. Kulyapin, Fiz. Tverd. Tela (St. Petersburg) **44** (5), 893 (2002) [Phys. Solid State **44**, 932 (2002)].
12. J. F. Cochran and B. Heinrich, Phys. Rev. B **45** (22), 13096 (1992).
13. D. L. Mills, Phys. Rev. B **45** (22), 13100 (1992).

Translated by O. Borovik-Romanova

Physics of the Solid State, Vol. 46, No. 5, 2004, pp. 872–876. Translated from Fizika Tverdogo Tela, Vol. 46, No. 5, 2004, pp. 846–850.

MAGNETISM AND FERROELECTRICITY

Effect of the Interaction between the Magnetic and Phonon Subsystems on the Magnetic Properties of a Ferromagnet: Model Calculations

V. Yu. Bodryakov and A. A. Povzner

Ural State Technical University, ul. Mira 19, Yekaterinburg, 620002 Russia

e-mail: povz@kf.ustu.ru

Received July 29, 2003

Abstract—Thermodynamical analysis and model calculations for an isotropic ferromagnet show that inclusion of the interaction between the magnetic and phonon subsystems (in particular, through a magnetization-dependent Debye temperature) causes renormalization of the equation of the magnetic state and a temperature dependence of the thermodynamic coefficients of the Landau expansion, which are usually assumed to be constant. One of the consequences of this dependence is, for example, an experimentally observed difference between the "true" and paramagnetic Curie temperatures of a ferromagnet. © *2004 MAIK "Nauka/Interperiodica".*

Previously, in a study of ferromagnetic gadolinium, we showed [1] that, around the Curie point, the characteristic Debye temperature of a ferromagnet $\theta(M, T)$ can be approximated by a sum of the "nonmagnetic" contribution θ_{para} and a magnetic part θ_m, which, in turn, can be represented by a double expansion in even powers of magnetization M and distance to the Curie point $t = T - T_c$:

$$\theta = \theta_{para} + \theta_{00} + \frac{1}{2}\theta_{10}M^2 + \frac{1}{2}\theta_{11}M^2 t + \frac{1}{4}\theta_{20}M^4 + \ldots, \quad (1)$$

where θ_{para} is the paramagnetic part of the Debye temperature, $\theta_{ij}(T)$ are thermodynamic coefficients of the series, and $M = M(T, H)$ is the molar magnetization in a magnetic field H (which is assumed to be normalized). The term θ_{00} can be interpreted as a jump in Debye temperature at the Curie point [2]. However, we have not made a detailed thermodynamic analysis of the effect of representing θ in the form of expansion (1) on the resulting magnetic properties of a ferromagnet. We perform such an analysis in the present paper and supplement it with model calculations performed using specially designed software.

Qualitative justification of expansion (1) is based on the dependence of the Debye temperature on molar volume V and bulk modulus K (see, i.e., [3–6]) and on the dependences of these quantities on M^2 and t:

$$\theta = \frac{\hbar(6\pi^2 N_A)^{1/3}}{k_B}\sqrt{\frac{3}{\mu}}\Xi^{1/2}K^{1/2}V^{1/6}. \quad (2)$$

Here, $\hbar$ is Planck's constant, N_A is Avogadro's number, k_B is Boltzmann's constant, μ is the molar mass, and Ξ is a function that depends on the Poisson ratio σ of a material (this function is supposed to be independent of temperature and magnetization).

Expansion (1) can also include higher order terms; however, as shown below, even the first four terms are sufficient to describe a number of features of the magnetization and magnetic susceptibility of a ferromagnet beyond the standard Landau theory of second-order phase transitions. Furthermore, neither the physical limits and validity of the Landau theory itself nor the precision of the experiments warrant these additional terms.

Thus, in the full thermodynamic potential consisting of a temperature- and magnetization-independent part Φ_0, the phonon (lattice) contribution Φ_p, the electron contribution Φ_e, and the exchange term Φ_m

$$\Phi = \Phi_0 + \Phi_p + \Phi_e + \Phi_m, \quad (3)$$

not only the exchange term

$$\Phi_m = \frac{1}{2}\alpha M^2 + \frac{1}{4}\beta M^4 - HM, \quad (4)$$

depends on magnetization but also the phonon contribution [by means of varying the Debye temperature (1)]

$$\Phi_p = 3R\left[\frac{3}{8}\theta + f(z)\right]. \quad (5)$$

Symbols α and β in Eq. (4) stand for the temperature-dependent coefficients of the Landau theory and it is presumed that $\alpha = a(T - T_C)$, with $a = \text{const} > 0$ and $\beta = \text{const} > 0$. For the derivatives of the introduced function $f(z) = \ln(1 - e^{-z}) - \frac{1}{3}D(z)$ with respect to variable $z = \theta/T$, we have relations [4] $f'(z) = D(z)/z$ and $f''(z) = -C_{VR}(z)/z^2$, where $D(z)$ is the tabulated Debye function,

$C_{VR}(z)$ is the tabulated Debye specific heat normalized to unity, and R is the gas constant.

The equation of the magnetic state for a ferromagnet is determined by minimizing the thermodynamic potential with respect to the order parameter (magnetization):

$$\left(\frac{\partial\Phi}{\partial M}\right)_{TPH} = \left(\frac{\partial\Phi_p}{\partial M}\right)_{TPH} + \left(\frac{\partial\Phi_m}{\partial M}\right)_{TPH} = 0. \quad (6)$$

This equation contains not only the exchange part, as in the traditional Landau theory approach, but also the phonon contribution, which can be read as a consequence of interaction between the magnetic and phonon subsystems of a ferromagnet:

$$\frac{H}{M} = 3R\theta_{10}\left[\frac{3}{8} + \frac{D(z)}{z}\right] + \left\{a + 3R\theta_{11}\left[\frac{3}{8} + \frac{D(z)}{z}\right]\right\}(T - T_C) + \left\{\beta + 3R\theta_{20}\left[\frac{3}{8} + \frac{D(z)}{z}\right]\right\}M^2. \quad (7)$$

Inclusion of the magnetization–phonon interaction (MPI) causes renormalization of the equation of the magnetic state of a ferromagnet, which still can be presented in the traditional form used in the Landau theory but with renormalized thermodynamic coefficients and Curie temperature:

$$\frac{H}{M} = a^*(T - T_C^*) + \beta^* M^2, \quad (8)$$

where

$$a^* = a + 3R\theta_{11}\left[\frac{3}{8} + \frac{D(z)}{z}\right], \quad (9)$$

$$T_C^* = T_C + \frac{3R\theta_{10}\left[\frac{3}{8} + \frac{D(z)}{z}\right]}{a + 3R\theta_{11}\left[\frac{3}{8} + \frac{D(z)}{z}\right]}, \quad (10)$$

$$\beta^* = \beta + 3R\theta_{20}\left[\frac{3}{8} + \frac{D(z)}{z}\right]. \quad (11)$$

Instead of the traditional expression for the spontaneous (at $H = 0$) magnetization of a ferromagnet $M_s^2 = -\frac{a(T - T_C)}{\beta}$, taking into account Eqs. (9)–(11), we obtain $M_s^2 = -\frac{a^*(T - T_C^*)}{\beta^*}$, where thermodynamic coefficients a^* and β^* explicitly depend on temperature in a rather complicated manner. Apparently, the MPI-induced shift in the Curie temperature is relatively small in the majority of cases. The initial (exchange) Curie temperature T_C could be interpreted as a thermodynamic parameter characterizing pure exchange interaction of a ferromagnet. The "true" (technical) Curie temperature T_C^* is a characteristic of the ferromagnet including the MPI.

It should be noted that, unlike the Curie temperature T_C^*, the renormalized thermodynamic coefficients a^* and β^* do not contain θ_{10}. In other words, the effect of the MPI on the magnetic properties of a ferromagnet manifests itself in higher order terms than in the simple expression $\theta \sim M^2$, as was supposed, for example, in [7, 8]. Therefore, it is worthwhile considering the MPI only for ferromagnets where this interaction (called also magnetoelastic) is strong enough. An example is Invar alloys. For ferromagnets where the MPI is not strong and it is sufficient to allow for terms $\theta \sim M^2$ in the Debye temperature, the classical Landau theory works sufficiently well.

We will not dwell on a detailed (complicated) thermodynamic analysis of the expressions written above. We only note that the Landau theory with renormalized thermodynamic coefficients provides a good description of the magnetic properties of low-temperature ferromagnets ($T, T_C \ll \theta$) even if the MPI is not weak. In high-temperature ferromagnets ($T, T_C \geq \theta$), the MPI can cause significant changes in the results of the traditional Landau theory.

We also note that, when the MPI is sufficiently strong and the condition $T_C^* \leq 0$ is met, the material does not become ferromagnetic at any finite temperature, though the exchange interaction can cause ferromagnetic ordering in absence of the MPI. A necessary (but not sufficient) condition for the ferromagnetic state to occur is $\theta_{10} \leq 0$. Another case where a material remains paramagnetic for all finite temperatures corresponds to $\beta^* \leq 0$, which occurs (for $\beta > 0$) if $\theta_{20} \leq 0$. It is conceivable that one of these possibilities is realized for paramagnetic scandium [9, 10]. Unfortunately, we cannot consider this issue in more detail because of the scarcity of experimental data for Sc.

In general, because of the slower variation of $D(z)/z$ with temperature in comparison with a linear variation with $t = T - T_C$ in the vicinity of the Curie point, the temperature dependence of the spontaneous magnetization of a ferromagnet is qualitatively similar to that predicted from the traditional Landau theory. The effects due to the MPI begin to manifest themselves only at a sufficient distance from the Curie point.

The most convenient characteristic of a ferromagnet for describing its behavior in the temperature region far from the magnetic transition point is the initial magnetic susceptibility $\chi = \left(\frac{\partial M}{\partial H}\right)_{TP}$ (at $H \longrightarrow 0$) or its

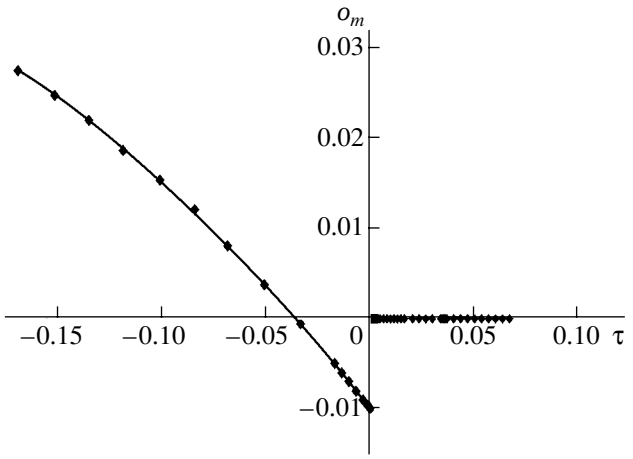

Fig. 1. Temperature dependence of the magnetic part of the reduced Debye temperature of a ferromagnet with magnetization–phonon interaction calculated for case I.

inverse χ^{-1}. It follows from the equation of the magnetic state (8) that $\chi^{-1} = a^*(T - T_C^*)$ at $T > T_C^*$ and $\chi^{-1} = -2a^*(T - T_C^*)$ at $T < T_C^*$; i.e., Ginzburg's rule of two [11] also holds for a ferromagnet with MPI. The linear temperature dependence of $\chi^{-1}(T)$ (following from the Landau theory) is extensively employed by experimentalists to estimate the Curie temperature [12]. Such an estimation is fairly rough and not infrequently gives a value of the paramagnetic Curie point $T_{C,p}$ (crossing point of the temperature axis and the line extrapolating $\chi^{-1}(T)$ from the high-temperature region) that is several dozen kelvins higher than the actual Curie temperature T_C^*. This disagreement has not yet been explained convincingly.

With inclusion of the MPI, the temperature dependence of $\chi^{-1}(T)$ becomes nonlinear at elevated temperatures ($T \gg \theta$):

$$\chi^{-1}(T) = \left\{a + 3R\theta_{11}\frac{T}{\theta}\right\}(T - T_C). \qquad (12)$$

In particular, if $\theta_{11} > 0$, the $\chi^{-1}(T)$ dependence progressively deviates upwards from the linear dependence with increasing temperature; therefore, the straight line interpolating it at elevated temperatures crosses the T axis at a higher point than T_C^*. Furthermore, the crossing temperature $T_{C,p}$ depends both on the strength of the MPI (via θ_{11}) and on the temperature range used for the linear interpolation. The way to rectify the problem is clear: a quadratic instead of a linear interpolation of the $\chi^{-1}(T)$ dependence will bring $T_{C,p}$ and T_C^* into better agreement.

With the analytical expressions presented above, we performed numerical computations of the model using specially designed software. For generality, the results of the calculations are expressed in terms of reduced quantities (Figs. 1–4). The following values of the parameters were used (in relative units) in all calculations: $a = 1.0$, $\beta = 0.1$, $H = 0$, $T_C = 300$, and $\theta_{para} = 200$.

Calculations were performed for two different cases (I, II) corresponding to two possible kinds of behavior of the temperature dependence of $\theta_m(T)$, namely, an increase and a decrease in θ_m, respectively, following the characteristic jump at the Curie point T_C as the temperature is decreased in the ferromagnetic region. The values of the thermodynamic parameters used in calculations are listed in the table. The temper-

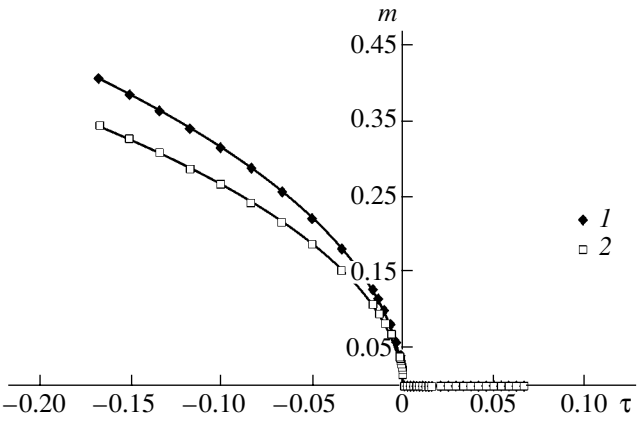

Fig. 2. Temperature dependence of the reduced magnetization of a ferromagnet calculated for case I (*1*) without and (*2*) with inclusion of the MPI.

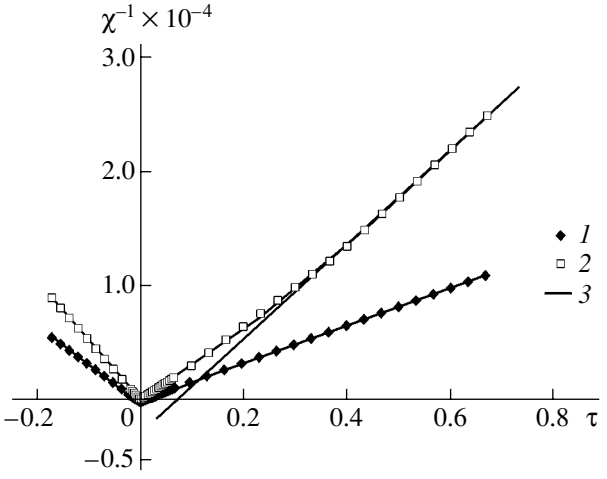

Fig. 3. Temperature dependence of the reduced magnetic susceptibility of a ferromagnet calculated for cases I and II (*1*) without and (*2*) with inclusion of the MPI. (3) A linear approximation in the high-temperature region.

ature dependence of the quantity $o_m(T) = \theta_m(T)/\theta_{para}$ is given by

$$o_m = o_{00} + \frac{1}{2}o_{10}m^2 + \frac{1}{2}o_{11}m^2\tau + \frac{1}{4}o_{20}m^4 + \ldots, \quad (13)$$

where the reduced thermodynamic coefficients, magnetization, and temperature are defined as $o_{ij} = \theta_{ij}/\theta_{para}$, $m = M(T, H)/M(0, 0)$, and $\tau = (T - T_C)/T_C$.

The temperature dependence of the magnetic contribution to the reduced Debye temperature $o_m(T)$ for case I ($o_{10}, \theta_{10} > 0$) is presented in Fig. 1. This kind of behavior of the Debye temperature is typical, for example, of gadolinium [1, 2]. The temperature dependences of the spontaneous magnetization calculated with and without regard for the MPI are shown in Fig. 2. It is seen that, though the $m(T, 0)$ dependence does not change qualitatively and is similar to that predicted from the Landau theory, the value of the magnetization itself is reduced significantly when the MPI is taken into account. At the same time, the difference between T_C and T_C^* is rather small (see table).

The temperature dependence of the inverse reduced initial susceptibility $\chi^{-1}(T) = \left(\frac{\partial m}{\partial H}\right)^{-1}_{TP}$ (at $H \longrightarrow 0$) of a ferromagnet calculated for case I with and without regard for the MPI is shown in Fig. 3. It can be seen that the MPI significantly increases the slope of the $\chi^{-1}(T)$ dependence both in the ferromagnetic and paramagnetic regions; furthermore, the $\chi^{-1}(T)$ dependence is not linear in the higher temperature region. The linear approximation of the $\chi^{-1}(T)$ at high temperatures does not cross the temperature axis either at T_C or at T_C^* but at a much higher paramagnetic Curie temperature $T_{C,p}$ (see table).

Figure 4 (as well as Fig. 1) presents the temperature dependence of the magnetic contribution to the reduced Debye temperature $o_m(T)$ calculated for case II (for parameters $o_{10}, \theta_{10} < 0$).

This kind of behavior of the Debye temperature is apparently typical of nickel and iron–nickel Invar alloys. The lack of experimental data on this subject prevents more definite conclusions. The $m(T, 0)$ dependences for this case and for the selected values of the parameters are qualitatively similar to those calculated in case I, and we do not present them. We only note a small decrease in the Curie temperature T_C^* relative to T_C as opposed to case I (see table).

Figure 3 also gives an idea about the temperature dependence of the inverse reduced initial susceptibility $\chi^{-1}(T)$ of a ferromagnet calculated for case II with and without regard for the MPI. This dependence, in accordance with the thermodynamic consideration performed above, is similar to the $\chi^{-1}(T)$ dependence in case I in spite of the drastic change in the temperature

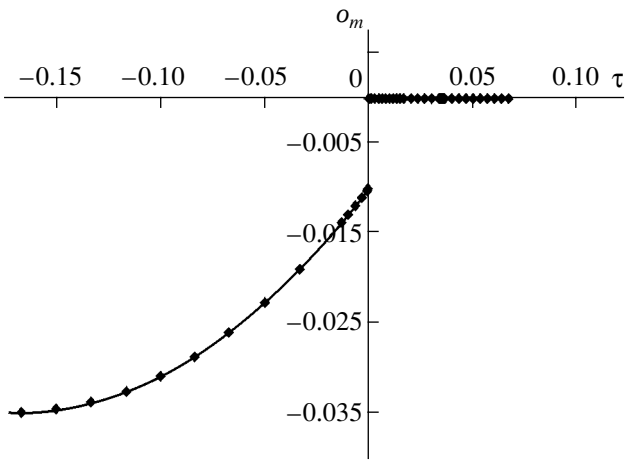

Fig. 4. Temperature dependence of the magnetic part of the reduced Debye temperature of a ferromagnet calculated for case II.

dependence of $o_m(T)$ in case II. The $\chi^{-1}(T)$ dependence in case II is not linear for higher temperatures in the paramagnetic region of a ferromagnet. The linear approximation of the $\chi^{-1}(T)$ at high temperatures (as in case I) does not cross the temperature axis either at T_C or at T_C^* but at a much higher paramagnetic Curie temperature $T_{C,p}$ (see table).

Thus, the following main results were obtained in the present work based on a thermodynamic analysis and model calculations.

(1) Using a phenomenological expression for the temperature dependence of the magnetic part of the Debye temperature, which is due to interaction between the magnetic and phonon subsystems of a ferromagnet, it was shown that the inclusion of the MPI leads to renormalization of the thermodynamic potential of the ferromagnet and the equation of the magnetic state.

(2) It was shown that inclusion of the MPI gives rise to a temperature dependence of the thermodynamic coefficients, which are considered constant in the traditional Landau theory.

Thermodynamic parameters (in arbitrary units) used in calculations

Parameter	Case I	Case II
θ_{00}	–2	–2
θ_{10}	0.04	–0.04
θ_{11}	0.02	0.02
θ_{20}	0.00396	0.00408
T_C^*	300.866	299.134
$T_{C,p}$	321.30	321.27

(3) The inclusion of the MPI causes either an increase or a decrease in the Curie temperature depending on the signs of the thermodynamic coefficients and the relations between them. However, the temperature dependence of the spontaneous magnetization of a ferromagnet may not change qualitatively and remain close to that predicted from the Landau theory. The magnitude of magnetization changes in this case.

(4) The most pronounced effect of the MPI is a modification of the temperature dependence of the inverse initial magnetic susceptibility, especially in the higher temperature region.

(5) It was shown that the MPI could be one of the reasons for the well-known discrepancy between the true and paramagnetic Curie temperatures of a ferromagnet.

REFERENCES

1. V. Yu. Bodryakov, A. A. Povzner, and S. A. Nikitin, Eur. Phys. J. B **4** (4), 441 (1998).
2. M. Rosen, Phys. Rev. **174** (2), 504 (1968).
3. V. Yu. Bodryakov, A. A. Povzner, and O. G. Zelyukova, Fiz. Met. Metalloved. **87** (4), 13 (1999).
4. V. Yu. Bodryakov and A. A. Povzner, Fiz. Met. Metalloved. **89** (5), 15 (2000).
5. V. Yu. Bodryakov and A. A. Povzner, *Self-Consistent Thermodynamic Model of Crystalline Lattice of Solids* (UGTU–UPI, Yekaterinburg, 2002), Part 1.
6. V. Yu. Bodryakov and A. A. Povzner, Zh. Tekh. Fiz. **73** (7), 136 (2003) [Tech. Phys. **48**, 931 (2003)].
7. V. M. Zverev and V. P. Silin, Zh. Éksp. Teor. Fiz. **93** (2), 709 (1987) [Sov. Phys. JETP **66**, 401 (1987)].
8. V. M. Zverev, Zh. Éksp. Teor. Fiz. **112** (5), 1863 (1997) [JETP **85**, 1019 (1997)].
9. É. V. Goloshina, V. P. Dyakina, and V. E. Startsev, Fiz. Met. Metalloved. **83** (3), 5 (1997).
10. V. Yu. Bodryakov, V. V. Petrushkin, and A. A. Povzner, Fiz. Met. Metalloved. **89** (4), 5 (2000).
11. L. D. Landau and E. M. Lifshitz, *Course of Theoretical Physics*, Vol. 5: *Statistical Physics*, 3rd ed. (Nauka, Moscow, 1976; Pergamon, Oxford, 1980), Part 1.
12. K. P. Belov, *Magnetic Transitions* (Fizmatgiz, Moscow, 1959; Consultants Bureau, New York, 1961).

Translated by G. Tsydynzhapov

Physics of the Solid State, Vol. 46, No. 5, 2004, pp. 877–880. Translated from Fizika Tverdogo Tela, Vol. 46, No. 5, 2004, pp. 851–853.

MAGNETISM AND FERROELECTRICITY

Finite Lifetime of Spiral Domains in the Anger State of Multidomain Magnetic Films

G. S. Kandaurova, L. N. Kartagulov, and V. N. Mal'tsev

Ural State University, pr. Lenina 51, Yekaterinburg, 620083 Russia

e-mail: vladimir.maltsev@usu.ru

Received August 26, 2003

Abstract—The finite lifetime T_g of a dynamic spiral domain in the anger state in a multidomain film with perpendicular magnetic anisotropy is estimated theoretically in the framework of a dissipative model. The finite lifetime of spiral domains is investigated as a function of the frequency of an external ac magnetic field that varies according to a harmonic law. © *2004 MAIK "Nauka/Interperiodica".*

1. INTRODUCTION

In [1], we stated that, in an external ac magnetic field, the domain structure of garnet ferrite films with perpendicular magnetic anisotropy transforms into an excited state, which is referred to as the anger state [1]. In this state, there can exist stable ordered dynamic domain structures of different types [2]. It has been established that the formation of dynamic spiral domains in a garnet ferrite film placed in an external ac magnetic field depends on the field amplitude and frequency. Spiral domain structures, like all ordered dynamic domain structures, are characterized by the amplitude–frequency region of their existence, i.e., the ranges of magnetic-field amplitudes and frequencies at which these structures are stable. However, each spiral domain exists over a finite period of time and then collapses and disappears [1, 2]. The period of stability of a spiral domain is determined by the lifetime T_g, which, in turn, depends on the parameters of the ac magnetic field [1]. Despite intensive investigations into the properties of dynamic spiral domains, a number of questions essential to the understanding of the specific features of spiral domains remain unclear. In particular, it remains to be seen why spiral domains can exist only over a finite period of time, i.e., have a finite lifetime T_g, and why the amplitude–frequency region of their existence is limited. At present, theoretical approaches to the description of ordered dynamic domain structures are being developed. In our recent work [3], the upper limit of the field amplitude range of existence of dynamic spiral domains was investigated as a function of the magnetic-field frequency in the framework of the so-called dissipative model. Moreover, it was shown that the stability of spiral domains decreases with an increase in the magnetic-field amplitude and increases with an increase in the field frequency. However, according to the dissipative model, the lifetime of an individual spiral domain in the region of dynamic stability is infinite, which is inconsistent with experimental data. In this respect, the existing theory needs to be further refined and, in particular, has to be complemented in such a way as to take into account the finite lifetime of an individual domain.

2. MODEL OF THE SPIRAL DOMAIN

The dynamics of a spiral domain will be described in the framework of the dissipative model proposed in our previous work [3]. Within this model, an isolated spiral domain is treated as a stripe domain twisted into an Archimedean spiral. The thickness of domain walls is taken to be equal to zero, and the domain-wall energy is expressed in terms of the surface energy density σ of the domain walls. The pitch of the spiral p and the width of the stripe domain forming the spiral are assumed to be constant. The size of the spiral domain is characterized by an outer radius R, which can change when moving the end of the outer turn of the spiral domain, i.e., upon twisting and untwisting of the spiral. The energy of an external ac harmonic magnetic field dissipates in the film due to frictional forces acting on the end of the outer turn of the spiral domain during motion. The time dependence of the outer radius of the spiral domain for different parameters of an external ac magnetic field can be determined from numerical solutions of the dynamic equation [3]

$$k^*\frac{dR}{dt} = -\frac{d}{dR}(E_m + E_w + E_H). \quad (1)$$

Here, $k^* = k[1 + (R/p)^2]$ is the frictional coefficient of the end of the outer turn, E_m is the magnetostatic energy, E_w is the domain-wall energy, and E_H is the Zeeman energy. In the general form, dynamic equation (1) can be approximated by the relationship

$$k^*\frac{dR(t)}{dt} = -(A\sin t + B)R(t) + C,$$

1063-7834/04/4605-0877$26.00 © 2004 MAIK "Nauka/Interperiodica"

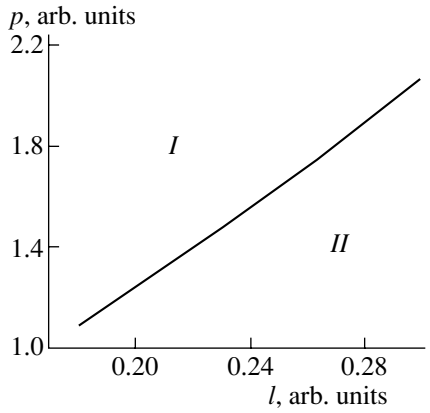

Fig. 1. Regions of dynamic stability of spiral domains.

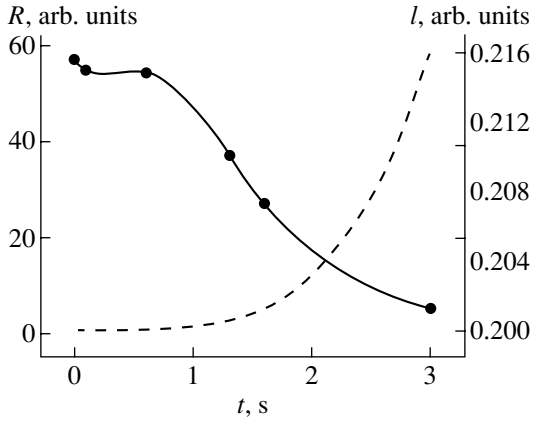

Fig. 2. Time dependences of the reduced (to the film thickness) outer radius R of a spiral domain (solid line) and the reduced characteristic length l of the film (dashed line).

where A is a coefficient dependent on the width of the stripe domain in the spiral-domain turns and B and C are coefficients dependent on the amplitude and frequency of the external ac magnetic field, respectively. Moreover, the coefficient C is proportional to the surface energy density σ. Hence, it follows that the dynamic behavior of the spiral domain depends on these coefficients.

Theoretical investigations into the static properties of spiral domains have revealed that, in the absence of an external ac magnetic field, there exist two regions of dynamic stability of spiral domains (Fig. 1). These regions are determined by the pitch p of the spiral and the reduced characteristic length of the film $l = \sigma/2\pi M^2 h$, where h is the film thickness and M is the magnetization. In the absence of an external magnetic field, the upper region (*I*) corresponds to the case of spiral domains with an infinite radius, whereas spiral domains in the lower region (*II*) have a finite radius. The results of the calculations performed in [3] demonstrated that, in an external ac magnetic field, the outer radius R of a spiral domain oscillates about an equilibrium value if the amplitude and frequency of the magnetic field correspond to the region of existence of the spiral domain. It is worth noting that the spiral domains in region *II* are less stable than the domains in region *I*. This can be explained by the fact that the former domains have a finite equilibrium radius R_0 and, at a large amplitude of radius oscillations, which depends on the amplitude and frequency of the magnetic field, the spiral domain can collapse.

The finite lifetime can be determined using several approaches. For example, the parameters p and l (or, what amounts to the same thing, the surface energy density σ of domain walls) can vary with time; as a result, the spiral domain goes from region *I* to region *II* and, hence, becomes less stable (Fig. 1). This can be achieved under the following conditions: (i) with parameter p kept constant, the surface energy density σ (parameter l in Fig. 1) increases with time, for example, due to the formation of different-type defects in the domain wall; (ii) with parameter l kept constant, the pitch p of the spiral decreases with time; and (iii) with a combination of the first two conditions. Moreover, it can be assumed that the stability loss of a spiral domain is associated with the enhancement of the effect exerted by the domain environment after the spiral domain reaches a specific size.

In this work, we assumed that the surface energy density of domain walls (and, correspondingly, the characteristic length of the film) increases with time at a constant pitch of the spiral. Consequently, the length l involved in dynamic equation (1) is a function of time. Time dependences of the outer radius of the spiral domain $R(t)$ were determined from numerical solutions of dynamic equation (1). In our calculations, we took into account both monotonic functions $l(t)$ and functions that vary with time in a random jumpwise manner. For the latter functions, the jumps were limited in magnitude and occurred at random intervals.

3. COMPUTATIONAL RESULTS AND DISCUSSION

According to our calculations, the outer radius R of the spiral domain decreases with a monotonic increase in the reduced characteristic length l of the film. As an example, Fig. 2 shows the time dependence of the spiral-domain radius averaged over the period of the external ac magnetic field in the case when the reduced characteristic length l obeys the following relationship:

$$l = l_0(1 + at^4), \tag{2}$$

where $l_0 = 0.2$ and $a = 0.001$. It can be seen from this figure that, at an instant of time T_g, the outer radius of the spiral domain becomes equal to zero. Therefore, the finite lifetime of the spiral domain can be obtained by introducing the time dependence of the surface energy

density into the model. The finiteness of the lifetime of the spiral domain is associated with the dependence of the equilibrium radius R_0 on the characteristic length l [3]. Actually, an increase in the characteristic length l leads to a decrease in the equilibrium radius R_0. When the equilibrium radius R_0 coincides with the amplitude of oscillations of the outer radius R, the spiral domain collapses. For the same reason, a decrease in the coefficient a with the parameters of the external ac magnetic field kept constant results in an increase in the lifetime of the spiral domain.

As follows from the calculation performed for the characteristic length $l(t)$ defined by expression (2), the lifetime T_g depends on the frequency of the external ac magnetic field. The frequency dependence of the lifetime T_g for constant values of the field amplitude and the coefficient a is depicted in Fig. 3a. In the framework of the model under consideration, the monotonic increase in the lifetime T_g with an increase in the frequency of the external ac magnetic field can be explained as follows. The spiral domain collapses when the amplitude of oscillations of the spiral-domain radius R becomes equal to the equilibrium radius R_0. Moreover, an increase in the frequency of the external ac magnetic field leads to a decrease in the amplitude of oscillations of the outer radius R of the spiral domain [3]. Consequently, the equilibrium radius R_0, at which the dynamic spiral domain collapses, also decreases with an increase in the magnetic-field frequency. However, the smaller the equilibrium radius R_0, the longer the time required to attain this radius for a constant coefficient a in expression (2).

Furthermore, according to experimental data [1], the frequency dependence of the lifetime T_g of a spiral domain can exhibit a nonmonotonic behavior. The disagreement between the experimental and theoretical frequency dependences of the lifetime of spiral domains indicates that the finite lifetime of the spiral domain is determined not only by the change in the surface energy density of domain walls with time. Therefore, in addition to the time dependence of the surface energy density, it is necessary to take into account the frequency dependences of other parameters of the spiral domain. As was shown in our previous work [3], an increase in the frequency of the external ac magnetic field is attended by a decrease in the pitch of the spiral. This implies that the equilibrium radius R_0 of the spiral domain decreases. Thus, the equilibrium radius R_0 decreases with an increase in the characteristic length l and a decrease in the pitch p of the spiral. Figure 3b illustrates the variation in the lifetime of spiral domains with an increase in the frequency of the external ac magnetic field in the case when the model accounts for the frequency dependence of the pitch p of the spiral. It can be seen from Fig. 3b that an increase in the field frequency leads to a decrease in the lifetime of the spiral domain.

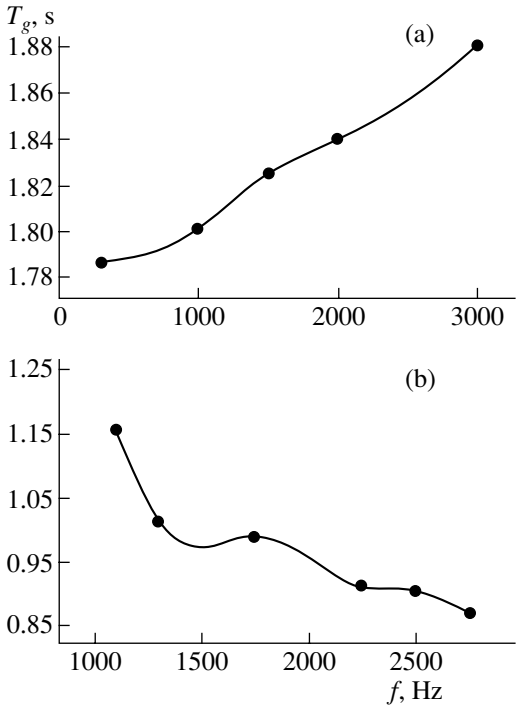

Fig. 3. Dependences of the lifetime T_g of the spiral domain on the frequency of the ac magnetic field (a) without and (b) with the inclusion of the frequency dependence of the pitch p of the spiral.

It should also be noted that the above calculations did not reveal any fundamental differences between the case of a monotonic change in the surface energy density of domain walls and the case where the surface energy density varies with time in a random manner. It was found that an increase in the characteristic length l leads to a decrease in the radius of the spiral domain and, vice versa, a decrease in the characteristic length l results in an increase in the radius of the spiral domain. This means that the spiral domains vary in size according to the surface energy density of the domain walls.

The experimental results obtained in [4] demonstrated that the nucleation and growth of a dynamic spiral domain is accompanied by an increase in the number of spiral turns. Then (over the period of time T_g), the number of spiral turns varies in a random manner but remains equal, on average, to N. Thereafter, the number of spiral turns drastically decreases and the spiral domain collapses. Since the true time dependences of the surface energy density σ and characteristic length l are unknown, we can attempt to fit them in such a way as to obtain not only the lifetime but also a dependence $N(t)$ similar to the dependence $N(t)$ observed in the experiment. The change in the number of turns for an individual spiral domain in a disordered dynamic domain structure over the period of its lifetime was obtained in [4] for a garnet ferrite film 9.5 μm thick at $l_0 = 2.17$ μm with an amplitude of the ac magnetic field

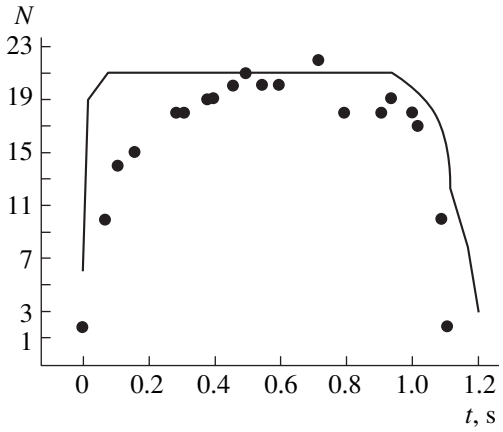

Fig. 4. Time dependence of the number N of turns in the spiral domain for the specified dependence $l(t)$. Points are the experimental data taken from [4].

$H_0 = 0.33$ (in units of $4\pi M_s$) and a frequency $\nu = 2.56$ kHz. In [4], the lifetime of the spiral domain was equal to 1.2 s. A similar time dependence of the number of turns in a spiral domain can also be obtained with the use of the function $l(t) = 0.22(1 + 0.001t^{30})$. Figure 4 presents the experimental dependence of the number of spiral turns on time (points) and the results of calculations (solid line) performed with the above function $l(t)$ for the parameters of the film and ac magnetic field used in the experiment. Moreover, in these calculations, we assumed that the film is subjected to a dc magnetic bias field $H_b = 0.45$ (in relative units).

It can be seen from Fig. 4 that the theoretical results are in satisfactory agreement with the experimental data. However, this agreement was achieved only after a dc magnetic field (which was absent in the experiment) was introduced into our calculations. The point is that, in the theoretical model used in this work, we deal with an isolated spiral domain, whereas a real spiral domain is affected by a disordered domain environment. Possibly, this effect of the domain environment on real spiral domains is simulated to some extent by the dc magnetic field introduced into the calculations.

4. CONCLUSIONS

Thus, in this work, the finite lifetime of a dynamic domain structure of the spiral-domain type was determined theoretically for the first time. The calculations demonstrated that the finite lifetime of a spiral domain can be associated with the increase in the surface energy density with time. Moreover, we cannot rule out that the finite lifetime of spiral domains depends to a considerably greater extent on factors different than those discussed above. In order to elucidate conclusively all the factors responsible for the finite lifetime of spiral domains, it is necessary to carry out further experimental and theoretical investigations.

ACKNOWLEDGMENTS

This work was supported in part by the Ural Russian Foundation for Basic Research (RFFI-Ural) in the framework of the scientific program "Basic Research in the Field of Natural Sciences," the scientific program "Russian Universities" of the Ministry of Education of the Russian Federation, and the US Civilian Research and Development Foundation for the Independent States of the Former Soviet Union (CRDF) (project no. REC-005).

REFERENCES

1. G. S. Kandaurova and A. É. Sviderskiĭ, Zh. Éksp. Teor. Fiz. **97** (4), 1218 (1990) [Sov. Phys. JETP **70**, 684 (1990)].
2. G. S. Kandaurova, Usp. Fiz. Nauk **172** (10), 1165 (2002) [Phys. Usp. **45**, 1051 (2002)].
3. V. N. Mal'tsev, G. S. Kandaurova, and L. N. Kartagulov, Fiz. Tverd. Tela (St. Petersburg) **45** (4), 658 (2003) [Phys. Solid State **45**, 691 (2003)].
4. G. S. Kandaurova, A. A. Rusinov, and V. Kh. Osadchenko, Dokl. Akad. Nauk (2003) (in press).

Translated by O. Borovik-Romanova

Physics of the Solid State, Vol. 46, No. 5, 2004, pp. 881–884. Translated from Fizika Tverdogo Tela, Vol. 46, No. 5, 2004, pp. 854–857.

MAGNETISM AND FERROELECTRICITY

Magnetic and Magnetoelastic Properties of the TbMnSi and $Tb_{0.5}La_{0.5}MnSi$ Compounds

T. I. Ivanova, S. A. Nikitin, M. V. Maslennikova, and Z. S. Umkhaeva

Lomonosov Moscow State University, Vorob'evy gory, Moscow, 119992 Russia

e-mail: ivanova@rem.phys.msu.su

Received September 5, 2003

Abstract—X-ray diffraction studies showed substitution of nonmagnetic lanthanum for terbium in the TbMnSi polycrystalline compound to initiate a structural transition from a TiNiSi-type orthorhombic structure (for TbMnSi) to a CeFeSi-type tetragonal phase (for $Tb_{0.5}La_{0.5}MnSi$). Magnetic measurements (of the magnetization, magnetostriction, thermal expansion) performed on $Tb_{0.5}La_{0.5}MnSi$ revealed a change in the character of magnetic ordering, the appearance of a ferromagnetic component in the Mn magnetic moment, a strong increase in magnetization as compared to TbMnSi, and the appearance of a spontaneous magnetic moment. Insertion of the lanthanum ion onto the rare-earth sublattice of TbMnSi brings about a change in the unit cell size and, hence, in the Mn–Mn, Mn–Si, and *R*–Mn interatomic distances, which causes, in turn, a change in the character of exchange interactions in $Tb_{0.5}La_{0.5}MnSi$ and the formation of a complex magnetic structure.

1. INTRODUCTION

The rare-earth manganese silicides *R*MnSi (where *R* stands for a rare-earth metal) are convenient subjects for studying the relation between the magnetic and crystal structures of these compounds [1–11]. Rare-earth compounds with silicon and manganese crystallize in a CeFeSi-type tetragonal (space group *P*4/*nmm*) [1] or TiNiSi-type orthorhombic *Pnma* structure [9]. The *R*MnSi isostructural alloys can be visualized as being made up of alternating layers of manganese, silicon, and a rare-earth element arranged perpendicular to the lattice *c* axis. Unlike the sublattices of other 3*d* transition metals, the Mn sublattice has an appreciable localized magnetic moment (1.5–3 μ_B); moreover, the *R*MnSi compounds have fairly high Curie temperatures and complex magnetic structures. The actual type of magnetic ordering depends substantially on the Mn–Mn, *R*–Mn, and Mn–Si interatomic distances, which determine the width and occupation of the 3*d* band resulting from hybridization of the Mn and Si atoms, as well as the exchange interaction pattern, both in-plane and between the layers. Neutron diffraction studies have revealed that, for $d_{Mn–Mn} \le 2.84$ Å, the manganese atoms in the planes are ferromagnetically ordered and that for $d_{Mn–Mn} > 2.90$ Å the ordering is antiferromagnetic [3, 6].

One of the most promising compounds in the *R*MnSi family is TbMnSi, which can exist in two crystal modifications, tetragonal and orthorhombic [2, 9]. Studies of the magnetic characteristics of TbMnSi in its tetragonal phase [2] shows it to be ferromagnetic with T_C = 265 K. Neutron diffraction measurements of TbMnSi [9] revealed its antiferromagnetic ordering in the TiNiSi crystallographic phase. The CeFeSi $\longrightarrow$ TiNiSi structural transition is known to occur in the *R*MnSi compounds for R^{3+} = 0.9 Å (R^{3+} is the radius of a free trivalent ion) and R^{3+}_{Tb} = 0.92 Å [5].

This study was aimed at investigating the effect exerted on the crystal and magnetic structures of TbMnSi by the substitution of nonmagnetic lanthanum for rare-earth terbium in the $Tb_{0.5}La_{0.5}MnSi$ compound.

2. EXPERIMENTAL TECHNIQUE AND SAMPLES

The $Tb_xLa_{1-x}MnSi$ compounds were prepared from high-purity rare-earth metals (terbium, lanthanum), 99.9 wt %-pure electrolytically produced manganese, and 99.9999 at. % single-crystal silicon. The terbium was purified by double vacuum distillation, and lanthanum, by arc zone recrystallization in an arc-shaped hollow extruded in a copper hearth. The compounds were synthesized in an electric arc furnace equipped with a non-expendable tungsten electrode on a water-cooled hearth in a purified-helium environment maintained at an excess pressure. The uniformity of the composition was provided by multiple remelting and homogenization anneals, which were conducted in evacuated quartz ampoules at a temperature of 700°C for 200 h.

Microstructure analysis and x-ray diffraction studies made with a DRON-3 diffractometer showed the compounds to be close to being single-phase. The lattice parameters were derived from the powder diffraction patterns.

1063-7834/04/4605-0881$26.00 © 2004 MAIK "Nauka/Interperiodica"

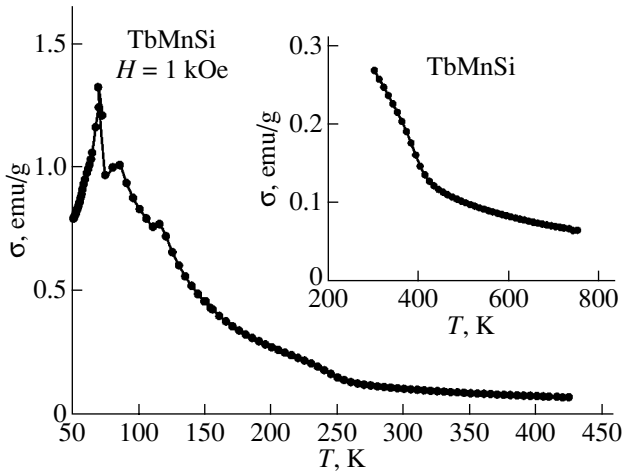

Fig. 1. Temperature dependence of the specific magnetization of TbMnSi in a magnetic field of 1.0 kOe.

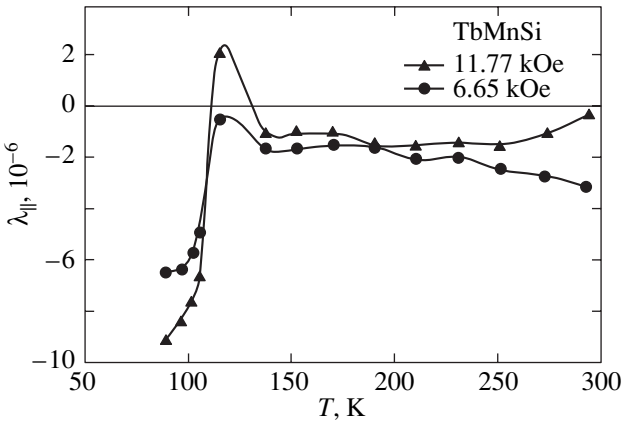

Fig. 2. Temperature dependence of the longitudinal magnetostriction $\lambda_{\|}(T)$ of TbMnSi in magnetic fields of 11.77 and 6.65 kOe.

The experimental studies were performed on polycrystalline samples of TbMnSi and $Tb_{0.5}La_{0.5}MnSi$. We measured the magnetization on a pendulum magnetometer in the temperature range 78–600 K in magnetic fields of up to 12 kOe (MSU) and with a SQUID magnetometer within the range 4.2–400 K in fields of up to 5 kOe (Institute of Low-Temperature and Structural Research, Wroclaw, Poland). The magnetostriction was studied following the tensometric technique in fields of up to 10 kOe at temperatures from 78 to 300 K (MSU).

3. EXPERIMENTAL RESULTS AND DISCUSSION

The magnetic measurements were conducted on a sample of the TbMnSi alloy, which crystallizes in a TiNiSi-type orthorhombic structure. X-ray diffraction analysis of the TbMnSi and $Tb_{0.5}La_{0.5}MnSi$ alloys under study revealed that substitution of lanthanum for terbium drives a transition from the orthorhombic (for TbMnSi) to tetragonal CeFeSi-type structure (for $Tb_{0.5}La_{0.5}MnSi$).

3.1. TbMnSi

The temperature dependence of the specific magnetization of TbMnSi exhibits three maxima in the low-temperature domain (at T_1 = 39 K, T_2 = 60.7 K, T_3 = 131 K), at which phase transitions in this compound take place (Fig. 1). Neutron diffraction studies [9] demonstrate a transition to collinear antiferromagnetism for $T \geq T_3$; near 300 K, the magnetic moments are aligned with the [100] axis, with the magnetic moment of terbium being apparently induced by a nonzero local molecular field. At low temperatures, below T_3, the projections of the wave vector q_x characterizing complex antiferromagnetic structures undergo sharp changes. In particular, in the temperature interval T_3–T_2, the magnetic moments of terbium and manganese form noncollinear helical structures in the (001) plane. Below T_2, the (001) magnetic helix plane apparently persists. However, the angles between the Tb and Mn magnetic moments are strongly temperature-dependent. This may account for the presence of the maxima on the $\sigma(T)$ curve. At T = 2 K, a plane helical structure exists in all rare-earth manganese silicides [9]. The Néel temperature, as derived from the temperature dependence of the magnetization, was found to be 410 K (see inset to Fig. 1). The magnetic susceptibility in the paramagnetic state obeys the Curie–Weiss law. We used the linear part of the inverse magnetic susceptibility to derive the paramagnetic Curie temperature θ_p = 31.07 K and the effective magnetic moment $\mu_{eff} = 10.17\mu_B$, which are close to the values given in [9]. The effective magnetic moment of the manganese ion calculated from the relation $\mu_{eff}^{Mn} = \sqrt{\mu_{eff}^2 - x(\mu_{eff}^{Tb})^2}$ is 3.07 μ_B (where x is the rare-earth ion concentration and μ_{eff}^{Tb} is the effective magnetic moment of the free Tb^{3+} ion). The results of magnetoelastic measurements performed on a polycrystalline TbMnSi sample agree with the data from the magnetization studies. The temperature dependence of the longitudinal magnetostriction $\lambda_{\|}(T)$ exhibits a distinct maximum in the region of the phase transition at T_3 = 131 K (Fig. 2). The temperature dependences of thermal expansion and of the thermal expansion coefficient measured on the same sample (not displayed in the figure) also exhibit a feature near T_3. Thus, the temperature of the phase transition to collinear antiferromagnetism for $T > T_3$ in the TbMnSi compound was obtained following three magnetic techniques, namely, by measuring the magnetization, magnetostriction, and thermal expansion.

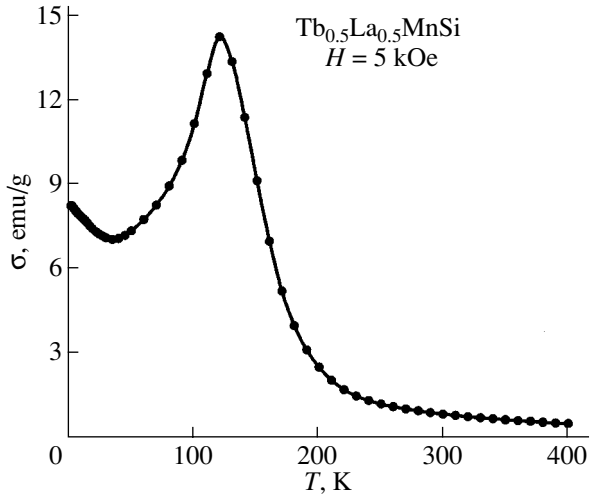

Fig. 3. Temperature dependence of the specific magnetization of $Tb_{0.5}La_{0.5}MnSi$ in a field of 5.0 kOe.

3.2. $Tb_{0.5}La_{0.5}MnSi$

X-ray diffraction measurements showed the substitution of the nonmagnetic lanthanum for Tb to initiate the formation of a tetragonal antiferromagnet, which is to a large extent single phase, with the formula $Tb_{0.5}La_{0.5}MnSi$ and to change the character of the magnetization curve (Fig. 3). The $\sigma(T)$ curve exhibits a maximum at T_1 = 136 K, which practically does not shift in temperature but is greater than the peak in the $\sigma(T)$ curve for TbMnSi by almost a factor of 3. This maximum should also apparently be identified with the transition to collinear antiferromagnetism for $T > T_1$. When cooled to low temperatures (4.2–30 K), the magnetization is seen to increase, which can be assigned to ordering on the terbium magnetic sublattice in the low-temperature region and (when cooled still further) to the formation of a plane helical structure at liquid-helium temperatures [9]. To determine the Néel temperature with a higher accuracy (T_N = 240 K), one should have, besides magnetic data, additional neutron diffraction information on the $Tb_{0.5}La_{0.5}MnSi$ compound. In the paramagnetic region (T > 300 K), the temperature dependence of inverse susceptibility of $Tb_{0.5}La_{0.5}MnSi$ obeys the Curie–Weiss law; the calculated parameters were found to be θ_p = 274.9 K and $\mu_{eff} = 5.67\mu_B$. The isotherms of specific magnetization of $Tb_{0.5}La_{0.5}MnSi$ obtained at T = 4.2 and 77 K (not shown in the figure) exhibit the appearance of a spontaneous magnetic moment. Magnetostriction measurements performed on a $Tb_{0.5}La_{0.5}MnSi$ polycrystalline sample reveal a clearly pronounced maximum in the $\lambda_{\parallel}(T)$ curves near the phase transition at T = 136 K (Fig. 4). The temperature behavior of thermal expansion $\Delta L/L(T)$ (Fig. 5) and of the thermal expansion coefficient $\alpha(T)$ studied on the $Tb_{0.5}La_{0.5}MnSi$ sample has two extrema at T = 136 and 240 K, which are close to the phase transition points for this compound. The data obtained in the x-ray diffraction and magnetic measurements carried out for TbMnSi and $Tb_{0.5}La_{0.5}MnSi$ are listed in the table.

To sum up, substitution of nonmagnetic lanthanum for Tb in the TbMnSi alloy brings about a change in the crystal structure, a sharp increase in magnetization, and the appearance of a ferromagnetic moment in the $Tb_{0.5}La_{0.5}MnSi$ compound. The observed effects can be explained as follows. The introduction of lanthanum onto the rare-earth sublattice modifies the unit cell parameters (the atomic radius of lanthanum is larger than that of terbium, R_{La} = 1.061 Å, R_{Tb} = 0.92 Å), the atomic coordinates, and the Mn–Mn, *R*–Mn, and Mn–Si interatomic distances. Competition between the *R*–*R*, *R*–Mn, and Mn–Mn exchange interactions gives rise

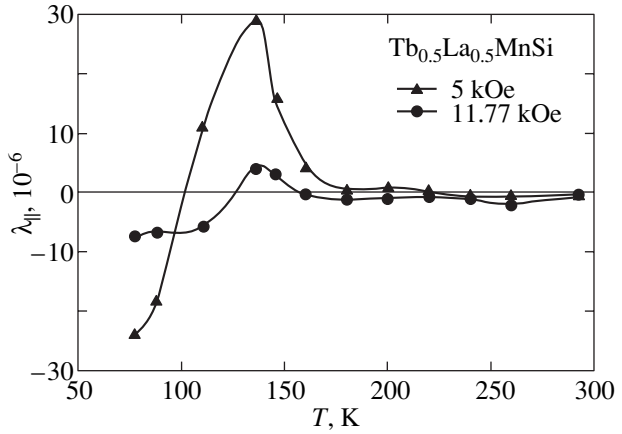

Fig. 4. Temperature dependence of the longitudinal magnetostriction $\lambda_{\parallel}(T)$ of $Tb_{0.5}La_{0.5}MnSi$ in magnetic fields of 11.77 and 5.0 kOe.

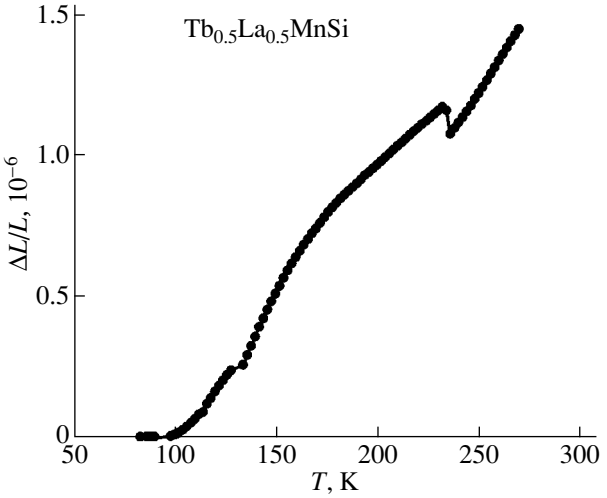

Fig. 5. Temperature dependence of thermal expansion $\Delta L/L(T)$ of the $Tb_{0.5}La_{0.5}MnSi$ compound.

Main magnetic and crystallographic characteristics of the TbMnSi and $Tb_{0.5}La_{0.5}MnSi$ compounds (T_{SR} are the magnetic ordering temperatures)

Compound	Space group	*a*, Å	*b*, Å	*c*, Å	T_{SR}, K	θ_p, K	μ_{eff}, μ_B	μ_{Mn}^{eff}, μ_B	d_{Mn-Mn}, Å	d_{Mn-Si}, Å
TbMnSi	*Pnma* (orthorhombic)	6.981	4.089	7.971	$T_1 = 39$ $T_2 = 70$ $T_3 = 131$ $T_N = 410$	31.07	10.17	3.07	2.990	2.550
$Tb_{0.5}La_{0.5}MnSi$	*P*4/*nmm* (tetragonal)	4.080	–	7.250	$T_1 = 130$ $T_N = 250$	274.9	5.67	1.97	2.885	2.639

to the formation of a complex magnetic structure in $Tb_{0.5}La_{0.5}MnSi$. It is common knowledge that the nature of the rare-earth element *R* (more specifically, the magnitude of its magnetic moment and the ionic radius) also has a considerable impact on the character of magnetic ordering in the *R*MnSi compounds (for instance, the magnetic moment of the manganese ion grows linearly with the radius of the rare-earth ion in both crystal structures, CeFeSi and TiNiSi) [3, 9]. The Mn–Mn interatomic distances in TbMnSi (TiNiSi) and $Tb_{0.5}La_{0.5}MnSi$ (CeFeSi) are 2.990 and 2.885 Å, respectively, with $d_{Mn-Mn} = 2.885$ Å lying close to the critical value separating the regions of ferro- and antiferromagnetic ordering in the *R*MnSi compounds. The increase in the Mn–Si interatomic distances in $Tb_{0.5}La_{0.5}MnSi$ brings about a decrease in the extent of hybridization between the Mn and Si orbitals and, hence, an increase in the magnetic moment. The large positive values of the Curie paramagnetic temperature (274.9 K) found for $Tb_{0.5}La_{0.5}MnSi$ argue for the existence of ferromagnetic coupling both between the manganese layers and within them. The appearance of a ferromagnetic component in the Mn magnetic moment initiates a strong increase in the magnetization of $Tb_{0.5}La_{0.5}MnSi$ and the formation of a spontaneous magnetic moment.

ACKNOWLEDGMENTS

This study was supported by the Russian Foundation for Basic Research (project no. 01-02-17977) and the federal program of support for leading scientific schools (project no. NSh-205.2003.2).

REFERENCES

1. R. Welter, G. Venturini, and B. Malaman, J. Alloys Compd. **206**, 55 (1994).
2. R. Welter, G. Venturini, E. Ressouche, and B. Malaman, J. Alloys Compd. **210**, 273 (1994).
3. G. Venturini, I. Ijjaali, E. Ressouche, and B. Malaman, J. Alloys Compd. **256**, 65 (1997).
4. R. Welter, I. Ijjaali, G. Venturini, and B. Malaman, J. Alloys Compd. **265**, 196 (1998).
5. A. Szytula, *Crystall Structures and Magnetic Properties of RTX Rare Earth Intermetallics* (Jagiellonian Univ. Press, Krakow, Poland, 1998), p. 82.
6. I. Ijjaali, R. Welter, G. Venturini, B. Malaman, and E. Ressouche, J. Alloys Compd. **270**, 63 (1998).
7. S. A. Nikitin, T. I. Ivanova, I. A. Tskhadadze, K. P. Skokov, and I. V. Telegina, J. Alloys Compd. **280** (1–2), 16 (1998).
8. S. A. Nikitin, O. V. Nekrasova, T. I. Ivanova, Yu. F. Popov, and R. S. Torchinova, Fiz. Tverd. Tela (Leningrad) **33** (6), 1640 (1991) [Sov. Phys. Solid State **33**, 923 (1991)].
9. R. Welter, G. Venturini, I. Ijjaali, and B. Malaman, J. Magn. Magn. Mater. **205**, 221 (1999).
10. I. Ijjaali, R. Welter, G. Venturini, and B. Malaman, J. Alloys Compd. **292**, 4 (1999).
11. S. A. Nikitin, T. I. Ivanova, Yu. A. Ovchenkova, M. V. Maslennikova, G. S. Burkhanov, and O. D. Chistyakov, Fiz. Tverd. Tela (St. Petersburg) **44** (2), 297 (2002) [Phys. Solid State **44**, 308 (2002)].

Translated by G. Skrebtsov

Physics of the Solid State, Vol. 46, No. 5, 2004, pp. 885–890. Translated from Fizika Tverdogo Tela, Vol. 46, No. 5, 2004, pp. 858–863.

MAGNETISM AND FERROELECTRICITY

Magnetic Structure and Properties of a Bulk $Fe_{72}Al_5P_{10}Ga_2C_6B_4Si_1$ Alloy in the Amorphous and Nanocrystalline States

G. E. Abrosimova*, A. S. Aronin*, Yu. P. Kabanov*, D. V. Matveev*, and V. V. Molokanov**

**Institute of Solid State Physics, Russian Academy of Sciences, Chernogolovka, Moscow oblast, 142432 Russia*
e-mail: matveev@issp.ac.ru
***Baĭkov Institute of Metallurgy and Materials Sciences, Russian Academy of Sciences, Leninskiĭ pr. 49, Moscow, 117911 Russia*

Received September 16, 2003

Abstract—The structure forming under controlled crystallization of a bulk $Fe_{72}Al_5P_{10}Ga_2C_6B_4Si_1$ amorphous alloy has been studied using differential scanning calorimetry, transmission electron microscopy, and x-ray diffraction. Crystallization of the alloy was established to result in the formation of a nanocrystalline structure consisting of three phases. The domain structure and magnetic properties of amorphous and nanocrystalline samples were investigated using the magnetooptic indicating film technique (MOIF) and a vibrating-sample magnetometer. The coercive force and the saturation magnetization of the amorphous samples were found to be 1 Oe and 130 emu/g, respectively. It was shown that the formation of the nanocrystalline structure entails a dramatic decrease in domain size (down to 1–4 μm) as compared to an amorphous sample (~1 mm). Simultaneously, a decrease in the saturation magnetization and a strong increase in the coercive force of the samples were observed. © *2004 MAIK "Nauka/Interperiodica".*

1. INTRODUCTION

Amorphous and nanocrystalline alloys feature remarkable mechanical and magnetic properties and are attracting considerable interest, in particular, because of their application potential. Most of the available amorphous alloys are produced by melt quenching on a rapidly rotating disk. In this case, the melt cooling rate is 10^5–10^6 K/s, and the samples thus obtained are 30–50-μm-thick ribbons. The synthesis and fabrication of bulk metal glasses [1–3] have again focused attention on amorphous metallic materials. The development of new alloys characterized by a high viscosity in molten state has made it possible to production them in the amorphous state at cooling rates below 100 K/s [1–5]. The critical cooling rate needed to obtain some metallic glasses in the amorphous state is so low that the $Pd_{40}Ni_{40}P_{20}$ alloy, for instance, has been prepared in bulk form as a sphere ~25 mm in diameter [6]. A number of systems have been prepared in the form of bulk amorphous alloys [1, 4, 5]. They exhibit unique properties; for example, some zirconium-based alloys have a high yield point of 840–2100 MPa, an elastic strain of ~4%, and high plasticity and are corrosion-resistant [7].

Since 1995, when bulk metal glasses were first prepared by melt quenching, a number of bulk ferromagnetic amorphous alloys of various compositions have been prepared, such as Fe–(Al,Ga)–(P,C,B) [8], Fe–Ga–(P,C,B) [9], (Nb,Pr)–Fe–(Al,Si) [10, 11], Fe–(Cr,Mo)–B–C [12], and others. The crystallization of Fe-based binary alloys was studied in considerable detail in [13, 14]. Fe-based multicomponent metal glasses heated before crystallization typically exhibit a large region of existence of a supercooled liquid, with the width of this temperature region exceeding 50 K. Iron-based bulk amorphous alloys exhibit high magnetic softness with a maximum saturation magnetization of 1.3 T and a coercive force of less than 5 A/m. It is known that iron-based nanocrystalline alloys (for instance, Finemet) prepared by amorphous alloy crystallization exhibit very high magnetic characteristics [15], but they are obtained in the form of ~30-μm-thick ribbons, which imposes limitations on their possible application. The maximum thickness of the samples of bulk iron-based alloys is ~3 mm for Fe–(Al,Ga)–(P,C,B), Fe–Ga–(P,C,B), and Fe–(Cr,Mo)–B–C and ~12 mm for (Nb,Pr)–Fe–(Al,Si). These alloy systems are convenient subjects for investigation due to the possibility of preparing ribbon-shaped samples with a thickness of 0.2 mm up from them and because the heating-driven phase transformations and changes in the properties occur similarly in both ingots and ribbon-shaped samples.

The present communication reports on a study of the structure, magnetic properties, and magnetization switching of a bulk $Fe_{72}Al_5P_{10}Ga_2C_6B_4Si_1$ alloy in the amorphous state, the possibility of forming nanocrys-

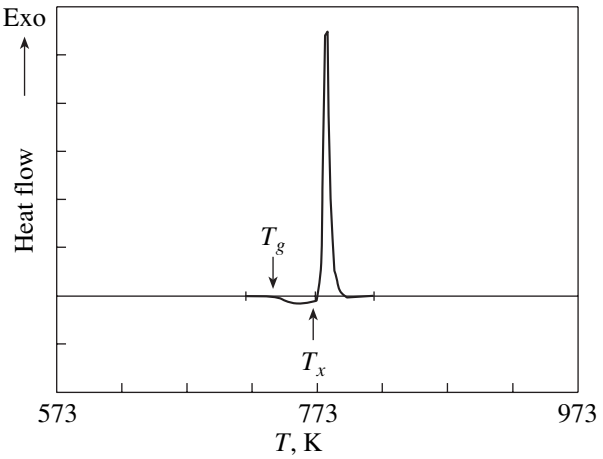

Fig. 1. DSC curve of a bulk $Fe_{72}Al_5P_{10}Ga_2C_6B_4Si_1$ amorphous alloy.

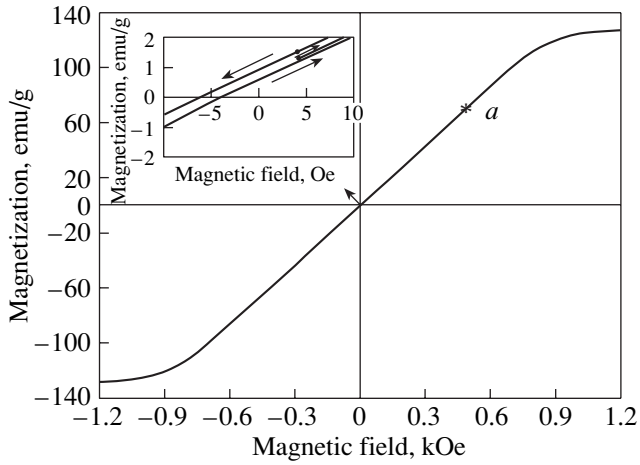

Fig. 2. Magnetization curve of a $Fe_{72}Al_5P_{10}Ga_2C_6B_4Si_1$ amorphous alloy.

talline structure in it by heating, and the magnetic structure and properties of the alloy.

2. EXPERIMENTAL TECHNIQUE

Bulk samples and thick ribbons of the $Fe_{72}Al_5P_{10}Ga_2C_6B_4Si_1$ amorphous alloy were prepared by melt quenching. The starting materials were more than 99.8% pure. The main studies were performed on ribbon samples with a cross section of ~0.2 × 2 mm. The glass formation temperature (T_g), the temperature of the onset of crystallization (T_x), and the crystallization enthalpy (ΔH) of the alloy were determined by DSC with a SETARAM differential scanning calorimeter at a heating rate of 10 K/min.

The samples were annealed in a tin bath heated to the desired temperature. The in-plane saturation magnetization of the annealed and starting samples and their coercive force were measured on a vibrating-sample magnetometer at room temperature.

The structure and phase composition of the starting and annealed samples were investigated using x-ray diffraction and transmission electron microscopy. The x-ray diffraction measurements were performed on SIEMENS D-500 and DRON 4.0 diffractometers with CuK_α and CoK_α radiation. The electron microscope studies were carried out on a JEOL-100 CX II electron microscope.

The domain structure was studied with the use of magnetooptic indicating films (MOIF) [16]. The indicator was a single-crystal iron-garnet film with in-plane magnetization. The film was placed directly on the sample under study. The stray fields at its edges, domains, and other magnetic defects gave rise to local deviations in the direction of magnetization out of the plane of the indicator film. They were revealed in the double Faraday effect in polarized light reflected from the lower surface of the film coated by an aluminum mirror. To study the magnetic structure, samples thinned preliminarily by mechanical means to a thickness of a few micrometers were subsequently mirror polished.

3. EXPERIMENTAL RESULTS AND DISCUSSION

The DSC curve of the starting alloy shown in Fig. 1 was used to determine the temperatures of glass formation (T_g) and of the onset of crystallization (T_x) and the crystallization enthalpy (ΔH): T_g = 748 K, T_x = 771 K, and ΔH = 103.3 J/g. The value of ΔH obtained and the pattern of the DSC curves of the alloy are typical of metal glass crystallization. The corresponding x-ray diffractogram of the as-prepared alloy exhibits only broad diffuse maxima characteristic of the amorphous structure.

Figure 2 displays the hysteresis curve of the as-prepared (amorphous) sample obtained by applying a magnetic field in the sample plane. The coercive force and the saturation magnetization of the sample, as derived from this curve, are 1 Oe and 130 emu/g, respectively. The deviation of this curve from zero (see inset) is caused by the demagnetizing factor related to the sample shape. The values of the coercive force and of the saturation magnetization and the shape of the hysteresis curve are typical of bulk amorphous, magnetically soft iron-based materials [17].

Figure 3a displays a magnetooptic image of the starting sample obtained under application of a magnetic field (the magnetic field applied to the sample corresponds approximately to point *a* in Fig. 2). This micrograph clearly shows regions with differently directed magnetizations separated by domain walls revealed in the form of bright and dark broken lines. The domain size is ~1 mm. The domain walls are bowed, possibly due to their pinning at imperfections in

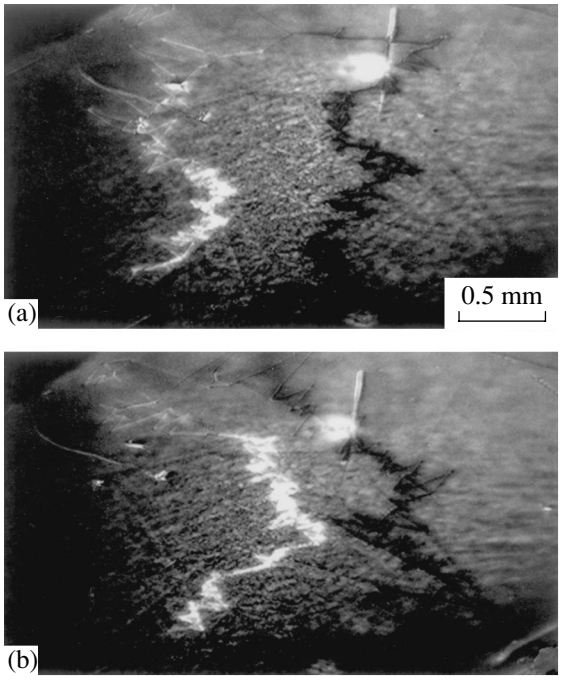

Fig. 3. Domain structure forming under magnetization reversal of the $Fe_{72}Al_5P_{10}Ga_2C_6B_4Si_1$ amorphous alloy.

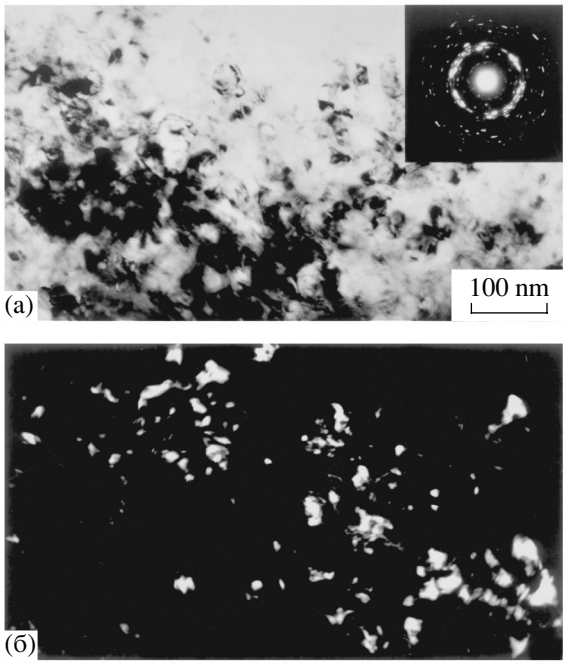

Fig. 4. Microstructure of the $Fe_{72}Al_5P_{10}Ga_2C_6B_4Si_1$ alloy annealed at 783 K for 5 h. (a) Bright-field image, (b) dark-field image.

the sample. The sawtooth shape of the domain-wall images should be attributed to the formation of intrinsic domain walls in the indicator film in weak fields (for the walls, it is energetically preferable to be pinned at the domain boundaries of the sample under study) and is in no way related to the magnetic structure of the sample. As is evident from Fig. 3b, a change in the magnetic field caused the domain walls to shift. As the sample is further magnetized, these domain walls annihilate to make the magnetic structure of the sample uniform.

Domain structure in amorphous metallic glasses was observed in [18, 19]. It consists, as a rule, of labyrinthine domains ranging in size from 10 μm to ~1 mm and depends on the actual alloy composition and other conditions. As pointed out in [20], the presence of strains in a sample brings about a change in the domain structure and, in particular, a decrease in the size of domains and a change in their shape. In our case, the domains were large (~1 mm) and their shape did not exhibit any distinct pattern. This suggests that the structure is fairly uniform and has only a small in-plane anisotropy.

Our structural studies showed the sample crystallization to produce three crystalline phases, namely, a bcc phase with the lattice parameter a = 0.286 nm; a phase of the Fe_3P type, which has a tetragonal lattice of space group $I\bar{4}$ and parameters a = 0.9035 nm and c = 0.4415 nm; and an fcc phase with lattice parameter a = 0.379 nm. Figure 4 presents the microstructure and an electron diffraction pattern (inset) of a sample annealed at 783 K for 5 h. At this and longer durations, the structure forming under these thermal processing conditions is nanocrystalline. The electron diffraction pattern of such a sample is seen to consist of a large number of reflections. The dark-field image (Fig. 4b) obtained in the reflection specified by the arrow (inset to Fig. 4a) reveals numerous crystalline precipitations 10–20 nm in size with unequal axes and a few grains up to 50 nm in size.

The formation of a nanocrystalline structure entails a change in the magnetic properties: the saturation magnetization decreases, and the coercive force

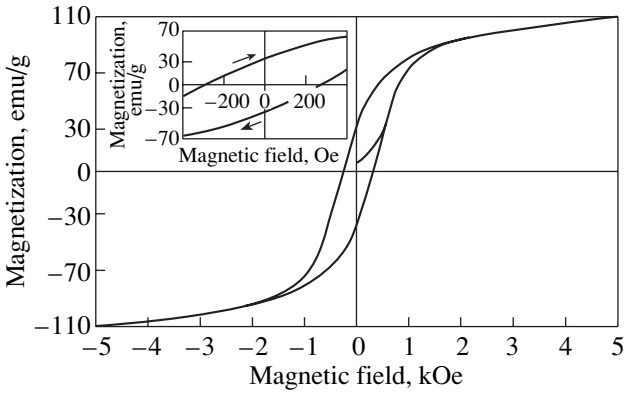

Fig. 5. Hysteresis curve of a sample of the $Fe_{72}Al_5P_{10}Ga_2C_6B_4Si_1$ amorphous alloy obtained after annealing at 783 K for 10 h.

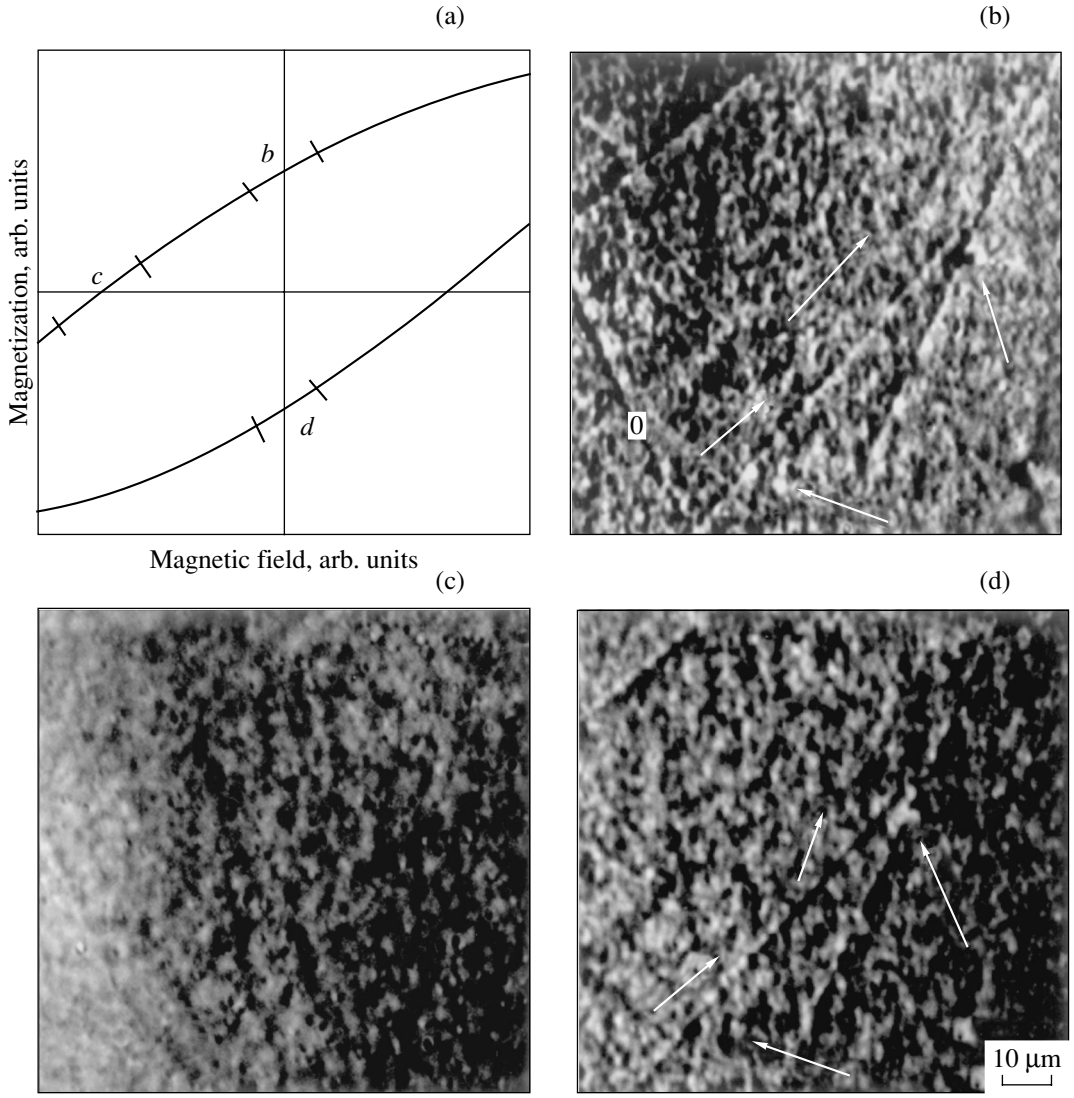

Fig. 6. Magnetooptic image of a sample of the $Fe_{72}Al_5P_{10}Ga_2C_6B_4Si_1$ amorphous alloy annealed for 5 h at 783 K. (a) Conventional hysteresis curve and (b) magnetooptic image (photomicrograph) of the sample obtained after the removal of the magnetic field that magnetized the sample to saturation, (c) photomicrograph obtained under application of a negatively oriented field $H \approx H_c$ to the sample, and (d) photomicrograph obtained after removal of the magnetic field of negative polarity.

increases. Figure 5 displays a hysteresis curve of a sample obtained after annealing at 783 K for 10 h. The coercive force and saturation magnetization of the sample extracted from this curve are 275 Oe and 110 emu/g, respectively. The domain structure changed accordingly.

Figure 6 shows a magnetooptic image of the sample annealed at 783 K for 5 h obtained under application of various magnetic fields. The sample was preliminarily polished (with a few scratches left purposefully to allow better observation of the change in the magnetization orientation). The images of the magnetic structure (Figs. 6b–6d) correspond to sections *b*, *c*, and *d* on the magnetization curve (Fig. 6a). The magnetooptic image of the sample obtained after removal of the in-plane magnetic field ($H = 0$) that magnetized the sample to saturation is shown in Fig. 6b. One clearly sees small magnetic regions with differently oriented magnetic moments (the magnetic moment has a large component directed perpendicular to the sample plane toward the indicator film in the bright regions and away from the film in the dark regions). These regions vary in size from 1 to 4 μm and are randomly distributed over the sample (some of them are identified with arrows). A subsequent increase in the field of negative polarity gradually washes the contrast nonuniformities out. Figure 6c presents a magnetooptic image obtained under application of a negatively oriented field $H \approx H_c$ to the sample. The magnetic contrast in this photomicrograph is seen to diminish noticeably and become more uni-

form, which implies that the average in-plane sample magnetization is close to zero. The magnetooptic image of the sample obtained after removal of the magnetic field of negative polarity is displayed in Fig. 6d. The microdomain magnetization direction is seen to have changed (the arrows specify some microdomains that changed their direction of magnetization as compared to Fig. 6b). As the field is increased still further, the nonuniformities in the image contrast are seen to disappear gradually, which corresponds to a change in the microdomain magnetization direction with an increase in the magnetic field to above H_c.

The character of the contrast variation in the image of magnetostatic fields observed to occur in central regions of the sample under variation of the magnetic field suggests that the magnetization reversal of samples with such a nanocrystalline structure takes place through incoherent rotation of the stray magnetic fields. The microdomain dimensions far exceed the size of the nanocrystals, which, as already mentioned, is 10–50 nm. As follows from previous studies of nanocrystalline alloys [21], the smallest size of the regions within which exchange interaction aligns the magnetic moments parallel to one another under application of a magnetic field is dictated by the ferromagnetic coupling length L_{ex}^0 given by the relation

$$L_{ex}^0 = (A/K_1)^{1/2}, \quad (1)$$

where K_1 is the magnetocrystalline anisotropy constant and A is the exchange parameter. The length L_{ex}^0 is far larger than the nanocrystal size; therefore, the magnetization reversal of nanocrystalline samples cannot occur in each single nanocrystal. One domain may contain many grains. As a consequence, the effective anisotropy is averaged over several nanocrystals and becomes weaker. The degree of averaging of the magnetocrystalline anisotropy can be determined in terms of the so-called random-anisotropy model, which was originally developed for amorphous systems [22]. For grains of a size D smaller than the ferromagnetic coupling length, the averaged anisotropy $\langle K \rangle$ affecting the magnetization reversal can be cast as [23]

$$\langle K \rangle = K_1^4 D^6 / A^3. \quad (2)$$

Thus, our results suggest that, in our case, L_{ex}^0 is as large as a few microns.

Images of the domain structure in nanocrystalline alloys were obtained earlier in [24–26]. These observations were made on magnetically soft alloys of the Finemet type. Kerr measurements [25] showed that the magnetic structure, for instance, of the $Fe_{73.5}Cu_1Nb_3Si_{13.5}B_9$ nanocrystalline alloy, consists of bowed domains up to 300 μm in size separated by 180° walls; note that a high-resolution image obtained by the Kerr technique revealed domain walls with a distinct substructure and a width of ~2 μm, which indicates a low effective anisotropy of the material. Magnetic force microscopy measurements [26] performed on a $Fe_{91}Zr_7B_2$ nanocrystalline alloy also showed the width of the 180° domain wall to be ~2 μm. In our case, the formation of nanocrystals brought about a strong decrease in the domain size as compared to the amorphous sample. This apparently indicates an increase in the anisotropy involved in the formation of a multiphase state. The decrease in the saturation magnetization brought about by nanocrystallization is also most likely connected with a change in the phase composition. As already mentioned, the nanostructure thus formed consists of three phases, more specifically, of a bcc phase (the α-Fe type), a Fe_3P-type phase, and an fcc phase. The α-Fe phase is not dominant (whereas the amount of Fe(Si) may be as high as 70–80% in Finemet). In our case, the formation of a small amount of a phase with the highest magnetization during crystallization brings about a decrease in the saturation magnetization of the alloy as a whole. To reach a qualified conclusion as to the nature of the observed phenomena, a more comprehensive investigation of the chemical composition of the phases would be needed.

4. CONCLUSIONS

Thus, we have studied the magnetic structure and properties of a bulk $Fe_{72}Al_5P_{10}Ga_2C_6B_4Si_1$ amorphous alloy, their variation under heating, and the correlation with structural changes. It was shown that, in the amorphous state, this alloy has a magnetic structure made up of domains with a size comparable to that of the sample and is magnetically soft. A nanocrystalline structure with grains 10–50 nm in size was found to form when the alloy is heated. The domains shrink in size to a few microns, which apparently indicates an increase in anisotropy in the course of formation of the multiphase state, an increase in the coercive force, and a decrease in the saturation magnetization. The observed variations in the structure and properties correlate with the phase composition of the forming nanocrystalline structure.

ACKNOWLEDGMENTS

This study was supported by the Russian Foundation for Basic Research (project no. 03-02-17227), the program of the Presidium of the Russian Academy of Sciences “Fundamental Problems in the Physics and Chemistry of Nanoscale Systems and Materials,” and the program of the Department of Physical Sciences of the Russian Academy of Sciences “New Materials and Structures.”

REFERENCES

1. A. Inoue, T. Zhang, and T. Masumoti, Mater. Trans., JIM **33**, 177 (1990).

2. A. Inoue, T. Zhang, N. Nishiyama, K. Ohba, and T. Masumoti, Mater. Trans., JIM **34**, 1234 (1993).
3. A. Peker and W. L. Johnson, Appl. Phys. Lett. **63**, 2342 (1993).
4. A. Inoue, Mater. Trans., JIM **36**, 866 (1995).
5. A. Inoue, T. Zhang, and T. Itoi, Mater. Trans., JIM **38**, 359 (1997).
6. A. J. Drehman, A. L. Greer, and D. Turnbull, Appl. Phys. Lett. **41**, 716 (1982).
7. L. Q. Xing, D. M. Herlach, M. Cornet, C. Bertrand, J.-P. Dallas, M.-H. Trichet, and J.-P. Chevalier, Mater. Sci. Eng. A **226–228**, 874 (1997).
8. A. Inoue and G. S. Gook, Mater. Trans., JIM **36**, 1180 (1995).
9. B. Shen and A. Inoue, Mater. Trans., JIM **41**, 873 (2000).
10. A. Inoue, T. Zhang, and A. Takeuchi, Mater. Trans., JIM **37**, 1731 (1996).
11. A. Inoue, T. Zhang, W. Zhang, and A. Takeuchi, Mater. Trans., JIM **37**, 99 (1996).
12. S. Pang, T. Zhang, K. Asami, and A. Inoue, Acta Mater. **50**, 489 (2002).
13. G. E. Abrosimova and A. S. Aronin, Fiz. Tverd. Tela (Leningrad) **32**, 1742 (1990) [Sov. Phys. Solid State **32**, 1014 (1990)].
14. G. E. Abrosimova, A. S. Aronin, and V. A. Stel'mukh, Fiz. Tverd. Tela (Leningrad) **33**, 3570 (1991) [Sov. Phys. Solid State **33**, 2006 (1991)].
15. Y. Yoshizawa, K. Yamauchi, T. Yamane, and H. Sugihara, J. Appl. Phys. **64**, 6047 (1988).
16. L. M. Dedukh, V. S. Gornakov, Yu. P. Kabanov, and V. I. Nikitenko, Pis'ma Zh. Éksp. Teor. Fiz. **64**, 778 (1996) [JETP Lett. **64**, 826 (1996)].
17. A. Inoue, A. Takeuchi, and B. Shen, Mater. Trans., JIM **42**, 970 (2001).
18. R. Smith, G. Jones, and D. Lord, IEEE Trans. Magn. **24**, 1868 (1988).
19. H. Krontmüller, J. Phys. Colloq. **41** (C8), 618 (1981).
20. G. Brown, M. Hawley, D. Markiewich, F. Spaepen, and E. Barth, J. Appl. Phys. **85**, 4415 (1999).
21. G. Herzer, J. Magn. Magn. Mater. **112**, 258 (1992).
22. R. Alben, J. Becker, and M. Chi, J. Appl. Phys. **49**, 1653 (1978).
23. G. Herzer, Mater. Sci. Eng. A **133**, 1 (1990).
24. O. Kohmoto, N. Uchida, E. Aoagi, T. Chon, and K. Higara, Mater. Trans., JIM **31**, 820 (1990).
25. R. Schäfer, A. Hubert, and G. Herzer, J. Appl. Phys. **69**, 5325 (1991).
26. K. Suzuki, D. Wexler, J. Cadogan, V. Sahajwalla, A. Inoue, and T. Masumoto, Mater. Sci. Eng. A **226–228**, 586 (1997).

Translated by G. Skrebtsov

Physics of the Solid State, Vol. 46, No. 5, 2004, pp. 891–901. Translated from Fizika Tverdogo Tela, Vol. 46, No. 5, 2004, pp. 864–874.

MAGNETISM AND FERROELECTRICITY

Magnetic and Magnetooptical Properties of Multilayer Ferromagnet–Semiconductor Nanostructures

V. E. Buravtsova*, E. A. Gan'shina*, V. S. Gushchin*, S. I. Kasatkin, A. M. Murav'ev**, N. V. Plotnikova**, and F. A. Pudonin*****

** Moscow State University, Vorob'evy gory, Moscow, 119899 Russia*

e-mail: guschin@genphpys.phys.msu.ru

*** Institute of Control Sciences, Russian Academy of Sciences, Moscow, 117997 Russia*

**** Lebedev Physical Institute, Russian Academy of Sciences, Leninskiĭ pr. 53, Moscow, 117924 Russia*

Received July 18, 2003; in final form, September 18, 2003

Abstract—The magnetic and magnetooptical properties of spin-tunneling multilayer permalloy–silicon carbide nanoheterostructures deposited by rf sputtering have been studied. Magnetometric and magnetooptical methods are used to show that the magnetic–semiconducting nanostructures have a complex magnetic structure and to track the evolution of the magnetic properties of these structures as functions of the magnetizing field and the thickness and sequence order of ferromagnetic and semiconducting layers in them. The induction response and the field and orientation dependences of the transversal Kerr effect are found to have anomalies. The experimental results are interpreted under the assumption that there is exchange interaction between the ferromagnetic and semiconducting layers through a thin magnetically ordered transition layer formed inside the interface. © *2004 MAIK "Nauka/Interperiodica".*

1. INTRODUCTION

The unusual magnetic, transport, and optical properties of some artificial layered ferromagnet–nonmagnetic material structures with a layer thickness varying from several angstroms to several tens of angstroms are of great interest. This interest is related to the alternating effective exchange interaction found in Fe/Cr multilayers [1]; the interaction was established to be a complex function of both the thickness of the antiferromagnetic Cr layer and the interface quality [2–4]. Magnetic nanostructures attracted considerable attention after the discovery of giant magnetoresistance in Fe/Cr and some other structures [3]; extensive study of this effect has led to the development of a new field in solid-state physics, spintronics. Magnetoresistive (MR) nanostructures consisting of two 3*d*-ferromagnet layers separated by a nonmagnetic material are of particular interest. As for the mechanism of spin-dependent resistance, there are spin-valve MR structures in which an interlayer consists of nonmagnetic metals (Cu, Ag, Au) or antiferromagnets (Cr, Mn, etc.) and spin-tunneling nanostructures with an interlayer of a dielectric (Al_2O_3, SiO_2, etc.). For practical applications, the most promising materials are spin-tunneling MR structures, in which a giant magnetoresistance of more than 40% has been obtained at room temperature [2]. They have been used to fabricate an experimental magnetic-field transducer with a sensitivity of $\approx 10^{-6}$ Oe [5], an MR random-access memory with a capacity of 256 kb [6], and a spin transistor [7].

Unfortunately, such technical achievements are not always supported experimentally and theoretically: the physical mechanisms of antiferromagnetic ordering of the magnetic moments in neighboring magnetic layers separated by a nonmagnetic material have not been completely established, the causes of magnetoresistance having opposite signs in similar structures differing only in the type of the nonmagnetic interlayer have not been revealed, etc. Moreover, a number of problems have currently appeared in studying ferromagnet–semiconductor nanoheterostructures (magnetic–semiconducting structures). Such structures are of special interest, since, on the one hand, they retain spin polarization when a current passes through them and, on the other hand, their parameters can be changed by applying a magnetic field. These properties are necessary for operating magnetic transistors and diodes. Apart from the possible spin polarization of an electrical current, magnetic–semiconducting nanostructures exhibit interesting magnetooptical (MO) effects [8], which widens the field of application of such structures. Therefore, studying the ferromagnet–semiconductor interaction is a challenging problem [9, 10].

Silicon carbide, SiC, is a promising semiconducting material for creating magnetic–semiconducting nanostructures and designing spintronic elements [11]. This semiconductor has a large band gap (more than 2.0 eV in its various crystalline modifications), a breakdown field of ~2.0 MV/cm, a heat conductivity of 4.9 W/(cm K), and a melting temperature of 2830°C. Moreover, silicon carbide is characterized by birefringence; there-

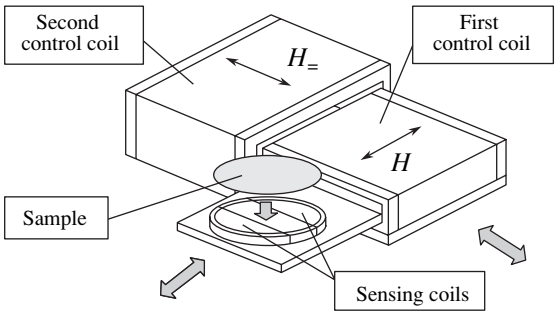

Fig. 1. Control coils of the device for measuring the magnetic properties of films.

fore, we can expect that nanostructures based on it will have interesting MO properties.

In this work, we study the magnetic and MO properties of spin-tunneling multilayer $Fe_{22}Ni_{78}$/SiC/$Fe_{22}Ni_{78}$ MR structures having various thicknesses and configurations of magnetic and nonmagnetic layers grown by rf sputtering of polycrystalline targets. As a result of this work, we revealed a magnetic interaction between the ferromagnet (FeNi) and nonmagnetic semiconductor (SiC).

2. PREPARATION OF MAGNETIC–SEMICONDUCTING STRUCTURES

Multilayer nanostructures were fabricated by rf sputtering of massive polycrystalline targets made of permalloy, silicon carbide, and other materials on a Sputron-II (Balzers) setup. Films were deposited on glass-ceramic substrates in an argon atmosphere with an initial pressure of below 5×10^{-7} Torr at a temperature of 70°C. The deposition rate was 3.38 nm/min for silicon carbide and 4.45 nm/min for the $Fe_{22}Ni_{78}$ permalloy. To create a uniaxial anisotropy in magnetic films, they were deposited in a constant magnetic field ($H_=$ = 50 Oe) applied along the substrate plane. The films deposited under these conditions feature good homogeneity and sharp interfaces, which is typical of rf sputtering. Moreover, the study of quantum-confinement effects in various metallic films (including Ni and Fe) corroborated the fact that the transition regions between a film and a substrate and between different-type layers do not exceed one or two atomic layers [12]. This conclusion was based on the fact that the quantum-confinement parameters of a film, which are extremely sensitive to its homogeneity through thickness, were independent of the substrate type. This means that the transition layer, which is the region of interaction between the film and substrate, has a small thickness. The layer thicknesses in the films were determined from the rate and time of sputtering; their values are given in the corresponding figures. For three fixed thicknesses of FeNi layers (d_m = 20, 30, 60 Å), we prepared three series of FeNi/SiC/FeNi nanostructures (symmetric structures) with a variable thickness d_s of the SiC layer (from 9 to 27 Å with a 3-Å interval) in each series. Moreover, we prepared two series of nanostructures that had separating Ti layers with a variable thickness and a SiC layer located at the top or bottom of the structures (asymmetric structures). Each series was grown in one technological cycle, and each sample was prepared under the same technological conditions in the same place in the vacuum chamber.

3. EXPERIMENTAL

3.1. Induction Method

The magnetic properties of the nanostructures were studied using the induction method. The magnetometer-based device described in [13, 14] allowed us to obtain information on the magnetic state of thin films, namely, clarify the character of magnetization reversal (whether it occurs via the motion of domain walls or the rotation of magnetization vectors), determine the coercive force H_c, establish the orientation of the easy (EA) and the hard axis (HA) of magnetization, measure the magnetic anisotropy field H_k, reveal and estimate the exchange interaction between magnetic films, and determine the uniformity of magnetic parameters across the surface of a sample and their dependences on the magnetic anisotropy field. The device makes it possible to measure the magnetic properties of both ultrathin magnetic films with a total thickness of the magnetic layers of ~5 nm and thick magnetic films (several micrometers thick). The strength of the alternating and static magnetic fields used in the device did not exceed 90 Oe.

The scheme of a compact unit that includes a sample holder, two control coils, and a system of sensing coils is shown in Fig. 1. The first control coil produces an alternating magnetic field H along the structure plane. The second control coil creates a static field $H_=$, which also lies in the sample plane and is normal to H; this field is used to measure the magnetic anisotropy. The sensing coils convert the variation of a magnetic flux into an induction signal.

3.2. Magnetooptical Method

The MO characteristics of the nanostructures were studied using the transversal Kerr effect (TKE). The spectral characteristics were measured in the energy range 0.5–4.3 eV; the field characteristics, in the magnetic-field range 0–1400 Oe; and the orientation characteristics, in the angular range $0° < \theta < 360°$. With this method, one can measure a change in the intensity of the light reflected by a sample when it is magnetized in a field that is oriented normally to the plane of light incidence and lies in the sample plane. The value and sign of the TKE are determined from the ratio $\delta = (I -$

$I_0)/I_0 = \Delta I/I_0$, where I and I_0 are the light intensities reflected by a structure in a magnetized or a demagnetized state, respectively. Since the values of the TKE in ferromagnetic metals and alloys do not exceed a few thousandths, modulation techniques are used to study the TKE in magnetic structures. In this case, TKE is generated and recorded via light intensity modulation upon magnetization reversal of a sample in an alternating magnetic field [15]. The value of δ is proportional to the light modulation depth. The dispersion of TKE spectra was measured in a field with an amplitude of 1400 Oe over the entire energy range. In this field, all samples were magnetized to saturation. The measurements were performed at a light incidence angle of φ = 70° at room temperature.

4. RESULTS AND DISCUSSION

Figure 2 shows the induction signal that is characteristic of the FeNi/SiC/FeNi nanostructures and arises upon magnetization reversal in the magnetic field H. The signal (Fig. 2a) consists of one positive and one negative pulse; that is, the response of the magnetic system is represented by the differential susceptibility of the sample. The shape of a hysteresis loop reconstructed by integrating this signal with respect to time is shown in Fig. 2b. This character of response of magnetic systems corresponds to a strong interaction between magnetic layers in a multilayer structure, when the magnetization reversal occurs simultaneously in all layers. When the interlayer interaction is weak, each magnetic layer undergoes magnetization reversal independently and the number of pulses in a read signal increases (see below).

In the anisotropic FeNi/Ti/FeNi and spin-tunneling FeNi/Al_2O_3/FeNi structures [11, 17] studied earlier, a magnetization reversal signal was generated at a certain applied magnetic field $H = H_t$ (H_t is the magnetization reversal field). As the amplitude of the applied field increased, the value of H_t either remained unchanged or insignificantly increased, which was explained by the contribution from domain walls at defects and sample edges to magnetization reversal. In the FeNi/SiC/FeNi structures studied in this work, the following behavior is observed with increasing H. Beginning from a certain value, the magnetization reversal field H_t decreases, then increases and, finally, levels off. For example, in the FeNi(20 Å)/SiC(21 Å)/FeNi(20 Å) sample, the magnetization reversal field decreases from $H_t = 4.8$ Oe at $H = 8$ Oe to $H_t = 4$ Oe at $H = 20$ Oe. A further increase in the amplitude of H results in an increase in H_t almost to the initial value. At $H \gg H_t$, the magnetization reversal field becomes equal to the coercive force. Thus, it is seen that the dependence of the magnetization reversal field on the amplitude of the applied field H is nonlinear in certain nanostructures.

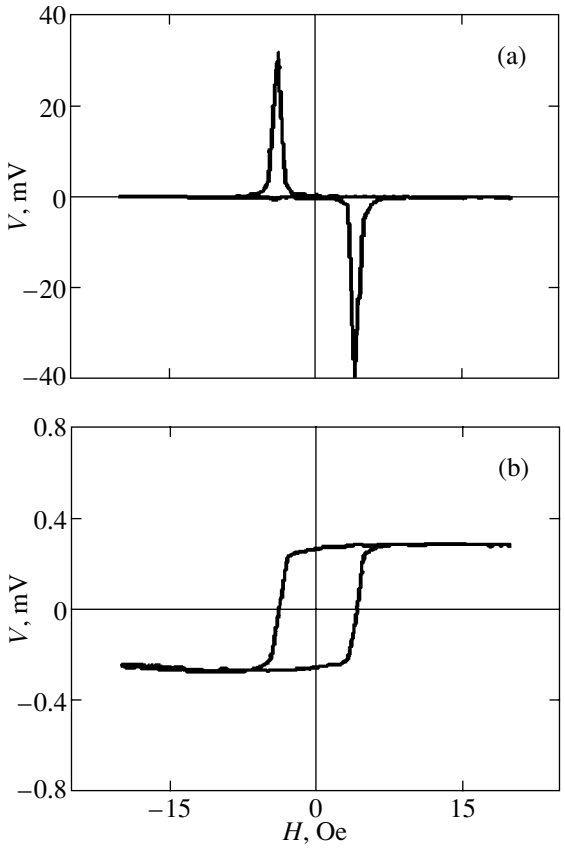

Fig. 2. Oscillograms of an FeNi/SiC/FeNi nanostructure: (a) magnetization reversal signals and (b) hysteresis loop.

The variation in the magnetization reversal field of a magnetic–semiconducting nanostructure with an amplitude of H indicates a change in the energy of the magnetic state of the permalloy films, which can be related to the effect of the nonmagnetic semiconducting SiC layer on both the process of magnetization reversal of the permalloy films and the magnetic properties of the nanostructures. The dependence of the magnetization reversal field on the amplitude of H is most pronounced for the semiconducting-layer thickness falling in the range $20 < d_s < 27$ Å and the magnetic-layer thickness $d_m = 20$ Å. However, the effect of the magnetic-layer thickness on the magnetic properties of the ferromagnetic FeNi/SiC/FeNi nanostructures is weaker than that of the semiconducting-layer thickness.

In the FeNi/SiC/FeNi nanostructure, the semiconducting layer interacts identically with the ferromagnetic layers because of the symmetric arrangement of the FeNi layers with respect to SiC. To determine the effect of the semiconducting layer on the interaction between the magnetic layers and to reveal the role of the substrate in the formation of the magnetic structure of a film, we grew two groups of asymmetric nanostructures, more specifically, FeNi(20 Å)/Ti(d_{Ti})/FeNi(20 Å) structures with a SiC(21 Å) layer located at the top or

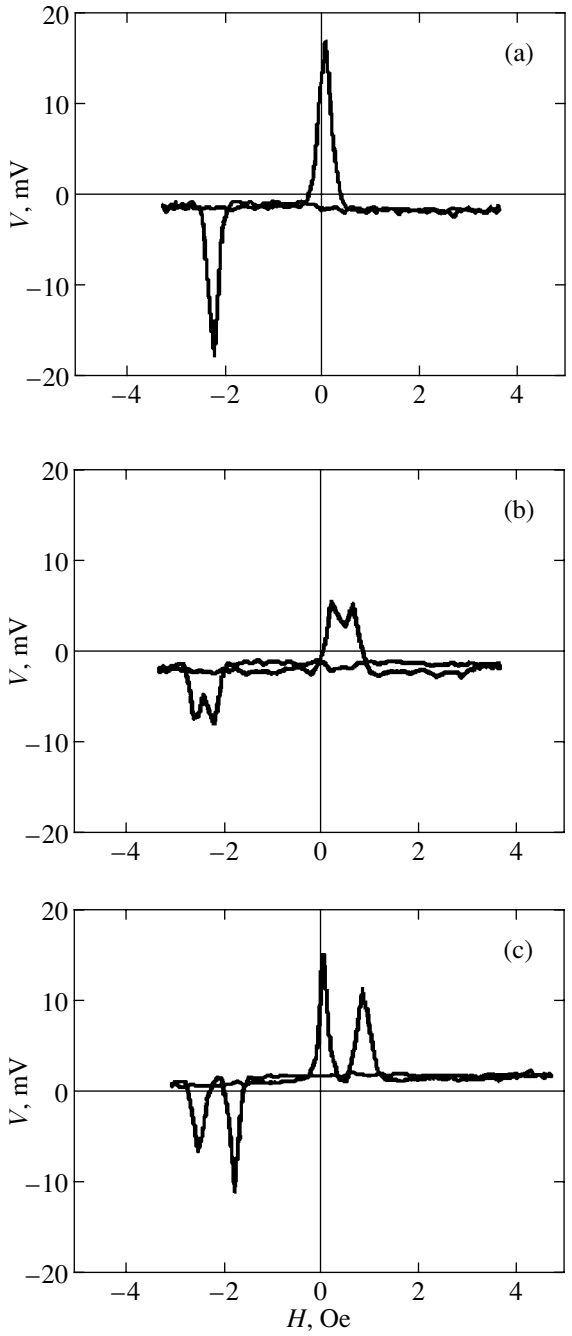

Fig. 3. Oscillograms of the magnetization reversal signals from FeNi(20 Å)/Ti(d_{Ti})/FeNi(20 Å)/SiC(21 Å) nanostructures at (a) d_{Ti} = 15, (b) 25, and (c) 50 Å.

bottom of the three-layer structure. The titanium-layer thicknesses were d = 15, 25, 35, and 50 Å, which allowed us to vary the exchange coupling between the ferromagnetic layers. Figure 3 shows the magnetization reversal signals for the FeNi(20 Å)/Ti(d_{Ti})/FeNi(20 Å)/SiC(21 Å) nanostructures, where d_{Ti} = 15, 25, and 50 Å. Similar spectra of the response of the ferromagnet to H were also obtained for the same compositions with the SiC layer located between the ferromagnetic layer and the substrate.

Figure 3a shows that, at d_{Ti} = 15 Å, the exchange interaction between the permalloy films exceeds the interaction between the semiconductor layer and the adjacent permalloy film; both permalloy films undergo magnetization reversal as a whole. At d_{Ti} = 25 Å, when the exchange interaction between the permalloy films weakens, the magnetization reversal signal is divided into two signals (Fig. 3b). This means that the ferromagnetic films start to undergo magnetization reversal individually (i.e., they have different values of coercive force H_c). As d_{Ti} increases further, the signals become completely separate and the variation in the values of H_c in the permalloy films becomes more pronounced. The separate magnetization reversal of the FeNi layers indicates that the coercive force of the FeNi film adjacent to SiC decreases, which can only be related to the appearance of a magnetic interaction between the FeNi layer and the nonmagnetic semiconducting SiC layer.

We also found that the magnetic interaction between the FeNi and SiC layers depends not only on the semiconducting-layer thickness but also on the applied magnetizing field. For the samples with d_{Ti} = 50 Å, magnetization reversal occurs as follows. As the H amplitude increases from zero to approximately 10 Oe, a single magnetization reversal signal with a maximum at H_t = 2.6 Oe is detected (Fig. 4a). This behavior indicates that magnetization reversal occurs simultaneously in both FeNi layers and that there is no effect of SiC on the magnetic parameters of the ferromagnetic films. As the amplitude of the applied field increases, the signal amplitude decreases and two other signals with peak positions at 1.7 and 3.4 Oe appear on either side of the signal (Fig. 4b). This behavior indicates the onset of individual magnetization reversal of the FeNi layers because of the increasing effect of the SiC layer on the adjacent FeNi layer. With a further increase in the amplitude of field H, the initial signal disappears (Fig. 4c) and the FeNi layers undergo magnetization reversal separately, which indicates a strong magnetic interaction between the nonmagnetic semiconducting SiC layer and the adjacent ferromagnetic FeNi layer.

These results show that the ferromagnetic FeNi layers and the semiconducting SiC layer interact with each other depending on the applied field. This field dependence of magnetization reversal can be explained as follows. The interdiffusion of the semiconductor and ferromagnet layers results in a thin (one- or two-atomic-layer-thick) interface whose magnetization increases with the magnetizing-field amplitude.

To obtain new information on the magnetic properties of the ferromagnet–semiconductor nanostructures under study, we used MO methods. The dynamic MO methods, which have a high sensitivity and give a large amount of information, showed themselves well in studying thin-film magnetic layer structures [18–20].

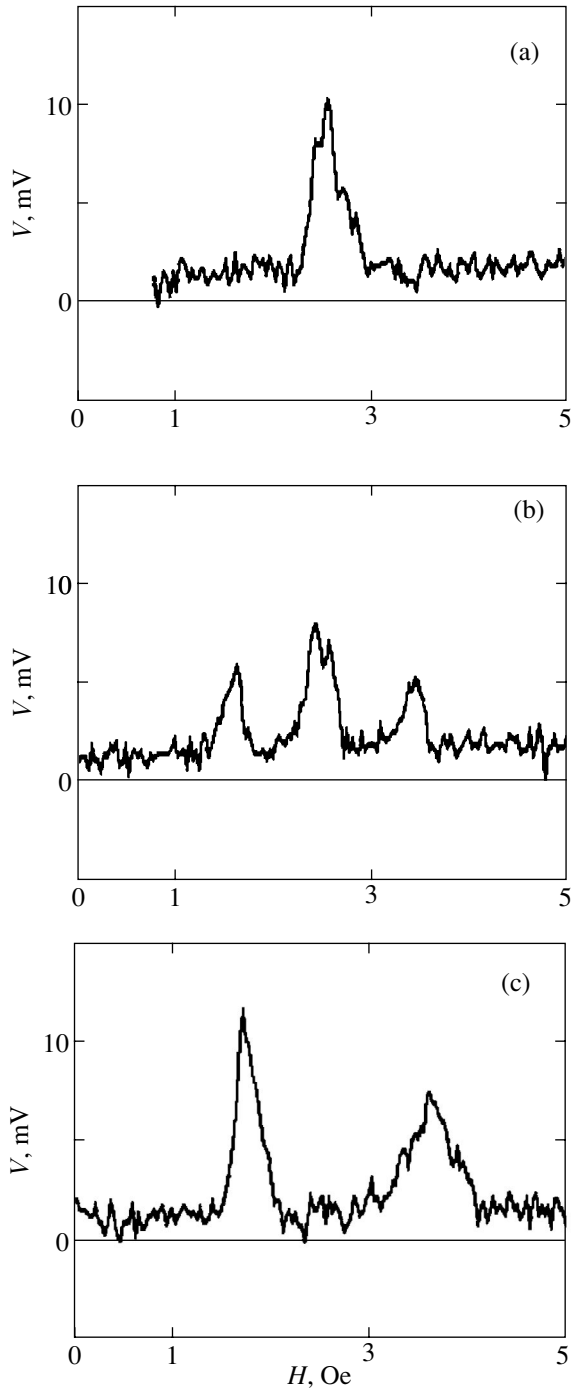

Fig. 4. Oscillograms of the one-polarity read signals from the FeNi(20 Å)/Ti(50 Å)/FeNi(20 Å)/SiC(21 Å) nanostructure recorded at a magnetizing-field amplitude of (a) 8, (b) 12, and (c) 20 Oe.

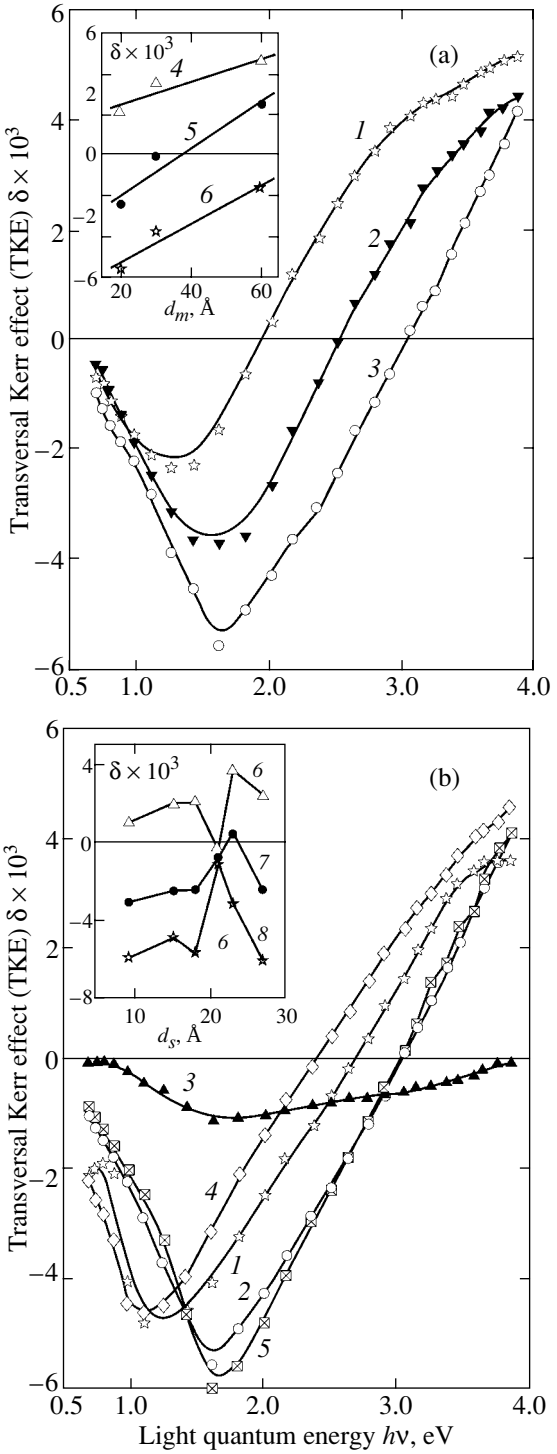

Fig. 5. Dispersion of the TKE in the nanoheterostructures: (a) (*1*) FeNi(60 Å)/SiC(18 Å)/FeNi(60 Å), (*2*) FeNi(30 Å)/SiC(18 Å)/FeNi(30 Å), and (*3*) FeNi(20 Å)/SiC(18 Å)/FeNi(20 Å); the inset shows the constant-energy dependences of the TKE on the permalloy layer thickness for *h*ν equal to (*4*) 3.45, (*5*) 2.5, and (*6*) 1.61 eV; (b) (*1*) FeNi(20 Å)/SiC(15 Å)/FeNi(20 Å), (*2*) FeNi(20 Å)/SiC(18 Å)/FeNi(20 Å), (*3*) FeNi(20 Å)/SiC(21 Å)/FeNi(20 Å), (*4*) FeNi(20 Å)/SiC(23 Å)/FeNi(20 Å), and (*5*) FeNi(20 Å)/SiC(27 Å)/FeNi(20 Å); the inset shows the constant-energy dependences of TKE on the silicon carbide layer thickness for *h*ν equal to (*6*) 3.45, (*7*) 2.5, and (*8*) 1.61 eV.

Figure 5 shows the frequency dependences of the TKE for various FeNi/SiC/FeNi nanostructures; they are mainly similar to the spectra of massive permalloys [21, 22]. It is seen that, in the near infrared region and the beginning of the visible region (0.7–2.0 eV), |δ| is

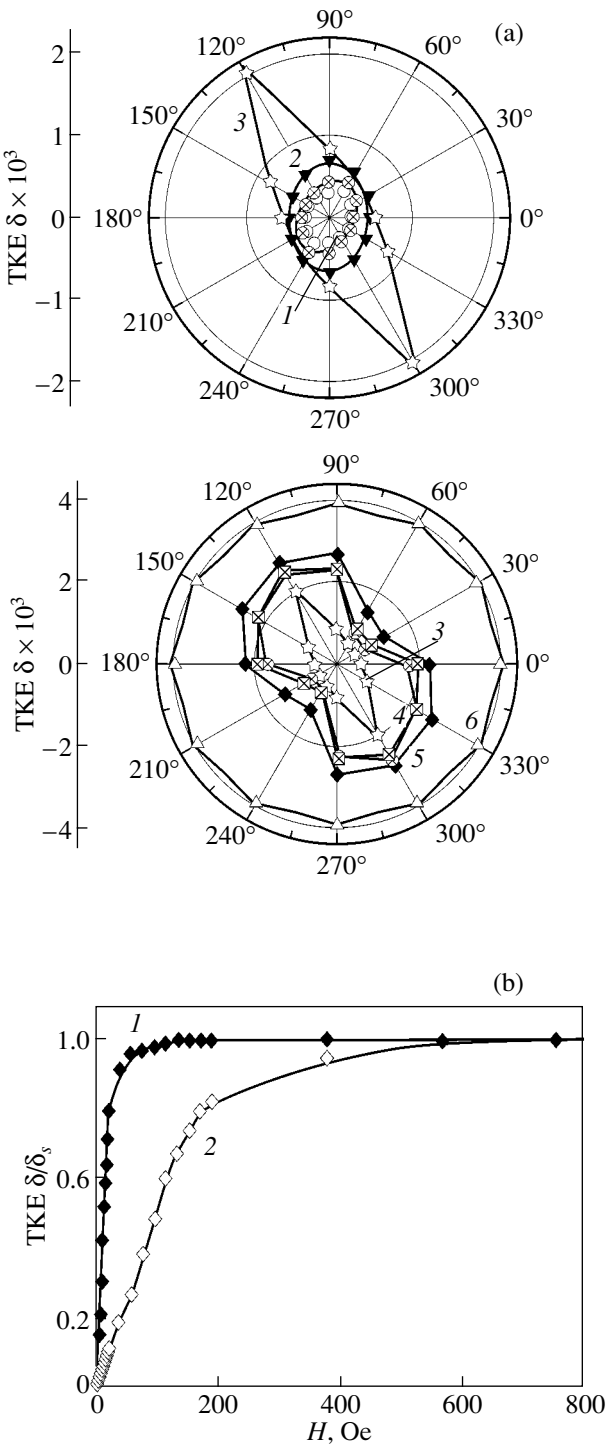

Fig. 6. (a) TKE polar diagrams of the FeNi(20 Å)/SiC(9 Å)/FeNi(20 Å) nanostructure at $h\nu$ = 2.5 eV: (*1*) H = 2, (*2*) 4, (*3*) 5, (*4*) 10, (*5*) 20, and (*6*) 1300 Oe. (b) Field dependence of the TKE at $h\nu$ = 2.5 eV measured along (*1*) the EA and (*2*) HA.

large in the samples with the minimum ferromagnetic-layer thickness. At the edge of the high-energy range of photons ($h\nu$ > 2.0 eV), the dependence of the TKE on the ferromagnetic-layer thickness is ordinary; namely, δ increases with d_{FeNi}, although there are no regular changes in the dispersion and value of the TKE.

The specific features of the $\delta(\nu)$ spectra can be explained as follows. As is known [23], the spectral features of the Kerr effects in low-dimensional structures are determined both by the dispersion of the diagonal and off-diagonal components of the permittivity tensor $[\varepsilon]$ and the thicknesses of the ferromagnetic layers and by the dispersion of the diagonal components of tensor $[\varepsilon]$ and the thickness of the nonmagnetic layer. The inset to Fig. 5 shows the concentration (thickness) dependences of the TKE in different spectral regions. As is seen from Fig. 5a, the values of δ increase virtually linearly with the ferromagnetic-layer thickness over the whole frequency range under study, with higher absolute values of TKE corresponding to smaller values of d_{FeNi}. This result agrees well with the formula

$$\delta_p = \left(A_1 + B_1\frac{d_{\mathrm{FeNi}}}{\lambda} + C_1\frac{d_{\mathrm{SiC}}}{\lambda}\right)\frac{d_{\mathrm{FeNi}}}{\lambda}\frac{\varepsilon_{xy}^{\mathrm{FeNi}}}{\varepsilon_{\mathrm{FeNi}}}\sin\varphi,$$

which was obtained in the Drude approximation and describes the MO properties of two-layer structures whose thickness is smaller than the skin depth [8]. In our case, the total thickness of the layer structure $d_{\mathrm{FeNi}} + d_{\mathrm{SiC}} + d_{\mathrm{FeNi}}$ is far less than both the light wavelength and skin depth. The apparent increase in the TKE of the nanostructures as the ferromagnetic-layer thickness decreases at $h\nu$ < 2.0 eV can be accounted for if we assume that the sign of coefficients A_1 and C_1 is the same and is opposite to that of B_1. Note that analogous changes in the sign and value of the TKE in the near IR region were observed when studying the dispersion $\delta(\nu)$ of a number of ferromagnetic metal–dielectric nanostructures [24].

The inset to Fig. 5b, which shows the dependences of the TKE in the FeNi/SiC/FeNi nanoheterostructures on the thickness of the silicon carbide layer, demonstrates nonlinear changes in the TKE with alternation of the maxima and minima, which is characteristic of multilayer structures. This fact, as well as the induction magnetometric measurements, indicates the existence of exchange interaction between the ferromagnetic layers through the semiconducting interlayer. When explaining the thickness dependence of the MO effects, we also took into account that quantum-confinement effects can substantially affect the MO properties, the frequency dependences of the MO spectra and of the coefficients A_1, B_1, and C_1, and the tensors $[\varepsilon]_{\mathrm{FeNi}}$ and $[\varepsilon]_{\mathrm{SiC}}$ because of small thicknesses of the layers in the layer nanostructures. The cause of the quantum-confinement effects is the quantization of the electronic energy spectrum (density of states) due to a change in the boundary conditions for the phase of the wave function of an electron at each interface in a ferromagnet–semiconductor multilayer nanostructure.

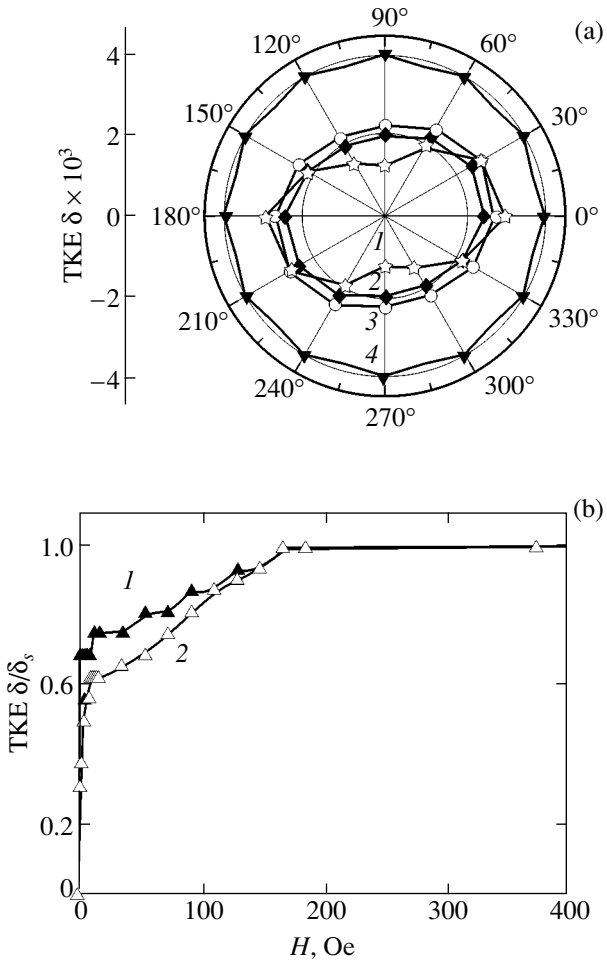

Fig. 7. (a) TKE polar diagrams of the FeNi(60 Å)/SiC(18 Å)/FeNi(60 Å) nanostructure at $h\nu$ = 3.05 eV: (*1*) H = 3.7, (*2*) 7.5, (*3*) 18.7, and (*4*) 750 Oe. (b) Field dependence of the TKE at $h\nu$ = 3.05 eV measured along (*1*) the EA and (*2*) HA.

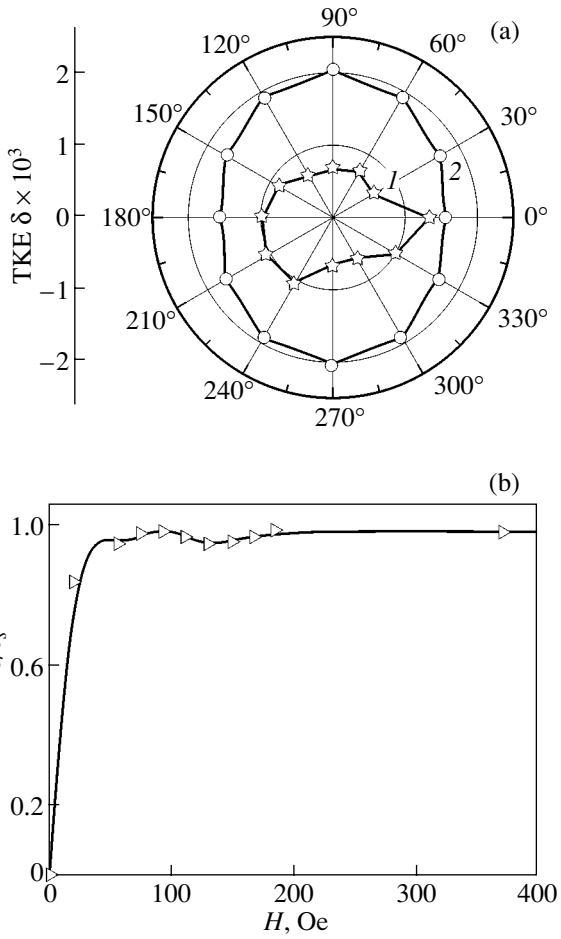

Fig. 8. (a) TKE polar diagrams of the FeNi(20 Å)/SiC(27 Å)/FeNi(20 Å) nanostructure at $h\nu$ = 3.36 eV: (*1*) H = 18 and (*2*) 180 Oe. (b) Field dependence of the TKE at $h\nu$ = 3.85 eV measured along the EA.

Figures 6–9 show the typical polar diagrams [orientation dependences of the TKE $\delta(\alpha)$] constructed in a wide field range for symmetric nanostructures. These figures also show the magnetization curves measured along the easy and hard axes of samples (these axes arose because a static magnetic field $H_=$ was applied along the plane of a sample during its sputtering). In all diagrams, the $H_=$ direction coincides with the 0–180° axis; the fields and photon energies used to measure the TKE are given in the corresponding figures.

As is seen from Figs. 6–9, the saturation field H_s depends substantially on the semiconducting-layer thickness; maximum values of H_s, 600 and 180 Oe, were observed in the structures with semiconducting-layer thicknesses d_s of 9 and 18 Å, respectively. In the samples with thick semiconducting layers, the saturation fields are much smaller; in the samples with d_s = 27 and 30 Å, H_s = 100 and 40 Oe, respectively. For these samples, the EA direction virtually coincides with the direction of the static magnetic field $H_=$, whereas for the samples with smaller d_s the EA direction deviates from the 0–180° direction. We call attention to steps in the $\delta(H)$ curves at low fields and to the intricate form of the $\delta(\alpha)$ orientation dependences, e.g., for the FeNi(20 Å)/SiC(27 Å)/FeNi(20 Å) sample (Fig. 8a). The $\delta(H)$ magnetization curve of this sample (Fig. 8b) is atypical: $\delta(H)$ decreases with increasing amplitude of the applied magnetic field H. On the whole, the magnetic anisotropy in these structures is uniaxial. However, as the magnetizing field increases, the easy axis in the FeNi(20 Å)/SiC(9 Å)/FeNi(20 Å) sample rotates from α = 60° to 120°, which indicates that an anisotropy other than the induced uniaxial anisotropy (e.g., exchange anisotropy) can be admixed to it. The results obtained suggest that the ferromagnetic layers in the samples with thick semiconducting layers are not exchange-coupled and that each layer is individually magnetized in the applied field. For thin SiC layers, the FeNi layers can interact through the semiconductor; that is, the ferromagnetic layers become exchange-cou-

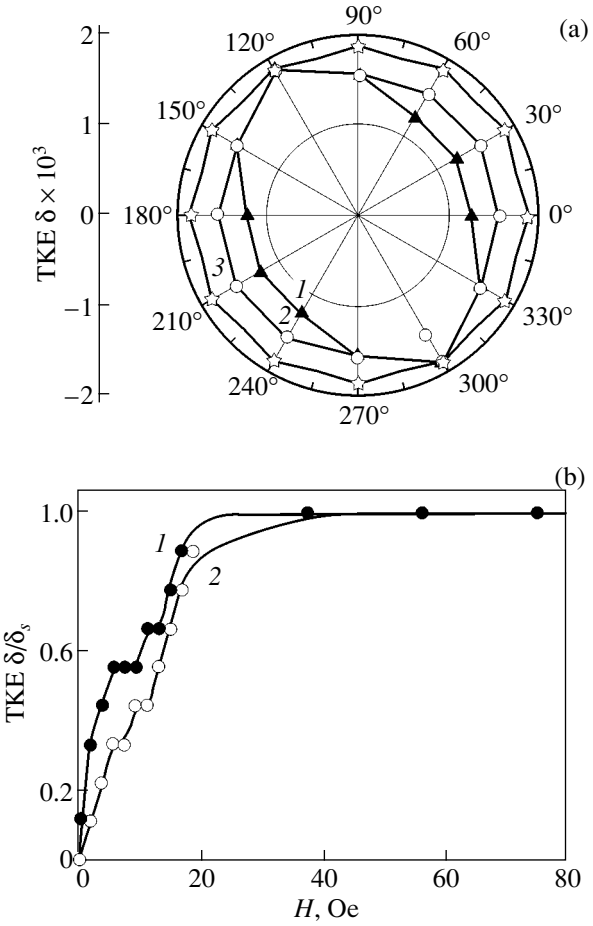

Fig. 9. (a) TKE polar diagrams of the FeNi(30 Å)/SiC(30 Å)/FeNi(30 Å) nanostructure at $h\nu$ = 2.16 eV: (*1*) H = 3.7, (*2*) 18.7, and (*3*) 1500 Oe. (b) Field dependence of the TKE at $h\nu$ = 2.16 eV measured along (*1*) the EA and (*2*) HA.

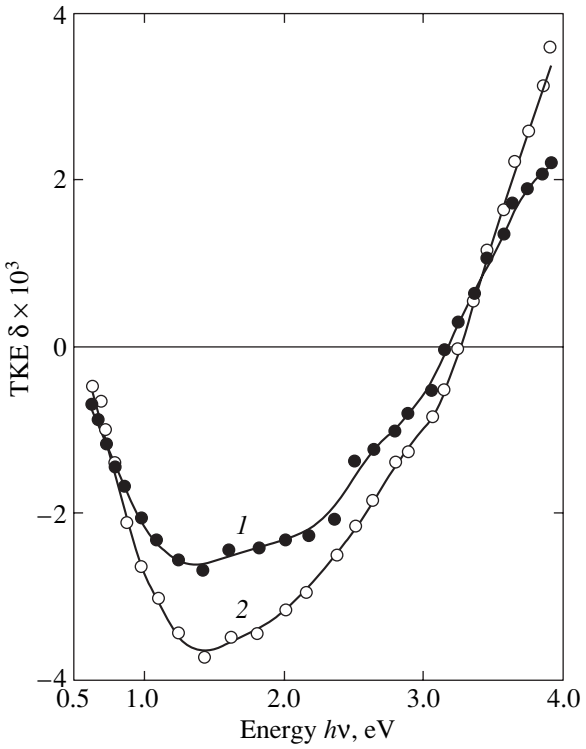

Fig. 10. Dispersion of the TKE in the asymmetric nanoheterostructures: (*1*) FeNi(20 Å)/Ti(12.5 Å)/FeNi(20 Å)/SiC(21 Å) and (*2*) SiC(21 Å)/FeNi(20 Å)/Ti(12.5 Å)/FeNi(20 Å).

pled. The coupling increases with a decrease in the semiconducting-layer thickness and, at certain semiconductor thicknesses, is likely to become antiferromagnetic. The latter is indicated by both the character of rotation of the EA and HA (Fig. 6) and the specific shapes of the $\delta(\alpha)$ diagrams and of the magnetization curves, which are represented by the ratio of the current value of δ to its maximum value δ_S at the field H = 1400 Oe. Possible antiferromagnetic interaction in such structures was noted in [8], where analogous $\delta(\alpha)$ dependences were observed in Fe/GaAs multilayers having various thicknesses of the semiconducting layer.

When studying asymmetric nanostructures using the induction method, we detected the effect of the semiconducting layer on the character of interaction between the ferromagnetic layers. However, the spectra of the response of the ferromagnets to the field H in the case where the semiconducting layer lies above or below the three-layered structure were found to be the same, since the induction method gives information on the magnetic parameters of the whole volume of a sample. Unlike this method, the magnetooptical method can provide data on the magnetic properties of only a few layers. As is seen from Fig. 10, the frequency dependences of the TKE for the samples SiC(21 Å)/FeNi(20 Å)/Ti(12.5 Å)/FeNi(20 Å) and FeNi(20 Å)/Ti(12.5 Å)/FeNi(20 Å)/SiC(21 Å) are different. The anisotropy and the field dependences of the TKE observed in these structures are also different (Figs. 11, 12); that is, the process of magnetization reversal and the magnetic parameters of the asymmetric nanoheterostructures depend on the location of the semiconductor (SC) layer with respect to the ferromagnetic (FM) layers in the three-layered structure FeNi(20 Å)/Ti(12.5 Å)/FeNi(20 Å).

A detailed consideration shows that the samples with the layer sequence SC/FM/TM/FM, where TM stands for a transition metal (titanium), exhibit a uniaxial anisotropy (Fig. 11); the EA makes an angle $\alpha = 30°$ with the field $H_=$ and does not change direction as the amplitude of the magnetizing field H increases. The saturation fields H_s for the EA and HA directions differ greatly (100 and 560 Oe, respectively; Fig. 11b). A large difference in the $\delta(H)$ curves is also observed in other mutually perpendicular directions (e.g., for $\alpha = 0°$ and 90°). In some cases, wide steps, which indicate delays in the process of magnetization reversal when

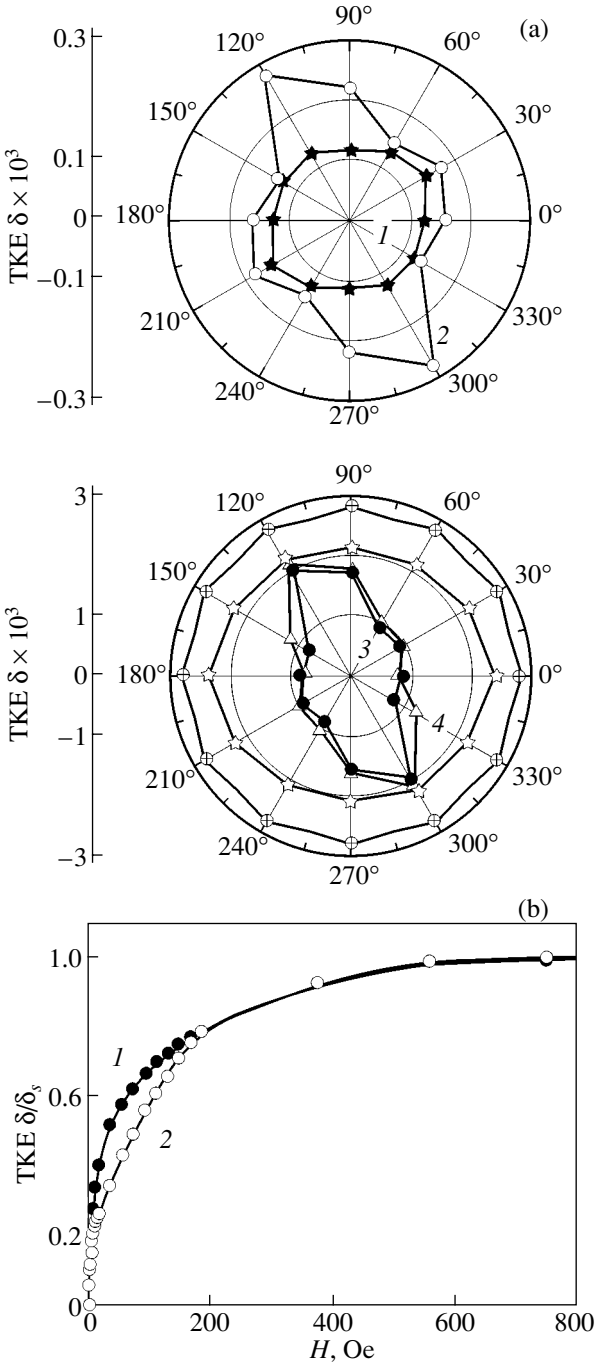

Fig. 11. (a) TKE polar diagrams of the SiC(21 Å)/FeNi(20 Å)/Ti(12.5 Å)/FeNi(20 Å) nanostructure at $h\nu$ = 2.5 eV: (*1*) H = 2, (*2*) 3, (*3*) 5, (*4*) 8, (*5*) 100, and (*6*) 562 Oe. (b) Field dependence of the TKE at $h\nu$ = 2.5 eV measured along (*1*) the EA and (*2*) HA.

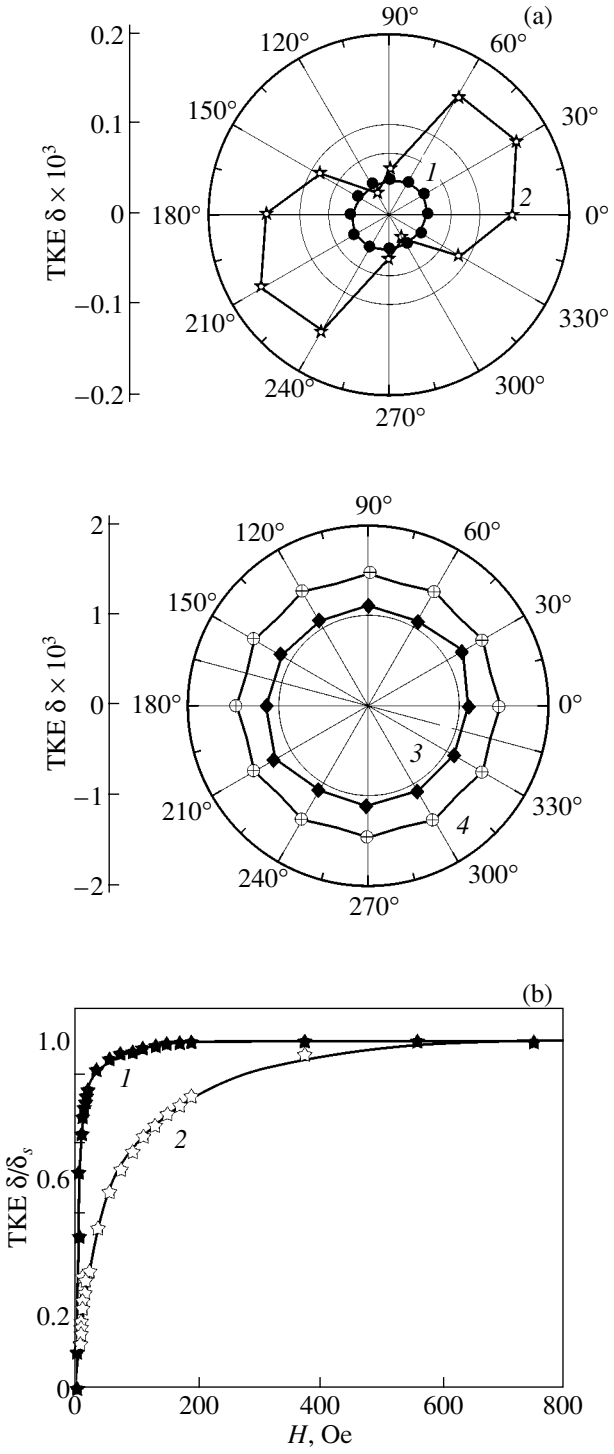

Fig. 12. (a) TKE polar diagrams of the FeNi(20 Å)/Ti(12.5 Å)/FeNi(20 Å)/SiC(21 Å) nanostructure at $h\nu$ = 2.5 eV: (*1*) H = 5, (*2*) 10, (*3*) 100, and (*4*) 562 Oe. (b) Field dependence of TKE at $h\nu$ = 2.5 eV measured along (*1*) the EA and (*2*) HA.

the amplitude of magnetic field H increases, appear in the magnetization curves.

In the case of a sample with the reverse sequence of layers, FM/TM/FM/SC, the $\delta(\alpha)$ polar diagrams and the magnetization curves behave in a complicated manner and differently in different directions (Fig. 12). The anisotropy cannot be described in a simple manner. In small fields (up to 5 Oe), the EA makes an angle $\alpha = 30°$ with the 0–180° direction, and then, in fields $H \geq 5$ Oe, another easy axis, perpendicular to this direction (α =

120°), appears suddenly. Beginning from 10 Oe, the TKE measured in this direction changes slowly as H increases, whereas in the perpendicular direction (α = 30°) the TKE increases rapidly. In a field of ~200 Oe, the anisotropy virtually disappears, although the sample is magnetized to only 80% in both directions. In small fields, the $\delta(H)$ curves also exhibit delays in the development of the effect.

The detected behavior of the $\delta(\alpha)$ orientation dependences and the corresponding $\delta(H)$ spectra, as well as the induction data, can be explained if, just as above, we assume exchange interaction between the ferromagnetic and semiconducting layers. This interaction can appear if a magnetically ordered interface layer (one or two atomic layers thick) forms as a result of interdiffusion between the permalloy and silicon carbide layers. This interaction is likely to be antiferromagnetic, which could explain the change in the EA and HA directions, the steps in the magnetization curves, and the changes in the number of responses in the magnetization-reversal signals of the nanostructures when the magnetizing field changes.

5. CONCLUSIONS

Spin-tunneling magnetoresistive symmetric (FeNi/SiC/FeNi) and asymmetric (FeNi/Ti/FeNi with a silicon carbide layer located either above or below the ferromagnet) nanoheterostructures have been synthesized, and their physical properties have been studied. The effects of the layer thicknesses and the magnetizing field on the response of the ferromagnet–semiconductor system have been studied. The response and magnetic properties of the nanostructures are found to depend nonlinearly on these parameters. The spectral, field, and orientation dependences of the magnetooptical TKE exhibit a number of anomalies, and the magnetooptical and magnetometric data are found to be closely correlated. The appearance of pulsed induction responses of the magnetic–semiconducting system and the anomalies in the $\delta(H)$ spectra and in the $\delta(\alpha)$ orientation dependences are shown to be caused by changes in the character of the magnetic anisotropy in both the asymmetric and symmetric nanostructures.

The experimental results obtained for magnetic–semiconducting nanostructures that differ in the thicknesses of the nonmagnetic and ferromagnetic layers and in their arrangement indicate that they have a complex magnetic structure and suggest that it is necessary to take into account the effect of the nonmagnetic semiconducting layer on the interaction between the ferromagnetic layers. Moreover, it is likely that the ferromagnetic layers affect the magnetic state of the semiconductor and that thin magnetic transition layers enriched in atoms of both ferromagnetic and semiconducting layers form at the interfaces in the nanostructures. The formation of this transition layer (superinterface) is assumed to cause an additional exchange interaction between it and a ferromagnetic layer. This interaction can appreciably affect the magnetic properties of the structures, the processes of magnetization reversal, and the MO properties of the structures. Our experimental results could be explained taking into account this interaction.

The results obtained show that our experimental techniques are efficient for studying the magnetic and MO properties of ferromagnet–semiconductor multilayers and the exchange interactions in them. The spin-tunneling magnetoresistive nanoheterostructures are shown to be promising materials for elements and devices in magnetic spintronics.

ACKNOWLEDGMENTS

This work was supported by the Russian Foundation for Basic Research (project nos. 01-02-16788, 01-02-16403) and the program “Russian Universities” (project no. UR.01.03.006).

REFERENCES

1. M. N. Baibich, J. M. Broto, A. Fert, F. Nguyen Van Dau, F. Petroff, P. Etienne, G. Creuzet, A. Frederich, and J. Chazelas, Phys. Rev. Lett. **61** (21), 2472 (1988).
2. S. S. Parkin, N. More, and K. P. Roche, Phys. Rev. Lett. **64** (19), 2304 (1990).
3. W. R. Bennet, W. Schwaracher, and W. F. Egelhoff, Phys. Rev. Lett. **65** (25), 3169 (1990).
4. T. Katayama, Y. Suzuki, M. Hayashi, and A. Thiaville, J. Magn. Magn. Mater. **126** (1–3), 527 (1993).
5. M. Tondra, J. M. Daughton, C. Nordman, D. Wang, and J. Taylor, J. Appl. Phys. **87** (9), 4679 (2000).
6. M. Bauer, R. Lopusnik, J. Fassbender, B. Hillebrands, J. Bangert, and J. Wecker, J. Appl. Phys. **91** (1), 543 (2002).
7. P. S. Anil Kumar, R. Jansen, O. M. Erve, R. Vlutter, S. D. Kim, and J. C. Lodder, Physica C **350**, 166 (2001).
8. I. D. Lobov, V. M. Maevskii, L. V. Nomerovannaya, M. M. Kirillova, A. A. Makhnev, and F. A. Pudonin, Phys. Met. Metallogr. **91** (1), S33 (2001).
9. M. Johnson, Phys. Rev. B **58** (15), 9635 (1998).
10. P. R. Hammar and M. Johnson, Phys. Rev. B **61** (11), 7207 (2000).
11. S. I. Kasatkin, A. M. Murav’ev, and F. A. Pudonin, Kratk. Soobshch. Fiz. **2**, 20 (2002).
12. L. A. Kuzik, Yu. E. Petrov, F. A. Pudonin, and V. A. Yakovlev, Zh. Éksp. Teor. Fiz. **105** (1), 215 (1994) [JETP **78**, 114 (1994)].
13. S. I. Kasatkin, A. M. Murav’ev, N. P. Vasil’eva, V. V. Lopatin, F. F. Popadinets, and A. V. Svatkov, Mikroélektronika, No. 2, 149 (2000).
14. S. I. Kasatkin, A. M. Murav’ev, and F. F. Popadinets, Zavod. Lab., No. 7, 23 (2001).
15. G. S. Krinchik and V. S. Gushchin, Zh. Éksp. Teor. Fiz. **56** (6), 1833 (1969) [Sov. Phys. JETP **29**, 984 (1969)].

16. S. I. Kasatkin, V. V. Lopatin, A. M. Murav'ev, P. I. Nikitin, F. F. Popadinets, F. A. Pudonin, and A. Yu. Toporov, Sens. Actuators **85**, 221 (2000).

17. S. I. Kasatkin, A. M. Murav'jev, P. I. Nikitin, F. A. Pudonin, A. Yu. Toporov, and M. V. Valeiko, Sens. Actuators **81** (1–3), 57 (2000).

18. E. A. Gan'shina, V. S. Guschin, S. A. Kirov, and N. E. Syr'ev, Fiz. Met. Metalloved. **78** (1), 63 (1994).

19. D. Weller, W. Reim, and K. Sporek, J. Magn. Magn. Mater. **93** (1), 183 (1991).

20. G. Y. Guo and H. Ebert, J. Magn. Magn. Mater. **156** (1–3), 173 (1996).

21. E. A. Gan'shina, D. N. Dzhuraev, A. G. Il'chuk, V. V. Litvintsev, and T. A. Tomas, Fiz. Met. Metalloved. **65** (3), 505 (1988).

22. E. Gan'shina, R. Kumaritova, A. Bogorodisky, M. Kuzmichov, and S. Ohnuma, J. Magn. Soc. Jpn. **23**, 379 (1999).

23. E. Can'shina, A. Granovsky, V. Guschin, M. Kuzmichev, P. Podrugin, A. Kravetz, and E. Shipil, Physica A (Amsterdam) **241** (1), 45 (1997).

24. E. A. Gan'shina, in *Nato ASI Series Frontiers in Magnetism of Reduced Dimension Systems* (Kluwer Academic, 1998), p. 397.

Translated by K. Shakhlevich

Physics of the Solid State, Vol. 46, No. 5, 2004, pp. 902–907. Translated from Fizika Tverdogo Tela, Vol. 46, No. 5, 2004, pp. 875–880.

MAGNETISM AND FERROELECTRICITY

Heat Capacity of the $Pb_5(Ge_{1-x}Si_x)_3O_{11}$ Ferroelectric System

A. A. Bush* and E. A. Popova**

** Moscow State Institute of Radioengineering, Electronics, and Automation, pr. Vernadskogo 78, Moscow, 119454 Russia*
e-mail: abush@ranet.ru

*** Moscow State University, Vorob'evy gory, Moscow, 119899 Russia*

Received August 21, 2003

Abstract—The temperature dependences of the molar heat capacity at constant pressure, C_p, of $Pb_5(Ge_{1-x}Si_x)_3O_{11}$ crystals with $x = 0$, 0.39, and 0.45 in the range 5–300 K, as well as of their permittivity, dielectric losses, and the pyroelectric effect, have been measured. Experimental data on the temperature behavior of the heat capacity are presented in the form of a sum of two Debye and one Einstein terms, $C_p(T) = 0.405C_{D1}(\Theta_{D1} = 160\ \text{K}, T) + 0.53C_{D2}(\Theta_{D2} = 750\ \text{K}, T) + 0.046C_E(\Theta_E = 47\ \text{K}, T)$. Besides a peak in the region of the ferroelectric Curie point $T_c = 450$ K for crystals with $x = 0$, the temperature dependences of the heat capacity did not reveal any other pronounced anomalies. © *2004 MAIK "Nauka/Interperiodica".*

1. INTRODUCTION

Crystals of the lead germanate $Pb_5Ge_3O_{11}$ and of the lead germanate-silicate $Pb_5(Ge_{1-x}Si_x)_3O_{11}$ exhibit clearly pronounced ferroelectric properties, with the Curie point T_c decreasing from 450 to 220 K as the silicon content increases up to ~70 at. % [1–4]. Because the Curie point occupies a convenient position on the temperature scale and these crystals can be potentially applied as a pyroelectric material and for use in ferroelectric storage devices and hologram recording and reading [1, 5–8], they have been attracting considerable interest from researchers over the past three decades. A large number of studies dealing with the structure of these materials and their dielectric, piezo- and pyroelectric, optical, mechanical, and other properties can be found in review [1].

Information available on the heat capacity of $Pb_5(Ge_{1-x}Si_x)_3O_{11}$ crystals are restricted to measurements performed on $Pb_5Ge_3O_{11}$ in the ranges 2–80 and 300–670 K [9, 10]; there are no data altogether on the temperature behavior of the heat capacity of the solid solution under study here. Such data are needed, however, to analyze the properties of the crystals and their variation with temperature. They are of interest, in particular, for proper interpretation of the pyroelectric characteristics of the crystals and for establishing the nature of the anomalous changes they undergo in their dielectric properties. In addition to the clearly pronounced maxima in the permittivity and the dielectric loss tangent at the Curie point, ε_m and $\tan\delta_m$, $Pb_5(Ge,Si)_3O_{11}$ crystals also exhibit anomalous changes in ε and $\tan\delta$ for $T < T_c$ [1, 4] in the form of weakly pronounced maxima in the permittivity at $T = T_1 \approx 240$ K (ε_1) and maxima in the loss tangent at ~230 K ($\tan\delta_1$). The origin of these anomalies remains unclear.

This communication reports on a measurement of the temperature behavior of the molar heat capacity of $Pb_5(Ge_{1-x}Si_x)_3O_{11}$ crystals with $x = 0$, 0.39, and 0.45 made in the range 6–300 K and analyzes both the results obtained and earlier data available on the high- and low-temperature regions [9, 10]. To determine the temperatures at which the properties of these crystals undergo anomalous changes, measurements of the temperature dependences of the permittivity, the loss tangent, and the pyroelectric constant were also performed.

2. PREPARATION OF THE CRYSTALS AND METHODS OF THEIR STUDY

The studies were conducted on $Pb_5(Ge_{1-x}Si_x)_3O_{11}$ single crystals up to a few mm^3 in volume grown by melt solution crystallization [4]. The phase composition of the samples and the orientation of the crystallographic axes in the crystals were checked with a DRON-4 x-ray diffractometer and a POLAM L-213M polarization microscope. The x-ray powder diffraction patterns of the crystals and the trigonal unit cell parameters derived from them ($a = 10.224(3)$ Å, $c = 10.664(3)$ Å for $x = 0$ and $a = 10.120(4)$ Å, $c = 10.547(4)$ Å for $x = 0.45$) are in good agreement with the data available for $Pb_5(Ge_{1-x}Si_x)_3O_{11}$ [1–4].

The molar heat capacity at constant pressure, C_p, was measured on crystals ~200 mg in mass in the range 6–300 K with the use of a standard THERMIS quasi-adiabatic microcalorimeter. The measurements were performed in the heating mode, with 10–15 min allotted for measurement of one point and with changing the temperature in steps of 1–2 K. The relative measurement accuracy improved with temperature from ~5% at 6 K to ~1% at 300 K.

The permittivity ε and the loss tangent $\tan\delta$ were measured with an E7-14 immitance meter at a frequency of 1.0 kHz in the temperature region 80–600 K for $x = 0$ and in the range 80–360 K for $x = 0.33$, 0.39, and 0.45. The pyroelectric effect was studied in the range 100–320 K by the quasi-static method on polarized crystals. The crystals were polarized by heating them above T_c with subsequent cooling in a dc electric field of ~400 V/cm. The pyroelectric constant γ was derived from the relation $\gamma = I/[S(dT/dt)]$, where I is the current that flows through the circuit formed by a sample and a V7-30 electrometer under uniform heating of the crystal at a rate $(dT/dt) \sim 0.1$ K/s and S is the area of the electrodes on the major crystal faces. The samples used in the measurements were single-crystal plates with the major faces perpendicular to the c axis. Silver paste electrodes were deposited on the major faces of the plates. The thickness of the plates was 0.5–1.0 mm, and their area was $S \sim 10$ mm^2.

3. EXPERIMENTAL RESULTS

Figure 1a presents the temperature dependences of the molar heat capacity $C_p(T)$ of $Pb_5(Ge_{1-x}Si_x)_3O_{11}$ crystals with $x = 0$, 0.39, and 0.45 measured in the range 4.2–300 K, as well as the $C_p(T)$ relations derived for $Pb_5Ge_3O_{11}$ from DSC data in the range 300–670 K [9]. Shown graphically in the bottom part of the figure is the temperature behavior of the permittivity ε, the loss tangent $\tan\delta$, and the pyroelectric constant γ for crystals with $x = 0$, 0.33, 0.39, and 0.45.

The maxima in the $\varepsilon(T)$ relations seen at 450, 320, 278, and 269 K for $x = 0$, 0.33, 0.39, and 0.45, respectively, are obviously associated with the ferroelectric phase transitions the crystals undergo. These data on the Curie point T_c are borne out by the maxima in the pyroelectric constant observed to occur in the region of these temperatures and by the absence of a pyroelectric effect at higher temperatures. For crystals with $x < 0.39$, the $\varepsilon(T)$ plots also reveal anomalies in the vicinity of $T = T_1 \approx 240$ K $< T_c$, which are accompanied by maxima in the $\tan\delta(T)$ graphs at ~230 K. The concentration-induced changes in the maximum values of ε and $\tan\delta$ at T_c and T_1 and in the positions of these maxima are in line with the report from [4] that an increase in Si content in crystals in the region of $x = 0$–0.39 reduces T_c, ε_m, and $\tan\delta_m$ and increases T_1, ε_1, and $\tan\delta_1$; at $x = 0.39$, the two anomalies at T_c and T_1 merge into one ($T_m = T_1$) with an abrupt increase in $\varepsilon_m(=\varepsilon_1)$, after which T_c, ε_m, and $\tan\delta_m$ decrease with increasing Si content.

In the temperature region where spontaneous polarization undergoes a change, the $C_p(T)$ dependence of $Pb_5Ge_3O_{11}$ exhibits an additional anomalous contribution to the heat capacity, which features a peak (characteristic of second-order phase transitions) at the Curie point. In addition to this peak, the $C_p(T)$ relation was

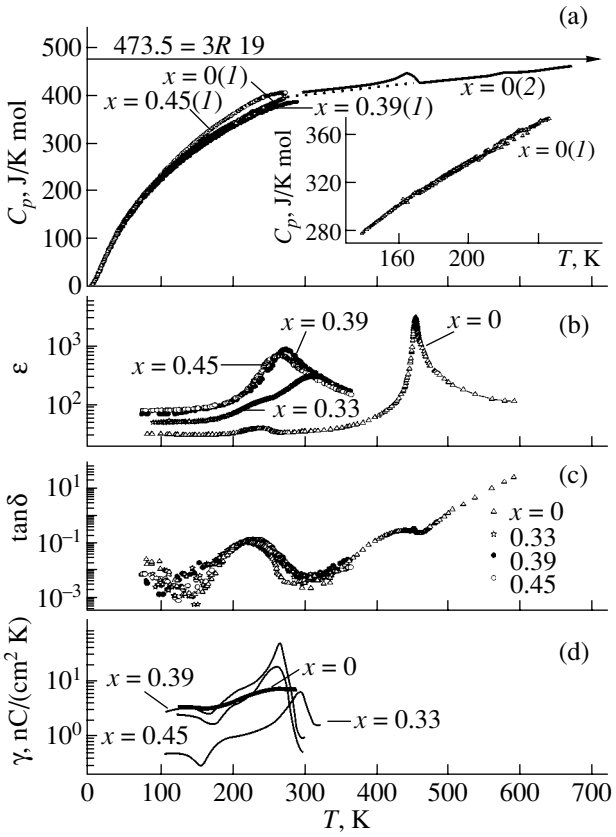

Fig. 1. Temperature dependences of the following quantities measured for the $Pb_5(Ge_{1-x}Si_x)_3O_{11}$ crystals with $x = 0$, 0.33, 0.39, and 0.45: (a) the molar heat capacity C_p at constant pressure: (*1*) our data and (*2*) data from [9]; (b, c) the permittivity ε and the loss tangent $\tan\delta$ measured along the c axis at a frequency of 1 kHz; and (d) the pyroelectric constant γ along the c axis.

reported in [9] to have a weakly pronounced maximum at $T = 570$ K. In the region of the low-temperature anomalies in the dielectric properties of the crystals (near $T_1 \sim 230$ K), the $C_p(T)$ relation exhibits an increased scatter of experimental points, but this scatter remains largely within experimental error (see inset to Fig. 1a). Above 670 K, the heat capacity C_p approaches the classical Dulong–Petit limit of $3Rs$, where R is the universal gas constant and s is the number of atoms in the formula unit of $Pb_5Ge_3O_{11}$ ($s = 19$).

The excess heat capacity associated with the ferroelectric phase transition was found by subtracting from the measured heat capacity its regular part C_{pn} defined by the baseline in the $C_p(T)$ graph. The baseline was derived by extrapolating the heat capacity from the temperature region above T_c (466–500 K) to the region lying below T_c (300–310 K), excluding the phase transition region. Estimation of the entropy of the transition ΔS from the excess heat capacity near T_c yields $\Delta S = \int (C_p - C_{pn})dT/T \approx 2.5$ J/K mol. This estimate is sub-

stantially smaller than $R\ln 2 = 5.76$ J/K mol, the figure predicted for the order–disorder transitions [11], which suggests the ferroelectric phase transition in $Pb_5Ge_3O_{11}$ to occur through the displacive mechanism or to be of a nature intermediate between the displacive and the order–disorder mechanisms.

The temperature dependences of the heat capacity of the $Pb_5(Ge_{1-x}Si_x)_3O_{11}$ solid solutions with $x = 0.39$ and 0.45 are basically similar to the $C_p(T)$ behavior of the lead germanate with $x = 0$. This similarity stems apparently from the fact that the major contribution to the lattice heat capacity of crystals of this system is due to the low-frequency vibrations of the Pb–O bonds, which change insignificantly in Si $\longrightarrow$ Ge substitutions. However, in contrast to the $C_p(T)$ relations for crystals with $x = 0$, the $C_p(T)$ relations for solid solutions do not exhibit clearly pronounced anomalies in the region of their T_c. This observation was quite unexpected, because the ferroelectric phase transition in these crystals becomes manifest in the temperature dependences of the dielectric properties and of the pyroelectric effect (Fig. 1). This behavior can be accounted for by the noticeable decrease in the spontaneous polarization of the crystals (from 4.8 $\mu C/cm^2$ at $x = 0$ to 1.7 $\mu C/cm^2$ for $x = 0.33$) and the diffuseness of the ferroelectric phase transition observed when Ge is replaced by Si (see Fig. 1, as well as [1–4]). The solid solutions can also undergo qualitative changes in their structure and properties for $x \geq 0.39$. This assumption is supported by the observation that, at this concentration, T_c coincides with T_1 and the dielectric characteristics of the crystals undergo abrupt changes. The slight decrease in the heat capacity of the solid solutions with $x = 0.39$ in comparison with the pure lead germanate can be assigned to the decrease in the molar mass of the phase resulting from the Si substituting for Ge. This substitution should exert a similar effect on the heat capacity of the $x = 0.45$ solid solution as well. In contrast to C_p at $x = 0.39$, however, its heat capacity increases as compared to C_p at $x = 0$ (Fig. 1). This growth may originate from the above-mentioned qualitative changes in the crystal structure occurring for $x > 0.39$.

When cooled down to the lowest temperatures attained, these crystals do not exhibit the rise $C_pT^{-3} \sim T^{-3/2}$, which has been observed in $LiNbO_3$, $LiTaO_3$, $BaTiO_3$, TGS, and KDP ferroelectric crystals and attributed to the domain wall contribution [12].

The normalized room-temperature molar heat capacity defined as $C_p^* = C_p/s$ was found to be $C_p^* = 21.0$ J/K mol for these crystals, which is noticeably in excess of analogous figures available for ferroelectric crystals $Li_2Ge_7O_{15}$ ($C_p^* = 17.6$ J/K mol) and $NaLiGe_4O_9$ ($C_p^* = 17.9$ J/K mol) [13]. In accordance with the atomic mass effect, the phonon frequencies of lead germanate should be lower than those of the lithium–sodium germanate, which brings about a decrease in the Debye temperature and, accordingly, in the heat capacity of lead germanate (containing heavier atoms).

4. ANALYSIS AND DISCUSSION OF THE RESULTS

Since the crystals under study re dielectrics, the major contribution to the heat capacity should be due to the elastic lattice vibrations. In the harmonic approximation, this contribution is defined as [14, 15]

$$C_V = k_B \int_0^{\omega(\max)} (\hbar\omega/k_BT)^2 \exp(\hbar\omega/k_BT) \times g(\omega)d\omega/[\exp(\hbar\omega/k_BT) - 1]^2,$$

where C_V is the molar heat capacity at constant volume, k_B is the Boltzmann constant, ω is the lattice mode frequency, ω_{max} is the highest frequency in the spectrum, $\hbar$ is Planck's constant, and $g(\omega)$ is the normal-vibration frequency distribution function, for which the normalization condition $\int_0^{\omega(\max)} g(\omega)d\omega = 3N$ is met, with N being the number of atoms in the lattice. Using the thermodynamic relation $C_p - C_V = 9\alpha^2BV_mT$ [15] (α is the temperature coefficient of linear expansion, B is the bulk compression modulus, V_m is the molar volume) and accepting the available data $\alpha \approx 7.8 \times 10^{-6}$ K^{-1} [2], $B \approx 0.7 \times 10^{11}$ N/m^2 [16], and $V_m = 1.92 \times 10^{-4}$ m^3, C_p can be found to differ from C_V by no more than ~1.0% at 300 K, and this difference tends to zero with decreasing temperature. Therefore, we neglect the difference between C_V and C_p in what follows.

To calculate C_p using the above relation, one needs the spectrum of normal mode frequencies. Determination of this spectrum is a problem of staggering complexity; therefore, various approximations are usually invoked [14, 15], in which the distribution function is assumed to be equal either to $g_E(\omega) = 3N\delta(\omega - \omega_E)$ (the Einstein model) or to $g_D(\omega) = 9N\omega^2/\omega_{max}^3$ for $\omega \leq \omega_{max}$ and $g_D(\omega) = 0$ for $\omega > \omega_{max}$ (the Debye model) or again to their superposition $\Sigma_i x_i g_E(\omega) + \Sigma_j y_j g_D(\omega)$.

In the Einstein model, the heat capacity is defined as $C_E = 3RsE(\Theta_E/T)$, where $E(x) = x^2\exp(x)/[\exp(x) - 1]^2$ is the Einstein function; ω_E and $\Theta_E = \hbar\omega_E/k_B$ are the Einstein characteristic frequency and temperature, respectively. In the Debye model, $C_D = 3RsD(\Theta_D/T)$, where $D(\Theta_D/T) = 3(T/\Theta_D)^3\int_0^{\Theta(D)/T} x^4\exp(x)dx/[\exp(x) - 1]^2$ is the Debye heat capacity function. In Debye's theory of lattice heat capacity, the crystal is treated as an isotropic continuous elastic medium, with only the contribution of the acoustic lattice vibrations taken into account directly. The optical mode contribution can be included only by properly setting the number of degrees of free-

dom. Considered in the framework of these assumptions, the Debye temperature is determined by the acoustic wave velocity in the crystal according to the relation $\Theta_D = (\hbar/k_B)(6\pi^2 N/V)^{1/3}c$, where V is the crystal volume and c is the average reciprocal cubed sound velocity, $3/c^3 = 1/c_L^3 + 2/c_T^3$, with c_L and c_T being the velocities of the longitudinal and transverse sonic waves, respectively.

The experimental relations can be conveniently compared with the Einstein and Debye models in the C_pT^{-3}–$\log T$ vs. $\log T$ coordinates, in which the Debye contribution to $C_p(T)$ manifests itself as a horizontal section in the low-temperature domain ($T < \Theta_D/10$) and the Einstein term, as a characteristic maximum (Fig. 2), whose position is related to the Einstein temperature through $T_{max} \approx \Theta_E/4.928$ and to the Einstein frequency ν_E (in cm^{-1}) as $T_{max} \approx 3.4/\nu_E$.

This analysis was carried out for a number of ferroelectric and related crystals using a comparatively simple scheme to calculate the parameters [12]. The data on the heat capacity were presented in the form of a sum, $C_p = C_D(\Theta_D, T) + 3RrE(\Theta_E/T) + C_{LT}$, including the Debye function, the Einstein function, and the low-temperature ($T < 10$ K) domain wall contribution $C_{LT} \sim T^{3/2}$, with three fitting parameters for the C_D and C_E contributions, namely, $-\Theta_E$, Θ_D, and r (r is the number of atoms in the formula unit that contribute to the Einstein term). The Debye temperature (needed to calculate the Debye contribution) was derived from the low-temperature part of the heat capacity relation, which for low enough temperatures ($T < \Theta_D/50$ [15]) assumes the form $C_p(T) = \beta T^3$, with $\beta = 12\pi^4 Rs/5\Theta_D^3$. The value of r was extracted from the graph of the relation $C_E(T) = C_p(T) - C_D(T)$, which, when plotted in the $\ln[T^2C_E(T)] - 1/T$ vs. $1/T$ coordinates, can be approximated with a straight line in the low-temperature domain, because at low temperatures the $C_E(T)$ relation can be cast as $C_E(T) = 3Rr(\Theta_E/T)^2\exp(-\Theta_E/T)$. Fairly good agreement between the experimental and calculated heat capacity data was reached for a number of crystals ($KTaO_3$, $LiNbO_3$, $BaTiO_3$, TGS, KDP, TlCl, and others) with discrepancies of not over 5%.

The C_pT^{-3} vs. $\log T$ relation measured on $Pb_5(GeSi)_3O_{11}$ crystals was found to differ strongly from the predictions based on the simple single-term Debye model in that it has a distinct maximum at $T_{max} =$ 9.5 K for $x = 0$ and 0.39 (10.5 K for $x = 0.45$); C_pT^{-3} at T_{max} exceeds the value of C_DT^{-3} predicted within the Debye model by a factor of 2.3 (Fig. 2). The Debye region within which $C_p = \beta T^3$ lies below 3 K. The presence of a peak in the C_pT^{-3} graph implies that no combination of Debye terms can fit the data on C_p. The peak in the $C_p(T)T^{-3}$ relation, according to [12], implies that the heat capacity contains a contribution from the Einstein term with a low-frequency characteristic mode

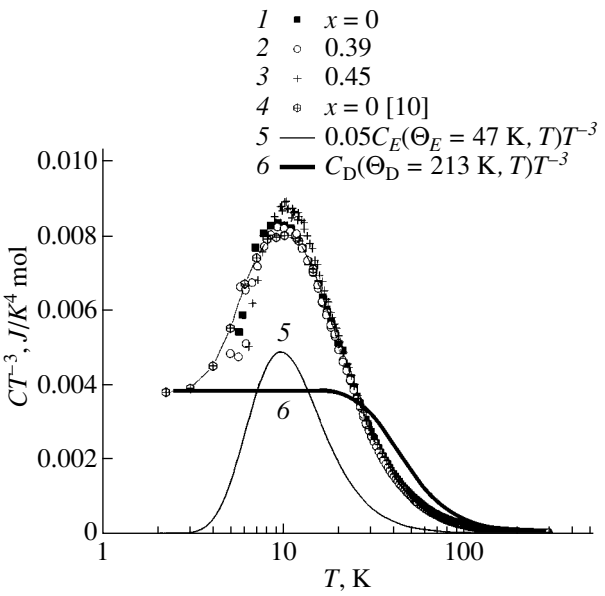

Fig. 2. C_pT^{-3} vs. $\log T$ dependences: (*1–4*) experimental plots for $Pb_5(Ge_{1-x}Si_x)_3O_{11}$ crystals constructed using (*1–3*) our data for $x = 0$, 0.39, and 0.45 and (*4*) data from [10] for $x = 0$; (*5*) plots drawn using the Einstein model $C_E = 3RsE(\Theta_E/T)$ with $\Theta_E = 47$ K and $s = 19$; and (*6*) the Debye model $C_D = 3RsD(\Theta_D/T)$ with $\Theta_D = 213$ K and $s = 19$.

$\nu_E = 32.5$ cm^{-1} and a characteristic Einstein temperature $\Theta_E = 47$ K. This Einstein contribution becomes insignificant for $T \lesssim T_{max}/4$ compared to the Debye term, because below T_{max} it falls off exponentially with temperature. The mode frequencies $\nu_1 = 30.3$ and $\nu_2 = 37.7$ cm^{-1} observed in the Raman spectrum of the crystals at 110 K [17] are close to the value $\nu_E = 32.5$ cm^{-1} obtained here.

The limiting low-temperature calorimetric Debye temperature $\Theta_D(0)$, as derived from the values of C_p [10] for $T < 3$ K under the assumption of 3×19 vibrational degrees of freedom per formula unit, is 213 K. This value is close to the figure calculated from the sound velocities measured in crystals at $T = 300$ K [18], namely, $\Theta_D = 216$ K. Figure 3 plots the temperature dependence of the Debye calorimetric temperature $\Theta_D(T)$, which was extracted from the $C_p(T)$ graph using tabulated values of the Debye function $D(\Theta_D/T)$. As the temperature increases from 2 to 280 K, Θ_D grows from 213 to 550 K, with a minimum of 160 K passed in the region of 10 K. This minimum in $\Theta_D(T)$ should apparently be associated with the maximum in the $C_p(T)T^{-3}$ relation. A distinct minimum in the $\Theta_D(T)$ relation is also observed in the region of the Curie point of the crystals. The strong temperature dependence of Θ_D reflects a deviation of the phonon spectrum $g(\omega)$ of $Pb_5Ge_3O_{11}$ crystals from the parabolic Debye dependence.

In view of the currently available data on $\Theta_D(0)$ and Θ_E, the experimental relation $C_p(T)$, according to [12],

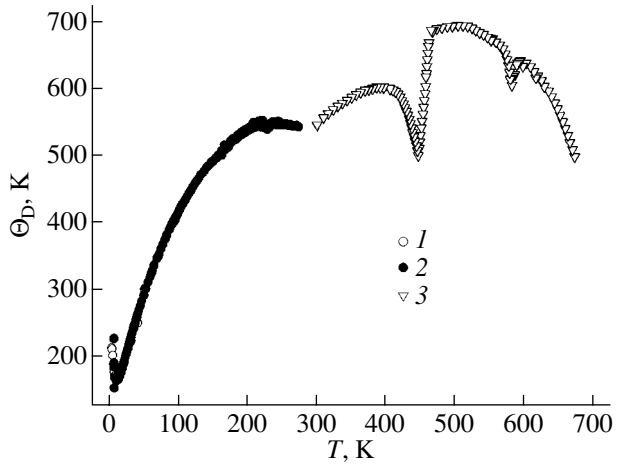

Fig. 3. Characteristic Debye temperature calculated for $Pb_5Ge_3O_{11}$ from the relation $C_p(T) = (3 \times 19)RD(\Theta_D/T)$ for various temperatures with the use of (*1*) our data, (*2*) data from [10], and (*3*) data from [9] on $C_p(T)$ under the assumption of 3×19 vibrational degrees of freedom per formula unit.

should represent a combination of two major terms, $C_p(T) = C_D(\Theta_D = 213\ \text{K}, T) + (r/s)C_E(\Theta_E = 47\ \text{K}, T)$. For $T > 26.5$ K, however, the $C_D(\Theta_D = 213, T)T^{-3}$ curve passes above the experimental $C_p(T)T^{-3}$ curve (Fig. 2); therefore, it does not appear possible to fit the $C_pT^{-3}(T)$ relation with the above sum $C_D + (r/s)C_E$. This observation, as well as the deviation from the $C_p = \beta T^3$ dependence in the top part of the region $T < (213\ \text{K})/50$, suggests that the low-temperature limiting Debye temperature thus found is overestimated.

The substantial differences between the masses of the Pb, Ge, and O atoms and between the force constants of the Pb–O and Ge–O bonds, as well as the available data on the crystal structure of $Pb_5Ge_3O_{11} = Pb_5[GeO_4][Ge_2O_7]$ [1], give grounds to consider the $[GeO_4]$ rigid tetrahedral groups as effective atoms at low temperatures. This reduces the number of vibrational degrees of freedom per formula unit from 3×19 to 3×8. The low-temperature limiting Debye temperature determined within this assumption decreases to $\Theta_D(0) = 160$ K. Note that, if we accept the above reduction in the number of vibrational degrees of freedom, the Debye temperature derived from sound-velocity data will likewise decrease from 216 to 162 K, because the number of atoms per unit volume in the corresponding expression decreases.

A proper fitting revealed that the experimental $C_p(T)$ relation can be represented as a sum of two Debye and one Einstein contributions, $C_p(T) = 0.405C_{D1}(\Theta_{D1} = 160\ \text{K}, T) + 0.53C_{D2}(\Theta_{D2} = 750\ \text{K}, T) + 0.046C_E(\Theta_E = 47\ \text{K}, T)$. The calculated values of the heat capacity differ by no more than 3% from the measurements, with the exception of the range 25–90 K and of the region near T_c (430–452 K), where this difference grows to

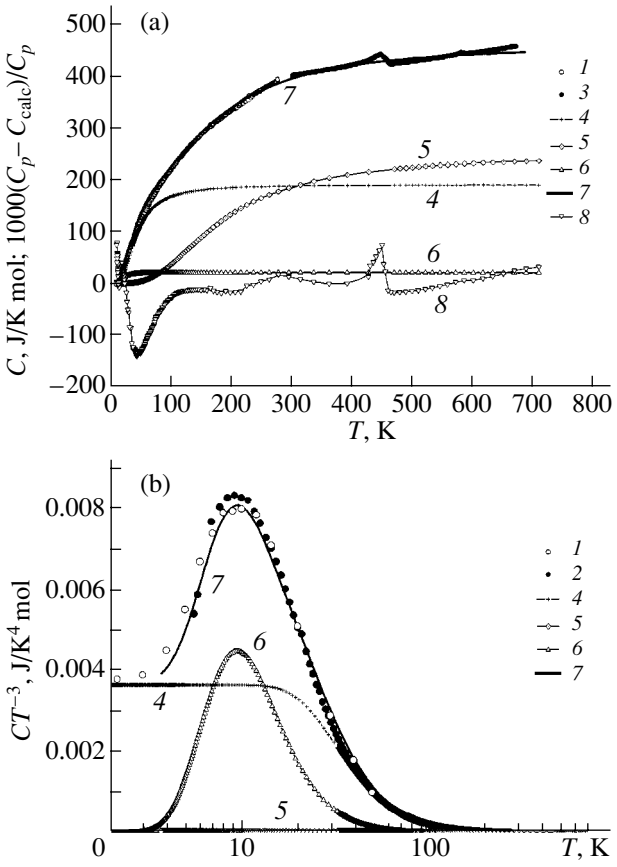

Fig. 4. Temperature dependences of (a) the molar heat capacity C and the relative difference, $(C_p - C_{calc})/C_p$, between the measured, C_p, and calculated, $C_{calc} = C_{D1} + C_{D2} + C_E$, heat capacities and (b) the molar heat capacity divided by the temperature cubed, CT^{-3}: (*1–3*) experimental graphs constructed using our data and the data from [9] and [10], respectively; (*4–7*) plots calculated from the relations $C_{D1} = 0.405 \times 3RsD(\Theta_{D1}/T)$ with $\Theta_{D1} = 160$ K, $C_{D2} = 0.53 \times 3RsD(\Theta_{D2}/T)$ with $\Theta_{D2} = 750$ K, $C_E = 0.046 \times 2RsE(\Theta_E/T)$ with $\Theta_E = 47$ K, and $C_{calc} = C_{D1} + C_{D2} + C_E$, respectively; (*8*) $1000(C_p - C_{calc})/C_p$.

maximum values of –15% and +7.5% at 40 and 450 K, respectively (Fig. 4a).

The fitting parameters of the expansion were suggested by the following reasoning. The low-temperature limiting Debye temperature Θ_{D1} was derived from the relation $C_p(T) = (12\pi^4 Rs^*/5\Theta_{D1}^3)T^3$, which is valid for crystals for $T < 3$ K, assuming the effective number of atoms per formula unit s^* to be 8. The relative contribution from $C_{D1}(\Theta_{D1})$ is determined reliably by the low-temperature plateau in the $C_p(T)^*T^{-3}$ dependence for $T < 3$ K. The relative contribution and the characteristic temperature of the Einstein term are determined by the magnitude and position of the peak in the $C_p(T)T^{-3}$ relation. The high-temperature region was approximated by the Debye term, whose characteristic temperature was estimated from the data on the temperature

dependence (presented above) of the calorimetric Debye temperature and on the frequencies of the modes observed in the IR and Raman spectra of the crystals [4, 17].

Based on the values of Θ_{D1}, Θ_{D2}, and Θ_E, one may conclude that the C_{D1} and C_E contributions are determined by the low-frequency vibrational modes of the crystal and the C_{D2} contribution, by the high-frequency modes. The separation of the vibrational modes of the $Pb_5[GeO_4][Ge_2O_7]$ crystals into two low- and high-frequency groups originates from the composition and structure of the crystals and is in accord with experimental studies of the IR and Raman spectra [4, 17]. Because the force constants of the Ge–O bonds are considerably larger than those of the other crystal bonds, the vibrational modes split into two groups; more specifically, 90 vibrational modes are connected with the internal vibrations of the $[GeO_4]$ tetrahedra, and 81 low-frequency modes are associated with the translational and rotational vibrations of the Pb cations and the $[GeO_4]$ tetrahedral groups [17]. The fraction of high-frequency modes in the phonon spectrum of the crystals, 90/171 = 0.526, is close to that of the C_{D2} contribution to the heat capacity.

The $C_p(T)T^{-3}$ relation, with T replaced by $\nu = 4.928T/1.4388$, is reported [19–21] to closely approximate the $g(\nu)/\nu^2$ function (with ν in cm^{-1}). From this it follows that the density of vibrational states has a maximum at $\nu_0 = 32.5\ cm^{-1}$ corresponding to the maximum in C_pT^{-3} located at 9.5 K. The deviation of the real from the Debye vibrational density of states, $g_D(\nu) \sim \nu^2$, in the vicinity of $32.5\ cm^{-1}$ accounts for the excess growth in C_pT^{-3} near 9.5 K. As the temperature increases, C_pT^{-3} tends rapidly to zero, which drastically reduces the amount of information that can be gained on the high-frequency region of the $g(\nu)$ phonon spectrum from the $C_p(T)T^{-3}$ curve.

5. CONCLUSIONS

Thus, analysis of the temperature dependence $C_p(T)T^{-3}$ permits us to make a rough reconstruction of the phonon spectrum of $Pb_5Ge_3O_{11}$ crystals. This analysis has been employed to present the phonon spectrum of the crystals as a linear combination of three, two Debye and one Einstein, terms. This representation is actually nothing more than a smoothed model of the real phonon spectrum of the crystals under study, which obviously has a substantially more complex frequency composition. However, this model offers the possibility of qualitatively describing the behavior of the heat capacity over a broad temperature range.

ACKNOWLEDGMENTS

This study was supported by the Russian Foundation for Basic Research, project no. 02-02-17798.

REFERENCES

1. A. A. Bush and Yu. N. Venevtsev, *Monocrystals with Ferroelectrics and Related Properties in the PbO–GeO_2 System and Their Possible Applications* (NIITÉKhIM, Moscow, 1981).
2. H. Iwasaki, S. Miyazawa, H. Kiyomada, K. Sugii, and N. Niizeki, J. Appl. Phys. **43** (12), 4907 (1972).
3. W. Eysel, R. W. Wolfe, and R. E. Newnham, J. Am. Ceram. Soc. **56** (3), 185 (1973).
4. A. A. Bush and Yu. N. Venevtsev, Kristallografiya **26** (2), 349 (1981) [Sov. Phys. Crystallogr. **26**, 198 (1981)].
5. C. R. Jones, N. Show, and A. W. Vere, Electron. Lett. **8** (14), 346 (1972).
6. R. Watton, C. Smith, and G. R. Jones, Ferroelectrics **14**, 719 (1976).
7. T. Li and S. T. Hsu, Integr. Ferroelectr. **34** (1–4), 1495 (2001).
8. S. Mendricks, X. Yue, R. Pankrath, H. Hesse, and D. Kip, Appl. Phys. B: Lasers Opt. **68** (5), 887 (1999).
9. S. A. Ivanov, S. A. Cherneĭ, V. P. Mikhal'chenko, S. G. Tarasov, and Yu. N. Venevtsev, Fiz. Tverd. Tela (Leningrad) **21** (9), 2545 (1979) [Sov. Phys. Solid State **21**, 1467 (1979)].
10. E. Gmelin and G. Burns, Phys. Rev. B **38** (1), 442 (1988).
11. B. A. Strukov and A. P. Livanyuk, *Physical Principles of Ferroelectric Phenomena in Crystals* (Nauka, Moscow, 1995).
12. W. N. Lawless, Phys. Rev. B **14** (1), 134 (1976).
13. K. Morikawa, T. Atake, M. Wada, and T. Yamaguchi, J. Phys. Soc. Jpn. **67** (6), 1994 (1998).
14. M. Born and K. Huang, *Dynamical Theory of Crystal Lattices* (Clarendon, Oxford, 1954; Inostrannaya Literatura, Moscow, 1958).
15. C. Kittel, *Introduction to Solid State Physics*, 5th ed. (Wiley, New York, 1976; Nauka, Moscow, 1978).
16. G. R. Barsch, L. J. Bomczar, and R. E. Newnham, Phys. Status Solidi A **29**, 241 (1975).
17. D. J. Lockwood, H. J. Hosea, and W. Taylor, J. Phys. C **13** (8), 1539 (1980).
18. Y. Ohmachi and N. Uchida, J. Appl. Phys. **43** (8), 3583 (1972).
19. I. M. Lifshitz, Zh. Éksp. Teor. Fiz. **26**, 551 (1954).
20. R. G. Chambers, Proc. Phys. Soc. London **78**, 941 (1961).
21. A. Junod, T. Jarlbord, and J. Muller, Phys. Rev. B **27** (3), 1568 (1983).

Translated by G. Skrebtsov

Physics of the Solid State, Vol. 46, No. 5, 2004, pp. 908–914. Translated from Fizika Tverdogo Tela, Vol. 46, No. 5, 2004, pp. 881–887.

MAGNETISM AND FERROELECTRICITY

Dielectric and Optical Properties of $Pb(Mg_{1/3}Nb_{2/3})_{0.8}Ti_{0.2}O_3$ (PMNT-0.2) Ferroelectric Relaxor Single Crystals

L. S. Kamzina*, I. P. Raevskiĭ, S. M. Emel'yanov**, S. I. Raevskaya**, and E. V. Sahkar****

**Ioffe Physicotechnical Institute, Russian Academy of Sciences, Politekhnicheskaya ul. 26, St. Petersburg, 194021 Russia*

***Institute of Physics, Rostov State University, Rostov-on-Don, 344090 Russia*

Received October 13, 2003

Abstract—The dielectric and optical (optical transmission, small-angle light scattering, birefringence) properties of PMNT-0.2 single crystals and their variation induced by a dc electric field have been studied. The birefringence was found to increase anomalously at the transition from the rhombohedral ferroelectric to the inhomogeneous relaxor phase (the spontaneous ferroelectric transition temperature T_{sp}). Below T_{sp}, the dielectric and optical properties were observed to exhibit anomalies originating from reorientation and growth of domains in size. Unlike ferroelectric relaxors of the type of $PbB'_{1/3}B'_{2/3}O_3$ and $PbB'_{1/2}B'_{1/2}O_3$, in PMNT-0.2 neither induction of the ferroelectric phase by an electric field nor thermally stimulated destruction of the ferroelectric state occurs through the percolation mechanism (i.e., they are not accompanied by anomalously narrow maxima in small-angle light scattering). This is attributed to the inhomogeneous structure of the relaxor phase, as a result of which the phase transition does not take place simultaneously in various regions of the crystal. © *2004 MAIK "Nauka/Interperiodica"*.

1. INTRODUCTION

Solid solutions $(1 - x)Pb(Mg_{1/3}Nb_{2/3})O_3$–$xPbTiO_3$ (PMNT–*x*), which serve as classical model objects for investigating the physics of ferroelectric relaxors, have been given considerable attention recently [1–9]. This can be attributed to both the obvious application potential of these materials, which exhibit unique dielectric, piezoelectric, electrostriction, and other properties, and the possibility of varying the characteristics of these compounds within a broad range, from typical relaxor characteristics to properties inherent in normal ferroelectrics, by properly varying the content of $PbTiO_3$. In the classical ferroelectric relaxor PMN, despite the formation of polar nanoregions (3–5 nm) below $T_B \approx 360$°C and an increase in their number and average size under a further lowering of temperature, no structural phase transition occurs and the crystal remains in the macroscopically cubic phase down to 5 K [2, 4, 10]. At the same time, in PMNT–*x* compositions, in addition to relaxor behavior, x-ray diffraction showed a transition to the rhombohedral phase to occur even as low as at $x \approx 0.05$ [4, 5]. At $x \approx 0.10$ in ceramics [6] and at $x \approx 0.20$ in crystals [7], this spontaneous transition from the macroscopically cubic relaxor phase to the rhombohedral ferroelectric state becomes evident already in the temperature dependence of ε and manifests itself as a step, whose temperature position is practically independent of frequency [11]. At the same time, one observes a considerable frequency dependence both of the temperature T_m of the maximum of ε and of the magnitude of this maximum, ε_m; this dependence persists up to the morphotropic phase boundary, which separates the rhombohedral from tetragonal phases and is seen at $x \approx 0.31$ [3, 7]. The rhombohedral ferroelectric phase can be induced in PMN only under application of an electric field [2, 7, 12, 13]. This process is kinetic in character and occurs in two stages; in the first of them, the number of polar regions increases, while their size remains practically unchanged with time, and in the second, these regions coalesce to form an infinite cluster [12, 13]. The second stage starts a certain time τ after the field application (this delay time depends strongly on the field and temperature), after the polar regions have already filled up a large enough part of the sample volume. In PMNT crystals, just as in PMN, the electric field induces a phase transition and the critical field at which the ferroelectric phase formation occurs in a time comparable to the duration of the experiment decreases with increasing *x*, to vanish for $x \approx 0.15$–0.20 [7], which can be identified with the onset of the spontaneous transition from the relaxor to the ferroelectric state.

The properties of the PMNT (in particular, the specific features of formation of the ferroelectric phase) were studied primarily by structural and dielectric methods. However, optical methods of crystal studies [transmission, birefringence, small-angle light scattering (SAS)] are more sensitive and provide more information than the dielectric techniques, particularly when investigating processes associated with the variation in

the size of inhomogeneities during phase transitions. These methods were employed successfully in studies of phase transitions in these compounds. Studies of the birefringence were used to follow the kinetics of the ferroelectric-state initiation in PMN and PMNT-0.1 crystals [13]. A study [14] of the phase transition induced in PMN crystals revealed a narrow peak in the temperature dependence of SAS intensity, which indicates that the transition is of percolation nature and that a large-scale structure is formed upon this transition. If the phase transition occurs by percolation, then the average size of the new phase cluster at the percolation threshold approaches the dimensions of the sample; in this case, a large-scale nonuniform structure forms and the phase transition should be accompanied by the appearance of narrow SAS intensity peaks (a minimum in transmission). The temperature dependence of the SAS intensity obtained in stoichiometric $PbSc_{1/2}Nb_{1/2}O_3$ (PSN) and $PbSc_{1/2}Ta_{1/2}O_3$ (PST) crystals [15, 16] with various degrees of ion ordering exhibits, in the absence of electric field, a narrow peak at the temperature of the spontaneous phase transition from the relaxor to the ferroelectric state.

PMNT crystals with compositions close to the morphotropic region have recently been attracting particular interest. These crystals exhibit a considerably higher piezoelectric sensitivity than ceramics of the same composition, which is due to the possibility of applying a field along a chosen crystallographic direction [17–19]. A distinctive feature of such crystals is the coexistence, within a broad temperature range, of phases differing in symmetry (cubic, rhombohedral, tetragonal, monoclinic) [18, 19]. This ability to reside in a variety of phases is characteristic of solid solutions of many relaxors and may originate both from a concentration inhomogeneity and from a spatially nonuniform degree of ordering among *B* cations in different valence states. Our earlier studies of $(1 - x)PbSc_{1/2}Nb_{1/2}O_3$–$(x)BaSc_{1/2}Nb_{1/2}O_3$(PBSN–*x*) solid solutions revealed that single crystals with $x = 0.04$ are similar in terms of their optical properties to pure PSN. As the Ba content increased to $x = 0.06$, crystals became increasingly more heterophase and initiation of the ferroelectric phase by an electric field was no longer accompanied by a narrow SAS intensity peak; i.e., this phase did not occur through the percolation mechanism [20, 21]. This suggests that the electric-field-induced variations in the properties of heterophase relaxor crystals are characterized by specific features.

The present communication reports on a study of the dielectric and optical properties of PMNT-0.2 crystals and of their variation by an electric field within a broad temperature range. The choice to use PMNT-0.2 crystals in the study was motivated by the fact that, first, these compounds are characterized by the coexistence of phases with different symmetries (cubic, rhombohedral) and different properties (relaxor, ferroelectric) and, second, these crystals have been investigated to a considerable detail using x-ray diffraction, which should greatly facilitate interpretation of the results obtained [8, 9, 22].

No studies of the dielectric and optical properties of PMNT-0.2 single crystals have been carried out previously. The temperature dependences of ε of the PMNT-0.2 compounds and their variation in a dc electric field have been investigated in ceramic samples only [3]. X-ray diffraction measurements showed that, in PMNT-0.2, as in PMN, an electric field drives a phase transition above a certain critical field level [8]. This field-driven transition was accompanied by nonuniform microstrains of the structure and lasted a fairly long time, up to 40 min, in fields of a few kV/cm. However, the phase diagram (field vs. temperature) of PMNT-0.2 crystals differs from that of PMN in that there is a spontaneous ferroelectric transition at zero field. The observed anomalies were not always clearly pronounced, which frequently made their experimental detection quite difficult.

2. GROWTH OF SINGLE CRYSTALS AND EXPERIMENTAL TECHNIQUE

Transparent yellow cube-shaped PMNT-0.2 crystals, with edges of up to 6 mm and (001) faces of the perovskite basis, were grown by spontaneous crystallization from a melt solution with a PbO–B_2O_3 mixture serving as the solvent [23]. The composition of the crystals was determined with a combination scanning electron microscope–microprobe Camebax-Micro. Plate-shaped samples for the investigation were cut parallel to the (001) natural crystal faces and polished.

The dc electric field was applied in the [100] direction, and light was propagated along [001]. A variety of electric field application modes was employed: zero-field cooling (ZFC), zero-field heating (ZFH), field heating after ZFC (FHaZFC), field cooling (FC), field heating after field cooling (FHaFC), and zero-field heating after field cooling (ZFHaFC). After each field application, the samples were heated at a temperature of 150°C for 0.5 h prior to taking the next measurement. The rate of sample temperature change was varied from 2 to 18°C/min.

A He–Ne laser was employed for optical measurements. We studied optical transmittance and small-angle light scattering in the transmission geometry [24]. The birefringence of a sample was derived from the relation $I = I_0 \sin^2 \pi \Delta n d/\lambda$, where I_0 is the incident intensity; I is the light intensity transmitted through the sample placed between two crossed polarizers, with the optical axis of the sample making an angle of 45° with the polarization of the incident light; Δn is the birefringence; λ is the wavelength of light; and d is the sample thickness.

Dielectric measurements were carried out at frequencies of 0.1–100 kHz with a P5083 ac bridge and an E4-7 *Q* meter.

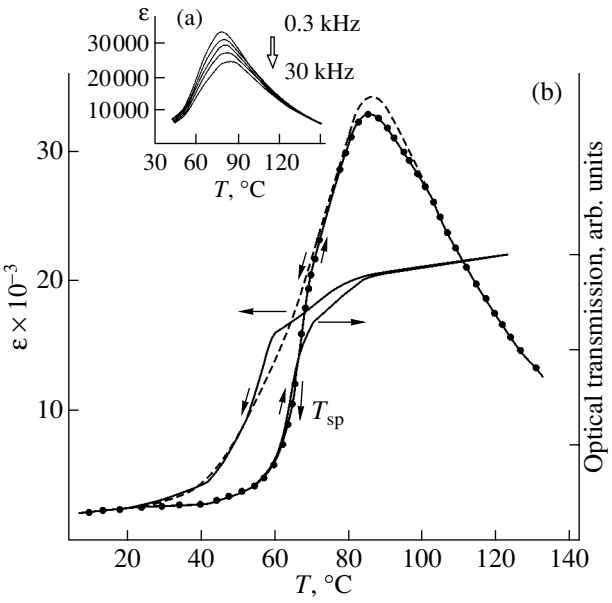

Fig. 1. Temperature behavior (a) of the permittivity ε at various measuring field frequencies and (b) of the permittivity ε at a frequency of 1 kHz and the optical transmittance measured under heating and cooling on PMNT-0.2 single crystals.

3. EXPERIMENTAL RESULTS AND DISCUSSION

Figure 1 presents temperature dependences of ε obtained at various measuring field frequencies (Fig. 1a) and of the optical transmittance and ε measured under heating and cooling (Fig. 1b) on a PMNT-0.2 single crystal. The temperature dependences of ε display, in addition to a diffuse maximum near $T_m \approx 80$–85°C, a knee at temperatures 15–20°C below T_m, which corresponds to the spontaneous transition between the relaxor and the ferroelectric phases and whose position on the temperature axis is practically frequency-independent. The frequency dispersion of ε grows sharply above the temperature of the knee (Fig. 1a). To estimate the degree of diffuseness of the ε peak, we used the following relation, which proved to be valid for describing the properties of a large number of relaxors of various types [25]:

$$\frac{\varepsilon_A}{\varepsilon} = 1 + 0.5\frac{(T - T_A)^2}{\sigma^2}, \qquad (1)$$

where ε_A ($>\varepsilon_m$) and T_A ($<T_m$) are the maximum value of the static permittivity and the temperature of this maximum, respectively, and σ is the parameter of transition diffuseness. In contrast to the widely used analogous Isupov formula [1] with ε_m and T_m in place of ε_A and T_A, the value of σ determined from Eq. (1) does not depend on frequency. The best fit to experimental data under independent variation of the parameters is reached with $\varepsilon_A = 46940$, $T_A \approx 65$°C, and $\sigma \approx 27$ K. The quadratic Curie–Weiss law holds up to temperatures of $T_{CW} \approx$ 280–290°C. For temperatures above ≈300°C, the linear Curie–Weiss law with the parameters $T_{CW} \approx 190$°C and $C \approx 1.3 \times 10^5$ K holds.

When plotted in the Arrhenius coordinates, the dependence of T_m on f deviates strongly from a straight line, which indicates a non-Debye relaxation character typical of ferroelectric relaxors [11]. At the same time, the T_m vs. f dependence is fitted well by the Vogel–Fulcher law

$$f = f_0 \exp[-\Delta E/k(T_m - T_0)], \qquad (2)$$

where f_0 is the attempt frequency of hopping over a potential barrier ΔE, k is the Boltzmann constant, and T_0 is the Vogel–Fulcher temperature defined as the temperature of static electric-dipole freeze-out or of the transition to the dipole glass state [11]. For PMNT-0.2, $f_0 \sim 7 \times 10^{10}$ Hz, which is close to the values of f_0 for classical ferroelectric relaxors [11]. The value $T_0 \approx$ 64°C approximately coincides with the temperature of the knee in $\varepsilon(T)$ (the temperature of the spontaneous ferroelectric transition T_{sp}), which is characteristic of other relaxors undergoing a spontaneous transition to the ferroelectric state. The activation energy ΔE in the Vogel–Fulcher law for PMNT-0.2 ($\Delta E \approx 0.026$ eV) is also close to the values observed in compounds featuring a spontaneous relaxor–ferroelectric transition ($\Delta E \approx$ 0.023 eV for PST [11]), whereas in $PbMg_{1/3}Nb_{2/3}O_3$, for instance, where the relaxor state is stable, the values of ΔE are substantially higher (≈0.07–0.1 eV [11]).

As seen from Fig. 1, the anomaly in the ε curve corresponding to the spontaneous phase transition at T_{sp} is not clearly defined, whereas optical transmittance grows strongly at this temperature (Fig. 1b). The temperature hysteresis of ≈10–11°C observed in dielectric and optical measurements is a major feature of a first-order phase transition. By contrast, the behavior of optical transmittance at the spontaneous phase transition in PMNT-0.2 crystals differs from the analogous relations observed in PST, PSN, and PBSN-0.04 [15, 16, 20], where this transition follows the percolation pattern and is accompanied by a minimum in optical transmittance (a SAS peak). A possible reason for the different nature of the spontaneous phase transition in this crystal is the nonuniformity of the phase existing above the T_{sp} temperature. This suggestion fits well with x-ray diffraction measurements [9], which indicate the presence of three inhomogeneous phases preceding the appearance of the rhombohedral ferroelectric phase at $T_{sp} \sim$ 55–65°C under cooling, namely, of an ergodic dipole glass ($T_{DG1} \sim$ 120–130°C), a nonergodic dipole glass ($T_{DG2} \sim$ 90–100°C), and a mixed phase ($T_M \sim$ 65–80°C) with coexisting ferroelectric and glass regions. At these temperatures, one also observes anomalies in the temperature evolution of the shape of the (224) reflection and in the integrated intensity of the (005) reflection, which are assigned in [9] to a substantial rearrangement of the crystal structure, because these anomalies indicate a change in the size and number of polar clusters and/or appearance of additional nonuniform strains in the crystal caused by atomic dis-

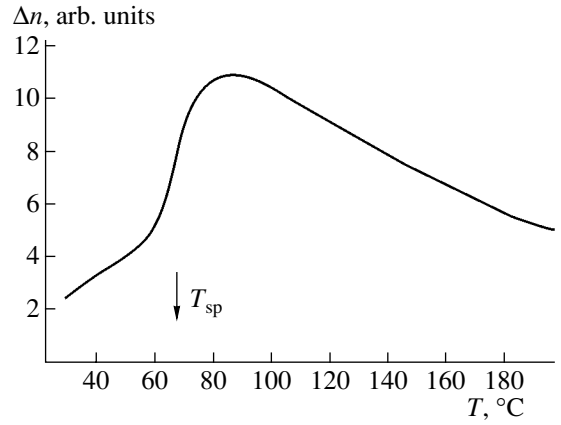

Fig. 2. Temperature dependence of the birefringence in a PMNT-0.2 crystal.

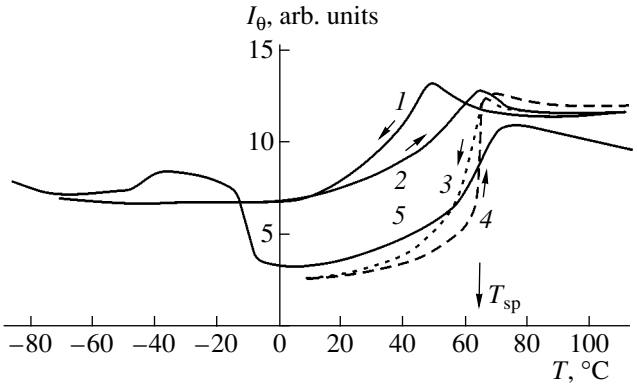

Fig. 3. Temperature dependences of the small-angle light scattering SAS (scattering angle 40′) measured in various modes of application of the 1-kV/cm-electric field: (*1*) ZFC, (*2*) ZFHaZFC, (*3*) FC, (*4*) ZFHaFC, and (*5*) FHaZFC.

placements, which distort the centrosymmetric pattern of cubic unit cells.

It is apparently such a distortion of the centrosymmetric pattern of cubic cells and the appearance of random atomic displacements that can account for the anomalous temperature dependence of the birefringence observed by us (Fig. 2). In place of the expected absence of Δn above T_{sp}, a feature characteristic of the relaxor phase of such crystals as PMN and PMNT-0.1 [15], we observed a maximum in Δn near T_{sp}. The birefringence decreased with increasing temperature, to become weakly dependent on temperature only substantially above T_{DG1} ($T \sim 200$°C).

The mixed phase of the PMNT-0.2 crystal ($T_{sp} < T < T_M$) is inherently nonergodic; i.e., the state of this crystal depends on its thermodynamic path in the *T*–*E* diagram. The properties of the crystal in this phase can depend not only on the electric field strength but also on the actual regime of its application. A study of the variation of the intensity and shape of x-ray reflections in an electric field revealed [22] that, if an [100]-oriented electric field applied to the mixed phase, which contains both regions of the ferroelectric rhombohedral phase and randomly nonuniform, spontaneously strained regions of the dipole glass phase, exceeds a certain threshold level of $(1–4) \times 10^5$ V/cm, this field drives the ferroelectric transition with relaxation times of 40–50 min.

Our studies of the optical transmittance and more sensitive SAS measurements performed in electric fields of up to 2.5 kV/cm in various field application modes did not reveal any anomalies associated with the onset of a ferroelectric transition at temperatures above T_{sp}. Figure 3 plots temperature dependences of the SAS intensity obtained in heating and cooling runs in the absence (curves *1*, *2*) and under application of a dc electric field of 1 kV/cm (curves *3*–*5*). The increase in the SAS intensity and the small broad maximum observed in the region of the spontaneous phase transition T_{sp} are related to the growth in size of the domains and to the formation of fairly large macrodomain regions. This anomaly is particularly clearly manifested when the sample is cooled in an electric field (FC regime, curve *3*) and when the ferroelectric state is destroyed at T_{sp} under heating (ZFHaFC regime, curve *4*). No anomalously narrow peak was observed in the temperature dependence of the SAS intensity (which would indicate the percolation character of the transition) even in an electric field. At the same time, in the FC regime (curve *3*), the temperature at which the SAS intensity decays is higher than when no field is applied (curve *1*), which suggests that the ferroelectric transition is nevertheless initiated. One could propose several explanations for the absence of the induced transition in our case. The nonuniform structure of the relaxor phase, more specifically, the coexistence, within a broad temperature interval, of regions of macroscopic cubic and rhombohedral phases whose volume fractions depend on temperature and on the electric field strength [9], may result in the phase transition not being driven simultaneously in various regions of the crystal. Another explanation could be that the time required for the phase transition to come to an end is very long (for PMNT-0.2 crystals subjected to an electric field of 1–2 kV/cm, this time is about 50 min [22]), so at the crystal cooling rates used (1–8°C/min) no equilibrium state is reached and the infinite ferroelectric-phase cluster does not form.

In crystals acted on by an electric field, we found low-temperature anomalies in the dielectric properties and optical transmittance that were not observed earlier in PMNT. Figures 4 and 5 display the temperature dependences of the loss tangent ($\tan\delta$), ε (Fig. 4), and optical transmittance (Fig. 5) obtained in the FHaZFC mode in various electric fields. No anomalies were observed in the temperature behavior of $\tan\delta$ (curve *1*, Fig. 4) and ε (curve *1*, inset to Fig. 4) below T_{sp} in a zero electric field, whereas in an electric field a small maximum appears in ε (curves *2*, *3* in inset to Fig. 4) and

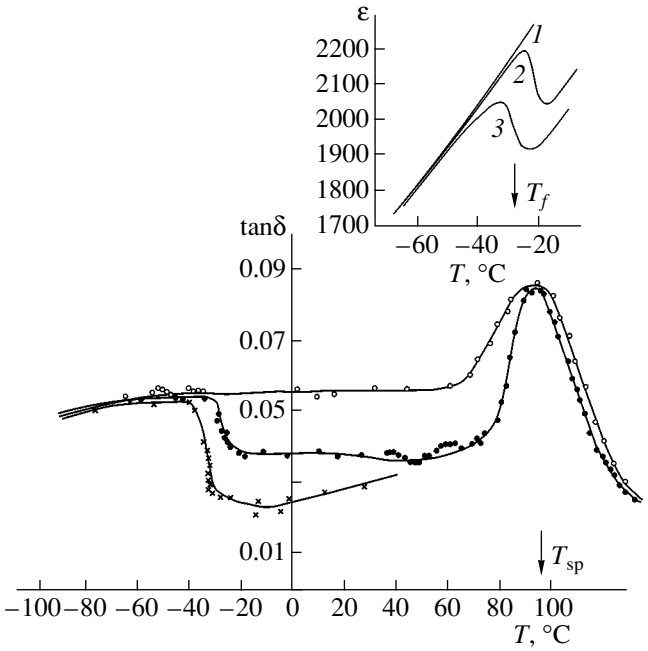

Fig. 4. tanδ and ε (inset) measured vs. temperature at 50 kHz in the FHaZFC mode in various electric fields *E*: (*1*) 0, (*2*) 1.5, and (*3*) 2.2 kV/cm.

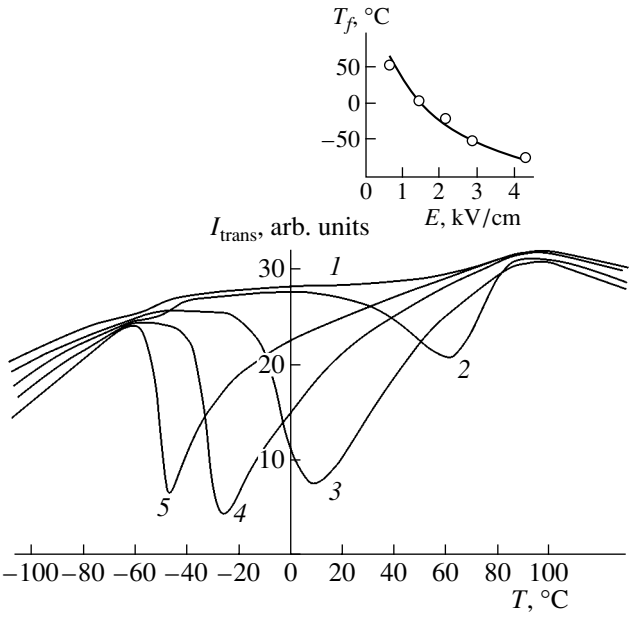

Fig. 5. Temperature dependences of optical transmittance measured in the FHaZFC mode in various electric fields *E*: (*1*) 0.25, (*2*) 0.6, (*3*) 1.3, (*4*) 1.8, and (*5*) 2.6 kV/cm. Inset: the temperature of the anomaly T_f plotted vs. electric field.

there is a sharp decrease in tanδ (curves *2*, *3*) at a certain temperature T_f. The temperature positions of these anomalies are seen to shift to lower temperatures with increasing electric field. The anomalies in the temperature dependences of optical transmittance near T_f (curves *2*–*5*, Fig. 5) are even more distinct. The minimum in the optical transmittance curve indicates an increase in scattering, particularly at small angles, which is associated with an increase in the size of the inhomogeneities and, hence, with a phase transition. Analogous low-temperature anomalies have been observed in an electric field in studies of the dielectric properties of the unpoled PLZT 8/65/35 ceramic [26] and of the PST ceramic undergoing a spontaneous phase transition [27]. It was conjectured in [26] that the low-temperature anomaly in ε observed in an electric field is associated with a transition from the micro- to macroscopic phase and the appearance of polarization, whereas in compounds (such as the PST) that have already transferred spontaneously to the ferroelectric phase with no electric field applied, the anomaly in ε is assigned to domain reorientation in an electric field [27].

Application of an electric field to a PMNT-0.2 crystal, which in the absence of an electric field resides in the ferroelectric polydomain rhombohedral phase at low temperatures, results in a growth in the size of the domains and in their reorientation. At a constant heating rate, the temperature of this transition shifts toward low temperatures with increasing field strength (Figs. 4, 5). In fields below 0.5 kV/cm, no low-temperature anomaly was observed to exist (curve *1* in Fig. 5). Below T_f, an electric field is not capable of reorienting the spontaneously formed ferroelectric domain structure. As the temperature grows and approaches T_f, the thermal energy needed to change (unfreeze) this domain structure increases, and this makes it possible for the ferroelectric domains to change their orientation in the electric field. This new domain configuration maintained by an electric field will now persist until thermal energy destroys the ferroelectric state, which corresponds to a transition to the relaxor state at T_{sp}.

As the sample heating rate decreases at a fixed bias field, T_f decreases (Fig. 6). Such a dependence of the temperature T_f on the sample heating rate was observed earlier only in the relaxors PMN [14], PLZT [26], and PBSN-6 [21] and was attributed to the polarization reorientation processes in a glasslike state occurring with long relaxation times. In compounds whose low-temperature phase is ferroelectric, this type of dependence was observed for the first time. Thus, either the electric field used in our experiments is not capable of reorienting domains and making them larger during the experiment or the ferroelectric phase is not completely uniform, with disordered regions existing at low temperatures. To more accurately determine the changes in the sample properties occurring near and above T_f in an electric field, one should employ a quasi-static method of measurement [7] instead of the dynamic method used in this study. Note that the displacement of the T_f temperature in PMNT-0.2 crystals observed under variation of the sample heating rate is two times slower than

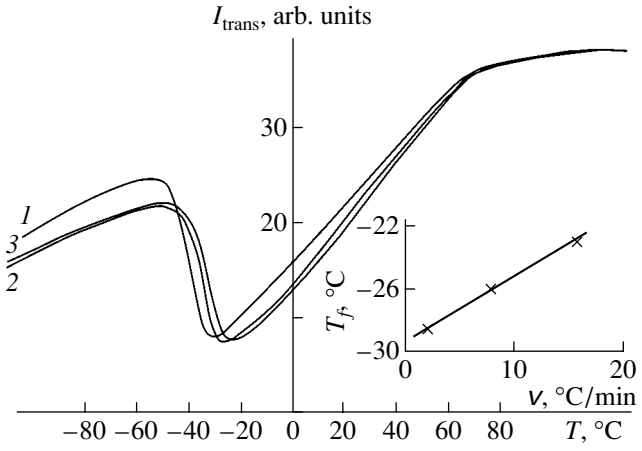

Fig. 6. Temperature dependences of optical transmittance measured in the FHaZFC mode in a field of 1.8 kV/cm at various sample heating rates: (*1*) 2, (*2*) 8, and (*3*) 16°C/min. Inset: the temperature of the anomaly T_f plotted vs. sample heating rate.

that in typical relaxors residing in a glasslike state at low temperatures.

4. CONCLUSIONS

Thus, we have succeeded in detecting, by optical means, an anomalous increase in birefringence in PMNT-0.2 crystals at the transition to the relaxor phase, which is probably caused by the cubic cells changing from centrosymmetric and by the onset of additional random atomic displacements. Below T_{sp}, anomalies in the dielectric and optical properties were observed to occur in an electric field, which originate from the field-induced reorientation and increase in the size of domains. Unlike the ferroelectric relaxors of the type of $PbB'_{1/3}B''_{2/3}O_3$ and $PbB'_{1/2}B''_{1/2}O_3$ studied earlier, as well as solid solutions with a low content of the second component (PBSN-4), neither initiation of the ferroelectric phase by an electric field nor thermally stimulated destruction of the ferroelectric state in PMNT-0.2 single crystals occurs through the percolation mechanism (i.e., they are not accompanied by the appearance of narrow maxima in small-angle light scattering). This is assigned to the inhomogeneous structure of the relaxor phase, in other words, to the coexistence, within a broad temperature interval, of macroscopic regions of the cubic and rhombohedral phases, with their volume fractions depending on the temperature and the electric field strength. Due to this inhomogeneity, the phase transition does not proceed simultaneously over the crystal.

ACKNOWLEDGMENTS

The authors are indebted to O.E. Kvyatkovskiĭ and A.A. Bokov for helpful discussions.

This study was supported by the Russian Foundation for Basic Research (project nos. 01-02-17801, 01-03-33119) and the program of the Department of Physical Sciences of the Russian Academy of Sciences.

REFERENCES

1. G. A. Smolenskiĭ, V. A. Bokov, V. A. Isupov, N. N. Kraĭnik, R. E. Pasynkov, A. I. Sokolov, and N. K. Yushin, *The Physics of Ferroelectric Phenomena* (Nauka, Leningrad, 1985).
2. L. T. Cross, Ferroelectrics **76**, 241 (1987).
3. O. Noblanc, P. Gaucher, and G. Calvarin, J. Appl. Phys. **79** (8), 4291 (1996).
4. B. Dkhil, J. M. Kiat, G. Kalvarin, G. Baldinozzi, S. B. Vakhrushev, and S. Suard, Phys. Rev. B **65** (2), 024104 (2001).
5. Z.-G. Ye, Y. Bing, G. Gao, A. A. Bokov, P. Stephens, B. Noheda, and G. Shirane, Phys. Rev. B **67** (10), 104104 (2003).
6. O. Bidault, E. Husson, and A. Morell, J. Appl. Phys. **82** (11), 5674 (1997).
7. E. Colla, N. Yushin, and D. Viehland, J. Appl. Phys. **83** (6), 3298 (1998).
8. I. P. Zakharchenko, O. A. Bunina, P. N. Timonin, Yu. A. Trusov, and V. P. Sakhnenko, Kristallografiya **43** (1), 71 (1998) [Crystallogr. Rep. **43**, 64 (1998)].
9. I. P. Zakharchenko, O. A. Bunina, P. N. Timonin, and V. P. Sakhnenko, Kristallografiya **45** (6), 1043 (2000) [Crystallogr. Rep. **45**, 961 (2000)].
10. N. de Mathan, E. Husson, G. Calvarin, J. R. Gavarri, A. W. Hewat, and A. Morell, J. Phys.: Condens. Matter **3**, 8159 (1991).
11. F. Chu, I. M. Reaney, and N. Setter, Ferroelectrics **151** (1–4), 343 (1994).
12. B. Dkhil and J. M. Kiat, J. Appl. Phys. **90** (9), 4576 (2001).
13. K. Fujishiro, T. Iwase, Y. Uesu, Y. Yamada, B. Dkhil, J. M. Kiat, S. Mori, and N. Yamamoto, J. Phys. Soc. Jpn. **69** (7), 2331 (2000).
14. L. S. Kamzina, N. N. Kraĭnik, and O. Yu. Korshunov, Fiz. Tverd. Tela (St. Petersburg) **37** (9), 2765 (1995) [Phys. Solid State **37**, 1523 (1995)].
15. L. S. Kamzina and A. L. Korzhenevskiĭ, Pis'ma Zh. Éksp. Teor. Fiz. **50** (3), 146 (1989) [JETP Lett. **50**, 163 (1989)].
16. L. S. Kamzina and N. N. Kraĭnik, Fiz. Tverd. Tela (St. Petersburg) **42** (9), 1664 (2000) [Phys. Solid State **42**, 1712 (2000)].
17. S. Park and T. R. Shrout, J. Appl. Phys. **82**, 1804 (1997).
18. Z.-G. Ye and M. Dong, J. Appl. Phys. **87** (5), 2312 (2000).
19. C.-S. Tu, C.-L. Tsai, V. H. Scmidt, H. Luo, and Z. Yin, J. Appl. Phys. **89** (12), 7908 (2001).
20. L. S. Kamzina, I. P. Raevskiĭ, V. V. Eremkin, and V. G. Smotrakov, Fiz. Tverd. Tela (St. Petersburg) **44** (9), 1676 (2002) [Phys. Solid State **44**, 1754 (2002)].

21. L. S. Kamzina, I. P. Raevskiĭ, V. V. Eremkin, V. G. Smotrakov, and E. V. Sahkar, Fiz. Tverd. Tela (St. Petersburg) **45** (6), 1061 (2003) [Phys. Solid State **45**, 1112 (2003)].
22. I. N. Zakharchenko, O. A. Bunina, P. N. Timonin, Y. A. Trusov, and V. P. Sakhnenko, Ferroelectrics **199** (1–4), 187 (1997).
23. S. M. Emel'yanov, N. P. Protsenko, V. A. Zagoruĭko, T. V. Sokolova, and S. M. Zaĭtsev, Izv. Akad. Nauk SSSR, Neorg. Mater. **27** (3), 431 (1991).
24. L. S. Kamzina and N. N. Krainik, Ferroelectrics **223**, 27 (1999).
25. A. A. Bokov, Y.-H. Bing, W. Chen, Z.-G. Ye, S. A. Bogatina, I. P. Raevski, S. I. Raevskaya, and E. V. Sahkar, Phys. Rev. B **68** (5), 052102 (2003).
26. Y. Xi, C. Zhili, and L. E. Cross, J. Appl. Phys. **54** (6), 3399 (1983).
27. F. Chu, G. R. Fox, and N. Setter, J. Am. Ceram. Soc. **81** (6), 1577 (1998).

Translated by G. Skrebtsov

Physics of the Solid State, Vol. 46, No. 5, 2004, pp. 915–921. Translated from Fizika Tverdogo Tela, Vol. 46, No. 5, 2004, pp. 888–894.

LATTICE DYNAMICS AND PHASE TRANSITIONS

Calorimetric and X-ray Diffraction Studies of the $(NH_4)_3WO_3F_3$ and $(NH_4)_3TiOF_5$ Perovskite-Like Oxyfluorides

I. N. Flerov*, M. V. Gorev*, V. D. Fokina*, A. F. Bovina*, and N. M. Laptash**

**Kirensky Institute of Physics, Siberian Division, Russian Academy of Sciences, Akademgorodok, Krasnoyarsk, 660036 Russia*

e-mail: flerov@ksc.krasn.ru

***Institute of Chemistry, Far East Division, Russian Academy of Sciences, pr. Stoletiya Vladivostoka 159, Vladivostok, 690022 Russia*

Received July 15, 2003

Abstract—The heat capacity and unit cell parameters of the $(NH_4)_3WO_3F_3$ and $(NH_4)_3TiOF_5$ perovskite-like oxyfluorides were measured in the temperature interval from 80 to 300 K; the existence of two and one phase transitions in these compounds, respectively, was demonstrated, and their thermodynamic parameters were determined. The effect of a hydrostatic pressure of up to 0.5 GPa on the phase transition temperatures was studied. Triple points and high-pressure phases were found in the *T* vs. *p* diagrams. An analysis of entropy changes suggests that all the structural transformations revealed are associated with the ordering of structural blocks.

1. INTRODUCTION

The perovskite-like fluoride compounds with general chemical formula $A_3M^{3+}F_6$ have cubic symmetry with space group $Fm\bar{3}m$ ($Z = 4$) in the high-temperature phase and belong to the cryolite–elpasolite family [1]. It was shown in [2] that the original cubic symmetry persists under partial substitution of oxygen for the fluorine ions, i.e., in $A_3MO_xF_{6-x}$ compounds (with the value of *x* depending on the actual valence of the central *M* atom), because the atoms of fluorine and oxygen are distributed at random over the lattice. The point symmetry of the O_xF_{6-x} octahedra was found from IR and Raman spectra to be lower than cubic, C_{4V} (for $x = 1$) and C_{2V} (for $x = 3$) [3, 4].

The perovskite-like oxyfluorides with atomic cations, like the related fluorides, have a distorted structure at room temperature and undergo, with increasing temperature, single or sequential structural transformations [5, 6]. Our present knowledge of the structure of the original and distorted phases of the oxyfluorides is inadequate. The symmetry of the cubic phase has been refined only for $Rb_2KMoO_3F_3$ [7] solely using a model that assumes the oxygen and fluorine atoms to be distributed over the 24*e* positions, for which the thermal vibration anisotropy was found to be essential. A variety of symmetries of the low-temperature phase (which exists, for instance, in $K_3MoO_3F_3$ at room temperature and is a result of two successive phase transitions) have been proposed, from trigonal [8] and orthorhombic [2] to monoclinic [9]. The phase transitions occurring in $A_3M^{3+}F_6$ and $A_3MO_xF_{6-x}$ are different in nature [1, 3]. The fluorides in distorted phases are ferroelastics, whereas the oxyfluorides undergo ferroelectric and ferroelastic transformations. Substitution of a spherical cation with the tetrahedral ammonium ion in fluorides brings about a noticeable lowering of the temperature at which the cubic phase loses stability. On the other hand, the nonsphericity of cation *A* may initiate additional disorder resulting from disordering of the tetrahedra in the 4*b* and/or 8*c* positions [1]. In connection with the low symmetry of the fluorine–oxygen octahedra, it was unclear how such effects would become manifest in the perovskite-like oxyfluorides.

Information on phase transitions in ammonium oxyfluorides has thus far been lacking. We performed a synthesis and investigation of the $(NH_4)_3WO_3F_3$ and $(NH_4)_3TiOF_5$ compounds to look for and study their possible phase transitions. For this purpose, we used differential scanning calorimetry, x-ray diffraction, adiabatic calorimetry, and differential thermal analysis (DTA) under pressure.

2. SAMPLE PREPARATION AND TRIAL EXPERIMENTS

The ammonium oxyfluorides $(NH_4)_3WO_3F_3$ and $(NH_4)_3TiOF_5$ were prepared from hot $(NH_4)_2WO_2F_4$ and $(NH_4)_2TiF_6$ solutions with excess NH_4F, with subsequent gradual addition of an NH_4OH solution to pH = 8 (until the first signs of precipitation of a white sediment appear). Such fast crystallization produces small, transparent, colorless crystals of octahedral

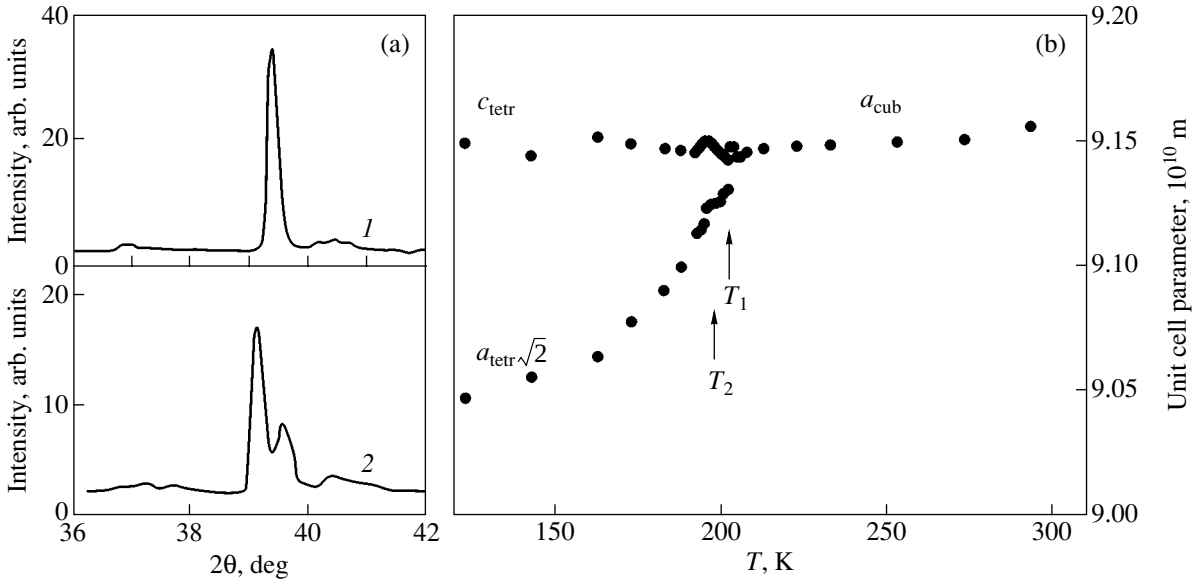

Fig. 1. X-ray characterization of $(NH_4)_3WO_3F_3$: (a) (400) reflection at (*1*) 293 and (*2*) 123 K and (b) temperature dependence of the unit cell parameters.

shape with an edge of about 5 μm. Following separation of the crystalline precipitate from the mother growth solution, larger octahedra crystallized under slow evaporation in air with edges about 40 μm long.

At room temperature, both cryolites were found to have cubic symmetry ($Fm\bar{3}m$, $Z = 4$) with the unit cell parameters $a_0 = 0.9156$ nm for $(NH_4)_3WO_3F_3$ and 0.9113 nm for $(NH_4)_3TiOF_5$. No peaks associated with residual impurities of the starting components or foreign phases were observed in the diffraction patterns.

The preliminary thermophysical studies of the two cryolites were performed using differential scanning microcalorimetry (DSM). We measured the heat capacity of the samples of the compounds prepared by fast and slow crystallization. The measurements were conducted in the temperature range from 120 to 330 K in heating and cooling runs at a rate of 8 K/min. The sample mass was about 0.1–0.2 g. The heat capacity of the $(NH_4)_3WO_3F_3$ oxyfluoride was found to behave anomalously under heating; namely, it revealed a sharp peak with a maximum at the temperature $T_1 = 201 \pm 1$ K. A shoulder was observed in the rising part of the peak at $T_2 \approx 199$ K. A conjecture was put forward that this compound undergoes a sequence of two phase transitions. Measurements carried out under cooling provided supportive evidence of this conjecture; namely, the heat capacity peak split in two because of a difference in hysteresis of the phase transition temperatures ($\delta T_1 \approx 3$ K, $\delta T_2 \approx 5$ K). Because the intermediate phase exists in a very narrow temperature interval, we could determine only the total enthalpy change, $\Sigma\Delta H_i = 3200 \pm 320$ J/mol, associated with the phase transition sequence.

In the $(NH_4)_3TiOF_5$ compound, DSM revealed only one phase transition at $T_0 = 270 \pm 1$ K with a temperature hysteresis $\delta T_0 \approx 11$ K. The enthalpy change for this compound was found to be considerably larger, $\Delta H_0 = 5000 \pm 500$ J/mol.

The calorimetric data obtained with DSM on samples prepared in various crystallization regimes are in satisfactory agreement within the error of measurement for both compounds.

To verify that the anomalies in the heat capacity are indeed related to structural transformations, we carried out x-ray studies of both compounds within a broad temperature range. The structural distortion of tungsten oxyfluoride was reflected in the broadening and splitting of the (*h*00) and (*hk*0) reflections setting in at T_1. Figure 1a shows a characteristic transformation of the (400) reflection. The pattern of the splitting did not change under a further decrease in temperature. The data obtained were insufficient for determining the symmetry of the distorted phases; therefore, Fig. 1b displays the temperature dependence of the parameters of a pseudotetragonal cell with the following relations: $a_{tetr} \approx a_{cub}/\sqrt{2}$ and $c_{tetr} \approx a_{cub}$. The behavior of the parameters exhibits two singular points at the temperatures T_1 and T_2, which can be identified with the phase transitions revealed by DSM in tungsten oxyfluoride.

The existence of a phase transition in $(NH_4)_3TiOF_5$ at 270 K was also confirmed by x-ray diffraction. A comparison of the x-ray diffractograms of this compound obtained at room temperature and 123 K (Fig. 2a) suggests, however, that the phase transition, besides causing the reflection splitting for $T < T_0$, gives rise to the appearance of additional peaks signaling the presence of a superstructure. One may thus conclude

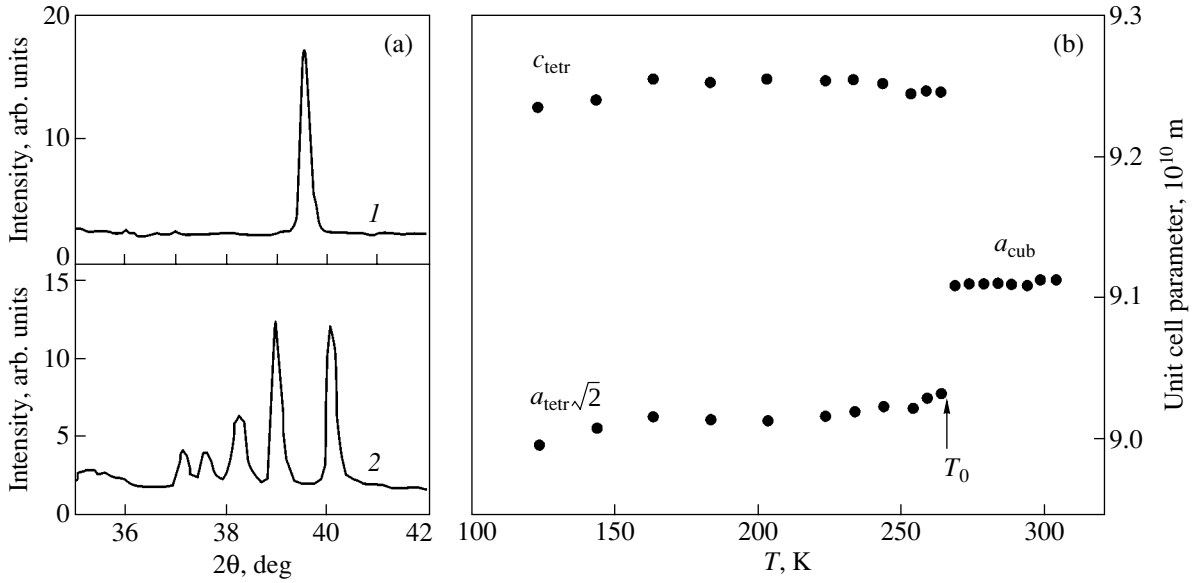

Fig. 2. X-ray characterization of $(NH_4)_3TiOF_5$: (a) (400) reflection at (*1*) 293 and (*2*) 123 K and (b) temperature dependence of the unit cell parameters.

that the symmetry of the low-temperature phase in titanium oxyfluoride is different from that of the distorted phases in the tungsten compound. Nevertheless, most of the lines in the powder x-ray diffraction pattern of $(NH_4)_3TiOF_5$ can also be indexed with the use of a tetragonal pseudocell. The $a_i(T)$ relation is plotted in Fig. 2b. The abrupt change in the cell parameters and the sharp heat capacity peak suggest that the structural transformation in the $(NH_4)_3TiOF_5$ compound is a clearly pronounced first-order phase transition.

3. HEAT CAPACITY MEASUREMENTS

The enthalpy change at the phase transition derived from DSM measurements is quite often found to be an underestimate, particularly in studies of transformations far from the tri-critical point, because this method has a relatively low sensitivity to pretransition phenomena occurring in the heat capacity behavior. Therefore, to refine the thermodynamic parameters of the phase transitions revealed in the compounds under study, we carried out comprehensive measurements of the temperature dependence of the heat capacity of $(NH_4)_3WO_3F_3$ and $(NH_4)_3TiOF_5$ with an adiabatic calorimeter within the temperature range from 80 to 300 K.

The samples to be studied, with a mass of about 1 g, were hermetically sealed in an indium container in a helium environment. The measurements were conducted in a discrete (ΔT = 2.5–4.0 K) and a continuous (dT/dt = 0.14 K/min) heating mode. The method of quasi-static thermograms with average heating and cooling rates $|dT/dt| \approx 0.04$ K/min was employed in the immediate vicinity of the phase transitions. The temperatures were measured with a platinum resistance thermometer.

Figure 3a displays the temperature dependence of the heat capacity of the $(NH_4)_3WO_3F_3$ compound measured over a broad temperature range. The region of the anomalies, which was studied from thermograms, is shown in more detail in Fig. 3b. Two heat capacity peaks were found to exist at temperatures $T_1 = 200.1 \pm 0.1$ K and $T_2 = 198.5 \pm 0.1$ K. The temperature hysteresis was $\delta T_1 = 2.2$ K and $\delta T_2 = 5.1$ K. The results obtained are in satisfactory agreement with the DSM measurements. When processing adiabatic calorimeter data, we likewise did not succeed in separating the heat

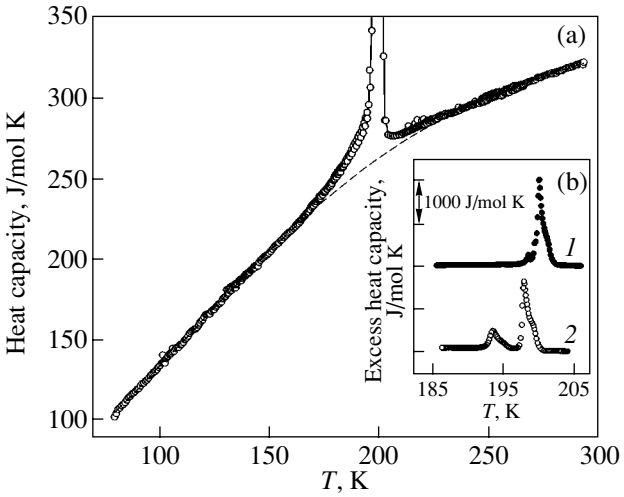

Fig. 3. Temperature dependence (a) of the heat capacity of $(NH_4)_3WO_3F_3$ over a broad temperature range and (b) of the excess heat capacity at the phase transitions measured (*1*) under heating and (*2*) under cooling. The dashed line represents the lattice heat capacity.

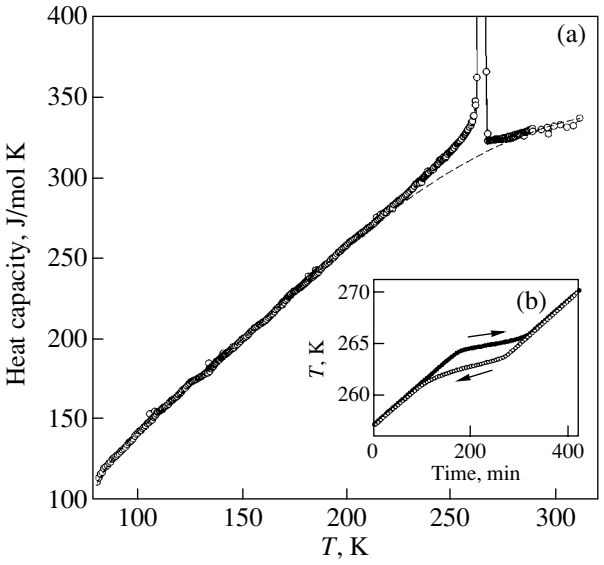

Fig. 4. (a) Temperature dependence of the heat capacity of $(NH_4)_3TiOF_5$ over a broad temperature range; The dashed line represents the lattice heat capacity. (b) Thermograms obtained in the heating and cooling modes near T_0.

capacity anomalies associated with the phase transition sequence. Therefore, we calculated the total enthalpy change in the two phase transitions by integrating the excess heat capacity $\Delta C_p(T)$ over temperature, derived by subtracting the lattice contribution from the total heat capacity. The temperature dependence of the regular heat capacity, obtained through polynomial fitting of experimental data outside the phase transition region, is shown in Fig. 3a with a dashed line. The average scatter of experimental data from the smoothed curve did not exceed 1%. By properly varying the temperature intervals within which the anomalous heat capacity was cut out, it was established that the anomaly exists within a broad temperature region below (T_1 – 40 K) and above (T_1 + 29 K) the temperature of the phase transition from the cubic phase. It is obvious, however, that the excess heat capacity near the temperatures of the transformations provides the main contribution to the enthalpy change. The calculated total enthalpy change was found to be $\Sigma\Delta H_i = 3370 \pm 250$ J/mol. The total change in the enthalpy in the two phase transitions was found (by integrating the function $\Delta C_p(T)/T$ over temperature) to be $\Sigma\Delta S_i = 16.9 \pm 1.2$ J/mol K.

The measured specific heat capacity of the $(NH_4)_3TiOF_5$ oxyfluoride is shown graphically in Fig. 4a. As in the DSM experiments, we observed one heat capacity anomaly. The refined phase transition temperature is $T_0 = 264.7 \pm 0.1$ K. The anomalous heat capacity was isolated in a way similar to that used to analyze the heat capacity of the tungsten compound. The excess heat capacity of $(NH_4)_3TiOF_5$ also exists within a broad temperature region, from (T_0 – 75 K) to (T_0 + 25 K). The changes in the enthalpy and entropy were determined in the same way as was done for tungsten oxyfluoride, namely, by integrating the corresponding functions, $\Delta C_p(T)$ and $\Delta C_p(T)/T$, to yield $\Delta H_0 = 4820 \pm 250$ J/mol and $\Delta S_0 = 18.1 \pm 1.0$ J/mol K.

Figure 4b presents thermograms obtained for the titanium compound under heating and cooling. Absorption of the latent heat of the transition during the sample heating was observed to occur in the interval $T_0 \pm 0.7$ K. This yielded $\delta H_0 = 4200 \pm 220$ J/mol for the latent heat and $\delta S_0 = 15.4 \pm 0.8$ J/mol K for the entropy jump. The value of the temperature hysteresis, $\delta T_0 = 2.3$ K, was found to be substantially smaller than that extracted from DSM experiments.

4. PHASE DIAGRAMS

Thus, both calorimetric and x-ray diffraction data suggest that $(NH_4)_3WO_3F_3$ undergoes, at atmospheric pressure, a sequence of phase transitions $G_0(Fm\bar{3}m) \longrightarrow G_1 \longrightarrow G_2$ and that $(NH_4)_3TiOF_5$ undergoes only one transformation, $G_0 \longrightarrow G_1'$. The experience gained in investigating related fluorides [10, 11] gave us grounds to believe that the ammonium oxyfluorides could likewise turn out be sensitive to external pressure.

The effect of external pressure on phase transition temperatures in both ammonium oxyfluorides was studied on samples prepared by fast crystallization. The transition temperature and its variation with pressure were measured by DTA. The sensor was a thermocouple fabricated by attaching copper wires with tin–lead solder to a germanium parallelepiped. A quartz bar was pasted as a reference to one junction of the thermocouple, and a small copper container with the substance to be measured, to the other junction. The sample mass was ~0.1 g. A pressure of up to 0.5 GPa was produced in a cylinder–piston-type chamber connected to a multiplier. A mixture of transformer oil with pentane served as the pressure-transmitting medium. The pressure and temperature in the chamber were measured with a manganin resistance manometer and a copper–constantan thermocouple, with errors of $\pm 10^{-3}$ GPa and ±0.3 K, respectively. The position of the phase boundaries in the T vs. p diagrams was established under increasing and decreasing hydrostatic pressure.

Figure 5 presents a T vs. p phase diagram of $(NH_4)_3WO_3F_3$. At atmospheric pressure, the temperature dependence of the DTA signal exhibited only one anomaly. We did not observe a splitting of the peak associated with the $G_0 \longrightarrow G_1 \longrightarrow G_2$ sequence, most likely because the DTA is less sensitive than DSM, which reliably detected both transitions, as already mentioned, in the cooling run only. Unfortunately, the DTA method employed by us does not allow us to perform measurements in the cooling mode.

This pattern of the phase diagram suggests that the G_1 phase found in the $(NH_4)_3WO_3F_3$ cryolite at atmospheric pressure disappears rapidly with increasing pressure and that the phase boundary observed to exist

up to the pressure of the triple point revealed in the diagram should be identified with the $G_0 \longrightarrow G_2$ transition. The coordinates of the triple point are p_{trp} = 0.183 GPa and T_{trp} = 199.6 K. The thermodynamic parameters of the phase transitions at atmospheric and high pressure are listed in the table. The temperature at which the cubic phase loses stability changes with increasing pressure at a very low rate, and the sign reversal of the quantity dT_1/dp is likely to occur, within the accuracy with which this quantity is determined. At the triple point, the G_0–G_2 phase boundary splits. At pressures above p_{trp}, tungsten oxyfluoride undergoes a sequence of two phase transitions, $G_0 \longrightarrow G_3 \longrightarrow G_2$. The temperature of the $G_0 \longrightarrow G_3$ transformation grows nonlinearly with increasing pressure. The initial shift of the transition temperature occurring at $p = p_{trp}$ is ~435 K/GPa. The G_3–G_2 phase boundary is linear and has a negative dT/dp coefficient.

The analysis of the DTA data also yielded the values of the enthalpy changes at the phase transitions taking place at high pressure. This was done by subtracting the baseline from the temperature-dependent DTA signal and calculating the area bounded by the anomaly corresponding to the phase transition. The area obtained for the transformation at atmospheric pressure ($G_0 \longrightarrow G_2$) in relative units was assumed equal to the enthalpy change $\Sigma\Delta H$ = 3370 J/mol (found in heat capacity measurements using adiabatic calorimetry) in the phase transition sequence $G_0 \longrightarrow G_1 \longrightarrow G_2$. The enthalpy changes in the successive pressure-induced phase transformations $G_0 \longrightarrow G_3$ and $G_3 \longrightarrow G_2$ were derived from the ratio of the areas bounded by the corresponding DTA peaks (see table). Near the triple point, the relation connecting the enthalpies of these phase transitions, $\Delta H(G_0 \longrightarrow G_2) = \Delta H(G_0 \longrightarrow G_3) + \Delta H(G_3 \longrightarrow G_2)$, should be met. As seen from a comparison of the above data, this relation is satisfied within the error with which the quantities ΔH are determined. The increase in the error of determining ΔH at high pressures originates from the increase in heat losses, which, in turn, is caused by the increase in the thermal conductivity of the pressure-transmitting liquid.

The T vs. p phase diagram of the $(NH_4)_3TiOF_5$ oxyfluoride is shown in Fig. 6. Its pattern is more complex than that of the tungsten compound. Two high-pressure phases and two triple points were revealed having the following parameters: T_{1trp} = 265.7 K, p_{1trp} = 0.196 GPa, and T_{2trp} = 249.2 K, p_{2trp} = 0.291 GPa. At the first triple point, the $G_0 \longrightarrow G_1'$ phase-transition line splits into two lines, corresponding to the $G_0 \longrightarrow G_2'$ and $G_2' \longrightarrow G_1'$ transitions. The latter transition operates within a comparatively narrow pressure interval (approximately 0.1 GPa). At the second triple point, the phase boundaries $G_2' \longrightarrow G_1'$, $G_2' \longrightarrow G_3'$, and $G_1' \longrightarrow G_3'$ terminate. The displacements of all phase transition temperatures identified in the phase diagram of titanium oxyfluoride are presented in the table. The slope of the $G_1' \longrightarrow G_3'$ phase boundary would suggest that this transformation also occurs at atmospheric pressure near 120 K. As follows, however, from our calorimetric measurements (see Section 3), there are no heat capacity anomalies in $(NH_4)_3TiOF_5$ in the temperature interval from T_0 to 80 K. Hence, it may be conjec-

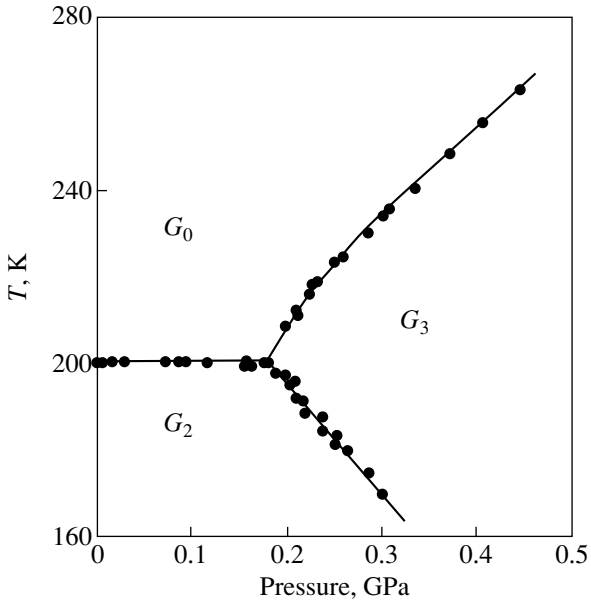

Fig. 5. T vs. p diagram of $(NH_4)_3WO_3F_3$.

Thermodynamic parameters of the phase transitions in $(NH_4)_3WO_3F_3$ and $(NH_4)_3TiOF_5$ revealed by T vs. p diagrams

Phase transition	$(NH_4)_3WO_3F_3$			$(NH_4)_3TiOF_5$				
	G_0–G_2	G_0–G_3	G_3–G_2	G_0–G_1'	G_0–G_2'	G_2'–G_1'	G_2'–G_3'	G_1'–G_3'
dT/dp, K/GPa	–2.5 ± 5	~435	–252 ± 14	6.3 ± 0.5	223 ± 9	–176 ± 12	–59 ± 12	425 ± 17
ΔH, J/mol	3370 ± 250	1000 ± 250	1900 ± 480	4820 ± 720	1320 ± 260	3400 ± 680	5300 ± 1060	1890 ± 380
ΔS, J/mol K	16.9 ± 1.2	5.0 ± 1.3	9.5 ± 2.4	18.1 ± 1.0	5.0 ± 1.0	12.8 ± 2.6	21.3 ± 4.3	7.6 ± 1.5
$\Delta V/V$, %	0.04	1.9	–2.1	0.1	1.0	–2.0	–1.1	2.8

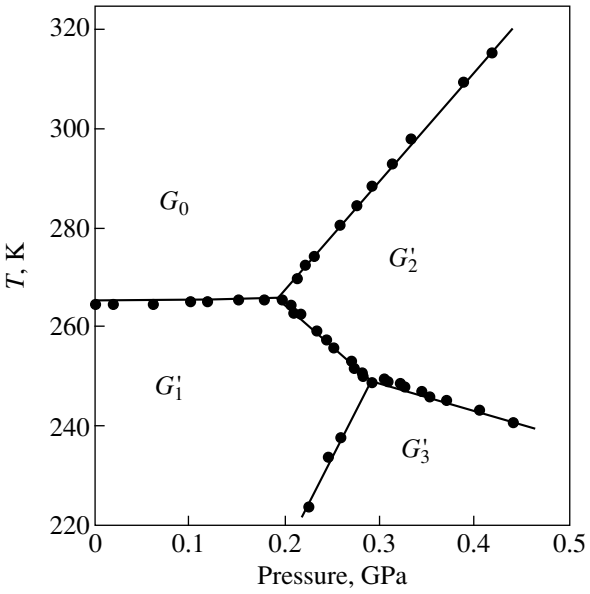

Fig. 6. T vs. p diagram of $(NH_4)_3TiOF_5$.

tured that, at pressures below 0.2 GPa, the $G_1' \longrightarrow G_3'$ is nonlinear, with rising dT/dp.

We used the method employed earlier to analyze the phase diagram of tungsten oxyfluoride to determine the enthalpy changes characteristic of the structural transformations in the titanium compound (see table). The enthalpies for the corresponding phase transition lines terminating at the triple points agree satisfactorily in relative magnitude within the experimental error.

5. DISCUSSION OF THE RESULTS

Our calorimetric, x-ray diffraction, and DTA measurements performed under pressure revealed phase transitions and pressure-induced phases in the $(NH_4)_3WO_3F_3$ and $(NH_4)_3TiOF_5$ ammonium oxyfluorides with cryolite structure. Substitution of the spherical atomic cation by the tetrahedral ammonium cation brought about, as expected, a substantial lowering of the temperature at which the cubic phase loses stability. For instance, the phase transitions from the cubic phase in the $K_3WO_3F_3$ and K_3TiOF_5 compounds take place at 452 K [5] and 490 K [6], respectively, with the simultaneous formation of the ferroelectric and ferroelastic states. In view of the single crystals used here being too small, we did not carry out studies of the permittivity and polarization, which leaves the question of the existence of ferroelectricity in the distorted phases of $(NH_4)_3WO_3F_3$ and $(NH_4)_3TiOF_5$ open. Observations performed with a polarization microscope showed that the nature of the structural transformations in both oxyfluorides investigated here is at least ferroelastic.

Although the results of our studies are insufficient to establish the symmetry of the distorted phases, we can maintain with confidence that the symmetry is different for $(NH_4)_3WO_3F_3$ and $(NH_4)_3TiOF_5$, because the latter was found to change translational symmetry at T_0.

As follows from calorimetric data, the phase transitions detected in our study are first-order transformations. Knowing the ratio between the jump in the entropy and its total change, one can determine the extent to which the transition is close to the tri-critical point. For the $G_0 \longrightarrow G_1'$ transformation in titanium oxyfluoride, this ratio is $\delta S_0/\Delta S_0 = 0.84$. The appreciable difference between the values of T_0 and δT_0 for this compound, as determined by DSM and from quasi-static thermograms, clearly indicates a noticeable dependence of the hysteresis phenomena on the temperature scanning rate and also provides supportive evidence of the phase transition being far from the tri-critical point.

The intermediate phase G_1 in $(NH_4)_3WO_3F_3$ exists in a very narrow temperature interval (T_1–T_2 = 1.6 K) and apparently disappears in the T vs. p diagram at low pressures. Therefore, the degree of closeness to the tri-critical point could be estimated only for the $G_0 \longrightarrow G_2$ transition by assuming, because the entropy is an additive quantity, that the relation $\delta S(G_0 \longrightarrow G_2) = \delta S(G_0 \longrightarrow G_1) + \delta S(G_1 \longrightarrow G_2)$ is valid. The total latent heat found from the thermograms is $\Sigma\delta H_i = 2700 \pm 150$ J/mol. In defining the entropy jump as $\delta S(G_0 \longrightarrow G_2) = \Sigma\delta H_i/T_1$, we found that the $G_0 \longrightarrow G_2$ phase transition in this compound is also fairly far from the tri-critical point, $\delta S(G_0 \longrightarrow G_2)/\Delta S(G_0 \longrightarrow G_2) = 0.8$. We may recall that some ammonium–fluorine cryolites and elpasolites, for instance, $(NH_4)_3ScF_6$ [10] and $Cs_2NH_4GaF_6$ [11], likewise exhibit large ratios $\delta S_0/\Delta S_0 = 0.86$.

Using the available information on the entropies of the phase transitions and the displacement of transformation temperatures induced by hydrostatic pressure, we used the Clapeyron–Clausius relation $dT/dp = (\Delta V/V)/\Delta S$ to estimate the relative changes in unit cell volume $\Delta V/V$ at phase transitions in the vicinity of the triple points (see table). Note that the pressure-induced phase transitions in $(NH_4)_3WO_3F_3$ and $(NH_4)_3TiOF_5$ are apparently more clearly pronounced first-order transformations, because the unit cell volume change for these compounds is several times larger than $\Delta V/V$ for transitions at atmospheric pressure.

The data listed in the table also suggest that the entropy change for all phase transitions in both ammonium oxyfluorides is typically $\Delta S/R \geq \ln 2$. We can therefore conclude with confidence that the observed structural distortions are associated with the ordering of some structural elements. Note also that the phase transitions $G_0 \longrightarrow G_2$ in $(NH_4)_3WO_3F_3$ and $G_0 \longrightarrow G_1'$ in $(NH_4)_3TiOF_5$ entail the same entropy change $\Delta S/R$ of approximately $\ln 8$, despite the difference in symmetry between the distorted phases. Figure 7 displays the temperature dependence of the excess entropy. As

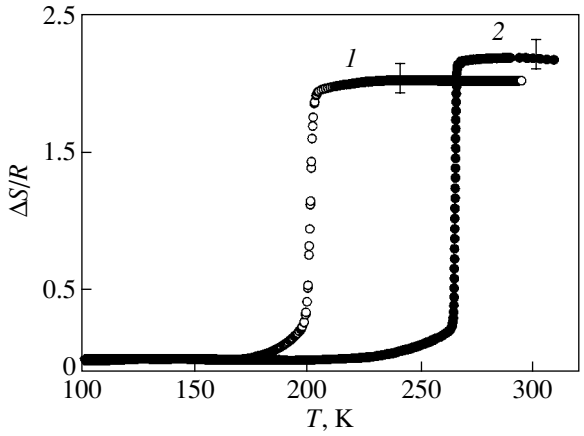

Fig. 7. Temperature dependence of the excess entropy of (*1*) $(NH_4)_3WO_3F_3$ and (*2*) $(NH_4)_3TiOF_5$. *R* is the universal gas constant.

shown by DSM studies, the change in entropy observed in a number of tungsten oxyfluorides of cryolite structure with atomic cations is typically $\Delta S/R \le \ln 2$ [5]. Thus, it is obvious that substitution of tetrahedral for spherical cations brings about a larger disorder in the $Fm\bar{3}m$ cubic structure. On the other hand, phase transitions from the cubic phase occurring in $(NH_4)_3ScF_6$ and $Cs_2NH_4CaF_6$ are also accompanied by an entropy change of ln8 [10, 11]. Such a large value of $\Delta S/R$ was assigned to partial ordering of the $M^{3+}F_6$ octahedra (ln4) and ordering of the ammonium tetrahedra in the 4*b* position (ln2). We do not currently have at our disposal data on the structure of either cubic or distorted phases of $(NH_4)_3WO_3F_3$ and $(NH_4)_3TiOF_5$. Therefore, we believe that consideration of any model concepts accounting for the established transition entropies would be premature.

However, the relation between the entropies near the triple points observed in the phase diagrams of both oxyfluorides indicates that the pressure-induced consecutive phase transitions also belong to order–disorder-type transformations.

ACKNOWLEDGMENTS

The authors are grateful to S.V. Mel'nikova for providing results of optical polarization studies.

This study was supported by the Russian Foundation for Basic Research (project nos. 03-02-16079, 03-02-06728, 01-03-32719) and the Department of Physical Sciences of the Russian Academy of Sciences (project no. 2.2.6.1).

REFERENCES

1. I. N. Flerov, M. V. Gorev, K. S. Aleksandrov, A. Tressaud, J. Grannec, and M. Couzi, Mater. Sci. Eng. R **24** (3), 81 (1998).
2. G. von Pausewang and W. Rüdorff, Z. Anorg. Allg. Chem. **364** (1–2), 69 (1969).
3. K. von Dehnicke, G. Pausewang, and W. Rüdorff, Z. Anorg. Allg. Chem. **366** (1–2), 64 (1969).
4. M. Couzi, V. Rodriguez, J.-P. Chaminade, M. Fouad, and J. Ravez, Ferroelectrics **80**, 109 (1988).
5. G. Peraudeau, J. Ravez, P. Hagenmüller, and H. Arend, Solid State Commun. **27**, 591 (1978).
6. M. Fouad, J. P. Chaminade, J. Ravez, and P. Hagenmüller, Rev. Chim. Miner. **24**, 1 (1987).
7. S. C. Abrahams, J. L. Bernstein, and J. Ravez, Acta Crystallogr. B **37** (7), 1332 (1981).
8. Z. G. Ye, J. Ravez, J.-P. Rivera, J.-P. Chaminade, and H. Schmid, Ferroelectrics **124**, 281 (1991).
9. F. J. Brink, R. L. Withers, K. Friese, G. Madariaga, and L. Noren, J. Solid State Chem. **163**, 267 (2002).
10. I. N. Flerov, M. V. Gorev, and T. V. Ushakova, Fiz. Tverd. Tela (St. Petersburg) **41** (3), 523 (1999) [Phys. Solid State **41**, 468 (1999)].
11. M. V. Gorev, I. N. Flerov, A. Tressaud, A. I. Zaitsev, and E. Durand, Solid State Sci. **4** (1), 15 (2002).

Translated by G. Skrebtsov

Physics of the Solid State, Vol. 46, No. 5, 2004, pp. 922–926. Translated from Fizika Tverdogo Tela, Vol. 46, No. 5, 2004, pp. 895–898.

LATTICE DYNAMICS AND PHASE TRANSITIONS

Effect of Electric Field on the Metal–Insulator Transition with the Formation of Superstructure

P. P. Boriskov, A. A. Velichko, and G. B. Stefanovich

Petrozavodsk State University, Petrozavodsk, 185640 Russia

e-mail: gstef@mainpgu.karelia.ru

Received March 25, 2003; in final form, September 4, 2003

Abstract—The mechanism of the effect of an electric field on the metal–insulator transition with the formation of superstructure is considered with allowance for the field modulation of the electronic spectrum. Experimental data on the switching effect in vanadium dioxide are interpreted on the basis of this modified model. © *2004 MAIK "Nauka/Interperiodica".*

The effect of an electric field on the metal–insulator phase transition (MIT) has been attracting considerable attention for a long time [1–5]. Obviously, the studies of high-field effects are highly informative from the point of view of elucidating the MIT mechanism. Moreover, the idea of using MIT for practical purposes in micro- and optoelectronics is without doubt very promising.

For many transition-metal oxides, in particular, for vanadium dioxide, the problem of the MIT mechanism still remains a subject of controversy. Two alternative models [6, 7] are traditionally considered: a structural phase transition (for one-dimensional systems, this is the Peierls transition) and the electronic Mott transition. In recent experiments on the switching effect in vanadium dioxide–based sandwich structures, we have shown [8, 9] that, at low ambient temperatures, in addition to Joule heating in the channel, high-field effects play an important role if the switching temperature is much smaller than the equilibrium MIT temperature (Fig. 1) and the maximum free carrier concentration is 1–2 orders of magnitude smaller than the critical Mott concentration ($\leq 10^{19}$ cm^{-3} for VO_2). Therefore, one can assume that, at high enough electric fields in VO_2 sandwich switches, a direct field dependence of the MIT temperature should be observed.

In contrast to quasi-one-dimensional (Peierls) systems with incommensurate superstructure, vanadium dioxide has no conductivity related to collective degrees of freedom, i.e., to charge density waves (CDWs) [10, 11]. However, deformation of a CDW (for example, in an electric field) can result in variation of the free carrier density; due to this, perturbations of the CDW affect the conductivity of a material even at subthreshold fields [11]. In this study, in the framework of such an approach, we consider the mechanism of the direct effect of the field on the transition; this mechanism implies that the model of MIT with the formation of superstructure includes field modulation of the electronic spectrum.

The conduction band of VO_2 in the metal state is formed due to the overlap of the wave functions of 3*d* states of vanadium atoms forming parallel chains along the *C* axis of the crystal. The MIT mechanism with superstructure formation in vanadium dioxide is related to Peierls instability of the one-dimensional a_1 band (with $x^2 - y^2$ symmetry), since the distance between the cations along the *C* axis is known to be much smaller than the distance between the nearest neighbors in per-

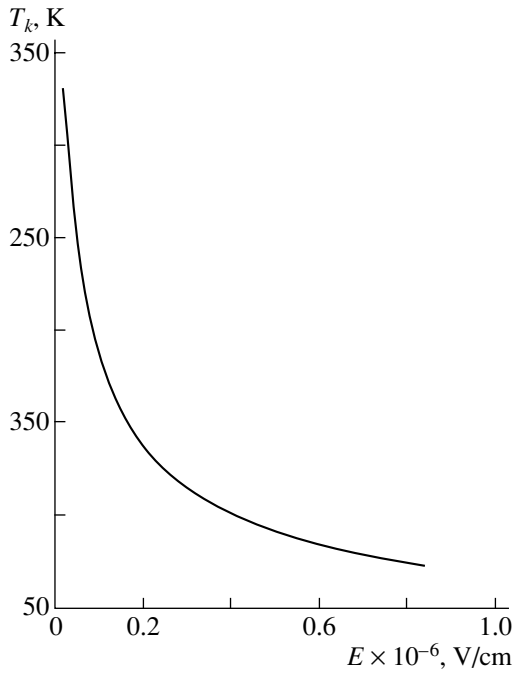

Fig. 1. Field dependence of the critical switching temperature T_k. As $E \longrightarrow 0$, T_k tends to the equilibrium value of the MIT temperature equal to 340 K for vanadium dioxide.

1063-7834/04/4605-0922$26.00 © 2004 MAIK "Nauka/Interperiodica"

pendicular directions. In this case, the MIT is described by the structural phase transition of a chain of equidistant vanadium atoms along the *C* axis to a state in which the distances between the nearest neighbor atoms alternate and the chain has a zigzag form (Fig. 2).

It is convenient to analyze the spectrum of strongly localized states of valence 3*d* electrons in the Wannier function representation; in this representation, the Hubbard Hamiltonian is [12]

$$H = \sum_{n,\sigma}\left[(\varepsilon_1-\mu)a^+_{n\sigma}a_{n\sigma}+\frac{U}{2}a^+_{n,\sigma}a_{n,\sigma}a^+_{n,-\sigma}a_{n,-\sigma}\right] + \sum_{n,n',\sigma}B(\mathbf{R}_n,\mathbf{R}_{n'})a^+_{n\sigma}a_{n'\sigma}, \quad (1)$$

where $a^+_{n,\sigma}$ ($a_{n,\sigma}$) is the creation (annihilation) operator at the site with the translation vector $\mathbf{R}_n$, ε_1 is the energy of the atomic one-electron level, μ is the chemical potential, *U* is the intra-atomic repulsion, $B(\mathbf{R}_n, \mathbf{R}_{n'})$ is the overlap integral of wave functions (the transfer integral), and σ is the spin projection ($\uparrow$, $\downarrow$).

The singlet dielectric pairing that gives rise to the CDW state is due to electron–phonon interaction described by the Fröhlich Hamiltonian

$$H_{\text{e–ph}} = \frac{1}{\sqrt{N}}\sum_{k,q,\sigma}\eta(\mathbf{q})(b_q+b^+_{-q})a^+_{k,\sigma}a_{k-q,\sigma}, \quad (2)$$

where $\eta(\mathbf{q})$ is the electron–phonon interaction constant, b^+_{-q} (b_q) is the phonon creation (annihilation) operator, $a^+_{k,\sigma}$ ($a_{k,\sigma}$) is the Fermi creation (annihilation) operator in the Bloch representation, $\mathbf{k}$ is the wave vector, and *N* is the number of atoms.

Since a phonon Bose condensate with $\mathbf{q} = \mathbf{Q}$ ($\langle b_{\mathbf{Q}}\rangle \neq 0$) exists in a state with CDW, Hamiltonian (2) with operators in the Wannier representation assumes the following form in the mean-field approximation [13]:

$$H' = \frac{1}{\sqrt{N}}\sum_{n,\sigma}\eta(Q)(b_Q+b^+_{-Q})a^+_{n,\sigma}a_{n,\sigma}\exp(-i\mathbf{Q},\mathbf{R}_n). \quad (3)$$

Introducing the electron–phonon interaction (3) into Hamiltonian (1), we obtain a self-consistent equation for the band gap Δ [10, 13],

$$\lambda^{-1} = \int_0^W d\varepsilon(2\nu(\varepsilon))^{-1} \times\left\{\tanh\left[\frac{\nu(\varepsilon)+g}{2k_BT}\right]+\tanh\left[\frac{\nu(\varepsilon)-g}{2k_BT}\right]\right\}, \quad (4)$$

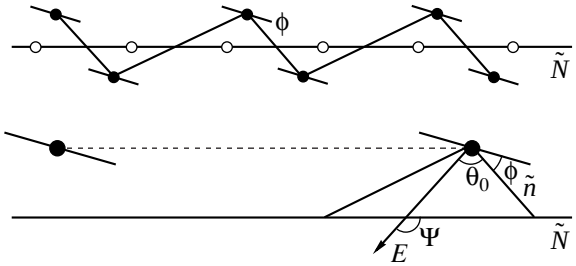

Fig. 2. Schematic configuration of vanadium atoms for a chain in the metal phase (open circles, which are at the same distance *b* from each other) and in the insulator phase (solid circles, the distances between which alternate, 2*a* and 2*c*). Here, ϕ is the angle between the axis of the atomic wave function of the 3*d* state and the direction to the nearest neighbor atom in the insulator phase.

where $\nu(\varepsilon) = \sqrt{\varepsilon^2+\Delta^2}$, *g* is the transfer integral in second order of the tight-binding approximation producing modulation of the Fermi surface, *W* is the band width, and λ specifies the singlet (CDW) solution.

The presence of parameter *g* in the model (we call it the warping parameter) results in the appearance of solutions to Eq. (4) that allow for a temperature jump of the gap, i.e., the first-order phase transition. The dependence of these solutions on parameter *g* also demonstrates the instability of the dielectric phase with respect to a modulation of the Fermi surface.

Now, we consider the effect of a dc field on the electron system in the model under consideration.

The matrix element of the interaction of electrons with the electric field $\mathbf{E}$ ($e > 0$) is

$$S(\mathbf{R}_n,\mathbf{R}_{n'}) = e\int w^*(\mathbf{r}-\mathbf{R}_n)(\mathbf{E}\mathbf{r})w(\mathbf{r}-\mathbf{R}_{n'})d^3r. \quad (5)$$

Expressing the Wannier functions $w(\mathbf{r}-\mathbf{R}_n)$ in terms of the Bloch functions $u(\mathbf{k}, \mathbf{r})$ [14], we can write Eq. (5) for a field directed along the *X* axis in the form

$$S(\mathbf{R}_n,\mathbf{R}_{n'}) = \frac{eE}{N^2}\sum_{\mathbf{k},\mathbf{k}'}\exp(\mathbf{k}\mathbf{R}_n-\mathbf{k}'\mathbf{R}_{n'}) \times\int\exp[-i(\mathbf{k}-\mathbf{k}')\mathbf{r}]u^*(\mathbf{k},\mathbf{r})xu(\mathbf{k}'\mathbf{r})d^3r = \frac{eE}{N^2}\sum_{\mathbf{k},\mathbf{k}'}\exp[\mathbf{k}\mathbf{R}_n-\mathbf{k}'\mathbf{R}_{n'}] \times\left\{i\frac{\partial}{\partial k_x}\delta(\mathbf{k}-\mathbf{k}')+X(\mathbf{k})\delta(\mathbf{k}-\mathbf{k}')\right\}, \quad (6)$$

where $X(\mathbf{k}) = i\int u^*(\mathbf{k},\mathbf{r})\partial/\partial k_x u(\mathbf{u},\mathbf{r})d^3r$.

The first term in braces in Eq. (6) determines the motion of the center of gravity of the electron wave packet in the field *E* [14]. If the quasimomentum relaxation time is much smaller than the characteristic time

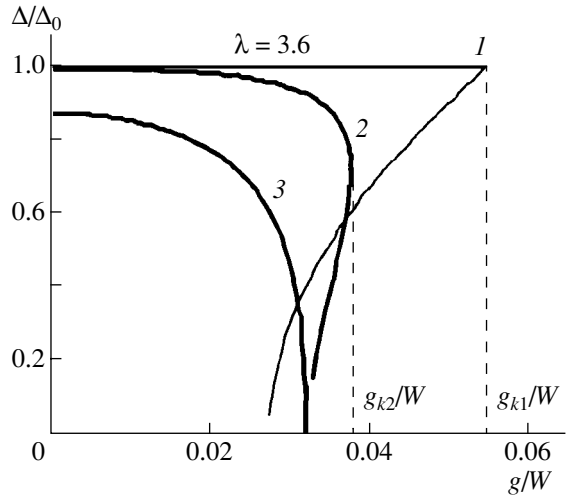

Fig. 3. Dependence of the band gap Δ on the warping parameter g plotted in the normalized coordinates for different values of k_BT/W: (*1*) 0.0001, (*2*) 0.02, and (*3*) 0.01; g_k is the critical warping parameter, and Δ_0 is the gap in the spectrum at zero temperature.

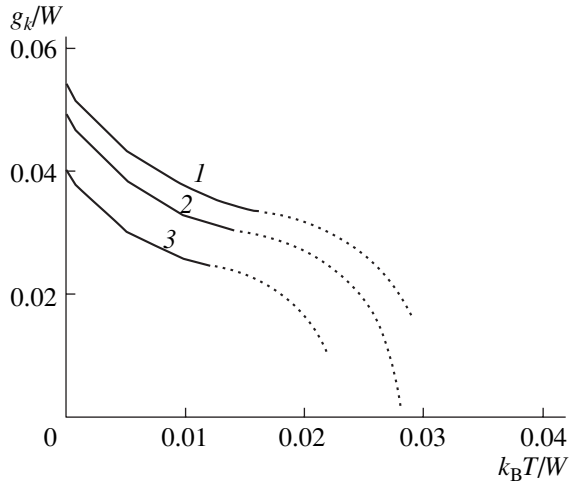

Fig. 4. Temperature dependence of the critical warping parameter g_k for different values of λ: (*1*) 3.6, (*2*) 3.7, and (*3*) 3.9. The dotted lines correspond to the temperature range where no jump in the gap is observed (see curve *3* in Fig. 3).

$\hbar k_F/eE$ of the field-induced variation of the packet (k_F is the Fermi quasimomentum), we can assume that the matrix element of the interaction is determined mainly by the second term in braces in Eq. (6). We note that such behavior of the electron system practically corresponds to the conditions of the dc current, where the mean free path is much smaller than the period $L_b \sim \hbar v_F/eEa$ of spatial oscillations of band electrons (v_F is the Fermi velocity, a is the lattice constant). Taking into account $\delta(\mathbf{k} - \mathbf{k}')$, we can write the second term in braces in Eq. (6) as

$$S^p(\mathbf{R}_n, \mathbf{R}_{n'}) = \frac{eE}{N}\sum_k \exp\{ik(\mathbf{R_n} - \mathbf{R_{n'}})\}X(\mathbf{k}). \quad (7)$$

Thus, in the presence of a field, the electronic system is described by the Hubbard Hamiltonian with a polarization contribution [similar to the third term in Eq. (1)] that describes the field-induced d-electron transitions between sites

$$H'' = \sum_{n, n', \sigma} S^p(\mathbf{R}_n, \mathbf{R}_{n'})a^+_{n\sigma}a_{n',\sigma}. \quad (8)$$

In a first approximation, we take into account the nearest neighbor contributions to sum (8), which produce homogeneous band broadening in an applied field. In a second-order approximation, we include the overlap of wave functions of the next-to-nearest neighbors. In this case, an inhomogeneous field-induced contribution to the electronic spectrum appears, which determines the applied field-dependent modulation of the Fermi surface.

Since $g(E) = g_0 + S^p(\mathbf{h})$, where g_0 is the modulation of the Fermi surface in the absence of the field and $\mathbf{h} = \mathbf{R}_n - \mathbf{R}_{n\pm2}$, the dependence of the gap in the energy spectrum on the warping parameter calculated by Eq. (4) (Fig. 3) can be represented as the external field dependence. It is seen from Fig. 3 that a critical field corresponding to the critical warping parameter g_k exists at which the gap collapses. The critical warping parameter decreases with increasing temperature (Fig. 4), which agrees with the results of a numerical simulation of the switching effect in vanadium dioxide–based sandwich structures [8, 9] (Fig. 1). With the problem stated in this way, the solution to Eq. (4) can qualitatively describe the MIT with superstructure formation in the presence of a dc electric field and the field and temperature dependence of the band gap.

To estimate the field-induced contribution to the warping parameter, we calculate the interaction matrix element (5) for various directions of the electric field. For the next-to-nearest neighbors, we have

$$S(\mathbf{h}) = eE\int\Psi(\mathbf{r})(x\sin\theta_0 + z\cos\theta_0)\Psi(\mathbf{r} - \mathbf{h})d^3r. \quad (9)$$

Here, the atomic electron wave function of the 3d state in the spherical coordinates ρ, θ, φ is

$$\Psi(r) = \frac{1}{81\sqrt{6\pi}}\exp\left\{-\frac{\tilde{Z}\rho}{3a_B}\right\}\left(\frac{Z\rho}{a_B}\right)^2(1 - 3\cos^2\theta), \quad (10)$$

where a_B is the Bohr radius, $\tilde{Z}$ is the charge of the atomic core (in units of the elementary charge), and θ_0 is the axial angle [in the (X, Z) plane] between the direction of the electric field and the axis of the atomic wave function.

In Fig. 5, the matrix element (9) is plotted as a function of the field direction with respect to the C axis deter-

mined by the angle $\psi = \theta_0 + \phi + \arccos[(b^2 + c^2 - a^2)/2bc]$ (Fig. 2). The data used in the calculation are taken from [6, 15]: $b = 0.285$ nm is the interatomic distance in the chain in the metal phase, $2a = 0.312$ nm and $2c = 0.265$ nm are the distances in the insulator phase, $W \cong 1.1$ eV is the width of the one-dimensional conduction band, $R = 0.046$ nm is the effective radius of the atomic wave function, and $\phi = 0.032$. The quantity (9) strongly depends on the Bohr radius a_B. In the calculations, we used two values: $a_B = R$, corresponding to strong localization of 3*d* electrons, and $a_B = \varepsilon_a R/6$, corresponding to the case of medium localization for permittivity $\varepsilon \approx 30$–100 ($\varepsilon_a = 65$ is the mean value) and an electron effective mass of vanadium dioxide $m^* \approx 6m$ (m is the free electron mass) [7].

It can be seen from Fig. 5 that the matrix element vanishes for the direction parallel to the axis of the 3*d*-electron wave functions ($\psi \sim 23°$) and reaches a maximum for a perpendicular field direction ($\psi \sim 113°$). The maximum value of $S(\mathbf{h})$ is of the same order of magnitude as the warping parameter corresponding to the gap collapse (Figs. 3, 4).

Thus, the above estimation confirms the conclusion that, in the framework of the model suggested, a high electric field (~10^6 V/cm) can produce the necessary modulation of the vanadium dioxide electronic spectrum for the direct effect of the field on the MIT to be observed.

Two remarks should be made in connection with this conclusion. Numerical analysis of the experimental data on the switching effect [8, 9] shows that, at low ambient temperatures (high switching fields), the effect of field generation of carriers in vanadium dioxide also occurs, producing a shift in the chemical potential (in Eq. (4), the chemical potential is constant). However, according to our estimates, the maximum change in electron density ($T = 15$ K, $E \sim 10^6$ V/cm) up to the switching threshold corresponds to a chemical potential shift of less than 0.005 eV, i.e., much smaller than the obtained maximum values of the warping parameter (Fig. 5).

From a thermodynamic point of view, one can reasonably speak of the system undergoing a MIT and about polarization of its ground state $\Delta = \Delta(E)$ only if E satisfies the condition $\hbar v_F/eE \ll \Delta$, when particle creation by tunneling is exponentially suppressed [4]. Thus, the equilibrium value of the gap Δ is determined by temperature and its field dependence produces a slight deviation from thermodynamic equilibrium (weakly nonsteady state). In this respect, we note the results of [16], where the case in which particle creation by tunneling gives rise to a weak incommensurability between the CDW and the lattice was considered; this feature led to the conclusion that a slight increase in the MIT temperature takes place in high electric fields (>10^7 V/cm). In this study, the field dependence of the transition temperature should be considered a manifestation of the effect of the field on the MIT (excluding the neighborhood of the transition critical point, where $\hbar v_F/eE > \Delta$).

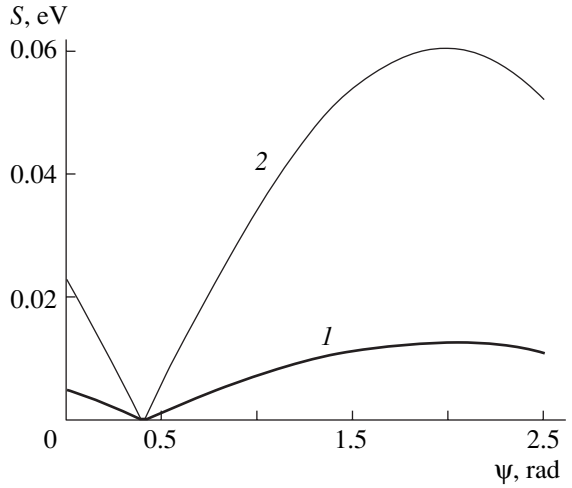

Fig. 5. Dependence of the field-induced contribution to the parameter of the Fermi surface warping $S \equiv S^P(\mathbf{h})$ on the angle ψ for (*1*) $a_B = R$ and (*2*) $\varepsilon_a R/6$; $E = 10^6$ V/cm.

ACKNOWLEDGMENTS

This study was supported by the Ministry of Education of the Russian Federation (project nos. PD02-1.2-183, E02-3.4-437) and the U.S. Civilian Research and Development Foundation (grant nos. PZ-013-02, ST-013-02).

REFERENCES

1. A. Chenevas-Paule, J. Phys. (Paris) **37**, 4 (1976).
2. V. N. Andreev, A. G. Aronov, and F. A. Chudnovskiĭ, Zh. Éksp. Teor. Fiz. **61**, 705 (1971) [Sov. Phys. JETP **34**, 376 (1972)].
3. V. V. Mokrousov and V. N. Kornetov, Fiz. Tverd. Tela (Leningrad) **16** (10), 3106 (1974) [Sov. Phys. Solid State **16**, 2005 (1974)].
4. I. V. Krive and A. S. Rozhavskiĭ, Zh. Éksp. Teor. Fiz. **81** (5), 1811 (1981) [Sov. Phys. JETP **54**, 959 (1981)].
5. A. L. Pergament, G. B. Stefanovich, and F. A. Chudnovskiĭ, Fiz. Tverd. Tela (St. Petersburg) **36** (10), 2988 (1994) [Phys. Solid State **36**, 1590 (1994)].
6. A. A. Bugaev, B. P. Zakharchenya, and F. A. Chudnovskiĭ, *Metal–Semiconductor Phase Transition and Its Application* (Nauka, Leningrad, 1979).
7. N. F. Mott, *Metal–Insulator Transitions* (Taylor and Fransic, London, 1974; Nauka, Moscow, 1979).

8. P. P. Boriskov, A. A. Velichko, A. L. Pergament, G. B. Stefanovich, and D. G. Stefanovich, Pis'ma Zh. Tekh. Fiz. **28** (10), 13 (2002) [Tech. Phys. Lett. **28**, 406 (2002)].
9. P. P. Boriskov, A. A. Velichko, A. L. Pergament, and G. B. Stefanovich, in *Proceedings of All-Russian Scientific Conference on the Physics of Semiconductors and Semimetals* (St. Petersburg, 2002), p. 13.
10. Yu. V. Kopaev, Fiz. Tverd. Tela (Leningrad) **12**, 3 (1970) [Sov. Phys. Solid State **12**, 1 (1970)].
11. G. Gruner, Rev. Mod. Phys. **60** (4), 1129 (1988).
12. J. Hubbard, Proc. R. Soc. London, Ser. A **276**, 238 (1963).
13. G. V. Loseva, S. G. Ovchinnikova, and G. A. Petrakovskiĭ, *Metal–Insulator Transition in Sulfides of 3d Metals* (Nauka, Novosibirsk, 1983).
14. J. Callaway, *Energy Band Theory* (Academic, New York, 1964; Mir, Moscow, 1969).
15. A. L. Semenov, Fiz. Tverd. Tela (St. Petersburg) **42** (10), 1842 (2000) [Phys. Solid State **42**, 1891 (2000)].
16. A. L. Semenov, Fiz. Tverd. Tela (St. Petersburg) **42** (6), 1125 (2000) [Phys. Solid State **42**, 1160 (2000)].

Translated by I. Zvyagin

Physics of the Solid State, Vol. 46, No. 5, 2004, pp. 927–941. Translated from Fizika Tverdogo Tela, Vol. 46, No. 5, 2004, pp. 899–912.

LATTICE DYNAMICS AND PHASE TRANSITIONS

Soft Polar Modes and Phase States of $Ca_{1-x}Pb_xTiO_3$ Solid Solutions

A. A. Volkov*, G. A. Komandin*, B. P. Gorshunov*, V. V. Lemanov, and V. I. Torgashev*****

**General Physics Institute, Russian Academy of Sciences, ul. Vavilova 38, Moscow, 117942 Russia*
***Ioffe Physicotechnical Institute, Russian Academy of Sciences, Politekhnicheskaya ul. 26, St. Petersburg, 194021 Russia*
****Rostov State University, Rostov-on-Don, Russia*

Received October 20, 2003

Abstract—Dielectric spectra $\varepsilon'(\nu)$ and $\varepsilon''(\nu)$ of $Ca_{1-x}Pb_xTiO_3$ ceramic samples ($x = 0$, 0.15, 0.2, 0.4) have been studied in the frequency range $\nu = 7$–1000 cm^{-1} at temperatures from 5 to 300 K using IR Fourier spectroscopy and submillimeter-range techniques. In the low-frequency range, polar phonons were established to undergo temperature-induced evolution. The results obtained are discussed in terms of the Landau theory of second-order phase transitions for coupled soft modes. The existence of one (or several) phase state(s) in the intermediate concentration region of $Ca_{1-x}Pb_xTiO_3$ solid solutions is tentatively assumed. © *2004 MAIK "Nauka/Interperiodica".*

1. INTRODUCTION

Calcium titanate, $CaTiO_3$, is a progenitor of the extensive family of perovskite crystals, which encompass a large variety of compounds, such as ferroelectrics and antiferroelectrics, high-temperature superconductors, manganites exhibiting colossal magnetoresistance, etc. Classical ferroelectrics, such as $BaTiO_3$, $PbTiO_3$, and $KNbO_3$, and incipient ferroelectrics $SrTiO_3$ and $KTaO_3$ have a perovskite structure [1]. The permittivity ε of the latter compounds, like that of normal ferroelectrics, depends strongly on temperature. It grows under cooling to extremely large values, $\varepsilon \sim 10^4$, but does not exhibit a peaked anomaly. At low temperatures, $\varepsilon(T)$ saturates near 40 K, but no ferroelectric phase transition takes place. Therefore, such compounds are called incipient ferroelectrics.

Dynamic theory of the crystal lattice relates the temperature divergence of the permittivity in perovskites to a decrease in the frequency of the soft polar mode of F_{1u} symmetry, whose existence is reliably supported by the temperature behavior of infrared absorption and reflectance spectra. It is presently believed that the static dielectric anomalies in $SrTiO_3$ and $KTaO_3$ are fully determined by the temperature behavior of the soft mode described by the Lyddane–Sachs–Teller relation [2]. In this respect, the basic perovskite $CaTiO_3$ has not been studied in sufficient detail. In $CaTiO_3$, the permittivity varies from 170 to 330 as the temperature is lowered from room to liquid-helium temperature [3], i.e., not as strongly as that in $SrTiO_3$ and $KTaO_3$. Viewed from the standpoint of the dynamic theory of ferroelectricity, this assumes the existence in $CaTiO_3$ of a lattice instability in the form of a polar soft mode and that this compound is prone to a ferroelectric phase transition. This assumption was substantiated by the apparently first observation [4] of the corresponding temperature behavior of IR reflectance spectra. Quite recently, new data on the soft mode in $CaTiO_3$ were published [5, 6].

Impurities are capable of inducing the transition to the ferroelectric state. This phenomenon was studied in considerable detail for $SrTiO_3$: Ca [7], $SrTiO_3$ doped by other impurities [8], as well as for the Li and Nb impurities in $KTaO_3$ [9]. The $Ca_{1-x}Pb_xTiO_3$ solid solutions have thus far been investigated only on the $PbTiO_3$ side ($x \geq 0.5$) [10–12]. In this connection, investigation of the dielectric properties and the possibility of inducing ferroelectricity by varying the composition of $Ca_{1-x}Pb_xTiO_3$ on the $CaTiO_3$ side appears of interest from the standpoint of both applied and fundamental research as an approach to determining the microscopic causes of instability of these solid solutions against ferroelectric fluctuations and their transformation from the incipient to real state. A positive answer to the question of whether ferroelectricity can be induced was obtained [13] in a study of the permittivity $\varepsilon(\nu)$ in the frequency range 10 Hz $< \nu <$ 1 MHz and of the hysteresis loops. It was established that the temperature of the phase transition to the ferroelectric state increases linearly with increasing lead concentration, until at $x > 0.28$ the solid solution transfers to the polar state for $T > 0$.

It was also shown in [13, 14] that $Ca_{1-x}Pb_xTiO_3$ solid solutions have relaxor properties at certain con-

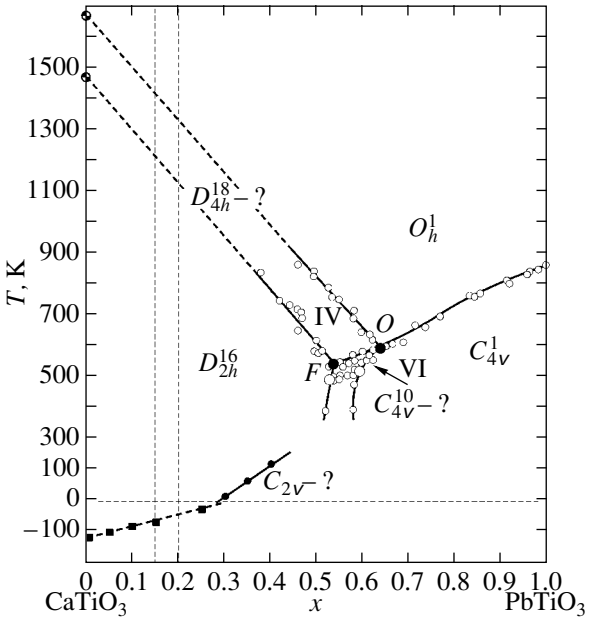

Fig. 1. Experimental phase diagram of the $Ca_{1-x}Pb_xTiO_3$ solid solution system derived from optical [17] (small open circles) and dielectric [13] (small filled circles and squares) measurements. The solid phase-transition lines are drawn through the points, and the dashed lines are their extrapolations. Phases IV and VI have tentatively tetragonal structure, and phase V, orthorhombic. The multiphase points *O* and *F* (large filled circles) are the assumed analogs of the corresponding points on the theoretical phase diagram in Fig. 16. The large open circles identify the three-phase points whose reliability requires additional investigation. Dashed vertical lines refer to the samples studied in this work.

centrations *x*. For instance, studies of the dielectric behavior of ceramics with low Pb contents revealed [13] that, while compositions with $x < 0.3$ behave similarly to pure perovskite, for $x > 0.3$ they exhibit a dependence of the diffuse maximum in $\varepsilon'(T)$ on the measuring field frequency and the maxima $\varepsilon'(T_{max})$ and $\varepsilon''(T_{max})$ do not coincide on the temperature scale. Neutron diffraction study of a $(Ca_{0.5}Pb_{0.5})TiO_3$ solid solution suggests that its structure is orthorhombically distorted by octahedron tilting and displacement of the Pb^{2+}/Ca^{2+} ions from their central perovskite sites [14]. This solid solution has the same symmetry as calcium titanate, $Pnma$–D_{2h}^{16} [15]. Investigation of the real and imaginary parts of the dielectric tensor led to the conclusion [14] that $(Ca_{0.5}Pb_{0.5})TiO_3$ has relaxor properties, which originate from structural frustration caused by the tilting of the TiO_6 octahedra in the $CaTiO_3$ matrix. In the $x = 0.1$ and 0.2 compositions, the structure remains orthorhombic; the orthorhombic distortions decrease substantially at $x = 0.3$ and 0.4 (the corresponding symmetry was not determined with adequate precision), while for $x > 0.5$ the lattice is tetragonal, as established by a TEM inspection of the corresponding solid solutions [16]. While no evidence of ordering of the lead and calcium atoms was found in the $x = 0.1$ and 0.2 compositions, partial ordering was shown to occur at $x = 0.3$ [16].

$Ca_{1-x}Pb_xTiO_3$ crystals were optically studied and an *x* vs. *T* diagram was constructed for $0.38 < x < 1$ in [17]. Figure 1 presents these data together with the results reported in [13]. We can see that there are several different phase states in the region $0.5 < x < 0.7$.

Such a complex concentration behavior of the $Ca_{1-x}Pb_xTiO_3$ solid solution system should manifest itself not only on the macroscopic but also on the microscopic level. This stimulated our investigation of the spectral response of these solid solutions using IR and submillimeter-range spectroscopy. The present communication reports on the results obtained in a study of the dielectric spectra $\varepsilon'(\nu)$ and $\varepsilon''(\nu)$ of $Ca_{1-x}Pb_xTiO_3$ ceramic samples ($x = 0$, 0.15, 0.2, 0.4) measured in the frequency range $\nu = 7$–1000 cm^{-1} at temperatures of 5–300 K. We are planning to extend our studies to values of *x* from 0.4 to 1.0 in order to cover the whole system of $Ca_{1-x}Pb_xTiO_3$ solid solutions. The results obtained in this work are discussed in terms of the Landau theory of phase transitions for coupled soft modes. A *T*–*x* phase diagram based on this theory was constructed for this solid solution system.

2. EXPERIMENTAL

Samples were prepared using standard ceramic technology [13]. The starting materials were OSCh 16-2 grade calcium carbonate $CaCO_3$, OSCh 5-2 grade titanium dioxide TiO_2, and OSCh 5-3 grade lead oxide PbO. Following calcination at 1150°C for 20 h, the samples were finally sintered for 1 h at 1390°C in sealed Pt crucibles in an environment of excess lead oxide. X-ray diffraction analysis showed the samples to be single-phase and have perovskite structure. All samples had a density of 0.92–0.95 of the theoretical x-ray value.

Samples in the form of polished pellets 1 cm in diameter and 0.05 to 0.3 mm thick were used to measure submillimeter-range spectra of transmittance in the region from 3 to 18 cm^{-1} at temperatures from 5 to 300 K and IR reflectance spectra in the range 30–1000 cm^{-1} at room temperature. In the former case, the measurements were carried out on an Epsilon custom-made BWT spectrometer [18], and in the latter, with a Bruker-113v Fourier spectrometer.

Quantitative information on the phonon line parameters was obtained from a dispersion analysis performed in terms of the model of additive oscillators with damping. The $\varepsilon'(\nu)$, $\varepsilon''(\nu)$, and $R(\nu)$ spectra were least squares fitted using the relations

$$\varepsilon'(\nu) = \varepsilon_\infty + \sum_i \frac{\Delta\varepsilon_i \nu_i^2(\nu_i^2 - \nu^2)}{(\nu_i^2 - \nu^2)^2 + \gamma_i^2\nu^2}, \quad (1)$$

$$\varepsilon''(\nu) = \sum_i \frac{\Delta\varepsilon_i \nu_i^2 \nu\gamma_i}{(\nu_i^2 - \nu^2)^2 + \gamma_i^2\nu^2}, \quad (2)$$

$$R(\nu) = \left|\frac{\sqrt{\varepsilon(\nu)} - 1}{\sqrt{\varepsilon(\nu)} + 1}\right|^2. \quad (3)$$

Here, ε_∞ is the high-frequency dielectric constant, ν_i is the natural frequency, γ_i is the damping constant, and $\Delta\varepsilon_i$ is the dielectric contribution, with $\Delta\varepsilon_i\nu_i^2 = f_i$ being the oscillator strength for each mode.

3. CRYSTAL STRUCTURE AND FACTOR-GROUP ANALYSIS

Calcium titanate has an ideal cubic perovskite structure with space group $Pm3m$–O_h^1 at temperatures $T >$ 1580 K. As the temperature is lowered, $CaTiO_3$ undergoes a sequence of phase transitions, whose temperatures and the symmetry of whose resulting phases have not thus far been established unambiguously [19, 20]. The phase sequence is assumed to be the same as that in $SrZrO_3$, namely, $Pm3m \longrightarrow I4/mcm \longrightarrow Cmcm \longrightarrow Pnma$ [21]. For $T <$ 1380 K, the structural distortion becomes stabilized, to be finally described by a rhombic unit cell with parameters a = 5.444 Å, b = 7.644 Å, and c = 5.367 Å and symmetry $Pnma$–D_{2h}^{16} (Fig. 2a) [15, 22]. The deviations from cubic structure are small, with the parameter of the reduced unit cell ($a/\sqrt{2}$, $b/2$, $c/\sqrt{2}$) being 3.82 Å. The unit cell contains four formula units; therefore, there are 60 vibrational degrees of freedom in the rhombic calcium titanate.

Based on the rhombic structure of $CaTiO_3$, Cochran and Zia [23] found that the distortion of the cubic perovskite cell requires three soft modes (at the *M*, *R*, and *X* points) for its description. Subsequent analysis revealed, however, that the observed displacements of atoms can be described in terms of only two soft modes at the *M* and *R* points of the cubic Brillouin zone and that the modes at the *X* points should instead be considered to be secondary order parameters [24, 25]. Figure 2b shows the transformation of the first Brillouin zone under these distortions. The high-temperature phase transitions enrich the Γ point spectrum of the D_{2h}^{16} phase of $CaTiO_3$ with new lines as compared to the spectrum of ideal perovskite. The degeneracy of the threefold degenerate modes at the zone center of the cubic phase is lifted, and zone folding transfers the modes from the *M*, *R*, and *X* points at the boundary to the zone center (Fig. 2b). Figure 3 displays the corresponding correlations of the representations. To make the pattern complete, correlations of the symmetry types for the phase transition in $PbTiO_3$ are also shown.

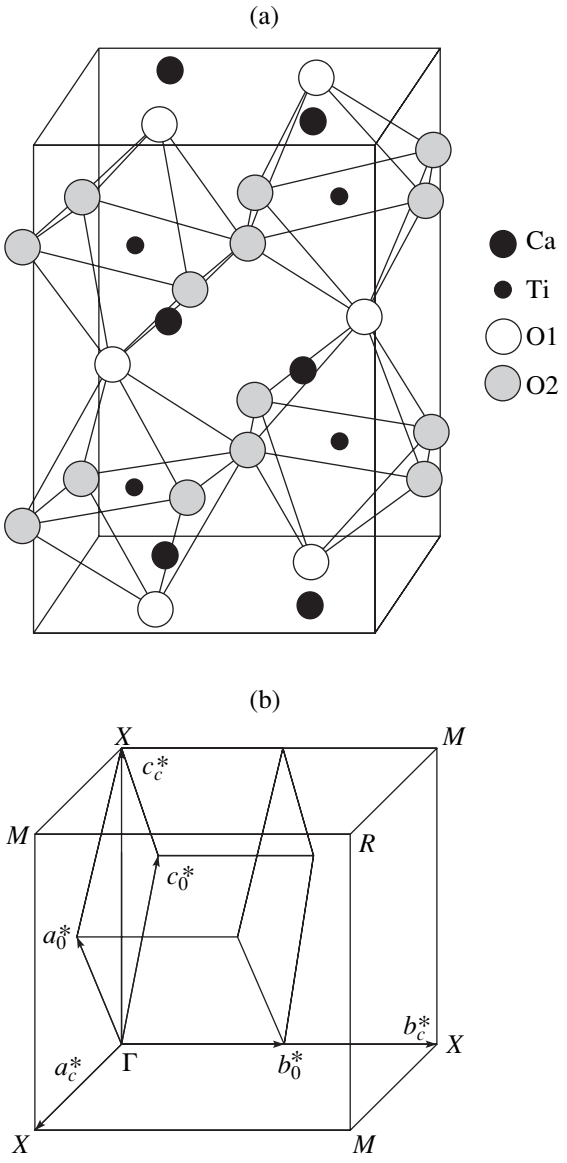

Fig. 2. (a) Unit cell of orthorhombic $CaTiO_3$ and (b) Brillouin zones of the simple cubic, Γ_c, and orthorhombic, Γ_o, unit cells. Points *M*, *R*, and *X* of the cubic cell pass into the center of the Brillouin zone of the orthorhombic cell as the $Pm3m \longrightarrow Pnma$ antiferrodistorsive phase transition occurs.

Ab initio calculations of the soft mode frequencies for calcium titanate have been performed in a number of publications. It turned out that the polar soft mode frequency for the cubic calcium titanate is imaginary for $T = 0$ and is equal (in cm^{-1}) to 153*i* [27] or 140*i* [28]. This means that if the calcium titanate were cubic, it would be a ferroelectric with a fairly high ferroelectric transition temperature. Analogous calculations performed for the rhombic phase yield about 90 cm^{-1} for

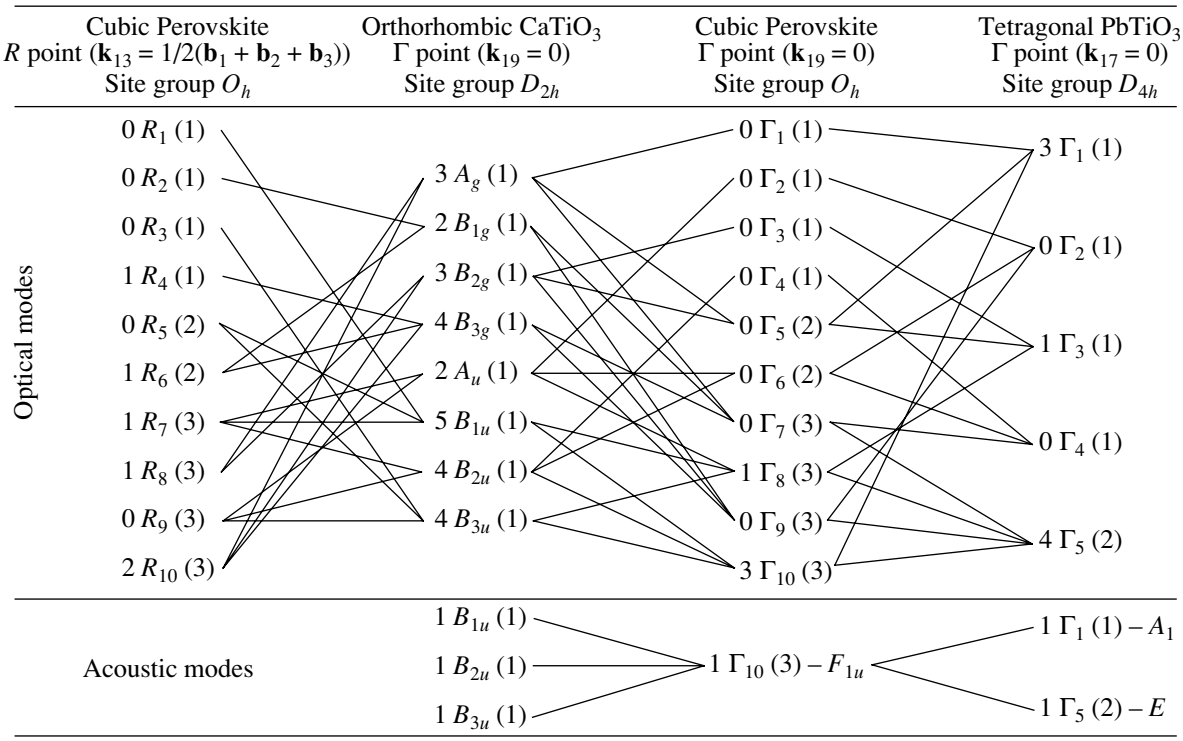

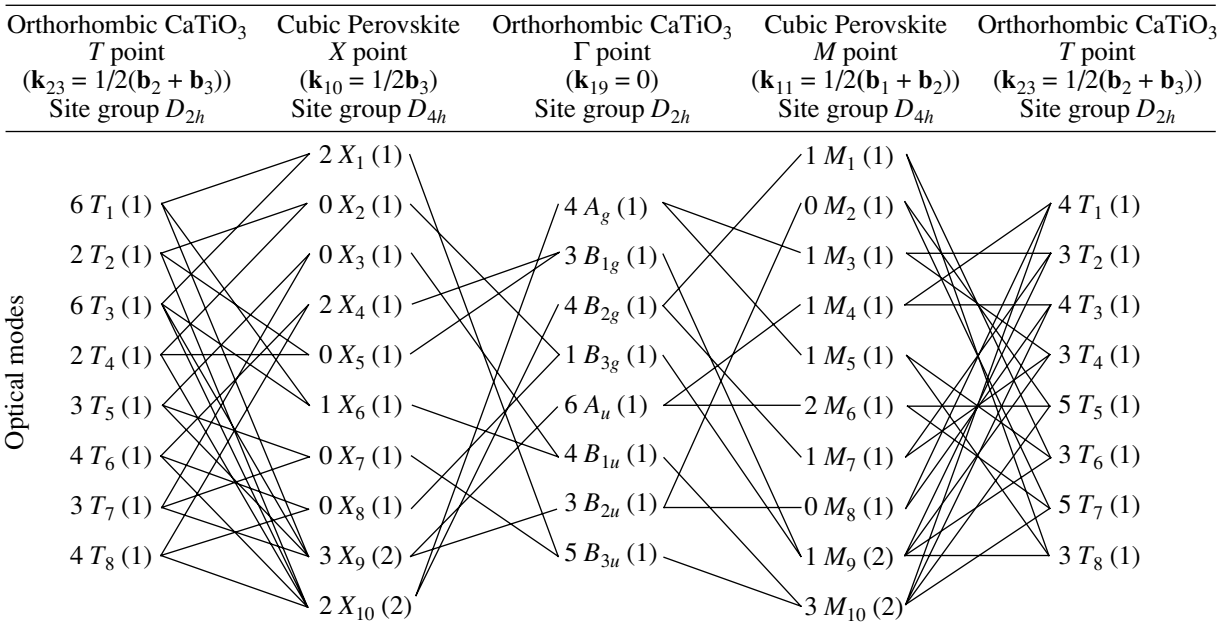

Composition of the mechanical representation for $CaTiO_3$ and selection rules

O_h^1-phase: F_{2u} (Γ_8) [silent] + $4F_{1u}$ (Γ_{10}) [IR]

D_{2h}^{16}-phase: $7A_g$ [Raman] + $5B_{1g}$ [Raman] + $7B_{2g}$ [Raman] + $5B_{3g}$ [Raman] + $8A_u$ [silent] + $10B_{1u}$ [IR] + $8B_{2u}$ [IR] + $10B_{3u}$ [IR]

Fig. 3. Composition of the mechanical representations and correlation diagrams for the symmetry types of the *Pm*3*m* cubic perovskite, tetragonal *P*4*mm* $PbTiO_3$ phase, and orthorhombic *Pnma* phase of $CaTiO_3$. The notation in the representations is in accordance with that from [26]. The numbers preceding the symbol of an irreducible representation indicate how many times it enters the mechanical representation, and the numbers following it (in parentheses) specify the dimension of the small irreducible representation. The acoustic and optic modes are decoupled. To make the figure more revealing, we show below the composition of mechanical representations for the centers of the Brillouin zones of the cubic and rhombic $CaTiO_3$ phases, the representations for the cubic phase being given in both spectroscopic notation and according to [26]; the activity of modes in Raman scattering and IR absorption is specified in brackets after the symbol of the irreducible representation (silent means that the mode is inactive in both Raman scattering and IR absorption).

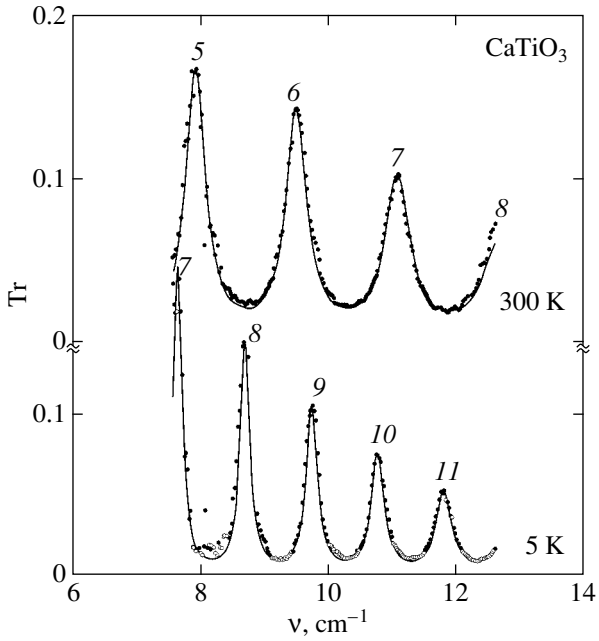

Fig. 4. Submillimeter-range transmittance spectra of a $CaTiO_3$ ceramic plate of thickness d = 0.245 mm recorded at 5 and 300 K. Points are experiment, and lines are calculations made using the Fresnel relation for the transmittance of a plane dielectric layer with parameters ε' and ε" given in Fig. 8. The numerals identify the peak numbers m.

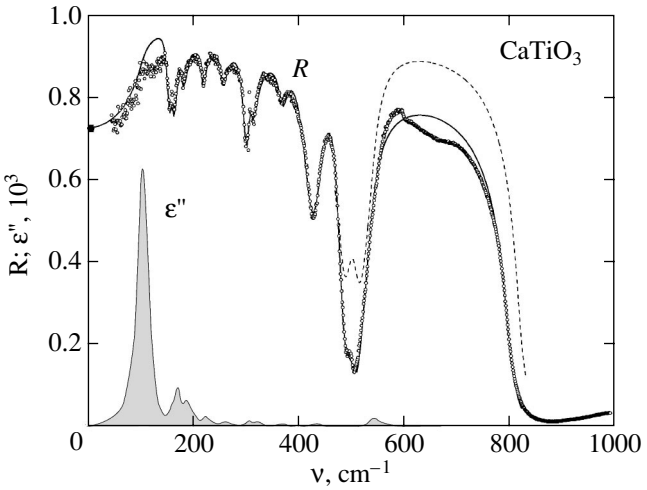

Fig. 5. Infrared reflectance spectrum $R(\nu)$ of a ceramic $CaTiO_3$ sample measured at 295 K and the absorption spectrum ε"(ν) derived from it by dispersion analysis. The points in the $R(\nu)$ spectrum are experiment, and the solid and the dashed lines represent model description using thirteen oscillators, with and without inclusion of coupling between the two oscillators extreme in frequency, respectively. The filled circle on the left is the reference value of R calculated from submillimeter-range data for ε' and ε".

the soft mode frequency [28]. In this case, there should be no ferroelectric phase transition, exactly what is observed experimentally.

4. SUBMILLIMETER AND INFRARED SPECTRA

4.1. Calcium Titanate

Figure 4 presents submillimeter-range transmittance spectra Tr(ν) of a ceramic plane-parallel $CaTiO_3$ plate with a thickness d = 0.245 mm. The spectra feature oscillatory curves typical of transparent samples and indicating interference of plane monochromatic electromagnetic waves in the sample (the Fabry–Perot effect). In these conditions, maxima in the transmittance appear with varying radiation frequency every time an integer number of half-waves fit into the sample thickness:

$$m(\lambda/2) = nd,$$

where m is the number of the interference maximum, λ is the radiation wavelength, and n is the refractive index. The positions of the peaks of transmittance Tr(ν) on the frequency scale and their separation are determined by the magnitude of the refractive index $n(\nu)$, and the values of Tr(ν) at the maxima and the oscillation swing are governed by the extinction coefficient $k(\nu)$ (the imaginary part of the refractive index). The contraction of the interference pattern in Fig. 4 observed under sample cooling indicates an increase in the refractive index at low temperatures. Note that the refractive index is independent of frequency both at 295 and at 5 K, which is indicated by the equidistant peak positions in frequency at both temperatures.

Table 1. Frequencies ν_i, dielectric contributions $\Delta\varepsilon_i$, and damping coefficients γ_i of IR-active modes in $CaTiO_3$ obtained by dispersion analysis of the reflectance spectrum $R(\nu)$ displayed in Fig. 5

i	ν_i, cm^{-1}	$\Delta\varepsilon_i$	γ_i, cm^{-1}
1	108.7	140 ± 2	19.6
2	170.6	10.10	16.2
3	187.3	2.70	10.1
4	223.0	1.40	8.5
5	252.5	1.90	56.3
6	260.9	0.40	14.5
7	307.0	0.40	11.7
8	312.4	0.10	19.7
9	323.5	0.90	25.4
10	373.2	0.40	30.2
11	441.3	0.80	43.7
12	449.1	0.20	24.7
13	541.6	1.30	27.4

Note: The accuracy of determination of ν_i and γ_i is ±0.1 cm^{-1}, and that of $\Delta\varepsilon_i$ for i = 2–13 is ±0.05. The measurements were made at room temperature. The coupling between the first and thirteenth oscillators is $\delta_{1-13} = 63 \pm 3$; $\varepsilon_\infty = 5.20 \pm 0.05$.

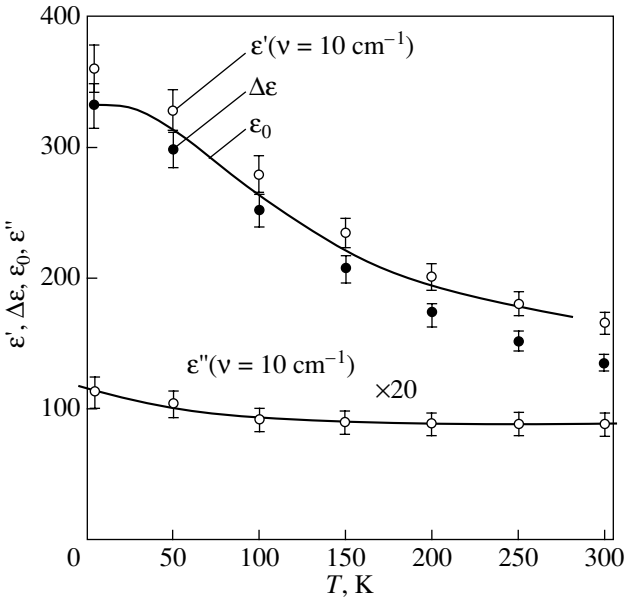

Fig. 6. Temperature dependences of the real and imaginary parts of the permittivity ε' and ε'' of $CaTiO_3$. Open circles are submillimeter-range measurements made at ν = 10 cm^{-1}, filled circles are the calculated dielectric contribution Δε from the soft mode, and the solid line represents static permittivity [13].

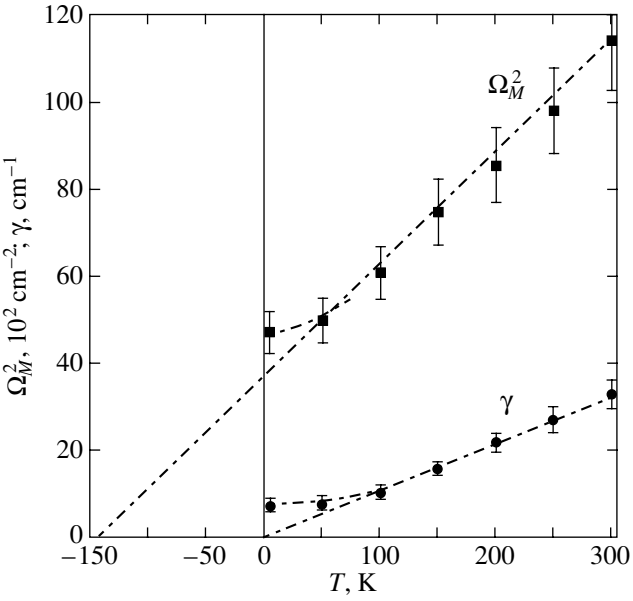

Fig. 7. Temperature dependences of the soft mode frequency and damping in a ceramic $CaTiO_3$ sample obtained by fitting the oscillator model to experiment (Fig. 5).

The solid lines in Fig. 4 are fits to the experimental Tr(ν) relation made using the Fresnel expression for the transmittance of a plane dielectric layer. This fitting procedure makes it possible to derive the real and imaginary parts of the refractive index $n(\nu, T)$ and $k(\nu, T)$, the real and imaginary parts of the permittivity $\varepsilon'(\nu, T)$ and $\varepsilon''(\nu, T)$, and the reflectance $R(\nu, T)$ [18].

Figure 5 shows infrared reflectance spectra $R(\nu)$. The solid line displays the results of a dispersion analysis performed by least squares fitting using Eqs. (1)–(3). The $R(\nu)$ spectrum was modeled by a sum of thirteen harmonic oscillators (as follows from a factor-group analysis (see Fig. 3), the IR spectrum should contain 25 lines of symmetry $9B_{1u} + 7B_{2u} + 9B_{3u}$; a possible explanation for the smaller observed number of these lines is proposed in [6]). All the oscillators were assumed to be independent, and only the coupling of the first to the last oscillator (solid line in Fig. 5) was taken into account. We made use of the imaginary coupling δ_{1-13} traditionally employed in the case of perovskites [29]. As seen from Fig. 5, the inclusion of this coupling is essential for frequencies above 500 cm^{-1}. The values of the parameters thus obtained are listed in Table 1.

Reflection IR spectroscopy has a well-known shortcoming in that it cannot provide good accuracy for measuring reflectance spectra $R(\nu)$ at low frequencies, below approximately 100 cm^{-1}. We sidestepped this drawback in the calculations by assigning a large weight to the high-precision low-frequency value $R = 0.73 \pm 0.01$ (filled circle on the left of Fig. 5), which was derived from submillimeter data on n and k. Shown in the bottom part of Fig. 5 is a model absorption spectrum obtained using 13 oscillators and corresponding to the experimental $R(\nu)$ spectrum. Figure 5 illustrates a complex and not obvious relation between the reflectance, $R(\nu)$, and absorption, $\varepsilon''(\nu)$, spectra; indeed, strong and large variations of R at high frequencies are paralleled by only weak ε'' fluctuations, whereas at low frequencies the much weaker dispersion of $R(\nu)$ is contrasted by a high lattice peak.

As seen from Table 1, the major contribution to the static permittivity ε_0 comes from only one mode, the lowest frequency mode, with a dielectric contribution $\Delta\varepsilon \approx 140$. The remaining 12 vibrations combined with ε_∞ yield about 26, i.e., ~15% of the total value. Assuming the temperature-induced variations in $\varepsilon'(T)$ and $\varepsilon''(T)$ observed in the submillimeter range to be due to the temperature evolution of this strongest mode (we call it soft) of frequency Ω_M, i.e., disregarding the temperature variations of the remaining contributions, we obtain the following temperature dependence for the soft mode contribution: $\Delta\varepsilon(T) = \varepsilon'(T) - 26$. This relation is plotted in Fig. 6 with filled circles. We further assume the soft mode oscillator strength $f(T) = \Delta\varepsilon(T)\Omega_M^2(T)$, just like ε_∞, to be independent of temperature, which is equivalent to the assumption that the Lyddane–Sachs–Teller relation holds. This assumption is substantiated by the almost perfect coincidence of the submillimeter values of the permittivity ε' with the static permittivity ε_0 measured at low frequencies [13] and, hence, by the absence of lower frequency excitations complementary

to the soft mode. With known room-temperature values of $\Delta\varepsilon$ and Ω_M (Table 1), we find the reference oscillator strength at room temperature, $f = 1.7 \times 10^6$ cm^{-2}, and use this constant value of f to calculate the temperature behavior of the soft mode frequency $\Omega_M(T)$ from the $\Delta\varepsilon(T)$ dependence (Fig. 7).

The $\Delta\varepsilon(T)$ and $\Omega_M(T)$ relations obtained in this way were employed to derive the temperature dependence of the soft mode damping $\gamma(T)$. To do this, we used Lorentzians at fixed temperatures for given $\Delta\varepsilon$ and Ω_M to model frequency dependences of the permittivity $\varepsilon'(\nu)$ and $\varepsilon''(\nu)$ with the values of γ at which the calculated low-frequency tails of the $\varepsilon'(\nu)$ and $\varepsilon''(\nu)$ lines would pass through the experimental values ε' and ε'' in the submillimeter range (Fig. 8). The temperature dependence of damping, $\gamma(T)$, obtained in this way is plotted in Fig. 7.

The data presented in Fig. 8 give the complete frequency and temperature pattern of the soft mode behavior in $CaTiO_3$ constructed following the above technique. It appears appropriate to note here that because the frequency of the soft mode is low and its intensity is high, observation of the soft mode using the traditional IR reflectance method is highly problematic. Figure 9 compares the absorption spectra due to the soft mode with the corresponding reflectance spectra. We see that the remarkably strong frequency- and temperature-induced transformations of the soft mode are very weakly manifested in the reflectance spectra. The soft mode parameters can be successfully extracted from such spectra only if absolute measurements of the reflectance are made with a high enough accuracy (not worse than 1%) throughout the spectrum covered.

4.2. $Ca_{1-x}Pb_xTiO_3$ Solid Solutions

These solid solutions were measured following a technique similar to that described in the preceding section. Figures 10 and 11 present the sets of spectra obtained in this study at various temperatures, namely, the IR reflectance (for frequencies above 20 cm^{-1}) and the submillimeter transmittance and phase (insets below 20 cm^{-1}) for samples with $x = 0.15$ and 0.4. The spectra of the real and imaginary parts of the permittivity in the low-frequency domain are displayed in Figs. 12 and 13.

The reflectance spectra have a pattern typical of perovskites and resemble those of pure $CaTiO_3$ (see Subsection 4.1, as well as [4–6, 30]). In $Ca_{1-x}Pb_xTiO_3$ samples (as in $CaTiO_3$), only the three lowest frequency modes provide the main contribution to the macroscopic dielectric behavior of the samples. The combined contribution to $\varepsilon_0 = \varepsilon_\infty + \Sigma_i \Delta\varepsilon_i$ coming from the remaining ($i > 3$) high-frequency lines does not exceed 15%. Note the radically different temperature behavior of the spectra of the sample with a low lead content ($x = 0.15$) and of the sample with $x = 0.4$. The frequency range below ~200 cm^{-1} for the former sample can be

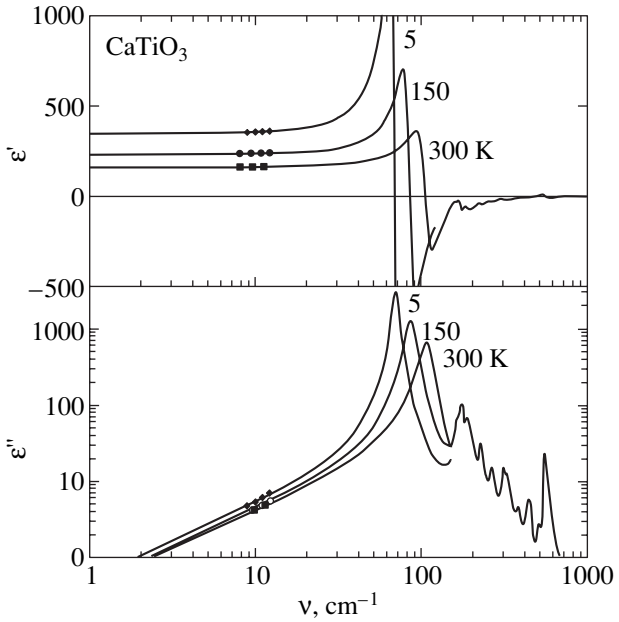

Fig. 8. Frequency and temperature dependences of $\varepsilon'(\nu, T)$ and $\varepsilon''(\nu, T)$ associated with the soft mode in $CaTiO_3$. Points are experiment (Fig. 4), and lines represent model calculations involving thirteen oscillators with the parameters listed in Table 1.

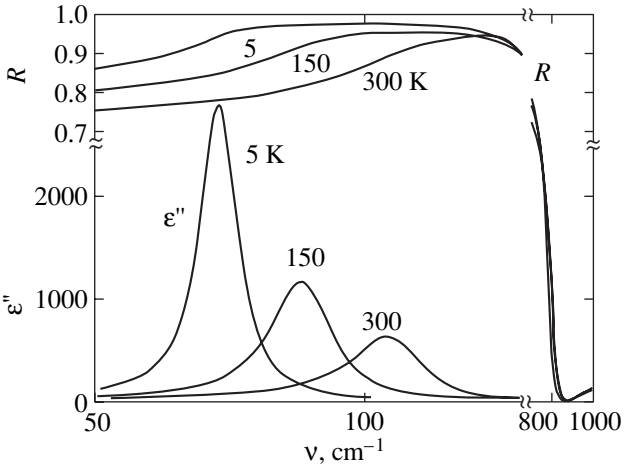

Fig. 9. Comparison of $R(\nu)$ and $\varepsilon''(\nu)$ spectra obtained at different temperatures for $CaTiO_3$.

satisfactorily approximated by three lines (labeled in Fig. 12 by M_1, M_2, M_3). At 300 K, the static value of the permittivity extrapolated from spectra of the $x = 0.15$ sample is $\varepsilon_0 \approx 250$; this quantity grows steadily to become about three times higher at 5 K. As seen from Fig. 12, this growth is caused by the simultaneous softening of all three lines indicated above. By contrast, the temperature behavior of the lines of the $x = 0.4$ sample is radically different; indeed, only the lowest frequency mode M_1 is relatively unstable in temperature, the temperature dependence of the mode being not monotonic

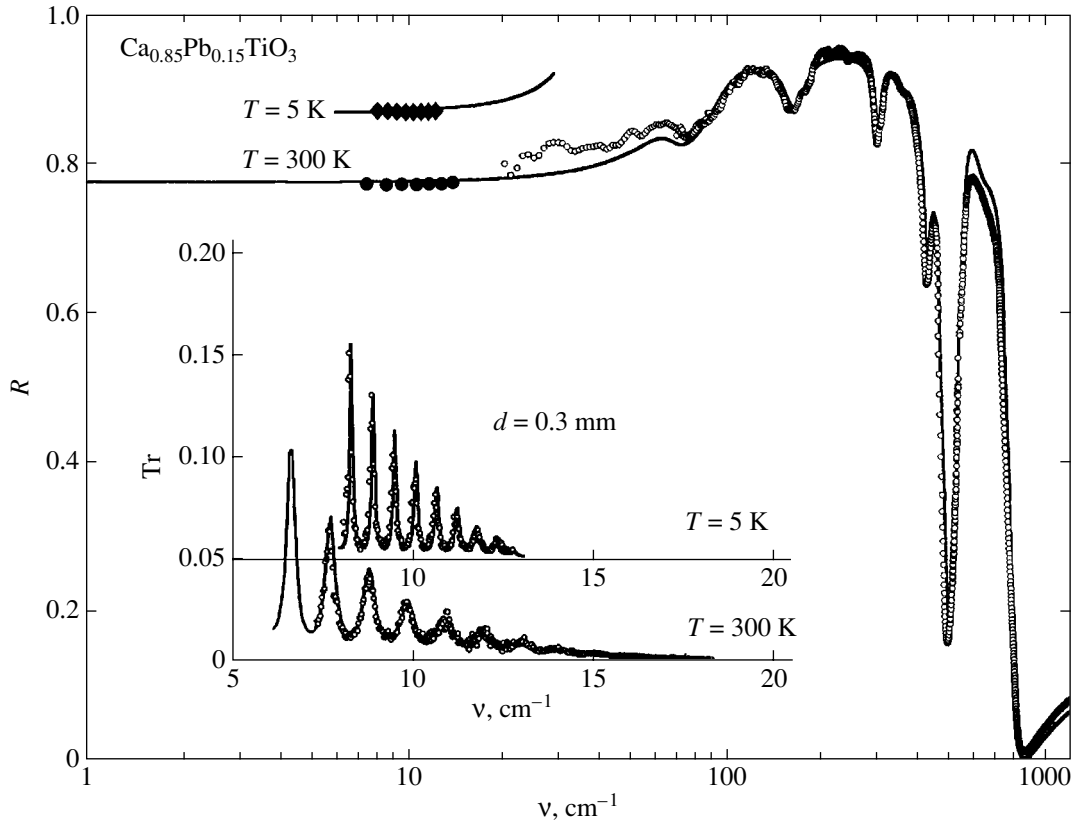

Fig. 10. Reflectance $R(\nu)$ and transmittance $\mathrm{Tr}(\nu)$ (inset) spectra obtained at 5 and 300 K on a $Ca_{1-x}Pb_xTiO_3$ sample with $x = 0.15$. Points are experiment, and lines represent fitting with the model of additive oscillators described by Eqs. (1)–(3). Sample thickness $d = 0.3$ mm.

(Fig. 13). In the beginning, as the temperature is lowered, the mode softens, but below ~180 K it starts to harden again, with the static dielectric contributions at high and low temperatures being approximately the same ($\varepsilon_0 \approx 650$). There is one more difference which we believe to be significant; namely, the width of the M_1 mode in the sample with $x = 0.4$ is very large as compared with that of the sample with a low lead content (cf. Figs. 12, 13). Its profile retains the resonance character of an overdamped oscillator (negative $\varepsilon'(\nu)$ at high frequencies). This qualitative description is illustrated in Figs. 14 and 15.

Figure 14 illustrates the temperature behavior of the squared frequencies of modes M_1, M_2, and M_3 obtained for $x = 0$, 0.15, 0.2, and 0.4. The samples with a low lead content exhibit softening of all three resonances (for M_3, it is small), a feature characteristic of the conventional temperature dependence of soft modes. All these modes are definitely coupled. In samples with $x = 0$, 0.15, and 0.2, the temperature and concentration dependences of the soft modes M_1, M_2, and M_3 and of the static permittivity ε_0 taken from [13] are seen to be correlated in accordance with the Lyddane–Sachs–Teller expression (in-phase variation of the soft-mode frequencies and inverse static permittivity). The temperature of the transition to the polar state remains, however, negative, as follows from extrapolating the graphs for the M_1 and M_2 modes, but is higher than that for pure $CaTiO_3$ (the extrapolated value is $T_0 = -142$ K in our study (Fig. 7) and $T_0 = -110$ K in [6]). This does not hold for the $x = 0.4$ sample. The variation of the M_1 mode frequency with temperature is nonmonotonic here, which implies possible phase transitions for $T_c > 70$ K. Note that the M_2 and M_3 modes are indistinguishable (their frequencies are probably very similar; we denoted them by $M_{2,3}$) and practically independent of temperature.

Figure 15a plots temperature dependences of the dielectric contributions due to resonances. For samples with $x < 0.3$, the static [13] and our total dynamic values correlate satisfactorily on the quantitative level, $\varepsilon_0 = \varepsilon_\infty + \Sigma_i \Delta\varepsilon_i$ ($i = 3$), throughout the temperature range covered. On the other side, for $x = 0.4$, the dielectric contribution from the M_1 mode reaches its maximum [$\varepsilon(T) \sim 950$)] near 180 K, which is close to the high-temperature maximum of the low-frequency permittivity $\varepsilon(T)$ plotted in Fig. 15b. Note that linear extrapolation of the high-temperature part of the $\nu^2(T)$ dependence for this line (Fig. 14) and an analogous extrapolation for the low-frequency $\varepsilon^{-1}(T)$ dependence shown in Fig. 15b yield approximately the same temperature (~70 K). The same applies to the extrapolations of the

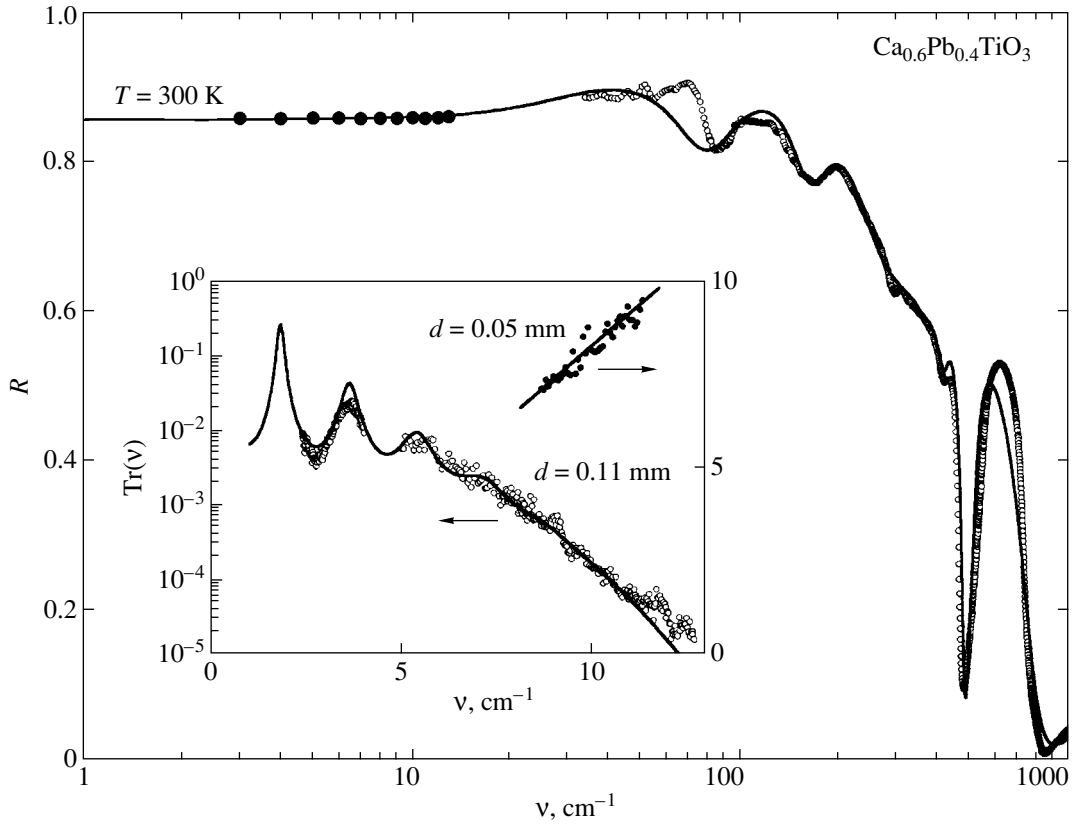

Fig. 11. Spectra of reflectance $R(\nu)$, transmittance $\mathrm{Tr}(\nu)$, and phase shift $\varphi(\nu)$ (inset) obtained at 300 K on $Ca_{1-x}Pb_xTiO_3$ samples of various thicknesses with $x = 0.4$. Points are experiment, and lines represent fitting with the model of additive oscillators described by Eqs. (1)–(3).

low-temperature parts of both dependences to zero near 250 K. The absence of the double-humped feature in the $\Delta\varepsilon(T)$ graph (Fig. 15) is most likely due to the large step ΔT chosen for measuring the spectra. Thus, in the sample with $x = 0.4$, we also have a correlation between the static and dynamic data. The small quantitative discrepancy may be associated with the fact that the static and spectroscopic measurements were conducted on different samples (but prepared using the same technology). Note that at $x = 0.4$ a solid solution is difficult to prepare and samples may be irreproducible. Finally, we note a certain analogy (the presence of two maxima, albeit inverted in intensity on the temperature scale) in the behavior of $\varepsilon(T)$ in the $Ca_{1-x}Pb_xTiO_3$ sample with $x = 0.4$ and in ceramics [31] and $CdTiO_3$ crystals [32].

Table 2 lists, for various $Ca_{1-x}Pb_xTiO_3$ compositions, the oscillator parameters for the three lowest frequency lines obtained at 5 and 300 K using the above spectral fitting.

5. DISCUSSION AND PHASE DIAGRAM OF $Ca_{1-x}Pb_xTiO_3$ SOLID SOLUTIONS

To gain a better understanding of the experimental results obtained, let us consider a simple model within the phenomenological theory by Landau.

The $CaTiO_3$ perovskite is cubic ($Pm\bar{3}m$–O_h^1 symmetry) above 1580 K and undergoes a sequence of three phase transitions [15]

$$Pnma\text{–}D_{2h}^{16} \overset{1380\ \mathrm{K}}{\longleftrightarrow} Cmcm\text{–}D_{2h}^{17}$$

$$\overset{1500\ \mathrm{K}}{\longleftrightarrow} I4/mcm\text{–}D_{4h}^{18} \overset{1580\ \mathrm{K}}{\longleftrightarrow} Pm\bar{3}m\text{–}O_h^1.$$

These high-temperature phase transitions are described as resulting from distortions because of the threefold degenerate phonon modes at the R and M points of the Brillouin zone being unstable. The eigenvectors of these modes display pure rotation of the TiO_6 octahedra (in-phase or anti-phase for the adjacent octahedral; see Fig. 2a) about different axes of the perovskite cell [33]. The phase of symmetry $I4/mcm$–D_{4h}^{18} is realized when only one component of the threefold degenerate mode at the R point condenses. Additional condensation of one component of the unstable M mode gives rise to a phase transition to the orthorhombic $Cmcm$–D_{2h}^{17} and $Pnma$–D_{2h}^{16} phases, with one more R-mode component condensing in the latter case. The situation becomes still more complex when the rotations are complemented by displacements of Ti ions

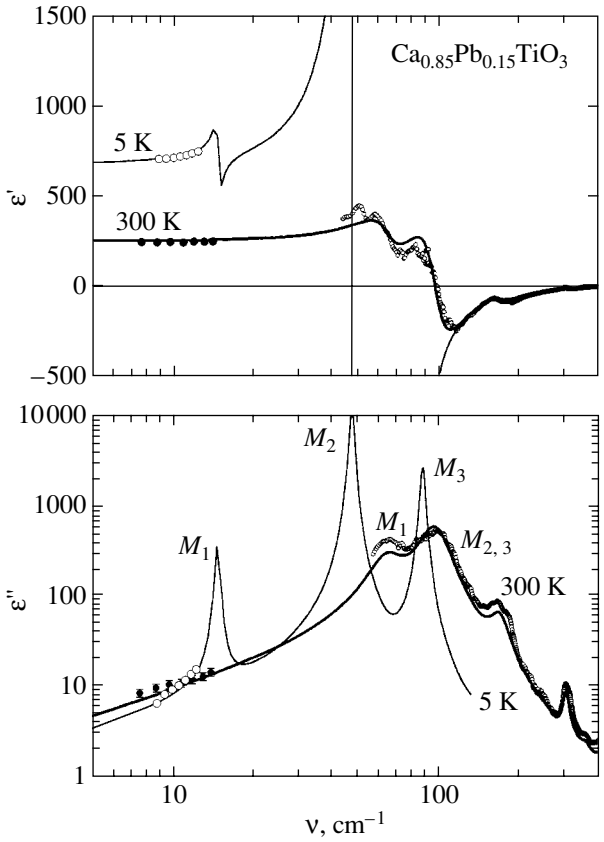

Fig. 12. Spectra of the real, ε'(ν), and imaginary, ε"(ν), parts of the permittivity of a $Ca_{1-x}Pb_xTiO_3$ sample with $x = 0.15$. Points are experiment, and lines represent fitting with the model of additive oscillators described by Eqs. (1)–(3). The letters M_1, M_2, and M_3 denote the three lowest frequency lines in the spectra.

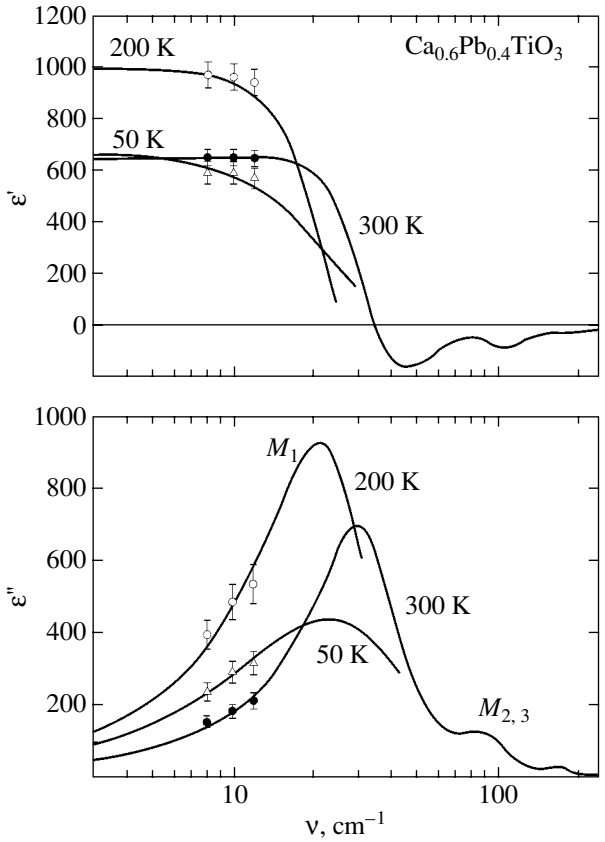

Fig. 13. Spectra of the real, ε'(ν), and imaginary, ε"(ν), parts of the permittivity of a $Ca_{1-x}Pb_xTiO_3$ sample with $x = 0.4$ at various temperatures. Points are experiment, and lines represent fitting with the model of additive oscillators described by Eqs. (1)–(3). The letters M_1 and $M_{2,3}$ denote the two lowest frequency lines in the spectra.

from their octahedral sites, for which the zone-center mode of symmetry F_{1u} is responsible. Structural distortions associated with all the above three soft modes were analyzed in [34] using the group-theoretical method, and 60 low-symmetry phases were indicated. Note that the above communication does not list all symmetry-allowed distortions, whose number can be shown to amount to 92, but consideration of this point is beyond the scope of the present paper. It is essential here that the ferroelectric phases $Pmc2_1$–C_{2v}^2, $Pmn2_1$–C_{2v}^7, and $Pma2_1$–C_{2v}^9 originate from the $Pnma$–D_{2h}^{16} phase when one or two components (of equal amplitude) of the threefold degenerate F_{1u} mode also condense [34].

In what follows, we use Landau's thermodynamic theory for second-order transitions, which is based essentially on the assumption of the possibility of expanding the nonequilibrium potential $\Phi(\eta)$ in powers of the "small" parameter η (the order parameter) and keeping only low-order terms. In our case, the order parameter should be made up of basis functions of the representations corresponding to the displacement modes M_5, R_8, and Γ_{10} (F_{1u}). (We employ here the notation of irreducible representations developed by Kovalev [26].) Because each of the M_5, R_8, and Γ_{10} modes is threefold degenerate, the order parameter η is nine-dimensional [$(m_1, m_2, m_3)(r_1, r_2, r_3)(g_1, g_2, g_3)$]. The solutions of the equations of state for the above phases (and a few others as well) are vectors in representation space; they are listed in Table 3 and are similar to the corresponding vectors specified in [34]. Since these model-independent solutions for each mode are characterized by a single parameter, the corresponding effective thermodynamic Landau potential can be written in the "isotropic" form with biquadratic interaction between modes (neglecting the threefold mode degeneracy and the need to introduce anisotropic terms into the potential):

$$\Phi = \alpha_2 m^2 + \alpha_4 m^4 + \beta_2 r^2 + \beta_4 r^4 + \gamma_2 g^2 + \gamma_4 g^4 - \delta_{22} m^2 r^2 - \varepsilon_{22} m^2 g^2 - \eta_{22} r^2 g^2 + \ldots. \quad (4)$$

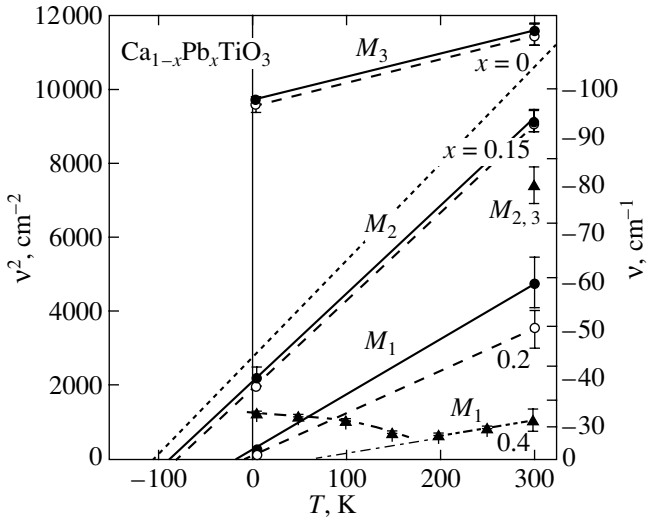

Fig. 14. Temperature behavior of the low-frequency modes in $Ca_{1-x}Pb_xTiO_3$ solid solutions (M_1, M_2, and M_3 indicate the three lowest frequency lines in the spectra) for different values of x: $x = 0.15$ (filled circles, solid lines), $x = 0.2$ (open circles, dashed lines), and $x = 0.4$ (triangles, dash-dotted lines). The right-hand (nonlinear) scale provided for convenience duplicates the left-hand one. The dashed line originating from point $T_0 = -105$ K compares the soft-mode behavior in pure $CaTiO_3$ [16].

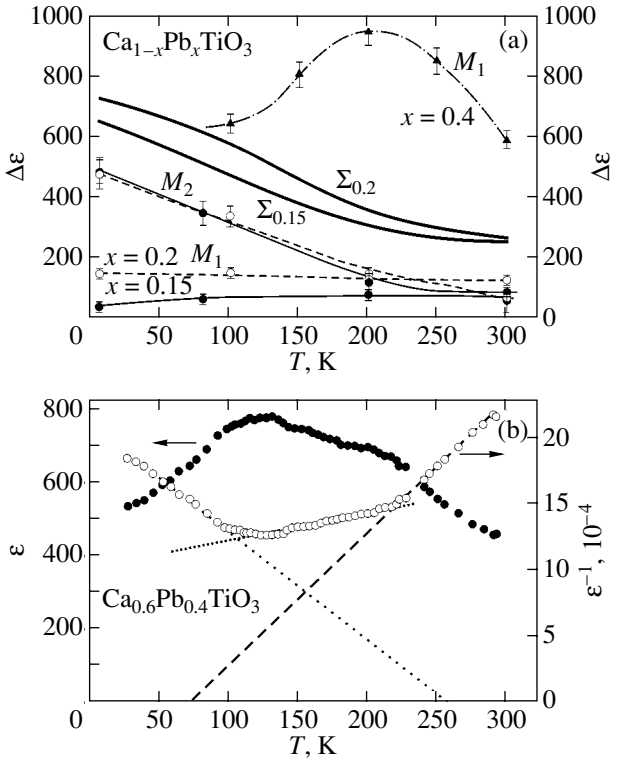

Fig. 15. Temperature behavior of the oscillator parameters of low-frequency modes in $Ca_{1-x}Pb_xTiO_3$ solid solutions. M_1, M_2, and M_3 label the three lowest frequency lines in the spectrum. (a) Dielectric contribution $\Delta\varepsilon(T)$ for the M_1 and M_2 modes; notation is the same as in Fig. 14; $\Sigma_{0.15}$ and $\Sigma_{0.2}$ are the total dielectric contributions from the lowest frequency modes in the $x = 0.15$ and 0.2 samples, respectively. (b) Temperature behavior of $\varepsilon(T)$ and $\varepsilon^{-1}(T)$ for the $x = 0.4$ sample measured at a field frequency of 1 kHz. The dashed and dotted straight lines plot the Curie–Weiss linear relations for $\varepsilon^{-1}(T)$.

Potential (4) is a function of components of the three modes m, r, and g (no longer degenerate) and is truncated to the fourth order of invariants in the pure modes and to their biquadratic coupling. The Greek letters denote the constants of the potential, which, in general, depend on external conditions (temperature, pressure, crystal composition, etc.). We assume here that mode coupling lowers the energy of the system, i.e., that $\delta_{22} > 0$, $\varepsilon_{22} > 0$, and $\eta_{22} > 0$. In addition, we assume (as is usually done in the Landau theory) that only the constants α_2, β_2, and γ_2 in the quadratic terms are linear functions of the temperature and concentration:

$$\alpha_2 = \alpha_{mT}(T - T_M) + \alpha_{mx}(x - x_M),$$

$$\beta_2 = \beta_{rT}(T - T_R) + \beta_{rx}(x - x_R),$$

$$\gamma_2 = \gamma_{gT}(T - T_\Gamma) + \gamma_{gx}(x - x_\Gamma).$$

The equations of state of model (4) are $\partial\Phi/\partial m = \partial\Phi/\partial r = \partial\Phi/\partial g = 0$ and allow the following eight solutions:

$$(0)\ m = r = g = 0;$$

$$(1)\ m \neq 0,\quad r = 0,\quad g = 0:\quad m^2 = -\frac{\alpha_2}{2\alpha_4};$$

$$(2)\ m = 0,\quad r \neq 0,\quad g = 0:\quad r^2 = -\frac{\beta_2}{2\beta_4};$$

$$(3)\ m = 0,\quad r = 0,\quad g \neq 0:\quad g^2 = -\frac{\gamma_2}{2\gamma_4};$$

$$(4)\ m \neq 0,\quad r \neq 0,\quad g = 0:$$

$$m^2 = -\frac{\beta_2\delta_{22} + 2\beta_4\alpha_2}{4\alpha_4\beta_4 - \delta_{22}^2},\quad r^2 = -\frac{\alpha_2\delta_{22} + 2\alpha_4\beta_2}{4\alpha_4\beta_4 - \delta_{22}^2};$$

$$(5)\ m \neq 0,\quad r = 0,\quad g \neq 0:$$

$$m^2 = -\frac{\gamma_2\varepsilon_{22} + 2\gamma_4\alpha_2}{4\alpha_4\gamma_4 - \varepsilon_{22}^2},\quad g^2 = -\frac{\alpha_2\varepsilon_{22} + 2\alpha_4\gamma_2}{4\alpha_4\gamma_4 - \varepsilon_{22}^2}; \quad (5)$$

$$(6)\ m = 0,\quad r \neq 0,\quad g \neq 0:$$

$$r^2 = -\frac{\gamma_2\eta_{22} + 2\gamma_4\beta_2}{4\beta_4\gamma_4 - \eta_{22}^2},\quad g^2 = -\frac{\beta_2\eta_{22} + 2\beta_4\gamma_2}{4\beta_4\gamma_4 - \eta_{22}^2};$$

$$(7)\ m \neq 0,\quad r \neq 0,\quad g \neq 0:$$

$$m^2 = \frac{1}{2}\frac{(4\beta_4\gamma_4 - \eta_{22}^2)\alpha_2 + (2\gamma_4\delta_{22} + \varepsilon_{22}\eta_{22})\beta_2 + (2\beta_4\varepsilon_{22} + \delta_{22}\eta_{22})\gamma_2}{\delta_{22}\varepsilon_{22}\eta_{22} - (4\alpha_4\beta_4 - \delta_{22}^2)\gamma_4 + \alpha_4\eta_{22}^2 + \beta_4\varepsilon_{22}^2},$$

$$r^2 = \frac{1}{2}\frac{(4\alpha_4\gamma_4 - \varepsilon_{22}^2)\beta_2 + (2\gamma_4\delta_{22} + \varepsilon_{22}\eta_{22})\alpha_2 + (2\alpha_4\eta_{22} + \delta_{22}\varepsilon_{22})\gamma_2}{\delta_{22}\varepsilon_{22}\eta_{22} - (4\alpha_4\beta_4 - \delta_{22}^2)\gamma_4 + \alpha_4\eta_{22}^2 + \beta_4\varepsilon_{22}^2},$$

$$g^2 = \frac{1}{2}\frac{(4\alpha_4\beta_4 - \delta_{22}^2)\gamma_2 + (2\alpha_4\eta_{22} + \varepsilon_{22}\delta_{22})\beta_2 + (2\beta_4\varepsilon_{22} + \delta_{22}\eta_{22})\alpha_2}{\delta_{22}\varepsilon_{22}\eta_{22} - (4\alpha_4\beta_4 - \delta_{22}^2)\gamma_4 + \alpha_4\eta_{22}^2 + \beta_4\varepsilon_{22}^2}.$$

The correspondence between these solutions and the model-independent solutions listed in Table 3 is fairly obvious, with the exception of the D_{2h}^{17} and D_{2h}^{16} phases, on the one hand, and the polar orthorhombic phases C_{2v}^2, C_{2v}^7, and C_{2v}^9, on the other, which are "indistinguishable" within model (4). Because the symmetry of the polar phases still remains unknown, this does not make the proposed form of the potential invalid. The same applies to the two rhombic phases, D_{2h}^{17} and D_{2h}^{16}, the former not having been established

Table 2. Numerical values of the oscillator parameters for the three lowest frequency modes M_1, M_2, and M_3 in $Ca_{1-x}Pb_xTiO_3$ solid solutions calculated for 5 and 300 K

Sample	*T*, K	Mode	Oscillator parameters			
			ν, cm^{-1}	Δε	γ, cm^{-1}	total dielectric contributions
$x = 0$	300	1	81	24.5	60	$\Sigma\Delta\varepsilon_M = 138.3$
		2	106	90.0	21	$\Sigma\Delta\varepsilon_{IR} = 22.3$
		3	130	23.8	17	$\varepsilon_\infty = 5$
	5	1	66.2	131.1	17.0	$\Sigma\Delta\varepsilon_M = 392.1$
		2	73.4	210.4	13.5	$\Sigma\Delta\varepsilon_{IR} = 22.3$
		3	107.8	50.6	13.2	$\varepsilon_\infty = 5$
$x = 0.15$	300	1	69	88	60	$\Sigma\Delta\varepsilon_M = 233$
		2	95	60	21	$\Sigma\Delta\varepsilon_{IR} = 7.3$
		3	105	85	17	$\varepsilon_\infty = 5$
	5	1	18.2	41.5	60	$\Sigma\Delta\varepsilon_M = 657.2$
		2	47	491.0	21	$\Sigma\Delta\varepsilon_{IR} = 7.3$
		3	87	124.7	17	$\varepsilon_\infty = 5$
$x = 0.20$	300	1	59	126.3	9	$\Sigma\Delta\varepsilon_M = 261.9$
		2	95	66.8	36	$\Sigma\Delta\varepsilon_{IR} = 8.1$
		3	107	68.8	107	$\varepsilon_\infty = 5$
	5	1	15.6	151.7	0.9	$\Sigma\Delta\varepsilon_M = 731.2$
		2	41.0	480.0	4.2	$\Sigma\Delta\varepsilon_{IR} = 8.1$
		3	97.0	99.5	35.0	$\varepsilon_\infty = 5$
$x = 0.4$	300	1	33	512	35	$\Sigma\Delta\varepsilon_M = 595$
		2.3	89	83	34	$\Sigma\Delta\varepsilon_{IR} = 13.8$
						$\varepsilon_\infty = 5$
	5	1	29	643	20.0	$\Sigma\Delta\varepsilon_M = 686$
		2.3	87	43	21.0	$\Sigma\Delta\varepsilon_{IR} = 13.8$
						$\varepsilon_\infty = 5$

Note: ν is resonance frequency, Δε is dielectric contribution, γ is damping constant, ε_∞ is high-frequency (electronic) permittivity, $\Sigma\Delta\varepsilon_M$ is the total dielectric contribution from the M_1, M_2, and M_3 modes to static permittivity, and $\Sigma\Delta\varepsilon_{IR}$ is the same from the remaining higher frequency modes.

reliably [15]. Note, however, that the stability regions of the latter phases become different after adding to Eq. (4) both sixth-order terms and terms responsible for the coupling anisotropy.

By analyzing the positive definiteness of the corresponding Hessian and checking the reality of the roots of the equations of state (5), we constructed a phase diagram; one of its cross sections is presented in Fig. 16. By virtue of the above assumptions, the x and T axes in Fig. 16 are straight lines. The x–T plane is superposed on the β_2–γ_2 plane to better reveal the most essential qualitative details of the experimental pattern.

(1) The existence of two (or three) high-temperature phase transitions $O_h^1 \rightleftharpoons D_{4h}^{18}$ at T_{c1} and to the D_{2h}^{16} phase at T_{c2} (we recall that, in the model at hand, the region of existence of the D_{2h}^{17} phase coincides with that of D_{2h}^{16} and, thus, is not considered subsequently as a separate area).

(2) The position of the concentration axis x is chosen such that the phase transition at T_{c3} for $x = 0$ (pure $CaTiO_3$) to one of the polar phases takes place at negative temperatures. The transition temperature increases linearly with concentration (the T_{c3}–T'_{c3} line of second-order phase transitions in Fig. 16 is a straight line, which agrees with the linear dependence $T_0^B \sim (x - x_c)$ established experimentally in [13]) and shifts toward the region of positive temperatures, until finally, for $T > T'_{c3}$, the phase transition occurs to the polar ferroelectric state at $T > 0$. Our spectroscopic data do not allow us to pinpoint to which of the three low-symmetry C_{2v} phases the solid solutions transfer because of the impossibility of performing polarization measurements on ceramic samples. Identification of the C_{2v}^9 phase in Fig. 16 with the polar state was made under the assumption that the B_{2u} mode is unstable [recall that the threefold degenerate $\Gamma_{10}(F_{1u})$ perovskite mode in the D_{2h}^{16} phase is split into three components, $B_{1u} + B_{2u} + B_{3u}$]. On the other hand, our samples with $x = 0.15$ and 0.2 revealed two essentially soft lines (M_1, M_2). This may indicate the possibility of a sequence of at least two phase transitions to different polar phases involving a change in the direction of the polarization vector. Model (4) should be complicated in this case by taking into account the threefold degeneracy of the F_{1u} mode. Near the $x \approx 0.3$ concentration, the diagram (see Fig. 1 and [13, Fig. 3]) should have a three-phase point and a wedge-shaped region for the monoclinic phase separating two C_{2v} phases of different symmetries.

(3) As the lead concentration is increased still further, a tetragonal ferroelectric phase of symmetry C_{4v}^{10} arises between T_{c4} and T_{c5}. The existence of an intermediate phase may account for the shape of the spectral density of the $x = 0.4$ sample. As already mentioned, its spectrum has a broad line M_1 in the low-frequency region. On the one hand, this allows the conclusion that this sample can be considered a relaxor (strong low-frequency dispersion). On the other hand, at these concentrations, one may expect the existence of several more phases differing from both the D_{2h}^{16} perovskite and the C_{4v}^1 polar phase of the lead titanate (see Fig. 1). As suggested by our simple model, these two phases should be separated by the C_{4v}^{10} phase (in Fig. 1, this may be the region of phase VI) or by a phase belonging to a subgroup of lower symmetry, C_{2v}^{20} or C_{2v}^{22}, which has the same enlarged unit cell as the perovskite, i.e., four times larger than that of $PbTiO_3$. The existence of an intermediate phase (or of several phases) could weaken the frustration of the polarization vector directions. By virtue of this phase being tetragonal, the polar $\Gamma_{10}(F_{1u})$ mode of the cubic perovskite splits here into a doublet $A_1 + E$ ($\Gamma_1 + \Gamma_5$ in Fig. 3 in the notation of [26]). As follows from Fig. 13, two lines (M_1, $M_{2,3}$) are indeed

Table 3. Some model-independent solutions (characterized by a single parameter for each mode) of the equations of state for the order parameter transforming according to the reducible representation $M_5 \oplus R_8 \oplus \Gamma_{10}$ of the $Pm\bar{3}m$–O_h^1 space group

No.	Order parameter			Space group and its number
1	$m_1 00$	000	000	$P4/mbm$–D_{4h}^5 (N 127)
2	000	$r_1 00$	000	$I4/mcm$–D_{4h}^{18} (N 140)
3	000	000	$g_1 00$	$P4mm$–C_{4v}^1 (N 99)
4	$00m_3$	$0r_2r_2$	000	$Pnma$–D_{2h}^{16} (N 62)
	$00m_3$	$00r_3$	000	$Cmcm$–D_{2h}^{17} (N 63)
5	$m_1 00$	000	$00g_3$	$P4bm$–C_{4v}^2 (N 100)
6	000	$r_1 00$	$g_1 00$	$I4cm$–C_{4v}^{10} (N 108)
	$m_1 00$	r_1–$r_1 0$	g_1–$g_1 0$	$Pmc2_1$–C_{2v}^2 (N 26)
7	$00m_3$	$0r_2r_2$	$0g_2g_2$	$Pmn2_1$–C_{2v}^7 (N 31)
	$00m_3$	$0r_2r_2$	$g_1 00$	$Pna2_1$–C_{2v}^9 (N 33)

Note: The numbers of representations are given according to the notation used in [26]. The column labeled "order parameter" defines the order parameter and is separated into three subcolumns identifying the components of the threefold degenerate perovskite modes that condense at the corresponding phase transition, namely, M_5 (m_i), R_8 (r_i), and Γ_{10} (g_i), respectively. The space groups are written in both the Hermann–Mauguin and Schëonflies notations. Their numbers are give in accordance with the International Crystallography Tables.

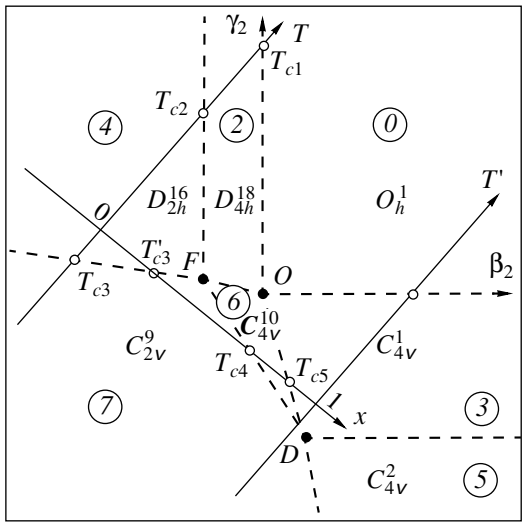

Fig. 16. A cut of the diagram of phase states by the (β_2, γ_2) plane for model (4). The numbered circles refer to the solutions of the equations of state (5), and the symmetry groups of the phases correspond to Table 3. Dashed lines identify second-order phase transitions. Solid lines are the T and x axes with the origin at the point ($x = 0$, $T = 0$). Constants of the potential: $\alpha_4 > 0$, $\beta_4 > 0$, $\gamma_4 > 0$, $\delta_{22} > 0$, $\varepsilon_{22} > 0$, $\eta_{22} > 0$.

present in the spectrum for $x = 0.4$. Interestingly, the frequency of the $M_{2,3}$ line is very close numerically to the value of the soft transverse phonon in $PbTiO_3$ [35, 36], whereas the M_1 line frequency lies closer to the lowest frequency perovskite mode. It is possibly this peculiar crossover that facilitates (at the microscopic level) the transition of the $Ca_{1-x}Pb_xTiO_3$ solid solution from the rhombic atomic packing in $CaTiO_3$ to tetragonal in $PbTiO_3$, with a decrease in the cell volume by a factor of 4.

In our opinion, further discussion would benefit considerably if it were based on a thorough study of samples spanning a broader range of concentrations x, from 0.3 to 1.0. As already mentioned, such studies are planned for the near future. Model (4) should be naturally made appropriate for this purpose by taking into account the fact that the coupled modes are multidimensional and by extending the potential expansion to higher orders.

6. CONCLUSIONS

The IR-spectroscopic investigation of the dynamic behavior of $Ca_{1-x}Pb_xTiO_3$ solid solutions on the $CaTiO_3$ side has established a quantitative analogy with static results [13], which suggests that in this system there are no low-frequency excitations (a central peak) in addition to the soft modes; i.e., we have not found any evidence of a transition of $Ca_{1-x}Pb_xTiO_3$ to the relaxor state.

The dynamic behavior of the $Ca_{1-x}Pb_xTiO_3$ solid solutions at low optical frequencies follows a radically different pattern. The optical spectrum of samples with $x < 0.3$ qualitatively resembles that of orthorhombic perovskite. As the lead concentration increases, the spectrum softens, which signals an approach to the ferroelectric transition temperature. This observation correlates with macroscopic measurements of $\varepsilon(T)$ in the low-frequency domain and with the conclusion made in [13] concerning a transformation of ferroelectricity from the incipient (for $x < 0.28$) to real (for $x > 0.28$) behavior with increasing lead concentration. Note the significant difference between the spectral patterns at low frequencies in the pure $CaTiO_3$ perovskite and in $Ca_{1-x}Pb_xTiO_3$. More specifically, in the former compound, the splitting of the polar mode F_{1u} into three components is small, whereas the solid solutions clearly show three components, with two of them being substantially soft. This may suggest a cascade of at least two (or three) incipient phase transitions to polar phases with differently oriented spontaneous polarization vectors. The spectrum of samples with $x = 0.4$ exhibits a basic difference. It is dominated at low frequencies by a strong and broad resonance line with a nonmonotonic evolution in temperature, which assumes the possibility of existence of several phase transitions (probably of the first order) of a nature that is still to be established. A simple phenomenological model with biquadratic coupling between soft modes located at the center and boundary of the Brillouin zone of the cubic phase is proposed. The model offers an explanation for the increase in the temperature of the phase transition to one of the polar phases with increasing lead concentration, with the phase transition temperature T_{c3} depending linearly on x. In addition, this model allows us to make a hypothesis on the possible existence of one or several phase states at intermediate concentrations. The existence of such an intermediate phase (or phases) is capable of smoothening the frustration by setting preferential polarization orientation in $Ca_{1-x}Pb_xTiO_3$ solid solutions.

ACKNOWLEDGMENTS

This study was supported by the Russian Foundation for Basic Research (project no. 03-02-16720), a grant from the President of the Russian Federation (no. NSh-2168.2003.2), and the program of the Department of Physical Sciences, Russian Academy of Sciences.

REFERENCES

1. M. E. Lines and A. M. Glass, *Principles and Applications of Ferroelectrics and Related Materials* (Clarendon, Oxford, 1977; Mir, Moscow, 1981).
2. R. A. Lyddane, R. G. Sachs, and E. Teller, Phys. Rev. **59**, 673 (1941).
3. V. V. Lemanov, A. V. Sotnikov, E. P. Smirnova, M. Weihnacht, and R. Kunze, Solid State Commun. **110**, 611 (1999).

4. A. S. Knyazev, Yu. M. Poplavko, V. A. Zakharov, and V. V. Alekseev, Fiz. Tverd. Tela (Leningrad) **15**, 3006 (1973) [Sov. Phys. Solid State **15**, 2003 (1973)].
5. V. Zelezhy, M. F. Limonov, D. Usvyat, V. V. Lemanov, J. Petzelt, and A. A. Volkov, Ferroelectrics **272**, 113 (2002).
6. V. Železhy, E. Cockayne, J. Petzelt, M. F. Limonov, D. Usvyat, V. V. Lemanov, and A. A. Volkov, Phys. Rev. B **66**, 224303 (2002).
7. J. G. Bednorz and K. A. Müller, Phys. Rev. Lett. **52**, 2289 (1984).
8. V. V. Lemanov, Ferroelectrics **226**, 133 (1999).
9. B. E. Vugmeister and M. D. Glinchuk, Rev. Mod. Phys. **62**, 993 (1990).
10. E. Sawaguchi and M. L. Charters, J. Am. Ceram. Soc. **42**, 157 (1959).
11. T. Yamamoto, M. Saho, K. Okazaki, and E. Goo, Jpn. J. Appl. Phys. **26** (2), 57 (1987).
12. B. Jiménez and R. Jiménez, Phys. Rev. B **66**, 014104 (2002).
13. V. V. Lemanov, A. V. Sotnikov, E. P. Smirnova, and M. Weihnacht, Appl. Phys. Lett. **81**, 886 (2002).
14. R. Ranjan, N. Singh, D. Pandey, V. Siruguri, P. S. R. Krishna, S. K. Paranjpe, and A. Banerjee, Appl. Phys. Lett. **70**, 3221 (1997).
15. B. J. Kennedy, C. J. Howard, and B. C. Chakoumakos, J. Phys.: Condens. Matter **11**, 1479 (1999).
16. R. Ganesh and E. Goo, J. Am. Ceram. Soc. **80**, 653 (1997).
17. V. V. Eremkin, V. G. Smotrakov, L. E. Balyunis, S. I. Shevtsova, and A. T. Kozakov, Kristallografiya **39**, 155 (1994) [Crystallogr. Rep. **39**, 137 (1994)].
18. A. A. Volkov, Yu. G. Goncharov, G. V. Kozlov, S. P. Lebedev, and A. M. Prokhorov, Infrared Phys. **25**, 369 (1985).
19. T. Vogt and W. W. Schmahl, Europhys. Lett. **24**, 281 (1993).
20. T. Matsui, H. Shigematsu, Y. Arita, Y. Hanajiri, N. Nakamitsu, and T. Nagasaki, J. Nucl. Mater. **247**, 72 (1997).
21. M. Ahtee, A. Glaser, and A. Hewat, Acta Crystallogr. B **34**, 752 (1978).
22. H. F. Kay and P. C. Bailey, Acta Crystallogr. **10**, 219 (1957).
23. W. Cochran and A. Zia, Phys. Status Solidi **25**, 273 (1968).
24. C. Darlington, Phys. Status Solidi B **66**, 231 (1976).
25. K. S. Aleksandrov, Ferroelectrics **14**, 801 (1976).
26. O. V. Kovalev, *Irreducible Representations of the Space Groups* (Akad. Nauk Ukr. SSR, Kiev, 1961; Gordon and Breach, New York, 1965).
27. W. Zhong, R. D. King-Smith, and D. Vanderbilt, Phys. Rev. Lett. **72**, 3618 (1994).
28. E. Cockayne and B. P. Burton, Phys. Rev. B **62**, 3735 (2000).
29. A. S. Barker, Jr., in *Ferroelectricity*, Ed. by E. F. Weller (Elsevier, Amsterdam, 1967).
30. C. H. Perry, B. N. Khanna, and G. Rupprecht, Phys. Rev. A **135**, 408 (1964).
31. M. E. Guzhva, V. V. Lemanov, and P. A. Markovin, Fiz. Tverd. Tela (St. Petersburg) **43**, 2058 (2001) [Phys. Solid State **43**, 2146 (2001)].
32. Y. J. Shan, H. Mori, H. Imoto, and M. Itoh, Ferroelectrics **270**, 381 (2002).
33. A. M. Glaser, Acta Crystallogr. B **28**, 3384 (1972); Acta Crystallogr. A **31**, 756 (1975).
34. H. T. Stokes, E. H. Kisi, D. M. Hatch, and C. J. Howard, Acta Crystallogr. B **58**, 934 (2002).
35. G. Burns and B. A. Scott, Phys. Rev. B **7**, 3088 (1973).
36. I. Fedorov, J. Petzelt, V. Zelezny, G. A. Komandin, A. A. Volkov, K. Brooks, Y. Huang, and N. Setter, J. Phys.: Condens. Matter **7**, 4313 (1995).

Translated by G. Skrebtsov

Physics of the Solid State, Vol. 46, No. 5, 2004, pp. 942–947. Translated from Fizika Tverdogo Tela, Vol. 46, No. 5, 2004, pp. 913–918.

LOW-DIMENSIONAL SYSTEMS AND SURFACE PHYSICS

Formation of a System of InGaAs Quantum Wires in a Gallium Arsenide Matrix

L. K. Orlov and N. L. Ivina

Institute of the Physics of Microstructures, Russian Academy of Sciences, Nizhni Novgorod, 603950 Russia

e-mail: orlov@ipm.sci-nnov.ru

Received July 1, 2003

Abstract—The formation of a system of one-dimensional quantum conductors in porous multilayer $In_xGa_{1-x}As/GaAs$ structures with a two-dimensional charge-carrier gas in the $In_xGa_{1-x}As$ layers is discussed. The transition from the single-crystalline to porous matrix is studied with scanning atomic force microcopy. A decrease in the dimensionality of the electron–hole gas in the objects, i.e., a transition from the two-dimensional to a one-dimensional system, is established by analyzing the dependences of the position and width of a spectral line in the photoluminescence spectra on the etching time. Both multilayer periodic superlattices and a structure with a single $In_xGa_{1-x}As$ layer located near the surface of gallium arsenide are studied. The electrophysical characteristics of electrons in the porous superlattices are measured as functions of temperature. They confirm the formation of a new structure and indicate a change in the mechanism of electron scattering in the quasi-one-dimensional transport channels formed in the system. © *2004 MAIK "Nauka/Interperiodica".*

Interest in porous semiconducting materials has noticeably increased over the past few years, since they can be used to fabricate low-dimensional objects, such as two-dimensional surfaces [1, 2], quantum wires [3, 4], and tunneling-coupled chains of zero-dimensional granules [5, 6], directly during electrochemical etching. One of the ideas for creating a system of quantum wires is to fill pores in a starting dielectric matrix (porous Si and opal or zeolite crystals [7, 8]) with a metallic or semiconducting material. However, it is difficult to actualize the idea of using a porous material to form low-dimensional inclusions, including those having the properties of quantum superlattices [8], in its planes, since it is difficult to produce filaments of another material that have a nanometer-scale cross section, perfect crystal structure, small scatter of parameters, and good electrical properties inside the pores of the initial matrix.

We propose an alternative, which consists in the creation of numerous quantum wires in the bulk of a semiconducting matrix. The method of fabricating two-dimensional systems of quantum wires is based on their self-formation during electrolytic etching of layered heteroepitaxial structures in which nanometer-thick layers with a two-dimensional electron–hole gas are built during their epitaxial growth [9–11]. To prove the successful realization of forming two-dimensional systems of quantum wires in porous multilayer heterostructures, it is necessary to analyze the properties of such structures by various techniques using as many possible structure types as possible to complete the analysis performed in [9–11].

In this work, we study the crystal structure and the properties of an electron–hole gas before and after electrochemical etching of samples using atomic force microscopy, photoluminescence (PL), and the Hall effect. Using both multilayer and one-layer structures, we analyze the shift and width of spectral photoluminescence lines depending on the etching time (i.e., on the cross-sectional dimension of wires making up a quantum network) in greater detail than was done in [10]. As the initial matrix, we chose epitaxial $GaAs/In_xGa_{1-x}As$ single-layer and multilayer semiconducting heterostructures (including periodic ones) grown by gas-phase epitaxy on semi-insulating GaAs (100) substrates at atmospheric pressure [12]. $In_xGa_{1-x}As$ layers in the initial samples formed single or double quantum wells. The structures were doped selectively by a donor impurity to a concentration of 10^{16}–10^{17} cm^{-3}. The total number N of the $In_xGa_{1-x}As$ quantum-confining layers in the structures was varied from one to ten. The data on the composition and thickness of the layers in the structures under study are given in the table. Quantum wells of a multilayer structure in the GaAs matrix were separated by a distance D of several tens of nanometers.

The procedure for fabricating two-dimensional systems made up of one-dimensional conductors consisted in etching vertical channels that intersect the $In_xGa_{1-x}As$ layers built in the GaAs matrix. Electrochemical etching was performed in an alcoholic solution of hydrofluoric acid at current densities of 20–40 mA/cm^2 in the presence of ultraviolet illumination. Electric currents were directed along the structure layers, i.e., along the surface of a sample. Pores that appear in a structure during etching then grow, thus decreasing the thickness of transverse barriers. This can eventually affect the characteristics of electrons (holes) localized

in the ternary-compound layers. In particular, when a porous crystal is based on structures containing a two-dimensional electron gas, the dimensionality of its electron subsystem is expected to decrease due to the appearance of an additional spatial restriction imposed on two-dimensional charge carriers not only in the direction normal to the layer plane but also in the plane formed by the two-dimensional network. The properties of the formed planar system of quasi-one-dimensional wires can be substantially different from those of the initial semiconducting structure.

The formation of a porous structure is confirmed by micrographs of the surface of a sample taken on a scanning probe microscope (Fig. 1) [9, 10]. Before etching (Fig. 1a), the surface had a banded shape with a groove depth of 4 nm. This surface structure can be related to growth steps; however, it can also be caused by the surface quality of the wafers used for epitaxy. After etching (Fig. 1b), the surface structure changes radically and acquires a shape typical of porous systems. The sample surfaces contained a significant number of pores with a visible depth of up to 100 nm. The geometry of etching (the electrolyte–semiconductor contact and the metallic (Au) contact are located on one side of a wafer) was chosen so that the current lines in a heterostructure grown on the semi-insulating GaAs substrate were directed both transversely and longitudinally to the sample surface, mainly along the $In_xGa_{1-x}As$ layers having a sufficiently high two-dimensional conductivity. The geometry of the current lines is likely to favor the etching of samples in both transverse and longitudinal (along the layer planes in a heterostructure) directions to form a two-dimensional network of a complex filament weave in the $In_xGa_{1-x}As$ layers.

As a method to reveal the effect of the formation of systems of quantum wires in the plane of a two-dimensional $In_xGa_{1-x}As$ layer upon etching, we can choose any optical method (e.g., photoluminescence) that has been shown to be effective for testing other low-dimensional objects. Photoluminescence spectra were recorded using a standard MDR-23 grating spectrometer with excitation induced by a helium–neon laser. As a detector, we used either a photomultiplier or a cooled Ge diode. The photoluminescence line of a heterostructure to be measured is clearly visible at liquid-nitrogen temperature and allows us (by recording the changes in the position and width of this spectral line) to track a possible transformation of the two-dimensional spectrum of the electron–hole gas of the system to a one-dimensional spectrum upon electrochemical etching of the heterostructure. Upon etching of the heterostructure, the emission line is expected to shift toward higher frequencies and, simultaneously, to decrease in width due to the sharp increase in the density of electron states when the dimensionality of the system decreased. This assumption was supported by our first experiments [10].

Parameters of the GaAs/InGaAs/GaAs structures under study

Sample no.	x	Number of InGaAs layers	d_1, nm	d_{qw}, nm	d_b, nm	D, nm
1—3253	0.15	1		9		–
2—3253	0.15	3		7, 9, 11		30
3—2053	0.25	10	21	7	7	70
4—2039	0.25	8	15	5	5	70
5—2040	0.25	10	23	9	5	70

Note: d_{qw} is the thickness of an individual quantum well, d_b is the thickness of the barrier in a double quantum well, $d_1 = 2d_{qw} + d_b$ is the thickness of a double quantum well, and x is the indium content in the ternary compound.

The heterostructures with a small number of quantum wells (samples *1*, *3*; see table), which are located near the outer surface of the structures, require special etching conditions for the etching of micropores in a sample not to be accompanied by etching of the sample surface [11]. In this case, we can track the effect of microporosity on the photoluminescence properties of a structure even with a single $In_xGa_{1-x}As$ layer buried

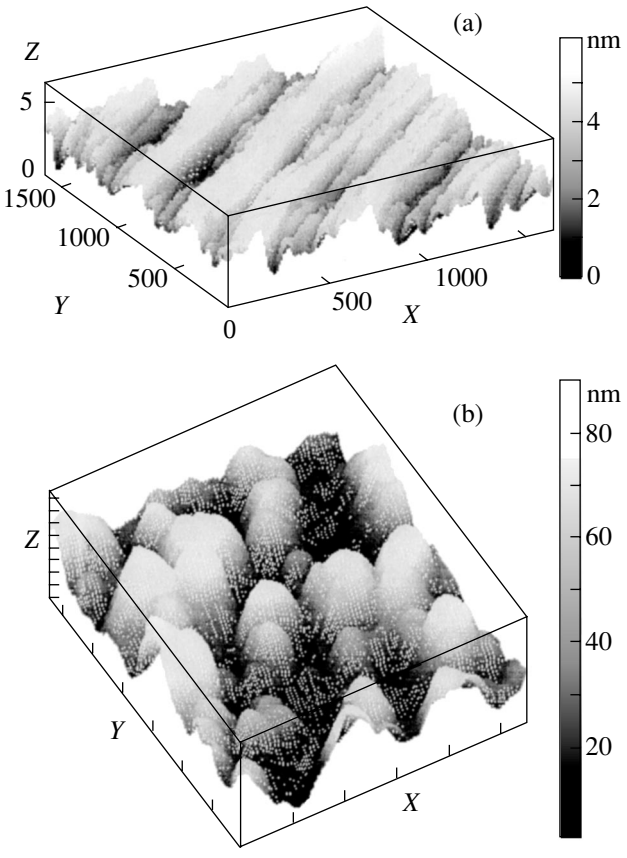

Fig. 1. Images of the surface of sample *4* taken by scanning atomic force microcopy (a) before and (b) after etching.

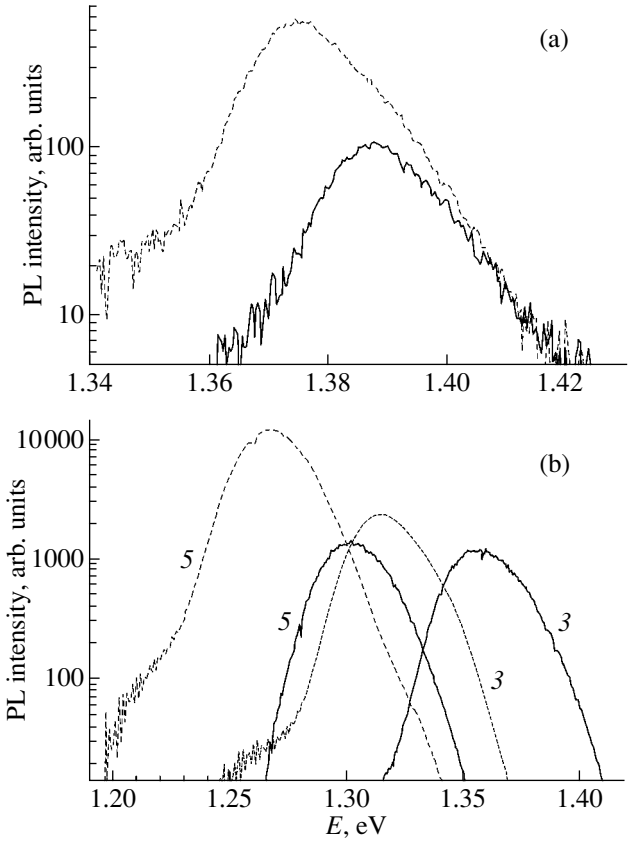

Fig. 2. Photoluminescence spectra recorded at $T = 77$ K for samples (a) *1* and (b) *3* and *5* before (dashed lines) and after (solid lines) etching over (a) 23 (sample *1*) and (b) 110 min (samples *3*, *5*).

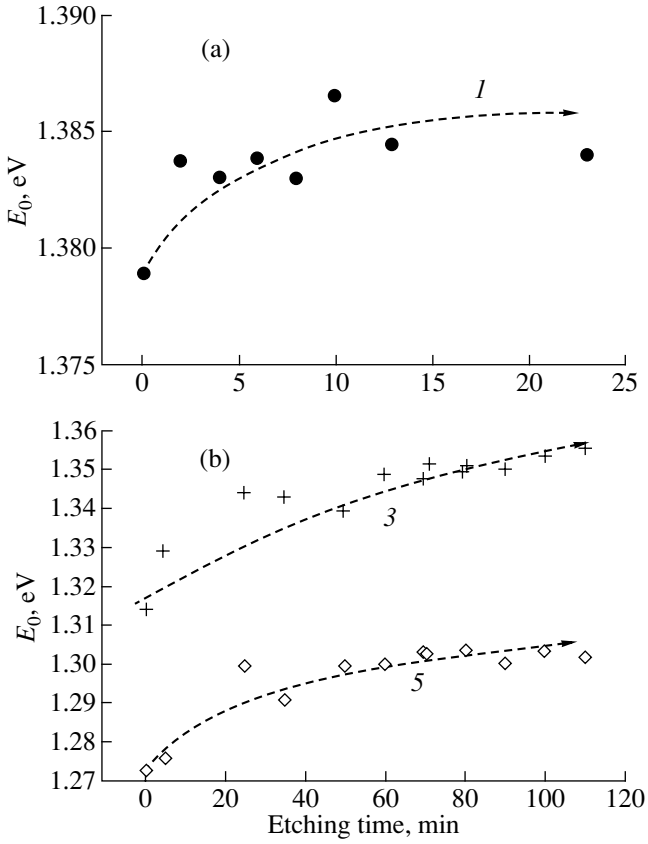

Fig. 3. Dependence of the photoluminescence peak E_0 on the etching time for samples (a) *1* and (b) *3* and *5*. The dashed lines illustrate the corresponding tendencies.

at a distance of only about 1 μm from the outer surface. The characteristic photoluminescence spectrum recorded at $T = 77$ K for one of the structures (sample *1*; see table) with one quantum-confinement $In_{0.15}Ga_{0.85}As$ layer is shown in Fig. 2a (dashed line). The shape of this resonance peak recorded after etching of the sample for 23 min is also given in Fig. 2a (solid line). The emission line of the two-dimensional $In_{0.15}Ga_{0.85}As$ porous layer is seen to shift slightly toward the short-wavelength region of the spectrum.

A similar short-wavelength shift in the photoluminescence line was detected for all porous structures under study, including porous superlattices (samples *3*–*5*) containing a sequence of double symmetrical quantum wells (Fig. 2b). Unlike sample *4*, which was comprehensively studied earlier [9, 10], the total etching time for samples *3* and *5* was increased to about two hours. It should be noted that the initial spectra of all superlattices (dashed lines in Fig. 2) had a relatively large width at half-maximum W (about 30 meV), which was caused by the natural scatter of the layer parameters, and could be described by Gaussian curves with a high accuracy. The spectral line widths of the superlattices were greater than the spectral line width recorded from one layer by a factor of 1.5–2. The accuracy of measuring the spectra was within 0.1–0.3 meV and was specified by the resolutions of the diffraction gratings.

The dependence of the shift in the photoluminescence line on the etching time is shown in Fig. 3. As noted in [10], the short-wavelength shift in the photoluminescence line, which is characteristic of all samples under study, is most likely due to an additional spatial restriction in the transport structural channels, which appears when the two-dimensional channels transform into one-dimensional channels in the two-dimensional network in the plane of the $In_xGa_{1-x}As$ layers. As shown in [13], a small etching-induced change in the elastic deformation of the layers results in the reverse effect, i.e., to a decrease in the band gap by less than 5 meV, which causes a slight shift in the position of the photoluminescence line toward the long-wavelength region of the spectrum. Competition between the mechanisms that lead to shifts in the photoluminescence line in opposite directions upon etching can cause the scatter of points in the $E_0(t)$ dependences given in Fig. 3. An increase in the etching time for structures *1* and *2* raises the probability of etching the upper $In_xGa_{1-x}As$ layer, which imposes a restriction on the etching time. This was demonstrated in [11] for structure *2* with three

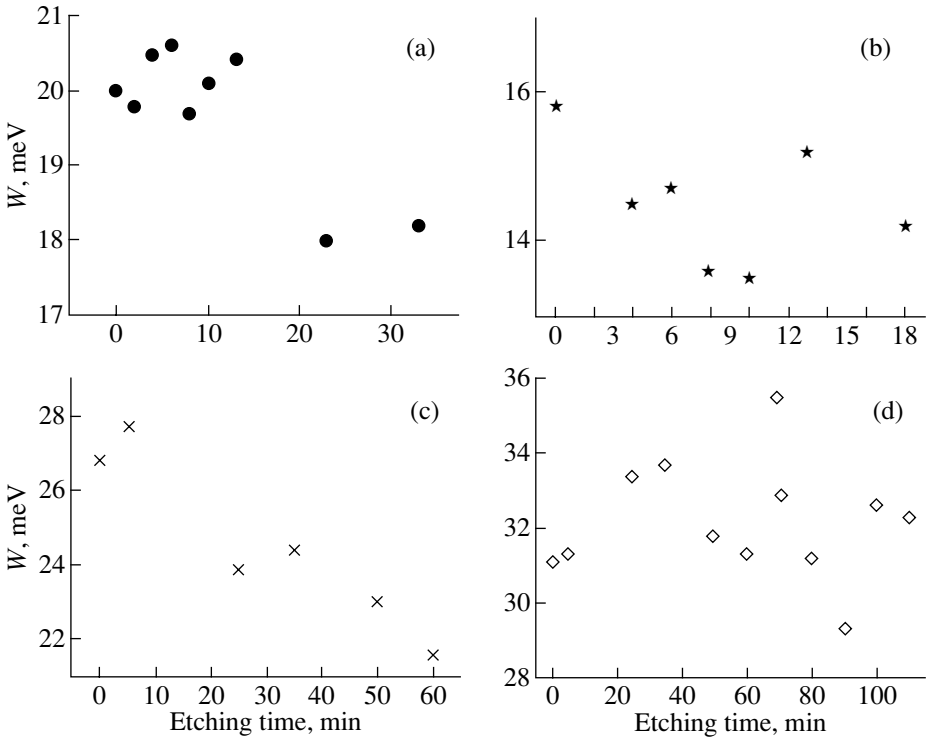

Fig. 4. Dependence of the photoluminescence line width at half-maximum W on the etching time of samples (a) *1*, (b) *2* (the PL line corresponds to the intermediate InGaAs layer), (c) *4*, and (d) *5*.

$In_xGa_{1-x}As$ layers of different thicknesses. For the superlattices, the total etching time can be substantially increased; therefore, the shift in the spectral line becomes more pronounced due to an additional quantum-confinement effect and the scatter of points in the $E_0(t)$ dependences is smaller (Fig. 3b). For the shift in the photoluminescence line, the simplest model assuming a rectangular section of a quantum wire formed gives $\Delta E = \Delta E_e + \Delta E_h = \pi^2\hbar^2/2d_2^2(1m_e + 1/m_h)$, where $m_{e(h)} = 0.06(0.4)m_0$ is the effective electron (hole) mass in the $In_{0.25}Ga_{0.75}As$ layer. Then, we have $\Delta E \approx 40$ meV, which corresponds to a wire cross-sectional width $d_2 \approx$ 13 nm.

The decrease in the dimensionality of the spectrum of charge carriers in the semiconductor that causes the transition of the two-dimensional system to a quasi-one-dimensional system would inevitably change the character of the density of states in the energy spectrum of the electron subsystem. In the structure with a two-dimensional electron gas, the energy dependence of the density of states is a step function, $\rho(E) \sim \sum_n (E - E_{nl})^0$. The additional decrease in the dimensionality of the electron spectrum by unity during the formation of a system of quantum wires in the heterostructure layers leads to a more pronounced resonance-type energy dependence of the density of states in the one-dimensional subband, $\rho(E) \sim (E - E_{nw})^{-1/2}$. Here, E_{nl} and E_{nw} are the edges of the energy subbands in the quantum layer and quantum wire, respectively. Similarly to structures with quantum dots, an increase in the density of states in the vicinity of energy band edges results in a decrease in the spectral line widths in the photoluminescence spectrum, which can be used for fabricating heterolasers.

As compared to sample *1* having one quantum layer (Fig. 2a), the initial spectral lines of the single-crystal superlattices (Fig. 2b) have a large width of the resonance line ($W \sim$ 27–32 meV), which is caused by the scatter of the structural parameters (e.g., the scatter in the thickness of a quantum well within both one and several superlattice periods). Etching of some samples results in a decrease in the line width by several millielectronvolts. For instance, this is clearly visible in structure *4* (Fig. 4c), where W varies with etching time from 27 to 21 meV during one-hour etching. A similar dependence was detected for samples *1* and *2* having a small number of quantum wells, where half-hour etching led to a 2-meV decrease in the initial spectral line width (Figs. 4a, 4b). This fact indicates that the effect of the additional spatial restriction in the formed network of quantum wires is more pronounced than the expected effect of increased statistical inhomogeneities that appear upon etching. Obviously, it is unlikely that absolutely smooth mirror boundaries of wires of the same size form during etching. The roughness of their boundaries favors the appearance of additional states

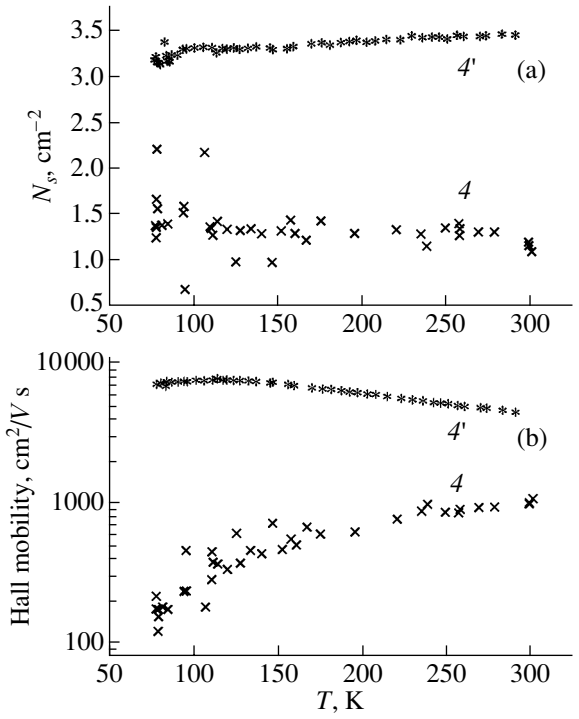

Fig. 5. Temperature dependences of (a) the surface concentration and (b) the Hall mobility of electrons obtained by the Van der Pauw method for (*4'*) single-crystal and (*4*) porous sample *4*.

(such as the Tamm and Shockley states) in the system. Moreover, charge states on the pore surfaces can block one-dimensional channels, thus resulting in additional inhomogeneities in the system [14] and, hence, additional broadening of the spectral lines. This behavior is clearly visible in Figs. 4b and 4d, where additional inhomogeneities appearing upon the etching of pores in multilayer structures *2* and *5* lead to a significant scatter in the experimental data from measurement to measurement. However, despite a strong scatter in the line widths depending on the etching time, a tendency toward a decrease in line width is also obvious. The dependences indicate that the mechanisms operating in opposite directions (statistical inhomogeneity and an increase in the density of states in the electronic spectrum) have approximately the same efficiency and are relatively sensitive to etching.

During etching, the integrated intensity of the photoluminescence lines decreases for virtually all structures [10]. The decrease in the radiation efficiency is related to a decrease in the volume of an active emitting layer because of its etching-out. On the other hand, the deterioration of the mirror surface characteristics of the system upon etching, which leads to a decrease in the intensity of the reflected signal of the exciting laser, would result in an increase in the fraction of power absorbed in a sample. This absorption, in turn, can increase the photoluminescence efficiency in some cases [1].

Studying one-dimensional quantum objects is of great interest in terms of both their specific optical and transport properties [15, 16]. However, in networks of quantum wires fabricated by electrolytic etching in planar layered quantum heterostructures, an increase in the role of surface states and the shielding effect [14] (which favors various percolation effects apart from breakage of the wires) can strongly complicate the character of the dependences for a heterostructure carrying a current. This complication is indicated by the Hall effect data measured on porous sample *4* (Fig. 5) and their comparison with the results obtained on the starting single-crystal samples [17]. The appearance of the additional, rather efficient scattering mechanism, which is related to the boundary states and charges on the well-developed surface of pores, not only decreases the electron concentration and mobility in a porous $In_xGa_{1-x}As$ layer as compared to the single-crystal layer but also radically changes the temperature dependence of the mobility (Fig. 5b). In the porous samples with an unstabilized surface, the electron scattering by the boundaries dominates over the electron–phonon scattering in the channels even at room temperature, thus causing a decrease in the electron mobility with decreasing measurement temperature.

ACKNOWLEDGMENTS

We are grateful to N.A. Alyabina, B.N. Zvonkov, and R.A. Rubtsova, NIFTI NNGU, for supplying the single-crystal samples and their assistance in sample etching and measurements and to N.V. Vostokov (IFM RAN) for taking surface images on a scanning probe microscope.

This work was supported in part by the Ministry of Education of the Russian Federation (project no. E02-3.4-347) and the Russian Foundation for Basic Research (project no. 01-02-16778).

REFERENCES

1. Yu. N. Buzynin, S. A. Gusev, Yu. N. Drozdov, Z. F. Krasil'nik, A. V. Murel', D. G. Revin, V. N. Shashkin, and I. V. Shuleshova, Poverkhnost, No. 5, 40 (1996).
2. N. S. Averkiev, L. P. Kazakova, É. A. Lebedev, Yu. V. Rud', A. N. Smirnov, and N. N. Smirnova, Fiz. Tekh. Poluprovodn. (St. Petersburg) **34**, 757 (2000) [Semiconductors **34**, 732 (2000)].
3. A. D. Grozaw and N. I. Leporda, Fiz. Tverd. Tela (St. Petersburg) **38**, 1924 (1996) [Phys. Solid State **38**, 1063 (1996)].
4. D. P. Yu, Y. J. Xing, Q. L. Hang, *et al.*, Physica E (Amsterdam) **9**, 305 (2001).
5. E. S. Demidov, Pis'ma Zh. Éksp. Teor. Fiz. **71**, 513 (2000) [JETP Lett. **71**, 351 (2000)].
6. E. S. Demidov, V. V. Karzanov, and V. G. Shengurov, Pis'ma Zh. Éksp. Teor. Fiz. **67**, 794 (1998) [JETP Lett. **67**, 839 (1998)].

7. V. N. Bogomolov, A. I. Zadorozhniĭ, T. M. Pavlova, V. P. Petranovskiĭ, V. P. Podkhalyuzin, and A. L. Kholkin, Pis'ma Zh. Éksp. Teor. Fiz. **31**, 406 (1980) [JETP Lett. **31**, 378 (1980)].
8. V. N. Bogomolov, A. I. Zadorozhniĭ, and T. M. Pavlova, Fiz. Tekh. Poluprovodn. (Leningrad) **15**, 2029 (1981) [Sov. Phys. Semicond. **15**, 1176 (1981)].
9. L. K. Orlov, N. L. Ivina, N. A. Alyabina, B. N. Zvonkov, and E. S. Demidov, Phys. Status Solidi A **3**, 981 (2003).
10. L. K. Orlov and N. L. Ivina, Pis'ma Zh. Éksp. Teor. Fiz. **75**, 584 (2002) [JETP Lett. **75**, 492 (2002)].
11. L. K. Orlov, N. L. Ivina, N. A. Alyabina, N. V. Vostokov, B. N. Zvonkov, and E. S. Demidov, in *Proceedings of International Conference on Solid State Crystals: Material Sciences and Applications, Zakopane, Poland, 2002* (2003), p. 38.
12. V. Ya. Aleshkin, B. N. Zvonkov, E. R. Lin'kova, A. V. Murel', and Yu. A. Romanov, Fiz. Tekh. Poluprovodn. (St. Petersburg) **27**, 931 (1993) [Semiconductors **27**, 504 (1993)].
13. L. K. Orlov, N. L. Ivina, Yu. N. Drozdov, and N. A. Alyabina, Pis'ma Zh. Tekh. Fiz. **28** (24), 1 (2002) [Tech. Phys. Lett. **28**, 1018 (2002)].
14. S. G. Petrosyan and A. Ya. Shik, Fiz. Tekh. Poluprovodn. (St. Petersburg) **26**, 763 (1992) [Sov. Phys. Semicond. **26**, 430 (1992)].
15. J. Voit, Rep. Prog. Phys. **58**, 977 (1995).
16. F. D. M. Haldane, J. Phys. C: Solid State Phys. **14**, 2585 (1981).
17. L. K. Orlov, N. L. Ivina, R. A. Rubtsova, and Yu. A. Romanov, Fiz. Tverd. Tela (St. Petersburg) **42** (3), 537 (2000) [Phys. Solid State **42**, 548 (2000)].

Translated by K. Shakhlevich

Physics of the Solid State, Vol. 46, No. 5, 2004, pp. 948–953. Translated from Fizika Tverdogo Tela, Vol. 46, No. 5, 2004, pp. 919–923.

LOW-DIMENSIONAL SYSTEMS AND SURFACE PHYSICS

Interwell Excitons in Semimagnetic Semiconductor Double Quantum Wells in an External Magnetic Field

A. V. Vertsimakha, S. B. Lev, and V. I. Sugakov

Institute for Nuclear Research, National Academy of Sciences of Ukraine, Kiev, 03680 Ukraine

e-mail: sugakov@kinr.kiev.ua

Received July 23, 2003

Abstract—The use of semimagnetic semiconductor double quantum wells in an external magnetic field is suggested for the separation of exciton charges. The exciton energies and wave functions, as well as the oscillator strengths, are calculated for (Zn, Be, Mg)Se/ZnSe/(Zn, Be, Mg)Se/(Zn, Mn)Se/(Zn, Be, Mg)Se double quantum wells for different interwell barrier widths and different external magnetic fields. It is shown that, in a certain range of magnetic fields, the lowest energy corresponds to the interwell (indirect) exciton. Moreover, its lifetime can be several orders of magnitude greater than the lifetime of an exciton localized in one well. © *2004 MAIK "Nauka/Interperiodica".*

1. INTRODUCTION

Over the past several years, the study of interwell excitons (with spatially a separated electron and hole; these excitons are also referred to as indirect excitons in the literature) in two-dimensional semiconductor structures has attracted growing attention. The basic feature of such systems is the occurrence of excitons having a long lifetime due to localization of the electron and the hole in different wells and, accordingly, weak overlap of their wave functions. Due to this feature, large exciton densities can be created in heterostructures and their collective properties can be studied. A number of new interesting phenomena observed in systems with high densities of collectively interacting interwell excitons were studied in [1–4]. In order for such excitons to accumulate, it is necessary that they correspond to the lowest excited state of the system. In [1–4], this condition was satisfied by applying an external electric field to the system. In this study, we suggest a method of creating lowest energy interwell excitons by using double quantum wells in semimagnetic semiconductors. Due to the exchange interaction between the carriers and the spins of magnetic impurities, exciton levels in such semiconductors have a strong dependence on an external magnetic field [5, 6]. It follows from our calculations described below that, for a specially chosen distribution of magnetic ions in the wells and barriers, it is possible to obtain structures for which the main excited exciton state corresponds to the interwell exciton in a certain range of magnetic fields. The lifetime of such excitons is orders of magnitude greater than the lifetime of direct excitons. One of the advantages of using a magnetic rather than an electric field is the absence of photocurrent and charge redistribution, which complicate the interpretation of the results.

We studied the semimagnetic semiconductor $Zn_{1-x}Mn_xSe$-based systems. Such heterostructures (for example, $Zn_{1-x}Mn_xSe$/ZnSe) attract interest as materials for the creation of "spin superlattices," in which space separation of charge carriers with different spin projections on the direction of the magnetic field is possible [7, 8]. To fabricate spin superlattices with strong carrier localization in quantum wells, (Zn, Be, Mg)Se ternary compounds were used as barrier layer materials [9]. In this study, we discuss double wells with such barriers.

We calculated the energy and lifetime of direct and interwell excitons in a (Zn, Be, Mg)Se/ZnSe/(Zn, Be, Mg)Se/Znn$_{1-x}$Mn$_x$Se/(Zn, Be, Mg)Se double quantum well. A number of interesting effects related to the intersection of different exciton levels with varying magnetic field should be observed in this system. In this case, the spatial characteristics of the lowest excited exciton state (the direct–indirect exciton transition), the energy level positions, and the radiation lifetimes change.

2. MODEL AND METHOD FOR CALCULATING THE EXCITON SPECTRUM

We study a system with two quantum wells (Fig. 1). One of the wells is formed by a layer of nonmagnetic ZnSe crystal, and the other is a layer of a semimagnetic $Zn_{1-x}Mn_xSe$ solid solution. The wells are separated by a nonmagnetic (Zn, Be, Mg)Se barrier layer.

Due to the giant Zeeman splitting in the semimagnetic layer [5, 6], one can control the depths of potential wells for the electron and hole in this layer by varying an external magnetic field. For the σ^+ component of the excitonic transition, the depth of the quantum well formed by the semimagnetic semiconductor increases

with magnetic field, while for the σ^- component the depth of the well decreases. At a temperature of 1.6 K, an increase in the magnetic field from 0 to 3 T results in a deepening of the potential well for holes by almost 40 meV for relative concentration $x = 0.05$ of the Mn^{2+} magnetic impurity in the $Zn_{1-x}Mn_xSe$ layer. The variation in the well depths for the electron and hole in a magnetic field produces an appreciable shift of the carrier quantum-confinement levels. However, the depth of the potential well in a nonmagnetic layer does not depend on the magnetic field (at the low external magnetic fields considered). In other words, for the system studied, the depth of one of the potential wells can be controlled by an external magnetic field. In what follows, we show that there is a threshold value of the magnetic field at which the interwell exciton becomes the lowest energy state.

The Hamiltonian of the system is

$$H = H_0(\mathbf{r}_e, \mathbf{r}_h) + V_e(x, z_e, H, s_{e,z}) + V_h(x, z_h, H, s_{h,z}), \quad (1)$$

where $H_0(\mathbf{r}_e, \mathbf{r}_h)$ is the free-exciton Hamiltonian; $\mathbf{r}_{e(h)} = (\boldsymbol{\rho}_{e(h)}, z_{e(h)})$ is the electron (hole) position vector; z is the crystal growth direction; $z_{e(h)}$ is the z coordinate of the electron (hole); $\rho = |\boldsymbol{\rho}_e - \boldsymbol{\rho}_h|$, $\boldsymbol{\rho}_e$, and $\boldsymbol{\rho}_h$ are the electron and hole position vectors in the layer plane; x is the concentration of impurity ions; H is the external magnetic field directed along the growth axis z of the structure; and $s_{e(h),z}$ is the projection of the electron (hole) spin on the magnetic field direction.

The last two terms in Eq. (1), which are the potentials for the electron and hole, are written as

$$V_e(x, z_e, H, s_{e,z}) = V_e(z_e) + \Delta V_e(x, H, s_{e,z}) \times [\Theta(L_1 + L_2 + d - z_e) - \Theta(L_1 + d - z_e)], \quad (2)$$

$$V_h(x, z_h, H, s_{h,z}) = V_h(z_h) + \Delta V_h(x, H, s_{h,z}) \times [\Theta(L_1 + L_2 + d - z_h) - \Theta(L_1 + d - z_h)], \quad (3)$$

where $\Theta(x)$ is the step function and L_1, L_2, and d are the widths of the quantum-well layers and the interlayer barrier, respectively.

The potentials $V_e(x, z_e, H, s_{e,z})$ and $V_h(x, z_h, H, s_{h,z})$ are expressed as a sum of two terms, the first of which is independent of an external magnetic field and the second, $\Delta V_{e(h)}$, describes the exchange interaction in the semimagnetic layer and depends on the magnetic field and on the carrier spin projections. As noted above, the exchange interaction between the carriers and the localized spins of impurity ions results in splitting of the exciton levels with different spin polarizations. In the presence of magnetic impurities in the layer, the variation in the band gap due to an external magnetic field is determined by

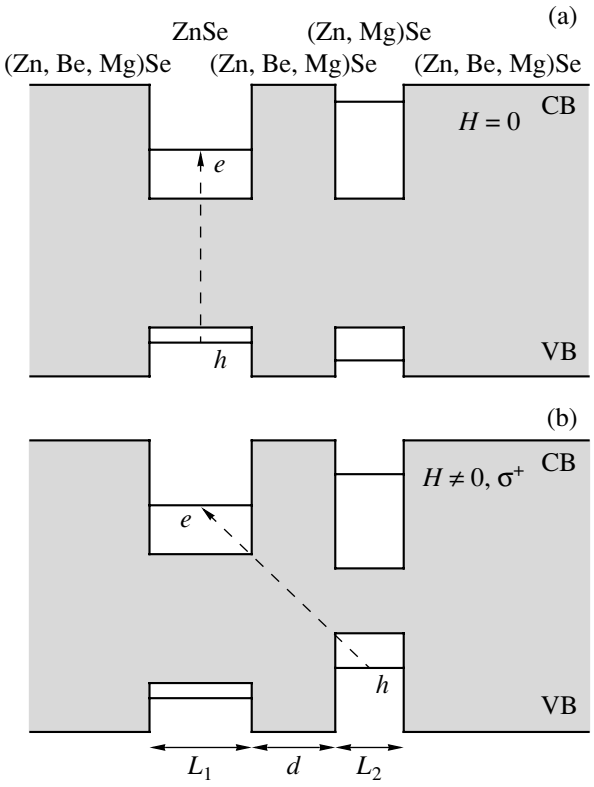

Fig. 1. Diagram of a heterostructure and positions of energy band edges (a) in the absence and (b) in the presence of an external magnetic field. Arrows show the formation of (a) a direct and (b) an indirect exciton.

$$\Delta V_e(x, H, s_{e,z}) = -xN_0\alpha\bar{s}_{\mathrm{Mn},z}(H)s_{e,z}, \quad (4)$$

$$\Delta V_h(x, H, s_{h,z}) = -x\frac{N_0\beta}{3}\bar{s}_{\mathrm{Mn},z}(H)s_{h,z}, \quad (5)$$

where $N_0\alpha$ and $N_0\beta$ are the electron and hole exchange integrals and $\bar{s}_{\mathrm{Mn},z}$ is the average projection of the spin of magnetic ions. Thus quantum-well potentials can be written as

$$V_e(x, z_e, H, s_{e,z}) = \begin{cases} (1 - Q_V)(E_g^{\mathrm{bar}} - E_g^1), & z_e \le 0, \\ 0, & 0 < z_e \le L_1, \\ (1 - Q_V)(E_g^{\mathrm{bar}} - E_g^1), & L_1 < z_e \le L_1 + d, \\ (1 - Q_V)(E_g^2 - E_g^1) + \Delta V_e(x, H, s_{e,z}), & \\ L_1 + d < z_e \le L_q + d + L_2, & \\ (1 - Q_V)(E_g^{\mathrm{bar}} - E_g^1), & L_1 + d + L_2 < z_e, \end{cases} \quad (6a)$$

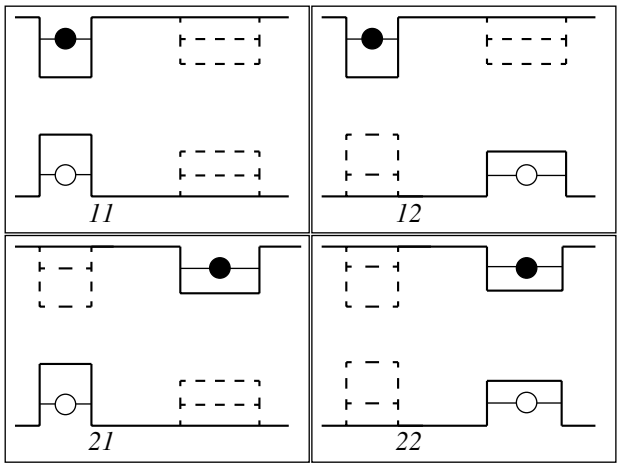

Fig. 2. Potential-well diagram illustrating the choice of wave functions. Numbers *ij* (11, 12, 21, 22) have the following meaning: an electron (a solid circle) is in well *i* and a hole (an open circle) is in well *j*. Solid lines represent the potential for which the solutions of the Schrödinger equation are chosen as basis functions. Dashed lines supplement this potential to the potential of the problem under study.

$$V_h(x, z_h, H, s_{e,h}) = \begin{cases} Q_V(E_g^{\text{bar}} - E_g^1), & z_h \le 0, \\ 0, & 0 < z_h \le L_1, \\ Q_V(E_g^{\text{bar}} - E_g^1), & L_1 < z_h \le L_1 + d, \\ Q_V(E_g^2 - E_g^1) + \Delta V_h(x, H, s_{h,z}), & \\ L_1 + d < z_h \le L_1 + d + L_2, & \\ Q_V(E_g^{\text{bar}} - E_g^1), & L_1 + d + L_2 < z_h, \end{cases} \quad (6b)$$

where E_g^{bar}, E_g^1, and E_g^2 are the band gaps in the barrier layer, ZnSe layer, and $Zn_{1-x}Mn_xSe$ layer, respectively. As noted above, the potential in the semimagnetic layer depends on the magnetic field and on the carrier spin orientation. For the system considered, the exciton binding energy is smaller than the distance between the one-particle energy levels in each well. Accordingly, for both electrons and holes, only the lowest quantum levels in each of the wells were taken into account.

To calculate the exciton energy for a system of double quantum wells, we used the following method. The wave function was chosen as a linear combination of the one-particle wave functions with fixed electron and hole localization radii. Let $\varphi_i(z_e)$ (i = 1, 2) be the one-particle electron wave function in an isolated well i (i.e., in the absence of the other well). For example, $\varphi_1(z_e)$ is the wave function of an electron in QW1 (QW stands for quantum well) in the absence of well QW2 (Fig. 2). For a hole in the valence band, we denote the corresponding wave functions by $\psi_i(z_h)$. As a basis, we choose the wave functions corresponding to the electron localized in well i and the hole localized in well j,

$$\Psi_{ji}(\rho, z_e, z_h) = \varphi_i(z_e)\psi_j(z_h)\sqrt{\frac{2}{\pi}}\frac{1}{\lambda}\exp\left(-\frac{\rho}{\lambda_{ij}}\right), \quad (7)$$

where λ_{ij} is a variational parameter determined by minimizing the energy of the system with Hamiltonian (1) and functions (7). Functions (7) do not take into account the possibility of carrier transitions between the wells; therefore, we construct the wave function of the system as a linear combination of functions (7):

$$\Psi = \sum_{i,j} a_{ij}\Psi_{ji}(\rho, z_e, z_h). \quad (8)$$

The coefficients a_{ij} are the probability amplitudes of finding the electron in well i and the hole in well j. The quantities a_{ij} and the exciton energies are determined from the equations

$$\det|\langle ij|H|km\rangle - E\langle ij|km\rangle| = 0. \quad (9)$$

Here and in what follows, we enumerate the levels E_ν starting from the lowest level, ν = 1, …, 4. In all calculations, we did not take into account paramagnetic effects at the boundary between the semimagnetic and nonmagnetic semiconductors. We also neglected the diamagnetic shift of the exciton lines, which is small for the 1*s* exciton state in the magnetic fields considered.

The exciton lifetime is inversely proportional to the overlap integral

$$I_\nu\left|\int\Psi_\nu(0, z, z)\right|^2, \quad (10)$$

which was calculated for each exciton state. Once the magnitude of the overlap integral is known, we can calculate different optical characteristics of the system, for example, reflection and absorption spectra. The required formulas can be found in [10, 11].

3. RESULTS AND DISCUSSION

We calculated the exciton energy and the overlap integral for a $Zn_{0.76}Be_{0.08}Mg_{0.16}Se/ZnSe/Zn_{0.76}Be_{0.08}Mg_{0.16}Se/Zn_{0.95}Mn_{0.05}Se/Zn_{0.76}Be_{0.08}Mg_{0.16}Se$ double quantum well using the following parameters: a band gap of the $Zn_{0.76}Be_{0.08}Mg_{0.16}Se$ barrier material E_g^{bar} = 3.2 eV [9], a ZnSe band gap E_g^1 = 2.822 eV, and a $Zn_{1-x}Mn_xSe$ band gap E_g^2 = 2.822 eV for x < 0.065, where x is the relative content of magnetic ions [8]. The parameter Q_V = 0.22 determines the ratio of the potential barrier height for holes to the band gap offset at the heteroboundary. The exchange integrals are $N_0\alpha$ = 0.26 eV and $N_0\beta$ = –1.31 eV [9]. The average projection of the manganese ion spin on the direction of the magnetic

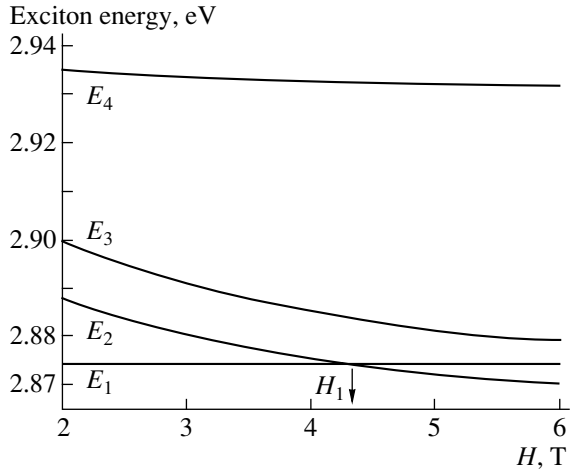

Fig. 3. Magnetic field dependence of the exciton energy for the σ component of the exciton transition; the interwell barrier width is 60 Å.

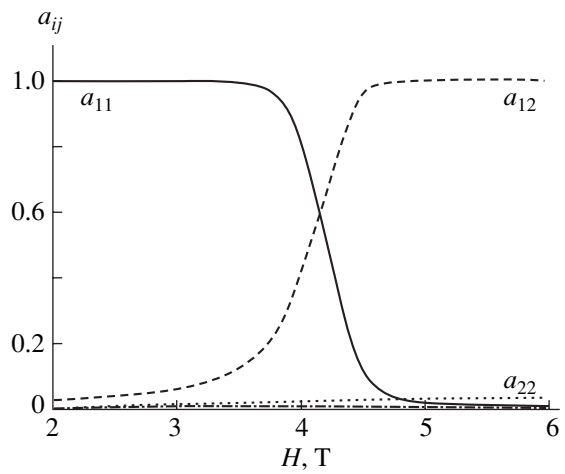

Fig. 4. Magnetic field dependence of the coefficients a_{ij} of the wave function of the lowest excited exciton state. The parameters of the system are the same as those in Fig. 3.

field was calculated in the mean-field approximation, $S_{\mathrm{Mn},z}(H) = -S_{\mathrm{eff}}B_{5/2}\left(\frac{5g\mu_B H}{2k_B(T+T_{\mathrm{eff}})}\right)$, where $B_{5/2}$ is the Brillouin function, $g = 2$, μ_B is the Bohr magneton, and k_B is Boltzmann's constant. For $x = 0.05$, the effective spin and temperature, which depend on the magnetic impurity content, are $S_{\mathrm{eff}} = 3/2$ and $T_{\mathrm{eff}} = 1.7$ K, respectively [9]. The electron effective mass is $m_e = 0.16m_0$, the heavy hole effective mass is $m_{hh,\perp} = 0.74m_0$ in the growth direction and $m_{hh,\parallel} = 0.28m_0$ in the direction perpendicular to the growth axis (m_0 is the free electron mass), and the permittivity is $\varepsilon = 9$ [9].

Figure 3 shows the calculated magnetic field dependence of the exciton energy in a double quantum well for the σ^+ component of the excitonic transition. The following values of the parameters were used in the calculation: a nonmagnetic well width $L_1 = 40$ Å, a width of the semimagnetic well $L_2 = 27$ Å, a barrier width $d = 60$ Å, and a relative content of magnetic impurity $x = 0.05$.

The curves in Fig. 3 correspond to four possible states of the 1*s* exciton labeled by E_1, E_2, E_3, and E_4 in ascending order of exciton energy.

We denote the field corresponding to the minimum separation of the lowest energy levels by H_1 (Fig. 3). For $H < H_1$, E_1 is the lowest energy direct-exciton state with the electron and hole localized in the same layer, namely, in the nonmagnetic quantum well QW1. The higher energy state E_2 is the interwell (indirect) exciton with the hole in the semimagnetic layer and the electron in the nonmagnetic layer. The level E_3 corresponds to the energy of the direct exciton in the semimagnetic layer QW2. Finally, the level E_4 is the energy of the second indirect exciton with the hole in the nonmagnetic layer and the electron in the semimagnetic layer.

The energies of these states vary with increasing magnetic field. For the σ^+ transition, the depths of the quantum wells for the electron and hole in the semimagnetic layer increase with field and the depth of the well for the hole increases faster than that for the electron, due to the greater value of the exchange integral. For a field H_0 ($H_0 < H_1$), the quantum confinement level for a hole in the semimagnetic well QW2 lies lower than that in well QW1. If we neglect the interaction between the electron and the hole, then, for $H > H_0$, the state with lower energy would correspond to the hole located in the semimagnetic quantum well QW2. However, if the Coulomb interaction is taken into account, then the energy of the direct exciton state still remains the lowest, since the absolute value of the binding energy of the direct exciton is much greater than the binding energy of the interwell exciton.

With a further increase in the field, the well for the hole in the semimagnetic layer becomes so deep that the transition of the hole from the nonmagnetic to the semimagnetic layer becomes energetically favorable for the exciton as a whole. The total energy of the interwell exciton for $H > H_1$ appears to be the minimum of the four possible states, though the absolute value of the binding energy of such an exciton is small.

In Fig. 4, the coefficients a_{ij} [defined in Eq. (8)] for the lowest exciton state are shown as functions of the magnetic field. As noted above, these coefficients determine the probability of finding the electron and the hole in the corresponding wells. It is seen from Fig. 4 that, for $H < H_1$, the coefficient a_{11} is the greatest; this means that both carriers are localized in the nonmagnetic layer QW1. For $H > H_1$, the coefficient a_{12} is the greatest; therefore, the lowest exciton state becomes indirect: the electron is localized in well QW1 and the hole in QW2. Thus, in magnetic fields close to H_1, the spatial configuration of the carriers forming the exciton in the lowest excited energy state changes.

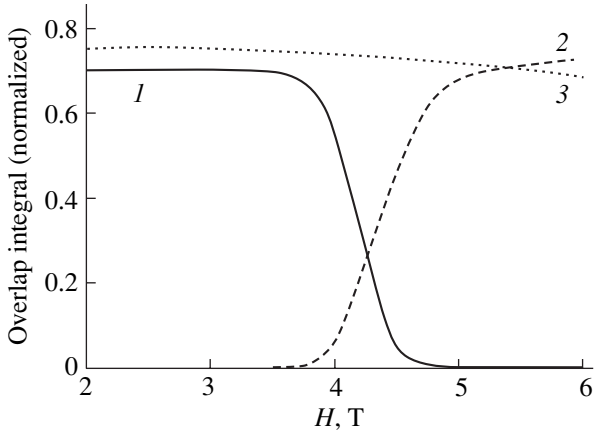

Fig. 5. Overlap integral as a function of the external magnetic field. Curves *1–3* describe the field dependence of the overlap integrals for the states with energies E_1, E_2, and E_3, respectively (see Fig. 3). The parameters of the system are the same as those in Fig. 3.

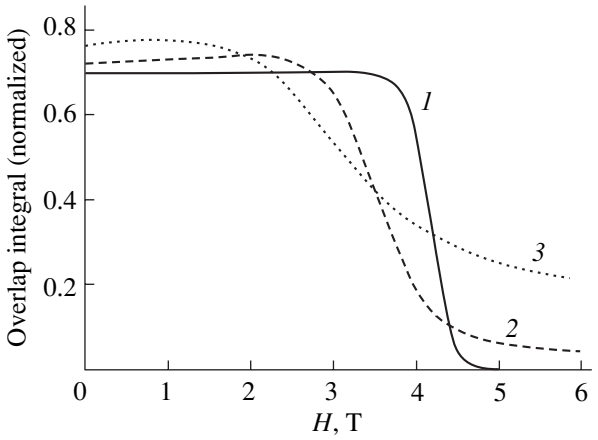

Fig. 6. Magnetic field dependence of the overlap integral for several values of the barrier width d between the quantum wells: (*1*) 60, (*2*) 40, and (*3*) 30 Å.

Figure 5 shows the overlap integrals for each of the states considered above. Overlap integral (10) is determined mainly by the spatial distribution of carriers. The overlap integral with wave functions of the carriers localized in the same layer (direct exciton) is greater than that for carriers localized in different layers of the structure (interwell exciton). Therefore, for $H < H_1$, the overlap integral for the lowest energy direct exciton state E_1 is much greater than that for the indirect state E_2 ($I_1 \gg I_2$ in Fig. 5). The situation is different for $H > H_1$. In this case, the lowest energy state is that of an indirect exciton, with the electron and hole being localized in different layers of the structure. The overlap integral (as well as the binding energy) for this lowest indirect state is much smaller than that for the direct excited state E_2 ($I_1 \ll I_2$ in Fig. 5). This modification of the state corresponds to an abrupt change in the magnitude of the overlap integral near $H = H_1$. The magnitude of the overlap integral and, therefore, the exciton lifetime depend on the parameters of the system. The lifetime of the interwell exciton state strongly increases with the width of the barrier separating the potential wells. For example, for $H > 3$ T, the lifetime of such an exciton in a system with barrier width $d = 40$ Å is an order of magnitude greater than the lifetime of the direct exciton. For an analogous structure with $d = 60$ Å, the difference becomes as large as two orders of magnitude (Fig. 6).

It is seen from Fig. 6 that the value of the field H_1 at which the transition from the state where the lowest energy exciton is direct to the state where the indirect exciton has the lowest energy increases with the barrier width. The wider the barrier, the smaller the absolute value of the binding energy of the indirect exciton, i.e., the greater the magnetic field that must be applied to make the well for a hole in the semimagnetic layer deep enough for the hole to pass to this well and for this transition to be energetically favorable for the exciton as a whole.

Thus, in a certain range of magnetic fields, the lowest energy state in the system considered is that of the indirect exciton.

4. CONCLUSIONS

We have found the exciton energy levels and wave functions in a double quantum well formed by semimagnetic semiconductors in an external magnetic field. We have shown that, for certain values of the magnetic field, resonances of different exciton states of the two-well system occur. In a certain range of magnetic fields, the interwell exciton corresponds to the lowest energy state and has a lifetime exceeding the direct-exciton lifetime by several orders of magnitude. Therefore, the system under study can be useful for creating high exciton densities.

ACKNOWLEDGMENTS

This study was supported in part by the program “Nanophysics and Nanoelectronics” of the National Academy of Sciences of Ukraine.

REFERENCES

1. L. V. Butov and A. I. Filin, Phys. Rev. B **58**, 1980 (1998).
2. A. V. Larionov, V. B. Timofeev, I. Khvam, and K. Soerensen, Pis’ma Zh. Éksp. Teor. Fiz. **75**, 233 (2002) [JETP Lett. **75**, 200 (2002)].
3. L. V. Butov, A. C. Gossard, and D. S. Chemla, Nature **418**, 751 (2002).

4. D. Shoke, S. Denev, Y. Liu, L. Pfeifer, and K. West, Nature **418**, 754 (2002).
5. A. V. Komarov, S. M. Ryabchenko, and O. V. Terletskiĭ, Zh. Éksp. Teor. Fiz. **73** (2), 608 (1977) [Sov. Phys. JETP **46**, 318 (1977)].
6. J. A. Gaj, R. Planel, and G. Fishman, Solid State Commun. **29**, 435 (1979).
7. M. von Ortenberg, Phys. Rev. Lett. **49**, 1041 (1982).
8. P. J. Klar, D. Wolverson, J. J. Davies, *et al.*, Phys. Rev. B **57**, 7103 (1998).
9. B. Konig, U. Zehnder, D. R. Yakovlev, *et al.*, Phys. Rev. B **60**, 2653 (1999).
10. E. L. Ivchenko and G. E. Pikus, *Superlattices and Other Heterostructures* (Springer, Berlin, 1995); E. L. Ivchenko, A. V. Kavokin, V. P. Kochereshko, *et al.*, Phys. Rev. B **46**, 7713 (1992).
11. V. I. Sugakov and G. V. Vertsimakha, J. Phys.: Condens. Matter **13**, 5635 (2001).

Translated by I. Zvyagin

Physics of the Solid State, Vol. 46, No. 5, 2004, pp. 954–968. Translated from Fizika Tverdogo Tela, Vol. 46, No. 5, 2004, pp. 924–937.

LOW-DIMENSIONAL SYSTEMS AND SURFACE PHYSICS

Dependence of the Surface Energy on the Size and Shape of a Nanocrystal

M. N. Magomedov

Institute of Geothermal Problems, Dagestan Scientific Center, Russian Academy of Sciences, pr. Kalinina 39a, Makhachkala, 367003 Russia

e-mail: mahmag@iwt.ru

Received May 7, 2003; in final form, August 26, 2003

Abstract—An expression is derived for the surface energy σ as a function of the size and shape of a nanocrystal. It is shown that the wider the deviation of the shape parameter f from unity, the more pronounced the decrease in the surface energy σ with a decrease in the number N of atoms in the nanocrystal. The dependences of the average coordination number, the surface energy, and the melting temperature on the number N exhibit an oscillatory behavior with maxima at points corresponding to numbers of atoms forming a defect-free cube. The surface energy decreases with an increase in the temperature T. It is found that the smaller the nanocrystal size or the greater the deviation of the nanocrystal shape from the thermodynamically most stable shape (a cube), the larger the quantity $-(d\sigma/dT)$. It is established that the nanocrystal undergoes melting when the surface energy decreases to a value at which it becomes independent of the nanocrystal size and shape. The conditions providing fragmentation and dendritization of the crystal are discussed. It is demonstrated that, at $N > 1000$, the dependence $\sigma(N)$ coincides, to a high accuracy, with the dependence of the surface tension of the nanocrystal on N. The inference is made that bimorphism is characteristic of nanocrystals. This implies that nanocrystals can have platelike and rodlike shapes with equal probability. © *2004 MAIK "Nauka/Interperiodica"*.

1. INTRODUCTION

Although the size dependence of the surface energy of condensed systems has been investigated theoretically in a large number of works [1–4], many problems remain unsolved even for a liquid phase [5, 6]. This is especially true in regard to the dependence of the surface energy on the nanocrystal shape. For liquids, this dependence is not very important because it is evident that a microdrop rapidly becomes spherical in shape. As regards nanocrystals, their shape in the general case can be arbitrary.

Let us consider a system consisting of N identical atoms at a temperature T and a pressure P. The change in the free energy of this system upon varying the temperature, the volume V, the number of atoms, and the surface area Σ can be represented in the form [7]

$$dF(T, V, N, \Sigma) = -SdT - PdV + \mu dN + \sigma d\Sigma. \quad (1)$$

Here, S is the entropy, μ is the chemical potential, and σ is the specific (per unit area) surface free energy (the function σ for a liquid phase is referred to as the surface tension). According to relationship (1), the function $\sigma(T, V, N)$ is defined by the expression

$$\sigma(T, V, N) = (dF/d\Sigma)_{T, V, N}. \quad (2)$$

For all theoretical approaches, the basic problem is to determine the derivative $(dF/d\Sigma)$ at constant values of the volume and the number of atoms in the system. Under the assumption that the system has a specific (as a rule, spherical or cubic) shape, function (2) is difficult to determine exactly, because the parameters Σ, V, and N cannot be treated independently at a given shape of the surface of the system.

As far back as 1948, Gibbs [8] paid attention to the difference in the energy of formation of a new crystal surface in two different processes, namely, upon cleavage of the crystal and extension of the already existing surface. In the former case, the surface area increases as a result of an increase in the number of surface atoms without a change in the surface density. In the latter case, the surface area increases through a change in the surface density at a constant number of surface atoms. The first process is associated with the change in the shape, and the energy increment is determined by the surface tension σ_{ten}. The change in the energy in the second process is caused by the surface stress σ_{str}; however, the question arises as to the thermodynamic equilibrium between the stretched surface and the volume [9]. In the general case, the surface energy σ can differ from the surface tension σ_{ten} of the crystal. In an isotropic case, these functions are related by the expressions [1, 10, 11]

$$\begin{aligned} \sigma_{ten} &= \sigma + \Sigma(d\sigma/d\Sigma)_{T, V, N}, \\ \sigma_{str} &= \sigma_{ten} + \Sigma(d\sigma_{ten}/d\Sigma)_{T, N}. \end{aligned} \quad (3)$$

It should be noted that, in the first expression, the surface area changes at a constant density due to a change in the shape. In the second expression, $d\Sigma$ appears as a result of the extension of the surface. If the function σ

does not depend on the surface area Σ, all three functions become equal to each other. This situation occurs in the thermodynamic limit: $N \longrightarrow \infty$, $V \longrightarrow \infty$, and $\Sigma/N \longrightarrow 0$ at $V/N = \text{const}$, when the function σ becomes independent of the shape parameters of the system [11]. However, as in the case of function (2), the derivative entering into expressions (3) are difficult to calculate exactly at a fixed shape of a finite nanocrystal ($N \neq \infty$).

Therefore, in the framework of existing theoretical approaches, the function $\sigma(T, V, N)$ can be found only approximately from an analysis of the dependence $F(V^{2/3})$ or $F(N^{2/3})$ under the assumption that the change in the argument $V^{2/3}$ or $N^{2/3}$ determines the change in the surface area. It is easily understood that, in the general case, this assumption is incorrect. In the present work, this problem was solved by analyzing the changes in the function $F(\Sigma)$ upon infinitesimal variations in the nanocrystal shape at fixed values of V and N.

2. THE AVERAGE VALUE OF THE FIRST COORDINATION NUMBER

Now, we consider a nanocrystal in the form of a rectangular parallelepiped faceted by the {100} planes. The nanocrystal is composed of N atoms, of which N_{po} atoms are arranged along the edge of the square base and $N_{ps} = fN_{po}$ atoms occupy the lateral edge of the parallelepiped. The total number of atoms in this system can be defined as $N = fN_{po}^3/\alpha$, where $f = N_{ps}/N_{po}$ is the shape parameter, $\alpha = \pi/6k_y$ is the microstructure parameter, and k_y is the packing coefficient. For regular lattices, the packing coefficient k_y takes the following values [12]:

$$k_y = \begin{cases} 2^{1/2}\pi/6 = 0.7405 \text{ (at } k_3 = 12), & \alpha = 0.707 \\ 2\pi/9 = 0.6981 \text{ (at } k_3 = 10), & \alpha = 0.750 \\ 3^{1/2}\pi/8 = 0.6802 \text{ (at } k_3 = 8), & \alpha = 0.770 \\ \pi/6 = 0.5236 \text{ (at } k_3 = 6), & \alpha = 1.000 \\ 3^{1/2}\pi/16 = 0.3401 \text{ (at } k_3 = 4), & \alpha = 1.540, \end{cases} \quad (4)$$

where k_3 is the first coordination number for an atom inside the parallelepiped.

In my earlier works [13, 14], it was shown that, depending on the number of atoms and the nanocrystal shape, the relative value of the averaged (over all atoms of the system) first coordination number is determined by the relationship

$$\begin{aligned} k_3^*(N, f) &= k_3(N, f)/k_3(N = \infty) \\ &= 1 - Z_s(f)(\alpha^2/N)^{1/3}, \\ Z_s(f) &= (1 + 2f)/3f^{2/3}. \end{aligned} \quad (5)$$

The volume, surface area, and diameter (the spacing between the most distant atoms) for the rectangular parallelepiped are given by the expressions

$$\begin{aligned} V &= N_{po}^3 f c^3 = N\alpha c^3, \\ \Sigma &= 2N_{po}^2(1 + 2f)c^2\alpha_s = 6c^2\alpha_s(N\alpha)^{2/3}Z_s(f), \\ d &= N_{po}(2 + f^2)^{1/2}c = 3^{1/2}c\alpha_d(N\alpha^{1/3})Z_d(f), \\ Z_d(f) &= f^{-1/3}[(2 + f^2)/3]^{1/2}, \end{aligned} \quad (6)$$

where c is the distance between the centers of the nearest neighbor atoms and α_s and α_d are the coefficients accounting for the atomic packing density in the face and edge of the nanocrystal, respectively. It can easily be seen that the volume $V(N)$ does not depend on the shape of the system. From formulas (5) and (6), we can derive the relationships for the dependence of the coordination number on the diameter and shape of the parallelepiped ($d^* = d/c$); that is,

$$k_3^*(d, f) = 1 - 3^{1/2}L_d(f)\alpha/d^*,$$

$$L_d(f) = Z_s(f)Z_d(f) = [(2f + 1)/3f][(2 + f^2)/3]^{1/2}.$$

The crystal–vacuum interface is assumed to be a Gibbs geometric surface [8].

3. OSCILLATIONS OF THE SIZE DEPENDENCES AND MAGIC NUMBERS OF ATOMS

It can be seen from Fig. 1 that the shape functions $Z_s(f)$, $Z_d(f)$, and $L_d(f)$ reach a minimum value (equal to unity for all the functions) for cubic nanocrystals (at $f = 1$). For platelike ($f < 1$) or rodlike ($f > 1$) nanocrystals, the values of the shape functions are greater than unity. Hence, as can be seen from Fig. 2, the function $k_3^*(f)$ at any value of N (or d) has a maximum at $f = 1$, i.e., for the thermodynamically most stable (cubic) shape of the nanocrystal. The cubic shape can be observed only at specific numbers of atoms in the nanocrystal: $N_{cube} = \text{INT}[N_{po}^3/\alpha]$, where $N_{po} = 2, 3, 4, \ldots$ and INT[x] is the integer part of the number x. The shape parameter f must satisfy the following conditions: $2/\text{INT}[N\alpha/2]^{1/2} \leq f \leq (1/2)\text{INT}[N\alpha/4]$, where the quantity on the left-hand side corresponds to a biatomic plate and the quantity on the right-hand side refers to a rod with a biatomic diameter. Under the model assumptions, a defect-free parallelepiped should have a minimum number of atoms, which depends on the shape parameter f and the microstructure parameter α; that is,

$$N_{min} = \begin{cases} \text{INT}[8/\alpha] & \text{for a cube} \quad (f = 1) \\ \text{INT}[8f/\alpha] & \text{for a rod} \quad (f > 1) \\ \text{INT}[8/\alpha f^2] & \text{for a plate} \quad (f < 1). \end{cases}$$

In this case, $N_{min}(f = 1) < N_{min}(f \neq 1)$; i.e., within the model under consideration, the nanocrystal with a minimum size is cubic in shape. Depending on the microstructure, the minimum size of the cube is determined by the following numbers of atoms:

$$N_{\min}(\text{cube}) = \text{INT}[2^3/\alpha]$$

$$= \begin{cases} \text{INT}[8/0.707] = 11 & \text{for a face-centered cubic structure} \quad (k_3 = 12) \\ \text{INT}[8/1.000] \equiv 8 & \text{for a hexagonal close-packed structure} \quad (k_3 = 6) \\ \text{INT}[8/1.540] = 5 & \text{for a diamond-like structure} \quad (k_3 = 4). \end{cases}$$

The exact values are as follows [1, 15]: $N_{\min}$(face-centered cubic structure) = 13, $N_{\min}$(hexagonal close-packed structure) ≡ 8, and $N_{\min}$(diamond-like structure) = 4. The above estimates clearly demonstrate that the accuracy of the method proposed in this work is satisfactory: the error in calculating the minimum number $N_{\min}$ of atoms even for close-packed structures is approximately equal to 15%.

For "noncubic" numbers of atoms (i.e., at $N \neq N_{\text{cube}}$), a defect-free parallelepiped can be plate- or rod-shaped; in this case, $k_3^*(N_{\text{cube}} \pm 1) < k_3^*(N_{\text{cube}})$. Taking into account that the quantity $k_3(N, f)$ determines the binding energy of the nanocrystal [13–15], it is interesting to consider the following features, which can easily be understood from analyzing the "isomorphs" $k_3(N)$, i.e., the "isomorphic" (calculated for f = const) dependences of the first coordination number on the number of atoms and the shape of nanocrystals (Fig. 2).

(i) Atoms of nanocrystals are characterized by magic numbers: nanocrystals with "cubic" numbers N_{cube} of atoms are energetically more stable than nanocrystals with $N = N_{\text{cube}} \pm 1$. As a consequence, the general size dependence $k_3(N)$ has a number of maxima.

(ii) The size dependences exhibit an oscillatory behavior: the general dependence $k_3(N)$ is oscillatory with maxima at points $k_3(N_{\text{cube}})$ and minima at points corresponding to numbers N of atoms forming only a defect-free rod of biatomic thickness.

From the data presented in Figs. 1 and 2, it is evident that the amplitude of these oscillations increases with a deviation of the shape parameter f from unity (within the above range of permissible values f). Since many lattice properties of nanocrystals are governed by the average coordination number $k_3(N)$, the dependences of these properties on N also exhibit an oscillatory behavior. The effects of magic numbers and oscillations in size dependences have long been observed in numerical

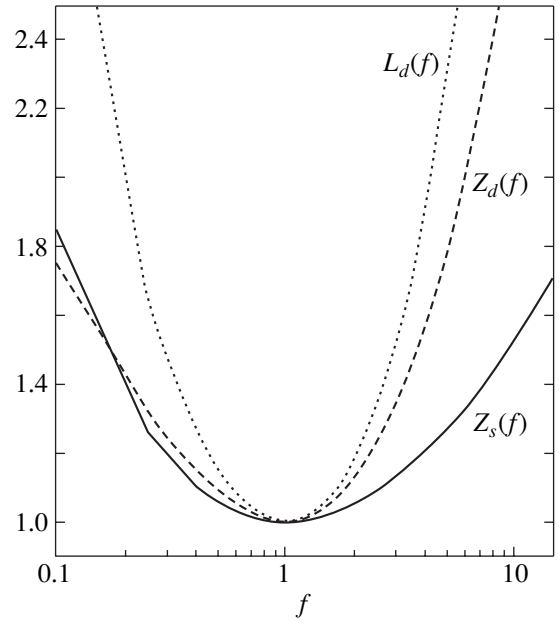

Fig. 1. Dependences of the shape functions $Z_s(f)$, $Z_d(f)$, and $L_d(f) = Z_s(f)Z_d(f)$ on the shape parameter f for cubic (f = 1), platelike (f < 1), and rodlike (f > 1) nanocrystals. All the shape functions reach a minimum value (equal to unity) for cubic nanocrystals (f = 1).

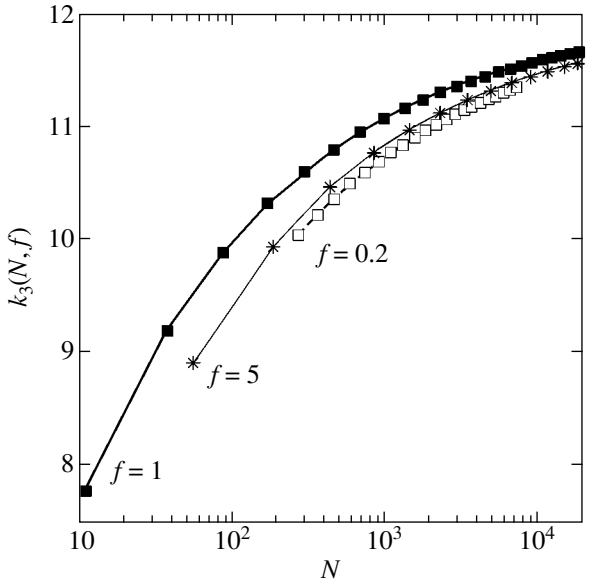

Fig. 2. Calculated dependences of the averaged (over all atoms) first coordination number on the number of atoms and the shape of nanocrystals with a face-centered cubic structure. Closed squares correspond to the cubic isomorph (f = 1), asterisks indicate the rodlike isomorph (f = 5), and open squares represent the platelike isomorph (f = 0.2). The minimum numbers of atoms are as follows: $N_{\min}$ = INT[8f/α] = INT[8 × 5/0.707] = 56 for the rodlike isomorph, $N_{\min}$ = INT[8/αf^2] = INT[8/0.707 × 0.04] = 282 for the platelike isomorph, and $N_{\min}$ = INT[8/α] = INT[8/0.707] = 11 for cubic nanocrystals. Symbols in the isomorphs indicate the permissible (at given values of f and α) numbers N of atoms in a nanocrystal with a specified shape.

and natural experiments (for details, see reviews [1, 15]).

4. CALCULATION OF THE SURFACE ENERGY OF A NANOCRYSTAL

Let us now assume that the interatomic interaction is governed by the Mie–Lennard-Jones pair potential [16]

$$\varphi(r) = [D/(b-a)]\{a[r_0/(c+r)]^b - b[r_0/(c+r)]^a\}. \quad (7)$$

Here, D is the depth of the potential well, r_0 is the coordinate of the minimum of the potential well, b is the stiffness parameter of the potential, and a is the parameter characterizing the long-range interaction.

Within the Einstein model of a vibrational spectrum, the free energy of the nanocrystal can be represented in the form [17]

$$F/Nk_Bk_3(N=\infty) = [k_3^*(N, f)/2](D/k_B)U(R) + 3[\Theta/k_3(N=\infty)] \times \{0.5 + (T/\Theta)\ln[1-\exp(-\Theta/T)]\}. \quad (8)$$

Here, k_B is the Boltzmann constant. In the nearest neighbor approximation, the potential energy $U(R)$ can be written as

$$U(R) = (aR^b - bR^a)/(b-a), \quad R = r_0/c.$$

In [18, 19], it was demonstrated that the characteristic Einstein temperature in the case of the interatomic potential (7) has the form

$$\Theta(T) = A_w\xi\{-1 + [1 + (6D/k_BA_w\xi^2)]^{1/2}\}\lambda(T/\Theta_0),$$
$$A_w = K_R[5k_3(N, f)ab(b+1)/192(b-a)]R^{b+2}, \quad (9)$$
$$K_R = \hbar^2/k_Br_0^2m, \quad \xi = 9/k_3(N=\infty),$$

where m is the atomic mass and Θ_0 is the Einstein temperature at $T = 0$. As was shown in [19], the function $\lambda(T/\Theta_0)$ at $T = 0$ and high temperatures ($T \gg \Theta_0$) is equal to unity. This function substantially changes only in the range $0 < T \ll \Theta_0$. Consequently, the dependence of the free energy (8) on the size and shape of the nanocrystals is determined only by the dependence of the average coordination number k_3 on N and f. Within this approach, it became possible to obtain the size dependences of the binding energy [13], the Debye temperature, the melting temperature, and the superconducting transition temperature [14], which are in good agreement with the experimental data.

From the foregoing it follows that the surface free energy (per unit area) can be defined by a relationship following from expression (2); that is,

$$\sigma(T, V, N) = (dF/dk_3^*)_{N,V,T}[(dk_3^*/df)_{\alpha,N}/(d\Sigma/df)_{\alpha,N,c}]. \quad (10)$$

Then, from formulas (5)–(9), we obtain the relationship

$$\sigma(T, V, N) = -[k_3(N=\infty)/12c^2\alpha_s]\{DU(R) + 3k_B[\Theta/k_3(N, f)]E(\Theta/T) \times [\Theta_0/(\Theta_0 + A_w\xi)]\vartheta(T/\Theta_0)\}, \quad (11)$$

where $E(\Theta/T) = 0.5 + [\exp(\Theta/T) - 1]^{-1}$ and $\vartheta(T/\Theta_0) = 1 - (T/\Theta_0)\{d\ln[\lambda(T/\Theta_0)]/d(T/\Theta_0)\}$. At high temperatures ($T > 0.3\Theta_0$), these functions can be simplified: $E(\Theta/T < 1) \cong T/\Theta_0$ and $\vartheta(T/\Theta_0 \gg 1) \cong 1$. Moreover, when the energy of zero-point vibrations is low compared to the chemical bond energy, i.e., at $6D \gg k_BA_w\xi^2$ (this condition is not satisfied only for quantum crystals of the He and Ne types), formula (9) can be rearranged to the relationship $\Theta_0 \cong (6DA_w/k_B)^{1/2}$ [19]. As a result, expression (11) can be simplified as follows:

$$\sigma(T, R, N) = -[k_3(N=\infty)/12c^2\alpha_s]\{DU(R) + [3k_BT/k_3(N, f)]\}. \quad (12)$$

From this relationship at high temperatures, we have

$$(d\sigma/dT)_V = -k_B/4c^2\alpha_sk_3^*(N, f). \quad (13)$$

For the isobaric dependence of the function $\sigma(T)$ at $N = \infty$ and $R = 1$, we obtain

$$(d\sigma/dT)_P = (d\sigma/dT)_V + (d\sigma/dV)_TV\alpha_p \cong (d\sigma/dT)_V - (2/3)\sigma\alpha_p, \quad (14)$$

where $\alpha_p = V^{-1}(dV/dT)_P$ is the coefficient of thermal expansion.

For macrocrystals ($N = \infty$) at zero pressure ($R = 1$) and melting temperatures T_m, functions (12)–(14) take the form

$$\sigma = (k_B/4r_0^2\alpha^{2/3})[k_3(N=\infty)(D/3k_B) - T_m], \quad (d\sigma/dT)_V = -k_B/4r_0^2\alpha^{2/3}, \quad (15)$$

$$(d\sigma/dT)_P \cong (d\sigma/dT)_V - 0.0533\sigma/T_m. \quad (16)$$

In this case, the quantity α_s was approximated as $\alpha_s \cong \alpha^{2/3}$. When calculating the quantity $(d\sigma/dT)_P$, the thermal expansion coefficient α_p at the melting temperature was estimated from the relationship $\alpha_pT_m \cong 0.08$ [20], which is satisfied for the metals presented in the table. Unfortunately, experimental data on the quantity $-(d\sigma/dT)_P$ for solids are unavailable in the literature; however, there is a considerable amount of reliable data for liquids [21]. The calculations demonstrated that the quantity $-(d\sigma/dT)_P$ for crystals is somewhat smaller than that determined for a liquid phase at the melting temperature in the experiment [21].

The table presents the results of calculations from formulas (15) and (16) for 25 metals. A comparison with the experimental estimates σ_{exp} [2, 22, 23] shows that the theoretical results are in good agreement with the experimental data. Therefore, relationships (12)

Calculated surface free energies of macrocrystals at melting temperatures and $R = 1$

Metal	r_0, nm [16]	D/k_B, K [16]	T_m, K [24]	$-(d\sigma/dT)_V$, formula (15)	$-(d\sigma/dT)_P$, formula (16)	σ, formula (15)	σ_{exp}
Face-centered cubic structure							
Cu	0.2549	6841.19	1356	67.0	135.5	1741	1730 [2] 1690–1780 [22] 1450–1810 [23]
Ag	0.2876	5736.99	1234	53.00	102.4	1142	1205 [2] 1050–2250 [23]
Au	0.2875	7411.60	1336	52.6	112.1	1490	1410 [2] 1250–1530 [23]
Al	0.2854	6630.61	932	53.4	131.6	1366	1020 [2] 940–1340 [23]
β-Co	0.249	8638.4	1765	70.0	139.4	2298	1800–2140 [22] 2465–2725 [23]
Pb	0.3477	3944.85	601	36.0	84.5	546	560 [2] 555–630 [23]
Ni	0.2478	8706.50	1728	70.8	143.2	2344	1725 [2] 1640–2500 [23]
Pt	0.2789	11367.70	2042	56.0	119.4	2428	1600–1965 [23]
Body-centered cubic structure							
Li	0.3008	4927.9	453.70	45.4	113.1	576	460 [2]
Na	0.3661	3303.3	370.97	30.7	67.9	259	230 [2]
K	0.4541	2730.6	336.40	19.9	41.8	138	130 [2]
Rb	0.4857	2506.6	312.00	17.4	36.4	111	104 [2]
Cs	0.5360	2360.0	301.80	14.3	29.5	86	80 [2]
V	0.2606	15581.1	2193	60.5	118.4	2381	2300 [2]
Nb	0.2865	21716.3	2740	50.1	103.9	2762	2100 [22] 2000–2264 [23]
Ta	0.2865	21303.8	3250	50.1	94.1	2681	2480 [2] 2410–2550 [23]
δ-Fe	0.2478	12574.6	1809	66.9	129.5	2123	2170 [2] 1750–2150 [22] 1720–2100 [23]
Cr	0.2495	12128.9	2176	66.0	114.8	1991	2400 [22] 2070–2110 [23]
Mo	0.2720	19822.1	2890	55.5	106.7	2775	2100 [22] 1865–2680 [23]
W	0.2737	25589.0	3650	54.9	106.7	3543	2610–3190 [22] 2668–2712 [23]
Hexagonal close-packed structure							
Mg	0.3188	2985.3	923	42.8	70.1	472	688 [2]
Zn	0.2762	2678.1	693	57.0	100.9	571	830–880 [23]
Cd	0.3112	2286.9	594	45.0	79.5	384	696 [2] 665–685 [23]
Ti	0.2930	9472.4	1940	50.7	100.8	1821	1700 [22, 23]
Zr	0.3199	12274.7	2125	42.5	92.6	1996	1850 [23]

Note: Data on the melting temperatures and structural parameters at these temperatures are taken from [24]. The surface energies σ and σ_{exp} are expressed in units of mJ/m^2, and the quantity $(d\sigma/dT)$ is given in μJ/m^2 K.

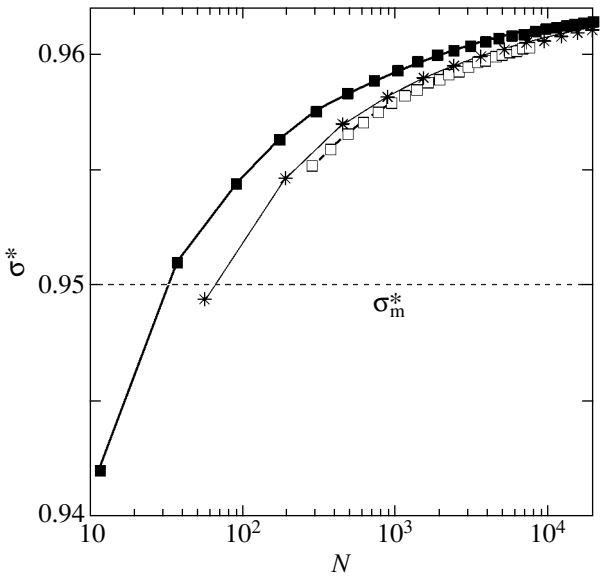

Fig. 3. Calculated dependences of the relative surface free energy $\sigma^* = 12\alpha_s\sigma r_0^2/k_3(N=\infty)D$ on the number of atoms and the shape of the surface of nanocrystals with a face-centered cubic structure. The relative temperature is given by $\tau = k_BT/D = 0.15$. Closed squares correspond to the cubic isomorph ($f = 1$), asterisks indicate the rodlike isomorph ($f = 5$), and open squares represent the platelike isomorph ($f = 0.2$). The horizontal dotted line shows the relative surface energy $\sigma_m^* = 0.95$ at which crystals undergo melting irrespective of the size N or shape f. In calculations, the distance between the centers of the nearest neighbor atoms is taken equal to the coordinate of the minimum of the potential well: $c = r_0$ (i.e., $R = 1$).

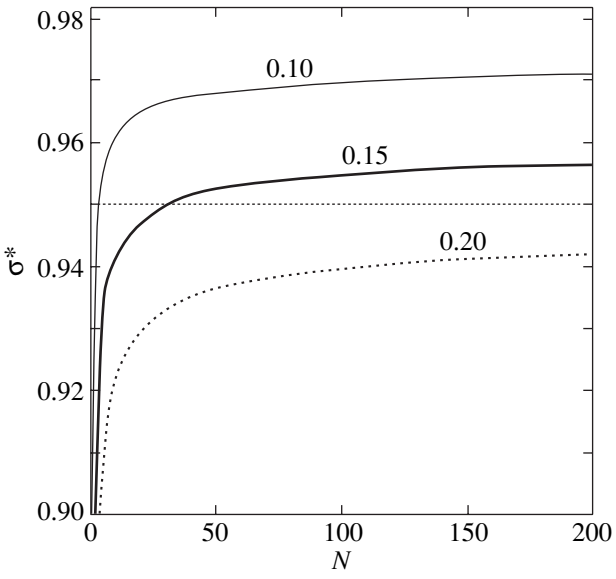

Fig. 4. Calculated dependences of the relative surface free energy $\sigma^* = 12\alpha_s\sigma r_0^2/k_3(N=\infty)D$ on the number of atoms and the temperature for isomorphic nanocrystals with cubic shape ($f = 1$). Nanocrystals have a face-centered cubic structure with $c = r_0$ (i.e., $R = 1$). Numbers near the curves correspond to the relative temperatures τ. The horizontal line shows the relative surface energy $\sigma_m^* = 0.95$ at which crystals undergo melting upon isochoric heating ($R = 1$) irrespective of the size N or the shape f of the surface.

and (13) can be used for analyzing the dependence of the surface energy on the size and shape of the surface of nanocrystals.

5. THE SURFACE ENERGY AS A FUNCTION OF THE SIZE AND SHAPE OF A NANOCRYSTAL

From formulas (5), (12), and (13) at $N \gg N_{\min} = 8$, we obtain the relationships

$$\begin{aligned}\sigma_N &= d\sigma/d(1/N^{1/3}) \cong -(k_BT/4c^2)Z_s^*(f) = \sigma_{TN}T,\\ \sigma_d &= d\sigma/d(c/d) \cong -(k_BT/4c^2)3^{1/2}\alpha^{1/3}L_d(f)\\ &= \sigma_{Td}T,\end{aligned} \quad (17)$$

Here, we introduced the following designations:

$$\begin{aligned}\sigma_{TN} &= [d(d\sigma/dT)_V/d(1/N^{1/3})]_c\\ &= -(k_B/12c^2)(2f^{1/3} + f^{-2/3}),\\ \sigma_{Td} &= [d(d\sigma/dT)_V/d(c/d)]_c\\ &= -(k_B/12c^2)\alpha^{1/3}(2 + f^{-1})(2 + f^2)^{1/2}.\end{aligned} \quad (18)$$

An analysis of these relationships demonstrates that the surface energy is a linear function of the argument $1/N^{1/3}$ (or c/d) and the slope of the size dependence of σ increases upon deviation of the parameter f from unity (Figs. 1, 2), i.e., upon distortion of the cube.

The dependence of the relative surface energy $\sigma^* = 12\alpha_s\sigma r_0^2/k_3(N=\infty)D$ on the number of atoms, the shape of the surface, and the temperature (at high temperatures) at $R = 1$ has the form [see formula (12)] $\sigma^* = 1 - [3\tau/k_3(N, f)]$. The dependences $\sigma^*(N, f)$ for nanocrystals with a face-centered cubic structure are plotted in Fig. 3. The relative temperature τ was taken to be $\tau = k_BT/D = 0.15$ (Fig. 3). The evolution of the function $\sigma^*(N)$ with an increase in the relative temperature from $\tau = 0.1$ to 0.2 (for cubic nanocrystals at high temperatures and $R = 1$) is illustrated in Fig. 4. It follows from the results obtained that the function σ^* only slightly depends on the size. For nanocrystals with a face-centered cubic structure (especially with a cubic shape), the surface energy σ^* can be considered to be independent of the size (and, correspondingly, of the shape). A similar inference was made for a liquid spherical drop by Bazulev *et al.* [6] on the basis of numerical simulations. It is this weak dependence $\sigma(N)$ that justifies the use of experimental data on $\sigma(N = \infty)$ in calculations of the thermal properties of nanocrystals, as has been done in many works. However,

as the temperature increases, the isomorphic size dependence $\sigma(N, f = \text{const})$ becomes more pronounced, especially for distorted nanocrystals (Figs. 2–4). Bazulev *et al.* [6] also found that the dependence $\sigma(N)$ becomes stronger when a spherical drop is transformed into an oblate elliptical drop. It should be noted that the general dependence $\sigma^*(N)$ exhibits an oscillatory behavior with maxima at the points N_{cube} where the function $k_3(N)$ has maxima (see Section 3).

6. THE CONSTANCY OF THE SURFACE ENERGY UPON MELTING

Now, we assume that the Lindemann criterion is valid upon melting of nanocrystals of arbitrary size [25–27]; that is,

$$\begin{aligned} R_m &\cong \text{const} \cong (1.1)^{-1} = 0.909, \\ \tau_m^*(N, f) &= [T_m(N, f)/T_m(N = \infty)] \\ &\cong [\Theta_0(N, f)/\Theta_0(N = \infty)]^2 \cong k_3^*(N, f). \end{aligned} \tag{19}$$

Then, from relationship (12), we obtain

$$\begin{aligned} &\sigma^*(T_m(N, f)) \\ &= R_m^2\{[-U(R_m)] - [3\tau_m(N, f)/k_3(N, f)]\} \\ &\cong R_m^2\{[-U(R_m)] - 3[\tau_m(N = \infty)/k_3(N = \infty)] \\ &\times [\tau_m^*(N, f)/k_3^*(N, f)]\} \cong R_m^2\{[-U(R_m)] \\ &- 3[\tau_m(N = \infty)/k_3(N = \infty)]\} \\ &= \sigma_m^*(k_3(N = \infty)), \end{aligned} \tag{20}$$

where $\sigma^* = 12\alpha_s\sigma r_0^2/k_3(N = \infty)D$ and $\tau = k_B T/D$. In this case, the relative surface energy σ_m^* at the melting temperature depends neither on the size nor on the shape of the nanocrystals. Relationship (20) implies that the relative surface energy of a nanocrystal (with any size and shape) at the melting temperature (which depends on N and f) is a constant determined by the nanocrystal microstructure. As can be seen from Fig. 5, the quantity $\tau_m(N = \infty) = k_B T_m(N = \infty)/D$ is nearly constant for the metals presented in the table: $\tau_m(N = \infty) \cong 0.15$ for hexagonal close-packed and body-centered cubic structures and 0.20 for face-centered cubic structures. Hence, from relationship (20) at $R_m \cong 1$, we can make the following estimates for metals with the corresponding microstructures:

$$\begin{aligned} \sigma_m^*(R_m = 1) &\cong 1 - [3\tau_m(N = \infty)/k_3] \\ &\cong \begin{cases} 1 - 3(0.15/12) = 0.963 & \text{for a hexagonal close-packed structure} \\ 1 - 3(0.20/12) = 0.950 & \text{for a face-centered cubic structure} \\ 1 - 3(0.15/8) = 0.944 & \text{for a body-centered cubic structure.} \end{cases} \end{aligned} \tag{21}$$

In Figs. 3 and 4, the relative surface energy $\sigma_m^* = 0.950$ is taken for face-centered cubic nanocrystals. It can be seen that the size at which a nanocrystal transforms into a liquid phase increases when the shape of the nanocrystal deviates from cubic shape (Fig. 3). Among the isomorphic (with a specified shape parameter f) nanocrystals, the nanocrystals with larger sizes undergo melting at higher temperatures (Fig. 4). Note that, for $\tau \geq \tau_m(N = \infty)$, the dependence $\sigma^*(N)$ lies below σ_m^* (see the isotherm for $\tau = 0.20$ in Fig. 4). Thus, reasoning from the Lindemann criterion (19), we obtain one more criterion for melting: a nanocrystal undergoes melting when the surface energy decreases to the value determined by relationship (20) and becomes independent of size and shape. It should be noted that estimates (21) for σ_m^* were carried out for isochoric ($R = 1$) heating. In the case of isobaric heating, the limiting value of σ_m^* should be smaller than estimates (21) due to a decrease in the parameter R. For example, from the Lindemann criterion at $a = 6$ and $b = 12$ (Lennard-Jones potential) and relationship (20), instead of estimates (21), we obtain the following estimates:

$$\sigma_m^*(R_m = 1.1^{-1}) \cong \begin{cases} 0.639 & \text{for a hexagonal cloe-packed structure,} \\ 0.628 & \text{for a face-centered cubic structure,} \\ 0.623 & \text{for a body-centered cubic structure.} \end{cases} \tag{22}$$

It should be taken into account that the dependences $\sigma^*(N)$ in Figs. 3 and 4 were plotted according to formula (12) at $R = 1$. If the calculations are performed for $R = 1.1^{-1}$, the curves in Figs. 3 and 4 should lie slightly below, but the qualitative pattern will remain unchanged, because the horizontal line for σ_m^* [according to estimates (22)] should also lie below. However, at $R_m = 1.1^{-1}$ and $\tau_m(N = \infty) = 0.2$, the calculated isotherms $\sigma^*(N)$ in Figs. 3 and 4 will be located below the level $\sigma_m^*(R_m = 1.1^{-1}) \cong 0.628$ that corresponds to the melting of a face-centered cubic macrocrystal. Since the melting temperature is a linear function of the depth of potential (7) (Fig. 5), the surface energy at the melting temperature of a nanocrystal is governed only by the microstructure and the parameters of the interatomic potential; that is,

$$\sigma(T_m(N, f)) = \sigma_m^*[k_3(N = \infty)D/12\alpha_s r_0^2]$$
$$\cong R_m^2\{[-U(R_m)] - [3\tau_m(N = \infty)/k_3(N = \infty)]\}$$
$$\times [k_3(N = \infty)D/12\alpha_s r_0^2] = \sigma_m(k_3, D, r_0).$$

The quantity $S_a(T_m) = 6\alpha_s(r_0/R_m)^2$ represents the surface area of a cube involving one atom at the melting temperature of the macrocrystal. The factor $E_s(T_m) = [k_3(N = \infty)/2]D[-U(R_m)] - (3/2)k_B T_m(N = \infty)$ is the sublimation energy (per atom) of the macrocrystal at the melting temperature (the second term is the mean energy per three degrees of freedom of the atom at the melting temperature of the macrocrystal). As a result, relationship (20) can be rewritten in the physically obvious form

$$\sigma_m(k_3, D, r_0) = E_s(T_m)/S_a(T_m). \quad (23)$$

Thus, for compounds with $T_m(N = \infty) \gg \Theta_0(N = \infty)$, the surface energy of a crystal (with any size and shape) at the melting temperature $T_m(N, f)$ is equal to the energy required to separate the macrocrystal into individual atoms [at $T_m(N = \infty)$], which is divided by the surface area of the free atoms thus formed at $T_m(N = \infty)$. That is why the surface area σ_m^* does not depend on the size and shape of the crystal and is determined only by the parameters of the interatomic potential (7) and the first coordination number $k_3(N = \infty)$. The surface energy $\sigma^* = 12\alpha_s\sigma r_0^2/k_3(N = \infty)D$ expressed in relative units [which are represented by a combination of the parameters of the interatomic potential (7)] appears to be independent of the parameters of the metal and, hence, becomes a characteristic that is approximately constant for metals with a particular microstructure. It is this situation that is described by expressions (20)–(23).

In the general case, experimental surface energies for different faces of a crystal differ from each other [15]. Since this difference is retained down to $T = 0$, it is most likely associated with the different atomic packing densities in faces with different $\{hkl\}$ indices. In particular, for a face-centered cubic structure, the number of nearest neighbors for an atom is equal to $k_2 = 6$ in the plane of the (111) face with the closest packing, $k_2 = 4$ in the plane of the (100) face, and $k_2 \cong 4$–2 in the plane of the (110) face in which atoms form chain structures [15]. Therefore, for these faces of face-centered cubic crystals, we have

$$\alpha_s \cong \pi/4k_y(2)$$

$$= \begin{cases} 0.8660 & \text{for the (111) face} \\ & \text{with } k_2 = 6 \text{ and } k_y(2) = 0.9069 \\ 0.7854 & \text{for the (100) face} \\ & \text{with } k_2 = 4 \text{ and } k_y(2) = 0.7854 \\ 1.1\text{–}1.5 & \text{for the (110) face} \\ & \text{with } k_2 \cong 4\text{–}2 \text{ and } k_y(2) \cong 0.7\text{–}0.5. \end{cases}$$

According to the above criterion for melting, the face melts when the surface energy of this face decreases to

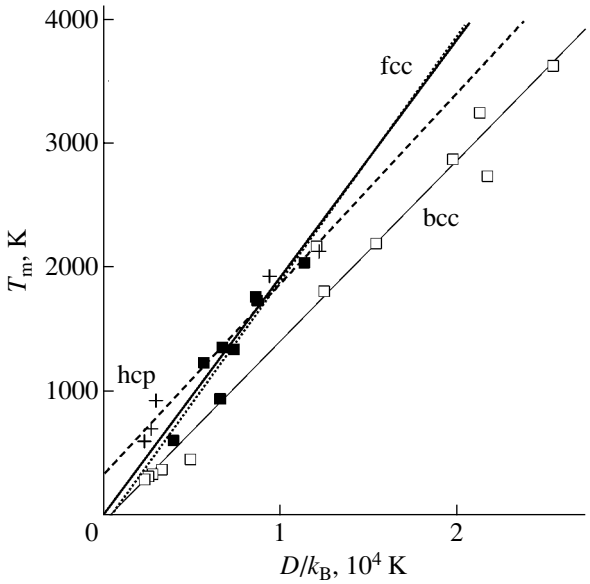

Fig. 5. Dependences of the melting temperature on the depth of the interatomic potential for metals with a face-centered cubic structure (closed squares), a body-centered cubic structure (open squares), and a hexagonal close-packed structure (crosses) presented in the table. Straight lines are the linear dependences $T_m = A(D/k_B) + B$. The heavy solid line indicates the dependence obtained in [21] at $A = 0.1923$ and $B = 0$. The other lines are constructed by computer processing of the data taken from the table. The dotted line corresponds to the dependence for a face-centered cubic structure: $A = 0.198$, $B = -93.207$, and the correlation coefficient $R_{cor} = 0.939$ (the dotted line virtually coincides with the heavy solid line). The thin solid line shows the dependence for a body-centered cubic structure: $A = 0.146$, $B = -52.248$, and $R_{cor} = 0.988$. The dashed line represents the dependence for a hexagonal close-packed structure: $A = 0.154$, $B = 338.914$, and $R_{cor} = 0.986$.

an energy [determined by expressions (20)–(23)] identical for all possible faces. Hence, it follows from relationship (12) that the melting temperatures for different crystal faces should also differ from each other. For example, for face-centered cubic structures, we have $T_m(111) > T_m(100) > T_m(110)$. It is this effect that has been experimentally observed for different faces of metals and semiconductors [28–30].

It can be seen from Fig. 3 that, at N = const, the surface energy is maximum for cubic nanocrystals (at $f = 1$). As a consequence, we can formulate the following regularities.

(i) The melting (or sublimation) temperature of a noncubic nanocrystal is less than that of the cubic isomer (i.e., the cubic nanocrystal with the same number N of atoms) under identical ambient conditions.

(ii) Consequently, the noncubic nanocrystal after melting (or evaporation) can immediately crystallize into a higher melting cubic isomeric form.

(iii) Upon transformation into the cubic isomeric nanocrystal, the heat of crystallization of a liquid (or gas) released from the noncubic nanocrystal is greater than the heat of melting (or sublimation) of the initial noncubic isomeric nanocrystal.

(iv) The noncubic nanocrystal should adhere to surrounding surfaces more easily than the cubic isomeric nanocrystal. The greater the deviation of the nanocrystal shape from cubic shape, the stronger the effect.

(v) The noncubic nanocrystal should enter into different chemical reactions more readily than the cubic isomeric nanocrystal. The greater the deviation of the nanocrystal shape from cubic shape, the higher the reactivity.

7. FRAGMENTATION AND DENDRITIZATION OF A CRYSTAL

As follows from relationships (11) and (12), the condition $\sigma < 0$ can be satisfied at specific values of R, T, N (or d), and f. In this case, it is energetically more favorable for the system to increase the surface area either through spontaneous decomposition into components (fragmentation) or through transformation of the structure of the surface into a skeleton structure (dendritization). According to expression (12), this fragmentation–dendritization condition is satisfied when the following inequality holds:

$$-k_3(N, f)U(R) < 3k_BT/D. \tag{24}$$

The "cold" fragmentation and dendritization [$-k_3(N, f)U(R) < 0$] was investigated in my previous work [13] when analyzing the binding energy of a nanocrystal at $T = 0$. At $T > 0$, the fulfillment of the fragmentation–dendritization condition (24) can be provided in different ways, namely, through (1) a variation in the pressure, i.e., in R at T, N, and f = const [13]; (2) an increase in the temperature T at R, N, and f = const [31]; (3) a decrease in the size N at R, T, and f = const [5]; or (4) a deviation of f from unity at R, T, and N = const (i.e., a deviation of the shape from cubic shape under isothermal and isochoric conditions).

When the fragmentation–dendritization condition (24) is ensured in any one of the aforementioned four ways, the crystal can undergo exothermal spontaneous decomposition into dendritic fragments with a maximum surface area (fragmentation–dendritization process). Inequality (24) can be rewritten in the form

$$R^b - (b/a)R^a + 3[(b-a)\tau/ak_3(N, f)] > 0, \quad R = r_0/c, \quad \tau = k_BT/D. \tag{25}$$

From relationship (25) at $b = 2a$, we found that condition (24) can be satisfied under uniform compression or uniform extension when the system obeys the following inequalities:

$$R^a_{com} > 1 + (1-\tau_{fr})^{1/2}, \quad R^a_{ext} < 1 - (1-\tau_{fr})^{1/2}, \quad \tau_{fr} = 3\tau/k_3(N, f). \tag{26}$$

Note that the smaller the quantity $k_3(N, f)$, the less the degree of compression (or extension) required for initiating the fragmentation–dendritization process.

Judging from the Lindemann criterion (19), we can assume that the relationship $\tau_m(N, f)/k_3(N, f) \cong \tau_m(N = \infty)/k_3(N = \infty)$ holds upon melting. Hence, it follows that, upon melting, the quantity $\tau_{fr}(T_m) = 3\tau_m(N, f)/k_3(N, f) \cong 3\tau_m(N = \infty)/k_3(N = \infty) \ll 1$ does not depend on the size and shape of the nanocrystal. Therefore, the values of $R_{com}(T_m)$ and $R_{ext}(T_m)$ that, according to inequalities (26), determine the degrees of compression and extension at the melting temperature (itself dependent on N and f), which are required for initiating the fragmentation–dendritization process, can turn out to be identical for any nanocrystal. In particular, for face-centered cubic crystals (Fig. 5), we have $\tau_m(N = \infty) \cong 0.2$, $\tau_{fr}(T_m) \cong 0.05$, $R_{com}(T_m) > 1.975^{1/a}$, and $R_{ext}(T_m) < 0.025^{1/a}$. At $a = 6$ (this is characteristic of van der Waals bonds [16]), the fragmentation–dendritization process upon melting of a crystal can proceed under the following conditions: $c(T_m)/r_0 < 0.893$ under compression and $c(T_m)/r_0 > 1.845$ under extension. At $a = 2$ (this holds true for diamonds, Si, Ge, α-Sn [32], a number of metals [16]), the above process can be initiated at $c(T_m)/r_0 < 0.712$ under compression and $c(T_m)/r_0 > 6.284$ under extension. These estimates indicate that it is more probable to observe the manifestation of the fragmentation–dendritization process upon melting under compression or extension of crystals in compounds with van der Waals bonds rather than in metals or semiconductors.

The experimental works devoted to the baric fragmentation revealed in crystals were discussed in my earlier work [13]. Moreover, the possibility of observing the size and thermal fragmentation of nanocrystals was also previously noted by other authors. In particular, the possible self-dispersion of 3d metal nanocrystals less than 20 nm in size was noted by Korobitsin

et al. [5], who calculated the surface energy of a cold nanocrystal. Zhukov [31] investigated the fragmentation of a chain consisting of 100 atoms by the molecular dynamics method. The results of all the aforementioned works confirm our inferences regarding the conditions for fragmentation and, hence, regarding the influence of the shape of the nanocrystal surface on the size dependence of the surface energy $\sigma(N, f)$.

8. RELATION BETWEEN THE SURFACE ENERGY σ AND THE ENERGIES OF SUBLIMATION AND VACANCY FORMATION

For macrocrystals of elemental substances, Pogosov [33] proposed the following phenomenological relationships:

$$4\pi r_0^2\sigma(N=\infty)/E_s(T=0) \cong C_s = 0.6\text{–}0.7 \cong 2/3, \quad (27)$$

$$\varepsilon_v/4\pi r_0^2\sigma(N=\infty) \cong C_v \cong 1/2. \quad (28)$$

Here, $E_s(T = 0)$ is the sublimation energy (per atom) of a macrocrystal at $T = 0$ and ε_v is the energy of formation of a vacancy (spherical in shape) in the bulk of the macrocrystal. Relationship (27) was derived under the assumption that, during the sublimation of a crystal composed of N atoms, the work is expended on forming the surface of free atoms and this work is proportional to the quantity $4\pi r_0^2\sigma(N = \infty)N$. However, expression (28) was deduced by assuming that the energy of vacancy formation is equal to only a portion of the work expended on forming a hollow surface of radius r_0 in an elastic continuum of the crystal. The validity of relationship (27) can easily be understood reasoning from expressions (12) and (20)–(23). In regard to expression (28), it should be noted that, in this case, the Lindemann criterion (19) enables one to obtain the estimate $\varepsilon_v/k_BT_m(N = \infty) \cong 10$ [34, 35]. Taking into account this estimate and the relationships $k_BT_m(N = \infty) \sim D \sim \sigma_m S_a(T_m)$, which follow from the data presented in Fig. 5 and estimates (22), the inference can be made that the approximate expression (28) is valid in the high-temperature range. Moreover, Devyatko *et al.* [36] calculated the energies of vacancy formation for different faces of a number of metals with a face-centered cubic structure and revealed the inequalities $\varepsilon_v(111) > \varepsilon_v(100) > \varepsilon_v(110)$. From these inequalities, expression (28), and the melting criteria (20)–(23), we obtain the relationship $T_m(111) > T_m(100) > T_m(110)$. The validity of this relationship (which was derived in a different way in Section 6) is confirmed by the experimental data presented in [28–30]. However, in the low-temperature range, the energy of vacancy formation ε_v considerably decreases with a decrease in the temperature [35, 37]. On the other hand, it can be seen from expression (12) and Fig. 4 that the surface energy σ increases with a decrease in the temperature. Therefore, expression (28) does not hold at low temperatures. That is why, in [33], expression (28) was found to be invalid for rare-gas crystals, which are characterized by a strong dependence $\varepsilon_v(T)$.

9. THE IDENTITY OF THE SURFACE ENERGY AND SURFACE TENSION

It should be noted that, in relationships (27) and (28), Pogosov [33] used the function $\sigma(N = \infty)$, i.e., the surface tension of macrocrystals, rather than the surface energy $\sigma_{ten}(N = \infty)$. According to formulas (3), (5), and (6), the surface tension $\sigma_{ten}(N)$ can be represented in the form

$$\sigma_{ten} = \sigma + \Sigma(d\sigma/dk_3^*)_{N,V,T}(dk_3^*/df)_{\alpha,N}/(d\Sigma/df)_{\alpha,N,c} = \sigma - (1-k_3^*)(d\sigma/dk_3^*)_{N,V,T}, \quad (29)$$

where $k_3^* = k_3^*(N, f)$.

From expression (12), in the high-temperature range, we have

$$\sigma_{ten} = \sigma - (1-k_3^*)k_BT/4c^2\alpha_s(k_3^*)^2 = \{k_3(\infty)D[-U(R)] - [3k_BT/(k_3^*)^2]\}/(12c^2\alpha_s), \quad (30)$$

$$(d\sigma_{ten}/dT)_V = -k_B/4c^2\alpha_s(k_3^*)^2. \quad (31)$$

It can be seen from these relationships that, compared to the surface energy σ, the surface tension σ_{ten} more rapidly decreases with both a decrease in N and an increase in the temperature. However, the difference between the quantities σ_{ten} and σ is small and vanishes at $N \longrightarrow \infty$. It follows from formula (30) that $\sigma_{ten} \longrightarrow \sigma$ at $k_3^*(N \longrightarrow \infty, f) \longrightarrow 1$.

Figure 6 depicts the isomorphic dependences $\sigma(N)$ and $\sigma_{ten}(N)$ for cubic ($f = 1$) and rodlike ($f = 5$) nanocrystals at the melting temperature $\tau = k_BT_m/D \cong 0.2$. In calculations, the distance between the centers of the nearest neighbor atoms was taken equal to that corresponding to the Lindemann criterion (19): $c = 1.1r_0$ (i.e., $R = 0.909$). As can be seen from Fig. 6, even at maximum values of T and c [when the first term in expression (30) is minimum and the second term is maximum], the difference between the functions $\sigma(N)$ and $\sigma_{ten}(N)$ is insignificant and, at $N > 1000$, these functions can be considered to be identical with a high accuracy. This inference is in agreement with the theoretical results obtained by Vogelsberger *et al.* [11]. Therefore, the results of the present work for the function $\sigma(N, f)$ are also valid for the function $\sigma_{ten}(N, f)$. The identity of these functions for macrocrystals of elemental substances, i.e., $\sigma_{ten}(N = \infty) = \sigma(N = \infty)$, was noted in the review by Kumikov and Khokonov [23], who analyzed the results of many experimental works.

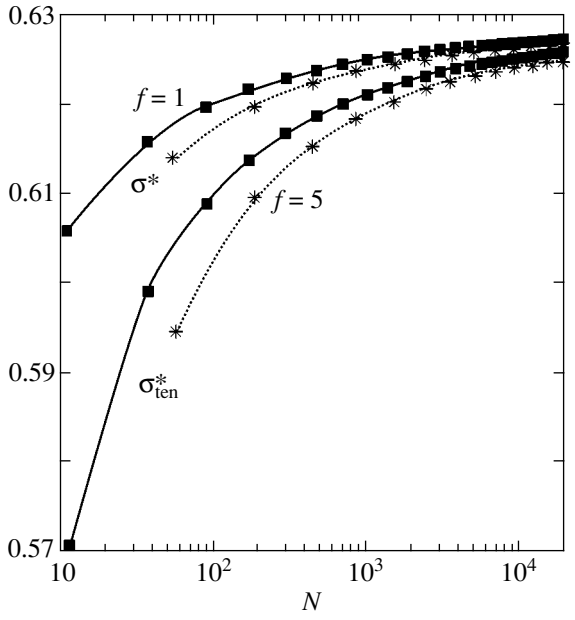

Fig. 6. Dependences of the surface energy $\sigma^* = 12\alpha_s\sigma r_0^2/k_3(N=\infty)D$ (two upper curves) and the surface tension $\sigma^*_{ten} = 12\alpha_s\sigma_{ten} r_0^2/k_3(N=\infty)D$ (two lower curves) on the number of atoms and the shape of the surface of nanocrystals with a face-centered structure at relative temperature $\tau = 0.2$. The exponents in potential (7) are as follows: $a = 6$ and $b = 12$. Squares and solid lines correspond to the isomorphs of cubic nanocrystals ($f = 1$), and asterisks and dotted lines indicate the isomorphs of rodlike nanocrystals ($f = 5$). The distance between the centers of the nearest neighbor atoms is taken equal to $c = 1.1r_0$ (i.e., $R = 0.909$).

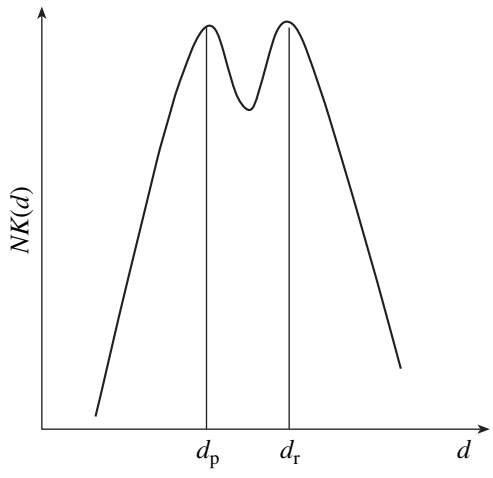

Fig. 7. Bimodal distribution of nanocrystals with an identical number N of atoms over the nanocrystal diameter d (which is frequently referred to as the nanocrystal size). The quantity $NK(d)$ is the number of isomeric nanocrystals with diameter d in an array. Vertical lines indicate the diameters of platelike nanocrystals (d_p) and rodlike nanocrystals (d_r) for which the distribution exhibits maxima.

The functional similarity of the equations for calculating the surface tension and the surface stress [see relationships (3)] suggests that, at $N > 1000$, the function $\sigma_{str}(N)$ should coincide, to a high accuracy, with the function $\sigma_{ten}(N)$; i.e., $\sigma_{str}(N) = \sigma_{ten}(N)$.

10. BIMORPHISM OF A NANOCRYSTAL

Figure 1 shows the dependences of the shape functions $Z_s(f)$, $Z_d(f)$, and $L_d(f)$. An analysis of these dependences indicates that three-dimensional nanocrystals can exhibit bimorphism. In essence, the phenomenon of bimorphism (literally, duplicity) lies in the identity of the shape functions for platelike and rodlike nanocrystals. As follows from the results obtained in Section 2 and relationships (8), (9), (11), (19), and (30), this identity implies the equality of the average coordination numbers, free energies, characteristic temperatures, surface energies, melting temperatures, and surface tensions for platelike and rodlike nanocrystals at α = const; that is,

$$\begin{aligned} k_3(\text{plate}) &= k_3(\text{rod}), \quad \Theta(\text{plate}) = \Theta(\text{rod}), \\ F(\text{plate}) &= F(\text{rod}), \quad \sigma(\text{plate}) = \sigma(\text{rod}), \\ T_m(\text{plate}) &= T_m(\text{rod}), \quad \sigma_{ten}(\text{plate}) = \sigma_{ten}(\text{rod}). \end{aligned} \tag{32}$$

The bimorphism can be observed in two cases, namely, at N = const and d = const.

(A) The bimorphism for isomeric (i.e., at N = const) nanocrystals takes place under the condition $k_3(N, f_p < 1) = k_3(N, f_r > 1)$, which can be reduced to the equation

$$Z_s(f_p < 1) = Z_s(f_r > 1), \tag{33}$$

where the subscripts p and r refer to platelike and rodlike shapes, respectively. Equality (33) suggests that oblate and prolate nanocrystals with a given number of atoms are characterized by the same parameters (32). Therefore, a nanocrystal involving a noncubic number of atoms ($N \neq N_{cube}$) can have platelike and rodlike shapes with equal probability. This leads to the following two effects.

(A.1) The bimodal distribution of isomeric nanocrystals over the diameter is schematically shown in Fig. 7. Cubic, platelike, and rodlike nanocrystals consisting of the same number of atoms can be formed under identical ambient conditions. Note that noncubic isomers [with equal values of N, $k_3(N)$, and Z and, correspondingly, with equal masses and binding energies] can have different diameters $d_r > d_p$; i.e., the size of rodlike nanocrystals is larger than that of platelike nanocrystals. From expressions (6), we can derive the following relationship for the difference between the diameters of noncubic nanocrystals:

$$\begin{aligned} \Delta d^* &= d^*(f_r) - d^*(f_p) \\ &= 3^{1/2}\alpha_d(N\alpha)^{1/3}[Z_d(f_r) - Z_d(f_p)], \end{aligned} \tag{34}$$

where the values of f_r and f_p are determined from condition (33). For example, it can be seen from Fig. 1 that the shape function $Z_s = 2^{1/3}$ is characteristic of both platelike ($f_p = 0.25$) and rodlike ($f_r = 5.1$) isomers. Consequently, nanocrystals with equal masses and parameters (32) have different diameters. (Note that the diameter of nanocrystals is traditionally measured using a microscope and is referred to as the nanocrystal size.) In our case, the diameters of noncubic nanocrystals with $Z_s = 2^{1/3}$ are as follows:

$$d^*/\alpha_d(N\alpha)^{1/3} = (2 + f^2)^{1/2} f^{-1/3}$$
$$= \begin{cases} 3.08 & \text{for a rod with } f_f = 5.10 \\ 2.28 & \text{for a plate with } f_p = 0.25. \end{cases}$$

Thus, nanocrystals are characterized by a bimodal size (diameter) distribution $NK(d)$. A similar bimodal distribution is schematically shown in Fig. 7. Some researchers observed bimodal distributions in experiments. In particular, Giorgio and Urban [38] found that the diameters of the majority of silver nanocrystals are equal either to 1–2 or to 4–5 nm. Anisichkin and Mal'kov [39] revealed that the sizes of diamond nanocrystals are equal to 3–3.5 or 5–5.5 nm. For copper nanocrystals, Ivanov-Omskiĭ *et al.* [40] obtained the nanocrystal size distribution function $NK(d)$ with two maxima at 2.0 and 2.7 nm. It should be noted that, up to now, the bimodality under consideration has not been justified theoretically. In this respect, the experimentally found bimodality of the distribution function $NK(d)$ is frequently treated as an experimental error. Unfortunately, at present, experimentally measured histograms of the nanocrystal size distribution $NK(d)$ have been processed using a standard procedure of fitting to a Gaussian unimodal distribution and thus calculating both the mean size of nanocrystals in an array and the variance of the distribution. Undeniably, the amount of experimental and theoretical data counting in favor of the bimodality of nanocrystal size distributions would be considerably larger if researchers were to have more closely examined the splitting of the maxima in histograms of the size distributions of nanocrystals and to have not treated the splitting of the distribution function $NK(d)$ [or $NK(N)$] as an experimental error (Fig. 7).

(A.2) At specific temperatures and a sufficiently small (noncubic!) number N of atoms, various internal fluctuations or external actions can initiate oscillations of the nanocrystal shape (at N = const) or, more specifically, reversible changes in the nanocrystal shape from platelike to rodlike. It is clear that these shape oscillations should occur most readily in nanocrystals of compounds with a low energy of interatomic interaction (for example, helium, hydrogen, neon, etc.). Note that, in experiments, the shape oscillations initiated in the nanocrystal (with a noncubic N!) under external actions (for example, upon exposure to acoustic or electromagnetic waves) should be accompanied by an anomalous absorption of the energy of the disturbance source. As follows from relationships (5) and (33), the resonance frequency of absorption is determined by the quantities N and α and also the interatomic interaction parameters.

(B) The bimorphism for isodiametric (at $d/c = d^* =$ const) nanocrystals is observed under the condition $k_3(d^*, f_p^* < 1) = k_3(d^*, f_r^* > 1)$, which can be reduced to the equation

$$L_d(f_p^* < 1) = L_d(f_r^* > 1). \quad (35)$$

When examining an array of isodiametric nanocrystals, i.e., nanocrystals chosen so that they have an identical diameter (the diameter of nanocrystals is usually measured using a microscope), we can observe the following two effects.

(B.1) The distribution $NK(N)$ of isodiametric nanocrystals over the number of atoms can appear to be bimodal. For identical diameters, the chosen (according to size under a microscope) nanocrystals can be either cubic or noncubic in shape. Some platelike and rodlike isodiametric nanocrystals can exhibit bimorphism in accordance with relationship (35). This means that parameters (32) for these nanocrystals should be equal to each other. Despite their sizes being equal, platelike and rodlike nanocrystals have different numbers of atoms: $N_p > N_r$. According to expressions (6), the difference between the numbers of atoms in these nanocrystals with noncubic surfaces can be represented as

$$\Delta N^{1/3} = [N(f_p)]^{1/3} - [N(f_r)]^{1/3}$$
$$= (d^*/3^{1/2}\alpha_d\alpha^{1/3})\{[Z_d(f_p^*)]^{-1} - [Z_d(f_r^*)]^{-1}\}. \quad (36)$$

Here, the parameters f_r^* and f_p^* are determined from condition (35).

(B.2) At a sufficiently high temperature and specific diameters d^*, the number of atoms in a noncubic nanocrystal can undergo oscillations. Under external actions or in response to internal fluctuations, a platelike nanocrystal can lose part of the atoms and transform into a rodlike nanocrystal with identical values of d^* and parameters (32) but different N. Then, this nanocrystal can capture atoms from the environment and regain its original shape. It is evident that, in experiments, the oscillations of the number of atoms in a noncubic nanocrystal (upon exposure to acoustic or electromagnetic waves) should result in an anomalous absorption of the energy of the disturbance source. The resonance frequency of absorption is determined by the quantities d^* and α and also the interatomic interaction parameters.

Let us now consider an array of noncubic nanocrystals that can exchange atoms. Under external actions (or in response to internal fluctuations), metastable noncubic (platelike or rodlike) shapes of nanocrystals can gradually transform into a more stable cubic shape, which is attended by an increase in the size of one type of crystals and a decrease in the size of the other type of

crystals. This relaxation of "cubization" of the shape with a change in the nanocrystal size should be accompanied by a release of energy due to the transformation of the array of nanocrystals into a thermodynamically more stable state. The energy gain is associated with the decrease in the total surface area of the array of nanocrystals owing to the cubization of the nanocrystal shape and the decrease in the degree of dispersion of the array as a whole.

11. SIMULTANEOUS PRECISION MEASUREMENT OF THE DIAMETER AND NUMBER OF ATOMS IN A NANOCRYSTAL OF ARBITRARY SHAPE

From relationships (34) and (36), it is easy to derive an "uncertainty relation" for the simultaneous precision measurement of the quantities d^* and N characterizing the nanocrystal size in an array; that is,

$$(\Delta d^*/N^{1/3})(\Delta N^{1/3}/d^*) = [Z_d(f_r) - Z_d(f_p)] \times \{[Z_d(f_p^*)]^{-1} - [Z_d(f_r^*)]^{-1}\}. \quad (37)$$

Here, the parameters f_r and f_p are determined from condition (33) and the quantities f_r^* and f_p^* are evaluated from condition (35).

The physical meaning of expression (37) is as follows. Let us assume that there is an array consisting of nanocrystals of a particular substance (α = const). From this array, we choose isomers, i.e., nanocrystals with identical numbers N of atoms and, consequently, with equal masses (as is the case with the selection of isomeric nanocrystals with the use of a mass spectrometer). By virtue of the bimorphism described by expression (33), the chosen isomeric nanocrystals are characterized by a bimodality (actually, uncertainty) of their diameters d^*. Now, we take nanocrystals with identical diameters d^* from the array (as is the case with the choice of nanocrystals equal in size under a microscope). Owing to the bimorphism described by relationship (35), the chosen isodiametric nanocrystals exhibit a bimodality (uncertainty) of the number of atoms. Only when all nanocrystals are cubic in shape (at $f_r = f_p = f_r^* = f_p^* = 1$) does neither bimodality nor uncertainty of the size occur in the system.

The above uncertainty in the simultaneous precision measurement of the quantities d^* and the number N in the array of nanocrystals is of considerable (or even crucial) importance for theoretical estimation of the diameter d^* of nanoparticles chosen using a mass spectrometer (i.e., according to the number N or the mass) and the number N of atoms in nanocrystals chosen under a microscope (i.e., according to the diameter d). In the former case, there can appear a bimodality in the distribution of nanocrystals over the diameter d^* (Fig. 7) and an uncertainty in the modal size of chosen nanocrystals. This necessarily leads to errors in the obtained dependences of the properties on the diameter d. In the latter case, a similar bimodality can be observed in the distribution of nanocrystals over the number N of atoms: the chosen rodlike, cubic, and platelike nanocrystals with the same size will contain different numbers of atoms. This bimodality introduces errors in the representation of the experimentally measured properties as a function of N.

It should be noted that the bimodality in the size distribution of nanocrystals [$NK(d)$, $NK(N)$] most clearly manifests itself when an array of nanocrystals is produced through baric fragmentation, i.e., through preliminary (static or dynamic) compression of a macrocrystal under a pressure higher than a threshold value, followed by rapid unloading [13]. The point is that, after this explosive treatment of the macrocrystal, the fragments formed have a noncubic shape with the highest probability, i.e., a platelike or rodlike habit (the term "fragmentation form" is used in experimental works). Strange as it may seem, the formation of cubic nanocrystals upon baric fragmentation is less probable [13]. Therefore, nanocrystals produced through baric fragmentation (for example, detonation diamonds [39, 41]) are characterized by a fragmentation habit and bimodality in the size distribution. In particular, the length-to-width ratio of particles in an array of detonation diamonds is estimated, on average, to be $f \approx 1.8$ [41].

In the case when nanocrystals are formed at low (or slowly changing) pressures, the appearance of bimodality in the size distribution is unlikely. For this preparation procedure, the formation of cubic nanocrystals is energetically most favorable and, hence, is more probable [13]. Therefore, the behavior of the experimental dependence $NK(d)$ enables us to judge both the conditions at which a given array was produced and the pressures applied to the array in the course of its evolution. For example, nanocrystals with the same diameter d (or the same numbers N of atoms, i.e., the same masses) are chosen from a powder (array of nanocrystals) of unknown origin. Then, if an ensemble of chosen nanocrystals exhibits a pronounced bimodality in the distribution of nanocrystals over N (or d), this powder most likely was subjected to sharp baric treatment at pressures above a threshold value in the course of the production or evolution. This method of analyzing an array of nanocrystals for bimodality in the size distribution can be used to design disposable detectors of explosion pressures.

12. CONCLUSIONS

Thus, the main results obtained in this work can be summarized as follows.

(1) The surface free energy σ (at $N \gg 8$, all the inferences made for σ are also valid for the function σ_{ten}) decreases with a decrease in the nanocrystal size: the functions $\sigma(N^{-1/3})$ and $\sigma(c/d)$ linearly decrease with an increase in the argument $N^{-1/3}$ or c/d.

(2) The greater the deviation of the nanocrystal shape from cubic shape, the more pronounced the decrease in the surface free energies $\sigma(N^{-1/3})$ and $\sigma(c/d)$ with an increase in the argument.

(3) At high temperatures, the surface free energy σ upon isochoric heating linearly decreases with an increase in the temperature. The smaller the nanocrystal size (for a particular shape) or the greater the deviation of the nanocrystal shape (at a given N) from the thermodynamically most stable shape (a cube), the larger the quantity $-(d\sigma/dT)_V$.

(4) The surface free energy σ upon isobaric heating decreases more rapidly (nonlinearly) as compared to isochoric heating: $-(d\sigma/dT)_P > -(d\sigma/dT)_V$. The slope of the dependence $\sigma(T)$ increases either with an isomorphic (at f = const) decrease in the number N or upon an isomeric (at N = const) deviation of the nanocrystal shape from cubic shape.

(5) It was established using the Lindemann criterion for melting (19) that a nanocrystal undergoes melting when the surface energy decreases to a value [determined by relationships (20)–(23)] at which it becomes independent of the nanocrystal size and shape.

(6) For compounds with $T_m(N = \infty) > \Theta(N = \infty)$, the surface energy of a nanocrystal (with arbitrary size and shape) at the melting temperature $T_m(N, f)$ is equal to the energy required to separate a macrocrystal into individual atoms [at $T_m(N = \infty)$], which is divided by the surface area of the free atoms thus formed at $T_m(N = \infty)$.

(7) The dependences $k_3(N)$, $\Theta(N)$, $F(N)$, $\sigma(N)$, $T_m(N)$, and $\sigma_{ten}(N)$ (and their related other size dependences) exhibit an oscillatory behavior with maxima at points corresponding to the magic numbers N_{cube} of atoms forming a defect-free cube and with minima at points corresponding to numbers N of atoms forming only a defect-free rod of biatomic thickness.

(8) Under condition (24), a nanocrystal can undergo exothermal spontaneous decomposition into dendritic fragments with a maximum surface area (fragmentation–dendritization process). This process is more probable in compounds with van der Waals bonds.

(9) Nanocrystals can exhibit bimorphism. This phenomenon manifests itself in the fact that nanocrystals can have platelike and rodlike shapes with equal probability.

(10) The bimorphism leads to bimodality in the distribution of nanocrystals either over the number of atoms in a nanocrystal or over the nanocrystal diameter.

ACKNOWLEDGMENTS

The author would like to thank A.D. Filenko, K.N. Magomedov, and Z.M. Surkhaeva for their assistance in performing this study.

This work was supported by the Russian Foundation for Basic Research, project no. 02-03-33301.

REFERENCES

1. Yu. I. Petrov, *Physics of Small Particles* (Nauka, Moscow, 1982).
2. L. Kornblit and A. Ignatiev, Physica A (Amsterdam) **141** (2–3), 466 (1987).
3. N. T. Gladkikh, L. K. Grigor'eva, S. V. Dukarov, V. E. Zil'bervarg, V. I. Larin, É. L. Nagaev, and S. P. Chizhik, Fiz. Tverd. Tela (Leningrad) **31** (5), 13 (1989) [Sov. Phys. Solid State **31**, 728 (1989)].
4. V. I. Zubov, I. D. Morokhov, and N. P. Tret'yakov, Poverkhnost, No. 3, 20 (1990).
5. D. V. Korobitsin, V. S. Demidenko, I. A. Nechaev, and V. I. Simakov, Izv. Vyssh. Uchebn. Zaved., Fiz., No. 9, 110 (2000).
6. A. N. Bazulev, V. M. Samsonov, and N. Yu. Sdobnyakov, Zh. Fiz. Khim. **76** (11), 2057 (2002).
7. L. D. Landau and E. M. Lifshitz, *Course of Theoretical Physics*, Vol. 5: *Statistical Physics*, 3rd ed. (Nauka, Moscow, 1976; Pergamon, Oxford, 1980), Part 1.
8. J. W. Gibbs, *Thermodynamics. Statistical Mechanics*, in *The Collected Works of J. Willard Gibbs* (Yale Univ. Press, New Haven, Conn., 1948; Nauka, Moscow, 1982).
9. É. L. Nagaev, Usp. Fiz. Nauk **162** (9), 49 (1992) [Sov. Phys. Usp. **35**, 747 (1992)].
10. É. V. Veĭtsman, Zh. Fiz. Khim. **65** (3), 850 (1991).
11. W. Vogelsberger, H.-G. Fritsche, and E. Muller, Phys. Status Solidi B **148** (1), 155 (1988).
12. G. S. Zhdanov, *Solid State Physics* (Mosk. Gos. Univ., Moscow, 1961).
13. M. N. Magomedov, Fiz. Tverd. Tela (St. Petersburg) **45** (5), 908 (2003) [Phys. Solid State **45**, 953 (2003)].
14. M. N. Magomedov, Fiz. Tverd. Tela (St. Petersburg) **45** (7), 1159 (2003) [Phys. Solid State **45**, 1213 (2003)].
15. B. M. Smirnov, Usp. Fiz. Nauk **163** (10), 29 (1993) [Phys. Usp. **36**, 933 (1993)].
16. M. N. Magomedov, Zh. Fiz. Khim. **62** (8), 2103 (1988).
17. M. N. Magomedov, Zh. Fiz. Khim. **62** (1), 58 (1988).
18. M. N. Magomedov, Zh. Fiz. Khim. **61** (4), 1003 (1987).
19. M. N. Magomedov, Fiz. Tverd. Tela (St. Petersburg) **45** (1), 33 (2003) [Phys. Solid State **45**, 32 (2003)].
20. A. A. Zhukov, Zh. Fiz. Khim. **48** (3), 562 (1974).
21. E. T. Turkdogan, *Physical Chemistry of High-Temperature Technology* (Academic, New York, 1980).
22. D. M. Skorov, A. I. Dashkovskiĭ, V. N. Maskalets, and V. K. Khizhnyĭ, *Surface Energy of Metallic Solid Phases* (Atomizdat, Moscow, 1973).
23. V. K. Kumikov and Kh. B. Khokonov, J. Appl. Phys. **54** (3), 1346 (1983).
24. M. I. Shakhparonov, *Introduction to the Modern Theory of Solutions* (Vysshaya Shkola, Moscow, 1976).
25. M. O. Robbins, G. S. Grest, and K. Kremer, Phys. Rev. B **42** (9), 5579 (1990).
26. Min-Yao Zhou and Ping Sheng, Phys. Rev. B **43** (4), 3460 (1991).
27. V. I. Ievlev, Fiz. Tverd. Tela (Leningrad) **33** (5), 1610 (1991) [Sov. Phys. Solid State **33**, 909 (1991)].
28. Yu. V. Naĭdich, N. F. Grigorenko, and V. M. Perevertaĭlo, Zh. Fiz. Khim. **51** (11), 2984 (1977).

29. U. Breuer, O. Krauff, and H. P. Bonzel, Phys. Rev. B **41** (15), 10848 (1990).
30. B. A. Nesterenko and V. G. Lyapin, *Phase Transitions at Free Faces and Interphase Boundaries in Semiconductors* (Naukova Dumka, Kiev, 1990).
31. V. S. Zhukov, Fiz. Tverd. Tela (Leningrad) **32** (12), 3626 (1990) [Sov. Phys. Solid State **32**, 2102 (1990)].
32. M. N. Magomedov, Zh. Fiz. Khim. **63** (11), 2943 (1989).
33. V. V. Pogosov, Fiz. Tverd. Tela (St. Petersburg) **36** (9), 2521 (1994) [Phys. Solid State **36**, 1371 (1994)].
34. T. Gorecki, High Temp.-High Press. **11** (6), 683 (1979).
35. M. N. Magomedov, Metally, No. 5, 73 (1992).
36. Yu. N. Devyatko, S. V. Rogozhkin, V. I. Troyan, E. P. Gusev, and T. Gustavson, Zh. Éksp. Teor. Fiz. **116** (12), 2038 (1999) [JETP **89**, 1103 (1999)].
37. M. N. Magomedov, Pis'ma Zh. Tekh. Fiz. **27** (18), 36 (2001) [Tech. Phys. Lett. **27**, 773 (2001)].
38. S. Giorgio and J. Urban, J. Phys. F: Met. Phys. **18** (8), L147 (1988).
39. V. F. Anisichkin and I. Yu. Mal'kov, Fiz. Goreniya Vzryva **24** (15), 135 (1988).
40. V. I. Ivanov-Omskiĭ, A. B. Lodygin, and S. G. Yastrebov, Fiz. Tekh. Poluprovodn. (St. Petersburg) **36** (7), 797 (2002) [Semiconductors **36**, 743 (2002)].
41. V. M. Tovstogan, V. A. Lukash, Yu. I. Sozin, A. V. Belyankina, and A. A. Svirid, Fiz. Tekh. Vys. Davlenii, No. 2, 37 (1980).

Translated by O. Borovik-Romanova

Physics of the Solid State, Vol. 46, No. 5, 2004, pp. 969–974. Translated from Fizika Tverdogo Tela, Vol. 46, No. 5, 2004, pp. 938–944.

LOW-DIMENSIONAL SYSTEMS AND SURFACE PHYSICS

Electron-Beam-Initiated Crystallization of Iron–Carbon Films

S. M. Zharkov and L. I. Kveglis

Kirensky Institute of Physics, Siberian Division, Russian Academy of Sciences, Akademgorodok, Krasnoyarsk, 660036 Russia
e-mail: zharkov@iph.krasn.ru

Received September 15, 2003

Abstract—A structure formed in nanocrystalline iron–carbon films exposed to an electron beam was studied. Explosive crystallization (EC) with the formation of dendrite and cellular–dendritic instabilities at a rate of up to 1 cm/s was observed. It was shown that the dependence between the growth rate of dendrite branches (or cells) during EC and the rounding radius of dendrite branch tips can be approximately described by equations used to calculate the crystal growth in supercooled melts. To explain the EC mechanism, a model of a liquid zone formed at the crystallization front was used. It was shown that the liquid zone arises due to energy accumulated in the film in the nanocrystalline state. It was assumed that this energy was accumulated due to the energy of elastic stresses. © *2004 MAIK "Nauka/Interperiodica".*

1. INTRODUCTION

Materials with nanocrystalline structure have unique physical properties and are objects of close attention [1]. A nanocrystalline material represents a specific state of condensed matter with a high degree of nonequilibrium. The problem of thermal stability of the nanocrystalline state during crystallization under exposure to uniform or local heating is very interesting and important from both theoretical and practical viewpoints. Under conditions of a rather weak heat dissipation, crystallization can become self-enhanced. An intense release of latent heat causes significant self-heating of the crystallization front, which takes on the form of a thermal domain moving with a velocity of up to a few tens of meters per second. In this case, a liquid zone can be formed at the crystallization front. The crystallization of a sample under such conditions is generally referred to as explosive crystallization [2].

Explosive crystallization (EC) was first observed in amorphous germanium. Crystallization initiated by pulsed laser beams [3], thermal heating [4], and mechanical impact [5] have been studied. EC caused by a pulsed laser beam has been observed in amorphous (In, Ga)Sb films. Pulses with a duration of ~10^{-7} s form local polycrystalline regions in amorphous films (with a velocity of up to 5 m/s) [6]. In [7–9], EC initiated by an electron beam was observed in amorphous Fe–Ni, Dy–Co, Pr–Ni, and Fe films. As a result of crystallization, various dendrite structures were formed.

The type of instabilities arising at the phase interface during crystallization changes depending on the conditions of the process. If the crystallization front velocity is low and the heat dissipation is ideal, the crystallization front will be "smooth." In the case of steady growth in a supercooled melt, any bulges in the crystallization front should disappear, thus maintaining the smoothness of the front. In the case of unsteady growth, an increase in the degree of supercooling causes instabilities in the smooth crystallization front, characteristic of crystallization from the melt: small-scale sinusoidal perturbations of the Mullins–Sekerka type, dendritic instabilities, a cellular structure of the front [10], and fractal clusters described by the Witten–Sander model [11, 12]. The mechanisms for the formation of various instabilities during crystal growth were considered by Langer [10, 13].

This study is devoted to the crystallization of nanocrystalline iron–carbon films initiated by an electron beam in a transmission electron microscope. We analyze the dependence of the parameters of a microstructure formed during crystallization on the rate of crystallization. Studies of dendrite structures formed by annealing films in vacuum in films grown using the same technology [14–16], of the fractal oxidation of such films in air under pulsed laser beams [17], and of EC under an electron beam [18] have already been reported.

2. EXPERIMENTAL

Iron–carbon films with a carbon content of ~20 at. % were grown through pulsed-plasma evaporation in vacuum (10^{-6} Torr) onto various substrates (NaCl, MgO, LiF). The growth method is described in [16, 19]. The chemical composition was determined using Auger spectroscopy. The film thickness was 20–50 nm. The film microstructure and phase composition were studied using a PRÉM-200 transmission electron microscope, as well as by x-ray diffraction methods using x-ray synchrotron radiation (λ = 1.7482 Å). The films were separated from substrates in water or a fluoric acid solution and were placed onto electron-microscopic object-supporting grids. Crystallization in the films was initiated by an electron beam in the transmission elec-

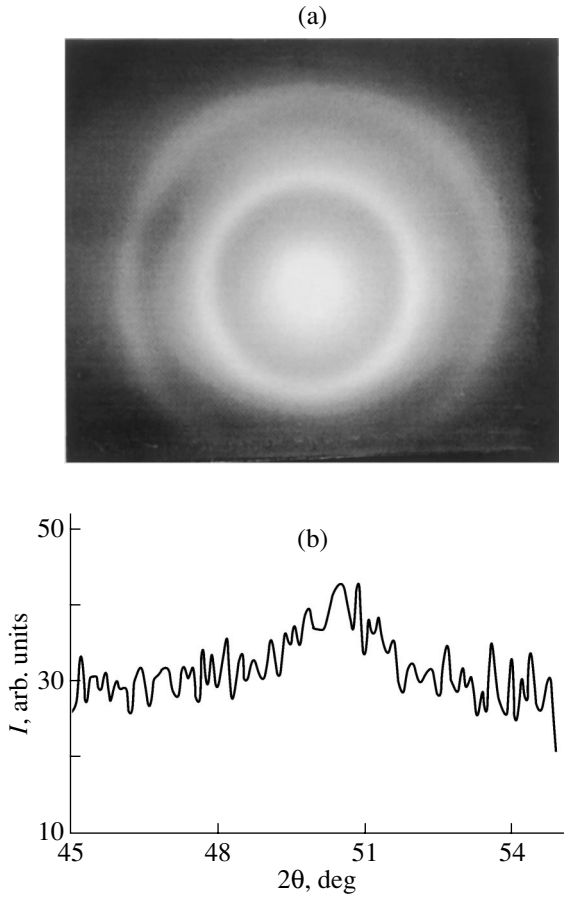

Fig. 1. (a) Electron diffraction pattern and (b) x-ray diffraction pattern obtained from an iron–carbon film in the initial state.

tron microscope in the mode of electron microscopy studies at an accelerating voltage of 125 kV and a beam current of 50–75 μA.

3. EXPERIMENTAL RESULTS

Electron diffraction patterns obtained from iron–carbon films in the initial state represent diffuse halos (Fig. 1a). In this case, the first diffraction reflection has a much higher intensity than the others. This fact suggests that the films under study are characterized by a nanocrystalline structure. The x-ray studies detect only one strongly broadened reflection (Fig. 1b). The x-ray diffraction peak broadening ($\Delta 2\theta$) is 2°–3° for various samples.

During electron microscopy studies, explosive crystallization was observed to occur in some films exposed to an electron beam. It is worth noting that the power of the electron beam incident on a sample corresponded to conventional conditions of electron microscopy studies. The crystallization rate determined visually during the studies varied from sample to sample and reached 1 cm/s. The typical electron microscopy image of the

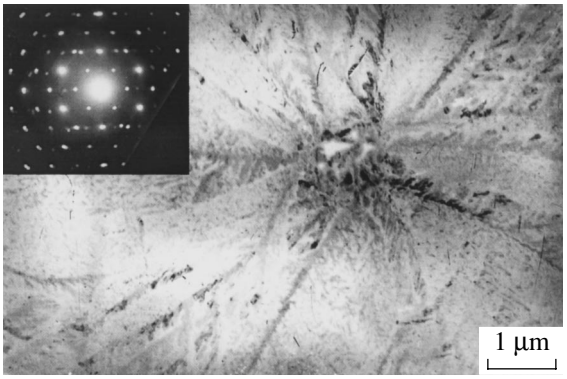

Fig. 2. Electron microscopy image of a dendrite crystal formed under an electron beam in the initial iron–carbon film. The inset shows an electron microdiffraction pattern obtained from a single dendrite branch.

film after such crystallization is shown in Fig. 2. The crystallization proceeded as follows. Initially, a crystallization center arose, from which dendrite-structure branches began to propagate in different directions. These branches, in turn, initiated new crystallization centers. The branch propagation velocity for the structure shown in Fig. 2 was ~0.25 cm/s. Due to crystallization, the film was in part covered with dendrite structures. The inset to Fig. 2 shows an electron diffraction pattern obtained by microdiffraction from a single dendrite branch. The electron diffraction pattern is spot-type and corresponds to none of the known structures of pure iron and iron–carbon compounds. The diffraction reflections in electron diffraction patterns obtained from noncrystalline film regions represented diffuse halos, as before.

In the case when it was impossible to achieve EC in the initial state, films were annealed in vacuum at T_{ann} = 100–150°C for 30 min. The electron diffraction patterns obtained from films after annealing did not differ from the electron diffraction patterns for the films in the initial state (Fig. 1a). Such films were again exposed to an electron beam, which as a rule caused crystallization. An electron microscopy image of a film after such crystallization is shown in Fig. 3. The inset to Fig. 3 shows the electron diffraction pattern obtained by microdiffraction from a single cell. The crystallization process was as follows. Initially, cells in the film grew at a rate of ~0.01 cm/s (Fig. 3, left). Then, secondary dendritic instabilities arose and developed. As a result, the film was covered in part by dendrite structures (Fig. 3, right) analogous to those observed during the crystallization of Fe–Ni films from a melt [20]. Eventually, the cellular structure was broken due to the development of secondary dendritic instabilities.

Figure 4 shows an electron microscopy image of the structure formed after a mechanical impact. An electron diffraction pattern (see inset to Fig. 4) obtained by microdiffraction from an area of ~0.5 μm shows spot reflections arranged similarly to those shown in Fig. 3.

Finally, one more group of films was observed. EC did not arise in them either in the initial state or after annealing at T = 100–150°C. However, crystallization began in such films after 5–10 min of exposure to an electron beam (at an accelerating voltage of 125 kV and a beam current of 50–75 μA, with the condenser aperture removed). The rate of this crystallization is low; as a result, a structure consisting of particles 30–150 nm in size is formed. Figure 5 shows an electron microscopy image of the structure formed after a 15 min of exposure to an electron beam. The electron diffraction pattern (see inset to Fig. 5) obtained by microdiffraction from an area of ~0.5 μm contains many randomly arranged spot reflections in place of diffuse halos.

4. DISCUSSION

If we assume that a diffraction peak in an x-ray pattern (Fig. 1b) is broadened only due to the size effect, then the size of crystallites composing the film in the initial state can be calculated using the Scherrer formula [21]

$$\Delta 2\theta = \frac{\lambda}{L\cos\theta_0}, \quad (1)$$

where $\Delta 2\theta$ is the diffraction peak width (in radians), λ is the x-ray wavelength (Å), θ_0 is the diffraction angle (deg), and L is the crystallite size (Å). At $\Delta 2\theta = 3°$, $\lambda = 1.7482$ Å, and $\theta_0 = 25°$, the largest crystallite size is ≈37 Å. This confirms the assumption of the nanocrystalline film structure based on the analysis of the intensity of diffraction reflections in an electron diffraction pattern (Fig. 1a).

We note that nonexplosive crystallization (Fig. 5) is caused by 15-min electron-beam heating and forms a structure consisting of unordered microcrystallites. This is confirmed by the randomly arranged spot reflections in the electron diffraction pattern (see inset to Fig. 5). In the case of EC, the process lasted a time of the order of a second or shorter. However, dendrite (Fig. 2) or cellular (Fig. 3) structures consisting of coherently oriented microcrystallites formed in this case. This is demonstrated by the spot electron diffraction patterns with regularly arranged reflections (see insets to Figs. 2, 3). The crystallization rate and the character of the structure formed by slow crystallization (Fig. 5) can be explained in terms of diffusion [22]. However, this mechanism cannot explain the formation of dendritic (Fig. 2) or cellular (Fig. 3) instabilities, let alone the EC rate. The values of diffusivity known for nanocrystalline materials are very large (~10^{-6} cm^2/s) [1]. However, according to [23], this can permit a growth rate of no higher than 0.2 μm/s, which is lower than the values observed in this study by a few orders of magnitude.

The character of the dendritic (Fig. 2) and cellular–dendritic (Fig. 3) structures observed after EC of nanocrystalline iron–carbon films corresponds to crystal growth in a supercooled melt [10, 13, 24]. As men-

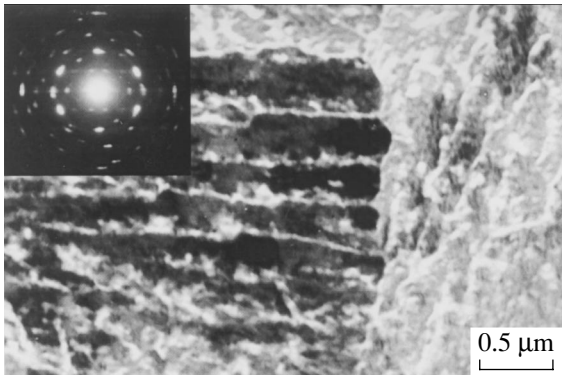

Fig. 3. Electron microscopy image of a cellular–dendritic structure formed under an electron beam in an iron–carbon film annealed in vacuum (T_{ann} = 100°C). The inset shows an electron microdiffraction pattern obtained from a single cell.

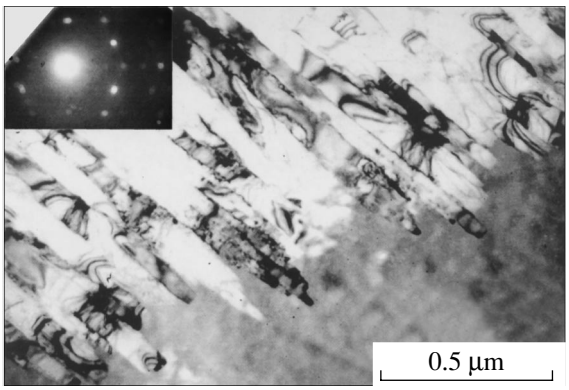

Fig. 4. Electron microscopy image of a structure formed in the initial iron–carbon film under mechanical impact. The inset shows an electron microdiffraction pattern obtained from a single cell.

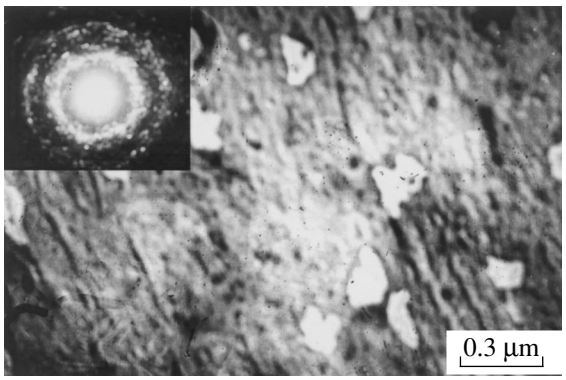

Fig. 5. Electron microscopy image of a structure formed in the initial iron–carbon film under an electron beam in 15 min. The inset shows an electron microdiffraction pattern obtained from an area of ≈0.5 μm.

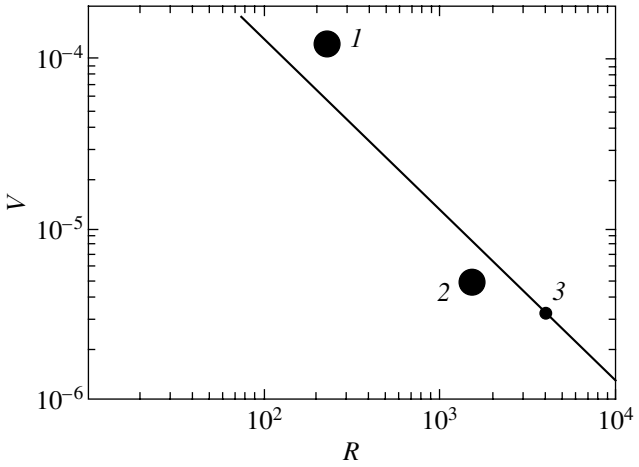

Fig. 6. Dimensionless growth rate V of a crystal in a supercooled melt vs. the rounding radius R of the crystalline needle tip [10]. The solid line corresponds to calculation [10] based on the Ivantsov equation. (*1*, *2*) The data for iron–carbon films with the structures shown in Figs. 2 and 3, respectively, studied in this work, and (*3*) the experimental result obtained in [10].

tioned above, EC can be accompanied by the formation of a liquid phase moving ahead of the crystallization front [2, 7]. The liquid phase can initiate various instabilities, including dendritic and cellular instabilities characteristic of crystallization from a melt.

As was shown by Ivantsov [25], the steady-state shape of a crystalline needle growing in a supercooled melt is a paraboloid of revolution. At a certain rounding radius $r = r_0$ of the needle tip, the growth rate of a needle will be highest. Experimentally, as the degree of supercooling ($T_{k,\infty} - T_0$) increases ($T_{k,\infty}$ is the temperature of the needle surface, T_0 is the melt temperature), the growth rate increases and the needle thickness decreases. A needle having the tip rounding radius r_0 and moving with the maximum possible velocity v_{max} at a given supercooling ($T_{k,\infty} - T_0$) will be most stable. Indeed, if a hill arises at the needle tip, it will gradually disappear, since its growth rate will be always lower than v_{max}; hence, the needle will retain its initial shape. Thus, it would be expected that the most probable needle shape will be that which provides its maximum growth rate. Figure 6 shows the dependence of the growth rate on the rounding radius of the tip of a crystalline needle growing in a supercooled melt calculated in [10] from the Ivantsov equation. Instead of the term "crystalline needle," we will use the terms "dendrite branch" and "cell." Based on the experimental data obtained in this study of the EC of nanocrystalline iron–carbon films, one can estimate the dimensionless rate V of dendrite or cellular growth and the dimensionless rounding radius R of the tip of a dendrite branch or cell: $V = v d_0/2D$ and $R = r/d_0$, where v is the growth rate of the dendrite branch or cell (cm/s), d_0 is the capillary length (~10^{-8} cm), D is the diffusivity (~10^{-5} cm^2/s), and r is the rounding radius of the tip of a dendrite branch or a cell (cm). The value of the capillary length d_0 is taken from [10], and the diffusivity D typical of molten metals is taken [26]. The dependences shown in Fig. 6 were constructed for the dimensionless supercooling $\Delta = (T_m - T)C_p/Q = 0.05$, where T_m is the melting point, T is the temperature of the supercooled melt, C_p is the specific heat, and Q is the latent heat.

By calculating the values of the dimensionless parameters V and R that correspond to our experimental data and plotting them in Fig. 6, we can approximately estimate to what extent the equations describing crystallization in the supercooled melt fit the EC processes in the films under study. The dendrite structure shown in Fig. 2 is characterized by the parameters $v \approx 0.25$ cm/s and $r = 15$–25 nm. For the cellular structure shown in Fig. 3, $v \approx 0.01$ cm/s and $r = 100$–160 nm. For the dendrite structure shown in Fig. 2, in the case of the maximum rounding radius $r = 2.5 \times 10^{-6}$ cm ($R = 250$) of the dendrite branch tip, $V = 1.25 \times 10^{-4}$ (circle *1* in Fig. 6). For the cellular structure shown in Fig. 3, at the maximum rounding radius $r = 1.6 \times 10^{-5}$ cm ($R = 1600$) of the cell tip, $V = 5 \times 10^{-6}$ (circle *2* in Fig. 6). We can see that the experimental values (Fig. 6) determined in this study are close to the curve calculated from the Ivantsov equation. Apparently, the dependence between the growth rate and the rounding radius of the tip of a dendrite branch (or a cell) for EC in the films under study can be approximately described by the formula obtained for the case of crystalline needle growth in a supercooled melt.

To find the dependences corresponding to this experiment, we need to know exact values of the quantities entering the equations (the capillary length, diffusivity, degree of supercooling, specific heat, latent heat, etc.). Accurate determination of these values is a separate intractable problem, since these characteristics nonlinearly depend on many parameters, such as the temperature gradients over the film surface, film thickness, and structural and concentration nonuniformities.

According to the estimations carried out, the local temperature of the films caused by an electron beam when initiating EC in nanocrystalline iron–carbon films was not higher than 200–250°C. The structures formed during EC are similar to those observed after annealing films in vacuum at T_{ann} = 300°C [14–16] or after mechanical impacts. Hence, the initiation of EC in the films under study requires a much lower energy than is required to melt the film [15]. The fact that the experimental results agree qualitatively with the dependences characteristic of crystal growth in the supercooled melt suggests that there is a liquid zone at the crystallization front. This zone provides conditions for the occurrence of dendritic and cellular instabilities. It is clear that the zone arose due to the release of energy stored in the film in the initial state. This energy should be at least sufficient for melting (surface melting [27, 28] or quasi-melting [29]) of nanocrystalline particles composing the film.

The mechanism for EC in the films under study is presumably as follows. An electron beam generates crystallization centers. A liquid zone arises at the front of crystallization; then, crystallization propagates over the film in the self-maintaining (autowave) mode. This mode is characterized by a release of the energy accumulated in the film during crystallization at the interface of two (solid and liquid) phases. During EC, nanoparticles that are molten on their edges aggregate with each other and form dendrite or cellular structures. Such structures exhibit scale invariance and, while having no translation symmetry, allow the formation of spot electron diffraction patterns. The crystallization model proposed can explain the fact that the dendrite (or cellular) structures, which caused spot electron diffraction patterns similar to those characteristic of single crystals, are formed from a structurally unordered nanocrystalline state in such a short time. The spot reflections in the electron diffraction pattern (Fig. 2) are distinct enough, which suggests that the crystal structure grown is perfect.

It is known that the EC front velocity reaches 1–50 m/s in some samples. However, impurity atoms in a material can decrease the crystallization rate by orders of magnitude [2]. The highest EC rates are observed in pure materials or in materials with low impurity contents (1–2 at. %). The crystallization rate of the films studied does not exceed 1 cm/s. These films contain ~20 at. % carbon, which explains the relatively low EC rates. It is most probable that a fraction of the carbon atoms in the initial state are at the surface of iron nanoparticles [15, 16]; carbon also enters into the composition of interstitial solid solutions, which do not form in the iron–carbon system in the equilibrium state [14–16].

As shown in [30, 31], the films are characterized by strong oriented and unoriented stresses, which can exceed the ultimate strength of a material in a bulk state. The strength of metal films is generally associated with their highly imperfect structure and can exceed the strength of the corresponding bulk materials by several times. As is known [32], structurally nonequilibrium regions in amorphous and nanocrystalline samples differ in energy from the thermodynamic equilibrium state by a "stress energy" with characteristic values of 5–20 kJ/mol. This energy is sufficient for a liquid zone to arise during the structural rearrangement caused by EC. It can be assumed that an energy of the same order of magnitude is accumulated in the nanocrystalline iron–carbon films under study. An argument in favor of this assumption can be a large number of bending extinction contours in an electron microscopy image (Fig. 4). The bending contours indicate bending of atomic planes caused by internal stresses. The lattice curvature radius calculated by analyzing the bending contours [33] is ≈1 μm. A comparison of the electron diffraction patterns shown in Figs. 3 and 4 shows that the atomic order formed during crystallization due to a mechanical impact (Fig. 4) is analogous to that formed by crystallization under an electron beam (Fig. 3).

The degree of nonequilibrium of nanocrystalline films (i.e., the energy accumulated in them) is controlled by technological conditions during their growth. Under nonequilibrium and nonuniform conditions, crystallization can bring about the formation of different (dendritic and cellular) structures in various films and even in a single film. These structures grow with different rates in various films. The crystallization rate is controlled by the degree of melt supercooling at the EC front and, hence, by the energy accumulated in the film. Determination of the degree of supercooling and the accurate latent heat is a separate complex problem. However, it is clear that, in films that accumulate large energy due to the technological conditions of their growth, the EC proceeds at a higher rate, requires a lower initiating energy, and results in the formation of dendrite structures (Fig. 2). In films that accumulate small energy, the crystallization initiation requires a larger energy and the process occurs at a lower rate with the formation of cellular structures (Fig. 3). In films that accumulate still smaller energy, crystallization is observed only after prolonged heating by an electron beam, is nonexplosive, and is not accompanied by the formation of cellular–dendrite structures. Finally, in equilibrium samples, crystal growth is impossible under an electron beam of such power.

The formation of dendrite and cellular instabilities during EC is a telling illustration for self-organization processes in nonequilibrium systems [34]. These instabilities occur especially often far from the equilibrium state under conditions of increasing instability of such systems. One should distinguish between the organization and self-organization phenomena; the latter is a spontaneous structurization process that occurs in an open nonequilibrium system and proceeds due to internal energy sources of the system itself, whereas the organization processes occur due to external energy sources. In the case under consideration, nonexplosive crystallization is caused by an electron beam (i.e., an external energy source) and corresponds to organization. EC is an example of self-organization, since the EC process (although initiated by an electron beam) occurs due to the energy accumulated in the film.

5. CONCLUSIONS

Thus, this study has shown that both ordinary and explosive crystallizations can take place in nanocrystalline iron–carbon films under an electron beam. The EC process occurs at a rate of up to 1 cm/s with the formation of dendritic or cellular–dendritic instabilities. Electron diffraction patterns obtained from films after EC are spot-type and do not correspond to any of the known structures of either pure iron or iron–carbon compounds. The crystallization model proposed explains the fact that the structures with spot-type electron diffraction patterns (similar to those characteristic of single crystals) are formed from a structurally unordered nanocrystalline state in such a short time.

The relation between the growth rate of dendrite branches (or cells) during EC and the rounding radius of the tip of a dendrite branch or a cell was approximately described by equations derived for the crystal growth in a supercooled melt. The following feature characteristic of crystallization in a supercooled melt was established: the higher the growth rate, the lower the rounding radius of the dendrite branch (or cell) tip. This allows us to conclude that EC in the films under study proceeds with the formation of a liquid phase at the crystallization front. The liquid zone arises due to the energy accumulated in the film in the nanocrystalline state rather than as a result of external exposure. It was assumed that crystallization under an electron beam is controlled by the energy accumulated in the film in the initial state.

ACKNOWLEDGMENTS

The authors are grateful to V.S. Zhigalov for putting the samples at their disposal and for his assistance in the experiment, S.V. Mytnichenko and A.V. Bessergenev for their assistance in the x-ray diffraction studies, V.G. Kesler for the study of the film chemical composition, and V.G. Myagkov for helpful discussions.

This study was supported by the Russian Foundation for Basic Research (project nos. 00-02-17358a, 03-02-16052a), the sixth competition of the Examination of Scientific Projects of Young Scientists of the Russian Academy of Sciences (1999, project no. 56), and INTAS (grant no. 00-100).

REFERENCES

1. H. Gleiter, Prog. Mater. Sci. **33**, 223 (1989).
2. V. A. Shklovskiĭ and V. M. Kuz'menko, Usp. Fiz. Nauk **157** (2), 311 (1989) [Sov. Phys. Usp. **32**, 163 (1989)].
3. R. Messier, T. Takamori, and R. Roy, Solid State Commun. **16** (3), 311 (1975).
4. R. Koba and C. E. Wickersham, Appl. Phys. Lett. **40** (8), 672 (1982).
5. A. Mineo, A. Matsuda, T. Kurosu, and M. Kikuchi, Solid State Commun. **13** (9), 1307 (1973).
6. C. E. Wickersham, G. Bajor, and J. E. Greene, Solid State Commun. **27** (1), 17 (1978).
7. O. Bostanjoglo and R. Liedtke, Phys. Status Solidi A **60** (2), 451 (1980).
8. V. G. Myagkov, L. I. Kveglis, and G. I. Frolov, Poverkhnost, No. 9, 131 (1992).
9. V. G. Myagkov, L. I. Kveglis, V. S. Zhigalov, and G. I. Frolov, Poverkhnost, No. 1, 105 (1994).
10. J. S. Langer, Rev. Mod. Phys. **52** (1), 28 (1980).
11. T. A. Witten and L. M. Sander, Phys. Rev. Lett. **47** (19), 1400 (1981).
12. B. M. Smirnov, Usp. Fiz. Nauk **149** (2), 177 (1986) [Sov. Phys. Usp. **29**, 481 (1986)].
13. J. S. Langer, Science **243**, 1150 (1989).
14. S. M. Zharkov, V. S. Zhigalov, L. I. Kveglis, Yu. V. Lisitsa, K. V. Renskaya, and G. I. Frolov, Pis'ma Zh. Éksp. Teor. Fiz. **65** (12), 872 (1997) [JETP Lett. **65**, 915 (1997)].
15. S. M. Zharkov, Candidate's Dissertation (Inst. of Physics, Siberian Division, Russian Academy of Sciences, Krasnoyarsk, 1999).
16. G. I. Frolov, V. S. Zhigalov, L. I. Kveglis, S. M. Zharkov, O. A. Bayukov, and A. L. Bas'ko, Fiz. Met. Metalloved. **88** (2), 85 (1999).
17. V. G. Myagkov, V. S. Zhigalov, and S. M. Zharkov, Dokl. Akad. Nauk **346** (2), 612 (1996) [Phys. Dokl. **41**, 55 (1996)].
18. S. M. Zharkov and L. I. Kveglis, Dokl. Akad. Nauk **383** (5), 617 (2002) [Dokl. Phys. **47**, 281 (2002)].
19. V. S. Zhigalov, G. I. Frolov, and L. I. Kveglis, Fiz. Tverd. Tela (St. Petersburg) **40** (11), 2074 (1998) [Phys. Solid State **40**, 1878 (1998)].
20. W. J. Boettinger, S. R. Coriell, A. L. Greer, A. Karma, W. Kurz, M. Rappaz, and R. Trivedi, Acta Mater. **48** (1), 43 (2000).
21. A. Guinier, *Theórie et Technique de la Radiocristallographie* (Dunod, Paris, 1956; Fizmatgiz, Moscow, 1961).
22. L. N. Paritskaya, Poroshk. Metall. (Kiev), No. 11, 44 (1990).
23. Yu. I. Vesnin, *Secondary Structure and Properties of Crystals* (Inst. Neorg. Khim. Sib. Otd. Ross. Akad. Nauk, Novosibirsk, 1997).
24. W. Kurz and D. J. Fisher, *Fundamentals of Solidification* (Trans. Tech., Switzerland, 1986).
25. G. P. Ivantsov, Dokl. Akad. Nauk SSSR **58** (4), 567 (1947).
26. *Physical Quantities. Handbook*, Ed. by I. S. Grigor'ev and E. Z. Meĭlikhov (Énergoatomizdat, Moscow, 1991).
27. A. Trayanov and E. Tosatti, Phys. Rev. Lett. **59** (19), 2207 (1987).
28. J. W. M. Frenken, P. M. J. Marée, and J. F. van der Veen, Phys. Rev. B **34** (11), 7506 (1986).
29. P. M. Ajayan and L. D. Marks, Phys. Rev. Lett. **63** (3), 279 (1989).
30. M. Ya. Fuks, Izv. Akad. Nauk SSSR, Ser. Fiz. **31** (3), 422 (1967).
31. V. A. Buravikhin, *Influence of Mechanical Stresses on the Magnetic Properties of Films* (Vost.-Sib. Kn., Irkutsk, 1968).
32. S. F. Timashev and L. I. Trakhtenberg, Zh. Fiz. Khim. **67** (3), 448 (1993).
33. V. Yu. Kolosov and A. R. Thölen, Acta Mater. **48** (8), 1829 (2000).
34. G. Nicolis and I. Prigogine, *Self-Organization in Non-Equilibrium Systems* (Wiley, New York, 1977; Mir, Moscow, 1979).

Translated by A. Kazantsev

Physics of the Solid State, Vol. 46, No. 5, 2004, pp. 975–982. Translated from Fizika Tverdogo Tela, Vol. 46, No. 5, 2004, pp. 945–952.

LOW-DIMENSIONAL SYSTEMS AND SURFACE PHYSICS

Electron-Stimulated Desorption of Rare-Earth Metal Atoms

V. N. Ageev, Yu. A. Kuznetsov, and N. D. Potekhina

Ioffe Physicotechnical Institute, Russian Academy of Sciences, Politekhnicheskaya ul. 26, St. Petersburg, 194021 Russia
e-mail: kuznets@ms.ioffe.rssi.ru

Received September 18, 2003

Abstract—The yield of europium and samarium atoms in electron-stimulated desorption from layers of rare-earth metals (REMs) adsorbed on the surface of oxidized tungsten has been measured as a function of the incident electron energy, surface coverage by REMs, degree of tungsten oxidation, and substrate temperature. The measurements were performed using the time-of-flight method with a surface-ionization-based detector within the substrate temperature interval 140–600 K. The yield studied as a function of electron energy has a resonance character. Overlapping resonance peaks of Sm atoms are observed at electron energies of 34 and 46 eV, and those of Eu atoms, at 36 and 41 eV. These energies correlate well with the REM 5*p* and 5*s* core-level excitation energies. The REM yield is a complex function of the REM coverage and substrate temperature. The peaks due to REM atoms are seen at low REM coverages only, and their intensity usually passes through a maximum with increasing coverage and substrate temperature. The concentration dependence of the REM atom yield is affected by the deposition of slow Ba^+ ions, but only if they are deposited after the REM adsorption. At higher REM coverages, additional peaks are observed at electron energies of 42, 54, and 84 eV, which originate from excitation of the 5*p* and 5*s* tungsten levels and result from desorption of SmO and EuO molecules. The temperature dependence of the intensity of these peaks is explained to be due to the order–disorder phase transition. The desorption of REM atoms is the result of their reversed motion through the adsorbed REM layer, and the SmO and EuO molecules desorb due to the formation of an antibonding state between the REM oxide molecules and the tungsten ions. © *2004 MAIK "Nauka/Interperiodica".*

1. INTRODUCTION

Bombardment of the surface of a solid by electrons may initiate desorption of charged and neutral particles. Desorption can result from the heating of the solid by electrons; this phenomenon is called thermal desorption for neutrals or surface ionization (SI) for charged particles. Particles can be removed from the surface through the transfer of kinetic energy from electrons to particles of the solid in an elastic collision. The efficiency of this process depends on the particle to electron mass ratio and decreases with increasing binding energy of the particle to the solid. In order to remove even such a light particle as a hydrogen atom chemisorbed on a metal surface, the electrons must have an energy on the order of 10 keV. Finally, particles can desorb from the surface of a solid through direct transfer of the potential energy of electronic excitation of adsorption bonds to the kinetic energy of desorbing particles. This phenomenon is called electron-stimulated desorption (ESD) [1–3].

While ESD is widely used in the analysis and modification of adsorbed layers and film coatings, its mechanism has still not been fully elucidated. This specifically applies to the ESD of neutrals because of the difficulties encountered in measuring their fluxes. We were the first to measure the yield and energy distributions of alkali atoms in their ESD from layers of alkali metals adsorbed on the surface of oxidized tungsten [4] and molybdenum [5], as well as of barium atoms in ESD from barium layers adsorbed on the surface of oxidized tungsten [6]. Those measurements showed that the mechanism of neutral ESD depends on the electronic structure of the adsorbate and of the substrate. It was found, in particular, that the main mechanism responsible for the ESD of alkali atoms from oxidized substrates includes hole formation in the 2*s* oxygen level, whose Auger decay involving the 2*p* electrons brings about neutralization of the adsorbed alkali metal ions. The desorption of atoms is governed by the competition between charge relaxation on the oxygen ion and reionization of the alkali atoms. If the oxygen ion recovers its negative charge at the expense of the substrate electrons faster than the reionization of the alkali metal atom occurs, the atom desorbs as a result of overlap between the electron shells of the atom and the negative oxygen ion [7].

This communication reports on the ESD of rare-earth metal (REM) atoms from REM layers adsorbed on the surface of oxidized tungsten. The choice of this subject was motivated by the following considerations. First, REMs are widely used in electronics and electrical engineering to fabricate luminophors, scintillators, permanent magnets, and HTSC ceramics [8, 9]. Second, these studies offer the possibility of checking our model, according to which the ESD of REM atoms should not be caused by hole creation in the 2*s* oxygen level, because the radius of REM atoms exceeds that of positive ions only slightly [6, 7]. In addition, REM

1063-7834/04/4605-0975$26.00 © 2004 MAIK "Nauka/Interperiodica"

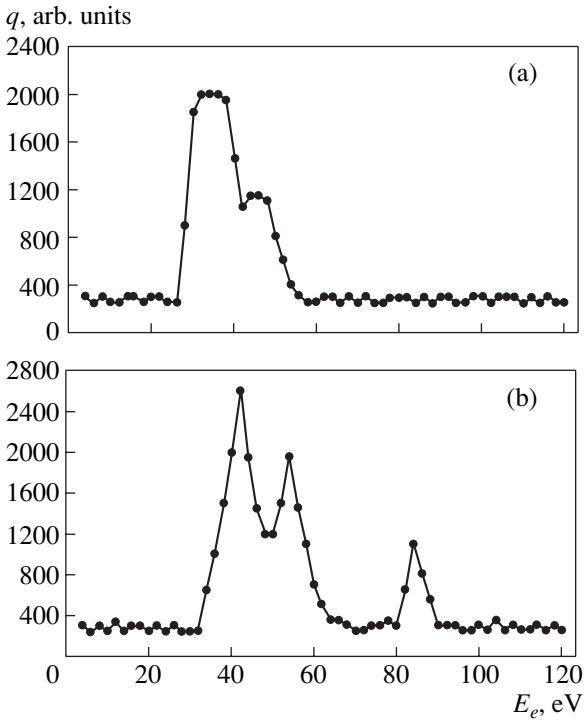

Fig. 1. ESD yield of neutrals from a Sm layer adsorbed on the oxygen-monolayer-coated tungsten surface at $T = 300$ K plotted vs. incident electron energy for samarium coverage Θ (a) 0.10 and (b) 0.70.

atoms have comparatively low ionization potentials, an essential feature making it possible to detect their fluxes using the SI technique [10].

2. EXPERIMENTAL TECHNIQUE

The experimental setup and the measurement technique employed were described in considerable detail in [11]. The measurements were conducted using the time-of-flight method with an SI detector, which permitted an increase in the efficiency of REM atom detection by more than an order of magnitude compared to the conventional method involving electron impact ionization of neutrals in a gas phase. A tungsten ribbon heated to $T = 2000$ K served as an emitter in the surface ionization detector. The substrates were textured tungsten ribbons with predominantly (100)-oriented faces. Following REM adsorption on the surface of clean tungsten, no ESD of REM atoms was detected, which means that the cross section of this process was less than 10^{-23} cm^2 (as estimated from the sensitivity of the instrument for detecting REM atoms). To establish the effect of tungsten oxidation on the ESD yield of REM atoms, the substrate was oxidized in two regimes; namely, in the first regime, an oxygen monolayer was grown on the tungsten surface (by heating the ribbon at an oxygen pressure of ~10^{-6} Torr at $T = 1600$ K for 300 s), and in the second, an oxide film about 5 monolayers thick was produced on the surface (oxygen pressure $\times 10^{-6}$ Torr, substrate temperature $T = 1100$ K, heating time 600 s) [12]. The amount of deposited REM was deduced from the time of deposition at a constant flux and was checked by Auger electron and thermal desorption spectroscopy [13]. The ribbon could be cooled in the interval from 160 to 300 K by varying the rate of gaseous nitrogen flow through the hollow current leads, with the gas cooled preliminarily in a copper tube immersed in liquid nitrogen. Heating the ribbon above $T = 300$ K was achieved by means of electric current. The residual gas pressure in the setup was below 5×10^{-10} Torr.

3. RESULTS

Our measurements of the neutral ESD yield during REM adsorption led to an unexpected result. The yield of neutrals as a function of electron energy was found to have a resonance character. Figure 1 plots the yield of neutral particles q from a layer of samarium adsorbed on the surface of an oxygen-monolayer-covered tungsten measured at $T = 300$ K as a function of electron energy E_e for two Sm coverages, $\Theta = 0.10$ and 0.70. The neutral appearance threshold is close to 26 eV. Above the threshold, the yield grows sharply with increasing electron energy to reach a maximum at the electron energy $E_e = 34$ eV. Another feature is seen on the high-energy side of this peak at $E_e = 46$ eV. Thus, the neutral yield plotted as a function of E_e consists of two overlapping peaks, at $E_e = 34$ and 46 eV. If the Sm coverage increases, the yield grows linearly with Θ for both peaks observed at low coverages, after which it passes through a maximum without a change in the peak shape at the same coverage Θ. The intensity of the peak at $E_e = 46$ eV is lower than that at $E_e = 34$ eV throughout the coverage range studied, and the 46-eV peak disappears at Sm coverages larger than $\Theta = 0.15$, whereas the peak at $E_e = 34$ eV persists up to the coverage $\Theta = 0.20$ (Fig. 2).

When, however, Sm is adsorbed on a tungsten oxide film, the dependence of the neutral ESD on coverage follows a different course. The yield q decreases with increasing Θ starting from very low coverages, at which the neutral current is already measurable (see [14, Fig. 3]).

The yield q of neutrals from a europium layer on oxidized tungsten plotted as a function of energy also has a resonance character. At low Θ, peaks are seen at $E_e = 36$ and 41 eV. Here, the yield appears abruptly at very low Eu coverages and decreases almost linearly with increasing Θ (Fig. 3) [15], but, in contrast to Sm, the Eu yield plotted vs. Θ falls off for any degree of tungsten oxidization and the concentration threshold is measurable, $\Theta^* = 0.03$ (curve *1* in Fig. 3).

Deposition of a small amount ($\Theta \sim 0.03$) of slow Ba^+ ions exerts a remarkable effect on the neutral yield, which depends on the order in which the Ba^+ ions and

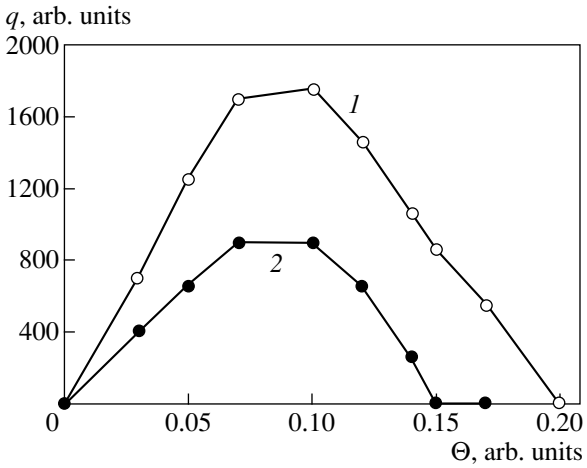

Fig. 2. ESD yield of neutrals from a Sm layer adsorbed on the oxygen-monolayer-coated tungsten surface at $T = 300$ K plotted vs. samarium coverage Θ for electron energy E_e equal to (*1*) 34 and (*2*) 46 eV.

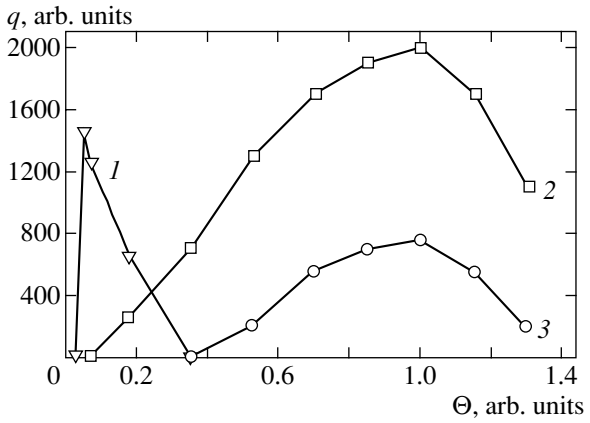

Fig. 3. ESD yield of neutrals from a Eu layer adsorbed on the oxygen-monolayer-coated tungsten surface at $T = 300$ K plotted vs. europium coverage Θ for electron energy E_e equal to (*1*) 36, (*2*) 54, and (*3*) 84 eV.

REM atoms were deposited. Deposition of Ba^+ ions on an oxidized tungsten substrate with adsorbed Eu shifts the maximum yield of neutrals toward lower Eu coverages, while deposition of Ba^+ ions made before deposition of Eu atoms has practically no effect on the yield of neutrals. A still stronger influence is produced by bombardment of Ba^+ ions after deposition of Sm on the yield of neutrals from the surface of tungsten coated by an oxygen monolayer after the Sm deposition. The smooth rise of the yield with increasing Sm coverage is replaced by a sharp growth in the yield after Ba^+ ion deposition at very low Sm coverages, as was observed when Sm was deposited on a W oxide film and in the case of Eu deposition. This effect is not observed if Ba^+ ions are deposited before Sm.

Additional peaks were observed at $E_e = 42$, 54, and 84 eV in ESD from oxidized tungsten for both REMs, but in the case of Sm they appear at the same coverage $\Theta = 0.20$ and their intensity grows linearly with Θ and then passes through a maximum at $\Theta = 1.0$ (Fig. 4), while in the case of Eu these peaks appear at different coverages but also pass through a maximum at $\Theta = 1.0$ (Fig. 3). The peaks of neutrals at $E_e = 34$ and 46 eV observed after Sm adsorption can be assigned to excitation of the Sm 5*p* and 5*s* levels, and those occurring at $E_e = 36$ and 41 eV after Eu adsorption, to the Eu 5*p* and 5*s* level excitation, whereas the peaks at $E_e = 42$, 54, and 84 eV observed with both REMs correlate with excitation of the W $5p_{1/2}$, $5p_{3/2}$, and 5*s* levels [16]. Note that the intensity of the peaks associated with excitation of the Sm and Eu core levels decreases with increasing degree of tungsten oxidation and that the intensity of the peaks related to the tungsten core-level excitation is practically independent of the degree of substrate oxidation.

The yield of neutrals is a very complex function of the surface coverage by REM and of the substrate temperature. Figure 5 presents graphs of the yield of neutrals during ESD from a Sm layer adsorbed on the surface of oxygen-monolayer-coated tungsten vs. temperature measured at Sm coverages below 0.10 and electron energy $E_e = 34$ eV. The yield falls off slowly with increasing T in the interval $T = 160$–280 K, to drop sharply to zero at $T \cong 350$ K. Note that for $\Theta < 0.10$ the yield increases smoothly with coverage (Fig. 2). For $\Theta > 0.10$, the temperature dependence of the yield of neutrals changes shape. Figure 6 displays the corresponding graphs obtained for $\Theta > 0.10$ and electron energy $E_e = 34$ eV. We readily see that, as T increases, the yield of neutrals passes through a maximum, which shifts with increasing coverage toward higher temperatures, while its intensity and width in temperature decrease. The temperature at which neutrals appear increases, and the temperature at which the

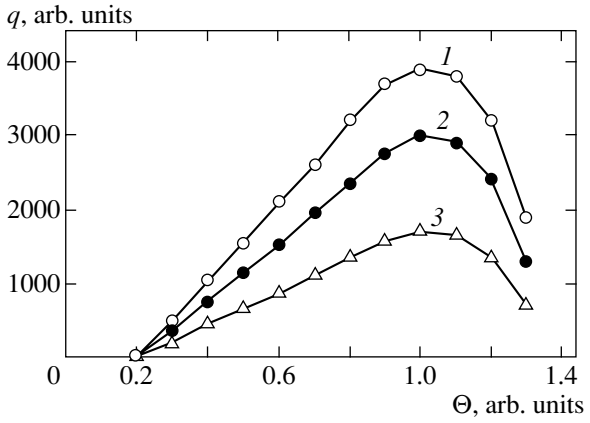

Fig. 4. ESD yield of neutrals from a Sm layer adsorbed on the oxygen-monolayer-coated tungsten surface at $T = 300$ K plotted vs. samarium coverage Θ for electron energy E_e equal to (*1*) 42, (*2*) 54, and (*3*) 84 eV.

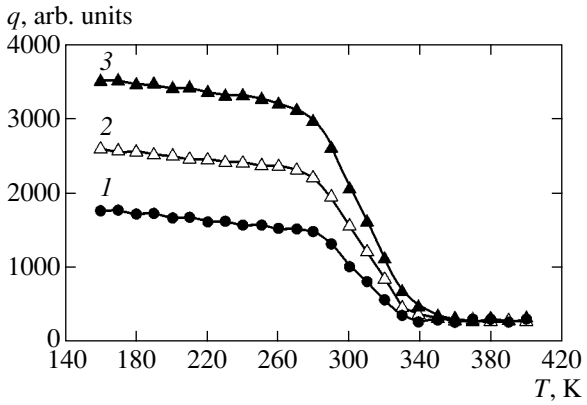

Fig. 5. ESD yield of neutrals from a Sm layer adsorbed on the oxygen-monolayer-coated tungsten surface plotted vs. substrate temperature for electron energy E_e = 34 eV and samarium coverages Θ (*1*) 0.03, (*2*) 0.05, and (*3*) 0.07.

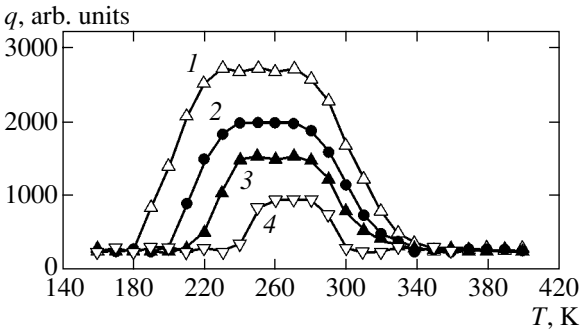

Fig. 6. ESD yield of neutrals from a Sm layer adsorbed on the oxygen-monolayer-coated tungsten surface plotted vs. substrate temperature for electron energy E_e = 34 eV and samarium coverages Θ (*1*) 0.12, (*2*) 0.15, (*3*) 0.17, and (*4*) 0.20.

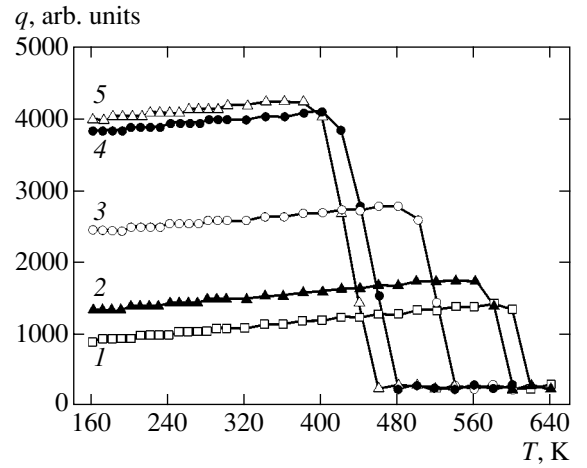

Fig. 7. ESD yield of neutrals from a Sm layer adsorbed on the oxygen-monolayer-coated tungsten surface plotted vs. substrate temperature for electron energy E_e = 42 eV and samarium coverages Θ (*1*) 0.40, (*2*) 0.50, (*3*) 0.70, (*4*) 0.90, and (*5*) 1.00.

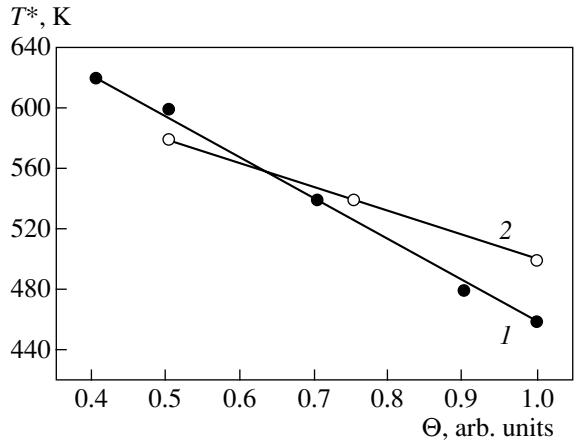

Fig. 8. Disappearance temperature of neutrals in ESD from a Sm adlayer deposited on a tungsten surface coated preliminarily by (*1*) an oxygen monolayer or (*2*) tungsten oxide plotted vs. samarium coverage Θ for incident electron energy E_e = 42 eV.

yield drops to zero decreases with increasing Θ. The temperature dependences of the yield of neutrals obtained at E_e = 46 eV behave similarly. Note that for Θ > 0.10 the q(Θ) dependence follows a falling course (Fig. 2).

The temperature dependence of the neutral ESD yield from tungsten oxide in the peak at E_e = 34 eV behaves similarly to that displayed in Fig. 6 for any Sm coverage, and q(Θ) is a falling-off relation starting from very low Θ.

The yield of neutral particles after Eu adsorption likewise passes through a maximum with increasing T at E_e = 36 and 41 eV, irrespective of the degree of tungsten oxidation; note that the temperature at which the yield becomes nonzero increases with Θ, while the disappearance temperature after Eu adsorption, unlike that for the Sm adsorption, does not depend on coverage.

The temperature dependences of the peak intensities for both REMs and electron energies E_e = 42, 54, and 84 eV behave in a fairly similar way for any degree of oxidation. Figure 7 plots the signal for E_e = 42 eV in the case of ESD from a Sm adlayer on an oxygen-monolayer-covered tungsten surface vs. the substrate temperature. At low T, the signal grows slowly with increasing T to drop subsequently to zero, with the disappearance temperature T* decreasing linearly with increasing Sm coverage; the slope of this relation increases with the degree of tungsten oxidation (Fig. 8). The rate of signal decay with increasing T does not depend on the concentration of deposited Sm, although the intensity of the signal grows approximately linearly with Θ. However,

in the case of Eu deposited under the same conditions, the $T^*(\Theta)$ relation is not a linear function even though it falls off with increasing Θ [17].

Throughout the temperature range covered, the ESD yield from adsorbed REM layers is reversible under variation of the substrate temperature; i.e., REM thermal desorption in this temperature range can be neglected.

4. DISCUSSION OF THE RESULTS

It was shown in [18] that if a tungsten ribbon is used as an SI-based detector of ESD-produced fluxes of neutrals, one cannot separate neutral atoms of REMs from the molecules of their oxides, because the rate of SmO and EuO dissociation on the W surface is higher than that of the thermal desorption of Sm and Eu atoms. This lead to the suggestion that the species departing from the surface after electron beam excitation of the REM core levels are neutral Sm and Eu atoms, whereas after the W excitation they are neutral SmO and EuO molecules, which are detected as REM ions. With this mechanism of ESD of neutrals, there is no need to explain how excitation transfers from tungsten to the REM ion via the oxygen ion. This hypothesis was verified by using a tungsten ribbon coated with an oxygen monolayer as an SI detector [19]. The rate of SmO and EuO dissociation on this surface is substantially lower than that on tungsten, so the particle fluxes generated by SI contain ions both of atoms of REMs and of molecules of their oxides. We have indeed succeeded in revealing a difference between the temperature dependences of the SI currents due to neutral particles desorbed from a Sm layer on oxidized tungsten following core level excitation of Sm and W [19].

The specific feature of the ESD of neutrals, which is observed under deposition of REM atoms on the surface of oxidized tungsten and above all needs to be discussed, is the resonance character of the yield of neutrals as a function of the energy of the incident electron. The yield of alkali metal atoms from oxidized tungsten exhibited a distinct threshold corresponding to the core-level excitation energy of substrate atoms or adatoms (oxygen 2*s*, lithium 1*s*, cesium 5*s*), after which the yield grew sharply with increasing E_e and then passed through a maximum, whose width depended on the localization of the primary excitation and constituted ~300 eV under excitation of the oxygen 2*s* level or ~100 eV in the case of excitation of the adatom core level [4–7]. Here, the dependence of the alkali-metal ESD yield was determined to a considerable extent by the dependence of the ionization cross section of the corresponding core level in the gas-phase atom on E_e and by the secondary-electron contribution.

In contrast to the case of alkali metals, the dependence of the ESD yield of REM atoms on E_e has resonance peaks. The resonance peaks in the REM atom ESD originate from the 5*p* and 5*s* REM atom core-level excitation, and those of the REM oxide molecule yield, from excitation of the $5p_{1/2}$, $5p_{3/2}$, and 5*s* tungsten atom core levels. The small width of these peaks is due apparently to the small region of the free-electron band to which core electrons transfer in the course of excitation. This strongly localized region of the conduction band can derive from empty 5*d* states of the REM or tungsten atoms, which descend in the field produced by the 5*p* and 5*s* holes of the corresponding atoms to form the $5p$–$5d_{ex}$ core exciton. The possibility of formation of a quasi-bound state of Eu and Sm adatoms chemisorbed on oxidized tungsten is supported by calculations and the spectrum of x-ray absorption in lanthanum oxide, which revealed the existence of a strong resonance peak near the $2p$–$5d_{ex}$ transition [20]. At higher excitation energies, where the 2*p* electron transfers to the free state (i.e., becomes ionized), the absorption probability is about 50 times lower than that in the exciton formation region. Resonance photoemission from REMs is also assigned to excitation to a discrete intermediate state, which decays through autoionization [21, 22].

We believe that the ESD of SmO and EuO molecules occurs as a result of destruction of the adsorption bond between the oxygen and tungsten in the course of tungsten core-exciton formation. Resonance excitation of the W 5*p* and 5*s* core levels correlates with the observation of resonance transition-metal photoemission initiated by the decay of intermediate quasi-bound states [23]. The decrease in the yield peak intensity observed in going over from the peak associated with excitation of the W $5p_{3/2}$ to the peak related with excitation of the W 5*s* level correlates with the lower probability of excitation of deeper levels by electrons [24].

The difference between the temperature and concentration dependences of the ESD yield of Eu and Sm atoms, on the one hand, and the EuO and SmO molecules, on the other, suggests that the ESD mechanisms of these particles are likewise different.

We believe that the ESD of Eu and Sm atoms, which lower the substrate work function and, hence, reside on the surface in ionic form [13], is initiated by core exciton formation in the Eu^+ and Sm^+ ions; these excitons consist of a REM 5*p* or 5*s* hole and an electron in the $5d_{ex}$ state, which sinks in the core hole field and may reach the band gap of oxidized tungsten. After transition of this electron to the conduction band, the charge of the adsorbed ion increases by unity and is driven by the image forces toward the surface [25], where it undergoes complete neutralization with the filling of both the core hole and the valence level. The neutralization of the adatom may disturb the electronic state of the nearest neighbor oxygen ion by reducing its charge. If charge relaxation at the oxygen ion occurs faster than reionization of the neutral particle thus formed, the electron shells spread apart and the neutral particle escapes from the surface. During its motion through the REM adlayer, the neutral particle may become reion-

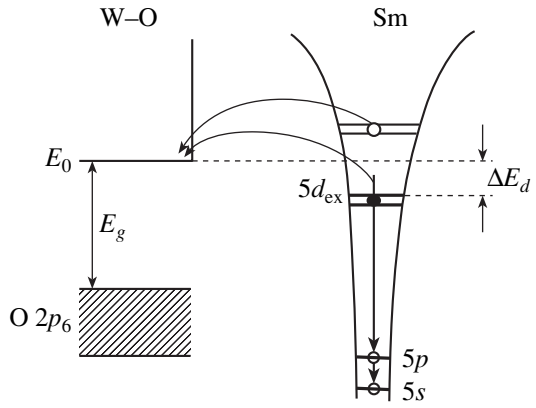

Fig. 9. Scheme of relaxation of the $5d_{ex}$ excited state of an adsorbed Sm ion with a hole in the $5p$ level. E_0 is the conduction band bottom of oxidized tungsten, E_g is the band gap of oxidized tungsten, and ΔE_d is the shift of the $5d_{ex}$ exciton level with respect to the conduction band bottom of oxidized tungsten.

ized, with the probability depending on the actual adlayer density. If the neutral particle survives, it departs from the surface; the yield of neutral atoms is lower, the larger is Θ (curve *1* in Fig. 3).

The rise of the REM reionization probability with increasing Θ correlates with the experiments performed in [26] and calculations made in [27] for Li^+ scattering from an Al(100) face coated partially by alkali metals. The probability of Li^+ neutralization has no threshold and grows approximately linearly with increasing alkali metal coverage and decreasing kinetic energy of the Li^+ ions. Because the kinetic energy of REM atoms in ESD is substantially lower than that found in studies [26, 27] and, by analogy with the alkali metals [4], should not exceed a few tenths of an electronvolt, this charge exchange effect should become observable already at low coverages, which, according to the results obtained for the $q(\Theta)$ relation in this mechanism (curve *1*, Fig. 3), is less than $\Theta = 0.05$. The reionized atoms remain on the surface, because their kinetic energy is too low to overcome the image force barrier.

The different temperature dependences of q (Figs. 5, 6) and different dependences of the yield of Sm and Eu atoms on Θ (Fig. 2; curve *1* in Fig. 3) obtained for this ESD mechanism are determined by the exciton level position relative to the substrate conduction-band bottom (Fig. 9). Ionization of the exciton with formation of the doubly charged ion is connected with the $5d_{ex}$ exciton transferring to the conduction band.

If the $5d_{ex}$ exciton level is above the conduction band bottom of oxidized tungsten, the electron can transfer spontaneously to the conduction band of the substrate, thus making the formation of doubly charged REM ions possible at any temperature. It is apparently this situation that occurs when Sm is deposited to $\Theta \leq 0.10$ on tungsten covered by an oxygen monolayer. In this case (Fig. 5), the yield of Sm atoms, rather than having a temperature threshold, falls off slowly with increasing T (which can be assigned to an increase in the number of filled states in the conduction band near the Fermi level) and the yield of Sm atoms grows linearly with increasing Θ at low ($\Theta \leq 0.10$) coverages (Fig. 2).

If the $5d_{ex}$ level lies in the band gap, this transition requires a certain activation energy; its probability increases with temperature, and, hence, atoms appear starting from a certain threshold temperature. As Θ increases, the $5d_{ex}$ level sinks because the electron interacts with positive charges of its neighbors, as well as because the adatom moves away from the surface through lateral interactions in the adsorbed layer. The barrier ΔE_d (Fig. 9) rises, and the probability of the $5d_{ex}$ electron transferring to the conduction band decreases, which results, apart from an increase in reionization (in the adlayer) of the neutrals desorbing from the surface, in the $q(\Theta)$ dependence of the yield of neutrals falling off with increasing Θ.

It is apparently this situation that is realized in the ESD of Eu atoms for any degree of W oxidation, starting with the lowest Θ (curve *1* in Fig. 3), and in the ESD of Sm atoms (when adsorbed on a W oxide film) at any Θ, starting with very low coverages, or with Sm adsorbed on oxygen-monolayer-covered W, starting with $\Theta > 0.10$ (Fig. 2).

Thus, there is a correlation between the pattern of the temperature dependence of the REM atom yield and its concentration dependence. If at low Θ the appearance of REM atoms has a temperature threshold, then the dependence of the yield on coverage $q(\Theta)$, after the appearance at low Θ, decreases almost linearly with increasing Θ (curve *1*, Fig. 3). The yield depends on temperature only weakly at low T, to drop sharply thereafter; the $q(\Theta)$ dependence first grows linearly with increasing Θ and, on passing a broad maximum, falls off linearly (Fig. 2). The appearance of a falling branch in $q(\Theta)$ coincides with the onset of an REM atom ESD appearance threshold in the temperature dependence $q(T)$ (Fig. 6). This correlation is indirect evidence of the validity of our model of ESD of REM neutrals from the surface of oxidized tungsten.

The dependence of the REM ESD atom yield on the order in which the Ba^+ ions and REM atoms are deposited finds can be explained by the deposition of slow Ba^+ ions on the oxygen-monolayer-covered W surface with chemisorbed REM ions changing the positions of the Sm^+ and Eu^+ ions as a result of their Coulombic interaction with the Ba^+ ions. It may be conjectured that the $5d_{ex}$ level for Sm on the oxygen monolayer, which at low Θ was above the substrate conduction band bottom, is forced by the Sm^+ ions that have changed position below the band bottom, with the result that the slow rise in the Sm atom yield for $\Theta < 0.10$ switches to a steep drop after the Ba^+ ion deposition, even for very low Θ. On the other hand, deposition of neutral Sm

atoms on the surface of oxidized tungsten with preliminarily chemisorbed Ba^+ ions does not affect the position of REM atoms with respect to the surface because of the absence of Coulomb interactions in the course of the deposition and, hence, does not influence the shape of the concentration and temperature dependences of the Sm and Eu atom yield in ESD.

The ESD of SmO and EuO molecules can be assigned to the formation of tungsten core excitons, which gives rise to an antibonding state coupling the tungsten ions and the REM oxide molecules. As T increases, so does the amplitude of the molecule oxide vibrations, which favors a slight increase in the molecule yield for $T < 450$ K (Fig. 7), because an increase in T brings about an increase in the rate of molecule removal (compared to the exciton lifetime).

An increase in the REM concentration on the surface entails a linear decrease in the disappearance temperature of the EuO and SmO molecules with increasing Θ (Fig. 8), with the slope of this straight line increasing with respect to the temperature axis as the degree of tungsten oxidation increases. Because this relation is reversible under variation of T, this effect could possibly be considered to be a result of a structural phase transition in the near-surface layer of the tungsten–oxygen–REM system.

The W(100) face undergoes reconstruction driven by temperature [28] or oxygen adsorption [29]. Adsorption of REMs at coverages above 0.20 is likely to bring about the formation of REM bonding to oxygen, while an increase in temperature modifies the surface layer structure.

The concentration thresholds for the ESD of SmO and EuO molecules [$\Theta^*(\mathrm{SmO}) = 0.20$, $\Theta^*(\mathrm{EuO}) = 0.07$] are possibly associated with the formation of ordered regions in the W–O–REM near-surface layer. It is from these regions that the SmO and EuO molecules leave following excitation of the W core levels. At low T and Θ, there are surface structures that are not matched with the substrate [29]. As T and Θ increase, ordered regions appear, which favor the escape of SmO and EuO molecules and are destroyed at high $T \geq T^*$. The temperature at which the order is destroyed decreases with increasing Θ (Fig. 8). An analogous effect of a nearly linear decrease in the order–disorder phase transition temperature was observed with LEEDS to occur with increasing cobalt coverage of the Si(111) face [30].

The intensity of interactions among atoms which bring about disordering depends on the degree of substrate oxidation, and it is this effect that manifests itself in the slope of the dependence of the SmO and EuO molecule ESD disappearance temperature T^* on Θ.

5. CONCLUSIONS

Thus, the dependence of the ESD yield from Eu and Sm layers adsorbed on the surface of oxidized tungsten on electron energy has a resonance pattern, with the yield peaks of the Eu and Sm atoms being related to excitation of the REM core levels and the yield peaks of the EuO and SmO molecules, to tungsten core-level excitation. The temperature and concentration dependences of the REM atom yield can be explained in terms of the position of the level of their excitons relative to the conduction band bottom of oxidized tungsten, and the temperature and concentration dependences of the REM oxide molecule yield should be assigned to the onset of the order–disorder phase transition in the adlayer of REM atoms.

ACKNOWLEDGMENTS

The authors are indebted to A.A. Kaplyanskiĭ and P.A. Rodnyĭ for helpful discussions.

This study was supported by the Russian state program “Surface Atomic Structures” (project no. 1152) and, in part, by the Russian Foundation for Basic Research (project no. 03-02-17523).

REFERENCES

1. V. N. Ageev, Prog. Surf. Sci. **47**, 55 (1994).
2. T. E. Madey, Surf. Sci. **299/300**, 824 (1994).
3. R. D. Ramsier and J. T. Yates, Surf. Sci. Rep. **12**, 246 (1991).
4. V. N. Ageev, Yu. A. Kuznetsov, and N. D. Potekhina, Fiz. Tverd. Tela (St. Petersburg) **38** (2), 609 (1996) [Phys. Solid State **38**, 335 (1996)].
5. V. N. Ageev and Yu. A. Kuznetsov, Phys. Low-Dimens. Semicond. Struct., No. 1/2, 113 (1999).
6. V. N. Ageev, Yu. A. Kuznetsov, and N. D. Potekhina, Surf. Sci. **367**, 113 (1996).
7. V. N. Ageev, Yu. A. Kuznetsov, and N. D. Potekhina, Fiz. Tverd. Tela (St. Petersburg) **39** (8), 1491 (1997) [Phys. Solid State **39**, 1324 (1997)].
8. G. V. Tsyganova, N. Yu. Pasechnik, and N. N. Smirnova, Vysokochist. Veshchestva, No. 2, 43 (1991).
9. P. A. Rodnyi, Radiat. Meas. **33**, 605 (2001).
10. É. Ya. Zandberg and N. I. Ionov, *Surface Ionization* (Nauka, Moscow, 1969).
11. V. N. Ageev, O. P. Burmistrova, and Yu. A. Kuznetsov, Fiz. Tverd. Tela (Leningrad) **29** (6), 1740 (1987) [Sov. Phys. Solid State **29**, 1000 (1987)].
12. V. N. Ageev and N. I. Ionov, Fiz. Tverd. Tela (Leningrad) **11**, 3200 (1969) [Sov. Phys. Solid State **11**, 2593 (1969)].
13. V. N. Ageev and A. Yu. Afanas’eva, Fiz. Tverd. Tela (St. Petersburg) **43** (4), 739 (2001) [Phys. Solid State **43**, 772 (2001)].
14. V. N. Ageev, Yu. A. Kuznetsov, and T. E. Madey, Surf. Sci. **528** (1–3), 47 (2003).
15. V. N. Ageev, Yu. A. Kuznetsov, and T. E. Madey, J. Vac. Sci. Technol. A **19** (4), 1481 (2001).
16. *Practical Surface Analysis by Auger and X-ray Photoelectron Spectroscopy*, Ed. by D. Briggs and M. Seah (Wiley, New York, 1983; Mir, Moscow, 1987).

17. V. N. Ageev, Yu. A. Kuznetsov, and T. E. Madey, J. Electron Spectrosc. Relat. Phenom. **128**, 223 (2003).

18. V. N. Ageev, Yu. A. Kuznetsov, and N. D. Potekhina, Fiz. Tverd. Tela (St. Petersburg) **43** (10), 1894 (2001) [Phys. Solid State **43**, 1972 (2001)].

19. V. N. Ageev and Yu. A. Kuznetsov, Pis'ma Zh. Tekh. Fiz. **29** (24), 1 (2003) [Tech. Phys. Lett. **29**, 1011 (2003)].

20. A. Mori, Y. Kayanuma, and A. Kotani, Prog. Theor. Phys. Suppl. **106**, 75 (1991).

21. S. L. Molodtsov, Yu. Kucherenko, J. J. Hinarejos, S. Danzenbächer, V. D. P. Servedio, M. Richter, and C. Laubschat, Phys. Rev. B **60** (24), 16435 (1999).

22. W. D. Schneider, C. Laubschat, G. Kalkowski, J. Haase, and A. Puschmann, Phys. Rev. B **28** (4), 2017 (1983).

23. L. H. Tjeng, C. T. Chen, J. Ghijsen, P. Rudolf, and F. Sette, Phys. Rev. Lett. **67** (4), 501 (1991).

24. D. Woodruff and T. Delchar, *Modern Techniques of Space Science* (Cambridge Univ. Press, Cambridge, 1986; Mir, Moscow, 1989).

25. P. R. Antoniewicz, Phys. Rev. B **21** (9), 3811 (1980).

26. C. B. Weare and J. A. Yarmoff, Surf. Sci. **348**, 369 (1996).

27. D. G. Goryunov, A. G. Borisov, G. E. Makhmetov, D. Teillet-Billy, and J. P. Ganyacq, Surf. Sci. **401**, 206 (1996).

28. V. P. Zhdanov, *Elementary Physicochemical Processes on Surface* (Nauka, Novosibirsk, 1988).

29. H. Yamazaki, T. Kamisawa, T. Kokubun, T. Haga, S. Kamimizu, and K. Sakamoto, Surf. Sci. **477**, 174 (2001).

30. R. J. Phaneuf, Y. Hong, S. Horch, and P. A. Bennett, Phys. Rev. Lett. **78** (24), 4605 (1997).

Translated by G. Skrebtsov

Physics of the Solid State, Vol. 46, No. 5, 2004, pp. 983–988. Translated from Fizika Tverdogo Tela, Vol. 46, No. 5, 2004, pp. 953–958.

LOW-DIMENSIONAL SYSTEMS AND SURFACE PHYSICS

Electron-Microscopic Study of the Surface Layer of an Aluminum–Silicon Alloy after Laser Alloying with Tungsten Carbide

L. M. Sorokin*, L. P. Efimenko, A. E. Kalmykov*, and Yu. I. Smolin****

** Ioffe Physicotechnical Institute, Russian Academy of Sciences, Politekhnicheskaya ul. 26, St. Petersburg, 194021 Russia*

*** Grebenshchikov Institute of Silicate Chemistry, Russian Academy of Sciences, ul. Odoevskogo 24/2, St. Petersburg, 199155 Russia*

Received October 13, 2003

Abstract—Transmission electron microscopy is used to study the structure of the surface layer of an Al–7 wt % Si alloy subjected to laser alloying. The base volume is found to be occupied by an aluminum matrix having a braidlike structure. New phases have been revealed, and their composition, shape, and spatial distribution have been determined. © *2004 MAIK "Nauka/Interperiodica".*

1. INTRODUCTION

Heat treatment of materials with a laser beam is widely applied in science and engineering for alloying, coating deposition, melting for recrystallization to improve the initial properties, etc. (see, e.g., [1–8]). The specific feature of laser treatment is that a focused laser beam moving across the surface of a sample heats only a very small volume while the surrounding material remains unheated. This feature results in a significant temperature gradient, which enables one to retain a high quenching rate and, hence, high-temperature states on cooling to room temperature [2]. Studying these high-temperature states can be of interest.

We studied the A356A1 aluminum alloy subjected to laser alloying with tungsten carbide to increase its resistance to wear and corrosion. The equilibrium solubility of tungsten in aluminum is too low (smaller than 1%) to affect the protection properties of alloys significantly. Laser technology can provide high cooling rates and, thus, supersaturated solid solutions with an alloying element content that is higher than the equilibrium solubility by several orders of magnitude [1].

The A356A1 alloy contains (wt %) 7% Si, <0.2% Fe, <0.2% Cu, <0.35% Mg, <0.11% Zn, and the balance in Al. For alloying, we used a tungsten carbide WC powder with a mean particle size of about 10 μm. As a binder, we applied a 2% aqueous solution of organic resin. The thickness of the powder layer applied onto the alloy surface was ~0.1 mm. Melting was performed with a 2-kW continuous neodymium laser beam. The beam spot velocity was 0.2 m/s, and the track overlapping was ~20%. The laser treatment time for each point was ~0.01 s. The treatment was performed in a nitrogen atmosphere. The melt cooling rate in the surface layer was higher than 10^4 K/s.

The purpose of this work was to study the structure of the treated layer. Since rapid melt cooling results in strong grain refinement, we used transmission electron microscopy for examination (which provides a high resolution).

2. EXPERIMENTAL

Ultrathin (about 0.1-μm) layers for transmission electron microscopy were cut from the laser-treated surface layer. Cuts in the form of 0.1-mm flakes were placed onto a copper grid. For examination, we used an ÉM-125K electron microscope.

To identify phases that form during local solidification after *in situ* chemical reactions upon laser melting of the surface layer, we used bright-field and dark-field images taken from the same sites of a sample in the transmission diffraction-contrast mode. The diameter of the selector aperture was 30 μm. Before taking dark-field images, we obtained point electron diffraction patterns from regions that had an almost single-crystalline structure. These electron diffraction patterns were sections of the planes of the reciprocal lattice of the matrix phase. We used them to interpret the images. To find such regions, we move samples under a microscope. We aimed to obtain a point electron diffraction pattern on the microscope screen that was as close to the regular reflection network of the matrix as possible. In this case, reflections that are additional to the regular matrix network should belong to other phases. Of course, we took into account the possibility of matrix reflections from grains of other orientations that do not form the basic network of reflections. It was easy to distinguish them from the reflections of a phase other than the matrix; in rare instances, these reflections form a regular network. The interplanar spacings corresponding to these reflections were determined using the device con-

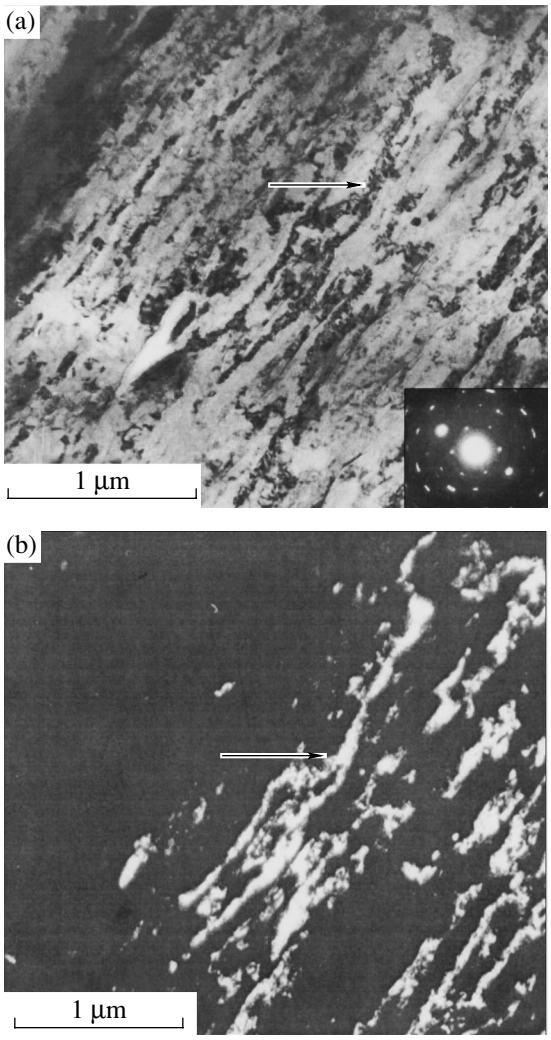

Fig. 1. (a) Bright-field image of the matrix; the arrow indicates one of the "braids." (b) Dark-field image of the same region in the matrix and the same braid as those in (a).

stant λL calculated from the positions of the (111) and (200) reflections of the matrix (solid solution of silicon in aluminum), which could be considered to be reflections of pure aluminum with sufficient accuracy.

The phase composition of the laser-treated surface layer was determined using x-ray diffraction patterns recorded on a Siemens D-500 diffractometer (CuK_α radiation).

The initial structure was analyzed with a CAMEBAX microprobe analyzer.

3. RESULTS AND DISCUSSION

The alloys were found to be a multiphase system where the aluminum-based matrix contained inclusions of various shapes, sizes, and compositions.

3.1. Matrix Structure

The bright-field image (Fig. 1a) shows dark areas in the form of elongated "braids." Electron microdiffraction patterns indicate that these areas contain aluminum only. The electron diffraction pattern taken from them is similar to a point electron diffraction pattern and is the (310) section of the reciprocal lattice (Fig. 1a, right bottom corner). The braids have a fine structure, which resembles a moiré fringe pattern with varying interband distances (from place to place). We studied dark-field images taken using the (200), (113), and (133) matrix reflections (Fig. 1a, right bottom corner). These images are characterized by a braidlike structure, with the braid parameters (length, curvature) being coincident with those visible in the bright-field image (compare Figs. 1a, 1b). This coincidence allows us to conclude that these areas are aluminum areas in the reflecting position. We failed to detect isolated dislocations or pileups, although they could be present upon rapid oriented solidification of the melt after laser melting of the surface. Solidification is oriented, since the melted layer lies on a cold substrate, namely, the initial Al–Si alloy. However, microblocks forming during solidification are slightly disoriented with respect to each other. The superposition of electron diffraction patterns taken from such differently oriented blocks can produce moiré fringes.

It should be noted that the electron diffraction pattern shows no signs of a severely deformed structure. Although the reflections consist of closely spaced points, they are not distorted and elongated; that is, they show no traces of asterism. Dark-field images taken in the matrix reflections demonstrate that the braidlike matrix areas are divided into separate fragments <0.1 μm in size. The absence of Debye rings of the matrix in the electron diffraction patterns indicates that the crystallographic orientations of the matrix fragments are close to each other. Without additional experiments, it is difficult to say whether the method of sample preparation (cuts prepared with a diamond knife) significantly affects the microstructure or not. This issue can be related to the nature of the braidlike matrix, since the deformation produced by the diamond knife results in disorientation of the matrix fragments, which can give rise to moiré fringes. Moreover, this matrix structure can be caused by the orientated solidification of the melt.

3.2. Inclusion Structure

The layer under study exhibits dark inhomogeneities (particles) in the bright-field image of the braidlike matrix (Fig. 2a). The inhomogeneities vary in size only slightly (from 0.3 to 1 μm) and are uniformly distributed. Some of them almost join with one another, leaving only a very small gap. In other cases, they stick together to form aggregates; the number of particles forming them can always be recognized. Since the sam-

ples are parallel-sided objects because of the method of their preparation, the dark contrast of the inhomogeneities can only be explained by the fact that they contain an element that has a greater atomic number and, thus, strongly absorbs electrons. In other words, these areas are enriched in tungsten. A thorough investigation of the contrast of the particles shows that there are smaller (10- to 30-nm) particles against the background of larger ones; the initial particles are made of individual narrow lamellae 50–100 nm in size. The direction of the lamellae coincides with that of the matrix braids. Apparently, rapid cooling during laser treatment causes twinning in carbide particles. Moreover, there are particles that have no lamellar structure. The smallest (10- to 20-nm) particles are more clearly visible against the background of these particles. Some of the smallest particles exhibit a contrast that is similar to that of small dislocation loops [9].

The particles that are about 1 μm in size are assumed to be tungsten carbide. As is seen from Fig. 2a, the tungsten-carbide particles have an oval shape with rounded edges that is close to an equiaxed shape. It should be noted that the size of the largest dark particles is smaller than the size (about 10 μm) of the initial tungsten-carbide particles used to prepare the paste applied onto the Al–Si alloy.

The data obtained can be interpreted as follows. The decrease in the sizes of the initial WC particles can be related to their cracking due to high thermal stresses that appear during high-energy laser treatment. Because of the interaction of the carbide particles with the surrounding Al–Si melt, their surface becomes smoother and their shape becomes rounded. The carbide particles can both dissolve in the melt and react with it to form chemical compounds.

To support our considerations, we took dark-field images using reflections that do not belong to aluminum. Although we could find regions giving almost point electron diffraction patterns, it was difficult to identify them because of the presence of polycrystalline regions. Nevertheless, we found that electron diffraction patterns taken from two-phase regions in a bright-field image contained reflections from planes having interplanar spacings substantially greater than the maximum values characteristic of aluminum, silicon, and tungsten carbide.

Figure 2b shows a dark-field image of the multiphase region (the same as that shown in Fig. 2a) taken in the reflections closest to the primary electron beam. The circle in the lower right-hand corner of Fig. 2a (in the electron diffraction pattern taken from the region shown in Fig. 2a) demonstrates the position of the selector aperture. In the dark-field image in Fig. 2b, only the regions that produce reflections entering into the aperture become bright. These reflections are both point reflections of various intensity and, probably, portions of Debye rings. Table 1 gives the interplanar spacings for them in comparison with the ASTM data for

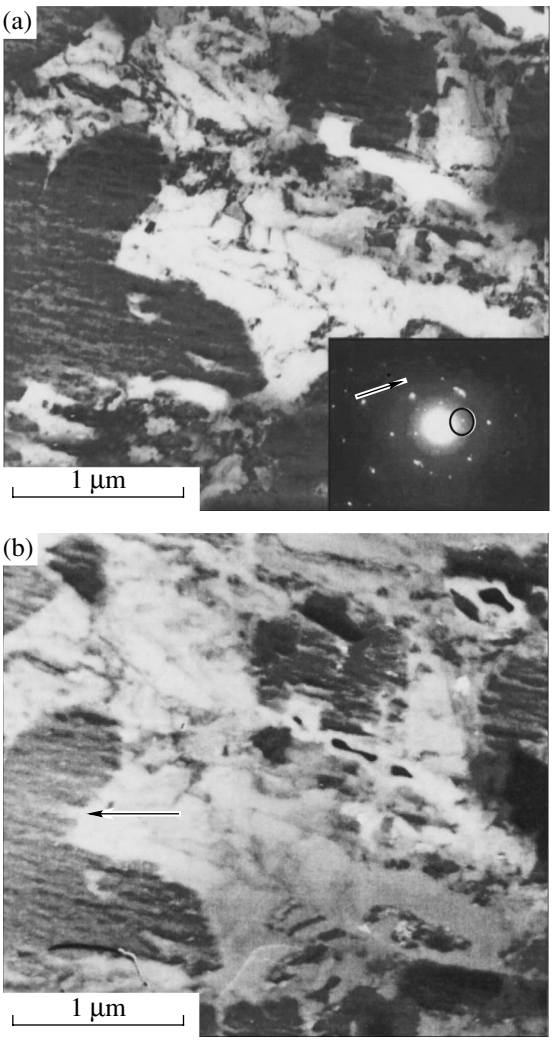

Fig. 2. (a) Bright-field image of the matrix with inclusions; the arrow indicates a carbide particle. (b) Dark-field image of the same region as that in (a).

binary and ternary compounds that can be made up of elements of the alloy. The reflections entering into the aperture are underlined. The dark-field image is seen to be taken in the reflections of the ternary compounds made up of elements of the alloy. In the dark-field image (Fig. 2b), 20- to 30-nm particles of these compounds are visible against the background of large particles (which are considered to be the initial tungsten-carbide particles) or at the periphery of the carbide particles. The dark-field image also demonstrates individual large particles, which are likely to consist of $W(SiAl)_2$. As compared to the smaller particles, these particles should give strong reflections in electron diffraction patterns. In the electron diffraction pattern, the strong reflection with d = 3.49 Å belongs to the $W(SiAl)_2$ phase (Table 1).

In Fig. 3, the dark-field image is taken using closely spaced reflections of both the matrix and a new phase (both reflections pass through the aperture). It is seen

Table 1. Experimental interplanar spacings (Å) calculated from electron diffraction patterns and the tabulated data

d_{exp}	ASTM data							
	$W(SiAl)_2$	Al_4C_3	β-Al_4SiC_4	α-Al_4SiC_4	$Al_4Si_2C_5$	Al	W_2C	WC
5.025			5.01					
3.57				3.614				
3.49	3.47							
2.87		2.872		2.836				2.84
2.26	2.23	2.248		2.231	2.227		2.276	
2.06	2.04	2.082			2.08	2.024		
1.76		1.787					1.749	
1.36	1.35	1.340						

that the matrix regions in the reflecting position have a braidlike structure. Moreover, a bright contrast is characteristic of small particles inside the initial carbide formations and at their periphery; these particles give reflections with an interplanar spacing $d = 2.22$ Å, measured using an experimental point electron diffraction pattern. The sizes of these particles and the character of their distribution within the carbide aggregates are identical to those in the dark-field image (Fig. 2b) taken only in a new-phase reflection. This finding suggests that the nature of the small particles in Fig. 3 is the same; namely, they consist of $W(SiAl)_2$. Indeed, according to the tabulated data (Table 1), this compound gives reflections with interplanar spacings d = 2.23 and 2.20 Å, which are close to the experimental value (2.26 Å). Similar reflections could be produced by the phases $Al_4Si_2C_5$ (2.227 Å) and W (2.23 Å). However, as noted above, the sizes of these particles and the character of their distribution are similar to those in Fig. 2b; therefore, we can conclude that the dark-field image in Fig. 3 also reveals $W(SiAl)_2$ particles.

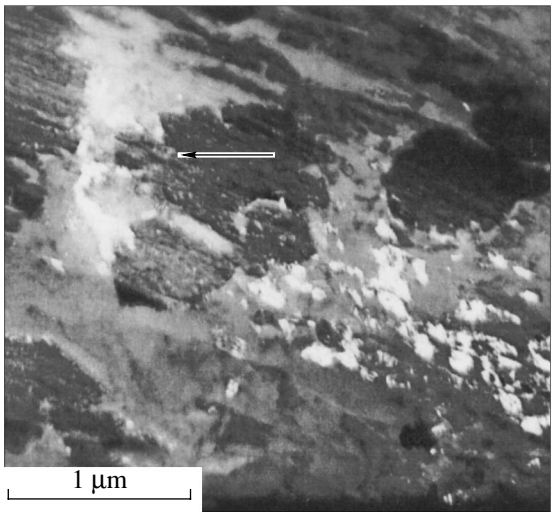

Fig. 3. Dark-field image of a multiphase region. The arrow indicates a $W(SiAl)_2$ particle.

It should be noted that all interplanar spacings (d = 4.07, 3.47, 2.23, 2.04 Å) calculated from electron diffraction patterns and related to the ternary compound $W(SiAl)_2$ are also present in the x-ray diffraction pattern. The electron diffraction patterns also contain traces of the phases Al_4C_3, W_2C, WC, and other compounds that were noted earlier as interaction products in the Al–Si–WC system.

Dahotre *et al.* [4] believe that Al_4C_3 particles form during laser treatment of the SiC/A356A1 composite, which is based on the same aluminum alloy that is studied in this work. In [4], platelike particles, which were considered to be Al_4C_3 particles, were observed. In this work, we failed to detect particles with this shape. This discrepancy can be explained as follows: the presence of the aluminum carbide in [4] was established using the only weak reflection in the x-ray diffraction pattern, which was identified as the (100) reflection from Al_4C_3 particles. However, according to the ASTM data, this reflection cannot arise from aluminum carbide. Moreover, the reflections at angles that are close to the angle indicated in the x-ray diffraction pattern are not the strongest for Al_4C_3. At the same time, platelike particles occupy a significant area in the electron micrographs given in [4] and, hence, should produce strong reflections. Thus, the data from [4] do not suggest that the platelike particles have the composition of aluminum carbide. In their next article [5], the authors affirmed that the platelike particles consisted of a mixture of the Al_4C_3 and $Al_4Si_2C_5$ compounds. To support this statement, they presented data obtained with an analytical electron microscope (more specifically, two electron diffraction patterns without key patterns, which were thought to correspond to the two compounds) and energy-dispersive spectroscopy (EDS) data. However, the EDS spectra had no carbon lines; this fact was considered to be caused by absorption of the corresponding radiation by the sample. The detector used in that work could detect light elements. The optical micrographs given in that work demonstrate that a significant portion

Table 2. Interplanar spacings (Å) of the X phase and the WO_2 oxide

X phase, TEM data	WO_2, ASTM data
4.85	4.795
3.46	3.452
2.83	2.831
1.99	2.154
	1.853
1.64	1.5987

of the sample surface is occupied by platelike particles, which should give a sufficiently strong carbon line.

In a multiphase region of the alloy, we found an X phase and determined its five interplanar spacings (Table 2); however, we failed to identify it. Electron diffraction patterns and the x-ray diffraction pattern contain reflections with interplanar spacings d = 4.85 and 4.75 Å, respectively, which cannot be assigned to the phases considered in this work. The WO_2 compound has a similar interplanar spacing (d = 4.795 Å). Moreover, we recorded electron diffraction patterns that were sections of the planes of the reciprocal lattice of single-crystalline particles other than the phases analyzed. The reflections make up a regular reflection network based on the reflections with d = 4.85 and 2.84 Å. Although the reflection with d = 2.84 Å can belong to WC, whose existence is not surprising, WC does not have the reflection with d = 4.85 Å. An example of such an electron diffraction pattern is shown in Fig. 4.

It should be noted that, when comparing the tabulated interplanar spacings with the experimental spacings calculated from electron diffraction patterns to identify possible phases, we took into account the relative intensities of reflections.

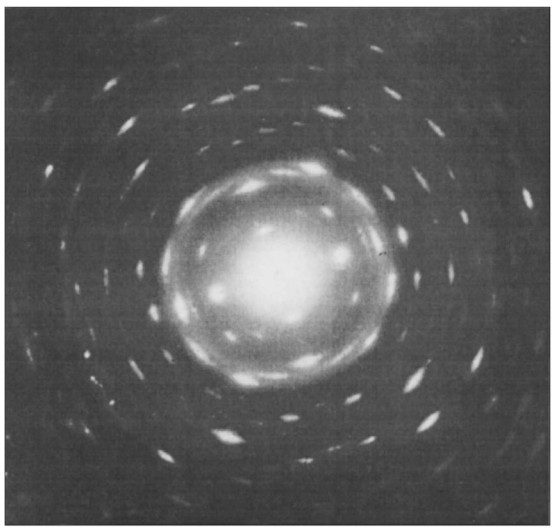

Fig. 4. Electron diffraction pattern of the X phase.

According to electron microprobe analysis, the initial alloy consists of 100- to 300-μm grains of an aluminum-based solid solution and layers of a fine-grained Al–Si eutectic with a particle size of 2–5 μm. X-ray diffraction patterns of the initial alloy taken before laser treatment exhibit strong sharp peaks of crystalline aluminum and silicon.

After he laser treatment, the size of all grains in the melting zone becomes smaller than 5 μm because of the high cooling rates. In x-ray diffraction patterns, the diffraction peaks of silicon are replaced with diffuse weak maxima, which can be related to both imperfections of the crystal structure and a small size of the silicon particles precipitating from the melt upon rapid cooling. Electron diffraction patterns taken with the help of a 1-μm selector aperture show pronounced rings made up of reflections from small silicon crystallites. This fact suggests that the starting silicon particles have a perfect crystal structure and that they decrease in size (which explains the character of the x-ray diffraction pattern).

The data on the phase composition of the alloying zone agrees with the results of the thermodynamic analysis of possible interaction reactions. The analysis shows that, in the Al–Si–WC system, the tungsten carbide WC is unstable and should be absent in the equilibrium state (just as W_2C). The presence of carbide particles in the laser-alloying zone is due to the fact that they do not melt during laser treatment; that is, the surface temperature does not exceed 2785°C. During the laser treatment (~0.01 s), the reaction between carbides and the Al–Si melt can occur only at the particle surface.

4. CONCLUSIONS

(1) The near-surface layer of the Al–Si alloy after laser-induced alloying with tungsten carbide has been found to be a multiphase system. The base volume is occupied by an aluminum matrix having a braidlike structure.

(2) The initial carbide WC has been found to partly decompose to form W_2C under the action of a laser beam.

(3) Carbide particles about one micrometer in size are uniformly distributed over the aluminum matrix and have a rounded shape. During laser treatment, the reaction between carbide particles and the Al–Si melt occurs only at the surface of the particles and results in the ternary compounds $W(SiAl)_2$, Al_4SiC_4, and $Al_4Si_2C_5$.

ACKNOWLEDGMENTS

We thank Professor N.B. Dahotre, Center for Laser Applications, University of Tennessee Space Institute, USA, for providing the samples.

This work was supported in part by the RAN-2003 scientific program of the St. Petersburg Scientific Center and the Russian Foundation for Basic Research (project no. 03-07-90108).

REFERENCES

1. A. G. Grigor'yants and A. N. Safonov, *Methods of Surface Laser Treatment* (Vysshaya Shkola, Moscow, 1987).
2. N. B. Dahotre, M. H. McCay, T. D. McCay, and M. M. Kim, J. Mater. Sci. **27**, 6426 (1992).
3. S. Nayak, L. Riester, H. M. Meyer III, and N. B. Dahotre, J. Mater. Res. **18** (4), 833 (2003).
4. N. B. Dahotre, T. D. McCay, and M. H. McCay, J. Appl. Phys. **65** (12), 5072 (1989).
5. N. B. Dahotre, M. H. McCay, and T. D. McCay, J. Mater. Res. **6** (3), 514 (1991).
6. A. Baidullaeva, E. F. Venger, A. I. Vlasenko, A. V. Lomovtsev, and P. E. Mozol', Fiz. Tekh. Poluprovodn. (St. Petersburg) **36** (7), 801 (2002) [Semiconductors **36**, 747 (2002)].
7. V. Yu. Fominski, R. I. Romanov, I. Smurov, and A. L. Smirnov, J. Appl. Phys. **93**, 5989 (2003).
8. D. E. Persson, S. Jacobson, and S. Hogmark, J. Laser Appl. **15**, 115 (2003).
9. *Direct Methods of Studies of Crystal Defects*, Ed. by A. M. Elistratov (Mir, Moscow, 1965).

Translated by K. Shakhlevich